BRAIN-IMAGE BASED COMPUTATION FOR SUPPORTING CLINICAL DECISION IN NEUROLOGICAL AND PSYCHIATRIC DISORDERS

EDITED BY: Lin Shi, Feng Feng and Weidong Cai

PUBLISHED IN: Frontiers in Neuroscience, Frontiers in Psychiatry and Frontiers in Neurology

frontiers Research Topics

frontiers

ISSN 1664-8714
ISBN 978-2-88966-675-1
DOI 10.3389/978-2-88966-675-1

About Frontiers

Frontiers is more than just an open-access publisher of scholarly articles: it is a pioneering approach to the world of academia, radically improving the way scholarly research is managed. The grand vision of Frontiers is a world where all people have an equal opportunity to seek, share and generate knowledge. Frontiers provides immediate and permanent online open access to all its publications, but this alone is not enough to realize our grand goals.

Frontiers Journal Series

The Frontiers Journal Series is a multi-tier and interdisciplinary set of open-access, online journals, promising a paradigm shift from the current review, selection and dissemination processes in academic publishing. All Frontiers journals are driven by researchers for researchers; therefore, they constitute a service to the scholarly community. At the same time, the Frontiers Journal Series operates on a revolutionary invention, the tiered publishing system, initially addressing specific communities of scholars, and gradually climbing up to broader public understanding, thus serving the interests of the lay society, too.

Dedication to Quality

Each Frontiers article is a landmark of the highest quality, thanks to genuinely collaborative interactions between authors and review editors, who include some of the world's best academicians. Research must be certified by peers before entering a stream of knowledge that may eventually reach the public - and shape society; therefore, Frontiers only applies the most rigorous and unbiased reviews.
Frontiers revolutionizes research publishing by freely delivering the most outstanding research, evaluated with no bias from both the academic and social point of view. By applying the most advanced information technologies, Frontiers is catapulting scholarly publishing into a new generation.

What are Frontiers Research Topics?

Frontiers Research Topics are very popular trademarks of the Frontiers Journals Series: they are collections of at least ten articles, all centered on a particular subject. With their unique mix of varied contributions from Original Research to Review Articles, Frontiers Research Topics unify the most influential researchers, the latest key findings and historical advances in a hot research area! Find out more on how to host your own Frontiers Research Topic or contribute to one as an author by contacting the Frontiers Editorial Office: frontiersin.org/about/contact

BRAIN-IMAGE BASED COMPUTATION FOR SUPPORTING CLINICAL DECISION IN NEUROLOGICAL AND PSYCHIATRIC DISORDERS

Topic Editors:
Lin Shi, The Chinese University of Hong Kong, China
Feng Feng, Peking Union Medical College Hospital (CAMS), China
Weidong Cai, The University of Sydney, Australia

Citation: Shi, L., Feng, F., Cai, W., eds. (2021). Brain-image Based Computation for Supporting Clinical Decision in Neurological and Psychiatric Disorders. Lausanne: Frontiers Media SA. doi: 10.3389/978-2-88966-675-1

Table of Contents

frontiers in Neuroscience

EDITORIAL
published: 03 March 2021
doi: 10.3389/fnins.2020.599523

Editorial: Brain-image Based Computation for Supporting Clinical Decision in Neurological and Psychiatric Disorders

Lin Shi[1]*, *Weidong Cai*[2] and *Feng Feng*[3]

[1] Department of Imaging and Interventional Radiology, The Chinese University of Hong Kong, Shatin, China, [2] School of Computer Science, The University of Sydney, Darlington, WA, Australia, [3] Department of Radiology, Peking Union Medical College Hospital (CAMS), Beijing, China

Keywords: neurological disease, psychiatric disease, magnetic resonance imaging, functional connectivity, structural connectivity, machine learning, radiomics

Editorial on the Research Topic

Brain-image Based Computation for Supporting Clinical Decision in Neurological and Psychiatric Disorders

Fast-paced developments in imaging and computational technologies in recent years have fostered breakthroughs in the conception and practice of neurology, neurosurgery, and psychiatry. This Research Topic presents a collection of recent researches on computational solutions for multimodal neuroimaging in brain disorders.

Structural imaging and its quantitative computational metrics are critical in assisting neurological disease diagnosis and assessment. A contribution by Zhang et al. explored the location of infarct core identified in diffusion weighted imaging (DWI) to distinguish intracranial atherosclerotic stenosis (ICAS) from embolic occlusion with good accuracy, which could help determine the most appropriate treatment strategy in the acute stage. Guo et al. studied the scanner-related reproducibility of white matter hyperintensity (WMH) in T2-FLAIR, which is crucial in the assessment of various white matter diseases, especially demyelinating, and small vessel diseases. The results showed that the best reproducibility occurred when 3D FLAIR images were acquired in the same MRI scanner, while WMH quantification variability reached the highest when WMH quantified in 2D FLAIR was compared with 3D FLAIR. The selection of quantification tools also made a big difference in reproducibility.

Computational imaging biomarkers can be applied to the study of mechanisms or predicting therapeutic strategies. Zhang et al. analyzed pre- and post- treatment resting-state functional MRI (rs-fMRI) images for dysphagia patients, examining the effect of intermittent theta burst stimulation (iTBS) after continuous TBS (cTBS) using static and dynamic functional connectivity and suggested that iTBS could reverse the aftereffects induced by cTBS on the contralateral suprahyoid muscle cortex. Rs-fMRI was also analyzed using regional homogeneity (ReHo), which detected significant differences among the data acquired at different times in patients with Nasopharyngeal Carcinoma (NPC) but not in healthy controls, suggesting the ReHo features may be indicative in predicting neurocognitive dysfunction in NPC (Yang et al.). Analysis of brain EEG features during the cognitive task could complement imaging studies to detect the temporal sensitive brain activity on-the-fly. Kim et al. present an EEG study to investigate the functional brain changes in subjects with Internet gaming disorder (IGD). They found that lower frontal theta activity might be a biomarker to detect diminished cognitive control in IGD.

Edited and reviewed by:
Vince D. Calhoun,
Georgia State University,
United States

***Correspondence:**
Lin Shi
shilin@cuhk.edu.hk

Specialty section:
This article was submitted to Brain Imaging Methods, a section of the journal Frontiers in Neuroscience

Received: *27 August 2020*
Accepted: *30 October 2020*
Published: *03 March 2021*

Citation:
Shi L, Cai W and Feng F (2021) Editorial: Brain-image Based Computation for Supporting Clinical Decision in Neurological and Psychiatric Disorders. Front. Neurosci. 14:599523. doi: 10.3389/fnins.2020.599523

The microarchitecture of the white matter provides sensitive and early evidence of brain changes. In the study by Liang et al., regional voxel-based group differences were found in inter-voxel diffusivity in T2 diabetes mellitus (DM) patients when compared with normal controls. These diffusion features were associated with T2DM risk factors. It is well-known that hippocampus volume asymmetry is an important visual clue for the detection of hippocampus sclerosis, which supports the proposition that white matter connectivity may also present as asymmetric. This is well-studied in a contribution by Zhao et al. using TBSS on diffusion tensor imaging (DTI) data. They found that the pattern of white matter asymmetry is distinct in TLE patients with left and right hippocampus sclerosis. In Jang et al., the authors investigated the diffusion metrics in MRI of the corticoreticulospinal tract (CRT), and analyzed the quantitative difference between mild traumatic brain injury (mTBI) patients with and without whiplash, and indicated that whiplash might be related to more severe axonal injuries in mTBI patients. The DTI data acquired in ADNI was employed in Liu et al. to develop a general framework that integrates deep learning, feature selection, causal inference, and genetic-imaging data analysis for predicting and understanding Alzheimer's Disease (AD).

Psychiatric diseases are usually reported with negative and inconsistent structural findings, but it is likely that statistical changes exist when microstructural or functional information is being studied. Fu et al. studied patients with schizophrenia and reported that IL-10, a regulatory cytokine assessed in venous blood, is associated with white matter integrity changes in DTI, using tract-based spatial statistics (TBSS) analysis. Another study in this Research Topic by Ding et al. explored the functional connectivity changes in schizophrenia. In this study global-brain FC was used on rs-fMRI data, indicating that schizophrenia patients and unaffected siblings shared enhanced GFC in the left superior frontal gyrus compared with normal controls. These findings separated those with schizophrenia and their siblings from normal controls. Lidaka et al. conducted a study of functional connectivity using rs-fMRI on a large sample ($n = 626$) of Autism Spectrum Disorder (ASD) and normal controls and found that patients with ASD exhibited thalamo-cortical hyperconnectivity and amygdala-cortical hypoconnectivity, which might be a potential neuroimaging biomarker of ASD. In another study of ASD, Zhou et al. propose a regularized learning framework to generate a high-order functional connectivity network (HoFCN) with high reliability and applied it to the identification of mild cognitive decline (MCI) and ASD from normal controls. This mathematics-based development was proven to be effective in making disease-related functional MRI changes in patients. Magnetic Resonance Spectroscopy (MRS) is a powerful tool and can be applied to the study of intracranial chemical composition with magnetic pulse sequences. Wang et al. introduced their work on using the MRS to quantify Gamma-Aminobutyric Acid (GABA) levels in women with depression and anxiety. In the postmenopausal stage, lower GABA levels were found in the depression group compared with the anxiety group, and both groups were lower than normal controls.

The development of computational methods, i.e., machine learning and radiomics, provides powerful tools to support systematic investigation for brain research. In Liu et al., the authors introduced their work on developing a machine learning prediction model based on radiomics features derived from MRI, to better characterize and distinguish neonatal acute bilirubin encephalopathy (ABE) from normal myelination in T1W MRI with high accuracy. The contribution by Zheng et al. also discusses how machine learning (namely support vector machine, SVM) was performed on the quantitative volumetry results of patients diagnosed with AD and vascular dementia (VaD). They generated a classification model with high accuracy, which indicated that there could be distinct brain atrophy patterns between these two major types of dementia.

The research efforts documented in these publications contribute to and further computational neuroradiology, and is particularly enlightening on potential future clinical applications.

AUTHOR CONTRIBUTIONS

All authors listed have made a substantial, direct and intellectual contribution to the work, and approved it for publication.

Conflict of Interest: The authors declare that the research was conducted in the absence of any commercial or financial relationships that could be construed as a potential conflict of interest.

frontiers in Neuroscience

ORIGINAL RESEARCH
published: 18 December 2018
doi: 10.3389/fnins.2018.00959

Improving Sparsity and Modularity of High-Order Functional Connectivity Networks for MCI and ASD Identification

Yueying Zhou[1], *Limei Zhang*[1], *Shenghua Teng*[2], *Lishan Qiao*[1,2*] *and Dinggang Shen*[3,4]

[1] School of Mathematics Science, Liaocheng University, Liaocheng, China, [2] College of Electronic and Information Engineering, Shandong University of Science and Technology, Qingdao, China, [3] Department of Radiology and BRIC, University of North Carolina at Chapel Hill, Chapel Hill, NC, United States, [4] Department of Brain and Cognitive Engineering, Korea University, Seoul, South Korea

High-order correlation has recently been proposed to model brain functional connectivity network (FCN) for identifying neurological disorders, such as mild cognitive impairment (MCI) and autism spectrum disorder (ASD). In practice, the high-order FCN (HoFCN) can be derived from multiple low-order FCNs that are estimated separately in a series of sliding windows, and thus it in fact provides a way of integrating dynamic information encoded in a sequence of low-order FCNs. However, the estimation of low-order FCN may be unreliable due to the fact that the use of limited volumes/samples in a sliding window can significantly reduce the statistical power, which in turn affects the reliability of the resulted HoFCN. To address this issue, we propose to enhance HoFCN based on a regularized learning framework. More specifically, we first calculate an initial HoFCN using a recently developed method based on maximum likelihood estimation. Then, we learn an optimal neighborhood network of the initially estimated HoFCN with sparsity and modularity priors as regularizers. Finally, based on the improved HoFCNs, we conduct experiments to identify MCI and ASD patients from their corresponding normal controls. Experimental results show that the proposed methods outperform the baseline methods, and the improved HoFCNs with modularity prior consistently achieve the best performance.

Keywords: high-order correlation, functional connectivity network, dynamic network, modularity, mild cognitive impairment, autism spectrum disorder

OPEN ACCESS

Edited by:
Lin Shi,
The Chinese University of Hong Kong, China

Reviewed by:
Suyash P. Awate,
Indian Institute of Technology Bombay, India
Pan Lin,
South-Central University for Nationalities, China

***Correspondence:**
Lishan Qiao
qiaolishan@lcu.edu.cn

Specialty section:
This article was submitted to Brain Imaging Methods, a section of the journal Frontiers in Neuroscience

Received: *15 September 2018*
Accepted: *03 December 2018*
Published: *18 December 2018*

Citation:
Zhou Y, Zhang L, Teng S, Qiao L and Shen D (2018) Improving Sparsity and Modularity of High-Order Functional Connectivity Networks for MCI and ASD Identification. Front. Neurosci. 12:959. doi: 10.3389/fnins.2018.00959

INTRODUCTION

Currently, resting state functional magnetic resonance imaging (rs-fMRI), which treats blood oxygen level dependent (BOLD) signals as indirect measures of neural activities, has been widely used in the fields of medicine and neuroscience (Liu et al., 2008; van den Heuvel and Hulshoff Pol, 2010; Liu F. et al., 2013). Based on rs-fMRI, the study of functional connectivity network (FCN) has become a prevalent way to understand brain working mechanism and provide promising biomarkers for diagnosing neural or mental disorders (Bullmore and Sporns, 2009; Fornito et al., 2015; Liu et al., 2017), such as autism spectrum disorder (ASD) (Weng et al., 2010; Wee et al., 2016), Alzheimer's disease (AD) (Wang et al., 2006; Sanz-Arigita et al., 2010), mild cognitive impairment

(MCI) (Rombouts et al., 2005; Qiao et al., 2016), major depressive disorder (Greicius et al., 2007; Cullen et al., 2014), schizophrenia (Jafri et al., 2008), and social anxiety disorder (Liu et al., 2015).

To date, researchers have developed many FCN estimation methods (Smith et al., 2011) from the simplest Pearson's correlation (PC) to the most complex dynamic causal modeling. In this paper, we mainly focus on the correlation-based methods due to their relative simplicity and reliability (Smith et al., 2013). Further, we suppose each node of the FCN corresponds to a brain region or a spatial region of interest (ROI) that has been well-defined according to a certain brain atlas, and each "edge" of the FCN corresponds to the relationship between BOLD signals that are extracted from the associated ROIs.

In the conventional correlation-based FCN models, PC is the most popular one for calculating the relationship between ROIs (Smith et al., 2013), but it only captures full correlation without removing the confounding effect from other ROIs. To ease this issue, partial correlations have been employed in calculating the relationship between ROIs for FCN construction (Marrelec et al., 2006). However, the estimation of partial correlation involves the calculation of an inverse covariance matrix, usually resulting in an ill-posed problem. Therefore, many studies adopted a regularizer in the model for more reliable partial correlation estimation (Friedman et al., 2008; Huang et al., 2009; Varoquaux et al., 2010). In fact, the regularizer also plays a role in encoding priors for FCN construction. For example, l_1-norm regularizer is commonly used for encoding sparsity prior of FCN (Lee et al., 2011), and also trace norm regularizer is used for low-rank prior (Liu G. et al., 2013; Qiao et al., 2016). In summary, most of the correlation-based FCN models can be formulated by a matrix-regularized learning framework, where different data fitting terms and regularized terms are combined for estimating FCNs. Please see **Table 1** in section Related Methods for more details.

Compared with the aforementioned FCN estimation methods based on low-order correlations, a novel concept of high-order correlation or high-order FCN (HoFCN) has been recently proposed (Chen et al., 2016; Zhang et al., 2016) for measuring more complex interaction information in the brain. Different from the low-order FCN that models the dependency between ROIs, HoFCN aims to capture relationships among different edges. To put it simply, we can consider the ecological chain (network) as an analogy, where the species are regarded as nodes and the ecological chains are the edges between the nodes. In such a way, ecological chains represent the low-order connection information of this network. However, there may exist some relationships among different ecological chains, and the flourishment or destruction of an ecological chain may affect another ecological chain. Therefore, we expect the relationships between edges can provide higher-order information in modeling FCN, compared with the low-order methods that only measure the relationship between nodes.

To date, several studies have suggested that HoFCNs can provide some useful and complementary information for disorder identification (Macke et al., 2011; Plis et al., 2014; Chen et al., 2016; Zhang et al., 2017). For instance, Plis et al. investigated the nonlinear interactions among brain regions in schizophrenia based on mutual information (Plis et al., 2014). Chen et al. proposed to estimate HoFCNs via correlation's correlation, and use a clustering strategy to reduce the dimensionality for efficient computation (Chen et al., 2016, 2017). Guo et al. constructed HoFCN based on minimum spanning tree and applied it for AD classification (Guo et al., 2017). Zhang et al. proposed the hybrid HoFCN for MCI identification based on the linear combination of low- and high-order FCNs (Zhang et al., 2017). Zhao et al. developed the multi-level HoFCN mainly based on PC and applied it for ASD diagnosis (Zhao et al., 2018).

Different from the heuristic methods for defining HoFCNs, Zhou et al. recently proposed to estimate HoFCN based on a rigorous probabilistic framework (Zhou et al., 2018), where a set of low-order correlation matrices (or low-order FCNs) are first calculated separately in sliding windows, and then these correlation matrices are considered as samples for achieving HoFCN by maximum likelihood estimation (MLE). Such a framework *not only* gives a clear theoretical explanation of HoFCN, *but also* provides a way of integrating dynamic information encoded in a sequence of low-order FCNs. However, the initially estimated low-order FCNs may be unreliable, since the use of limited volumes/samples in each sliding window will significantly reduce the statistical power. As such, the derived HoFCN may contain noisy connections inheriting from the low-order counterparts. To deal with this problem, we propose to improve the HoFCNs based on a regularized learning framework. To be specific, we adopt a two-step learning strategy. First, an initial HoFCN is estimated using the MLE method as proposed in Zhou et al. (2018). Then, an optimal neighborhood network of the initially estimated HoFCN is learnt to meet the sparsity and modularity regularizers, aiming, respectively to remove possible noisy connections and encode more informative structure (i.e., modularity) of the network. To verify the effectiveness of our proposed method, we apply the improved HoFCNs to identify subjects with MCI and ASD from normal controls (NCs), respectively. The experimental results show that our proposed methods outperform the baseline methods, and the improved

TABLE 1 | Correlation-based FCN estimation methods under a matrix-regularized learning framework, where $\|\cdot\|_F$, $\|\cdot\|_1$, $\|\cdot\|_*$, and $\|\cdot\|_{q,1}$ denote F-norm, l_1-norm, trace norm and $l_{q,1}$-norm of a matrix, respectively.

Method	Data fitting term	Regularized term
PC (Biswal et al., 1995)	$\left\|W - X^T X\right\|_F^2$	N/A
$PC_{sparsity}$ (Li et al., 2017)	$\left\|W - X^T X\right\|_F^2$	$\|W\|_1$
$PC_{scale-free}$ (Li et al., 2017)	$\left\|W - X^T X\right\|_F^2$	$\sum_{i,j=1}^{n} \gamma_{ij} \|W_{ij}\|$
SR (Lee et al., 2011)	$\|X - XW\|_F^2$	$\|W\|_1$
LR (Qiao et al., 2016)	$\|X - XW\|_F^2$	$\|W\|_*$
SLR (Qiao et al., 2016)	$\|X - XW\|_F^2$	$\lambda_1 \|W\|_1 + \lambda_2 \|W\|_*$
SGR (Wee et al., 2014)	$\|X - XW\|_F^2$	$\lambda_1 \|W\|_1 + \lambda_2 \|W\|_{q,1}$
WSR (Yu et al., 2017)	$\|X - XW\|_F^2$	$\|C \odot W\|_1$
WSGR (Yu et al., 2017)	$\|X - XW\|_F^2$	$\lambda_1 \|C \odot W\|_1 + \lambda_2 \|W\|_{q,1}$

HoFCN with modularity prior consistently achieves the best performance.

The rest of this paper is organized as follows. In section Related Methods, we introduce the correlation-based low-order and high-order FCN modeling methods. In section The Proposed Method, we propose our HoFCN learning strategy, including the motivation, model and algorithm. In section Experiments and Results, we evaluate our proposed method with applications to MCI and ASD identification. In section Discussions, we discuss our findings and several aspects that affect the final performance. Then, we conclude the paper in section Conclusion.

RELATED METHODS

In this section, we first summarize the existing correlation-based FCN methods into a matrix-regularized learning framework in **Table 1**. Then, we specifically describe several representative FCN estimation methods, including PC (Biswal et al., 1995), sparse representation (SR) (Lee et al., 2011) and the MLE-based HoFCN estimation (Zhou et al., 2018).

Pearson's Correlation

As the most popular and simplest method to estimate FCN, PC with its mathematical expression is defined as follows:

$$W_{ij} = \frac{(x_i - \bar{x}_i)^T (x_j - \bar{x}_j)}{\sqrt{(x_i - \bar{x}_i)^T (x_i - \bar{x}_i)}\sqrt{(x_j - \bar{x}_j)^T (x_j - \bar{x}_j)}} \quad (1)$$

where $x_i \in R^V,\ i = 1, 2, \cdots, P$, is the extracted time series from the ith ROI, V is the number of temporal image volumes, P is the total number of ROIs, $\bar{x}_i \in R^V$ is the mean of x_i, and $W_{i,j}$ is the correlation weight between the ith and jth ROIs. Without loss of generality, we suppose x_i is centralized by $x_i - \bar{x}_i$ and normalized by $\sqrt{(x_i - \bar{x}_i)^T (x_i - \bar{x}_i)}$, and thus we can express PC as $W_{ij} = {x_i}^T x_j$, or, its equivalent matrix form

$$W = X^T X, \quad (2)$$

where $X = [x_1, x_2, \cdots, x_P] \in R^{V \times P}$ is the rs-fMRI data matrix.

In practice, we can treat Equation (2) as the solution of the following optimization problem

$$min_W \left\| W - X^T X \right\|_F^2, \quad (3)$$

where $\|\cdot\|_F$ represents F-norm of a matrix. In this way, we can put PC into the matrix-regularized learning framework reported in **Table 1** for a unified understanding.

Sparse Representation

SR is one of commonly-used methods for calculating (regularized) partial correlation. The mathematical model of SR is given as follows:

$$min_W \sum_{i=1}^{n} \left\| x_i - \sum_{j \neq i} W_{ij} x_j \right\|^2 + \lambda \sum_{j \neq i} \left| W_{ij} \right|. \quad (4)$$

Similar to PC, it can be rewritten as the following matrix form,

$$min_W \|X - XW\|_F^2 + \lambda \|W\|_1,\ s.t.\ W_{ii} = 0,\ \forall i = 1, \cdots, P, \quad (5)$$

where $\|\cdot\|_F$ and $\|\cdot\|_1$ denote F-norm and l_1-norm of the matrix, respectively. The constraint $W_{ii} = 0$ plays a role in removing x_i from X to avoid trivial solution.

Based on the idea of sparsity, many extended SR methods have been developed for constructing FCNs, including sparse group representation (Wee et al., 2014), weighted sparse representation (Yu et al., 2017), weighted sparse group representation (Yu et al., 2017), sparse low-rank representation (Qiao et al., 2016) and sparse PC (Li et al., 2017), to name a few. Most of these methods can be unified in the matrix-regularized leaning framework as shown in **Table 1**.

MLE-Based HoFCN Estimation

As discussed in section Introduction, many HoFCN estimation methods have been proposed in recent years. Here, we only review the MLE-based method (Zhou et al., 2018) due to its clear probabilistic explanation, and shortly we will use this method (named $\text{HoFCN}_{\text{MLE}}$) as a baseline for developing our approach.

The $\text{HoFCN}_{\text{MLE}}$ method includes two main steps. First, a set of low-order FCNs are estimated in a series of sliding windows. Then, the resulted low-order FCNs are used as samples for estimating HoFCN by MLE with an assumption that the low-order FCN samples follow a matrix-variant normal distribution (Zhang and Schneider, 2010). As a result, the HoFCN, Ω, can be achieved by the following iteration formula (generally, with the identity matrix I as an initial estimation of Ω).

$$\Omega = \frac{1}{KP} \sum_{k=1}^{K} (W_k - M)\Omega^{-1}(W_k - M)^T \quad (6)$$

where W_k is the kth low-order FCN associated with the kth sliding window, and $M = \frac{1}{K}\sum_{k=1}^{K} W_k$ is the mean of all the low-order FCNs. Please refer to Zhou et al. (2018) for details of the theoretical formulation and probabilistic explanation.

THE PROPOSED METHOD

Motivation

As discussed earlier, despite its empirical effectiveness in identifying neuropsychiatric disorders, the typically estimated HoFCN may contain some noisy connections that inherit from the low-order FCNs. In general, the weak connections in HoFCN are removed according to a given threshold, prior to the statistical analysis or classification. However, the thresholding scheme is heuristic and only consider the sparsity aspect of FCN. Therefore, in this section we develop a more flexible approach for improving HoFCN based on the matrix-regularized learning framework, *not only* aiming to reduce noisy connections of HoFCN, *but also* introduce more informative structures (i.e., modularity) than just sparsity into HoFCN. In particular, we will consider both sparsity and modularity as the priors of HoFCN, due to their well-accepted neuroscientific basis (Sporns, 2011; Sporns and Betzel, 2016). To our best knowledge, this is the first work to employ the modularity prior in HoFCN estimation.

Model: Learning Neighborhood Networks With Regularizers

For reaching the above goals, we adopt a simple two-step learning strategy. First, we obtain an initial estimation of HoFCN (denoted by Ω_0) based on the MLE method as described in section MLE-based HoFCN Estimation. Second, we learn an optimal neighborhood network of the initially estimated HoFCN Ω_0 with sparsity and modularity priors, respectively, as regularizers of the objective function.

More specifically, sparsity can usually be encoded by l_1-norm regularizer (Lee et al., 2011), and thus the optimal neighborhood network of HoFCN with *sparsity* prior (named **S-HoFCN**) can be achieved as follows:

$$\min_{\Omega} \|\Omega - \Omega_0\|_F^2 + \mu \| \Omega\|_1, \tag{7}$$

where Ω_0 is the initially estimated HoFCN by MLE method, Ω is the improved HoFCN that needs to be sparse and simultaneously keep as the spatial neighbor of Ω_0, and μ is the regularized parameter for controlling the balance between the sparsity of Ω and its distance from Ω_0.

Furthermore, modularity means that some group structures exist in the network, where the nodes within a group are densely connected, while the nodes between groups are sparsely connected (Sporns and Betzel, 2016). Notably, it has been proved that the modularity of a network can be described by a combination of trace (nuclear) norm and l_1-norm under mild conditions (Liu G. et al., 2013; Qiao et al., 2016). Therefore, we optimize the neighborhood network of HoFCN with *modularity* prior (named **M-HoFCN**), as follows,

$$\min_{\Omega} \| \Omega - \Omega_0\|_F^2 + \mu_1 \| \Omega\|_1 + \mu_2 \|\Omega\|_*, \tag{8}$$

where μ_1 and μ_2 are regularized parameters used to control the balance between the three terms in the optimization problem. Specially, when $\mu_2 = 0$, Equation (8) reduces to S-HoFCN as given in Equation (7), meaning that the sparsity is a necessary but not sufficient condition for modularity. Note that the proposed models in both Equations (7, 8) are also fit for matrix-regularized learning framework described in **Table 1**.

Algorithm

Here, we only give the optimization algorithm for solving M-HoFCN, since S-HoFCN is a special case of M-HoFCN. Note that the objective function in Equation (8) is convex, but the l_1-norm and trace norm are both indifferentiable. To address this kind of optimization problem, a number of algorithms have been developed in the machine learning community (Tomioka and Sugiyama, 2009; Richard et al., 2012; Zhuang et al., 2012; Oymak et al., 2014). We choose the proximal method (Combettes and Pesquet, 2009; Bertsekas, 2012) to solve Equation (8), due to its simplicity and efficiency.

In particular, we first consider the data fitting term $f(\Omega) = \| \Omega - \Omega_0\|_F^2$ in Equation (8). Since it is differentiable, we can calculate its gradient with respect to Ω, and get $\nabla f(\Omega) = 2(\Omega - \Omega_0)$. As a result, we have the gradient descent step as follows,

$$\Omega_k = \Omega_{k-1} - \alpha_k \cdot \nabla f\left(\Omega_{k-1}\right), \tag{9}$$

where α_k is the step size.

Then, according to the definition of proximal operator (Combettes and Pesquet, 2009), the proximal operator of l_1-norm (i.e., $\mu_1 \| \Omega\|_1$) is given as follows,

$$\text{prox}_{\mu_1\|\cdot\|_1}(\Omega) = \left[sgn\left(\Omega_{ij}\right) \times \max\left(abs\left(\Omega_{ij}\right) - \mu_1\right), 0\right]_{p\times p}, \tag{10}$$

where $sgn(\cdot)$ and $abs(\cdot)$ are sign and absolute functions, respectively. Equation (10) in fact imposes a soft-threshold operation on the entries of Ω. Similarly, the proximal operator of trace norm $\mu_2 \|\Omega\|_*$ is equivalent to a shrinkage operation on the singular value of Ω (Ji and Ye, 2009), as follows.

$$\begin{aligned}\text{prox}_{\mu_2\|\cdot\|_*}(\Omega) \;=\; &Udiag\left(\max\left\{\sigma_1 - \mu_2, 0\right\},\right.\\ &\left.\cdots, \max\left\{\sigma_n - \mu_2, 0\right\}\right) V^T,\end{aligned} \tag{11}$$

where $Udiag(\sigma_1, \cdots, \sigma_n)V^T$ is the singular value decomposition of matrix Ω.

Finally, to circumvent the case that the current Ω_k moves out of the "feasible region" regularized by l_1-norm $\| \Omega\|_1$ and trace norm $\|\Omega\|_*$, we use the proximal operations $\text{prox}_{\mu_1\|\cdot\|_1}$ and $\text{prox}_{\mu_2\|\cdot\|_*}$ on Ω_k, respectively, as given in Equations (10, 11). Hence, we get a simple algorithm to solve Equation (8) as shown in **Table 2**.

EXPERIMENTS AND RESULTS

In this section, we first evaluate the proposed method by identifying subjects with MCI from NCs based on ADNI dataset (http://adni.loni.ucla.edu), and then conduct an ASD identification task based on ABIDE database (http://fcon_1000.projects.nitrc.org/indi/abide/) for further illustrating the generalization of the proposed method.

Data Acquisition and Preprocessing

For MCI identification, 137 subjects (including 68 MCIs and 69 NCs) were selected in our study. The subjects were age-matched and scanned by 3.0T Philips scanners. SPM8 (http://www.fil.ion.ucl.ac.uk/spm/) toolbox was used to process the acquired rs-fMRI data. For each subject, the scanning time was 7 min, corresponding to 140 volumes. Subjects with more than 2.5 min of large framewise displacement (FD > 0.5) were excluded before data inclusion. To keep signal stabilization, the first 3 volumes of each subject were also removed, and the remaining volumes were corrected for subsequent analysis.

TABLE 2 | Algorithm for solving M-HoFCN in Equation (8).

Initialize Ω with Ω_0

Iterate:

1. $\Omega \leftarrow \Omega - \alpha \cdot 2(\Omega - \Omega_0)$
2. $\Omega \leftarrow \text{prox}_{\mu_1\|\cdot\|_1}(\Omega) = [sgn\left(\Omega_{ij}\right) \times \max\left(abs\left(\Omega_{ij}\right) - \mu_1\right), 0]_{p\times p}$
3. $\Omega \leftarrow \text{prox}_{\mu_2\|\cdot\|_*}(\Omega) = Udiag(\max\left\{\sigma_1 - \mu_2, 0\right\}, \cdots, \max\left\{\sigma_n - \mu_2, 0\right\})V^T$

During the scan, a rigid-body transformation was applied to correct head motion, and the subjects with head motion larger than 2 mm or 2° were excluded. The rs-fMRI images were registered to the Montreal Neurological Institute (MNI) space and spatially smoothed by a Gaussian kernel with full width at half maximum of $6 \times 6 \times 6$ mm^3. To further reduce the influences of nuisance signals, regression of ventricle and white matter signals as well as Friston 24-parameter model (Friston et al., 1996) were also performed. Using Automated Anatomical Labeling (AAL) template (Tzourio-Mazoyer et al., 2002), the preprocessed BOLD signals were divided into 116 ROIs, among which 90 ROIs are in the cerebra and the rest 26 are in the cerebella. For each ROI, prior to FCN estimation, its mean rs-fMRI time series was band-pass filtered from 0.015 to 0.15 Hz. At last, all the mean time series of the whole brain were put into a data matrix $X \in R^{137\times116}$.

For ASD identification, we use the same preprocessed dataset as in Wee et al. (2016). Specifically, 92 subjects including 45 ASD patients and 47 typically developing NCs (with ages between 7 and 15 years old) from this dataset are selected. All rs-fMRI images were acquired using a standard echo-planar imaging sequence on a clinical routine 3T Siemens Allegra scanner. During 6 min rs-fMRI scanning procedure, the subjects were required to relax with their eyes focusing on a white fixation cross in the middle of the black background screen projected on a screen. The imaging parameters include the flip angle as 90°, 33 slices, TR/TE as 2000/15 ms with 180 volumes, and 4.0 mm voxel thickness. The fMRI data were preprocessed by SPM8. Specifically, the first 10 rs-fMRI volumes of each subject were discarded. The remaining volumes were calibrated as follows: (1) normalization to MNI space with resolution $3 \times 3 \times 3$ mm^3; (2) regression of nuisance signals (ventricle, white matter, global signals, and head-motion) with Friston 24-parameter model; (3) band-pass filtering (0.01–0.08 Hz); (4) signal de-trending. After that, the BOLD time series signals were partitioned into 116 ROIs, according to the AAL atlas. At last, we put these time series into a data matrix $X \in R^{170\times116}$.

FCN Construction

With the preprocessed rs-fMRI data, we calculate the improved HoFCNs using the proposed S-HoFCN and M-HoFCN methods, respectively. Moreover, for comparison, we construct FCNs based on the baseline methods including PC, SR and $\text{HoFCN}_{\text{MLE}}$.

In **Figure 1**, we show the adjacency matrices of a certain FCN constructed by five different methods for MCI identification. The regularized parametric values used in SR, S-HoFCN and M-HoFCN are $\lambda = 2^4$, $\mu = 2^{-3}$ and $\mu_1 = 2^4, \mu_2 = 2^{-3}$, respectively. For the high-order methods, the width of sliding windows is fixed to $N = 70$, and step size $s = 1$. As seen from **Figure 1**, the networks based on PC and $\text{HoFCN}_{\text{MLE}}$ are dense, meaning that both low-order and high-order correlations without sparsity constraints may cause some "noisy" connections. In contrast, the networks based on SR, S-HoFCN, and M-HoFCN are sparse due to the introduction of l_1-norm regularizer. Further, we note that M-HoFCN shows clearer modular structures than S-HoFCN, since the combination of l_1-norm and trace norm regularizers has been proved to result in modularity (Qiao et al., 2016). Finally, it is observed that the high-order FCNs shown in **Figures 1C–E** tend to have more fine-grained modularity than the low-order FCNs shown in **Figures 1A,B**, which is consistent with the conclusion that the HoFCNs may be able to capture more subtle network structures as discussed in Zhang et al. (2016).

Feature Selection and Classification

In our experiments, we adopt the edge weights of FCN or HoFCN as features for MCI/ASD identifications. Although the edge weights include the full information of the networks, it typically causes the curse of dimensionality, since the number of feature dimension, i.e., $116 \times (116-1)/2 = 6670$, is far greater than the sample size (i.e., the number of subjects). To address

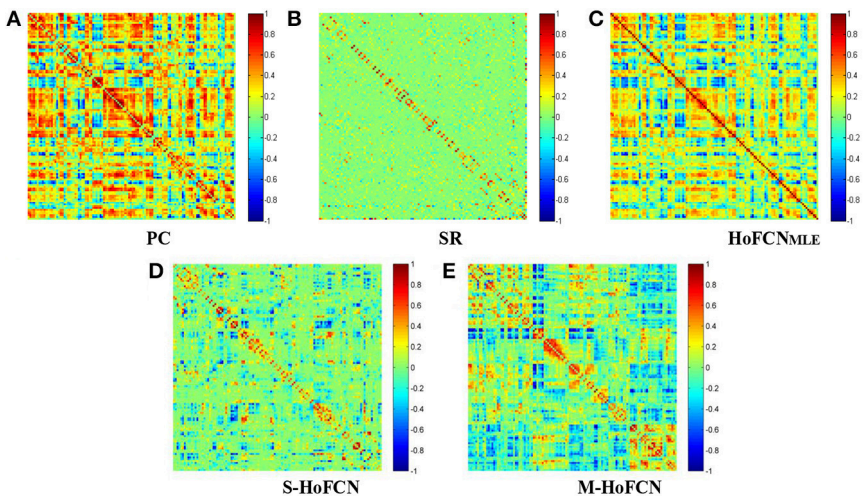

FIGURE 1 | The FBN adjacency matrices constructed by five different methods. **(A)** PC, **(B)** SR, **(C)** $\text{HoFCN}_{\text{MLE}}$, **(D)** S-HoFCN, and **(E)** M-HoFCN.

this problem, we first employ the two-sample t-test ($p = 0.05$) to select features before MCI/ASD classifications.

We use the linear support vector machine (SVM) (Chang and Lin, 2011) with default $C = 1$ for conducting the classification task. A leave-one-out cross validation (LOOCV) is adopted in our experiments to estimate the classification performance of different methods. It works in a way that in each run only one of T samples (subjects) is adopted for testing while the rest $T - 1$ samples are used for training a classifier. Therefore, we can obtain the final performance by averaging results of all the runs.

In general, one or more hyperparameters are involved in the FCN estimation methods. Specifically, for the regularization parameters (i.e., λ in SR, μ in S-HoFCN and μ_1, μ_2 in M-HoFCN), we conduct a line or grid search in the range of $(2^{-5}, 2^{-4}, \cdots, 2^0, \cdots, 2^4, 2^5)$. Note that no such parameters are involved in PC and $\text{HoFCN}_{\text{MLE}}$. For a fair comparation, we introduce a thresholding parameter into PC and $\text{HoFCN}_{\text{MLE}}$ to sparsify the initially estimated FCNs by removing the weakly connected edges. To be consistent, we employ 11 threshold values that correspond to different levels of sparsity $(1\%, 10\%, \cdots, 90\%, 100\%)$ for PC and $\text{HoFCN}_{\text{MLE}}$. For example, 10% means that the threshold value is set to remove 90% edges from the FCN, while 100% means all edges are preserved.

To obtain the optimal parameters for each method, we use an inner LOOCV procedure on the training data. Given a parametric value, in the current $T - 1$ training samples for the classification task, we use $T - 2$ samples to select features (t-test with $p = 0.05$) and train a classifier (SVM with $C = 1$), while the rest one to validate the performance of the trained classifier. Once the best validation performance is achieved by averaging the accuracies of all the inner LOOCV runs, we can determine the optimal value of the parameter for the current training samples. It is worth noting that there are sliding window parameters used in estimating the initial HoFCNs. We will have a detailed discussion about this problem in Section Sensitivity to Network Modeling Parameters.

In **Figure 2**, we display the pipeline of MCI identification used in our experiments. Based on the preprocessed fMRI data, we first estimate the initial HoFCNs based on the MLE method, and then improve the initially estimated HoFCNs by introducing

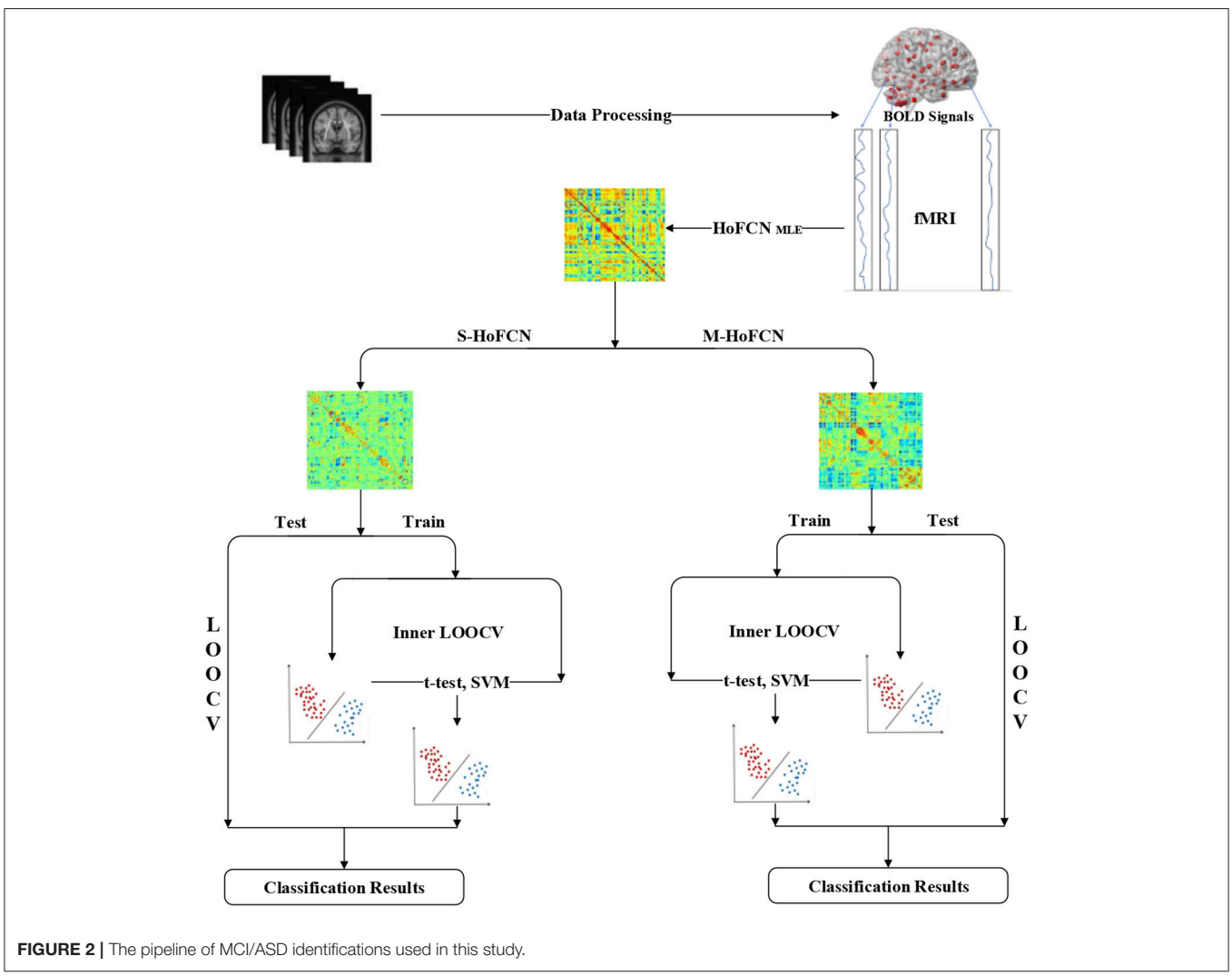

FIGURE 2 | The pipeline of MCI/ASD identifications used in this study.

sparsity and modularity priors, respectively. Finally, we apply the improved HoFCNs to identify patients suffering from MCI or ASD via the LOOCV scheme.

To evaluate the different FCN estimation methods, we adopt accuracy (ACC), sensitivity (SEN) and specificity (SPE) (Sokolova et al., 2006) as performance metrics. Their definitions are given in **Table 3**, where TP, TN, FP, and FN indicate true positive, true negative, false positive and false negative, respectively. Of note, in this work, we treat MCI/ASD patients as the positive class while the NCs as the negative.

Classification Results

In **Table 4**, we report the classification results of five different methods for MCI classification task. For the three HoFCN methods, we report the best result based on different sizes of sliding windows ($N = 50$, $s = 1$ for $\text{HoFCN}_{\text{MLE}}$; $N = 70$, $s = 2$ for S-HoFCN; and $N = 70$, $s = 6$ for M-HoFCN). As shown in **Table 4**, with respect to ACC and SPE, the proposed methods outperform the baseline methods, and they are consistently better than $\text{HoFCN}_{\text{MLE}}$. Especially for M-HoFCN, it achieves the best performance. Therefore, we argue that the modularity prior is of vital importance in removing the noisy connections and improving the reliability of HoFCNs. However, we note that, in terms of SEN, the proposed methods do not work well. In the next section, we will further investigate this phenomenon.

In **Table 5**, we simply report the best experimental results of ASD identification. For three HoFCN methods, s is fixed with 1, while $N = 90, 110, 70$ for $\text{HoFCN}_{\text{MLE}}$, S-HoFCN, and M-HoFCN, respectively. In terms of ACC, the proposed methods perform better than low-order FCNs, and better than the results reported in Wee et al. (2016). Similar to the results on MCI dataset, the M-HoFCN method also achieves the best performance, meaning that the modularity prior plays an important role in FCN modeling.

TABLE 3 | Definitions of the performance metrics involved in this paper.

Performance metric	Abbreviation	Definition
accuracy	ACC	$\frac{TP+TN}{TP+FP+TN+FN}$
sensitivity	SEN	$\frac{TP}{TP+FN}$
specificity	SPE	$\frac{TN}{TN+FP}$

TABLE 4 | The classification results based on five different methods for MCI identification, with $N = 50$, $s = 1$ for $\text{HoFCN}_{\text{MLE}}$, $N = 70$, $s = 2$ for S-HoFCN, and $N = 70$, $s = 6$ for M-HoFCN.

Method	ACC	SEN	SPE
PC	0.7956	0.8824	0.7101
SR	0.7810	0.8088	0.7536
$\text{HoFCN}_{\text{MLE}}$	0.8248	0.8824	0.7681
S-HoFCN	0.8540	0.8676	0.8406
M-HoFCN	0.8613	0.8382	0.8841

DISCUSSIONS

Sensitivity to Network Modeling Parameters

In this study, the involved parameters can be divided into two groups, i.e., sliding window parameters of HoFCNs and the regularization parameters (or threshold values) in the network estimation models. As discussed earlier, we have selected the optimal regularized parameter via inner LOOCV. In the following, we will discuss the sensitivity to the parameters of sliding windows (i.e., width N and step size s) of three HoFCN methods ($\text{HoFCN}_{\text{MLE}}$, S-HoFCN and M-HoFCN). To this end, we conduct experiments for MCI/ASD identifications under three cases:

Case 1: Varied window widths $N = 50$, 70, 90, 110 and fixed step size $s = 1$ for MCI identification. **Figure 3** shows the classification results of three HoFCN methods under this case. (Of note, in both **Figures 3–5**, we simply use MLE, S and M to represent the corresponding $\text{HoFCN}_{\text{MLE}}$, S-HoFCN and M-HoFCN methods, respectively.) It can be observed that our proposed methods perform better than $\text{HoFCN}_{\text{MLE}}$ and have the best performance at $N = 70$. For ACC, M-HoFCN has 100% possibilities to outperform $\text{HoFCN}_{\text{MLE}}$, and 75% possibilities to outperform S-HoFCN. For SEN and SPE, M-HoFCN has 75% possibilities to work better than $\text{HoFCN}_{\text{MLE}}$. That is, M-HoFCN is the best method for MCI classification. Additionally, we note that the bigger value of N tends to result in worse performance, which is consistent with the finding of choosing window sizes in Hindriks et al. (2016).

Case 2: Fixed window width $N = 70$ and varied step sizes $s = 1$, 2, 4, 6, 8 for MCI identification. We choose $N = 70$ since, as shown in **Figure 3**, the HoFCN methods tend to have the best performance at 70. In this way, we show classification results based on three HoFCN methods in **Figure 4**. By comparison, for ACC, the proposed methods have 100% possibilities to outperform $\text{HoFCN}_{\text{MLE}}$, and M-HoFCN has 80% possibilities to outperform S-HoFCN; for SEN and SPE, S-HoFCN and M-HoFCN both have 80% possibilities to perform better than $\text{HoFCN}_{\text{MLE}}$. As such, our proposed methods at least have 80% possibilities that perform better than $\text{HoFCN}_{\text{MLE}}$, and M-HoFCN has the best performance at $N = 70$, $s = 6$, while S-HoFCN at $N = 70$, $s = 2$. By using the fixed window

TABLE 5 | Comparison of the best classification results based on six different methods for ASD identification. Here, we empirically fix $s = 1$, and $N = 90$, 110, 70 for $\text{HoFCN}_{\text{MLE}}$, S-HoFCN and M-HoFCN, respectively.

Method	ACC	SEN	SPE
PC	0.6304	0.6222	0.6383
SR	0.5543	0.6000	0.5106
Wee et al., 2016	0.7070	0.8140	0.6120
$\text{HoFCN}_{\text{MLE}}$	0.7391	0.8000	0.6809
S-HoFCN	0.7391	0.7778	0.7021
M-HoFCN	0.7500	0.8000	0.7021

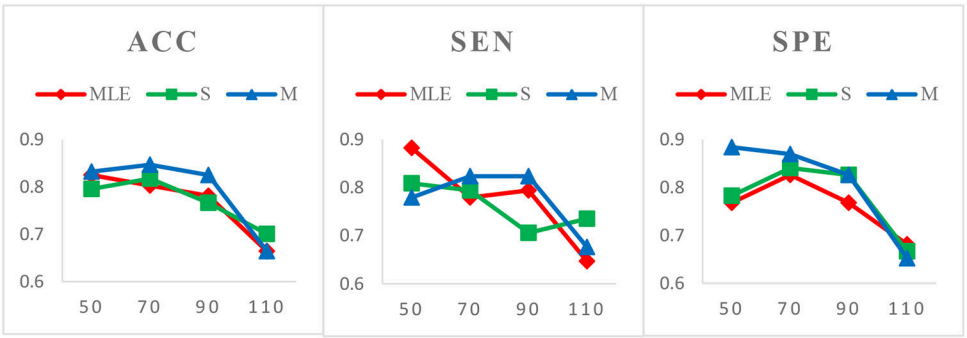

FIGURE 3 | Comparison of classification results based on three HoFCN methods for MCI identification, with varied window widths $N = 50, 70, 90, 110$ and fixed step size $s = 1$. The proposed methods (especially M-HoFCN) are consistently better than $\text{HoFCN}_{\text{MLE}}$, and they tend to have the best classification performance at $N = 70$.

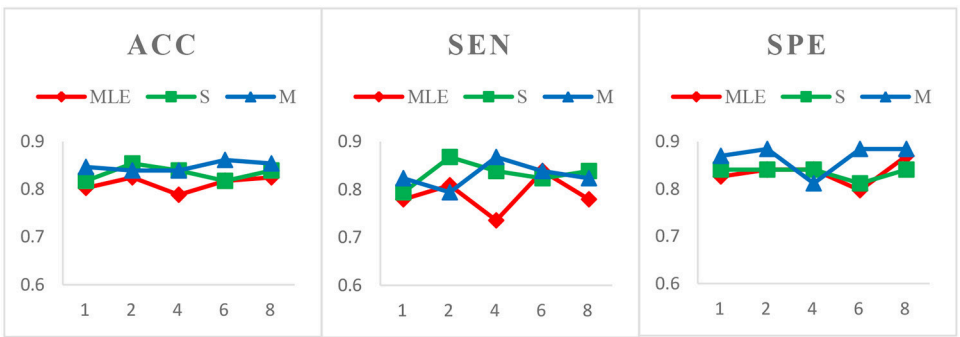

FIGURE 4 | Comparison of classification results based on three HoFCN methods for MCI identification, with different step size $s = 1, 2, 4, 6, 8$ and fixed window width $N = 70$. Our proposed methods have 80% possibilities to perform better than $\text{HoFCN}_{\text{MLE}}$.

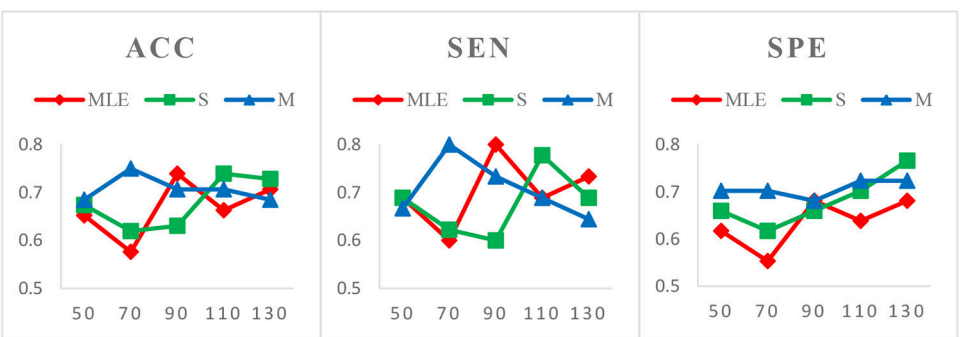

FIGURE 5 | Comparison of classification results based on three HoFCN methods for ASD identification, with varied $N = 50, 70, 90, 110, 130$ and fixed $s = 1$. Note that M-HoFCN achieves the best performance in average.

width $N = 70$, we find that the performances of three HoFCN methods with varied step sizes are relatively stable.

Case 3: Varied window widths $N = 50, 70, 90, 110, 130$ and fixed $s = 1$ for ASD identification. As shown in **Figure 5**, S-HoFCN has 80% possibilities to work better than $\text{HoFCN}_{\text{MLE}}$ for ACC and SPE, and 60% for SEN; M-HoFCN has 100% possibilities to outperform $\text{HoFCN}_{\text{MLE}}$ for SPE, and 60% for ACC and SEN. For different methods, $\text{HoFCN}_{\text{MLE}}$ gets the best performance at $N = 90$, while S-HoFCN at $N = 110$ and M-HoFCN at $N = 70$. Compared with the performance of three HoFCN methods, we found that M-HoFCN averagely achieves the best performance and it remains more stable than the other two methods. It is consistent with the finding in MCI identification.

Parcellation of the Brain

We adopt AAL atlas with 116 ROIs as network nodes in this work. To date, there exists different ROI definitions in different brain

anatomical/functional templates, such as AAL, Harvard-Oxford (http://www.fmrib.ox.ac.uk/fsl/), Eickhoff-Zilles (Eickhoff et al., 2005) and Automatic Non-linear Imaging Matching and Anatomical Labeling (ANIMAL) (Collins et al., 1995; Wang et al., 2009), etc. As reported in Wang et al. (2009), AAL and ANIMAL templates can lead to significant differences in network topological properties. Craddock et al. also revealed that ROI size had great impact on the network performance analysis, and 200 ROIs can offer better interpretability (Craddock et al., 2012). Therefore, we further conduct experiments for constructing FCNs with 200 ROIs from (Craddock et al., 2012), and take ASD classification as an example for evaluating the influence of different parcellation schemes on the final accuracy. Experimental results show that the proposed M-HoFCN still achieves the best ACC (0.6923), compared with PC (0.6248), SR (0.5167), $\text{HoFCN}_{\text{MLE}}$ (0.6811), and S-HoFCN (0.6730), which further illustrates the importance of using modularity prior in FCN estimation. Note, however, that the performance of most methods reduces greatly with 200 ROIs. The possible reason is that 200 ROIs, resulting in $200 \times (200-1)/2 = 19900$ edges, cause the challenge for feature selection or the "curse of dimensionality," since limited training samples are involved. In the future, we plan to further investigate the influence of differently selected templates on the network properties and the subsequent classification performance.

Head Motion Artifacts

As we know, the FCN estimation based on rs-fMRI data is sensitive to the head motion (Van Dijk et al., 2012; Power et al., 2014). To eliminate the influence of head motion artifacts, a commonly used method is data scrubbing that removes some volumes based on FD or DVARS (Power et al., 2012). However, in this study, we did not perform scrubbing operation to exclude volumes since dynamic information is necessarily encoded by the sliding window scheme for estimating initial low-order FCNs. The removal of volumes would disrupt the autocorrelation structure of data, which is problematic related to temporal filtering and dynamic information encoding (Janine et al., 2017). In fact, several related studies (Chen et al., 2016, 2017) also did not suggest scrubbing operation due to the same reason. Additionally, the data scrubbing often removes relatively high amount of data, thus reducing the statistical power, and, in practice, how to determine a suitable threshold of FD is still an open problem.

To further study the impact of head motion artifacts on the classification performance, we conduct the network modeling methods without regression of Friston 24-parameters. With fixed parameters such as $N = 70$ and $s = 1$, the experimental ACCs for ASD identification are PC (0.6750), SR (0.6104), $\text{HoFCN}_{\text{MLE}}$ (0.6511), S-HoFCN (0.6430), and M-HoFCN (0.6458), respectively. Compared with the results in **Table 5**, we note that most of the methods tend to decrease ACC, meaning that head motion artifacts have a significant influence on the classification performance. In other words, regressing out the head motion artifacts can contribute to achieve better (at least more discriminative) FCNs.

Top Discriminative Features

As previously mentioned in section Feature Selection and Classification, we adopt the edge weights of estimated FCN as features for classification. Here, we use two-sample t-test to re-select the features for MCI and ASD identification problems, respectively, based on the proposed M-HoFCN method, since it achieves the best performance. In particular, after constructing FCNs by M-HoFCN model ($N = 70$, $s = 6$ for MCI; and $N = 70$, $s = 1$ for ASD), we apply t-test to select discriminative features in order of their p-values (< 0.001). In this way, we select 72 and 67 discriminative features for MCI and ASD identification tasks, respectively, and visualize the features in **Figure 6**. Of note, the thickness of each arc represents the discriminative power that is inversely proportional to the corresponding p-value.

From **Figure 6A**, we found that the top discriminative features (i.e., functional connections) and their corresponding brain regions include right inferior frontal gyrus, bilateral hippocampus, bilateral parahippocampal gyrus, right pallidum, right caudate, left middle temporal gyrus, left cerebellum 6, etc. The findings are partially consistent with previous studies (Wolf et al., 2003; Albert et al., 2011; Solodkin et al., 2013). In particular, the right inferior frontal gyrus (Salvatore et al., 2015), bilateral hippocampus (Chen et al., 2016), bilateral parahippocampal gyrus (Echávarri et al., 2011), right pallidum (Supekar et al., 2008; Albert et al., 2011), right caudate (Albert et al., 2011), left middle temporal gyrus (Kosicek and Hecimovic, 2013; Chen et al., 2016), and left cerebellum 6 (Suk et al., 2015) are all reported as potential biomarkers for MCI or AD identification. However, currently it is an open problem for explaining these FCN-based biomarkers. In the future, we plan to provide further experimental evidences toward the biological explanation of those involved functional connectivity or brain regions.

In terms of the selected features as shown in **Figure 6B**, brain regions that may contribute to ASD identification in this work include the left precentral gyrus, right middle frontal gyrus, right hippocampus, bilateral parahippocampal gyrus, right amygdala, bilateral putamen, left caudate, bilateral pallidum, and bilateral middle temporal, many of which are widely reported in the previous studies associated with ASD identification (Sparks et al., 2002; Haznedar et al., 2006; Rojas et al., 2006; Toal et al., 2009; Ecker et al., 2010; Qiu et al., 2010).

Limitations

In this work, we only use PC as a cornerstone in construction of HoFCN due to its simplicity and popularity. However, as we described above, PC can only capture the full correlation, and thus partial correlation-based methods such as SR may be considered in practice. Besides, many researchers have devoted their efforts to FCN estimation methods based on group analysis. For example, Liu et al. proposed a hierarchical Markov random field model to capture both group and subject FCNs simultaneously, which can take within-subject coherence and between-subject consistency of the network label maps into account (Liu et al., 2014); Ghanbari et al. designed a multi-layer graph clustering algorithm to extract hub-networks

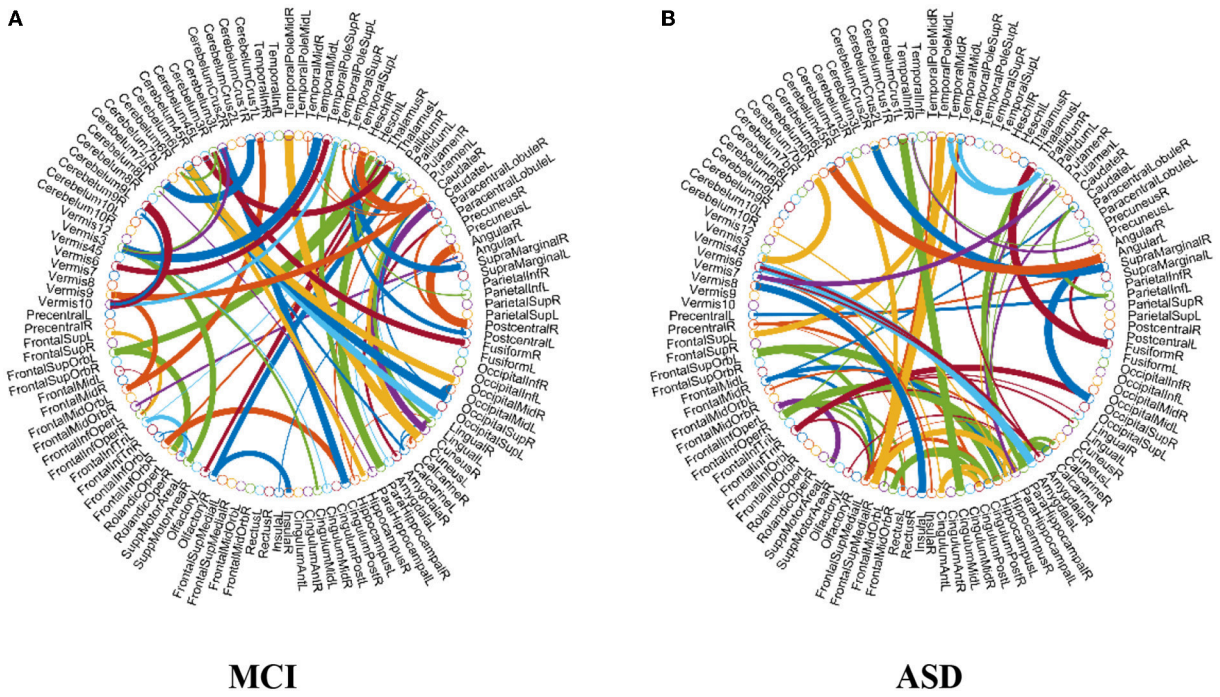

FIGURE 6 | The most discriminative features (network connections) involved in the classification tasks by using t-test with $p < 0.001$. Note that the thickness of the arcs is inversely proportional to the corresponding p-value for indicating the discriminative power of the features. **(A)** MCI and **(B)** ASD.

by non-negative matrix factorization and applied the hubs to characterize population commonalities and subject variations between ASD and typically developing children (Ghanbari et al., 2017); Kam et al. proposed a multiple FCN model using hierarchical clustering and applied it for ASD diagnosis (Kam et al., 2017). These methods provide a different understanding toward brain structure and group/subject analysis, which we can consider in our future studies.

CONCLUSION

In this paper, we develop an effective way of improving HoFCN estimation, by learning a neighborhood networks of the initial HoFCN with sparsity and modularity priors as regularizers, respectively. We apply our proposed methods to identify subjects with MCI and ASD from their corresponding NCs. In both MCI and ASD identifications, our proposed HoFCN methods consistently outperform the baseline methods. Especially, the M-HoFCN tends to achieve the best performance, which illustrates the importance of the modularity prior in FCN estimation.

AUTHOR CONTRIBUTIONS

DS put forward the idea of HoFCN and provided the preprocessed rs-fMRI data. LQ and YZ proposed to learn the neighborhood networks that meet sparsity and modularity for improved HoFCN estimation. YZ, LZ, and ST designed the procedures of MCI/ASD identification experiments. All authors developed the estimation algorithm and contributed to the preparation of the article, figures, and tables.

ACKNOWLEDGMENTS

We thank Yining Zhang for the insightful and helpful discussions. This work is partly supported by National Natural Science Foundation of China (61402215), and Natural Science Foundation of Shandong Province (ZR2018MF020).

REFERENCES

Albert, M. S., DeKosky, S. T., Dickson, D., Dubois, B., Feldman, H. H., Fox, N. C., et al. (2011). The diagnosis of mild cognitive impairment due to Alzheimer's disease: recommendations from the national institute on Aging-Alzheimer's Association workgroups on diagnostic guidelines for Alzheimer's disease. *Alzheimers Dement.* 7, 270–279. doi: 10.1016/j.jalz.2011.03.008

Bertsekas, D. P. (2012). "Chapter 4: Incremental gradient, subgradient, and proximal methods for convex optimization: a survey," in *Optimization for Machine Learning* (Cambridge, MA; London: MIT Press).

Biswal, B. B., Yetkin, F. Z., Haughton, V. M., and Hyde, J. S. (1995). Functional connectivity in the motor cortex of resting human brain using echo-planar MRI. *Magn. Reson. Med.* 34, 537–541. doi: 10.1002/mrm.1910340409

Bullmore, E., and Sporns, O. (2009). Complex brain networks: graph theoretical analysis of structural and functional systems. *Nature Rev. Neurosci.* 10, 186–198. doi: 10.1038/nrn2575

Chang, C. C., and Lin, C. J. (2011). LIBSVM: a library for support vector machines. *ACM Trans. Intell. Syst. Technol.* 2, 1–27. doi: 10.1145/1961189.1961199

Chen, X., Zhang, H., Gao, Y., Wee, C. Y., Li, G., and Shen, D. (2016). High-order resting-state functional connectivity network for MCI classification. *Hum. Brain Mapp.* 37, 3282–3296. doi: 10.1002/hbm.23240

Chen, X., Zhang, H., Lee, S. W., and Shen, D. (2017). Hierarchical high-order functional connectivity networks and selective feature fusion for MCI classification. *Neuroinformatics* 15, 1–14. doi: 10.1007/s12021-016-9321-x

Collins, D. L., Holmes, C. J., Peters, T. M., and Evans, A. C. (1995). Automated 3D modelbased neuroanatomical segmentation. Human brain mapping 3. *Hum. Brain Mapp.* 3, 190–208. doi: 10.1002/hbm.460030304

Combettes, P. L., and Pesquet, J. C. (2009). "Chapter 10: Proximal splitting methods in signal processing," in *Fixed-Point Algorithms for Inverse Problems in Science and Engineering, Springer Optimization and Its Applications, Vol. 49,* ed H. H. Bauschke (New York, NY: Springer Science+Business Media), 185–212. doi: 10.1007/978-1-4419-9569-8_10

Craddock, R. C., James, G. A., Hu, X. P., and Mayberg, H. S. (2012). A whole brain fMRI atlas generated via spatially constrained spectral clustering. *Hum. Brain Mapp.* 33, 1914–1928. doi: 10.1002/hbm.21333

Cullen, K. R., Westlund, M. K., Klimes-Dougan, B., Mueller, B. A., Houri, A., Eberly, L. E., et al. (2014). Abnormal amygdala resting-state functional connectivity in adolescent depression. *JAMA Psychiatry* 71, 1138–1147. doi: 10.1001/jamapsychiatry.2014.1087

Echávarri, C., Aalten, P., Uylings, H. B., Jacobs, H. I., Visser, P. J., Gronenschild, E. H., et al. (2011). Atrophy in the parahippocampal gyrus as an early biomarker of Alzheimer's disease. *Brain Struct. Funct.* 215, 265–271. doi: 10.1007/s00429-010-0283-8

Ecker, C., Rocha-Rego, V., Johnston, P., Mourao-Miranda, J., Marquand, A. F., Daly, E., et al. (2010). Investigating the predictive value of whole-brain structural MR scans in autism: a pattern classification approach. *Neuroimage* 49, 44–56. doi: 10.1016/j.neuroimage.2009.08.024

Eickhoff, S. B., Stephan, K. E., Mohlberg, H., Grefkes, C., Fink, G. R., Amunts, K., et al. (2005). A new SPM toolbox for combining probabilistic cytoarchitectonic maps and functional imaging data. *Neuroimage* 25, 1325–1335. doi: 10.1016/j.neuroimage.2004.12.034

Fornito, A., Zalesky, A., and Breakspear, M. (2015). The connectomics of brain disorders. *Nat. Rev. Neurosci.* 16, 159–172. doi: 10.1038/nrn3901

Friedman, J., Hastie, T., and Tibshirani, R. (2008). Sparse inverse covariance estimation with the graphical lasso. *Biostatistics* 9, 432–441. doi: 10.1093/biostatistics/kxm045

Friston, K. J., Williams, S., Howard, R., Frackowiak, R. S., and Turner, R. (1996). Movement-related effects in fMRI time-series. *Magn. Reson. Med.* 35, 346–355. doi: 10.1002/mrm.1910350312

Ghanbari, Y., Bloy, L., Tunc, B., Shankar, V., Roberts, T. P. L., Edgar, J. C., et al. (2017). On characterizing population commonalities and subject variations in brain networks. *Med. Image Anal.* 38, 215–229. doi: 10.1016/j.media.2015.10.009

Greicius, M. D., Flores, B. H., Menon, V., Glover, G. H., Solvason, H. B., Kenna, H., et al. (2007). Resting-state functional connectivity in major depression: abnormally increased contributions from subgenual cingulate cortex and thalamus. *Biol. Psychiatry* 62, 429–437. doi: 10.1016/j.biopsych.2006.09.020

Guo, H., Liu, L., Chen, J., Xu, Y., and Jie, X. (2017). Alzheimer classification using a minimum spanning tree of high-order functional network on fMRI dataset. *Front. Neurosci.* 11:639. doi: 10.3389/fnins.2017.00639

Haznedar, M. M., Buchsbaum, M. S., Hazlett, E. A., Licalzi, E. M., Cartwright, C., and Hollander, E. (2006). Volumetric analysis and three-dimensional glucose metabolic mapping of the striatum and thalamus in patients with autism spectrum disorders. *Am. J. Psychiatry* 163, 1252–1263. doi: 10.1176/ajp.2006.163.7.1252

Hindriks, R., Adhikari, M. H., Murayama, Y., Ganzetti, M., Mantini, D., Logothetis, N. K., et al. (2016). Can sliding-window correlations reveal dynamic functional connectivity in resting-state fMRI? *Neuroimage* 127, 242–256. doi: 10.1016/j.neuroimage.2015.11.055

Huang, S., Li, J., Sun, L., Liu, J., Wu, T., Chen, K., et al. (2009). "Learning brain connectivity of alzheimer's disease from neuroimaging data," in *Advances in Neural Information Processing Systems 22: Conference on Neural Information Processing Systems 2009* (Vancouver, BC), 808–816.

Jafri, M., Pearlson, G. D., Stevens, M., and Calhoun, V. D. (2008). A method for functional network connectivity among spatially independent resting-state components in schizophrenia. *Neuroimage* 39, 1666–1681. doi: 10.1016/j.neuroimage.2007.11.001

Janine, B., Stephen, S., and Beckmann, C. (2017). *Introduction to Resting State fMRI Functional Connectivity*. Oxford, UK: Oxford University Press.

Ji, S., and Ye, J. (2009). "An accelerated gradient method for trace norm minimization," in *Proceedings of the 26th Annual international conference on machine learning* (Montreal, QC), 457–464.

Kam, T. E., Suk, H. I., and Lee, S. W. (2017). Multiple functional networks modeling for autism spectrum disorder diagnosis. *Hum. Brain Mapp.* 38, 5804–5821. doi: 10.1002/hbm.23769

Kosicek, M., and Hecimovic, S. (2013). Phospholipids and Alzheimer's Disease: alterations, mechanisms and potential biomarkers. *Int. J. Mol. Sci.* 14, 1310–1322. doi: 10.3390/ijms14011310

Lee, H., Lee, D. S., Kang, H., Kim, B. N., and Chung, M. K. (2011). Sparse brain network recovery under compressed sensing. *IEEE Trans. Med. Imaging* 30, 1154–1165. doi: 10.1109/TMI.2011.2140380

Li, W., Wang, Z., Zhang, L., Qiao, L., and Shen, D. (2017). Remodeling pearson's correlation for functional brain network estimation and autism spectrum disorder identification. *Front. Neuroinform.* 11:55. doi: 10.3389/fninf.2017.00055

Liu, F., Guo, W., Fouche, J. P., Wang, Y., Wang, W., Ding, J., et al. (2015). Multivariate classification of social anxiety disorder using whole brain functional connectivity. *Brain Struct. Funct.* 220, 101–115. doi: 10.1007/s00429-013-0641-4

Liu, F., Guo, W., Liu, L., Long, Z., Ma, C., Xue, Z., et al. (2013). Abnormal amplitude low-frequency oscillations in medication-naive, first-episode patients with major depressive disorder: a resting-state fMRI study. *J. Affect. Disord.* 146, 401–406. doi: 10.1016/j.jad.2012.10.001

Liu, F., Wang, Y., Li, M., Wang, W., Li, R., Zhang, Z., et al. (2017). Dynamic functional network connectivity in idiopathic generalized epilepsy with generalized tonic-clonic seizure. *Hum. Brain Mapp.* 38, 957–973. doi: 10.1002/hbm.23430

Liu, G., Lin, Z., Yan, S., Sun, J., Yu, Y., and Ma, Y. (2013). Robust recovery of subspace structures by low-rank representation. *IEEE Trans. Pattern Anal. Mach. Intell.* 35, 171–184. doi: 10.1109/TPAMI.2012.88

Liu, W., Awate, S. P., Anderson, J. S., and Fletcher, P. T. (2014). A functional network estimation method of resting-state fMRI using a hierarchical Markov random field. *Neuroimage* 100, 520–534. doi: 10.1016/j.neuroimage.2014.06.001

Liu, Y., Wang, K., Yu, C., He, Y., Zhou, Y., Liang, M., et al. (2008). Regional homogeneity, functional connectivity and imaging markers of Alzheimer's disease: a review of resting-state fMRI studies. *Neuropsychologia* 46, 1648–1656. doi: 10.1016/j.neuropsychologia.2008.01.027

Macke, J. H., Opper, M., and Bethge, M. (2011). Common input explains higher-order correlations and entropy in a simple model of neural population activity. *Phys. Rev. Lett.* 106:208102. doi: 10.1103/PhysRevLett.106.208102

Marrelec, G., Krainik, A., Duffau, H., Pélégriniissac, M., Lehéricy, S., Doyon, J., et al. (2006). Partial correlation for functional brain interactivity investigation in functional MRI. *Neuroimage* 32, 228–237. doi: 10.1016/j.neuroimage.2005.12.057

Oymak, S., Jalali, A., Fazel, M., Eldar, Y. C., and Hassibi, B. (2014). Simultaneously structured models with application to sparse and low-rank matrices. *IEEE Trans. Inf. Theory* 61, 2886–2908. doi: 10.1109/TIT.2015.2401574

Plis, S. M., Sui, J., Lane, T., Roy, S., Clark, V. P., Potluru, V. K., et al. (2014). High-order interactions observed in multi-task intrinsic networks are dominant indicators of aberrant brain function in schizophrenia. *Neuroimage* 102, 35–48. doi: 10.1016/j.neuroimage.2013.07.041

Power, J. D., Barnes, K. A., Snyder, A. Z., Schlaggar, B. L., and Petersen, S. E. (2012). Spurious but systematic correlations in functional connectivity MRI networks arise from subject motion. *Neuroimage* 59, 2142–2154. doi: 10.1016/j.neuroimage.2011.10.018

Power, J. D., Mitra, A., Laumann, T. O., Snyder, A. Z., Schlaggar, B. L., and Petersen, S. E. (2014). Methods to detect, characterize, and remove motion artifact in resting state fMRI. *Neuroimage* 84, 320–341. doi: 10.1016/j.neuroimage.2013.08.048

Qiao, L., Zhang, H., Kim, M., Teng, S., Zhang, L., and Shen, D. (2016). Estimating functional brain networks by incorporating a modularity prior. *Neuroimage* 141, 399–407. doi: 10.1016/j.neuroimage.2016.07.058

Qiu, A., Adler, M., Crocetti, D., Miller, M. I., and Mostofsky, S. H. (2010). Basal ganglia shapes predict social, communication, and motor dysfunctions in boys with autism spectrum disorder. *J. Am. Acad. Child Adolesc. Psychiatry* 49, 539–551.e1–4. doi: 10.1016/j.jaac.2010.02.012

Richard, E., Savalle, P. A., and Vayatis, N. (2012). "Estimation of simultaneously sparse and low rank matrices," in *ICML'12 Proceedings of the 29th International Coference on International Conference on Machine Learning* (Edinburgh).

Rojas, D. C., Peterson, E., Winterrowd, E., Reite, M. L., Rogers, S. J., and Tregellas, J. R. (2006). Regional gray matter volumetric changes in autism associated with social and repetitive behavior symptoms. *BMC Psychiatry* 6:56. doi: 10.1186/1471-244X-6-56

Rombouts, S. A., Barkhof, F., Goekoop, R., Stam, C. J., and Scheltens, P. (2005). Altered resting state networks in mild cognitive impairment and mild Alzheimer's disease: an fMRI study. *Hum. Brain Mapp.* 26, 231–239. doi: 10.1002/hbm.20160

Salvatore, C., Cerasa, A., Battista, P., Gilardi, M. C., Quattrone, A., and Castiglioni, I. (2015). Magnetic resonance imaging biomarkers for the early diagnosis of Alzheimer's disease: a machine learning approach. *Front. Neurosci.* 9:307. doi: 10.3389/fnins.2015.00307

Sanz-Arigita, E. J., Schoonheim, M. M., Damoiseaux, J. S., Rombouts, S. A., Maris, E., Barkhof, F., et al. (2010). Loss of 'small-world' networks in Alzheimer's disease: graph analysis of FMRI resting-state functional connectivity. *PLoS ONE* 5:e13788. doi: 10.1371/journal.pone.0013788

Smith, S. M., Miller, K. L., Salimi-Khorshidi, G., Webster, M., Beckmann, C. F., Nichols, T. E., et al. (2011). Network modelling methods for FMRI. *Neuroimage* 54, 875–891. doi: 10.1016/j.neuroimage.2010.08.063

Smith, S. M., Vidaurre, D., Beckmann, C. F., Glasser, M. F., Jenkinson, M., Miller, K. L., et al. (2013). Functional connectomics from resting-state fMRI. *Trends Cogn. Sci.* 17, 666–682. doi: 10.1016/j.tics.2013.09.016

Sokolova, M., Japkowicz, N., and Szpakowicz, S. (2006). "Beyond Accuracy, F-Score and ROC: A Family of Discriminant Measures for Performance Evaluation," in *AI 2006: Advances in Artificial Intelligence: 19th Australian Joint Conference on Artificial Intelligence, Hobart, Australia*, eds A. Sattar, and B.-H. Kang (Berlin; Heidelberg: Springer Berlin Heidelberg), 1015–1021.

Solodkin, A., Chen, E. E., Van Hoesen, G. W., Heimer, L., Shereen, A., Kruggel, F., et al. (2013). *In vivo* parahippocampal white matter pathology as a biomarker of disease progression to Alzheimer's disease. *J. Comp. Neurol.* 521, 4300–4317. doi: 10.1002/cne.23418

Sparks, B. F., Friedman, S. D., Shaw, D. W., Aylward, E. H., Echelard, D., Artru, A. A., et al. (2002). Brain structural abnormalities in young children with autism spectrum disorder. *Neurology* 59, 184–192. doi: 10.1212/WNL.59.2.184

Sporns, O. (2011). *Networks of the Brain*. Cambridge, MA; London: MIT Press.

Sporns, O., and Betzel, R. F. (2016). Modular brain networks. *Annu. Rev. Psychol.* 67, 613–640. doi: 10.1146/annurev-psych-122414-033634

Suk, H. I., Wee, C. Y., Lee, S. W., and Shen, D. (2015). Supervised discriminative group sparse representation for mild cognitive impairment diagnosis. *Neuroinformatics* 13, 1–19. doi: 10.1007/s12021-014-9241-6

Supekar, K., Menon, V., Rubin, D., Musen, M., and Greicius, M. D. (2008). Network analysis of intrinsic functional brain connectivity in Alzheimer's disease. *PLoS Comput. Biol.* 4:e1000100. doi: 10.1371/journal.pcbi.1000100

Toal, F., Bloemen, O. J. N., Deeley, Q., Tunstall, N., Daly, E., Page, L., et al. (2009). Psychosis and autism: magnetic resonance imaging study of brain anatomy. *Br. J. Psychiatry* 194, 418–425. doi: 10.1192/bjp.bp.107.049007

Tomioka, R., and Sugiyama, M. (2009). Dual-augmented lagrangian method for efficient sparse reconstruction. *IEEE Signal Process. Lett.* 16, 1067–1070. doi: 10.1109/LSP.2009.2030111

Tzourio-Mazoyer, N., Landeau, B., Papathanassiou, D., Crivello, F., Etard, O., Delcroix, N., et al. (2002). Automated anatomical labeling of activations in SPM using a macroscopic anatomical parcellation of the MNI MRI single-subject brain. *Neuroimage* 15, 273–289. doi: 10.1006/nimg.2001.0978

van den Heuvel, M. P., and Hulshoff Pol, H. E. (2010). Exploring the brain network: a review on resting-state fMRI functional connectivity. *Eur. Neuropsychopharmacol.* 20, 519–534. doi: 10.1016/j.euroneuro.2010.03.008

Van Dijk, K. R. A., Sabuncu, M. R., and Buckner, R. L. (2012). The Influence of head motion on intrinsic functional connectivity MRI. *Neuroimage* 59, 431–438. doi: 10.1016/j.neuroimage.2011.07.044

Varoquaux, G., Gramfort, A., Poline, J. B., and Thirion, B. (2010). "Brain covariance selection: better individual functional connectivity models using population prior," in *Advances in Neural Information Processing Systems 23 (NIPS 2010)* (Vancouver, BC), 2334–2342.

Wang, J., Wang, L., Zang, Y., Yang, H., Tang, H., Gong, Q., et al. (2009). Parcellation- dependent small-world brain functional networks: a resting-state fMRI study. *Hum. Brain Mapp.* 30, 1511–1523 doi: 10.1002/hbm.20623

Wang, L., Zang, Y., He, Y., Liang, M., Zhang, X., Tian, L., et al. (2006). Changes in hippocampal connectivity in the early stages of Alzheimer's disease: evidence from resting state fMRI. *Neuroimage* 31, 496–504. doi: 10.1016/j.neuroimage.2005.12.033

Wee, C. Y., Yap, P. T., and Shen, D. (2016). Diagnosis of autism spectrum disorders using temporally distinct resting-state functional connectivity networks. *CNS Neurosci. Ther.* 22, 212–219. doi: 10.1111/cns.12499

Wee, C. Y., Yap, P. T., Zhang, D., Wang, L., and Shen, D. (2014). Group-constrained sparse fMRI connectivity modeling for mild cognitive impairment identification. *Brain Struct. Funct.* 219:641. doi: 10.1007/s00429-013-0524-8

Weng, S. J., Wiggins, J. L., Peltier, S. J., Carrasco, M., Risi, S., Lord, C., et al. (2010). Alterations of resting state functional connectivity in the default network in adolescents with autism spectrum disorders. *Brain Res.* 1313, 202–214. doi: 10.1016/j.brainres.2009.11.057

Wolf, H., Jelic, V., Gertz, H., Nordberg, A., Julin, P., and Wahlund, L. (2003). A critical discussion of the role of neuroimaging in mild cognitive impairment. *Acta Neurol. Scand.* 107, 52–76. doi: 10.1034/j.1600-0404.107.s179.10.x

Yu, R., Zhang, H., An, L., Chen, X., Wei, Z., and Shen, D. (2017). Connectivity strength-weighted sparse group representation-based brain network construction for MCI classification. *Hum. Brain Mapp.* 38, 2370–2383. doi: 10.1002/hbm.23524

Zhang, H., Chen, X., Shi, F., Li, G., Kim, M., Giannakopoulos, P., et al. (2016). Topographical information-based high-order functional connectivity and its application in abnormality detection for mild cognitive impairment. *J. Alzheimers Dis.* 54, 1095–1112. doi: 10.3233/JAD-160092

Zhang, Y., and Schneider, J. G. (2010). "Learning multiple tasks with a sparse matrix-normal penalty," in *Advances in Neural Information Processing Systems 23: 24th Annual Conference on Neural Information Processing Systems 2010.* (Vancouver, BC), 2550–2558.

Zhang, Y., Zhang, H., Chen, X., Lee, S. W., and Shen, D. (2017). Hybrid high-order functional connectivity networks using resting-state functional MRI for mild cognitive impairment diagnosis. *Sci. Rep.* 7:6530. doi: 10.1038/s41598-017-06509-0

Zhao, F., Zhang, H., Rekik, I., An, Z., and Shen, D. (2018). Diagnosis of autism spectrum disorders using multi-level high-order functional networks derived from resting-state functional MRI. *Front. Hum. Neurosci.* 12:182. doi: 10.3389/fnhum.2018.00184

Zhou, Y., Qiao, L., Li, W., Zhang, L., and Shen, D. (2018). Simultaneous estimation of low- and high-order functional connectivity for identifying mild cognitive impairment. *Front. Neuroinform.* 12:3. doi: 10.3389/fninf.2018.00003

Zhuang, L., Gao, H., Lin, Z., Ma, Y., Zhang, X., Yu, N. (2012). "Non-negative low rank and sparse graph for semi-supervised learning," in *Proceedings / CVPR, IEEE Computer Society Conference on Computer Vision and Pattern Recognition* (Washington, DC: IEEE Computer Society), 2328–2335.

Conflict of Interest Statement: The authors declare that the research was conducted in the absence of any commercial or financial relationships that could be construed as a potential conflict of interest.

frontiers in Neuroscience

ORIGINAL RESEARCH
published: 07 February 2019
doi: 10.3389/fnins.2019.00052

Increased Peripheral Interleukin 10 Relate to White Matter Integrity in Schizophrenia

Gui Fu[1†], Wenjing Zhang[1†], Jing Dai[2], Jieke Liu[1], Fei Li[1], Dongsheng Wu[1], Yuan Xiao[1], Chandan Shah[1], John A. Sweeney[1,3], Min Wu[1] and Su Lui[1]**

[1] Huaxi MR Research Center, Department of Radiology, West China Hospital of Sichuan University, Chengdu, China, [2] The Fourth People's Hospital of Chengdu, Sichuan, China, [3] Department of Psychiatry and Behavioral Neuroscience, University of Cincinnati, Cincinnati, OH, United States

OPEN ACCESS

Edited by:
Lin Shi,
The Chinese University of Hong Kong, China

Reviewed by:
Kai Yuan,
Xidian University, China
Elisabetta C. del Re,
Harvard Medical School, United States
Salem Hannoun,
American University of Beirut Medical Center, Lebanon

***Correspondence:**
Min Wu
wuminscu@scu.edu.cn
Su Lui
lusuwcums@tom.com

[†] These authors have contributed equally to this work

Specialty section:
This article was submitted to Brain Imaging Methods, a section of the journal Frontiers in Neuroscience

Received: 18 September 2018
Accepted: 21 January 2019
Published: 07 February 2019

Citation:
Fu G, Zhang W, Dai J, Liu J, Li F, Wu D, Xiao Y, Shah C, Sweeney JA, Wu M and Lui S (2019) Increased Peripheral Interleukin 10 Relate to White Matter Integrity in Schizophrenia. Front. Neurosci. 13:52. doi: 10.3389/fnins.2019.00052

Background: Schizophrenia is characterized by the disruption of microstructural white matter (WM) integrity, while the pathogenesis remains unclear. Inflammation has been associated with the WM pathology in schizophrenia. Interleukin 10 (IL-10) has been proven to be related to schizophrenia in both animal and human models. The aim of this study was to explore whether peripheral IL-10 was associated with microstructural WM integrity in schizophrenia.

Methods: A total of 47 patients with schizophrenia (SZ) and 49 healthy controls (HC) underwent diffusion tensor imaging and venous blood sampling. Tract-based spatial statistics was conducted to explore the differences in fractional anisotropy (FA), radial diffusivity (RD), mean diffusivity (MD), and axial diffusivity (AD) between patients and controls. A quantitative chemiluminescence assay was performed to measure peripheral IL-10 levels. General linear regression analysis using a stepwise method was applied to examine the relationship between peripheral IL-10 and diffusion measures.

Results: Compared with the HC, peripheral IL-10 levels were higher and a significant reduction of FA and AD, and increase of RD and MD were observed in SZ (corrected $p < 0.05$). A regression analysis revealed that peripheral IL-10 was negatively correlated with FA in the right posterior thalamic radiation and left inferior fronto-occipital fasciculus, in SZ ($\beta = -0.51$, $p = 0.01$; $\beta = -0.47$, $p = 0.02$, respectively) but not in HC ($\beta = -0.01$, $p = 0.95$; $\beta = -0.003$, $p = 0.98$, respectively), and the differences in regression curves were significant ($z = 2.50$, $p = 0.01$; $z = 2.37$, $p = 0.02$, respectively). IL-10 was negatively connected with MD in the right parietal arcuate fasciculus ($\beta = -0.40$, $p = 0.048$) and body of the corpus callosum ($\beta = -0.43$, $p = 0.03$) in SZ, while not in HC. The magnitude of correlation in the patient and control group was different ($z = 2.48$, $p = 0.01$ and $z = 2.61$, $p < 0.01$, respectively). In addition, IL-10 was positively correlated with RD in the right parietal arcuate fasciculus in patients ($\beta = 0.45$, $p = 0.04$) but not in HC ($\beta = 0.26$, $p = 0.94$), but the correlation coefficients were not significant ($z = 0.98$, $p = 0.32$).

Conclusion: Our findings demonstrated that elevated peripheral IL-10 levels were associated with the disruption of microstructural WM integrity in schizophrenia, supporting the notion that inflammation plays a regulatory role in the pathology of microstructural WM and is associated with schizophrenia.

Keywords: schizophrenia, interleukin 10, white matter, inflammation, diffusion tensor imaging

INTRODUCTION

Schizophrenia is considered a disconnection disorder characterized by disrupted white matter (WM) integrity (Viher et al., 2016; Di Biase et al., 2017; Kelly et al., 2018). Although the pathogenesis of disrupted WM integrity in schizophrenia remains unclear, neuroinflammation mediated by cytokines appears to be an important pathogenic mechanism (Frodl and Amico, 2014; Najjar and Pearlman, 2015). Moreover, evidence from genomic, blood, postmortem and neuroimaging studies indicates that inflammation plays an important role in the pathophysiological process of schizophrenia (Borovcanin et al., 2015; Najjar and Pearlman, 2015; Fond et al., 2016; Khandaker and Dantzer, 2016; Shivakumar et al., 2018; Xiu et al., 2018). For example, the polymorphisms of interleukin (IL) -10, IL-6 and tumor necrosis factor α (TNF-α) are related to a high risk of developing schizophrenia (Shivakumar et al., 2018; Xiu et al., 2018) and their levels in blood are higher in schizophrenia patients compared with healthy subjects (Kunz et al., 2011; Lee et al., 2017). Elevated expressions of IL-6, IL-1β, IL-8, and SERPINA (a serine protease inhibitor) were associated with a higher WM neuron density below the orbitofrontal cortex in schizophrenia (Fung et al., 2014). Besides, a neuroimaging study found that serum IL-6 and C-reactive protein (CRP) were associated with reduced fractional anisotropy (FA) of WM in schizophrenia, though there was no significant difference in IL-6 and CRP levels between schizophrenia patients and the controls (Prasad et al., 2015). The evidence indicates that the dysregulation of cytokines could lead to the pathophysiological changes of WM in schizophrenia.

Among these cytokines, IL-10, a regulatory cytokine, maintains the balance between pro-inflammatory and anti-inflammatory cytokines (Murray, 2006). Growing evidence has demonstrated that IL-10 is associated with schizophrenia. For example, it has been reported that increased IL-10 expression alleviates behavioral abnormalities in a mouse model (Meyer et al., 2008). In addition, a meta-analysis of genomic studies demonstrated that subjects with a single nucleotide polymorphism (SNP, rs1800872) and two haplotypes (A-C-A and G-C-C) of IL-10 are vulnerable to schizophrenia (Gao et al., 2014). Furthermore, a previous study found an elevation of systemic IL-10 in patients with schizophrenia compared with healthy controls (Kunz et al., 2011). Peripheral IL-10 levels were also correlated to the severity of clinical symptoms of schizophrenia (Xiu et al., 2016). Additionally, it was also observed that atypical antipsychotics could upregulate the blood IL-10 levels (Sugino et al., 2009).

Growing evidence suggests that IL-10 might be associated with WM anomalies (Pang et al., 2005; Vidal et al., 2013). A previous study on rhesus macaques found that higher IL-10 levels in serum were positively associated with WM volume in the regions below the inferior parietal sulcus, at the tail of the lateral lunate sulcus and with WM density in the dorsal prefrontal cortex (Willette et al., 2013). Additionally, *in vivo* studies indicated a link between peripheral IL-10 and microstructural WM integrity. The inflammatory score composited of blood IL-10 and other cytokines including TNF-α, IL-23, and IL-1β was negatively associated with lower FA in patients with Alzheimer's disease (Swardfager et al., 2017). In addition, peripheral IL-10 was negatively associated with FA and positively associated with radial diffusivity (RD) and mean diffusivity (MD) in patients with bipolar disorder, however, there were no controls in this study (Benedetti et al., 2016). To our knowledge, no *in vivo* study has examined the relationship between systemic IL-10 and microstructural WM integrity in schizophrenia.

Thus, the aim of the present study was to explore whether the changes of peripheral IL-10 were related to the disruption of microstructural WM integrity *in vivo* and clinical symptoms, as well as cognitive ratings in schizophrenia.

MATERIALS AND METHODS

Participants

Forty-seven patients with schizophrenia (28 males and 19 females; mean age [± *SD*], 31.85 ± 11.10 year, range: 21–52 year; mean education [± *SD*], 12.26 ± 2.76 year; mean duration of illness [± *SD*], 7.77 ± 6.99 year) were recruited from the Outpatient Center of the Department of Psychiatry, West China Hospital of Sichuan University. All Patients were diagnosed with schizophrenia using the Structured Clinical Interview for DSM-IV. All patients had received outpatient monotherapy with antipsychotic drugs for at least 6 months and reached the stable phase. All patients were medication free for 10–14 days before the study enrollment.

A total of 49 healthy subjects (22 males and 27 females; mean age [± *SD*], 34.63 ± 9.28 year, range: 26–50 year; mean education [± *SD*],14.49 ± 4.33 year) were recruited from the local area via the distribution of poster advertisements. They were screened using the non-patient version of the Structured Clinical Interview for DSM-IV, to exclude those with a history of psychiatric illness. Furthermore, none of their first-degree relatives had a known history of psychiatric illness. Exclusion criteria for both groups were: being left handed, history of neurological illness, autoimmune diseases (such as systemic lupus erythematosus, rheumatoid arthritis, and others)

or acute infectious illness within the 4 weeks prior to the study, thyroid dysfunction (assessed regularly by measuring the serum triiodothyronine, thyroxine, and thyroid-stimulating hormone in the Outpatient Center), administration of non-steroidal anti-inflammatory drugs or antibiotic drugs within the 4 weeks prior to the study, alcohol or illegal drug dependence/abuse and pregnancy. Magnetic resonance imaging (MRI) scanning, blood sampling and clinical assessment were completed on the same day.

The study was approved by the Ethics Committee of the West China Hospital of Sichuan University. All participants provided written informed consent after being informed about the details of the study.

MRI Protocol

The MR imaging scans were performed on a 3.0 Tesla Siemens Magnetom Skyra system. The diffusion tensor images (DTIs) were acquired and the parameters were: two b0 images and 60 images with *b*-value of 1000 s/mm; echo time (TE) 93.0 ms, repetition time (TR) 6800 ms, field of view (FOV) 230 mm × 230 mm × 150 mm, flip angle 90°, voxel size 1.8 mm × 1.8 mm × 3.0 mm, slices 50 and slice thickness 3.0 mm. All acquired images were inspected for significant scanning artifacts and gross brain abnormalities and none were observed in any participant.

Image Processing

The original DICOM images were shifted to NIFTI images using MRIcron software[1] and were then processed using the FDT toolbox of FSL 5.0.6[2]. Head motion and eddy current were corrected and the non-brain tissues were then removed. Diffusion eigenvectors, eigenvalues and FA were calculated. Tract-based spatial statistic (TBSS[3]) was then conducted for voxel-wise statistical analyses (Smith et al., 2006). Briefly, a non-linear registration tool (FNIRT) was used to register the individual FA map into the standard space. All transformed FA maps were combined into a four-dimensional image, averaged to form mean FA images, and finally a mean FA skeleton template was created. The FA threshold was defined at 0.2 to separate WM and non-WM areas, including gray matter, ventricles, and cerebrospinal fluid. Finally, the registered FA images were projected onto the FA skeleton which created a four-dimensional skeletonized image containing all subjects. Similar analyses were performed for axial diffusivity (AD), MD, and RD.

Peripheral IL-10 Measurement

Venous blood was collected from all subjects and heparin was the anticoagulant. Within 30 min of collection, blood samples were centrifuged at 1500 rpm for 20 min. Then, plasma samples were stored at −80°C until the concentrations were measured. The peripheral IL-10 concentrations were determined using the Q-Plex^{TM} Custom Assay and were measured twice. The mean values were calculated for the following statistical analysis.

[1]http://people.cas.sc.edu/rorden/mricron

[2]https://fsl.fmrib.ox.ac.uk/fsl/fslwiki/FSL

[3]https://fsl.fmrib.ox.ac.uk/fsl/fslwiki/TBSS

Clinical Measures

The severity of psychotic symptoms was evaluated by experienced psychiatrists using the Positive and Negative Syndrome Scale (PANSS), which includes three sub-scales (positive symptoms, negative symptoms, and general psychopathology). The cognitive test was conducted by trained and skilled research assistants using the Brief Assessment of Cognition in Schizophrenia (BACS). The BACS tests participants in four domains including verbal memory, processing speed, reasoning and problem solving, and working memory (Keefe et al., 2008). A composite score combining data across subtests was the primary outcome for the following analysis (Eng et al., 2013; Wang et al., 2017).

Statistical Analysis

The statistical analysis for non-imaging data was conducted using SPSS for windows, version 22.0. The continuous variables were compared using a two-sample *t*-test and the categorical variables were analyzed using a chi-square test. The *p*-value was two tailed at a significance level of < 0.05.

To explore the differences of diffusion parameters between schizophrenia patients and healthy controls, voxel-wise statistical analysis was conducted on the skeletonized images using FSL randomize (Winkler et al., 2014) with 5,000 permutations, with age and gender as covariates. Threshold-free cluster enhancements (TFCE) (Smith and Nichols, 2009) was used for the multiple comparison correction, with a significance level at $p < 0.05$. The Johns Hopkins University International Consortium for Brain Mapping (JHU ICBM-DTI-81) WM labels was used to identify the regions showing group differences in diffusion parameters. To explore the relationship between the diffusion parameters (FA, AD, MD, and RD) and peripheral IL-10 and between diffusion parameters and symptom scores, the DTI values for each subject were extracted from the regions with significant differences between these two groups (cluster size > 50 voxels) (see **Supplementary Table S1**). The cluster size was defined as the voxels with $p < 0.05$ and t-value > 3 and was highly conservative compared with previous studies (Dineen et al., 2009; Meng et al., 2018), based on the calculation method suggested by Bullmore et al. (1999).

Linear regression analysis using a stepwise method was performed to examine the relationship between serum IL-10 levels and DTI values (FA, AD, RD, and MD). The difference of correlation coefficients was calculated with the Fisher Z-Transformation test, via the application of the "cocor" package in R (Diedenhofen and Musch, 2015). In addition, the relationship between IL-10/DTI values and clinical variables (including BMI, illness duration, CPZ equivalent, PANSS scores, and BACS score) was investigated using Pearson correlation. False discovery rate (FDR) was applied for multiple comparison correction and statistical significance was defined as less than 0.05.

In the exploratory analysis, to investigate the differences of diffusion parameters between schizophrenia patients and healthy controls, voxel-wise statistical analysis was conducted on the skeletonized images using FSL randomize with 5,000 permutations, with IL-10 as covariate. Threshold-free cluster

enhancements (TFCE) was used for multiple comparison correction, with a significance level at $p < 0.05$. The Johns Hopkins University International Consortium for Brain Mapping (JHU ICBM-DTI-81) WM labels was used to identify the regions showing group differences in diffusion parameters. Findings are available in the **Supplementary Materials**.

RESULTS

Demographic and Clinical Data

The results of demographic and clinical variables are listed in **Table 1**. There were no significant differences in age and gender between the schizophrenia and control groups. There were differences in BMI (schizophrenia: 23.40 ± 3.19 kg/m^2; controls: 22.09 ± 3.01 kg/m^2, $p = 0.04$) and education (schizophrenia: 12.26 ± 2.76 year; controls: 14.49 ± 4.33 year, $p < 0.01$) between the two groups.

The levels of serum IL-10 were higher in patients than in controls (schizophrenia: 10.59 ± 0.24 pg/ml; controls: 9.27 ± 0.24 pg/ml, $p < 0.001$).

TBSS Results

Compared with healthy controls, a widespread reduction of FA were observed in patients, including the right superior longitudinal fasciculus, left inferior fronto-occipital fasciculus, bilateral sagittal stratum, corpus callosum (including genu, body, and splenium), bilateral posterior thalamic radiation (including the optic radiation), right posterior corona radiata and the left anterior corona radiata. A global increase in RD was also found in schizophrenia patients in the right sagittal stratum (include inferior longitudinal fasciculus and inferior fronto-occipital fasciculus), left posterior corona radiata, bilateral anterior corona radiata, body and splenium of the corpus callosum, bilateral superior longitudinal fasciculus and the left posterior thalamic radiation (include optic radiation) compared with the healthy controls. A widespread increase of MD was found in schizophrenia patients compared to the controls, with effects in the corpus callosum (including genu, body, and splenium), right superior corona radiata, right anterior corona radiata and the bilateral superior longitudinal fasciculus. In addition, significant AD reduction was found for the clusters in the right superior corona radiata, right anterior corona radiata and body, and the genu of callosum corpus (see **Figure 1**). In addition, when adjusting for IL-10, the TBSS results of inter-group comparisons were similar with the TBSS findings with age and gender as covariates (see **Supplementary Figure S2**).

Regression Analysis Between IL-10 Levels and Diffusion Measures

Regression analysis showed significant negative correlations between peripheral IL-10 and FA in the right posterior thalamic radiation ($\beta = -0.51$, $p = 0.01$) and left inferior fronto-occipital fasciculus ($\beta = -0.47$, $p = 0.02$) across patients, but not in the controls ($\beta = -0.01$, $p = 0.95$ and $\beta = -0.003$, $p = 0.98$, respectively). The correlation coefficients were statistically different between these two groups ($z = 2.50$, $p = 0.01$ and $z = 2.37$, $p = 0.02$, respectively). Significant negative correlations between IL-10 and MD were found in the right parietal arcuate fasciculus ($\beta = -0.39$, $p = 0.048$) and the body of the corpus callosum ($\beta = -0.43$, $p = 0.03$) in patients, but not in the controls. The correlation coefficients were significantly different ($z = 2.48$, $p = 0.01$ and $z = 2.61$, $p < 0.01$, respectively). In addition, we also found a positive correlation between IL-10 and RD in the right parietal arcuate fasciculus across patients ($\beta = 0.45$, $p = 0.04$) but not in the controls ($\beta = 0.26$, $p = 0.94$). There was no significant difference in the correlation coefficients ($z = 0.98$, $p = 0.32$) (see **Figure 2**). No significant correlation was found between AD changes and peripheral IL-10.

TABLE 1 | Demographic and clinical variables in patients with schizophrenia and healthy controls.

	Patients Mean (*SD*)	Controls Mean (*SD*)	*p*-Value
Age, years [range]	31.85 (11.10) [21–52]	34.63 (9.28) [26–50]	0.19
No. male/female	28/19	22/27	0.15
Handedness	Right	Right	
BMI, kg/m^2	23.40 (3.19)	22.09 (3.01)	0.04
Education, years	12.26 (2.76)	14.49 (4.33)	< 0.01
Illness duration, years	7.77 (6.99)		
Antipsychotic dosage (CPZ equivalent), mg/d	390.45 (174.76)		
PANSS			
Total	59.96 (18.23)		
Positive symptoms	9.71 (4.29)		
Negative symptoms	14.88 (6.76)		
General symptoms	24.96 (8.66)		
BACS			
Composite score	36.77 (12.87)		
IL-10, pg/ml	10.59 (0.24)	9.27 (0.24)	< 0.001

BMI, body mass index; CPZ, chlorpromazine; PANSS, Positive and Negative Syndrome Scale; BACS, Brief Assessment of Cognitive in Schizophrenia; SD, standard deviation.

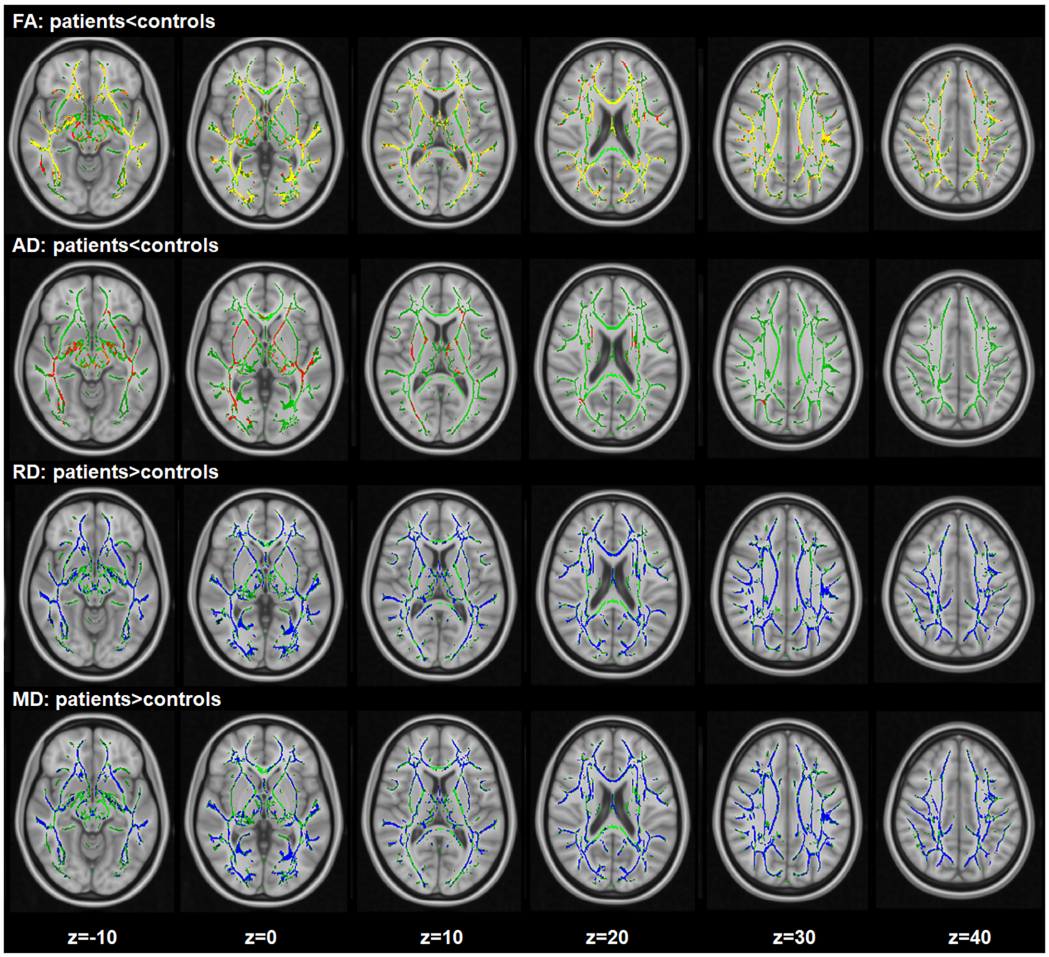

FIGURE 1 | Widespread changes of DTI measures in schizophrenia patients compared with healthy controls. Regions with significant decrease are highlighted in yellow-red/orange. Regions with significant increase are highlighted in blue. Results are shown overlaid on the Montreal Neurologic Institute (MNI) template (1 mm). FA, fractional anisotropy; RD, radial diffusivity; AD, axial diffusivity; MD, mean diffusivity.

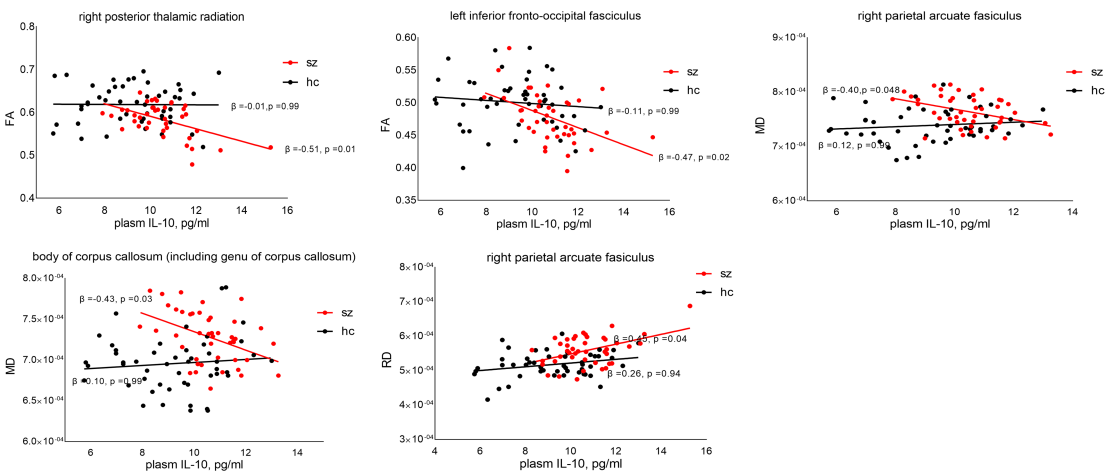

FIGURE 2 | Relationship between peripheral IL-10 and DTI values. *p*-Value was corrected by false discovery rate (FDR). FA, fractional anisotropy; RD, radial diffusivity; MD, mean diffusivity.

Association Between Demographic/Clinical Factors and Peripheral IL-10/DTI Values

There was no significant correlation between serum IL-10 and clinical variables (including BMI, dosage of antipsychotic medications in CPZ equivalents, PANSS scores, and BACS score). No significant correlation was found between DTI values and changes in illness duration or dosage of antipsychotic medications in CPZ equivalents, PANSS scores, and BACS score (see **Supplementary Figure S1**).

DISCUSSION

Focusing on IL-10, a key anti-inflammatory cytokine, the current study provided direct evidence supporting that elevated peripheral IL-10 was related to the disrupted WM integrity of certain bundles in schizophrenia. It therefore provides novel information about the role of cytokines, especially IL-10 in the neuropathology of schizophrenia and adds more evidence relevant to the neuroinflammatory model of schizophrenia.

In our study, systemic IL-10 levels were higher in schizophrenia patients than in healthy subjects, consistent with previous studies (Kunz et al., 2011) and further supporting that the dysregulation of systemic IL-10 is related to the pathogenesis of schizophrenia. Although it remains unclear why the association between systemic IL-10 and WM integrity only existed in schizophrenia patients but not in controls, we assumed that microstructural WM might be more sensitive to IL-10 in patients than healthy subjects. The assumption was supported by the evidence that peripheral cytokines could easily penetrate the blood–brain-barrier (BBB) due to the activated endothelial cell and increased permeability of BBB in schizophrenia (Khandaker and Dantzer, 2016). In addition, a study by Vanessa et al. found that premature newborns with WM injury, who had a high risk of developing mental illness (Baer et al., 2016), had higher IL-10 levels in both cerebrospinal fluid and plasm (Ellison et al., 2005).

How IL-10 might affect microstructural WM integrity remains unclear. Reduced FA values are thought to be related to the disrupted integrity of microstructural WM, impaired axonal membrane and/or demyelination (Beaulieu, 2002). Although the mechanism of reduced FA in schizophrenia is not well-known yet, it is important to note that high IL-10 levels in serum were negatively associated with reduced FA in the posterior thalamic radiata and the inferior fronto-occipital fasciculus in our study. A study *in vitro* found that IL-10 stimulated the activity of macrophage phagocytosis and microglia, which greatly increased myelin phagocytosis (Smith et al., 1998). In addition, a previous study found that IL-10 could enhance initial demyelination via inhibiting the production of interferon γ (IFN-γ) (Puntambekar et al., 2015) while another study suggested that the inflammatory score composited of IL-10, TNF-α, IL-1β, and IL-23 was negatively associated with lower FA within periventricular WM in Alzheimer's disease (Swardfager et al., 2017). Given that increased RD is related to demyelination (Song et al., 2005), the pattern that higher IL-10 is related to higher RD in schizophrenia, as observed in our study, further supports that IL-10 may be involved in the demyelination of WM. Additionally, IL-10 was also associated with the integrity of the axonal membrane (Atkins et al., 2007). The evidence suggests that WM injury may occur under high serum IL-10 in schizophrenia. However, reduced FA is related not only to myelin and axonal integrity but also to neurofilaments, extracellular water content, and track geometry (Jones et al., 2013). IL-10 has been reported to enhance re-myelination and neuron/axonal growth (Gaupp et al., 2008; Yang et al., 2009), and re-myelination can cause shorter internodes and thinner sheaths, which could increase MD (Peters, 2009; Jelescu et al., 2016). Parallel animal studies are required to clarify the role of IL-10 in these factors. Our study found that by adjusting for IL-10, a widespread FA/AD reduction and MD/RD increase in schizophrenia patients compared with controls. Peripheral IL-10 did not alter the abnormalities of WM in patients but peripheral IL-10 was related to WM integrity, indicating that the peripheral IL-10 may play a regulatory role in the disruption of microstructural WM integrity and the pathogenesis of schizophrenia.

Our study noted that peripheral IL-10 was associated with diffusion measures (FA and MD) in certain bundles including the right posterior thalamic radiation, left inferior fronto-occipital fasciculus, corpus callosum and the arcuate fasciculus. FA reduction of the right posterior thalamic radiation and the left inferior fronto-occipital fasciculus, and MD increase in the corpus callosum have been reported in previous neuroimaging studies of schizophrenia (Fitzsimmons et al., 2013; Gong and He, 2015; Sun et al., 2015; Kelly et al., 2018). The posterior thalamic radiation projects fibers to the parietal, temporal and occipital cortex and processes information on body image (Frieling et al., 2012) while the damage to the posterior thalamic radiation could result in self-perception deficits (Lee et al., 2016). In addition, the inferior fronto-occipital fasciculus connected directly to the frontal and occipital areas (Martino et al., 2010) and reduced FA in this tract was associated with positive symptoms, negative symptoms and auditory-verbal hallucinations in schizophrenia (Curcic-Blake et al., 2015; Oestreich et al., 2016). Furthermore, abnormality of the corpus callosum is associated with reality distortion (i.e., hallucinations and delusions) (Whitford et al., 2010) and negative symptoms in schizophrenia (de Witte et al., 2014). It was also noted that the dysregulation of systemic IL-10 was also related to the negative and general symptoms of schizophrenia (Xiu et al., 2014; Kapelski et al., 2016), as well as cognitive function (Xiu et al., 2016), indicating a link between systemic IL-10, WM integrity and clinical symptoms in schizophrenia. However, our study did not observe a significant association between peripheral IL-10 and clinical assessments in schizophrenia, which might be due to several confounding factors including the relatively small sample size and antipsychotic medication.

The present study had some limitations. First, the sample size was relatively small and studies with larger sample size are required to replicate our findings in the future. Second, the patients in our study were medication free but not drug-naïve, so the potential effects of antipsychotic medication could not be excluded completely. However, once

patients were diagnosed with schizophrenia, antipsychotics were immediately administered, before they underwent MRI scanning. Thus, studying patients who are medicated would render findings with a higher generalization. Additionally, investigating pathophysiological changes in patients who are in a clinically stable stage, is also important to identify more convincing findings, since patients at an earlier stage, for example first episode patients, may not have a stable pathophysiology underlying the illness. Third, the cross-sectional nature of our study was limited to determine whether there is a causative relationship between peripheral IL-10 and the alterations of WM integrity in schizophrenia. It is not clear about the longitudinal profile in patients, with respect to the course of schizophrenia. Forth, although IL-10 is a critical cytokine in the immune response, which is a complex process involving many factors. Therefore, future studies investigating more inflammatory mediators and examining their relationship with microstructural WM integrity are necessary for better understanding the pathophysiology of schizophrenia. Fifth, although TBSS analysis is a robust, sensitive and commonly used method in diffusion MR studies, future studies using more methods of DTI analysis are necessary to replicate our findings. Finally, the study only conducted the DTI analysis while an optimized design is necessary to verify the WM abnormalities that could affect DTI results.

In summary, our study revealed that patients with schizophrenia presented elevated peripheral IL-10 levels, which was also related to the deficits of certain WM bundles, including the right posterior thalamic radiation, left inferior fronto-occipital fasciculus, the body of corpus callosum and the arcuate fasciculus. This observation provided *in vivo* evidence supporting the role of IL-10 in structural dysconnectivity, relevant to the neuropathology of schizophrenia.

AUTHOR CONTRIBUTIONS

SL, MW, and JS conceived the study and designed the protocol. GF, WZ, JL, JD, DW, and YX conducted the experiments. GF and WZ conducted the statistical analyses. GF, WZ, FL, JS, CS, MW, and SL interpreted the study findings and contributed to developing the manuscript. GF wrote the first draft of the manuscript, which was reviewed by all authors. GF and WZ contributed equally to this work.

FUNDING

This study was supported by the National Natural Science Foundation of China (Grant Nos. 81671664 and 81621003). SL would also like to acknowledge the support from the Chang Jiang Scholars of China (Award No. Q2015154), the National Program for Support of Top-notch Young Professionals (National Program for Special Support of Eminent Professionals, Organization Department of the Communist Party of China Central Committee, Award No. W02070140), the Fundamental Research Funds for the Central Universities (Grant No. 2018SCUH0011), and the Science and Technology Project of the Health Planning Committee of Sichuan (Grant No. 18ZD035).

ACKNOWLEDGMENTS

We would like to acknowledge all participants of study and the staff of the Department of Psychiatry, West China Hospital of Sichuan University, in the implementation of this project.

SUPPLEMENTARY MATERIAL

The Supplementary Material for this article can be found online at: https://www.frontiersin.org/articles/10.3389/fnins.2019.00052/full#supplementary-material

FIGURE S1 | Relationship between antipsychotic dosage (CPZ equivalent) and DTI values/ peripheral IL-10 levels. FA, fractional anisotropy; RD, radial diffusivity; MD, mean diffusivity; CPZ, chlorpromazine.

FIGURE S2 | Widespread changes of DTI measures in schizophrenia patients compared with healthy controls (peripheral IL-10 as the covariate). Regions with significant decrease are highlighted in yellow-red/orange. Regions with significant increase are highlighted in blue. Results are shown overlaid on the Montreal Neurologic Institute (MNI) template (1 mm). FA, fractional anisotropy; RD, radial diffusivity; AD, axial diffusivity; MD, mean diffusivity.

TABLE S1 | Extracted regions with significant between-group differences in diffusion measures.

REFERENCES

Atkins, S., Loescher, A. R., Boissonade, F. M., Smith, K. G., Occleston, N., O'Kane, S., et al. (2007). Interleukin-10 reduces scarring and enhances regeneration at a site of sciatic nerve repair. *J. Peripher. Nerv. Syst.* 12, 269–276. doi: 10.1111/j.1529-8027.2007.00148.x

Baer, R. J., Chambers, C. D., Bandoli, G., and Jelliffe-Pawlowski, L. L. (2016). Risk of preterm birth by subtype among Medi-Cal participants with mental illness. *Am. J. Obstet. Gynecol.* 215, 519.e1–519.e9. doi: 10.1016/j.ajog.2016.06.017

Beaulieu, C. (2002). The basis of anisotropic water diffusion in the nervous system – a technical review. *NMR Biomed.* 15, 435–455. doi: 10.1002/nbm.782

Benedetti, F., Poletti, S., Hoogenboezem, T. A., Mazza, E., Ambree, O., de Wit, H., et al. (2016). Inflammatory cytokines influence measures of white matter integrity in Bipolar Disorder. *J. Affect. Disord.* 202, 1–9. doi: 10.1016/j.jad.2016.05.047

Borovcanin, M., Jovanovic, I., Dejanovic, S. D., Radosavljevic, G., Arsenijevic, N., and Lukic, M. L. (2015). Increase systemic levels of IL-23 as a possible constitutive marker in schizophrenia. *Psychoneuroendocrinology* 56, 143–147. doi: 10.1016/j.psyneuen.2015.03.003

Bullmore, E. T., Suckling, J., Overmeyer, S., Rabe-Hesketh, S., Taylor, E., and Brammer, M. J. (1999). Global, voxel, and cluster tests, by theory and permutation, for a difference between two groups of structural MR images of the brain. *IEEE Trans. Med. Imaging* 18, 32–42. doi: 10.1109/42.750253

Curcic-Blake, B., Nanetti, L., van der Meer, L., Cerliani, L., Renken, R., Pijnenborg, G. H., et al. (2015). Not on speaking terms: hallucinations and structural network disconnectivity in schizophrenia. *Brain Struct. Funct.* 220, 407–418. doi: 10.1007/s00429-013-0663-y

de Witte, L., Tomasik, J., Schwarz, E., Guest, P. C., Rahmoune, H., Kahn, R. S., et al. (2014). Cytokine alterations in first-episode schizophrenia patients before and after antipsychotic treatment. *Schizophr. Res.* 154, 23–29. doi: 10.1016/j.schres.2014.02.005

Di Biase, M. A., Cropley, V. L., Baune, B. T., Olver, J., Amminger, G. P., Phassouliotis, C., et al. (2017). White matter connectivity disruptions in early and chronic schizophrenia. *Psychol. Med.* 47, 2797–2810. doi: 10.1017/S0033291717001313

Diedenhofen, B., and Musch, J. (2015). cocor: a comprehensive solution for the statistical comparison of correlations. *PLoS One* 10:e0121945. doi: 10.1371/journal.pone.0121945

Dineen, R. A., Vilisaar, J., Hlinka, J., Bradshaw, C. M., Morgan, P. S., Constantinescu, C. S., et al. (2009). Disconnection as a mechanism for cognitive dysfunction in multiple sclerosis. *Brain* 132(Pt 1), 239–249. doi: 10.1093/brain/awn275

Ellison, V. J., Mocatta, T. J., Winterbourn, C. C., Darlow, B. A., Volpe, J. J., and Inder, T. E. (2005). The relationship of CSF and plasma cytokine levels to cerebral white matter injury in the premature newborn. *Pediatr. Res.* 57, 282–286. doi: 10.1203/01.PDR.0000148286.53572.95

Eng, G. K., Lam, M., Bong, Y. L., Subramaniam, M., Bautista, D., Rapisarda, A., et al. (2013). Brief assessment of cognition in schizophrenia: normative data in an English-speaking ethnic Chinese sample. *Arch. Clin. Neuropsychol.* 28, 845–858. doi: 10.1093/arclin/act060

Fitzsimmons, J., Kubicki, M., and Shenton, M. E. (2013). Review of functional and anatomical brain connectivity findings in schizophrenia. *Curr. Opin. Psychiatry* 26, 172–187. doi: 10.1097/YCO.0b013e32835d9e6a

Fond, G., Godin, O., Brunel, L., Aouizerate, B., Berna, F., Bulzacka, E., et al. (2016). Peripheral sub-inflammation is associated with antidepressant consumption in schizophrenia. Results from the multi-center FACE-SZ data set. *J. Affect. Disord.* 191, 209–215. doi: 10.1016/j.jad.2015.11.017

Frieling, H., Fischer, J., Wilhelm, J., Engelhorn, T., Bleich, S., Hillemacher, T., et al. (2012). Microstructural abnormalities of the posterior thalamic radiation and the mediodorsal thalamic nuclei in females with anorexia nervosa–a voxel based diffusion tensor imaging (DTI) study. *J. Psychiatr. Res.* 46, 1237–1242. doi: 10.1016/j.jpsychires.2012.06.005

Frodl, T., and Amico, F. (2014). Is there an association between peripheral immune markers and structural/functional neuroimaging findings? *Prog. Neuropsychopharmacol. Biol. Psychiatry* 48, 295–303. doi: 10.1016/j.pnpbp.2012.12.013

Fung, S. J., Joshi, D., Fillman, S. G., and Weickert, C. S. (2014). High white matter neuron density with elevated cortical cytokine expression in schizophrenia. *Biol. Psychiatry* 75, e5–e7. doi: 10.1016/j.biopsych.2013.05.031

Gao, L., Li, Z., Chang, S., and Wang, J. (2014). Association of interleukin-10 polymorphisms with schizophrenia: a meta-analysis. *PLoS One* 9:e90407. doi: 10.1371/journal.pone.0090407

Gaupp, S., Cannella, B., and Raine, C. S. (2008). Amelioration of experimental autoimmune encephalomyelitis in IL-4Ralpha-/- mice implicates compensatory up-regulation of Th2-type cytokines. *Am. J. Pathol.* 173, 119–129. doi: 10.2353/ajpath.2008.071156

Gong, Q., and He, Y. (2015). Depression, neuroimaging and connectomics: a selective overview. *Biol. Psychiatry* 77, 223–235. doi: 10.1016/j.biopsych.2014.08.009

Jelescu, I. O., Zurek, M., Winters, K. V., Veraart, J., Rajaratnam, A., Kim, N. S., et al. (2016). In vivo quantification of demyelination and recovery using compartment-specific diffusion MRI metrics validated by electron microscopy. *Neuroimage* 132, 104–114. doi: 10.1016/j.neuroimage.2016.02.004

Jones, D. K., Knosche, T. R., and Turner, R. (2013). White matter integrity, fiber count, and other fallacies: the do's and don'ts of diffusion MRI. *Neuroimage* 73, 239–254. doi: 10.1016/j.neuroimage.2012.06.081

Kapelski, P., Skibinska, M., Maciukiewicz, M., Pawlak, J., Zaremba, D., and Twarowska-Hauser, J. (2016). Family-based association study of interleukin 10 (IL10) and interleukin 10 receptor alpha (IL10RA) functional polymorphisms in schizophrenia in Polish population. *J. Neuroimmunol.* 297, 92–97. doi: 10.1016/j.jneuroim.2016.05.010

Keefe, R. S., Harvey, P. D., Goldberg, T. E., Gold, J. M., Walker, T. M., Kennel, C., et al. (2008). Norms and standardization of the Brief Assessment of Cognition in Schizophrenia (BACS). *Schizophr. Res.* 102, 108–115. doi: 10.1016/j.schres.2008.03.024

Kelly, S., Jahanshad, N., Zalesky, A., Kochunov, P., Agartz, I., Alloza, C., et al. (2018). Widespread white matter microstructural differences in schizophrenia across 4322 individuals: results from the ENIGMA Schizophrenia DTI Working Group. *Mol. Psychiatry* 23, 1261–1269. doi: 10.1038/mp.2017.170

Khandaker, G. M., and Dantzer, R. (2016). Is there a role for immune-to-brain communication in schizophrenia? *Psychopharmacology* 233, 1559–1573. doi: 10.1007/s00213-015-3975-1

Kunz, M., Cereser, K. M., Goi, P. D., Fries, G. R., Teixeira, A. L., Fernandes, B. S., et al. (2011). Serum levels of IL-6, IL-10 and TNF-alpha in patients with bipolar disorder and schizophrenia: differences in pro- and anti-inflammatory balance. *Braz. J. Psychiatr.* 33, 268–274. doi: 10.1590/S1516-44462011000300010

Lee, E. E., Hong, S., Martin, A. S., Eyler, L. T., and Jeste, D. V. (2017). Inflammation in schizophrenia: cytokine levels and their relationships to demographic and clinical variables. *Am. J. Geriatr. Psychiatry* 25, 50–61. doi: 10.1016/j.jagp.2016.09.009

Lee, S. J., Kim, B., Oh, D., Kim, M. K., Kim, K. H., Bang, S. Y., et al. (2016). White matter alterations associated with suicide in patients with schizophrenia or schizophreniform disorder. *Psychiatry Res. Neuroimaging* 248, 23–29. doi: 10.1016/j.pscychresns.2016.01.011

Martino, J., Brogna, C., Robles, S. G., Vergani, F., and Duffau, H. (2010). Anatomic dissection of the inferior fronto-occipital fasciculus revisited in the lights of brain stimulation data. *Cortex* 46, 691–699. doi: 10.1016/j.cortex.2009.07.015

Meng, L., Chen, Y., Xu, X., Chen, T., Lui, S., Huang, X., et al. (2018). The neurobiology of brain recovery from traumatic stress: a longitudinal DTI study. *J. Affect. Disord.* 225, 577–584. doi: 10.1016/j.jad.2017.08.075

Meyer, U., Murray, P. J., Urwyler, A., Yee, B. K., Schedlowski, M., and Feldon, J. (2008). Adult behavioral and pharmacological dysfunctions following disruption of the fetal brain balance between pro-inflammatory and IL-10-mediated anti-inflammatory signaling. *Mol. Psychiatry* 13, 208–221. doi: 10.1038/sj.mp.4002042

Murray, P. J. (2006). Understanding and exploiting the endogenous interleukin-10/STAT3-mediated anti-inflammatory response. *Curr. Opin. Pharmacol.* 6, 379–386. doi: 10.1016/j.coph.2006.01.010

Najjar, S., and Pearlman, D. M. (2015). Neuroinflammation and white matter pathology in schizophrenia: systematic review. *Schizophr. Res.* 161, 102–112. doi: 10.1016/j.schres.2014.04.041

Oestreich, L. K., McCarthy-Jones, S., and Whitford, T. J. (2016). Decreased integrity of the fronto-temporal fibers of the left inferior occipito-frontal fasciculus associated with auditory verbal hallucinations in schizophrenia. *Brain Imaging Behav.* 10, 445–454. doi: 10.1007/s11682-015-9421-5

Pang, Y., Rodts-Palenik, S., Cai, Z., Bennett, W. A., and Rhodes, P. G. (2005). Suppression of glial activation is involved in the protection of IL-10 on maternal *E. coli* induced neonatal white matter injury. *Brain Res. Dev. Brain Res.* 157, 141–149. doi: 10.1016/j.devbrainres.2005.03.015

Peters, A. (2009). The effects of normal aging on myelinated nerve fibers in monkey central nervous system. *Front. Neuroanat.* 3:11. doi: 10.3389/neuro.05.011.2009

Prasad, K. M., Upton, C. H., Nimgaonkar, V. L., and Keshavan, M. S. (2015). Differential susceptibility of white matter tracts to inflammatory mediators in schizophrenia: an integrated DTI study. *Schizophr. Res.* 161, 119–125. doi: 10.1016/j.schres.2014.09.043

Puntambekar, S. S., Hinton, D. R., Yin, X., Savarin, C., Bergmann, C. C., Trapp, B. D., et al. (2015). Interleukin-10 is a critical regulator of white matter lesion containment following viral induced demyelination. *Glia* 63, 2106–2120. doi: 10.1002/glia.22880

Shivakumar, V., Debnath, M., Venugopal, D., Rajasekaran, A., Kalmady, S. V., Subbanna, M., et al. (2018). Influence of correlation between HLA-G polymorphism and Interleukin-6 (IL6) gene expression on the risk of schizophrenia. *Cytokine* 107, 59–64. doi: 10.1016/j.cyto.2017.11.016

Smith, M. E., van der Maesen, K., and Somera, F. P. (1998). Macrophage and microglial responses to cytokines in vitro: phagocytic activity, proteolytic enzyme release, and free radical production. *J. Neurosci. Res.* 54, 68–78. doi: 10.1002/(sici)1097-4547(19981001)54

Smith, S. M., Jenkinson, M., Johansen-Berg, H., Rueckert, D., Nichols, T. E., Mackay, C. E., et al. (2006). Tract-based spatial statistics: voxelwise analysis of multi-subject diffusion data. *Neuroimage* 31, 1487–1505. doi: 10.1016/j.neuroimage.2006.02.024

Smith, S. M., and Nichols, T. E. (2009). Threshold-free cluster enhancement: addressing problems of smoothing, threshold dependence and localisation in cluster inference. *Neuroimage* 44, 83–98. doi: 10.1016/j.neuroimage.2008.03.061

Song, S. K., Yoshino, J., Le, T. Q., Lin, S. J., Sun, S. W., Cross, A. H., et al. (2005). Demyelination increases radial diffusivity in corpus callosum of mouse brain. *Neuroimage* 26, 132–140. doi: 10.1016/j.neuroimage.2005.01.028

Sugino, H., Futamura, T., Mitsumoto, Y., Maeda, K., and Marunaka, Y. (2009). Atypical antipsychotics suppress production of proinflammatory cytokines and up-regulate interleukin-10 in lipopolysaccharide-treated mice. *Prog. Neuropsychopharmacol. Biol. Psychiatry* 33, 303–307. doi: 10.1016/j.pnpbp.2008.12.006

Sun, H., Lui, S., Yao, L., Deng, W., Xiao, Y., Zhang, W., et al. (2015). Two patterns of white matter abnormalities in medication-naive patients with first-episode schizophrenia revealed by diffusion tensor imaging and cluster analysis. *JAMA Psychiatry* 72, 678–686. doi: 10.1001/jamapsychiatry.2015.0505

Swardfager, W., Yu, D., Ramirez, J., Cogo-Moreira, H., Szilagyi, G., Holmes, M. F., et al. (2017). Peripheral inflammatory markers indicate microstructural damage within periventricular white matter hyperintensities in Alzheimer's disease: a preliminary report. *Alzheimers Dement.* 7, 56–60. doi: 10.1016/j.dadm.2016.12.011

Vidal, P. M., Lemmens, E., Dooley, D., and Hendrix, S. (2013). The role of "anti-inflammatory" cytokines in axon regeneration. *Cytokine Growth Factor Rev.* 24, 1–12. doi: 10.1016/j.cytogfr.2012.08.008

Viher, P. V., Stegmayer, K., Giezendanner, S., Federspiel, A., Bohlhalter, S., Vanbellingen, T., et al. (2016). Cerebral white matter structure is associated with DSM-5 schizophrenia symptom dimensions. *Neuroimage Clin.* 12, 93–99. doi: 10.1016/j.nicl.2016.06.013

Wang, L. J., Huang, Y. C., Hung, C. F., Chen, C. K., Chen, Y. C., Lee, P. Y., et al. (2017). The Chinese version of the brief assessment of cognition in schizophrenia: data of a large-scale mandarin-speaking population. *Arch. Clin. Neuropsychol.* 32, 289–296. doi: 10.1093/arclin/acw100

Whitford, T. J., Kubicki, M., Schneiderman, J. S., O'Donnell, L. J., King, R., Alvarado, J. L., et al. (2010). Corpus callosum abnormalities and their association with psychotic symptoms in patients with schizophrenia. *Biol. Psychiatry* 68, 70–77. doi: 10.1016/j.biopsych.2010.03.025

Willette, A. A., Coe, C. L., Birdsill, A. C., Bendlin, B. B., Colman, R. J., Alexander, A. L., et al. (2013). Interleukin-8 and interleukin-10, brain volume and microstructure, and the influence of calorie restriction in old rhesus macaques. *Age* 35, 2215–2227. doi: 10.1007/s11357-013-9518-y

Winkler, A. M., Ridgway, G. R., Webster, M. A., Smith, S. M., and Nichols, T. E. (2014). Permutation inference for the general linear model. *Neuroimage* 92, 381–397. doi: 10.1016/j.neuroimage.2014.01.060

Xiu, M. H., Man, L. J., Wang, D., Du, X., Yin, G., Zhang, Y., et al. (2018). Tumor necrosis factor-alpha -1031T/C polymorphism is associated with cognitive deficits in chronic schizophrenia patients versus healthy controls. *Am. J. Med. Genet. B Neuropsychiatr. Genet.* 177, 379–387. doi: 10.1002/ajmg.b.32622

Xiu, M. H., Tian, L., Chen, S., Tan, Y. L., Chen, D. C., Chen, J., et al. (2016). Contribution of IL-10 and its -592 A/C polymorphism to cognitive functions in first-episode drug-naive schizophrenia. *Brain Behav. Immun.* 57, 116–124. doi: 10.1016/j.bbi.2016.03.005

Xiu, M. H., Yang, G. G., Tan, Y. L., Chen, D. C., Tan, S. P., Wang, Z. R., et al. (2014). Decreased interleukin-10 serum levels in first-episode drug-naive schizophrenia: relationship to psychopathology. *Schizophr. Res.* 156, 9–14. doi: 10.1016/j.schres.2014.03.024

Yang, J., Jiang, Z., Fitzgerald, D. C., Ma, C., Yu, S., Li, H., et al. (2009). Adult neural stem cells expressing IL-10 confer potent immunomodulation and remyelination in experimental autoimmune encephalitis. *J. Clin. Invest.* 119, 3678–3691. doi: 10.1172/JCI37914

Conflict of Interest Statement: The authors declare that the research was conducted in the absence of any commercial or financial relationships that could be construed as a potential conflict of interest.

frontiers in Neuroscience

ORIGINAL RESEARCH
published: 07 February 2019
doi: 10.3389/fnins.2019.00063

Local Diffusion Homogeneity Provides Supplementary Information in T2DM-Related WM Microstructural Abnormality Detection

Yi Liang[1,2†], Han Zhang[3†], Xin Tan[2], Jiarui Liu[1], Chunhong Qin[2], Hui Zeng[1], Yanting Zheng[1], Yujie Liu[1], Jingxian Chen[1], Xi Leng[2], Shijun Qiu[1,2] and Dinggang Shen[3,4*]*

[1] Medical Imaging Research Office, Guangzhou University of Chinese Medicine, Guangzhou, China, [2] Department of Medical Imaging, The First Affiliated Hospital of Guangzhou University of Chinese Medicine, Guangzhou, China, [3] Department of Radiology and BRIC, University of North Carolina at Chapel Hill, Chapel Hill, NC, United States, [4] Department of Brain and Cognitive Engineering, Korea University, Seoul, South Korea

OPEN ACCESS

Edited by:
Lin Shi,
Chinese University of Hong Kong, China

Reviewed by:
Bing Zhang,
Nanjing Drum Tower Hospital, China
Xiang-Zhen Kong,
Max Planck Institute for Psycholinguistics, Netherlands

***Correspondence:**
Shijun Qiu
qiu-sj@163.com
Dinggang Shen
dgshen@med.unc.edu

[†] These authors have contributed equally to this work

Specialty section:
This article was submitted to Brain Imaging Methods, a section of the journal Frontiers in Neuroscience

Received: 24 September 2018
Accepted: 22 January 2019
Published: 07 February 2019

Citation:
Liang Y, Zhang H, Tan X, Liu J, Qin C, Zeng H, Zheng Y, Liu Y, Chen J, Leng X, Qiu S and Shen D (2019) Local Diffusion Homogeneity Provides Supplementary Information in T2DM-Related WM Microstructural Abnormality Detection. Front. Neurosci. 13:63. doi: 10.3389/fnins.2019.00063

Objectives: We aimed to investigate whether an *inter-voxel* diffusivity metric (local diffusion homogeneity, LDH), can provide supplementary information to traditional intra-voxel metrics (i.e., fractional anisotropy, FA) in white matter (WM) abnormality detection for type 2 diabetes mellitus (T2DM).

Methods: Diffusion tensor imaging was acquired from 34 T2DM patients and 32 healthy controls. Voxel-based group-difference comparisons based on LDH and FA, as well as the association between the diffusion metrics and T2DM risk factors [i.e., body mass index (BMI) and systolic blood pressure (SBP)], were conducted, with age, gender and education level controlled.

Results: Compared to the controls, T2DM patients had higher LDH in the pons and left temporal pole, as well as lower FA in the left superior corona radiation ($p < 0.05$, corrected). In T2DM, there were several overlapping WM areas associated with BMI as revealed by both LDH and FA, including right temporal lobe and left inferior parietal lobe; but the unique areas revealed only by using LDH included left inferior temporal lobe, right supramarginal gyrus, left pre- and post-central gyrus (at the semiovale center), and right superior radiation. Overlapping WM areas that associated with SBP were found with both LDH and FA, including right temporal pole, bilateral orbitofrontal area (rectus gyrus), the media cingulum bundle, and the right cerebellum crus I. However, the unique areas revealed only by LDH included right inferior temporal lobe, right inferior occipital lobe, and splenium of corpus callosum.

Conclusion: Inter- and intra-voxel diffusivity metrics may have different sensitivity in the detection of T2DM-related WM abnormality. We suggested that LDH could provide supplementary information and reveal additional underlying brain changes due to diabetes.

Keywords: type 2 diabetes mellitus, diffusion tensor imaging, local diffusion homogeneity, white matter, fractional anisotropy

INTRODUCTION

Type 2 diabetes mellitus, a complex metabolic disorder characterized by increased blood glucose level, affects more than 425 million people, especially those younger than 65 years (International Diabetes Federation, 2017). T2DM patients could develop many severe complications, among which the increased risk of dementia has been more and more reported (Biessels et al., 2006; Kodl and Seaquist, 2008; McCrimmon et al., 2012). The deterioration of normal frontal lobe functions are frequently reported in T2DM studies (Kawamura et al., 2012; McCrimmon et al., 2012), possibly responsible to cognitive impairment, and malfunctioned executive control abilities (Xia et al., 2013; Cui et al., 2014; Garcia-Casares et al., 2014; Zhang et al., 2014). Since the dementia progression cannot be reversed and a heavy social burden could be elicited, it is of great important to identify potential image-based alterations for better understanding of the cognitive decline in T2DM (Hsu et al., 2012; Biessels and Reijmer, 2014; Brundel et al., 2014; Xia et al., 2017).

Recent evidence based on *in vivo* neuroimaging technique showed that the abnormal neural activities were even found in the T2DM subjects who still have normal cognition (Yang et al., 2016; Zhang et al., 2018). To this end, blood-oxygen-level-dependent (BOLD), functional magnetic resonance imaging (fMRI) has been used as a non-invasive brain functional imaging technique in several T2DM brain functional studies (Brundel et al., 2014). It was reported that the functional connectivity of the default mode network and executive control network in T2DM patients has been impaired despite no clinically significant cognitive decline was found (Yang et al., 2016). However, the neuropathology and pathophysiology of the early cognitive dysfunctions in T2DM are still not clear (Biessels et al., 2006; Kodl and Seaquist, 2008; Kawamura et al., 2012).

Another widely used complementary non-invasive MRI technique is diffusion tensor imaging (DTI), which has higher resolution and better signal-to-noise ratio than fMRI and can sensitively detect changes of constrained molecular water diffusivity in the WM (Alexander et al., 2007). DTI has long been used as a sensitive and objective technique searching for subtle changes in WM in many diseases (O'Donnell and Westin, 2011; Guo W. et al., 2012; Wang et al., 2015; Ding et al., 2018). It is reasonable that WM changes in specific fiber tracts might have led to disrupted information exchange, thus deteriorating functional integration among brain regions (Wakana et al., 2004; Alexander et al., 2007; Reijmer et al., 2013b; Biessels and Reijmer, 2014; Moheet et al., 2015) and further causing cognitive deficits in T2DM. However, for the T2DM patients who have not developed substantial cognitive impairment, only very few DTI studies have been published (Hsu et al., 2012; Zhang et al., 2014), most of which used conventional metrics such as fractional anisotropy (FA) (Beaulieu, 2002; O'Donnell and Westin, 2011; Guo W.B. et al., 2012). One of the limitations of the conventional DTI metrics is that they may not be adequately sensitive to the subtle changes in T2DM patients at the preclinical stage. For example, in a study by our group, we found significantly decreased FA in neurotypical, middle-aged T2DM patients in the fronto-cingulo-parietal areas, cerebellum vermis, and bilateral thalamus (Tan et al., 2016). However, different results have also been reported in other studies (Hsu et al., 2012; Zhang et al., 2014). It might be useful to use another (more sensitive) DTI metrics for T2DM studies.

From the method point of view, FA, and other conventionally used *intra-voxel* diffusivity indices all depend on an assumed tensor model (Alexander et al., 2007), while different models could lead to different results (O'Donnell and Westin, 2011). In a seminal paper (Gong, 2013), an *inter-voxel* measurement, local diffusion homogeneity (LDH), was proposed to reveal more comprehensive WM changes. LDH is a model-free diffusivity index calculated from raw diffusion-weighted images (DWI) that measures the inter-voxel similarity of the full diffusion profiles across a few closely located voxels. Specifically, Kendall's coefficient of concordance is used to quantify such an overall diffusivity similarity between a centered voxel and those of all its nearest neighborhood (Gong, 2013). For example, a higher LDH value may indicate local coherence enhancement of the fibers, possibly caused by changes in fiber myelination, diameter, or density (Gong, 2013; Liu et al., 2016, 2017).

In this study, we used LDH to study T2DM-related brain changes as helpful supplements to the previous FA-based studies, aiming to test whether it is highly feasible to use such an inter-voxel diffusivity metric in the assessment of T2DM-induced brain WM changes. The LDH- and FA-based results were systematically compared. In addition to the group difference comparisons, we also searched for possible associations between imaging phenotypes (LDH/FA) and certain clinical risk factors (BMI and SBP) for both T2DMs and healthy controls as another evidence of the systematic differences between inter- (LDH) and intra-voxel indices (FA). Our hypothesis is that LDH could detect additional WM alterations compared to FA, which might provide new insights into the neuropathology and pathophysiology underlying the cognitive dysfunction in T2DM.

MATERIALS AND METHODS

Participants

We focused on the T2DM patients without clinically significant cognitive decline or any significant brain diseases in the aim of searching for an early sign of the WM changes. This study was approved by the local ethics committee. Written informed consents from all participants were obtained. T2DM subjects were selected from hospitalized patients from the endocrinology department of the hospital, and healthy controls were from the volunteers over the same period. T2DM was diagnosed using fasting blood glucose >7.0 mmol/L on two separate occasions, or 2-h blood glucose level >11.1 mmol/L during a 75 g oral glucose tolerance test (American Diabetes, 2010; International Diabetes Federation, 2017). All the T2DM subjects

Abbreviations: ARWMCs, age-related white matter changes; BMI, body mass index; CST, corticospinal tract; DTI, diffusion tensor image; DWI, diffusion-weighted image; FA, fractional anisotropy; FOV, field of view; LDH, local diffusion homogeneity; MRI, magnetic resonance image; SBP, systolic blood pressure; T2DM, type 2 diabetes mellitus; TE, echo time; TR, repetition time; WM, white matter; WMHs, white matter hyperintensities.

received insulin via a pump or subcutaneous injection during hospitalization. All participants received a detailed neurological examination by experienced neurologists to make sure there were no significant cognitive complaints nor positive neurological symptoms. General clinical measurements and demographic information for each subject were collected, including biological tests, chest X-ray, electrocardiogram, BMI [weight (kg)/height (meter)^2], education level, blood pressure during rest, and duration of the disease (for T2DM patients only).

Exclusion criteria for both groups were as follows: impaired glucose tolerance or impaired fasting glucose (International Diabetes Federation, 2017), serious eye diseases, any sign of cognitive impairment or positive neurological symptoms, any history of neurologic abnormality, serious head injury (with loss of consciousness >5min), severe hypoglycemia or hyperlipemia, left or mixed-handedness, BMI > 30 kg/m^2, substance (e.g., alcohol, tobacco, psychoactive drug) abuse, hypertension (the cut-off values are based on the Seventh Report of the Joint National Committee on Prevention, Detection, Evaluation, and Treatment of High Blood Pressure (JNC 7), i.e., SBP = 140 mm Hg or a diastolic blood pressure = 90 mm Hg) (Whelton and Carey, 2017), hyperlipemia, specific abnormalities finding in conventional MRI scans, or other factors that might affect brain structure and function (e.g., chronic infections, organic failure, and psychiatric diseases). In addition, all the T2DM subjects took single-field fundus photography for the evaluation of diabetic retinopathy. Based on the International Clinical Disease Severity Scale for diabetic retinopathy, the subjects at the first stage (no apparent retinopathy) and the second stage (mild non-proliferative retinopathy) were included, while those at the third or higher stages, or with macular edema were excluded (Abbas et al., 2017).

Microvascular Disease Assessment

Small vascular disease [white matter hyperintensities (WMHs) or lacunar infarction] is commonly found in T2DM patients, especial the more elderly patients, and are also associated with neurological impairment (Kodl and Seaquist, 2008). Therefore, it is necessary to make sure these complications will not contribute to our results. WMHs and lacunar infarcts were quantitatively assessed using an age-related WM changes scale (ARWMCs) as described before (Wahlund et al., 2001). Two experienced radiologists blinded to group allocations separately performed the rating. The consensus was obtained through discussion between the two raters if they rated differently. All participants with lacunar infarcts or a rating score >2 were excluded.

MRI Acquisition

All participants received whole-brain MRI scans with a 3T scanner (SIGNA EXCITE GE Medical Systems, United States) and an 8-channel head coil. The scan time was within 1 week after enrollment and 2–3 h after a meal. First, the axial T1-weighted [repetition time (TR)/echo time (TE) = 2100/24 ms, field of view (FOV) = 22 cm × 22 cm, slice thickness = 5 mm with 1-mm gap], T2-weighted (TR/TE) = 4917/107 ms, FOV = 22 cm × 22 cm, slice thickness = 5 mm with 1-mm gap), and fluid-attenuated inversion recovery (TR/TE = 9000/120 ms, FOV = 24 cm × 24 cm, matrix size = 512 × 512, slice thickness = 5 mm with 1.5-mm gap) were scanned. These clinical scans were used for clinical evaluation to make sure there was no positive finding (e.g., infarction and malformations) from any subject. The high-resolution structural 3D T1-weighted images (256 × 256 image matrix with 160 continuous sagittal slices, 1-mm isotropic voxels) and DTI data (single-shot echo-planar imaging sequence, TR/TE = 12,000/75.5 ms, flip angle = 90°, FOV = 24 cm × 24 cm, matrix size = 128 × 128, axial slice thickness = 3 mm without gap, 25 optional non-linearly distributed directions with b values of 1000 s/mm^2 and one image with b = 0 s/mm^2, acquisition time = 5 min 36 s) were acquired.

Image Processing

All DTI data processing was implemented using a pipelined toolbox, PANDA[1] (Cui et al., 2013), which is based on the FSL[2] preprocessing pipeline. Eddy-current induced geometric distortions and head motion of all raw diffusion data were firstly corrected. The diffusivity along each diffusion-weighted gradient direction was calculated from the original DWI, which generated a series of diffusivity values at each voxel. Kendall's coefficient of concordance was applied to quantify the overall similarity of the diffusivity vectors between a centering voxel and its 26 neighborhoods and was attributed to this centering voxel as LDH (Gong, 2013). An LDH map was thus computed for each subject inside a WM mask that was generated by averaging the un-smoothed FA maps across all healthy controls followed by a threshold of FA > 0.25. For comparison, we also generated FA maps for each subject by fitting a diffusion tensor model for each voxel and calculating three eigenvalues (λ1, λ2, and λ3) for voxel-wise FA calculation. For each subject, both LDH and FA maps were generated in the native space. The individual FA maps were non-linearly registered to an FA template in FSL using FNIRT, and the deformation field was applied to each individual's LDH map to warp them into the common standard space. The LDH and FA maps were further spatially smoothed with a 6-mm full-width-at-half-maximum (FWHM) isotropic Gaussian kernel.

Group Comparison of Inter- and Intra-Voxel Metrics

To identify the potential T2DM imaging markers based on both LDH and FA, voxel-wise group comparisons between the T2DM subjects and healthy controls within the WM mask were conducted using two-sample t-tests for the LDH and FA maps, separately. The two-sample t-tests were conducted based on a general linear model with REST v1.8 toolbox (Song et al., 2011). Age, gender, and education level were considered as covariates during the group comparisons and were regressed out. All the statistical maps were corrected for multiple comparisons using a Monte Carlo simulation (AlphaSim), with parameters as follows: FWHM = 6 mm, 1000 simulations, and edge connection. Of note, there are alternative methods to conduct AlphaSim correlation with estimated smoothness from residual maps or

[1] http://www.nitrc.org/projects/panda

[2] http://fsl.fmrib.ox.ac.uk/fsl

statistical maps, which has been suggested as a standard when reporting fMRI results (Poldrack et al., 2008). A voxels level p value < 0.01 (two-tailed) and a cluster-level p-value < 0.05 with cluster size > 71 mm^3 were considered to be significant.

Correlation Between Diffusion Indices and Clinical Measurements

Overweight or obesity (commonly detected by BMI) was an independent risk factor for diabetes, and hypertension (measured by SBP cut points) have also been associated with increased risk of cognitive and cerebrovascular dysfunction (Biessels et al., 2006; Kodl and Seaquist, 2008; Kawamura et al., 2012). Hence, both BMI and SBP were chosen to measure the biological/clinical correlation with both diffusion indices within the T2DM group and control group, separately. Specifically, voxel-wise Pearson's correction analysis was used to calculate the correlations between diffusion matrixes (LDH and FA) and clinical measurements (BMI and SBP) in the same WM mask. These correlation analyses were also conducted in a voxel-wise manner based on a general linear model with REST v1.8 with the same nuisance covariates added and the same threshold strategy applied (AlphaSim corrected p value < 0.05). Such image–clinical measurement association analyses can also demonstrate different sensitivity between these two diffusion indices.

TABLE 1 | Demographic and clinical characteristics and diffusion metrics in the regions of interest.

	Controls (n = 32)	T2DM (n = 34)	p
Age (years)	56.31 ± 4.46	58.29 ± 4.19	0.067
Gender (M/F)	18/14	10/24	0.027
BMI (kg/m^2)	20.58 ± 1.47	24.36 ± 1.89	< 0.001
SBP (mmHg)	114.94 ± 5.65	124.38 ± 10.25	< 0.001
Diastolic (mmHg)	69.21 ± 4.71	76.26 ± 6.65	0.03
Education (years)	9.75 ± 1.32	10.50 ± 1.21	0.019
FDG (mmol/L)	5.28 ± 0.23	6.64 ± 2.00	< 0.001
TG (mmol/L)	1.46 ± 0.30	1.62 ± 0.44	0.101
TC (mmol/L)	4.54 ± 0.36	4.78 ± 0.98	0.205
HDL (mmol/L)	0.96 ± 0.12	1.01 ± 0.19	0.228
LDL (mmol/L)	2.46 ± 0.21	2.55 ± 0.47	0.267
HbA1c (%)	–	7.85 ± 1.34	–
Course of disease (y)	–	6.85 (3-14)	–
LDH at pons	0.48 ± 0.09	0.56 ± 0.08	0.001
LDH at L temporal pole	0.60 ± 0.05	0.64 ± 0.04	0.003
FA at L corona	0.42 ± 0.02	0.39 ± 0.03	< 0.001

Data are presented as means ± SD, numbers of male and female, or median (range). BMI, body mass index; SBP, systolic blood pressure; FDG, averaged fasting glucose; TG, triglyceride; TC, total cholesterol; HDL, high-density lipoprotein; LDL, low-density lipoprotein; HbA1c, glycosylated hemoglobin. LDH at pons, LDH at L temporal pole: LDH values extracted from pons and left temporal pole, respectively; FA at L corona, FA value extracted from left superior corona radiate.

RESULTS

Demographic and Clinical Characteristics

Demographic and clinical measurements of the 34 T2DM and 32 controls are summarized in **Table 1**. T2DM subjects had higher BMI, SBP, education level, and averaged fasting glucose than the healthy controls. Twenty (58.8%) and one (3%) T2DM subject were considered as overweight (BMI, 24–28 kg/m^2) and obesity (BMI $>$ 28 kg/m^2), respectively (Shang et al., 2013). Nine (26.5%) T2DM subjects with SBP greater than 130 mmHg were categorized as stage-1 hypertension. No control subject was found to have either a BMI $>$ 24 kg/m^2 or a SBP $>$ 130 mmHg.

Microvascular Disease Assessment

Most T2DM (n = 26) and control subjects (n = 28) had an ARWMCs scale of 0, while the remaining (eight subjects in T2DM and four in the control group) who were detected with WMHs $\geq$ 5 mm based on both T2 and FLAIR images had an ARWMCs scale of 1, involving bilateral frontal lobes (n = 4), superior radiation (n = 6), occipital lobes (n = 4) and left temporal lobe (n = 1). Lacunar infarction was not found in any of the participants. Four subjects in the T2DM group were classified as the second stage (mild-to-moderate, non-proliferative) retinopathy, and the rest had no apparent retinopathy (American Diabetes, 2010).

Group Differences in LDH and FA

Significantly higher LDH were found in the pons and the left temporal pole in T2DM subjects compared to the healthy controls (**Figures 1A,B**). There was no decreased LDH observed in the T2DM group. Decreased FA in the T2DM group was only found in the left superior corona radiate (**Figure 1C**). The mean LDH and FA values within these ROIs were listed in **Table 1** and clusters details were listed in **Table 2**.

Correlation Between Diffusion Indices and Clinical Measurements

No correlations were found between the clinical measures and the LDH/FA within the regions that showed the difference between the two groups. In the following exploratory voxel-wise correlation analysis, BMI- or SBP-associated LDH and FA in the WM were detected for both groups. We found that for the T2DM group, several clusters that presented correlations between BMI/SBP and LDH had similar locations with comparable sizes and peak values to those clusters that presented correlations between BMI/SBP and FA (**Table 3**, see also the blue-colored areas in **Figure 2**, which indicated the overlapping clusters using the LDH-based results). From the scatter plots in **Figure 2**, we found that increased LDH and FA in most of the regions were associated with greater BMI or SBP ($p < 0.05$, corrected). None of these correlations between diffusion metrics and clinical measurements were found in the healthy controls ($p > 0.05$), except the left temporal lobe, where increased LDH values were associated with lower BMI in both groups. All these results were obtained after adjusting for age, gender and education level. Further details are listed in **Table 3**.

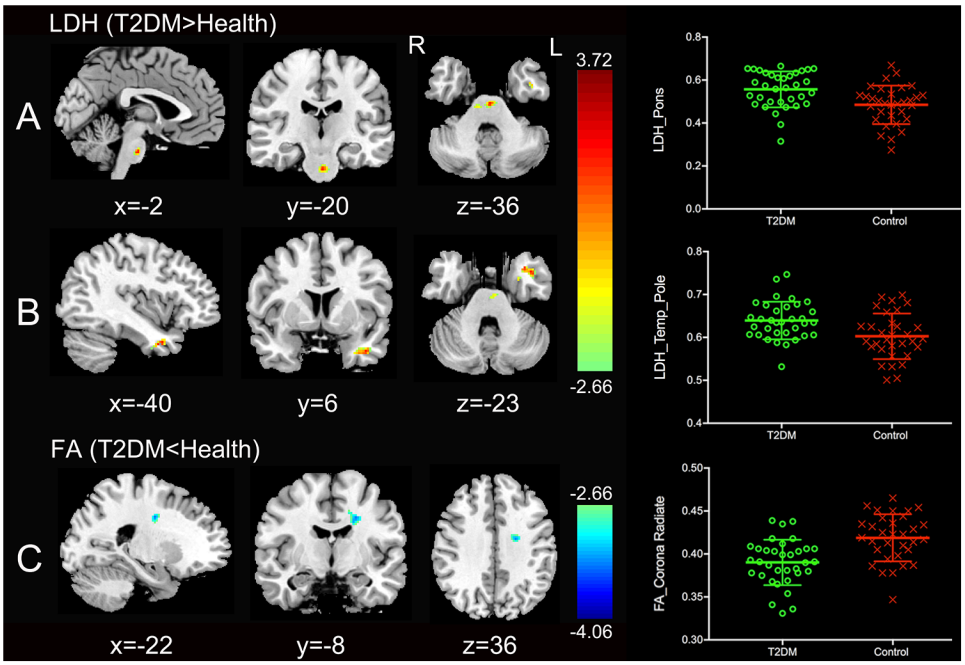

FIGURE 1 | Clusters of between-group differences of LDH and FA with age, gender and education level adjusted ($p < 0.05$, AlphaSim corrected). Significantly higher regional LDH were found in the pons **(A)** and the left temporal pole **(B)**, and significantly decreased FA were found in the left superior corona radiate **(C)** in T2DM subjects compared to the healthy controls. Color scale denotes the *t* values; x, y, z, Montreal Neurological Institutes coordinates; L, left; R, right. The scatter plots show LDH or FA values (means and SD) extracted from each region of interest (ROI) for each group.

TABLE 2 | Regions showing group differences in LDH and FA.

Region names (involved metrics)	Voxel size	MNI coordinates (mm)	Peak *T*
Pons (LDH)	109	−2 −20 −36	3.357
L Temporal Pole (LDH)	72	−40 6 −23	3.364
L Corona (FA)	82	−22 −8 36	−3.363

BA, brodmann area; LDH, local diffusion homogeneity; FA, fractional anisotropy; MCP, the middle cerebellar peduncle; CST, corticospinal tract; UF, uncinate fasciculus; ILF, inferior longitudinal fasciculus; SLF, superior longitudinal fasciculus.

BMI-Associated WM Changes

Four clusters (the yellow clusters in **Figure 2A**) presented BMI-associated WM changes *only* by using LDH, including left inferior temporal lobe, right supra-marginal gyrus; left pre-central gyrus and post-central gyrus (semiovale center), and right superior radiation. Two clusters (the violet clusters in **Figure 2A**) presented BMI-associated WM changes only by using FA, including the left inferior temporal lobe, and left calcarine cortex. There were two marked overlapping WM areas associated with BMI as revealed by both LDH and FA, including the right inferior temporal lobe and left inferior parietal lobe (the blue clusters in **Figure 2A**).

SBP-Associated WM Changes

Likewise, SBP-associated WM regions using only LDH are shown in **Figure 2B** (the yellow blobs), including the right inferior temporal lobe, the right inferior occipital lobe, and the splenium of corpus callosum. The SBP-associated WM regions using only FA located in the left superior corona radiation, the left parahippocampus, and the vermis. The overlapping SBP-associated regions revealed by both LDH and FA included the right temporal pole, bilateral orbitofrontal area (rectus gyrus), the media cingulum bundle, and the right cerebellum crus I (shown in blue in **Figure 2B**).

DISCUSSION

Major Findings and the Clinical Indications

To our best knowledge, this is the first study that comprehensively compare LDH and FA in a imaging-based clinical research, and the first study using LDH for DWI-based brain alteration detection in T2DM (American Diabetes, 2010; Liu et al., 2016, 2017; Zhuo et al., 2016). In this study, voxel-based intra-voxel (FA) and inter-voxel diffusivity metrics (LDH) were used in a whole-brain exploratory study to explore and compare their sensitivity in between-group comparison and brain-clinical association analysis. The results confirmed our hypothesis that (1) inter-voxel and intra-voxel diffusivity metrics had different sensitivity in T2DM-related WM microstructural abnormality detection, and (2) both metrics provided supplementary

TABLE 3 | Regions showing correlations between LDH/FA and BMI/SBP in T2DM.

	Region names	Voxel size	MNI coordinates (mm)	*r* value
BMI & LDH	R inferior temporal lobe (fusiform)*[1]	136	48 −26 −22	0.542
	L inferior temporal lobe (fusiform)	155	−52 −20 −28	0.592
	R supra-marginal gyrus	139	58 −14 30	−0.606
	L inferior parietal lobe (fusiform)*[2]	457	−46 8 36	0.661
	R superior radiation	75	30 0 24	−0.574
	L semiovale center/post-central gyrus	157	−44 −10 42	0.573
BMI & FA	R inferior temporal lobe (fusiform)*[1]	117	50 −24 −28	0.571
	L inferior & middle temporal lobe	104	−68 −34 −18	0.641
	L calcarine cortex (V1)	77	−2 −88 4	−0.714
	L inferior parietal lobe*[2]	338	−62 6 18	0.629
SBP & LDH	R temporal Pole&[1]	641	48 20 −30	−0.715
	R cerebellum_crus1&[2]	112	42 −68 −28	0.615
	R inferior temporal love	247	48 −40 −20	0.646
	B orbitofrontal area&[3]	276	12 40 −18	0.635
	R inferior Occipital lobe	171	30 −88 −4	0.659
	B cingulum bundle&[4]	256	6 −24 46	0.616
SBP & FA	R cerebellum_Crus1&[2]	136	46 −62 −34	0.620
	R temporal pole&[2]	343	40 22 −34	−0.664
	B orbitofrontal area&[3]	206	−2 40 −22	0.674
	L parahippocampus	168	−20 −44 −8	0.670
	Vermis	110	2 −56 2	−0.669
	L superior radiation	111	−26 8 34	0.546
	B cingulum bundle&[4]	71	6 −26 44	0.634

*BA, brodmann area; V1, primary visual cortex; OR, optic radiations; LDH, local diffusion homogeneity; FA, fractional anisotropy; BMI, body mass index; SBP, systolic blood pressure; UF, uncinate fasciculus; ILF, inferior longitudinal fasciculus; SLF, superior longitudinal fasciculus; FPUT, the fronto-parietal U-tracts connecting pre-central and post-central gyrus; CST, corticospinal tract; IFO, inferior fronto-occipital fasciculus; sCC, the fibers of splenium of corpus callosum; mCB, medial cingulum bundle; gCC, genu of corpus callosum; FX, fornix; ST, stria terminalis; R, right, L, left; B, bilateral. *Overlapping regions associated with BMI as revealed by both LDH and FA. &Overlapping regions associated with SBP as revealed by both LDH and FA. The number behind * or &: the pairing label for each overlapping region that presents the correlation between LDH/FA and BMI, or between LDH/FA and SBP.*

information to each other in the detection of WM changes for T2DM.

Group Difference in LDH and FA

LDH and FA Are Complementary for T2DM Imaging Marker Detection

We found increased LDH in the T2DM patients in the pons and the left temporal pole, while FA had no such changes. There are two possible reasons lead to such differences. First, LDH and FA are two different diffusion parameters with different sensitivity to WM impairments. LDH measures the *inter-voxel* similarity of the diffusivity profile in a local range, while FA measures *intra-voxel* diffusivity shape (Alexander et al., 2007). It has been speculated that LDH may be *more sensitive* to the microstructural coherence changes but less sensitive to the myelination changes than FA (Gong, 2013). Secondly, the pons and the left temporal pole contain WM tracts of complex nature (e.g., the crossing fibers) (Alexander et al., 2007; Kiernan, 2012). FA can be largely affected by the crossing fibers (Alexander et al., 2007; Gong, 2013). LDH, on the other hand, is a model-free index that has been suggested to be more tolerable to fiber crossing (Gong, 2013; Liu et al., 2016, 2017).

We also found that, in the left corona radiata, there was a group difference in FA but not LDH. This is consistent with previous findings using FA for T2DM imaging marker detection (Tan et al., 2016). Interestingly, the corona radiata also has crossing fibers. Therefore, we assumed that the left corona radiata could have adequate group difference, where the crossing-fiber influence of FA could not cancel out the detection of such a difference (Tan et al., 2016). For LDH, we speculated that this region might have little changes in the fiber orientation coherence, but more possibly subjecting demyelination (Gong, 2013).

Increased LDH in Pons and the Left Temporal Pole Reflect Compensatory Effect

Increased LDH indicates the enhancement of coherence of local fibers, which may be due to changes of the fiber myelination, diameter, or density differences along the WM tracts. We interpreted such an LDH increase as consequences of an early compensatory mechanism by neuroplasticity that could eventually disappear as the disease progresses (Gispen and Biessels, 2000; Gong, 2013). The increased LDH in the pons could reflect cerebellar compensation to the impaired cerebral functions, or probably result from the functional enhancement of the corticospinal tract (CST). These compensatory mechanisms can be generally mediated by anatomy pathways via the pons. Specifically, the pons contains fibers connecting the cerebellum (via the middle cerebellar peduncle) and the cerebral cortex

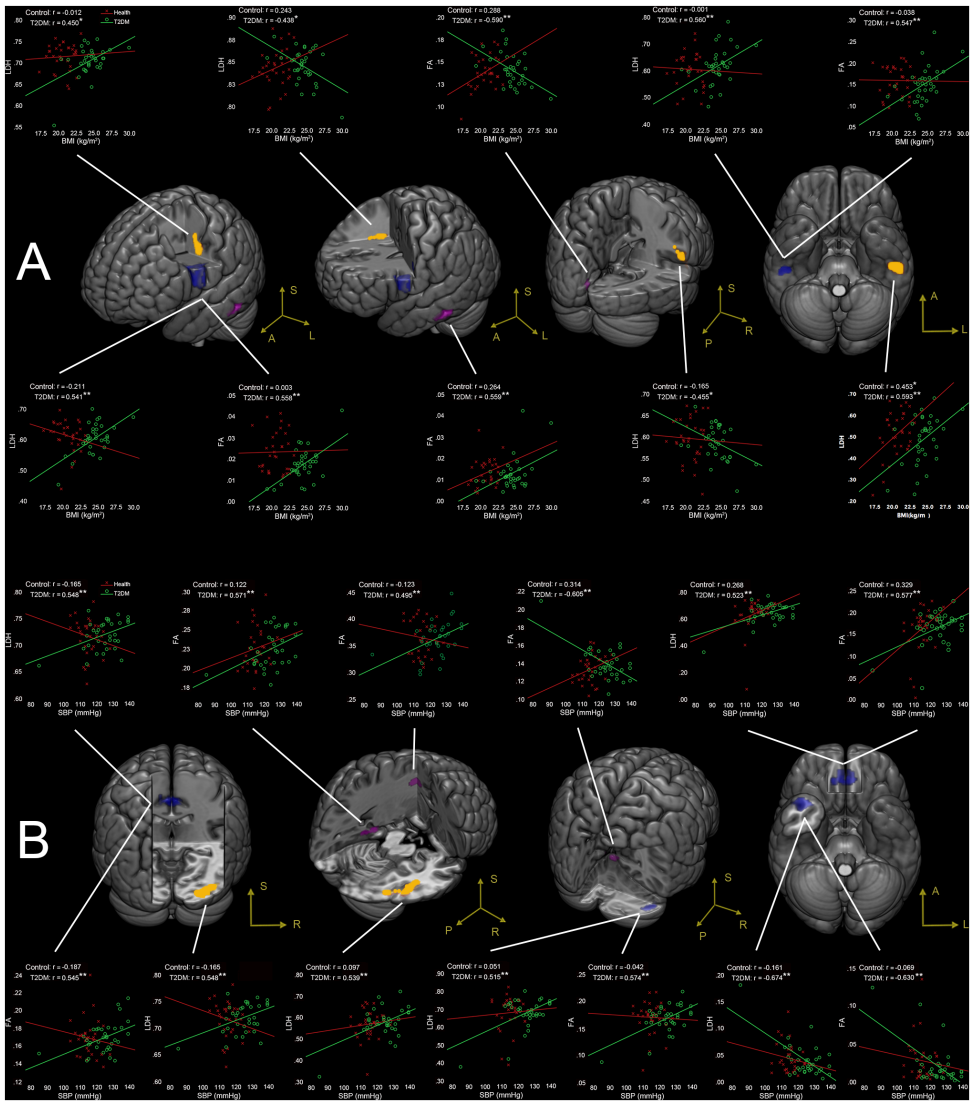

FIGURE 2 | (A) Correlations between BMI and LDH/FA, and **(B)** correlations between SBP and LDH/FA in T2DM subjects, with age, gender, and education level adjusted ($p < 0.05$, AlphaSim corrected). The yellow colored clusters show regions affected by BMI and SBP detected only by LDH. The violet colored clusters show regions affected by BMI and SBP only detected by FA. The blue colored clusters show regions affected by BMI and SBP detected by both LDH and FA. The scatter plots show the correlations between clinical measurement (BMI/SBP) and diffusion metrics (LDH/FA) for each cluster and each group. $^{*}p < 0.05$, $^{**}p < 0.01$. Due to very similar spatial patterns between the two overlapping correlation results, we only show the voxels with significant correlations to LDH to avoid too complex patterns and muddledness in the figure.

(via CST) (Wakana et al., 2004; Buckner, 2013) as a pivotal "relay station" and a connector. Several studies have found the possible compensation mechanisms by the cerebellum in T2DM patients (Xia et al., 2013; Cui et al., 2014; Wang et al., 2017). Although these studies were based on the subjects with different demographic and cognitive characteristics, the differences in the cerebellum could still be detected in all of these studies due to its compensatory ability to maintain intact cognitive functions (Stoodley et al., 2010; Buckner, 2013; Cui et al., 2014). On the other hand, T2DM patients could be easily affected by the diabetic peripheral neuropathy, which could further lead to altered sensory function (Ba-Tin et al., 2011). Moreover, T2DM subjects often have increased BMI or even obesity, which can impair fine motor control and cause movement disorder (Berrigan et al., 2006). All these impaired sensory and/or motor functions could be compensated by the increased LDH in the pons to enhance the CST for maintaining normative neural functions in the preclinical stage (Hsu et al., 2012; van Bloemendaal et al., 2016).

The left temporal pole has strong anatomical connections to paralimbic regions including hippocampus, parahippocampus, amygdala, hypothalamus, and insula (Olson et al., 2007; Kiernan, 2012). It also mediates several high-order cognitive functions, such as memory and emotion processing (Kodl and Seaquist, 2008; Kawamura et al., 2012; McCrimmon et al., 2012). These

regions particularly have abundant insulin receptors that are believed to be essential for memory and other cognitive functions (Kiernan, 2012; McCrimmon et al., 2012). In T2DM, hyperinsulinemia or insulin-resistance leads to reduced insulin receptors, which could affect the abovementioned regions and cause impaired cognitive functions (Kamal et al., 1999; van Bloemendaal et al., 2016; Alfaro et al., 2018). Therefore, the increased LDH in the temporal pole could reflect strengthened connections to these cognitive function-related regions and make compensation to maintain normal cognitive functions.

To further explore such a possible compensatory effect, we did a supplementary experiment focusing on WM structural connectivity networks and found reduced local efficiency at the right superior temporal pole ($p < 0.05$ after Bonferroni correction, see **Supplementary Material**). This finding provides another support for our claim, that is, the increased LDH in the left-sided temporal pole could be caused by reduced local efficiency in its right-sided counterpart. Such a compensatory hypothesis needed to be further investigated by future studies.

Correlation Between Diffusion Metrics and Clinical Measurements

In the T2DM group, different WM regions were associated with BMI and SBP, irrespective of which diffusion metrics (LDH or FA) was used. These results indicated not only different sensitivity of the two diffusivity metrics but also different impacts of obesity and hypertension on the brain (Biessels et al., 2006; Sery et al., 2014; Kullmann et al., 2015). In general, BMI-associated WM regions in the T2DM group mainly encompassed the bilateral association fibers (i.e., fibers that cross the inferior temporal lobe) and the fibers connecting the motor and somatosensory areas (pre- and post-central gyrus). Meanwhile, the SBP-associated WM regions in the T2DM group were more widely distributed, including fibers in the limbic system (left parahippocampus and the media cingulum bundle), association fibers extending to the temporal lobe, callosal fibers, and cerebellar WM (vermis and right cerebellum crus I). The current study showed consistent results with previous research (Hassing et al., 2004; Brundel et al., 2014; van Bloemendaal et al., 2016; Alfaro et al., 2018). For example, it has been reported that the significant alterations of odor-induced brain activations, especially the significantly decreased activation in the hippocampus and parahippocampus of the dominant hemisphere could occur before brain structural changes in T2DM with normal cognitive functions (Zhang et al., 2018). We noticed that in the current study, increased LDH and FA values in most of the regions (e.g., bilateral orbitofrontal area and the left parahippocampus) were associated with greater BMI or SBP; while inverse correlations between the clinical measurements and the diffusion metrics were mainly in the right hemisphere. Since greater BMI and SBP were associated with increased risks of cognitive dysfunctions (Hassing et al., 2004; Alfaro et al., 2018), the inverse brain-clinical associations in our study suggest potential damage of WM fiber structure in T2DM even before the onset of symptoms. Likewise, such brain-clinical associations in the opposite direction could also be explained as recruitment capacity to maintain the cognitive performance in circumstances of altered BMI or SBP (Biessels et al., 2006; Liu et al., 2017; Xia et al., 2017).

The mechanisms of how obesity and hypertension affect the human brains WM integrity have not been fully elucidated, because the T2DM *per se* and its metabolic syndromes could share common pathways, which lead to complex metabolic, inflammatory and microvascular disturbances (van Bloemendaal et al., 2016; Alfaro et al., 2018). All these factors may weigh into WM microstructural damages and cognitive decline; thus, it is difficult to differentiate the biological and neurological consequences of each individual factor (Biessels et al., 2006; Toth et al., 2006; Geha et al., 2017; Alfaro et al., 2018). Taken together, we propose that the correlations between brain imaging metrics and clinical measurements could be a probable result from brain plasticity and other compensatory mechanisms, which allow the brain to adapt according to the changes in environmental pressure, physiology, and pathology caused by T2DM in order to maintain a normative level of cognitive functions (Kamal et al., 1999; van Harten et al., 2006; Biessels and Reijmer, 2014; Concha, 2014; van Bloemendaal et al., 2016; van Bussel et al., 2017).

Strengths and Limitations

The current study features several strengths. First, to our best knowledge, it is the first to investigate inter-voxel diffusivity metrics in the T2DM brains. It is also the first comprehensive investigation that combines between-group comparisons and a brain-clinical measure association analysis, which together comprehensively reveal the T2DM-related brain alterations. Second, the two groups involved in this study had relative younger age and narrow age range compared to most of the other studies (Reijmer et al., 2013a; van Bussel et al., 2017; Xia et al., 2017). Such features could alleviate the cohort heterogeneity problem and reduce the nuisance effect of age (Gispen and Biessels, 2000; Biessels et al., 2006; Salthouse, 2009). Third, low microvascular risk (i.e., no infarction, no significant WMHs, and no apparent retinopathy) with no apparent cognitive impairments in the two groups could further minimize confounding effects (Peng et al., 2016).

One of the possible concerns is the unmatched education level and gender. However, we could not find out any significant gender- and education level-effect on the LDH and FA from a linear regression test. Meanwhile, all the main analysis were conducted with age, gender and education level as covariates to exclude their potential influences. Therefore, we believe that education level and gender could have an insignificant effect on the results. Due to the difficulty of collecting middle-aged cognitively normal T2DM patients, we intended to include as many subjects as possible in this study. Another limitation is that the true biological meaning of LDH is still unclear by now. Although we have made tentative explanations and interpretations in terms of potential neuromechanism and biological substrates of the LDH, these interpretations are stillhighly speculative. Future studies may need to manipulate the

WM changes with a specific disease or animal model to further investigate the neural basis of LDH changes.

CONCLUSION

Our study indicated that inter-voxel (local diffusion homogeneity, LDH) and intra-voxel (FA) metrics had different sensitivity in detection of T2DM-related WM microstructural abnormalities. The combination of FA and LDH could provide supplementary information and better reveal the underlying brain changes due to diabetes. We found interesting compensatory recruitment of the pons and the left temporal pole with increased LDH in T2DM compared to the healthy controls. Such a compensatory mechanism and the potential associations between risk factors and imaging findings in the middle-aged T2DM patients hold great clinical potential in detecting early imaging markers of T2DM.

ETHICS STATEMENT

This study was approved by the ethics committee of First Affiliated Hospital of Guangzhou University of Chinese Medicine. All subjects gave written informed consent in accordance with the Declaration of Helsinki.

AUTHOR CONTRIBUTIONS

HaZ, SQ, and DS contributed to conception and design of the study. YuL, HuZ, and XT organized the data. YiL performed the data analysis and drafted the manuscript. All authors revised the manuscript, and read and approved the submitted version.

FUNDING

This study was supported in part by the National Natural Science Foundation of China (91649117, 81471251, and 81771344), National Major Cultivation Fund (Natural Science) for the Innovative School Projects of Guangdong Provincial Department of Education (2014GKXM034), Guangzhou Science and Technology Planning Project (2018-1002-SF-0442), and NIH grant (AG041721).

SUPPLEMENTARY MATERIAL

The Supplementary Material for this article can be found online at: https://www.frontiersin.org/articles/10.3389/fnins.2019.00063/full#supplementary-material

REFERENCES

Abbas, Q., Fondon, I., Sarmiento, A., Jimenez, S., and Alemany, P. (2017). Automatic recognition of severity level for diagnosis of diabetic retinopathy using deep visual features. *Med. Biol. Eng. Comput.* 55, 1959–1974. doi: 10.1007/s11517-017-1638-6

Alexander, A. L., Lee, J. E., Lazar, M., and Field, A. S. (2007). Diffusion tensor imaging of the brain. *Neurotherapeutics* 4, 316–329. doi: 10.1016/j.nurt.2007.05.011

Alfaro, F. J., Gavrieli, A., Saade-Lemus, P., Lioutas, V. A., Upadhyay, J., and Novak, V. (2018). White matter microstructure and cognitive decline in metabolic syndrome: a review of diffusion tensor imaging. *Metabolism* 78, 52–68. doi: 10.1016/j.metabol.2017.08.009

American Diabetes (2010). Diagnosis and classification of diabetes mellitus. *Diabetes Care* 33(Suppl. 1), S62–S69. doi: 10.2337/dc10-S062

Ba-Tin, L., Strike, P., and Tabet, N. (2011). Diabetic peripheral microvascular complications: relationship to cognitive function. *Cardiovasc. Psychiatry Neurol.* 2011:723434. doi: 10.1155/2011/723434

Beaulieu, C. (2002). The basis of anisotropic water diffusion in the nervous system - a technical review. *NMR Biomed.* 15, 435–455. doi: 10.1002/nbm.782

Berrigan, F., Simoneau, M., Tremblay, A., Hue, O., and Teasdale, N. (2006). Influence of obesity on accurate and rapid arm movement performed from a standing posture. *Int. J. Obes.* 30, 1750–1757. doi: 10.1038/sj.ijo.0803342

Biessels, G. J., and Reijmer, Y. D. (2014). Brain changes underlying cognitive dysfunction in diabetes: what can we learn from MRI? *Diabetes* 63, 2244–2252. doi: 10.2337/db14-0348

Biessels, G. J., Staekenborg, S., Brunner, E., Brayne, C., and Scheltens, P. (2006). Risk of dementia in diabetes mellitus: a systematic review. *Lancet Neurol.* 5, 64–74. doi: 10.1016/S1474-4422(05)70284-2

Brundel, M., Kappelle, L. J., and Biessels, G. J. (2014). Brain imaging in type 2 diabetes. *Eur. Neuropsychopharmacol. J. Eur. Coll. Neuropsychopharmacol.* 24, 1967–1981. doi: 10.1016/j.euroneuro.2014.01.023

Buckner, R. L. (2013). The cerebellum and cognitive function: 25 years of insight from anatomy and neuroimaging. *Neuron* 80, 807–815. doi: 10.1016/j.neuron.2013.10.044

Concha, L. (2014). A macroscopic view of microstructure: using diffusion-weighted images to infer damage, repair, and plasticity of white matter. *Neuroscience* 276, 14–28. doi: 10.1016/j.neuroscience.2013.09.004

Cui, Y., Jiao, Y., Chen, Y. C., Wang, K., Gao, B., Wen, S., et al. (2014). Altered spontaneous brain activity in type 2 diabetes: a resting-state functional MRI study. *Diabetes* 63, 749–760. doi: 10.2337/db13-0519

Cui, Z., Zhong, S., Xu, P., He, Y., and Gong, G. (2013). Panda: a pipeline toolbox for analyzing brain diffusion images. *Front. Hum. Neurosci.* 7:42. doi: 10.3389/fnhum.2013.00042

Ding, Z., Zhang, H., Lv, X. F., Xie, F., Liu, L., Qiu, S., et al. (2018). Radiation-induced brain structural and functional abnormalities in presymptomatic phase and outcome prediction. *Hum. Brain Mapp.* 39, 407–427. doi: 10.1002/hbm.23852

Garcia-Casares, N., Berthier, M. L., Jorge, R. E., Gonzalez-Alegre, P., Gutierrez Cardo, A., Rioja Villodres, J., et al. (2014). Structural and functional brain changes in middle-aged type 2 diabetic patients: a cross-sectional study. *J. Alzheimers Dis.* 40, 375–386. doi: 10.3233/JAD-131736

Geha, P., Cecchi, G., Todd Constable, R., Abdallah, C., and Small, D. M. (2017). Reorganization of brain connectivity in obesity. *Hum. Brain Mapp.* 38, 1403–1420. doi: 10.1002/hbm.23462

Gispen, W. H., and Biessels, G. J. (2000). Cognition and synaptic plasticity in diabetes mellitus. *Trends Neurosci.* 23, 542–549. doi: 10.1016/S0166-2236(00)01656-8

Gong, G. (2013). Local diffusion homogeneity (LDH): an inter-voxel diffusion MRI metric for assessing inter-subject white matter variability. *PLoS One* 8:e66366. doi: 10.1371/journal.pone.0066366

Guo, W. B., Liu, F., Chen, J. D., Xu, X. J., Wu, R. R., Ma, C. Q., et al. (2012). Altered white matter integrity of forebrain in treatment-resistant depression: a diffusion tensor imaging study with tract-based spatial statistics. *Prog. Neuropsychopharmacol. Biol. Psychiatry* 38, 201–206. doi: 10.1016/j.pnpbp.2012.03.012

Guo, W., Liu, F., Liu, Z., Gao, K., Xiao, C., Chen, H., et al. (2012). Right lateralized white matter abnormalities in first-episode, drug-naive paranoid schizophrenia. *Neurosci. Lett.* 531, 5–9. doi: 10.1016/j.neulet.2012.09.033

Hassing, L. B., Hofer, S. M., Nilsson, S. E., Berg, S., Pedersen, N. L., McClearn, G., et al. (2004). Comorbid type 2 diabetes mellitus and hypertension exacerbates cognitive decline: evidence from a longitudinal study. *Age Ageing* 33, 355–361. doi: 10.1093/ageing/afh100

Hsu, J. L., Chen, Y. L., Leu, J. G., Jaw, F. S., Lee, C. H., Tsai, Y. F., et al. (2012). Microstructural white matter abnormalities in type 2 diabetes mellitus: a diffusion tensor imaging study. *Neuroimage* 59, 1098–1105. doi: 10.1016/j.neuroimage.2011.09.041

International Diabetes Federation (2017). *IDF Diabetes Atlas*, 8th Edn. Brussels: International Diabetes Federation.

Kamal, A., Biessels, G. J., Urban, I. J., and Gispen, W. H. (1999). Hippocampal synaptic plasticity in streptozotocin-diabetic rats: impairment of long-term potentiation and facilitation of long-term depression. *Neuroscience* 90, 737–745. doi: 10.1016/S0306-4522(98)00485-0

Kawamura, T., Umemura, T., and Hotta, N. (2012). Cognitive impairment in diabetic patients: can diabetic control prevent cognitive decline? *J. Diabetes Investig.* 3, 413–423. doi: 10.1111/j.2040-1124.2012.00234.x

Kiernan, J. A. (2012). Anatomy of the temporal lobe. *Epilepsy Res. Treat.* 2012:176157. doi: 10.1155/2012/176157

Kodl, C. T., and Seaquist, E. R. (2008). Cognitive dysfunction and diabetes mellitus. *Endocr. Rev.* 29, 494–511. doi: 10.1210/er.2007-0034

Kullmann, S., Schweizer, F., Veit, R., Fritsche, A., and Preissl, H. (2015). Compromised white matter integrity in obesity. *Obes. Rev.* 16, 273–281. doi: 10.1111/obr.12248

Liu, G., Tan, S., Dang, C., Peng, K., Xie, C., Xing, S., et al. (2017). Motor recovery prediction with clinical assessment and local diffusion homogeneity after acute subcortical infarction. *Stroke* 48, 2121–2128. doi: 10.1161/STROKEAHA.117.017060

Liu, H. H., Wang, J., Chen, X. M., Li, J. P., Ye, W., and Zheng, J. (2016). Reduced local diffusion homogeneity as a biomarker for temporal lobe epilepsy. *Medicine* 95:e4032. doi: 10.1097/MD.0000000000004032

McCrimmon, R. J., Ryan, C. M., and Frier, B. M. (2012). Diabetes and cognitive dysfunction. *Lancet* 379, 2291–2299. doi: 10.1016/S0140-6736(12)60360-2

Moheet, A., Mangia, S., and Seaquist, E. R. (2015). Impact of diabetes on cognitive function and brain structure. *Ann. N. Y. Acad. Sci.* 1353, 60–71. doi: 10.1111/nyas.12807

O'Donnell, L. J., and Westin, C. F. (2011). An introduction to diffusion tensor image analysis. *Neurosurg. Clin. N. Am.* 22, 185–196. doi: 10.1016/j.nec.2010.12.004

Olson, I. R., Plotzker, A., and Ezzyat, Y. (2007). The Enigmatic temporal pole: a review of findings on social and emotional processing. *Brain* 130, 1718–1731. doi: 10.1093/brain/awm052

Peng, J., Qu, H., Peng, J., Luo, T. Y., Lv, F. J., Chen, L., et al. (2016). Abnormal spontaneous brain activity in type 2 diabetes with and without microangiopathy revealed by regional homogeneity. *Eur. J. Radiol.* 85, 607–615. doi: 10.1016/j.ejrad.2015.12.024

Poldrack, R. A., Fletcher, P. C., Henson, R. N., Worsley, K. J., Brett, M., and Nichols, T. E. (2008). Guidelines for reporting an fMRI study. *Neuroimage* 40, 409–414. doi: 10.1016/j.neuroimage.2007.11.048

Reijmer, Y. D., Brundel, M., de Bresser, J., Kappelle, L. J., Leemans, A., Biessels, G. J., et al. (2013a). Microstructural white matter abnormalities and cognitive functioning in type 2 diabetes: a diffusion tensor imaging study. *Diabetes Care* 36, 137–144. doi: 10.2337/dc12-0493

Reijmer, Y. D., Leemans, A., Brundel, M., Kappelle, L. J., Biessels, G. J., and Utrecht Vascular Cognitive Impairment Study Group. (2013b). Disruption of the cerebral white matter network is related to slowing of information processing speed in patients with type 2 diabetes. *Diabetes* 62, 2112–2115. doi: 10.2337/db12-1644

Salthouse, T. A. (2009). When does age-related cognitive decline begin? *Neurobiol. Aging* 30, 507–514. doi: 10.1016/j.neurobiolaging.2008.09.023

Sery, O., Hlinecka, L., Balcar, V. J., Janout, V., and Povova, J. (2014). Diabetes, hypertension and stroke - does Alzheimer protect you? *Neuro Endocrinol. Lett.* 35, 691–696.

Song, X. W., Dong, Z. Y., Long, X. Y., Li, S. F., Zuo, X. N., Zhu, C. Z., et al. (2011). REST: a toolkit for resting-state functional magnetic resonance imaging data processing. *PLoS One* 6:e25031. doi: 10.1371/journal.pone.0025031

Shang, X., Li, J., Tao, Q., Li, J., Li, X., Zhang, L., et al. (2013) Educational level, obesity and incidence of diabetes among chinese adult men and women aged 18-59 years old: an 11-year follow-up study. *PLoS One* 8:e66479. doi: 10.1371/journal.pone.0066479

Stoodley, C. J., Valera, E. M., and Schmahmann, J. D. (2010). An fMRI study of intra-individual functional topography in the human cerebellum. *Behav. Neurol.* 23, 65–79. doi: 10.3233/BEN-2010-0268

Tan, X., Fang, P., An, J., Lin, H., Liang, Y., Shen, W., et al. (2016). Micro-structural white matter abnormalities in type 2 diabetic patients: a DTI study using TBSS analysis. *Neuroradiology* 58, 1209–1216. doi: 10.1007/s00234-016-1752-4

Toth, C., Schmidt, A. M., Tuor, U. I., Francis, G., Foniok, T., Brussee, V., et al. (2006). Diabetes, leukoencephalopathy and rage. *Neurobiol. Dis.* 23, 445–461. doi: 10.1016/j.nbd.2006.03.015

van Bloemendaal, L., Ijzerman, R. G., Ten Kulve, J. S., Barkhof, F., Diamant, M., Veltman, D. J., et al. (2016). Alterations in white matter volume and integrity in obesity and type 2 diabetes. *Metab. Brain Dis.* 31, 621–629. doi: 10.1007/s11011-016-9792-3

van Bussel, F. C., Backes, W. H., van Veenendaal, T. M., Hofman, P. A., van Boxtel, M. P., Schram, M. T., et al. (2017). Functional brain networks are altered in type 2 diabetes and prediabetes: signs for compensation of cognitive decrements? the maastricht study. *Diabetes* 66:560. doi: 10.2337/db17-er02a

van Harten, B., de Leeuw, F. E., Weinstein, H. C., Scheltens, P., and Biessels, G. J. (2006). Brain imaging in patients with diabetes: a systematic review. *Diabetes Care* 29, 2539–2548. doi: 10.2337/dc06-1637

Wahlund, L. O., Barkhof, F., Fazekas, F., Bronge, L., Augustin, M., Sjogren, M., et al. (2001). A new rating scale for age-related white matter changes applicable to MRI and CT. *Stroke* 32, 1318–1322. doi: 10.1161/01.STR.32.6.1318

Wakana, S., Jiang, H., Nagae-Poetscher, L. M., van Zijl, P. C., and Mori, S. (2004). Fiber tract-based atlas of human white matter anatomy. *Radiology* 230, 77–87. doi: 10.1148/radiol.2301021640

Wang, Z., Wang, J., Zhang, H., McHugh, R., Sun, X., Li, K., et al. (2015). Interhemispheric functional and structural disconnection in Alzheimer's Disease: a combined resting-state fMRI and DTI study. *PLoS One* 10:e0126310. doi: 10.1371/journal.pone.0126310

Wang, Z. L., Zou, L., Lu, Z. W., Xie, X. Q., Jia, Z. Z., Pan, C. J., et al. (2017). Abnormal spontaneous brain activity in type 2 diabetic retinopathy revealed by amplitude of low-frequency fluctuations: a resting-state fMRI study. *Clin. Radiol.* 72, 340.e1–340.e7. doi: 10.1016/j.crad.2016.11.012

Whelton, P. K., and Carey, R. M. (2017). The 2017 clinical practice guideline for high blood pressure. *Jama J. Am. Med. Assoc.* 318, 2073–2074. doi: 10.1001/jama.2017.18209

Xia, W., Chen, Y. C., and Ma, J. (2017). Resting-state brain anomalies in type 2 diabetes: a meta-analysis. *Front. Aging Neurosci.* 9:14. doi: 10.3389/fnagi.2017.00014

Xia, W., Wang, S., Sun, Z., Bai, F., Zhou, Y., Yang, Y., et al. (2013). Altered baseline brain activity in type 2 diabetes: a resting-state fMRI study. *Psychoneuroendocrinology* 38, 2493–2501. doi: 10.1016/j.psyneuen.2013.05.012

Yang, S. Q., Xu, Z. P., Xiong, Y., Zhan, Y. F., Guo, L. Y., Zhang, S., et al. (2016). Altered intranetwork and internetwork functional connectivity in type 2 diabetes mellitus with and without cognitive impairment. *Sci. Rep.* 6:32980. doi: 10.1038/srep32980

Zhang, J., Wang, Y., Wang, J., Zhou, X., Shu, N., Wang, Y., et al. (2014). White matter integrity disruptions associated with cognitive impairments in type 2 diabetic patients. *Diabetes* 63, 3596–3605. doi: 10.2337/db14-0342

Zhang, Z., Zhang, B., Wang, X., Zhang, X., Yang, Q. X., Qing, Z., et al. (2018). Altered odor- induced brain activity as an early manifestation of cognitive decline in patients with type 2 diabetes. *Diabetes Metab. Res. Rev.* 67, 994–1006. doi: 10.2337/db17-1274

Zhuo, C. J., Ma, X. L., Qu, H. R., Wang, L. N., Jia, F., and Wang, C. L. (2016). Schizophrenia patients demonstrate both inter-voxel level and intra-voxel level white matter alterations. *PLoS One* 11:e0162656. doi: 10.1371/journal.pone.0162656

Conflict of Interest Statement: The authors declare that the research was conducted in the absence of any commercial or financial relationships that could be construed as a potential conflict of interest.

frontiers in Neuroscience

ORIGINAL RESEARCH
published: 26 February 2019
doi: 10.3389/fnins.2019.00145

Enhanced Global-Brain Functional Connectivity in the Left Superior Frontal Gyrus as a Possible Endophenotype for Schizophrenia

*Yudan Ding[1], Yangpan Ou[1], Qinji Su[2], Pan Pan[1], Xiaoxiao Shan[1], Jindong Chen[1], Feng Liu[3], Zhikun Zhang[2], Jingping Zhao[1] and Wenbin Guo[1]**

[1] Department of Psychiatry, The Second Xiangya Hospital of Central South University, Changsha, China, [2] Mental Health Center, The Second Affiliated Hospital of Guangxi Medical University, Nanning, China, [3] Department of Radiology, Tianjin Medical University General Hospital, Tianjin, China

The notion of dysconnectivity in schizophrenia has been put forward for many years and results in substantial attempts to explore altered functional connectivity (FC) within different networks with inconsistent results. Clinical, demographical, and methodological heterogeneity may contribute to the inconsistency. Forty-four patients with first-episode, drug-naive schizophrenia, 42 unaffected siblings of schizophrenia patients and 44 healthy controls took part in this study. Global-brain FC (GFC) was employed to analyze the imaging data. Compared with healthy controls, patients with schizophrenia and unaffected siblings shared enhanced GFC in the left superior frontal gyrus (SFG). In addition, patients had increased GFC mainly in the thalamo-cortical network, including the bilateral thalamus, bilateral posterior cingulate cortex (PCC)/precuneus, left superior medial prefrontal cortex (MPFC), right angular gyrus, and right SFG/middle frontal gyrus and decreased GFC in the left ITG/cerebellum Crus I. No other altered GFC values were observed in the siblings group relative to the control group. Further ROC analysis showed that increased GFC in the left SFG could separate the patients or the siblings from the controls with acceptable sensitivities. Our findings suggest that increased GFC in the left SFG may serve as a potential endophenotype for schizophrenia.

Keywords: schizophrenia, global-brain functional connectivity, functional magnetic resonance imaging, endophenotype, network

OPEN ACCESS

Edited by:
Weidong Cai,
The University of Sydney, Australia

Reviewed by:
Minghao Dong,
Xidian University, China
Dominic T. Cheng,
Auburn University, United States

****Correspondence:***
Wenbin Guo
guowenbin76@csu.edu.cn

Specialty section:
This article was submitted to Brain Imaging Methods, a section of the journal Frontiers in Neuroscience

Received: *27 October 2018*
Accepted: *08 February 2019*
Published: *26 February 2019*

Citation:
Ding Y, Ou Y, Su Q, Pan P, Shan X, Chen J, Liu F, Zhang Z, Zhao J and Guo W (2019) Enhanced Global-Brain Functional Connectivity in the Left Superior Frontal Gyrus as a Possible Endophenotype for Schizophrenia. Front. Neurosci. 13:145. doi: 10.3389/fnins.2019.00145

INTRODUCTION

Characterized by disturbances of perception (Yoon et al., 2008), cognition (Barch and Csernansky, 2007), emotion (Holt et al., 2011), and thought (Corlett et al., 2007), schizophrenia is a devastating and complex mental disorder, affecting adults as well as adolescence with highly heterogeneous and multifaceted clinical syndromes instead of a single disease entity (Yu et al., 2017). The diagnosis of schizophrenia is largely dependent on the psychiatrists' evaluation and experience based on the comprehensive history records and laboratory examinations (Chin et al., 2018). In recent decades, great efforts have been made to identify reliable and objective biomarkers, such as electrophysiological (Turetsky et al., 2008; Smith et al., 2010; Edgar et al., 2012), neuropsychological

(Smith et al., 2010; Edgar et al., 2012; Schulze-Rauschenbach et al., 2015), and neuroimaging indices (Edgar et al., 2012; Turner et al., 2012; Moran et al., 2013).

It has been postulated that schizophrenia is a neurodevelopmental disorder with abnormal neural connectivity of discrete brain networks and genetic and environmental factors may contribute to such dysconnectivity (Maynard et al., 2001; Karlsgodt et al., 2008). To date, substantial neuroimaging studies reveal structural and functional aberrations in many brain areas in schizophrenia or high risk populations, or both of them, including the prefrontal, cingulate, temporal, cerebellar, hippocampal, and thalamic regions (Rubinov and Bullmore, 2013; Thermenos et al., 2013; Bois et al., 2015; Chung and Cannon, 2015) within various brain networks such as the default-mode network (DMN) (Bluhm et al., 2007; Zhou et al., 2007; Ongur et al., 2010), cerebellar-cerebral networks (Konarski et al., 2005; Phillips et al., 2015), and thalamo-cortical networks (Andreasen et al., 1996; Jones, 1997; Swerdlow, 2010). Unaffected siblings of patients with schizophrenia, a subgroup of high risk subjects with approximately 50% of genetic burden (Pergola et al., 2017), have about a 10-fold increased risk to develop schizophrenia than general population (Chang et al., 2002). Unaffected siblings are free from confounding variables caused by environmental or disease-associated factors, and thus having an advantage to assess brain function with limited confounding factors. For example, disturbed resting-state FC has been observed in the first-degree relatives (Jang et al., 2011), which was predominantly altered in schizophrenia (Lynall et al., 2010; Skudlarski et al., 2010). Therefore, similar brain abnormalities shared by patients with schizophrenia and unaffected siblings can be regarded as potential endophenotypes for schizophrenia. Endophenotypes are some heritable and characteristic changes certainly present in patients but are possible to appear in unaffected relatives. They segregate with the disease within families and can be biochemical, neuroanatomical, cognitive, endocrine, or neurophysiological parameters (Gottesman and Gould, 2003; Bertolino and Blasi, 2009).

However, results from resting-state functional magnetic resonance imaging (fMRI) of abnormal intrinsic neural activity and/or functional connectivity (FC) across brain areas within those networks were inconsistent: increased FC (Zhou et al., 2007), decreased FC (Bluhm et al., 2007), or both (Ongur et al., 2010). One possible factor accounting for the mixed findings is that the majority of neuroimaging studies adopted either seed-based region-of-interest (ROI) analysis or independent component analysis (ICA), both of which are, to some extent, dependent on prior assumptions rather than employing a whole-brain examination (McKeown et al., 2003; Mannell et al., 2010; Joel et al., 2011). Therefore, it is possible to miss the most significantly altered regions which may indicate the core pathophysiology of schizophrenia.

Another reason may be that heterogeneous samples with different illness duration and medication history have biased the findings. Results from some longitudinal MRI studies in patients with chronic schizophrenia have showed accelerated gray matter loss over time and such progressive structural alterations were more remarkable at the initial stage of illness (Yoshida et al., 2009; Chiapponi et al., 2013;Schnack et al., 2016). As for resting-state fMRI studies, researchers have revealed reduced FC within the executive control network (ECN), DMN and dorsal attention network (DAN) in medicated patients (Woodward et al., 2011), whereas no changes were found within the ECN network in first-episode, drug-naive patients with schizophrenia (Lui et al., 2009). Therefore, it is essential to recruit first-episode, drug-naive patients with schizophrenia to explore the intact connectivity of these networks.

In the present study, we aimed to explore global-brain FC (GFC) differences by comparing a group of first-episode, drug-naive patients with schizophrenia and unaffected siblings with healthy controls employing the voxel-wise model-free GFC method, which had been described in details in our previous study (Cui et al., 2018). Apart from the seed-based ROI method and ICA method, GFC is another method of functional connectome which consists of FC of anatomically different brain areas (Craddock et al., 2013). Unlike the ROI and ICA methods, GFC is not biased by *a priori* specification of brain areas like ROI and spares from controversial views on the number of components in the ICA method (Kelly et al., 2012). Thus, the GFC method was preferable in our study. Based on the dysconnectivity hypothesis of schizophrenia and aforementioned studies, we hypothesized that patients with schizophrenia would reveal abnormal GFC in brain regions pertain to certain networks especially the DMN and thalamo-cortical circuit. Another hypothesis was that disrupted GFC could serve as an endophenotype shared by patients with schizophrenia and unaffected siblings. In addition, receiver operating characteristic (ROC) curve was conducted to differentiate the patients and unaffected siblings from the controls. Finally, we also examined correlations between disrupted GFC and clinical variables such as illness duration and symptom severity assessed by Positive and Negative Syndrome Scale (PANSS).

MATERIALS AND METHODS

Participants

Forty-six patients with first-episode, drug-naive patients with schizophrenia, 46 non-affected siblings of patients with schizophrenia and 46 healthy controls took part in this study. All subjects were right handed, and aged from 18 to 37 years with more than 6 years of formal education. Handedness was determined by the Annett Hand Preference Questionnaire (Dragovic and Hammond, 2007). The study was in accordance with the Helsinki Declaration and approved by the local ethics committees of the Second Affiliated Hospital of Guangxi Medical University. All participants signed their written informed consent.

The included patients and siblings were recruited from the Mental Health Center, the Second Affiliated Hospital of Guangxi Medical University in China, and the controls were recruited from the local community. The diagnosis of schizophrenia was made by two research psychiatrists (W.G. and Z.Z.) according to the Structured Clinical Interview of the

Diagnostic and Statistical Manual of Mental Disorders-IV (DSM-IV) criteria, patient edition, whereas non-patient version was used for unaffected siblings and healthy controls to rule out any psychiatric conditions. No antipsychotic medications or other psychotropic agents were treated to the patients, and PANSS total scores referring symptom severity of them was more than 70 at baseline. All participants did a series of routine physical examinations including systems review and laboratory tests to exclude any significant medical conditions and shared the same exclusion criteria: neurological disorders or history of brain injury, history of nicotine dependence, alcohol or other substance dependence, or any contraindications to MRI scan. In addition, potential controls who had a first-degree relative diagnosed with psychiatric disorders were also excluded.

Imaging Acquisition and Preprocessing

Scanning was performed on a Siemens 3.0 T scanner. Participants with soft earplugs and foam, which could reduce scanner noise and head movement, were informed to lay still and remain awake with their eyes closed. After scanning, all subjects were asked some questions to claim that they did not fall asleep during the scanning. The images were acquired with a gradient-echo echo-planar imaging (EPI) sequence using the following parameters: repetition time/echo time (TR/TE) = 2000 ms/30 ms, 30 slices, 64 × 64 matrix, 90° flip angle, 24 cm field of view, 4 mm slice thickness, 0.4 mm slice gap, and 250 volumes lasting for 500 s.

Software DPABI was used to preprocess the imaging data (Yan et al., 2016). After slice timing and head motion correction, participants with over 2 mm maximal translation and 2° maximal rotation were excluded. Several covariates, including Friston-24 head motion parameters acquired through rigid body correction (de Kwaasteniet et al., 2013), signal from a ventricular region of interest, and signal from a region centered in the white matter, were removed. In addition, we applied mean frame-wise displacement (FD) according to a formula described previously (Liu et al., 2008; Power et al., 2012) to address the residual effects of motion as a covariate in group analyses. The global signal was not removed since it is still a controversial practice in the resting-state fMRI field (Hahamy et al., 2014). Then, we normalized the data to conventional EPI template in the Montreal Neurological Institute (MNI) space at a 3 mm × 3 mm × 3 mm resolution. Finally, the images were bandpass-filtered (0.01–0.08 Hz) and linearly detrended following spatially smoothed with a 4 mm full-width at half-maximum Gaussian kernel.

GFC Analysis

Voxel-wise GFC method, defined as FC between a selected voxel and all other voxels in a given gray matter mask, was used to create voxel-to-voxel maps by composing GFC values of all voxels for each subject. SPM8 in Matlab (Liu et al., 2015) was used to generate the gray matter mask by setting the threshold at probability > 0.2. According to Yan and colleagues (Chao-Gan and Yu-Feng, 2010), a threshold of 0.2 was used to create a gray matter mask in this study, which indicated that voxels with the probability > 0.2 would be classified as gray matter. The GFC was computed as:

$$GFC_{\mathrm{a}} = \Sigma_{\mathrm{b}=1}^{\mathrm{n}} \frac{r\,(T_{\mathrm{a}},\ T_{\mathrm{b}})}{n-1}$$

Where, Pearson's correlation coefficient (r) was calculated at the given voxels a and b for T_s, a pair of time series, followed by Fisher r-to-z transformation (Cui et al., 2018) and the GFC of a voxel was the coefficient of this voxel with all other voxels in the mask.

Statistical Analysis

When appropriate, demographical data including age, sex, and years of education and clinical data were compared by using Chi-square test and analysis of variance (ANOVA).

After performing analysis of covariance (ANCOVA), *post hoc t*-tests were carried out to compare group differences among patients with schizophrenia, unaffected siblings, and controls. Age and the mean FD were applied as covariates in the ANCOVA and *post hoc t*-tests. The results were corrected by the Gaussian random field (GRF) theory at $p < 0.05$ (voxel significance: $p < 0.001$, cluster significance: $p < 0.05$).

After identifying brain regions with abnormal GFC values showing significant differences by group comparisons, the mean GFC values were extracted from these regions for further ROC curves analysis, which was used to examine whether these regions could discriminate patients with schizophrenia or unaffected siblings from healthy controls as reliable markers.

Linear correlation analyses were performed between abnormal GFC and clinical variables in PANSS scores and illness duration in the patient group ($p < 0.05$). The Bonferroni correction was used to limit type I error.

RESULTS

Demographical and Clinical Characteristics

Two patients, 4 siblings, and 2 healthy controls were excluded due to excessive head motion. Therefore, the final analysis enrolled 44 patients, 42 non-affected siblings, and 44 healthy controls. The three groups had no significant differences in age, sex, education level, and FD values (see **Table 1**). The mean illness duration of the patients was 22.34 ± 7.01 months, and the mean PANSS total score was 90.70 ± 11.17.

Group Differences in the GFC Values

Compared with healthy controls, patients with schizophrenia and unaffected siblings shared enhanced GFC in the left superior frontal gyrus (SFG). In addition, as showed in **Table 2** and **Figure 1**, the patient group had increased GFC in other areas such as the bilateral PCC/precuneus, and decreased GFC in the left ITG/cerebellum Crus I relative to the control group. No other altered GFC values were observed in the siblings group relative to the control group (**Table 2** and **Figure 2**).

Correlation Results

After the Bonferroni correction ($p > 0.05/7 = 0.007$ for abnormal GFC values in the seven brain regions), no significant

correlations were found between GFC values and clinical variables in the patients.

ROC Results

Since the left SFG exhibited increased GFC in both the patients and the siblings, it might be considered as a marker to separate the patients or the siblings from the controls. To examine this potential, ROC analysis was conducted. As shown in **Figure 3**, to discriminate the patients or the siblings from the controls, the areas under the curve of the left SFG were 0.829 or 0.748, respectively. Further diagnostic analysis showed that the sensitivity and specificity to separate the patients or siblings from the controls were 70.45 or 85.71%, and 90.91 or 56.82%, respectively.

DISCUSSION

In the present study, we first tested abnormalities of voxel-wise brain-wide FC in first-episode, drug-naive patients with schizophrenia and non-affected siblings using the GFC analysis. The key finding was that the patients and the siblings shared enhanced GFC in the left SFG relative to the controls. Further ROC analysis showed that the GFC value in this area might serve as a marker with a relatively high sensitivity to discriminate the patients or the siblings from the controls. Compared to healthy controls, patients with schizophrenia showed disturbed GFC mainly in the thalamo-cortical network.

There are two important features of our study. First, we explored FC abnormalities in patients with schizophrenia in an unbiased way using the voxel-wise brain-wide method. To date, not a unanimous pattern of brain functional anomalies pertaining to schizophrenia has converged among researchers, though these studies have indicated importance of abnormalities in certain brain circuits. The reason may be that many previous studies in this field focused on some predefined brain areas using approaches based on ROI (Guo et al., 2015a). It is conceivable that different studies obtained different results by selecting different ROIs. Additionally, it is possible that the most important brain regions relating to the core pathological changes in schizophrenia were never covered in some studies. On the contrary, the GFC method used in our study investigated the FC abnormalities in a voxel-wise brain-wide and more importantly, an unbiased way.

The second important feature is the sample groups recruited in this study. First-episode, drug-naive patients with schizophrenia were recruited to explore the intact connectivity of these networks in the present study. Except patients with schizophrenia, unaffected siblings were also enrolled in the study. Taking into account that schizophrenia is a highly heritable and complex disorder, unaffected siblings of schizophrenia patients who share remarkable genetic backgrounds with the patients are at a high-risk state to develop the disease (Jang et al., 2011). In order to have a more comprehensive insight into the neural underpinnings of schizophrenia, it is essential to investigate this group of people without interference of clinical and treatment matters.

TABLE 1 | Baseline demographic and clinical characteristics of the study participants.

	Patients (n = 44)	Siblings (n = 42)	Controls (n = 44)	p-value
Gender (male/female)	28/16	28/14	23/21	0.35
Age (years)	23.45 ± 4.24	23.57 ± 3.62	23.55 ± 2.58	0.99
Education (years)	11.11 ± 2.46	12.13 ± 2.24	11.30 ± 1.67	0.11
FD (mm)	0.03 ± 0.03	0.03 ± 0.01	0.03 ± 0.02	0.34
Illness duration (months)	22.34 ± 7.01			
PANSS				
Positive symptom score	22.48 ± 5.37			
Negative symptom score	22.50 ± 6.38			
General symptom score	45.73 ± 6.97			
Total score	90.70 ± 11.17			

FD, framewise displacement; PANSS, the Positive and Negative Syndrome Scale; Values are expressed as mean ± SD.

TABLE 2 | Baseline group comparison in levels of GFC across groups.

Cluster location	Peak (MNI)			Number of voxels	T-value
	x	y	z		
Patients vs. Controls					
Left ITG/cerebellum Crus I	−45	−42	−24	55	−4.6571
Bilateral thalamus	6	−12	15	50	4.2670
Right angular gyrus	51	−57	33	139	4.6931
Bilateral PCC/precuneus	3	−54	33	67	4.0364
Left superior MPFC	−9	54	45	66	4.4945
Right superior frontal gyrus/middle frontal gyrus	39	24	48	150	5.0740
Left superior frontal gyrus	−9	27	60	113	5.1110
Siblings vs. Controls					
Left superior frontal gyrus	−15	66	9	28	4.1515

GFC, global-brain functional connectivity; ITG, inferior temporal gyrus; MPFC, medial prefrontal cortex; PCC, posterior cingulate cortex.

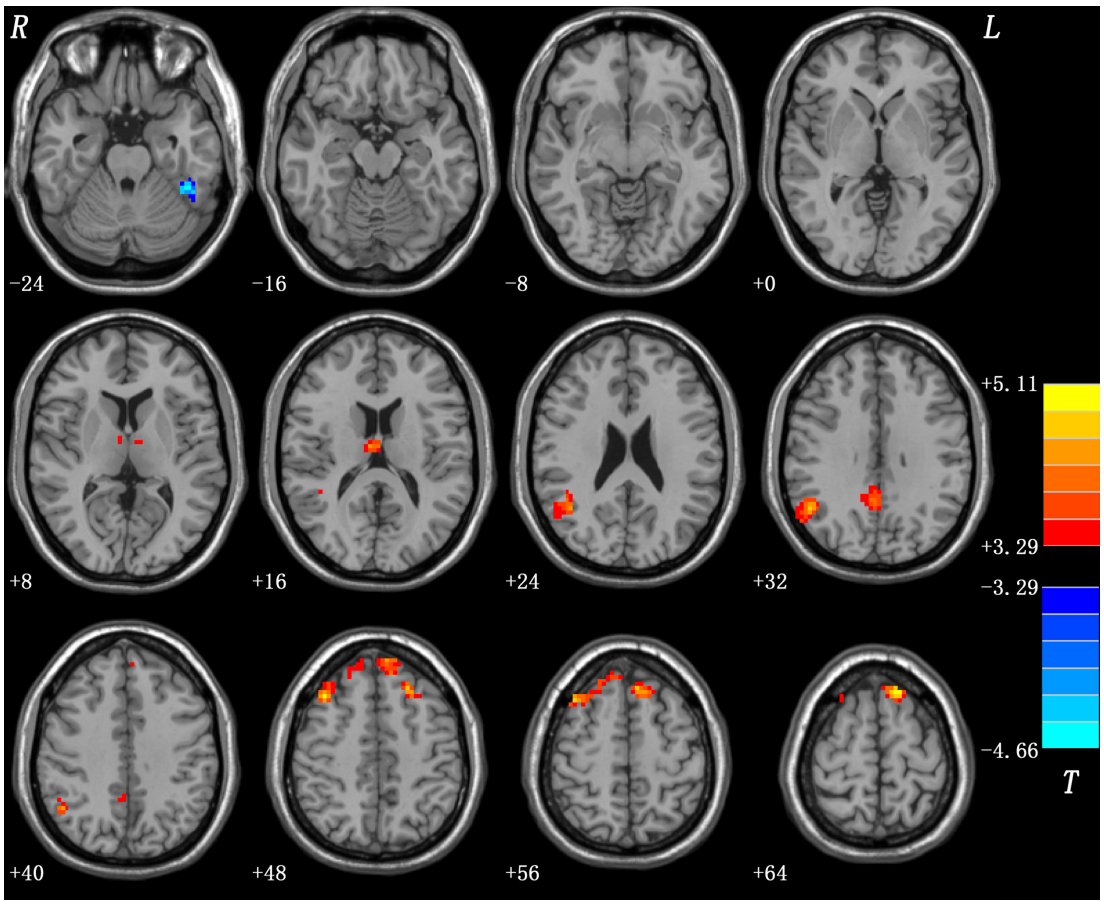

FIGURE 1 | Abnormal GFC in patients with schizophrenia relative to healthy controls. GFC, global-brain functional connectivity.

In addition, with more efforts putting into the effective treatment that could improve the clinical outcomes of patients with schizophrenia considerably, earlier identification and intervention are pushed to an urgent place (Chang et al., 2016). Investigating the vulnerability state and initial period of schizophrenia are help to address this issue.

The left SFG, involving in the impaired attention and cognitive domains (Wolf et al., 2008) including perception, working memory (Jenkins et al., 2018), and active imagery (Qiu et al., 2018), is one of the most consistently explored regions that may be a key hub in the pathophysiological processes of schizophrenia. In present study, increased GFC of the left SFG was found both in patients with schizophrenia and unaffected siblings and further ROC analysis exhibited that the GFC values of this region might be applied as a potential marker to differentiate the patients as well as the siblings from the controls with relatively high sensitivity. However, no correlations were found between the GFC value in this area and symptom severity or illness duration, which was somewhat out of our expectations. We supposed that the enhanced FC might be a trait alteration for schizophrenia independently of symptom severity and illness duration. The relatively small sample size was also a confounding factor. In addition, consistent with our results, many previous resting-state fMRI studies recorded no correlation between abnormal FC and clinical variables in patients with schizophrenia (Guo et al., 2015a). Actually, some researchers have reported a similar pattern of cognitive deficits between patients with schizophrenia and the first-degree relatives, including working memory, set shifting, and prepotent response (Johnstone et al., 2002; Brewer et al., 2005; Snitz et al., 2006). Similarly, a M100 magnetoencephalography study found greater left SFG M100 activity in not only patients with schizophrenia but also unaffected relatives (Chen et al., 2018). This shared auditory encoding abnormality indicated a compensatory adjustment by overactivating dorsal auditory pathway (Chen et al., 2013) and could also be regarded as a potential endophenotype.

The thalamus, associated with many brain functions such as cognitive and attention control (Carlesimo et al., 2011; Schmitt et al., 2017), goal-directed mental operation (Doucet et al., 2018), and experience and expression of emotion (Frodl et al., 2002), is a complex structure. Several neurobiological studies have postulated that the pathophysiology of schizophrenia involves abnormal functional interactions between the cortex and thalamus, the subcortical structure (Cheng et al., 2015). Our result of increased GFC in bilateral thalamus was consistent with previous studies, which found increased connectivity

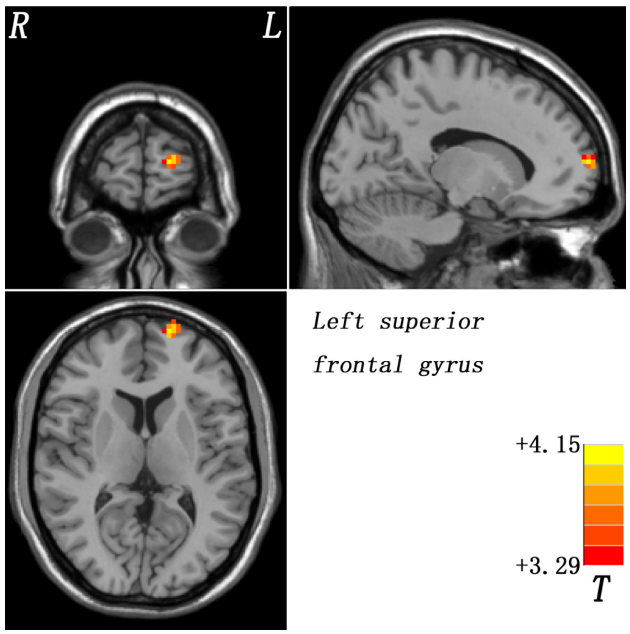

FIGURE 2 | Enhanced GFC in the left SFG in the siblings compared to the controls. GFC, global-brain functional connectivity; SFG, superior frontal gyrus.

between thalamus and motor and somatosensory cortical areas (Woodward et al., 2012). Compensatory effort or dedifferentiation is always considered as an explanation of hyperconnectivity of brain regions (Cabeza et al., 2002; Grady et al., 2005; Guo et al., 2013; Su et al., 2015), which may be affected by inflammation process in the early state of schizophrenia. In that state (Anticevic et al., 2015), astrocytes could be activated by proinflammatory cytokines like interleukin-6, and consequently the metabolism and blood flow increased (Liberto et al., 2004). It is noteworthy that numerous thalamic nuclei comprise the thalamus, and there are topographically parallel pathways linking these anatomical segregated nuclei to different cortical regions within the thalamo-cortical circuits (Alexander et al., 1986; Haber, 2003; Woodward et al., 2012). Pergola and colleagues found that gray matter volume of the mediodorsal thalamic nucleus was associated with schizophrenia but state-related, while the left anterior and midline thalamic nuclei was the most important region associated with familial risk (Pergola et al., 2017). Decreased connectivity between the prefrontal cortex and dorsomedial/anterior thalamus was also observed in previous studies (Woodward et al., 2012). It is still unclear whether the increased GFC in the bilateral thalamus documented by our study pertains to specific thalamic nuclei and whether there are associations between functional and structural imaging findings relating to thalamus. In addition, age is a vital factor that should be considered from a neurodevelopmental perspective. According to Fair and colleagues, there were significant differences in the thalamo-cortical FC between children, adolescents, and adults (Fair et al., 2010).

The DMN, including brain regions such as the posterior cingulate cortex (PCC)/precuneus, medial prefrontal cortex (MPFC), angular gyrus (Andrews-Hanna et al., 2014), and parahippocampal gyrus (Raichle et al., 2001), is one of the most consistently disturbed resting-state networks in patients with schizophrenia. MPFC is involved in the regulation of emotional behavior and self-referential processing in the DMN (Chen et al., 2012; Yu et al., 2014) and the angular gyrus plays an important role in the language process, spatial cognition, and memory retrieval (Uddin et al., 2010). Therefore, disturbed DMN network connectivity may be linked to part of poor performance seen in patients with schizophrenia. Some researchers also found unaffected siblings having altered regional activity in certain brain areas of the DMN (Guo et al., 2014a,c). However, one study showed no marked FC difference within the DMN between patients with schizophrenia and controls (Wolf et al., 2011). The

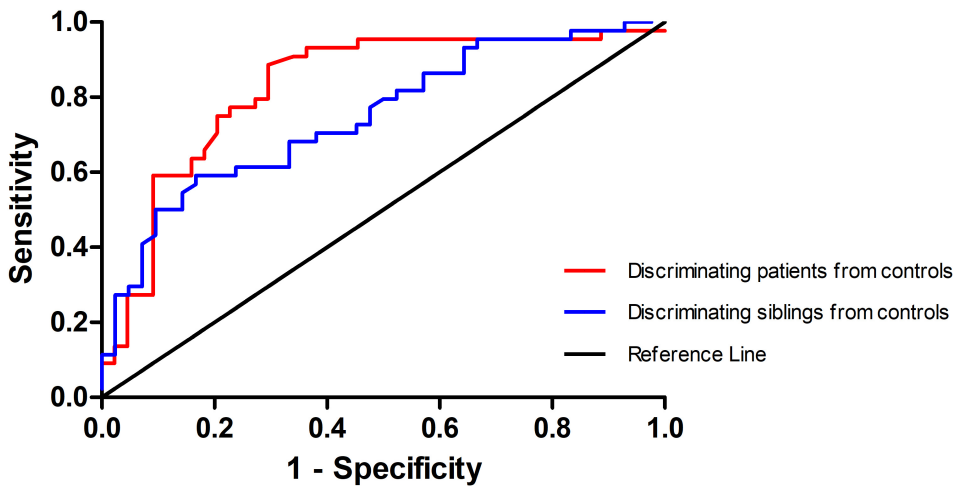

FIGURE 3 | Receiver operating characteristic (ROC) curve of separating the patients and the siblings from the controls by using the GFC values in the left SFG. GFC, global-brain functional connectivity; SFG, superior frontal gyrus.

inconsistency may result from sample heterogeneity, sample size, and analysis methods. For patients with schizophrenia, illness duration and potential medication effects are also confounding factors. Consistent with our results, the ITG, important for emotional processing, social cognition (Guo et al., 2014b), and facial perception (Schultz et al., 2000), has been reported to have reduced FC in patients with schizophrenia as compared with healthy controls (Vercammen et al., 2010). Previous evidence also suggests that the impairment of temporal lobe and constituent parts in schizophrenia patients may be an important element in the emergence of auditory hallucinations and thought disorder (Seok et al., 2007). Intriguingly, one study suggested that deficit schizophrenia, a subgroup of patients with poorer treatment response and greater possibility to become chronicity compared to non-deficit schizophrenia, demonstrated structural and functional abnormalities in ITG (Yu et al., 2017).

In addition to the relatively small sample size, there are some limitations in this study. First, the scanning did not conduct again in the patients group after treatment. A longitudinal study is better to portray the continuous GFC alteration of brain networks in vulnerable people and patients with schizophrenia. Second, structural alterations, including gray matter and white matter, were not examined in this study. According to some researchers (Guo et al., 2012, 2015b), there were structural alterations in the gray matter and white matter in patients with schizophrenia. Hence, structural alterations underlying GFC remain unclear. However, the neuroimaging data of patients, siblings, and controls were preprocessed in the same way in order to minimize the effects caused by lack of structural examination in the present study. Finally, the study was based on resting-state fMRI without tasks involved. Therefore, it may restrict the generalizability of this study and the interpretation of underlying pathophysiology should be caution.

CONCLUSION

In summary, this study is the first to explore voxel-wise brain-wide FC in first-episode drug-naive patients with schizophrenia and unaffected siblings. Dysconnectivity of the thalamo-cortical circuits may involve in the etiology of schizophrenia. Enhanced GFC in left SFG may serve as a potential endophenotype for schizophrenia.

DATA AVAILABILITY

All datasets generated for this study are included in the manuscript and/or the supplementary files.

AUTHOR CONTRIBUTIONS

WG and JZ designed the study. WG, QS, ZZ, YD, YO, and PP collected the original imaging data. WG, FL, XS, JC, and JZ managed and analyzed the imaging data. WG and YD wrote the first draft of the manuscript. All the authors contributed to and approved the final manuscript.

FUNDING

This study was supported by grants from the National Key R&D Program of China (2016YFC1307100 and 2016YFC1306900) and the National Natural Science Foundation of China (Grant Nos. 81571310, 81630033, 81771447, 81501451, and 81471363).

ACKNOWLEDGMENTS

The authors thank all individuals who served as the research participants.

REFERENCES

Alexander, G. E., DeLong, M. R., and Strick, P. L. (1986). Parallel organization of functionally segregated circuits linking basal ganglia and cortex. *Annu. Rev. Neurosci.* 9, 357–381. doi: 10.1146/annurev.ne.09.030186.002041

Andreasen, N. C., O'Leary, D. S., Cizadlo, T., Arndt, S., Rezai, K., Ponto, L. L., et al. (1996). Schizophrenia and cognitive dysmetria: a positron-emission tomography study of dysfunctional prefrontal-thalamic-cerebellar circuitry. *Proc. Natl. Acad. Sci. U.S.A.* 93, 9985–9990. doi: 10.1073/pnas.93.18.9985

Andrews-Hanna, J. R., Smallwood, J., and Spreng, R. N. (2014). The default network and self-generated thought: component processes, dynamic control, and clinical relevance. *Ann. N. Y. Acad. Sci.* 1316, 29–52. doi: 10.1111/nyas.12360

Anticevic, A., Hu, X., Xiao, Y., Hu, J., Li, F., Bi, F., et al. (2015). Early-course unmedicated schizophrenia patients exhibit elevated prefrontal connectivity associated with longitudinal change. *J. Neurosci.* 35, 267–286. doi: 10.1523/JNEUROSCI.2310-14.2015

Barch, D. M., and Csernansky, J. G. (2007). Abnormal parietal cortex activation during working memory in schizophrenia: verbal phonological coding disturbances versus domain-general executive dysfunction. *Am. J. Psychiatry* 164, 1090–1098. doi: 10.1176/ajp.2007.164.7.1090

Bertolino, A., and Blasi, G. (2009). The genetics of schizophrenia. *Neuroscience* 164, 288–299. doi: 10.1016/j.neuroscience.2009.04.038

Bluhm, R. L., Miller, J., Lanius, R. A., Osuch, E. A., Boksman, K., Neufeld, R. W., et al. (2007). Spontaneous low-frequency fluctuations in the BOLD signal in schizophrenic patients: anomalies in the default network. *Schizophr. Bull.* 33, 1004–1012. doi: 10.1093/schbul/sbm052

Bois, C., Whalley, H. C., McIntosh, A. M., and Lawrie, S. M. (2015). Structural magnetic resonance imaging markers of susceptibility and transition to schizophrenia: a review of familial and clinical high risk population studies. *J. Psychopharmacol.* 29, 144–154. doi: 10.1177/0269881114541015

Brewer, W. J., Francey, S. M., Wood, S. J., Jackson, H. J., Pantelis, C., Phillips, L. J., et al. (2005). Memory impairments identified in people at ultra-high risk for psychosis who later develop first-episode psychosis. *Am. J. Psychiatry* 162, 71–78. doi: 10.1176/appi.ajp.162.1.71

Cabeza, R., Anderson, N. D., Locantore, J. K., and McIntosh, A. R. (2002). Aging gracefully: compensatory brain activity in high-performing older adults. *Neuroimage* 17, 1394–1402. doi: 10.1006/nimg.2002.1280

Carlesimo, G. A., Lombardi, M. G., and Caltagirone, C. (2011). Vascular thalamic amnesia: a reappraisal. *Neuropsychologia* 49, 777–789. doi: 10.1016/j.neuropsychologia.2011.01.026

Chang, C. J., Chen, W. J., Liu, S. K., Cheng, J. J., Yang, W. C., Chang, H. J., et al. (2002). Morbidity risk of psychiatric disorders among the first degree

relatives of schizophrenia patients in Taiwan. *Schizophr. Bull.* 28, 379–392. doi: 10.1093/oxfordjournals.schbul.a006947

Chang, M., Womer, F. Y., Bai, C., Zhou, Q., Wei, S., Jiang, X., et al. (2016). Voxel-based morphometry in individuals at genetic high risk for schizophrenia and patients with schizophrenia during their first episode of psychosis. *PLoS One* 11:e0163749. doi: 10.1371/journal.pone.0163749

Chao-Gan, Y., and Yu-Feng, Z. (2010). DPARSF: a MATLAB toolbox for "Pipeline" data analysis of resting-state fMRI. *Front. Syst. Neurosci.* 4:13. doi: 10.3389/fnsys.2010.00013

Chen, J. D., Liu, F., Xun, G. L., Chen, H. F., Hu, M. R., Guo, X. F., et al. (2012). Early and late onset, first-episode, treatment-naive depression: same clinical symptoms, different regional neural activities. *J. Affect. Disord.* 143, 56–63. doi: 10.1016/j.jad.2012.05.025

Chen, Y. H., Edgar, J. C., Huang, M., Hunter, M. A., Epstein, E., Howell, B., et al. (2013). Frontal and superior temporal auditory processing abnormalities in schizophrenia. *Neuroimage Clin.* 2, 695–702. doi: 10.1016/j.nicl.2013.05.002

Chen, Y. H., Howell, B., Edgar, J. C., Huang, M., Kochunov, P., Hunter, M. A., et al. (2018). Associations and heritability of auditory encoding, gray matter, and attention in schizophrenia. *Schizophr. Bull.* doi: 10.1093/schbul/sby111 [Epub ahead of print].

Cheng, W., Palaniyappan, L., Li, M., Kendrick, K. M., Zhang, J., Luo, Q., et al. (2015). Voxel-based, brain-wide association study of aberrant functional connectivity in schizophrenia implicates thalamocortical circuitry. *NPJ Schizophr.* 1:15016. doi: 10.1038/npjschz.2015.16

Chiapponi, C., Piras, F., Fagioli, S., Piras, F., Caltagirone, C., and Spalletta, G. (2013). Age-related brain trajectories in schizophrenia: a systematic review of structural MRI studies. *Psychiatry Res.* 214, 83–93. doi: 10.1016/j.pscychresns.2013.05.003

Chin, R., You, A. X., Meng, F., Zhou, J., and Sim, K. (2018). Recognition of schizophrenia with regularized support vector machine and sequential region of interest selection using structural magnetic resonance imaging. *Sci. Rep.* 8:13858. doi: 10.1038/s41598-018-32290-32299

Chung, Y., and Cannon, T. D. (2015). Brain imaging during the transition from psychosis prodrome to schizophrenia. *J. Nerv. Ment. Dis.* 203, 336–341. doi: 10.1097/NMD.0000000000000286

Corlett, P. R., Murray, G. K., Honey, G. D., Aitken, M. R., Shanks, D. R., Robbins, T. W., et al. (2007). Disrupted prediction-error signal in psychosis: evidence for an associative account of delusions. *Brain* 130(Pt 9), 2387–2400. doi: 10.1093/brain/awm173

Craddock, R. C., Jbabdi, S., Yan, C. G., Vogelstein, J. T., Castellanos, F. X., Di Martino, A., et al. (2013). Imaging human connectomes at the macroscale. *Nat. Methods* 10, 524–539. doi: 10.1038/nmeth.2482

Cui, X., Liu, F., Chen, J., Xie, G., Wu, R., Zhang, Z., et al. (2018). Voxel-wise brain-wide functional connectivity abnormalities in first-episode, drug-naive patients with major depressive disorder. *Am. J. Med. Genet B Neuropsychiatr. Genet.* 177, 447–453. doi: 10.1002/ajmg.b.32633

de Kwaasteniet, B., Ruhe, E., Caan, M., Rive, M., Olabarriaga, S., Groefsema, M., et al. (2013). Relation between structural and functional connectivity in major depressive disorder. *Biol. Psychiatry* 74, 40–47. doi: 10.1016/j.biopsych.2012.12.024

Doucet, G. E., Moser, D. A., Luber, M. J., Leibu, E., and Frangou, S. (2018). Baseline brain structural and functional predictors of clinical outcome in the early course of schizophrenia. *Mol. Psychiatry* doi: 10.1038/s41380-018-0269-0

Dragovic, M., and Hammond, G. (2007). A classification of handedness using the Annett Hand Preference Questionnaire. *Br. J. Psychol.* 98(Pt 3), 375–387. doi: 10.1348/000712606X146197

Edgar, J. C., Hunter, M. A., Huang, M., Smith, A. K., Chen, Y., Sadek, J., et al. (2012). Temporal and frontal cortical thickness associations with M100 auditory activity and attention in healthy controls and individuals with schizophrenia. *Schizophr. Res.* 140, 250–257. doi: 10.1016/j.schres.2012.06.009

Fair, D. A., Bathula, D., Mills, K. L., Dias, T. G., Blythe, M. S., Zhang, D., et al. (2010). Maturing thalamocortical functional connectivity across development. *Front. Syst. Neurosci.* 4:10. doi: 10.3389/fnsys.2010.00010

Frodl, T., Meisenzahl, E. M., Zetzsche, T., Born, C., Groll, C., Jager, M., et al. (2002). Hippocampal changes in patients with a first episode of major depression. *Am. J. Psychiatry* 159, 1112–1118. doi: 10.1176/appi.ajp.159.7.1112

Gottesman, I. I., and Gould, T. D. (2003). The endophenotype concept in psychiatry: etymology and strategic intentions. *Am. J. Psychiatry* 160, 636–645. doi: 10.1176/appi.ajp.160.4.636

Grady, C. L., McIntosh, A. R., and Craik, F. I. (2005). Task-related activity in prefrontal cortex and its relation to recognition memory performance in young and old adults. *Neuropsychologia* 43, 1466–1481. doi: 10.1016/j.neuropsychologia.2004.12.016

Guo, W., Liu, F., Chen, J., Wu, R., Zhang, Z., Yu, M., et al. (2015a). Resting-state cerebellar-cerebral networks are differently affected in first-episode, drug-naive schizophrenia patients and unaffected siblings. *Sci. Rep.* 5:17275. doi: 10.1038/srep17275

Guo, W., Liu, F., Liu, J., Yu, L., Zhang, J., Zhang, Z., et al. (2015b). Abnormal causal connectivity by structural deficits in first-episode, drug-naive schizophrenia at rest. *Schizophr. Bull.* 41, 57–65. doi: 10.1093/schbul/sbu126

Guo, W., Liu, F., Liu, J., Yu, L., Zhang, Z., Zhang, J., et al. (2013). Is there a cerebellar compensatory effort in first-episode, treatment-naive major depressive disorder at rest? *Prog. Neuropsychopharmacol. Biol. Psychiatry* 46, 13–18. doi: 10.1016/j.pnpbp.2013.06.009

Guo, W., Liu, F., Liu, Z., Gao, K., Xiao, C., Chen, H., et al. (2012). Right lateralized white matter abnormalities in first-episode, drug-naive paranoid schizophrenia. *Neurosci. Lett.* 531, 5–9. doi: 10.1016/j.neulet.2012.09.033

Guo, W., Liu, F., Zhang, J., Zhang, Z., Yu, L., Liu, J., et al. (2014a). Abnormal default-mode network homogeneity in first-episode, drug-naive major depressive disorder. *PLoS One* 9:e91102. doi: 10.1371/journal.pone.0091102

Guo, W., Su, Q., Yao, D., Jiang, J., Zhang, J., Zhang, Z., et al. (2014b). Decreased regional activity of default-mode network in unaffected siblings of schizophrenia patients at rest. *Eur. Neuropsychopharmacol.* 24, 545–552. doi: 10.1016/j.euroneuro.2014.01.004

Guo, W., Yao, D., Jiang, J., Su, Q., Zhang, Z., Zhang, J., et al. (2014c). Abnormal default-mode network homogeneity in first-episode, drug-naive schizophrenia at rest. *Prog. Neuropsychopharmacol. Biol. Psychiatry* 49, 16–20. doi: 10.1016/j.pnpbp.2013.10.021

Haber, S. N. (2003). The primate basal ganglia: parallel and integrative networks. *J. Chem. Neuroanat.* 26, 317–330. doi: 10.1016/j.jchemneu.2003.10.003

Hahamy, A., Calhoun, V., Pearlson, G., Harel, M., Stern, N., Attar, F., et al. (2014). Save the global: global signal connectivity as a tool for studying clinical populations with functional magnetic resonance imaging. *Brain Connect.* 4, 395–403. doi: 10.1089/brain.2014.0244

Holt, D. J., Lakshmanan, B., Freudenreich, O., Goff, D. C., Rauch, S. L., and Kuperberg, G. R. (2011). Dysfunction of a cortical midline network during emotional appraisals in schizophrenia. *Schizophr. Bull.* 37, 164–176. doi: 10.1093/schbul/sbp067

Jang, J. H., Jung, W. H., Choi, J. S., Choi, C. H., Kang, D. H., Shin, N. Y., et al. (2011). Reduced prefrontal functional connectivity in the default mode network is related to greater psychopathology in subjects with high genetic loading for schizophrenia. *Schizophr. Res.* 127, 58–65. doi: 10.1016/j.schres.2010.12.022

Jenkins, L. M., Bodapati, A. S., Sharma, R. P., and Rosen, C. (2018). Working memory predicts presence of auditory verbal hallucinations in schizophrenia and bipolar disorder with psychosis. *J. Clin. Exp. Neuropsychol.* 40, 84–94. doi: 10.1080/13803395.2017.1321106

Joel, S. E., Caffo, B. S., van Zijl, P. C., and Pekar, J. J. (2011). On the relationship between seed-based and ICA-based measures of functional connectivity. *Magn. Reson. Med.* 66, 644–657. doi: 10.1002/mrm.22818

Johnstone, E. C., Lawrie, S. M., and Cosway, R. (2002). What does the Edinburgh high-risk study tell us about schizophrenia? *Am. J. Med. Genet.* 114, 906–912. doi: 10.1002/ajmg.b.10304

Jones, E. G. (1997). Cortical development and thalamic pathology in schizophrenia. *Schizophr. Bull.* 23, 483–501. doi: 10.1093/schbul/23.3.483

Karlsgodt, K. H., Sun, D., Jimenez, A. M., Lutkenhoff, E. S., Willhite, R., van Erp, T. G., et al. (2008). Developmental disruptions in neural connectivity in the pathophysiology of schizophrenia. *Dev. Psychopathol.* 20, 1297–1327. doi: 10.1017/S095457940800062X

Kelly, C., Biswal, B. B., Craddock, R. C., Castellanos, F. X., and Milham, M. P. (2012). Characterizing variation in the functional connectome: promise and pitfalls. *Trends Cogn. Sci.* 16, 181–188. doi: 10.1016/j.tics.2012.02.001

Konarski, J. Z., McIntyre, R. S., Grupp, L. A., and Kennedy, S. H. (2005). Is the cerebellum relevant in the circuitry of neuropsychiatric disorders? *J. Psychiatry Neurosci.* 30, 178–186.

Liberto, C. M., Albrecht, P. J., Herx, L. M., Yong, V. W., and Levison, S. W. (2004). Pro-regenerative properties of cytokine-activated astrocytes. *J. Neurochem.* 89, 1092–1100. doi: 10.1111/j.1471-4159.2004.02420.x

Liu, F., Zhu, C., Wang, Y., Guo, W., Li, M., Wang, W., et al. (2015). Disrupted cortical hubs in functional brain networks in social anxiety disorder. *Clin. Neurophysiol.* 126, 1711–1716. doi: 10.1016/j.clinph.2014.11.014

Liu, Y., Liang, M., Zhou, Y., He, Y., Hao, Y., Song, M., et al. (2008). Disrupted small-world networks in schizophrenia. *Brain* 131(Pt 4), 945–961. doi: 10.1093/brain/awn018

Lui, S., Deng, W., Huang, X., Jiang, L., Ma, X., Chen, H., et al. (2009). Association of cerebral deficits with clinical symptoms in antipsychotic-naive first-episode schizophrenia: an optimized voxel-based morphometry and resting state functional connectivity study. *Am. J. Psychiatry* 166, 196–205. doi: 10.1176/appi.ajp.2008.08020183

Lynall, M. E., Bassett, D. S., Kerwin, R., McKenna, P. J., Kitzbichler, M., Muller, U., et al. (2010). Functional connectivity and brain networks in schizophrenia. *J. Neurosci.* 30, 9477–9487. doi: 10.1523/JNEUROSCI.0333-10.2010

Mannell, M. V., Franco, A. R., Calhoun, V. D., Canive, J. M., Thoma, R. J., and Mayer, A. R. (2010). Resting state and task-induced deactivation: a methodological comparison in patients with schizophrenia and healthy controls. *Hum. Brain Mapp.* 31, 424–437. doi: 10.1002/hbm.20876

Maynard, T. M., Sikich, L., Lieberman, J. A., and LaMantia, A. S. (2001). Neural development, cell-cell signaling, and the "two-hit" hypothesis of schizophrenia. *Schizophr. Bull.* 27, 457–476. doi: 10.1093/oxfordjournals.schbul.a006887

McKeown, M. J., Hansen, L. K., and Sejnowsk, T. J. (2003). Independent component analysis of functional MRI: what is signal and what is noise? *Curr. Opin. Neurobiol.* 13, 620–629. doi: 10.1016/j.conb.2003.09.012

Moran, M. E., Hulshoff Pol, H., and Gogtay, N. (2013). A family affair: brain abnormalities in siblings of patients with schizophrenia. *Brain* 136(Pt 11), 3215–3226. doi: 10.1093/brain/awt116

Ongur, D., Lundy, M., Greenhouse, I., Shinn, A. K., Menon, V., Cohen, B. M., et al. (2010). Default mode network abnormalities in bipolar disorder and schizophrenia. *Psychiatry Res.* 183, 59–68. doi: 10.1016/j.pscychresns.2010.04.008

Pergola, G., Trizio, S., Di Carlo, P., Taurisano, P., Mancini, M., Amoroso, N., et al. (2017). Grey matter volume patterns in thalamic nuclei are associated with familial risk for schizophrenia. *Schizophr. Res.* 180, 13–20. doi: 10.1016/j.schres.2016.07.005

Phillips, J. R., Hewedi, D. H., Eissa, A. M., and Moustafa, A. A. (2015). The cerebellum and psychiatric disorders. *Front. Public Health* 3:66. doi: 10.3389/fpubh.2015.00066

Power, J. D., Barnes, K. A., Snyder, A. Z., Schlaggar, B. L., and Petersen, S. E. (2012). Spurious but systematic correlations in functional connectivity MRI networks arise from subject motion. *Neuroimage* 59, 2142–2154. doi: 10.1016/j.neuroimage.2011.10.018

Qiu, L., Yan, H., Zhu, R., Yan, J., Yuan, H., Han, Y., et al. (2018). Correlations between exploratory eye movement, hallucination, and cortical gray matter volume in people with schizophrenia. *BMC Psychiatry* 18:226. doi: 10.1186/s12888-018-1806-1808

Raichle, M. E., MacLeod, A. M., Snyder, A. Z., Powers, W. J., Gusnard, D. A., and Shulman, G. L. (2001). A default mode of brain function. *Proc. Natl. Acad. Sci. U.S.A.* 98, 676–682. doi: 10.1073/pnas.98.2.676

Rubinov, M., and Bullmore, E. (2013). Schizophrenia and abnormal brain network hubs. *Dialogues Clin. Neurosci.* 15, 339–349.

Schmitt, L. I., Wimmer, R. D., Nakajima, M., Happ, M., Mofakham, S., and Halassa, M. M. (2017). Thalamic amplification of cortical connectivity sustains attentional control. *Nat.* 545, 219–223. doi: 10.1038/nature22073

Schnack, H. G., van Haren, N. E., Nieuwenhuis, M., Hulshoff Pol, H. E., Cahn, W., and Kahn, R. S. (2016). Accelerated brain aging in schizophrenia: a longitudinal pattern recognition study. *Am. J. Psychiatry* 173, 607–616. doi: 10.1176/appi.ajp.2015.15070922

Schultz, R. T., Gauthier, I., Klin, A., Fulbright, R. K., Anderson, A. W., Volkmar, F., et al. (2000). Abnormal ventral temporal cortical activity during face discrimination among individuals with autism and Asperger syndrome. *Arch. Gen. Psychiatry* 57, 331–340. doi: 10.1001/archpsyc.57.4.331

Schulze-Rauschenbach, S., Lennertz, L., Ruhrmann, S., Petrovsky, N., Ettinger, U., Pukrop, R., et al. (2015). Neurocognitive functioning in parents of schizophrenia patients: attentional and executive performance vary with genetic loading. *Psychiatry Res.* 230, 885–891. doi: 10.1016/j.psychres.2015.11.031

Seok, J. H., Park, H. J., Chun, J. W., Lee, S. K., Cho, H. S., Kwon, J. S., et al. (2007). White matter abnormalities associated with auditory hallucinations in schizophrenia: a combined study of voxel-based analyses of diffusion tensor imaging and structural magnetic resonance imaging. *Psychiatry Res.* 156, 93–104. doi: 10.1016/j.pscychresns.2007.02.002

Skudlarski, P., Jagannathan, K., Anderson, K., Stevens, M. C., Calhoun, V. D., Skudlarska, B. A., et al. (2010). Brain connectivity is not only lower but different in schizophrenia: a combined anatomical and functional approach. *Biol. Psychiatry* 68, 61–69. doi: 10.1016/j.biopsych.2010.03.035

Smith, A. K., Edgar, J. C., Huang, M., Lu, B. Y., Thoma, R. J., Hanlon, F. M., et al. (2010). Cognitive abilities and 50- and 100-msec paired-click processes in schizophrenia. *Am. J. Psychiatry* 167, 1264–1275. doi: 10.1176/appi.ajp.2010.09071059

Snitz, B. E., Macdonald, A. W. III, and Carter, C. S. (2006). Cognitive deficits in unaffected first-degree relatives of schizophrenia patients: a meta-analytic review of putative endophenotypes. *Schizophr. Bull.* 32, 179–194. doi: 10.1093/schbul/sbi048

Su, Q., Yao, D., Jiang, M., Liu, F., Jiang, J., Xu, C., et al. (2015). Increased functional connectivity strength of right inferior temporal gyrus in first-episode, drug-naive somatization disorder. *Aust. N. Z. J. Psychiatry* 49, 74–81. doi: 10.1177/0004867414553949

Swerdlow, N. R. (2010). Integrative circuit models and their implications for the pathophysiologies and treatments of the schizophrenias. *Curr. Top. Behav. Neurosci.* 4, 555–583. doi: 10.1007/7854_2010_48

Thermenos, H. W., Keshavan, M. S., Juelich, R. J., Molokotos, E., Whitfield-Gabrieli, S., Brent, B. K., et al. (2013). A review of neuroimaging studies of young relatives of individuals with schizophrenia: a developmental perspective from schizotaxia to schizophrenia. *Am. J. Med. Genet. B Neuropsychiatr. Genet.* 162B, 604–635. doi: 10.1002/ajmg.b.32170

Turetsky, B. I., Greenwood, T. A., Olincy, A., Radant, A. D., Braff, D. L., Cadenhead, K. S., et al. (2008). Abnormal auditory N100 amplitude: a heritable endophenotype in first-degree relatives of schizophrenia probands. *Biol. Psychiatry* 64, 1051–1059. doi: 10.1016/j.biopsych.2008.06.018

Turner, J. A., Calhoun, V. D., Michael, A., van Erp, T. G., Ehrlich, S., Segall, J. M., et al. (2012). Heritability of multivariate gray matter measures in schizophrenia. *Twin Res. Hum. Genet.* 15, 324–335. doi: 10.1017/thg.2012.1

Uddin, L. Q., Supekar, K., Amin, H., Rykhlevskaia, E., Nguyen, D. A., Greicius, M. D., et al. (2010). Dissociable connectivity within human angular gyrus and intraparietal sulcus: evidence from functional and structural connectivity. *Cereb. Cortex* 20, 2636–2646. doi: 10.1093/cercor/bhq011

Vercammen, A., Knegtering, H., den Boer, J. A., Liemburg, E. J., and Aleman, A. (2010). Auditory hallucinations in schizophrenia are associated with reduced functional connectivity of the temporo-parietal area. *Biol. Psychiatry* 67, 912–918. doi: 10.1016/j.biopsych.2009.11.017

Wolf, N. D., Sambataro, F., Vasic, N., Frasch, K., Schmid, M., Schonfeldt-Lecuona, C., et al. (2011). Dysconnectivity of multiple resting-state networks in patients with schizophrenia who have persistent auditory verbal hallucinations. *J. Psychiatry Neurosci.* 36, 366–374. doi: 10.1503/jpn.110008

Wolf, R. C., Hose, A., Frasch, K., Walter, H., and Vasic, N. (2008). Volumetric abnormalities associated with cognitive deficits in patients with schizophrenia. *Eur. Psychiatry* 23, 541–548. doi: 10.1016/j.eurpsy.2008.02.002

Woodward, N. D., Karbasforoushan, H., and Heckers, S. (2012). Thalamocortical dysconnectivity in schizophrenia. *Am. J. Psychiatry* 169, 1092–1099. doi: 10.1176/appi.ajp.2012.12010056

Woodward, N. D., Rogers, B., and Heckers, S. (2011). Functional resting-state networks are differentially affected in schizophrenia. *Schizophr. Res.* 130, 86–93. doi: 10.1016/j.schres.2011.03.010

Yan, C. G., Wang, X. D., Zuo, X. N., and Zang, Y. F. (2016). DPABI: data processing and analysis for (resting-state) brain imaging. *Neuroinformatics* 14, 339–351. doi: 10.1007/s12021-016-9299-9294

Yoon, J. H., Tamir, D., Minzenberg, M. J., Ragland, J. D., Ursu, S., and Carter, C. S. (2008). Multivariate pattern analysis of functional magnetic resonance imaging data reveals deficits in distributed representations in schizophrenia. *Biol. Psychiatry* 64, 1035–1041. doi: 10.1016/j.biopsych.2008.07.025

Yoshida, T., McCarley, R. W., Nakamura, M., Lee, K., Koo, M. S., Bouix, S., et al. (2009). A prospective longitudinal volumetric MRI study of superior temporal gyrus gray matter and amygdala-hippocampal complex in chronic schizophrenia. *Schizophr. Res.* 113, 84–94. doi: 10.1016/j.schres.2009.05.004

Yu, M., Dai, Z., Tang, X., Wang, X., Zhang, X., Sha, W., et al. (2017). Convergence and divergence of brain network dysfunction in deficit and non-deficit schizophrenia. *Schizophr. Bull.* 43, 1315–1328. doi: 10.1093/schbul/sbx014

Yu, R., Chien, Y. L., Wang, H. L., Liu, C. M., Liu, C. C., Hwang, T. J., et al. (2014). Frequency-specific alternations in the amplitude of low-frequency fluctuations in schizophrenia. *Hum. Brain Mapp.* 35, 627–637. doi: 10.1002/hbm.22203

Zhou, Y., Liang, M., Tian, L., Wang, K., Hao, Y., Liu, H., et al. (2007). Functional disintegration in paranoid schizophrenia using resting-state fMRI. *Schizophr. Res.* 97, 194–205. doi: 10.1016/j.schres.2007.05.029

Conflict of Interest Statement: The authors declare that the research was conducted in the absence of any commercial or financial relationships that could be construed as a potential conflict of interest.

frontiers in Psychiatry

ORIGINAL RESEARCH
published: 16 April 2019
doi: 10.3389/fpsyt.2019.00252

Thalamocortical Hyperconnectivity and Amygdala-Cortical Hypoconnectivity in Male Patients With Autism Spectrum Disorder

Tetsuya Iidaka[1,2], Tomohiro Kogata[2], Yoko Mano[2] and Hidetsugu Komeda[3]*

[1] Brain & Mind Research Center, Nagoya University, Nagoya, Japan, [2] Department of Physical and Occupational Therapy, Graduate School of Medicine, Nagoya University, Nagoya, Japan, [3] Department of Education, Psychology, and Human Studies, Aoyama Gakuin University, Tokyo, Japan

Background: Analyses of resting-state functional magnetic resonance imaging (rs-fMRI) have been performed to investigate pathophysiological changes in the brains of patients with autism spectrum disorder (ASD) relative to typically developing controls (CTLs). However, the results of these previous studies, which have reported mixed patterns of hypo- and hyperconnectivity, are controversial, likely due to the small sample sizes and limited age range of included participants.

Methods: To overcome this issue, we analyzed multisite neuroimaging data from a large sample (n = 626) of male participants aged between 5 and 29 years (mean age = 13 years). The rs-fMRI data were preprocessed using SPM12 and DPARSF software, and signal changes in 90 brain regions were extracted. Multiple linear regression was used to exclude the effect of site differences in connectivity data. Subcortical–cortical connectivity was computed using connectivities in the hippocampus, amygdala, caudate nucleus, putamen, pallidum, and thalamus. Eighty-eight connectivities in each structure were compared between patients with ASD and CTLs using multiple linear regression with group, age, and age × group interactions, head movement parameters, and overall connectivity as variables.

Results: After correcting for multiple comparisons, patients in the ASD group exhibited significant increases in connectivity between the thalamus and 19 cortical regions distributed throughout the fronto-parietal lobes, including the temporo-parietal junction and posterior cingulate cortices. In addition, there were significant decreases in connectivity between the amygdala and six cortical regions. The mean effect size of hyperconnectivity (0.25) was greater than that for hypoconnectivity (0.08). No other subcortical structures showed significant group differences. A group-by-age interaction was observed for connectivity between the thalamus and motor-somatosensory areas.

Conclusions: These results demonstrate that pathophysiological changes associated with ASD are more likely related to thalamocortical hyperconnectivity than to amygdala-cortical hypoconnectivity. Future studies should examine full sets of clinical and behavioral symptoms in combination with functional connectivity to explore possible biomarkers for ASD.

Keywords: resting, functional magnetic resonance imaging, age, development, network, amygdala

OPEN ACCESS

Edited by:
Lin Shi,
The Chinese University of Hong Kong, China

Reviewed by:
Baxter P. Rogers, Vanderbilt University, United States
Meiling Li, Harvard Medical School, United States

****Correspondence:***
Tetsuya Iidaka
iidaka@met.nagoya-u.ac.jp

Specialty section:
This article was submitted to Neuroimaging and Stimulation, a section of the journal Frontiers in Psychiatry

Received: *06 December 2018*
Accepted: *02 April 2019*
Published: *16 April 2019*

Citation:
Iidaka T, Kogata T, Mano Y and Komeda H (2019) Thalamocortical Hyperconnectivity and Amygdala-Cortical Hypoconnectivity in Male Patients With Autism Spectrum Disorder. Front. Psychiatry 10:252. doi: 10.3389/fpsyt.2019.00252

INTRODUCTION

Autism spectrum disorder (ASD) is characterized by atypical social communication and restricted patterns of behavior, interest, or activities, both of which must be present in the early developmental period (1). Hyper- or hyporeactivity to sensory stimuli and unusual interest in sensory aspects of the environment are highly significant symptoms that are directly associated with subjective distress in daily life in affected patients (2). The distress caused by particular sensory stimuli can cause maladaptive behaviors in those who are unable to communicate appropriately in social situations. Although sensory hyper- and hyporesponsiveness are not unique to ASD, they appear to be more prevalent in this population than among individuals with other developmental disabilities or schizophrenia. Previous studies have investigated the neurophysiological basis of such disturbances in unimodal and multimodal sensory processing among patients with ASD, as well as disturbances in shifting attention to and from sensory stimuli (3, 4).

Extensive structural and functional neuroimaging studies have investigated alterations in patterns of brain connectivity in patients with ASD, relative to typically developing controls. Such studies often employ resting-state functional magnetic resonance imaging (rs-fMRI), a powerful tool for functional connectivity (FC) analysis that may help to elucidate pathophysiological correlates in the brains of patients with ASD. Both hypo- and hyperconnectivity have been observed in brain regions implicated in ASD. That is, the results of each study range from robust underconnectivity to robust overconnectivity depending on the age of participants and type of analysis pipeline. Indeed, previous research has indicated that, in FC analyses, overconnectivity or underconnectivity in patients relative to controls depends on the application of bandpass filtering and task regressors (5). In addition, the use of global signal regression (GSR) has always been debated because the global signal may also include neuronal activity within the whole brain (6). Thus, methodological variables have exerted indispensable effects on group differences reported in previous studies.

Mixed results have also been reported regarding differences in FC between patients with ASD and controls. For example, Glerean et al. suggested that the mixture of hypo- and hyperconnectivity reported across previous ASD studies is reflected in the composition of the default-mode and ventro-temporal-limbic subnetworks (7). In this study, the ASD group exhibited reduced interhemispheric connectivity in regions of typically high interhemispheric connectivity and increased interhemispheric connectivity in areas of typically reduced connectivity (8). In contrast, a study by Tyszka et al. demonstrated that neurotypical and high-functioning adults with autism displayed very similar patterns and strengths of resting-state connectivity, reporting no evidence for altered connectivity at the whole-brain level (9).

These seemingly contradictory findings may be the result of the small sample sizes utilized in previous studies. Abraham et al. demonstrated the high classification accuracy of ASD as compared with controls using a large (n = 871) multisite dataset known as the Autism Brain Imaging Data Exchange (ABIDE) database (10). In another study involving a larger sample size, 418 patients with ASD and 509 matched controls underwent whole-brain voxel-based rs-fMRI, which revealed that patients with ASD exhibited reduced cortical connectivity in the middle temporal gyrus/superior temporal sulcus and increased connectivity in the medial thalamus (11). Such findings indicate that the use of a large multisite dataset may help to elucidate the functional changes in brain connectivity associated with ASD.

A small sample size and limited age range make it difficult to reproduce the studies, as disease-specific patterns of brain activity may change across age groups, and analyses using multiple tests of connectivity fail after correcting for multiple comparisons. To overcome these issues, we analyzed a large rs-fMRI dataset from the ABIDE II database that included only male patients ranging in age from 5 to 29 years. Our primary hypothesis was that neurophysiological changes observed in the brains of patients with ASD are caused by dysconnectivity (hypo- and/or hyperconnectivity) between subcortical structures and cortical mantles. This hypothesis was driven by a recent developmental theory, which proposes that functional imbalances between the affective control system involving subcortical structures (e.g., amygdala and striatum) and the cognitive control system mediated by the prefrontal cortices may affect emotional and social behaviors during early to late adolescence (12). According to this model, sensory modulation in ASD (2, 3) most likely involves functional alterations in thalamocortical connectivity, as the thalamus is known to connect primary sensory input with higher-order cortical areas (13–15).

MATERIALS AND METHODS

Participants

The original imaging and demographic data were collected from the ABIDE II database (http://fcon_1000.projects.nitrc.org/indi/abide/index.html), which allows unrestricted usage for noncommercial research purposes. Although the dataset included both adults and children of both sexes, only male participants ranging from 5 to 29 years of age were included in the present study. Brain images and related data from 368 patients with ASD and 362 control participants with typical development (CTL) from 17 universities and research institutes were used for the initial analysis. Following exclusion of participants with excessive head movement during scanning and failure in the spatial normalization steps (for details, see the section Imaging Data Analysis), the results from the remaining 311 patients with ASD and 315 CTLs were reported. The mean ages (± s.d). in the ASD and CTL groups were 13.9 ± 5.3 and 13.4 ± 5.5 years, respectively. The participants' demographic data and the abbreviated names of each institution are listed in **Supplementary Table 1**. The ethics committee of the Nagoya University School of Medicine approved the usage of these anonymous data for research purposes.

Autism was diagnosed using the Autism Diagnostic Interview-Revised (ADI-R) (16) and Autism Diagnostic Observation Schedule (ADOS) (17) in almost all cases. The CTL participants were screened in clinical interviews conducted by experts in child psychiatry. Intelligent quotients (IQs) were measured in 301 patients with ASD and 310 CTLs; however, all but one

institute provided full scale IQ, while one institute (EMC) provided only performance IQ. Details regarding the diagnostic procedures and questionnaires used can be found on the ABIDE website. Age and IQ distribution for each group are shown in **Supplementary Figure 1**. There was no significant difference in mean age between the two groups (t-test, $p = 0.24$), although IQ was lower in the ASD group than in the CTL group (mean ± s.d. ASD; 106 ± 16, CTL; 114 ± 12, t-test, $p < 0.001$). Among the 311 patients with ASD, the ADOS score (17) was obtained from 188 (60%) patients. Ninety-four patients with ASD (30%) were receiving psychotropic medication at the time of scanning, while 185 (60%) were not. Data for medication status were unavailable for 32 (10%) patients. Among CTL participants, 12 (4%) were taking medication at the time of scanning, while 260 (83%) were not. Data for medication status were unavailable for 43 (14%) CTLs (**Supplementary Figure 2**).

Imaging Data Acquisition

At each institute, functional brain images were acquired using a 3-T scanner and a T2*-weighted gradient-echo echo-planar imaging (EPI) sequence, which is sensitive to blood oxygen level-dependent (BOLD) contrast. Participants were asked to lie still in the scanner while remaining awake. Although the scanning parameters, MRI vendor, voxel size, number of volumes, scanning time, and instructions whether to keep eyes open/closed varied among the institutes, the general experimental procedure used was uniform within each institute. The number of image volumes for each participant ranged from 120 to 947 (mean = 234), and scanning time ranged from 5 to 16.4 min (mean = 7.0). The details of the scanning parameters and experimental settings are provided in **Supplementary Table 2**.

Imaging Data Analysis

Preprocessing

Data were analyzed using SPM12 software (Wellcome Department of Imaging Neuroscience, London, UK, http://www.fil.ion.ucl.ac.uk/spm/) at the Brain and Mind Research Center of Nagoya University. After discarding the first 10 volumes, all volumes were spatially realigned to the mean volume, and the signal in each slice was temporally realigned to that obtained in the middle slice using sinc interpolation. No slice timing correction was applied for datasets with multiband acquisition. The resliced volumes were normalized to the Montreal Neurological Institute (MNI) space with a voxel size of 3 × 3 × 3 mm using an EPI template in SPM12. The normalized images were spatially smoothed with a 4-mm Gaussian kernel. After the preprocessing steps, several quality control steps were employed. Participants whose maximum head movement was greater than 3.0 mm and 3° and those whose normalized images did not correctly match the EPI template were removed from the study.

Resting-State Functional Connectivity Analyses

Preprocessed datasets were further processed using the Data Processing Assistant for Resting-State fMRI toolkit (DPARSF; http://www.rfmri.org, advanced version) (18). Processing was conducted according to the following steps: 1) removal of the linear and quadric trends in the time series; 2) temporal band-pass filtering (0.01–0.1 Hz) to reduce the effect of low-frequency drift and high-frequency noise; 3) regressing out the effect of head motion during scanning using six head motion parameters, six head motion parameters one time point before, and the 12 corresponding squared items (Friston 24-parameter model); and 4) controlling for nonneural noise in the time series by including covariates in the linear regression (i.e., the white matter and cerebrospinal fluid signals). Since sufficient empirical evidence has shown that the results of FC after GSR should be interpreted carefully, the global signal was not removed in the present study (6, 19, 20). Head motion is known to have substantial effects on the results of FC analyses (21). Image scrubbing of the time-series data was performed by deleting one time point before and two time points after the excessive head movement, as defined by framewise displacement (FD) greater than 0.5 (22). The group differences in mean FD value and the proportion of scrubbed volumes were investigated using a Mann–Whitney U-test (statistical threshold, $p < 0.05$, **Table 1**).

The residuals of the datasets after band-pass filtering, removal of the trends and nuisance covariates, and scrubbing were regarded as BOLD signal fluctuations originating from neuronal activity during the resting state. The Automated Anatomical Labeling (AAL) template (23), which is widely used for identifying brain regions in the MNI space, was applied to the normalized and smoothed time-series datasets of each participant. The AAL template is a standard brain template for creating intrinsic connectivity (24, 25), although other templates have been used for the same purpose [e.g., the Harvard-Oxford Atlas (9, 26) and voxel-wise lattice method (27, 28)]. The AAL template divides each hemisphere into 45 distinct regions. The average time-series data were computed in each of the 90 regions for each participant. We used the AAL template because it is implemented in DPARSF software, and a 90 × 90 correlation matrix is better suited to avoid issues with multiple comparisons in the data analysis, relative to other templates with higher spatial resolution.

The time-series data from each of the 90 regions were cross-correlated, and Pearson's correlation coefficients (r) between each brain region and the remaining 89 regions were computed for each participant. Individual r values were normalized to z values using Fisher's z-transformation. The z-transformed correlation coefficients were represented in a 90 × 90 FC matrix,

TABLE 1 | Group differences in head motion parameters.

	ASD	CTL	U-test
FD	0.22 (0.20)	0.19 (0.11)	$p = 0.051$
Scrubbed (%)	18.3 (17.8)	14.9 (16.7)	$p = 0.002$

FD, frame wise displacement; ASD, autism spectrum disorder; CTL, control. Scrubbed (%): the proportion of the scrubbed volumes in total scan volumes. Mean and SD in the parentheses. U-test: Mann–Whitney U-test.

which was symmetric with regard to the diagonal. Multiple linear regression was used to further control for site effect on the FC matrix by regressing out the *z*-transformed correlation coefficients for each matrix element on dummy variables for each site. The standardized residuals were used as an estimate of the FC of each region and every other region controlling for site effect (29). This process was conducted using MATLAB-based in-house software.

Extracting Subcortical–Cortical Functional Connectivity

Our *a priori* hypothesis was that subcortical–cortical connectivity is altered in patients with ASD relative to CTLs during the developmental period and early adulthood. Therefore, we extracted the subcortical–cortical connectivity values from the matrix elements created in the previous section. Six subcortical structures (i.e., the hippocampus, amygdala, caudate nucleus, putamen, pallidum, and thalamus) in the left and right hemispheres, as defined by the AAL template, were selected for this purpose. For each structure, 88 FC values with every other region were extracted by excluding the FC with a counterpart in an opposite hemisphere; for example, an FC between the left and right hippocampus was not included in the analysis. Finally, the FCs from subcortical structures in each of the left and right hemispheres were averaged; for example, we averaged connectivity values between the left hippocampus and region A and those between the right hippocampus and region A. Finally, overall mean connectivity, i.e., the average of all elements of the 6×88 subcortical and cortical connectivity matrix, was computed in each subject.

Group Differences in Subcortical–Cortical Functional Connectivity

Eighty-eight FCs in each of the six structures were compared between the ASD and CTL groups *via* multiple linear regression using the FC as a dependent variable and group, age, the age × group interaction, mean FD, and overall mean connectivity as independent variables. Age, mean FD, and overall mean connectivity were mean corrected. The analysis was conducted using Origin Pro software (https://www.originlab.com/). The statistical threshold was set at $p < 0.05$ after correction for multiple comparisons using a false-discovery rate (FDR) (30) in each structure. In the present study, a significant main effect of group on FC strength was obtained only for the thalamus and amygdala. The region names, adjusted *p*-values of the main effect of group, and the effect size of Hedges's *g* are listed in **Tables 2** and **3**. The cortical regions that survived the FDR correction were superimposed on the cortical surface using BrainNet Viewer (**Figures 1** and **2**, http://www.nitrc.org/projects/bnv/) (31). Among the significant results for the thalamus, FC values for four cortical regions with an effect size $g > 0.27$ are plotted in **Figure 1**. To investigate whether the significant results could be influenced by the group difference in intellectual function, FIQ was added as an independent variable in the multiple regression analysis. Finally, Pearson's correlation coefficients between the significant thalamocortical and amygdala-cortical connectivity values and social and communication subscales of the ADOS were investigated (statistical threshold, $p < 0.05$).

TABLE 2 | Cortical regions with significant hyperconnectivity with thalamus in ASD group.

No.	Region name	adj-p-value	E.S. (*g*)
1	Precentral_L	0.048	0.21
2	Frontal_Sup_L	0.033	0.23
3	Frontal_Sup_R	0.028	0.25
4	Frontal_Sup_Orb_R	0.025	0.25
5	Frontal_Mid_L	0.040	0.23
6	Frontal_Mid_Orb_R	0.042	0.24
7	Frontal_Sup_Medial_L	0.049	0.22
8	Frontal_Sup_Medial_R	0.023	0.26
9	Frontal_Med_Orb_R	0.033	0.22
10	Cingulum_Post_L	0.025	0.27
11	Cingulum_Post_R	0.023	0.28
12	Postcentral_L	0.043	0.24
13	Postcentral_R	0.023	0.26
14	Parietal_Sup_L	0.025	0.24
15	Parietal_Inf_L	0.033	0.24
16	SupraMarginal_L	0.023	0.29
17	Angular_L	0.023	0.27
18	Angular_R	0.049	0.23
19	Paracentral_Lobule_L	0.028	0.25

All p-values are adjusted and significant after FDR correction at p < 0.05. E.S. (g) indicates effect size of Hedges's g. Positive effect size indicates hyperconnectivity in ASD and negative effect size indicates hypoconnectivity in ASD as compared with CTL.

TABLE 3 | Cortical regions with significant hypoconnectivity with amygdala in ASD group.

No.	Region name	adj-*p*-value	E.S. (*g*)
1	Frontal_Inf_Oper_R	0.039	−0.07
2	Frontal_Inf_Tri_R	0.028	−0.07
3	Calcarine_L	0.039	−0.07
4	Lingual_L	0.020	−0.10
5	Fusiform_L	0.023	−0.09
6	Temporal_Sup_R	0.020	−0.08

All p-values are adjusted and significant after FDR correction at p < 0.05. E.S. (g) indicates effect size of Hedges's g. Positive effect size indicates hyperconnectivity in ASD and negative effect size indicates hypoconnectivity in ASD as compared with CTL.

Effect of Age and Age-by-Group Interaction on Functional Connectivity

Multiple linear regression using the FC values from the thalamus and amygdala revealed significant group differences in FC following FDR correction for multiple comparisons. Because these results included a main effect of age and age-by-group interaction terms, we used the main effect and interaction to investigate the region in which the relationship between connectivity and age may or may not differ between the ASD and CTL groups. The cortical regions in which the main effect and interaction terms were significant in the multiple linear regression analysis were reported. The statistical threshold was

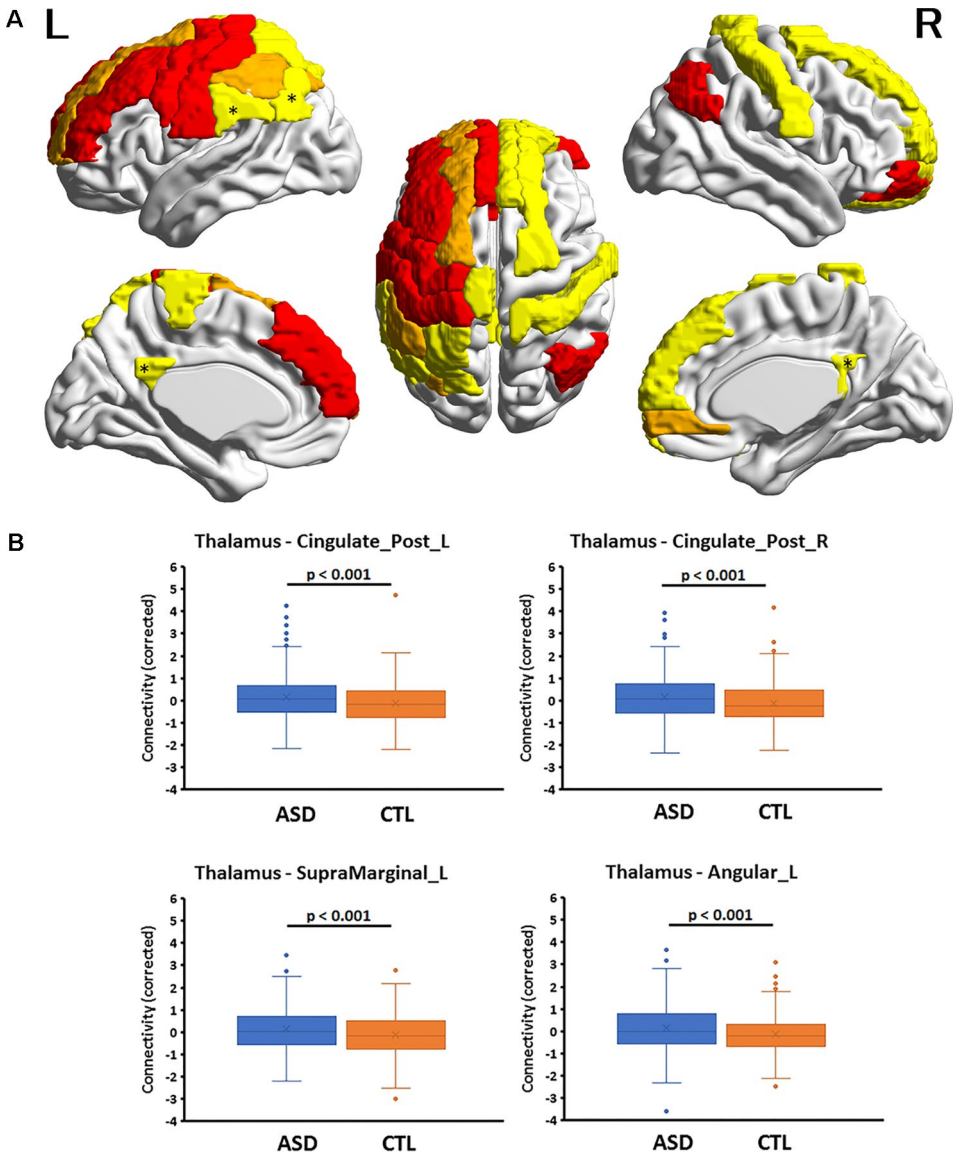

FIGURE 1 | (A) Cortical regions with hyperconnectivity with the thalamus in autism. Nineteen cortical regions in which connectivity with the thalamus was significantly greater for the autism spectrum disorder (ASD) group than for the control (CTL) group after false-discovery rate (FDR) correction were mapped on the surface of the template brain. Colored regions correspond to the regions listed in **Table 1**. The colors of the regions indicate levels of FDR adjusted *p*-value—yellow: $0.02 < p < 0.03$; orange: $0.03 < p < 0.05$; red: $0.04 < p < 0.05$. An asterisk indicates the region shown in the bottom. The figure was created using BrainNet Viewer. **(B)** Four representative regions with thalamocortical hyperconnectivity in autism. Boxplots of four thalamocortical functional connectivities for the ASD and CTL groups. Among the 19 connectivities that survived FDR correction, these 4 were highly significant (Hedges's $g > 0.27$) and were associated with the posterior cingulate cortex and temporo-parietal junction (TPJ, supramarginal and angular gyri), which are subdivisions of the default mode network. The mean connectivity values were significantly higher in the ASD group than in the CTL group. A boxplot shows the distribution of data into quartiles, the mean (cross;×), and outliers. The whisker lines indicate the outer boundaries of the upper and lower quartiles, while points outside the whiskers indicate outliers. These are representative results, and all connectivities that survived FDR correction are listed in **Table 1**.

set at $p < 0.05$, uncorrected for multiple comparisons. For the significant age-by-group interaction effect, the FC values and age for both groups are plotted in **Figure 3**. Pearson's correlation coefficient between age and FC in each group was computed without testing the statistical significance level because the interaction term was proven to be significant in the multiple regression analysis.

The Relationship among Age, Head Movement, Intellectual Function, and Connectivity

To explore the relationships among the age, FD, FIQ, and overall connectivity, Pearson's correlation coefficients were computed for each group (statistical threshold, $p < 0.05$, **Supplementary Table 4**). A multiple regression analysis was conducted including

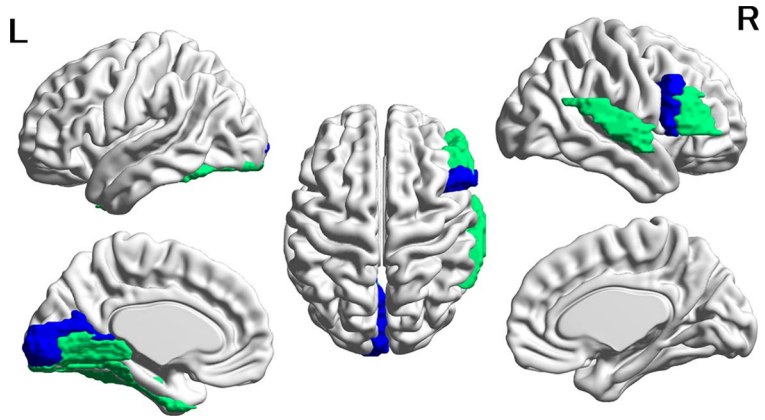

FIGURE 2 | Cortical regions with hypoconnectivity with the amygdala in autism. Six cortical regions in which connectivity with the amygdala was significantly greater for the CTL group than for the ASD group after FDR correction were mapped on the surface of the template brain. Colored regions correspond to the regions listed in **Table 2**. The colors of the regions indicate levels of FDR adjusted *p*-value—green: $0.02 < p < 0.03$; blue: $0.03 < p < 0.04$. The figure was created using BrainNet Viewer.

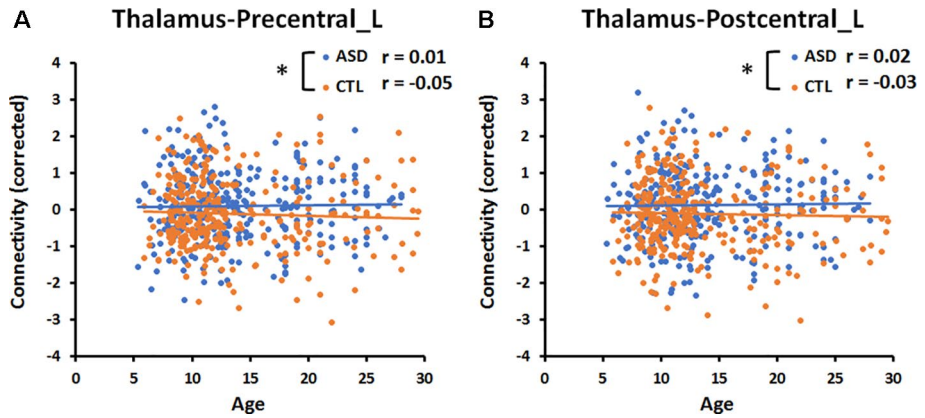

FIGURE 3 | Significant age-by-group interaction effect on thalamocortical connectivities. **(A)** The correlation between age and connectivity in the thalamus-precentral gyrus of the left hemisphere was weakly negative ($r = -0.05$) in the CTL group, but near zero ($r = 0.01$) in the ASD group. **(B)** The correlation between age and thalamus-postcentral gyrus of the left hemisphere was weakly negative ($r = -0.03$) in the CTL group, but weakly positive ($r = 0.02$) in the ASD group. An asterisk indicates a significant age-by-group interaction effect ($p < 0.05$, uncorrected). Blue and orange lines indicate the regression lines of ASD and CTL, respectively.

each of these values (age, FD, FIQ, and overall connectivity) as a dependent variable and age, group, and the age × group interaction term as independent variables (statistical threshold, $p = 0.05$).

Effects of Medication on Functional Connectivity in the ASD Group

In the present study, we included participants receiving any kind of psychotropic medication that may alter the FC in the brain because the exclusion of those participants would have reduced the sample size by 29%, potentially decreasing the statistical power of the dataset. To clarify the effects of medication on our results, we compared FC matrices between 94 patients with ASD who received psychotropic medication (on-med group) and 185 who did not (off-med group) at the time of scanning. The mean age and mean IQ were compared between the groups using t-tests. Eighty-eight FCs in the thalamus and amygdala were compared between the on- and off-med groups using the FC as a dependent variable, and group, age, the age × group interaction, mean FD, and overall mean connectivity as independent variables. Age, mean FD, and overall mean connectivity were mean corrected. Finally, mean FD and the proportion of scrubbed volumes were compared between the on- and off-med groups using a Mann–Whitney U-test (**Supplementary Table 5**). The statistical threshold was set at $p < 0.05$, uncorrected.

RESULTS

Group Differences in Head Motion Parameters

There was a trend towards significance ($p = 0.051$) in the difference in FD values between the ASD and CTL groups, and

the proportion of scrubbed volumes was significantly higher in the ASD group than in the CTL group (**Table 1**).

Group Differences in Subcortical–Cortical Functional Connectivity

Multiple linear regression analyses revealed that, among the six subcortical structures including the amygdala, hippocampus, caudate nucleus, pallidum, putamen, and thalamus, only those FCs connecting the thalamus and amygdala with several cortical regions exhibited significant main effects of group after correcting for multiple comparisons. In all 19 thalamocortical connectivities that survived correction for multiple comparisons, the mean FC values were greater in the ASD group than in the CTL group. The effect size of the group difference ranged from 0.21 to 0.29 (mean, 0.25, **Table 2** and **Figure 1**). In the ASD group, increased connectivity was observed between the thalamus and the frontal, cingulate, and parietal cortices of the left and right hemispheres. Regions exhibiting highly significant differences and medium effect sizes were identified in the left and right posterior cingulate cortices (PCCs; Cingulum_Post_L and Cingulum_Post_R), left supramarginal gyrus (SupraMarginal_L), and left angular gyrus (Angular_L). Boxplots of the FC values in the four regions for both groups are illustrated in **Figure 1**.

In contrast, in all six amygdala-cortical connectivities that survived correction for multiple comparisons, the mean FC values were lower in the ASD group than in the CTL group. The effect size of the group difference ranged from 0.07 to 0.10 (mean, 0.08, **Table 3** and **Figure 2**). In the ASD group, decreased connectivity was observed between the amygdala and the frontal, occipital, and temporal cortices of the left and right hemispheres. When the FIQ was included as an independent variable in the multiple regression analysis of these connectivities, the group difference remained significant (uncorrected p-values: 0.0007–0.025). There was no significant correlation between the connectivity values and the ADOS subscales (social and communication). The results of group difference in connectivity that did not survive FDR correction at $p < 0.05$ but were significant at uncorrected $p < 0.05$ are listed in **Supplementary Table 3**.

Effect of Age and Age-by-Group Interaction on Functional Connectivity

The multiple linear regression analysis revealed a significant ($p <$ 0.05, uncorrected) age-by-group interaction for the connectivity between the thalamus and left precentral gyrus (Precentral_L, $p = 0.02$, **Figure 3**), and for that between the thalamus and left postcentral gyrus (Postcentral _L, $p = 0.02$, **Figure 3**). The correlation between age and the connectivity between the thalamus and left pre- and postcentral gyri was near zero in the ASD group and weakly negative in the CTL group. There was no significant age-by-group interaction for the connectivity between the amygdala and six cortical regions.

The multiple linear regression analysis revealed a significant ($p < 0.05$, uncorrected) main effect of age for the connectivity between the thalamus and right superior frontal gyrus (Frontal_Sup_R, $r = 0.04$, $p = 0.01$), for that between the thalamus and right orbital gyrus (Frontal_Mid_Orb_R, $r = 0.06$, $p = 0.04$), and for that between the thalamus and left paracentral lobule (Paracentral_Lobule_L, $r = 0.05$, $p = 0.02$). There was no significant main effect of age for the connectivity between the amygdala and six cortical regions.

The Relationship among Age, Head Movement, Intellectual Function, and Connectivity

In the ASD group, there was a significant negative correlation between FD and age ($r = -0.17$, $p = 0.003$) and between FD and mean connectivity ($r = 0.27$, $p < 0.001$). In the CTL group, there was a significant negative correlation between the FD and FIQ ($r = -0.13$, $p = 0.02$) and between FD and mean connectivity ($r = 0.26$, $p < 0.001$). However, there was no significant group-by-age interaction effect on these correlations. For other insignificant results, see **Supplementary Table 4**.

Effects of Medication on Functional Connectivity in the ASD Group

No significant difference in mean age was observed between the on-med and off-med ASD groups (on-med, 13.2 ± 4.1, off-med, 13.5 ± 5.4, $p = 0.65$, **Supplementary Figure 3**, left); however, mean IQ significantly differed between the groups (on-med, 109 ± 17, off-med, 105 ± 16, $p = 0.045$, **Supplementary Figure 3**, right). Mean FD and the proportion of scrubbed volumes did not significantly differ between the on- and off-med groups (**Supplementary Table 5**). The multiple linear regression analysis revealed no significant main effect of medication on the FCs between the thalamus/amygdala and cortical regions (all $p > 0.05$, uncorrected). These results suggest that the effect of psychotropic medication on thalamocortical connectivity was relatively negligible in the present study.

DISCUSSION

In the present study, we analyzed a large rs-fMRI dataset from the ABIDE II database to determine whether neurophysiological changes observed in the brains of patients with ASD are caused by dysconnectivity between subcortical and cortical structures. Our findings indicated that the ASD group exhibited significantly increased connectivity between the thalamus and 19 cortical regions after FDR correction for multiple comparisons, relative to that observed in the CTL group. The mean effect size of the group difference was 0.25, and, therefore, the degree of difference was not small or negligible. The cortical regions comprised the frontal and parietal areas as well as the supramarginal and angular gyrus (i.e., temporo-parietal junction, TPJ) and bilateral PCCs. In the pre- and postcentral gyri of the left hemisphere, there were significant group differences in the relationship between connectivity and the participant's age, indicating that connectivity decreases as age increases among typically developing CTLs, but not among patients with ASD.

In addition, the present study revealed that the ASD group exhibited significantly decreased connectivity between the

amygdala and six cortical regions after FDR correction for multiple comparisons, relative to that observed in the CTL group. However, the mean effect size of the group difference was 0.08, and, therefore, the degree of difference in amygdala-cortical connectivity is smaller than that for thalamocortical connectivity. These group differences in connectivity were not influenced by the difference in intellectual function between the groups.

Thus, the results of the present study suggest that hyperconnectivity in thalamocortical pathways, and to a lesser extent hypoconnectivity in amygdala-cortical pathways, are associated with the pathophysiology of ASD. Furthermore, as the present results were obtained after regressing out the mean FD and overall mean connectivity values, the group differences in connectivity should be unrelated to the differences in head movement and regionally specific to the thalamus and amygdala.

Previous studies have reported conflicting results regarding patterns of hypo- and hyperconnectivity in patients with ASD. Most of these studies have observed reduced functional and structural connectivity among patients with ASD (32–35), while relatively few have described hyperconnectivity (36–38). However, such studies may not have sufficient statistical power due to the small sample size and limited age range, necessitating confirmation regarding the reliability and reproducibility of the findings. A very recent rs-fMRI study demonstrated that the FC between the thalamus and the primary and secondary auditory cortices was significantly higher in the ASD group than in the CTL group (39). Therefore, the results of the present study indicate that widespread cortical areas are overly connected to the thalamus, further supporting the notion of thalamocortical hyperconnectivity among patients with ASD.

Several other large-scale studies have used multisite neuroimaging data to investigate the neural underpinnings of ASD (11, 40, 41). Cheng et al. investigated differences in FC between 418 patients with ASD and 509 CTLs (11), reporting both hyper- and hypoconnectivity in the ASD group. However, the authors noted that the thalamus exhibited significantly greater connectivity with the rest of the brain in the ASD group than in the CTL group. Although our findings regarding thalamic hyperconnectivity were similar to those of Cheng et al. (11), they were unable to elucidate which regions of the brain were hyperconnected to the thalamus because their connectivity value was the average of the whole brain. In a study by Woodward et al., an older version of the ABIDE I database was used for analysis (228 patient–control pairs). The authors investigated only the cortical connectivity from and to the thalamus and revealed, similar to the present study, increased prefrontal, motor, somatosensory, and temporal cortex connectivity with the thalamus in the autism group as compared with the control group (41).

In a study by Cerliani et al. involving 166 patients with ASD and 193 CTLs (all male, age range: 6 to 50 years), the authors performed an independent component analysis (ICA) using an ABIDE dataset (40). One component involving the thalamus and basal ganglia exhibited significantly greater connectivity with several other components involving the motor, visual, and auditory areas as well as the superior temporal sulcus in the ASD group than in the CTL group. Their results are relevant to the results of the present study; however, the critical component did not differentiate the thalamus and other basal ganglia regions when the ICA was applied to the rs-fMRI data. In another recent study, Fu et al. observed dynamic hyperconnectivity between the hypothalamus/subthalamic region and several sensory areas (42). Taken together, the results of studies utilizing large multisite datasets indicate that ASD is associated with thalamocortical hyperconnectivity, rather than hypoconnectivity.

Thalamocortical pathways are critical to sensory processing and perception because they carry information received from the primary sensory organs to cortical areas specific to each sensory modality. Thalamic input to the cortex is important for the development of sensory and association cortices, and the thalamus appears to influence the formation of sensory representation in the cortices during early development (15). Therefore, abnormalities in sensory processing, which have been widely associated with ASD (4, 39), may be caused by developmental irregularities within the neuronal connectivity between the thalamus and sensory areas in the cortex. Additional studies have indicated that the thalamic reticular nucleus (TRN), which surrounds the thalamic projection circuit with inhibitory GABAergic neurons, may play a critical role in attention and sensory processing (14). The disruption of inhibitory mechanisms involving the TRN in patients with ASD may give rise to sensory hyperarousal and the hyperconnectivity patterns observed using rs-fMRI.

The mediodorsal nucleus (MDN) of the thalamus plays a key role in higher-order cognitive functions, such as working memory and attention, mechanisms of which appear to be based on the relationship between the MDN and the frontal and cingulate cortices. The MDN may interact with prefrontal cortices during the performance of higher-order cognitive tasks, and is also likely involved during social communication. The researchers have proposed that disruptions in cortico-cortical connectivity may occur during the early neurodevelopmental period, and that such disruptions are caused by alterations in connectivity between the thalamus and the cortex. Such significant alterations in cortico-cortical communication may contribute to many of the cognitive disruptions evident in neurodevelopmental disorders (43).

In the present study, the most significant differences between the ASD and CTL groups were observed in the TPJ and the posterior cingulate cortex. These areas are subcomponents of the default mode network and are considered to be related to several specific mental processes such as self-related thoughts and mind-wandering (44). Specifically, the TPJ is implicated in a variety of processes including multisensory integration and social cognition, most of which are impaired in patients with ASD (45). These findings indicate that the heightened connectivity observed in the ASD group of the present study may reflect TPJ malfunctioning.

On the other hand, a study that examined the FC patterns of the amygdala using rs-fMRI demonstrated that adolescents with ASD have decreased FC between the amygdala and the thalamus/putamen compared to CTLs (46). The patients with ASD showed weaker fronto-amygdala connectivity in the

right hemisphere (47). There was a significant reduction in connectivity between the amygdala and prefrontal, parietal, and occipital cortices in the ASD group compared with the CTL group (48, 49). In a study using younger subjects (mean age: 3.5 years), the ASD group showed significantly weaker connectivity between the amygdala and medial prefrontal cortices (50). The results of previous studies are in accordance with those of the present study showing a reduced connectivity pattern between the amygdala and several cortical regions in a large sample of patients with ASD. Although the amygdala is a critical structure involved in emotional perception and regulation in patients with ASD (47–50), the small effect size observed in the present study may preclude the possibility that the amygdala plays a principal role in the pathogenesis of the disease.

Notably, we observed a significant group-by-age interaction effect on patterns of FC in the pre- and postcentral gyri. These interaction effects are most likely derived from decreases in connectivity with age in the CTL group and fixed connectivity in the ASD group. Our findings suggest that this age range represents a critical period for neuronal development and maturation in CTLs. Previous reviews of age-related differences in brain structure have reported that gray matter volume decreases, while white matter volume increases, during puberty and early adolescence (51, 52). Therefore, unchanging connectivity may reflect neurodevelopmental delays or irregularities observed in the ASD group in this study.

The present study possesses several limitations of note. First, in order to maintain the statistical power of the large multisite dataset, we did not exclude patients taking medication from the study population. However, we observed no statistically significant differences in thalamocortical or amygdala-cortical connectivity between the medication groups, suggesting that medication exerts virtually no influence on connectivity in patients with ASD. Second, there was no significant correlation between the connectivity values and clinical symptoms in the ASD group. While we could not reveal the neural substrates of such symptoms in the ABIDE II database, future datasets that provide complete sets of symptom scales may enable us to reveal the relationship between connectivity and symptoms. Third, in the present study, the brain template did not differentiate subnuclei within the thalamus. Therefore, the resultant activity was an average of that in the whole thalamus. This may obscure the exact pattern of FC, as the thalamus is composed of several nuclei, each of which exhibits specific neuronal connections and functions (15, 43). Further analysis using an anatomical template delineating separate thalamic subnuclei (53) is therefore required.

CONCLUSIONS

Using a large dataset from multiple ABIDE II database sites, we demonstrated that hyperconnectivity between the thalamus and fronto-parietal cortices, most notably the left TPJ and bilateral PCC, is associated with the pathophysiology of ASD. Moreover, amygdala-cortical connectivity was significantly decreased in the ASD group. Future studies should collect full sets of clinical and behavioral data in combination with FC data to explore possible biomarkers for ASD.

AUTHOR CONTRIBUTIONS

TI contributed to data collection, analyzed and interpreted the data, and wrote the manuscript. TK contributed to the methods and data preparation. YM and HK made substantial contributions to interpretation of data and wrote the manuscript. All authors were involved in drafting the manuscript, and read and approved the final manuscript.

FUNDING

This study was supported by KAKENHI No. 17H05923 and No. 15H01846.

ACKNOWLEDGMENTS

The authors thank researchers and participants of ABIDE database.

SUPPLEMENTARY MATERIAL

The Supplementary Material for this article can be found online at: https://www.frontiersin.org/articles/10.3389/fpsyt.2019.00252/full#supplementary-material

SUPPLEMENTARY TABLE 1 | Participants demographics.

SUPPLEMENTARY TABLE 2 | Names of institutes and data acquisition parameters.

SUPPLEMENTARY TABLE 3 | Subcortical connectivity which did not survive FDR correction.

SUPPLEMENTARY TABLE 4 | Correlation between FD, age, full-IQ, and mean connectivity.

SUPPLEMENTARY TABLE 5 | Medication effect on head motion parameters.

SUPPLEMENTARY FIGURE 1 | Age and IQ distribution of the participants. Distributions of age at the time of scanning (top) and IQ (bottom) for the ASD (blue column) and CTL groups (orange column). The vertical axis indicates the number of participants. There was no significant group difference in mean age, although mean IQ was significantly lower ($p < 0.001$) in the ASD group than in the CTL group. IQ: intelligence quotient; ASD: autism spectrum disorder; CTL: control.

SUPPLEMENTARY FIGURE 2 | Medication status of participants in each group. The number in the column indicates the number of participants, while the scale below indicates the percentage.

SUPPLEMENTARY FIGURE 3 | Medication effect on age and IQ. Boxplot of age (left) and IQ (right) in the on- and off-medication ASD groups. Patients in the on-med group exhibited significantly higher mean IQ values than those of the off-med group ($p < 0.05$). IQ: intelligence quotient.

REFERENCES

1. American_Psychiatric_Association. *Diagnostic and statistical manual for mental disorders*. 5th edition. American Psychiatric Association, Arlington, VA, (2013).
2. Ben-Sasson A, Hen L, Fluss R, Cermak SA, Engel-Yeger B, Gal E. A meta-analysis of sensory modulation symptoms in individuals with autism spectrum disorders. *J Autism Dev Disord* (2009) 39:1–11. doi: 10.1007/s10803-008-0593-3
3. Marco EJ, Hinkley LB, Hill SS, Nagarajan SS. Sensory processing in autism: a review of neurophysiologic findings. *Pediatr Res* (2011) 69:48R–54R. doi: 10.1203/PDR.0b013e3182130c54
4. Mikkelsen M, Wodka EL, Mostofsky SH, Puts NAJ. Autism spectrum disorder in the scope of tactile processing. *Dev Cogn Neurosci* (2018) 29:140–50. doi: 10.1016/j.dcn.2016.12.005
5. Nair A, Keown CL, Datko M, Shih P, Keehn B, Muller RA. Impact of methodological variables on functional connectivity findings in autism spectrum disorders. *Hum Brain Mapp* (2014) 35:4035–48. doi: 10.1002/hbm.22456
6. Caballero-Gaudes C, Reynolds RC. Methods for cleaning the BOLD fMRI signal. *Neuroimage* (2017) 154:128–49. doi: 10.1016/j.neuroimage.2016.12.018
7. Glerean E, Pan RK, Salmi J, Kujala R, Lahnakoski JM, Roine U, et al. Reorganization of functionally connected brain subnetworks in high-functioning autism. *Hum Brain Mapp* (2016) 37:1066–79. doi: 10.1002/hbm.23084
8. Hahamy A, Behrmann M, Malach R. The idiosyncratic brain: distortion of spontaneous connectivity patterns in autism spectrum disorder. *Nat Neurosci* (2015) 18:302–9. doi: 10.1038/nn.3919
9. Tyszka JM, Kennedy DP, Paul LK, Adolphs R. Largely typical patterns of resting-state functional connectivity in high-functioning adults with autism. *Cereb Cortex* (2014) 24:1894–905. doi: 10.1093/cercor/bht040
10. Abraham A, Milham MP, Di Martino A, Craddock RC, Samaras D, Thirion B, et al. Deriving reproducible biomarkers from multi-site resting-state data: an Autism-based example. *Neuroimage* (2017) 147:736–45. doi: 10.1016/j.neuroimage.2016.10.045
11. Cheng W, Rolls ET, Gu H, Zhang J, Feng J. Autism: reduced connectivity between cortical areas involved in face expression, theory of mind, and the sense of self. *Brain* (2015) 138:1382–93. doi: 10.1093/brain/awv051
12. Shulman EP, Smith AR, Silva K, Icenogle G, Duell N, Chein J, et al. The dual systems model: review, reappraisal, and reaffirmation. *Dev Cogn Neurosci* (2016) 17:103–17. doi: 10.1016/j.dcn.2015.12.010
13. Ferrarelli F, Tononi G. The thalamic reticular nucleus and schizophrenia. *Schizophr Bull* (2011) 37:306–15. doi: 10.1093/schbul/sbq142
14. Krol A, Wimmer RD, Halassa MM, Feng G. Thalamic reticular dysfunction as a circuit endophenotype in neurodevelopmental disorders. *Neuron* (2018) 98:282–95. doi: 10.1016/j.neuron.2018.03.021
15. Lopez-Bendito G. Development of the thalamocortical interactions: past, present and future. *Neuroscience* (2018) 385:67–74. doi: 10.1016/j.neuroscience.2018.06.020
16. Lord C, Rutter M, Le Couteur A. Autism Diagnostic Interview-Revised: a revised version of a diagnostic interview for caregivers of individuals with possible pervasive developmental disorders. *J Autism Dev Disord* (1994) 24:659–85. doi: 10.1007/BF02172145
17. Lord C, Rutter M, DiLavore PC, Risi S. *Autism diagnostic observation schedule*. Los Angeles: Western Psychological Service (1999).
18. Chao-Gan Y, Yu-Feng Z. DPARSF: A MATLAB Toolbox for "pipeline" data analysis of resting-state fMRI. *Front Syst Neurosci* (2010) 4:13. doi: 10.3389/fnsys.2010.00013. eCollection 2010.
19. Fox MD, Zhang D, Snyder AZ, Raichle ME. The global signal and observed anticorrelated resting state brain networks. *J Neurophysiol* (2009) 101:3270–83. doi: 10.1152/jn.90777.2008
20. Murphy K, Birn RM, Handwerker DA, Jones TB, Bandettini PA. The impact of global signal regression on resting state correlations: are anti-correlated networks introduced? *Neuroimage* (2009) 44:893–905. doi: 10.1016/j.neuroimage.2008.09.036
21. Van Dijk KR, Sabuncu MR, Buckner RL. The influence of head motion on intrinsic functional connectivity MRI. *Neuroimage* (2012) 59:431–8. doi: 10.1016/j.neuroimage.2011.07.044
22. Power JD, Barnes KA, Snyder AZ, Schlaggar BL, Petersen SE. Spurious but systematic correlations in functional connectivity MRI networks arise from subject motion. *Neuroimage* (2012) 59:2142–54. doi: 10.1016/j.neuroimage.2011.10.018
23. Tzourio-Mazoyer N, Landeau B, Papathanassiou D, Crivello F, Etard O, Delcroix N, et al. Automated anatomical labeling of activations in SPM using a macroscopic anatomical parcellation of the MNI MRI single-subject brain. *Neuroimage* (2002) 15:273–89. doi: 10.1006/nimg.2001.0978
24. Lai MC, Lombardo MV, Chakrabarti B, Sadek SA, Pasco G, Wheelwright SJ, et al. A shift to randomness of brain oscillations in people with autism. *Biol Psychiatry* (2010) 68:1092–9. doi: 10.1016/j.biopsych.2010.06.027
25. Supekar K, Uddin LQ, Khouzam A, Phillips J, Gaillard WD, Kenworthy LE, et al. Brain hyperconnectivity in children with autism and its links to social deficits. *Cell Rep* (2013) 5:738–47. doi: 10.1016/j.celrep.2013.10.001
26. Di Martino A, Yan CG, Li Q, Denio E, Castillanos FX, Alaerts K, et al. The autism brain imaging data exchange: towards a large-scale evaluation of the intrinsic brain architecture in autism. *Mol Psychiatry* (2013) 19:659–67. doi: 10.1038/mp.2013.78
27. Anderson JS, Nielsen JA, Froehlich AL, DuBray MB, Druzgal TJ, Cariello AN, et al. Functional connectivity magnetic resonance imaging classification of autism. *Brain* (2011) 134:3742–54. doi: 10.1093/brain/awr263
28. Nielsen JA, Zielinski BA, Fletcher PT, Alexander AL, Lange N, Bigler ED, et al. Multisite functional connectivity MRI classification of autism: ABIDE results. *Front Hum Neurosci* (2013) 7:599. doi: 10.3389/fnhum.2013.00599
29. Drysdale AT, Grosenick L, Downar J, Dunlop K, Mansouri F, Meng Y, et al. Resting-state connectivity biomarkers define neurophysiological subtypes of depression. *Nat Med* (2017) 23:28–38. doi: 10.1038/nm.4246
30. Benjamini Y, Hochberg Y. Controlling the false discovery rate: a practical and powerful approach to multiple testing. *J R Stat Soc Series B Methodol* (1995) 57:289–300. doi: 10.1111/j.2517-6161.1995.tb02031.x
31. Xia M, Wang J, He Y. BrainNet Viewer: a network visualization tool for human brain connectomics. *PLoS One* (2013) 8:e68910. doi: 10.1371/journal.pone.0068910
32. Rudie JD, Brown JA, Beck-Pancer D, Hernandez LM, Dennis EL, Thompson PM, et al. Altered functional and structural brain network organization in autism. *Neuroimage Clin* (2012) 2:79–94. doi: 10.1016/j.nicl.2012.11.006
33. Nair A, Treiber JM, Shukla DK, Shih P, Muller RA. Impaired thalamocortical connectivity in autism spectrum disorder: a study of functional and anatomical connectivity. *Brain* (2013) 136:1942–55. doi: 10.1093/brain/awt079
34. Verly M, Verhoeven J, Zink I, Mantini D, Van Oudenhove L, Lagae L, et al. Structural and functional underconnectivity as a negative predictor for language in autism. *Hum Brain Mapp* (2014) 35:3602–15. doi: 10.1002/hbm.22424
35. Yerys BE, Herrington JD, Satterthwaite TD, Guy L, Schultz RT, Bassett DS. Globally weaker and topologically different: resting-state connectivity in youth with autism. *Mol Autism* (2017) 8:39. doi: 10.1186/s13229-017-0156-6
36. Ray S, Miller M, Karalunas S, Robertson C, Grayson DS, Cary RP, et al. Structural and functional connectivity of the human brain in autism spectrum disorders and attention-deficit/hyperactivity disorder: a rich club-organization study. *Hum Brain Mapp* (2014) 35:6032–48. doi: 10.1002/hbm.22603
37. Murdaugh DL, Maximo JO, Kana RK. Changes in intrinsic connectivity of the brain's reading network following intervention in children with autism. *Hum Brain Mapp* (2015) 36:2965–79. doi: 10.1002/hbm.22821
38. Abbott AE, Nair A, Keown CL, Datko M, Jahedi A, Fishman I, et al. Patterns of atypical functional connectivity and behavioral links in autism differ between default, salience, and executive networks. *Cereb Cortex* (2016) 26:4034–45. doi: 10.1093/cercor/bhv191
39. Linke AC, Jao Keehn RJ, Pueschel EB, Fishman I, Muller RA. Children with ASD show links between aberrant sound processing, social symptoms, and atypical auditory interhemispheric and thalamocortical functional connectivity. *Dev Cogn Neurosci* (2018) 29:117–26. doi: 10.1016/j.dcn.2017.01.007
40. Cerliani L, Mennes M, Thomas RM, Di Martino A, Thioux M, Keysers C. Increased functional connectivity between subcortical and cortical resting-state networks in autism spectrum disorder. *JAMA Psychiatry* (2015) 72:767–77. doi: 10.1001/jamapsychiatry.2015.0101

41. Woodward ND, Giraldo-Chica M, Rogers B, Cascio CJ. Thalamocortical dysconnectivity in autism spectrum disorder: an analysis of the Autism Brain Imaging Data Exchange. *Biol Psychiatry Cogn Neurosci Neuroimaging* (2017) 2:76–84. doi: 10.1016/j.bpsc.2016.09.002
42. Fu Z, Tu Y, Di X, Du Y, Sui J, Biswal BB, et al. Transient increased thalamic-sensory connectivity and decreased whole-brain dynamism in autism. *Neuroimage* (2019):191–204 doi.org/10.1016/neuroimage.2018.06.003
43. Ouhaz Z, Fleming H, Mitchell AS. Cognitive functions and neurodevelopmental disorders involving the prefrontal cortex and mediodorsal thalamus. *Front Neurosci* (2018) 12:33. doi: 10.3389/fnins.2018.00033
44. Raichle ME. The brain's default mode network. *Annu Rev Neurosci* (2015) 38:433–47. doi: 10.1146/annurev-neuro-071013-014030
45. Eddy CM. The junction between self and other? Temporo-parietal dysfunction in neuropsychiatry. *Neuropsychologia* (2016) 89:465–77. doi: 10.1016/j.neuropsychologia.2016.07.030
46. Guo X, Duan X, Long Z, Chen H, Wang Y, Zheng J, et al. Decreased amygdala functional connectivity in adolescents with autism: a resting-state fMRI study. *Psychiatry Res Neuroimaging* (2016) 257:47–56. doi: 10.1016/j.pscychresns.2016.10.005
47. Odriozola P, Dajani DR, Burrows CA, Gabard-Durnam LJ, Goodman E, Baez AC, et al. Atypical frontoamygdala functional connectivity in youth with autism. *Dev Cogn Neurosci* (2018). doi: 10.1016/j.dcn.2018.12.001
48. Rausch A, Zhang W, Haak KV, Mennes M, Hermans EJ, van Oort E, et al. Altered functional connectivity of the amygdaloid input nuclei in adolescents and young adults with autism spectrum disorder: a resting state fMRI study. *Mol Autism* (2016) 7:13. doi: 10.1186/s13229-015-0060-x
49. Rausch A, Zhang W, Beckmann CF, Buitelaar JK, Groen WB, Haak KV. Connectivity-based parcellation of the amygdala predicts social skills in adolescents with autism spectrum disorder. *J Autism Dev Disord* (2018) 48:572–82. doi: 10.1007/s10803-017-3370-3
50. Shen MD, Li DD, Keown CL, Lee A, Johnson RT, Angkustsiri K, et al. Functional connectivity of the amygdala is disrupted in preschool-aged children with autism spectrum disorder. *J Am Acad Child Adolesc Psychiatry* (2016) 55:817–24. doi: 10.1016/j.jaac.2016.05.020
51. Herting MM, Sowell ER. Puberty and structural brain development in humans. *Front Neuroendocrinol* (2017) 44:122–37. doi: 10.1016/j.yfrne.2016.12.003
52. Vijayakumar N, Op de Macks Z, Shirtcliff EA, Pfeifer JH. Puberty and the human brain: insights into adolescent development. *Neurosci Biobehav Rev* (2018) 92:417–36. doi: 10.1016/j.neubiorev.2018.06.004
53. Krauth A, Blanc R, Poveda A, Jeanmonod D, Morel A, Szekely G. A mean three-dimensional atlas of the human thalamus: generation from multiple histological data. *Neuroimage* (2010) 49:2053–62. doi: 10.1016/j.neuroimage.2009.10.042

Conflict of Interest Statement: The authors declare that the research was conducted in the absence of any commercial or financial relationships that could be constructed as a potential conflict of interest.

frontiers in Neuroscience

ORIGINAL RESEARCH
published: 24 April 2019
doi: 10.3389/fnins.2019.00309

Intermittent Theta-Burst Stimulation Reverses the After-Effects of Contralateral Virtual Lesion on the Suprahyoid Muscle Cortex: Evidence From Dynamic Functional Connectivity Analysis

Guoqin Zhang[1†], Xiuhang Ruan[1†], Yuting Li[2†], E Li[1], Cuihua Gao[1], Yanli Liu[1], Lisheng Jiang[3], Lingling Liu[1], Xin Chen[1], Shaode Yu[4], Xinqing Jiang[1], Guangqing Xu[5], Yue Lan[2,3*] and Xinhua Wei[1,2*]*

[1] Department of Radiology, Guangzhou First People's Hospital, Guangzhou Medical University, Guangzhou, China, [2] The Second Affiliated Hospital, South China University of Technology, Guangzhou, China, [3] Department of Rehabilitation Medicine, Guangzhou First People's Hospital, Guangzhou Medical University, Guangzhou, China, [4] Shenzhen Institutes of Advanced Technology, Chinese Academy of Sciences, Shenzhen, China, [5] Department of Rehabilitation Medicine, Beijing Tiantan Hospital, Capital Medical University, Beijing, China

Contralateral intermittent theta burst stimulation (iTBS) can potentially improve swallowing disorders with unilateral lesion of the swallowing cortex. However, the after-effects of iTBS on brain excitability remain largely unknown. Here, we investigated the alterations of temporal dynamics of inter-regional connectivity induced by iTBS following continuous TBS (cTBS) in the contralateral suprahyoid muscle cortex. A total of 20 right-handed healthy subjects underwent cTBS over the left suprahyoid muscle motor cortex and then immediately afterward, iTBS was applied to the contralateral homologous area. All of the subjects underwent resting-state functional magnetic resonance imaging (Rs-fMRI) pre- and post-TBS implemented on a different day. We compared the static and dynamic functional connectivity (FC) between the post-TBS and the baseline. The whole-cortical time series and a sliding-window correlation approach were used to quantify the dynamic characteristics of FC. Compared with the baseline, for static FC measurement, increased FC was found in the precuneus (BA 19), left fusiform gyrus (BA 37), and right pre/post-central gyrus (BA 4/3), and decreased FC was observed in the posterior cingulate gyrus (PCC) (BA 29) and left inferior parietal lobule (BA 39). However, in the dynamic FC analysis, post-TBS showed reduced FC in the left angular and PCC in the early windows, and in the following windows, increased FC in multiple cortical areas including bilateral pre- and postcentral gyri and paracentral lobule and non-sensorimotor areas including the prefrontal, temporal and occipital gyrus, and brain stem. Our results indicate that iTBS reverses the aftereffects induced by cTBS on the contralateral suprahyoid muscle cortex. Dynamic FC analysis displayed a different

OPEN ACCESS

Edited by:
Weidong Cai,
The University of Sydney, Australia

Reviewed by:
Sidong Liu,
Macquarie University, Australia
Feng Liu,
Tianjin Medical University General Hospital, China

***Correspondence:**
Guangqing Xu
guangchingx@163.com
Yue Lan
bluemooning@163.com
Xinhua Wei
weixinhua@aliyun.com

[†] These authors have contributed equally to this work as co-first authors

Specialty section:
This article was submitted to Brain Imaging Methods, a section of the journal Frontiers in Neuroscience

Received: *20 November 2018*
Accepted: *19 March 2019*
Published: *24 April 2019*

Citation:
Zhang G, Ruan X, Li Y, Li E, Gao C, Liu Y, Jiang L, Liu L, Chen X, Yu S, Jiang X, Xu G, Lan Y and Wei X (2019) Intermittent Theta-Burst Stimulation Reverses the After-Effects of Contralateral Virtual Lesion on the Suprahyoid Muscle Cortex: Evidence From Dynamic Functional Connectivity Analysis. Front. Neurosci. 13:309. doi: 10.3389/fnins.2019.00309

pattern of alteration compared with the static FC approach in brain excitability induced by TBS. Our results provide novel evidence for us in understanding the topographical and temporal aftereffects linked to brain excitability induced by different TBS protocols and might be valuable information for their application in the rehabilitation of deglutition.

Keywords: repetitive transcranial magnetic stimulation, theta-burst stimulation, magnetic resonance imaging, swallowing, dynamic functional connectivity analysis

INTRODUCTION

Swallowing disorders (i.e., dysphagia) are a common sequela of a range of diseases and disorders (González-Fernández and Daniels, 2008; Clave and Shaker, 2015). Patients with dysphasia are at risk of developing severe complications such as aspiration pneumonia, malnutrition, and dehydration, which have large impacts on the quality of life of patients (Martino et al., 2005). Despite various strategies that have been developed that aim to enhance swallowing recovery, efficient treatment options for dysphagia rehabilitation remain limited (Bath et al., 2000; Geeganage et al., 2012).

Transcranial magnetic stimulation (TMS) is a non-invasive method that can alter human cortex excitability and has started to attract attention for use in treating dysphagia. Increasing evidence has indicated that TMS may be a promising tool to facilitate neural reorganization in dysphagic patients (Khedr and Abo-Elfetoh, 2010; Michou et al., 2012; Doeltgen et al., 2015). TMS can modify the excitability at the site of stimulation as well as in remote brain areas that are functionally connected with the target site (brain network effect) (Suppa et al., 2008; Valchev et al., 2015; Steel et al., 2016). More recently, theta burst stimulation (TBS), a novel pattern of rTMS, was shown to produce significant and long-lasting aftereffects within very short stimulation periods (Huang et al., 2005).

There are two forms of TBS according to the stimulus pattern: intermittent TBS (iTBS) enhances cortical excitability, and in contrast, continuous TBS (cTBS) suppresses cortical excitability, which is usually explained by its long-term depression (LTD) of synaptic activity (Huang et al., 2005). The recent development of human temporary "virtual lesion" by using non-invasive magnetic stimulation at a low frequency has given us the opportunity to explore the cortical central mechanisms in improving swallowing function and recovery in a controlled environment before proceeding to clinical trials (Mistry et al., 2007; Cugy et al., 2016). Thus, as an entity for suppression of cortical excitability, cTBS can be used to create a "virtual lesion" in the swallowing cortex by transiently reducing the excitability of the targeted brain area.

It has been shown that swallowing is represented in multiple cortical regions bilaterally and swallowing functions are organized by a distributed brain network (Ertekin and Aydogdu, 2003). Although stimulating the lesioned or unlesioned hemisphere for dysphagia patients remains a controversial topic, converging evidence suggests unaffected hemisphere stimulation with TMS helps to rehabilitate swallowing function (Hamdy et al., 1998; Jefferson et al., 2009; Pisegna et al., 2016). Furthermore, our recent study indicated that iTBS could reverse the inhibitory effect induced by cTBS in the contralateral suprahyoid motor cortex (Lin et al., 2017). Most of the previous studies explored the aftereffect of TBS over the cortex by measuring the motor-evoked potentials (MEP) of peripheral muscles (Wu et al., 2012; Lin et al., 2017). However, our understanding of the underlying mechanisms linked to the neural networks between the two hemispheres of the swallowing cortex after TBS stimulation remains unclear.

Recently, resting-state functional MRI (Rs-fMRI) has been used in the investigation of the neural mechanism of TMS (Andoh et al., 2015; Bharath et al., 2015; Dichter et al., 2015; Valchev et al., 2015; Ji et al., 2017). The functional connectivity (FC) analysis calculating the temporal similarities was broadly used in Rs-fMRI studies; however, most of the studies only considered FC measurements using static FC (Biswal et al., 1995; Geerligs et al., 2014). It measures the correlations of signals between different brain regions during a scanning period, thus providing a relatively static pattern of brain activity coherence in the resting state (Wig et al., 2011). More recently, emerging evidence has proposed that human brain connectivity is most likely time-dependent and dynamic (i.e., dynamic FC) (Liu et al., 2017; Marusak et al., 2017; Robinson et al., 2017). Therefore, a dynamic FC analysis is a sensitive method to capture the time-varying information of FC and has been attracting increasing attention for use in characterizing the brain's intrinsic functional organization (Marusak et al., 2016; Preti et al., 2016). However, as far as we know, there is no previous study that explored the features of dynamic FC of TBS on the swallowing cortex to date.

The suprahyoid muscle is linked to the movement of the hyoid-throat complex and plays an important role in swallowing (Nam et al., 2013). The purpose of this study was to evaluate dynamic functional network connectivity in subjects given iTBS following contralateral cTBS, which acts to create a "virtual lesion" on the suprahyoid muscle cortex. Although stimulating the lesioned or unlesioned hemisphere for dysphagia patients remains a controversial topic, converging evidence suggests unaffected hemisphere stimulation with TMS helps to rehabilitate swallowing function (Hamdy et al., 1998; Jefferson et al., 2009; Pisegna et al., 2016). Furthermore, a recent study indicated that iTBS could reverse the inhibitory effect induced by cTBS in the contralateral suprahyoid motor cortex (Lin et al., 2017). Therefore, to verify if the contralateral iTBS can reverse the effect of cTBS which was used as a virtual lesion on the left side, we placed the iTBS on the right motor areas of the suprahyoid muscles. In this study, we hypothesized that iTBS might facilitate bilateral brain excitability though interhemispheric interactions between the

suprahyoid motor cortices and reverse the aftereffects of cTBS in the contralateral hemisphere. To verify this hypothesis, this study aimed to characterize the temporal dynamic features of whole-brain FC at a voxel level, to explore whether dynamic features of FC are linked to the underlying mechanism of iTBS in the treatment of a contralateral virtual lesion in the swallowing cortex.

MATERIALS AND METHODS

Participants

A total of 20 participants (10 women; mean age: 23.5 ± 4.4 years) took part in the study after giving written informed consent. We did not include subjects with a history of neurological and/or psychiatric disease, swallowing dysfunction, or substance abuse. The present study was approved by the clinical research ethics committee of Guangzhou First People's Hospital. The study was conducted in accordance with the Declaration of Helsinki (2008 revision).

Transcranial Magnetic Stimulation

The details of the TMS procedure have been described in a previous study (Lin et al., 2017; Ruan et al., 2017). In brief, motor evoked potentials (MEPs) to TMS were recorded from the suprahyoid muscle and right first dorsal interosseous (FDI) of the hand. Electrodes (Yiruide, Wuhan, China) were placed over the bilateral suprahyoid muscle surface and the surface of the FDI to detect the suprahyoid muscle electromyographic (EMG) responses. Electrodes were connected to an EMG recording system (Yiruide, Wuhan, China) with a preamplifier and amplifier.

Magnetic stimulation was performed using a handheld figure of eight coil (mean 70 mm outer diameter) connected to a Magstim super rapid stimulator (Yiruide Medical Equipment Co., Wuhan, China) to deliver single-pulse TMS. The stimulating coil was held tangentially to the skull with the coil handle pointing backward and laterally 45° away from the anterior-posterior axis (Mistry et al., 2007). The precise position of the TMS coil was tracked and recorded using the neuronavigation system (SofTaxic, E.M.S., Bologna, Italy) with a graphic user interface and a three dimensional (3D) optical digitizer (NDI, Polaris Vicra, ON, Canada).

rTMS was delivered using the theta burst stimulation (TBS) protocol as first described by Huang et al. (2005). Briefly, the coil was held in an identical orientation to single pulse TMS when performing TBS. The navigation system was used to determine the hot spot and active motor threshold (AMT) of FDI. The motor hot spot was determined as the site at which TMS consistently elicited the largest MEPs from the contralateral FDI. Then the stimulation intensity was gradually reduced until at least 5 times of 10 consecutive stimulations which induced MEP of ≥50 μV in the contralateral thumb abductor muscle, and the stimulation intensity was the ATM of the subject. After that, the navigation system was used to determine the hot spot of the suprahyoid motor cortex. The method was similar to determination of the FDI hot spot. TBS was applied over the hot spot of the suprahyoid motor cortex. The stimulation intensity was set to 80% of the AMT of the FDI.

The TBS protocol consisted of three pulses of stimulation delivered at 50 Hz and repeated at 5 Hz. In the iTBS pattern, a 2 s train of TBS was repeated every 10 s for a total of 190 s (600 pulses in total). By contrast, a 40 s train of uninterrupted TBS was administered for approximately 40 s (600 pulses in total) in the cTBS protocol. The stimulation intensity was set to 80% of the AMT of the FDI.

Experimental Design

The stimulation protocol was as follows: iTBS was performed on the right hemisphere immediately after completing cTBS on the left motor cortex of the suprahyoid muscles. Rs-fMRI datasets were acquired before and after the TBS implement on a different day (**Figure 1**).

MR Data Acquisition

Brain imaging was performed on a 3.0 T MRI scanner (Siemens, Erlangen, Germany) using a 16-channel phased-array head coil. The Rs-fMRI data were acquired before and immediately after each TBS session. The acquisition parameters for functional data were as follows: TR = 2000 ms, TE = 21 ms, FA = 90°, FOV = 240 × 240 mm, matrix = 64 × 64, slice thickness = 4.0 mm, and voxel size = 3.75 × 3.75 × 4.0 mm. During the Rs-fMRI scan, participants were instructed to relax with their eyes closed but not fall asleep. T1-weighted structural images were acquired using a three-dimensional magnetization-prepared rapid acquisition gradient-echo (MPRAGE) sequence (TR = 2530 ms, TE = 2.93 ms, FA = 7°, FOV = 256 mm, a 256 × 256 matrix and a slice thickness of 1.0 mm).

MR Data Preprocessing

Image preprocessing was carried out using the Data Processing Assistant for Rs-fMRI (DPARSF[1]) (Yan and Zang, 2010), which runs with the statistical parametric mapping software (SPM8[2]). Briefly, data pre-processing steps included removal of the first 10 image frames for signal equilibration; slice timing correction for acquisition delay between slices; realignment of the data to compensate for rigid body motion (excessive motion was defined as translation or rotation >2 mm or 2°); registration of the 3D structural images into the standard Montreal Neurological Institute (MNI) space; regression of white matter nuisance signals, cerebral spinal fluid BOLD-signal and 24 head-motion profiles to minimize the effect of head motion; registration of the functional images to the MNI space using the parameters of structural image normalization and with resampling to 3 × 3 × 3 mm^3; spatial smoothing using a Gaussian kernel of 4 mm full-width at half maximum (FWHM); and bandpass filtering (0.01–0.08 Hz) of the functional data to reduce

[1]http://rfmri.org/DPARSF

[2]http://www.fil.ion.ucl.ac.uk/spm

[3]http://www.restfmri.net

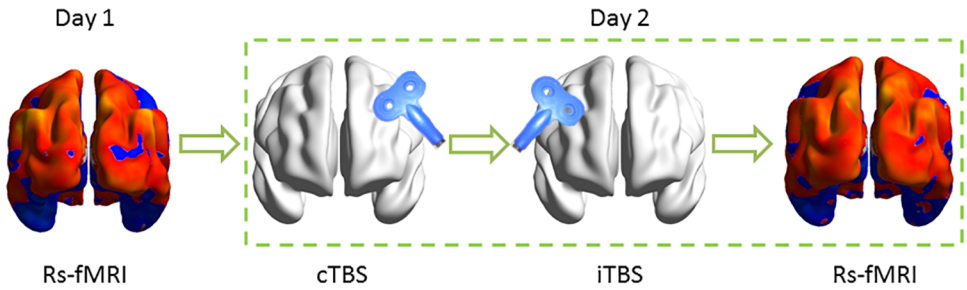

FIGURE 1 | Schematic of the experimental design. Resting-state functional MRI (Rs-fMRI) was acquired before and after theta burst stimulation (TBS) on the different day. In TBS stimulation, each subject received continuous TBS (cTBS) first on the left suprahyoid muscle cortex and immediately followed intermittent TBS (iTBS) on the right homologous area. The target area for TBS stimulation was guided by neuronavigation.

the effects of low-frequency drift and high-frequency noise (Biswal et al., 1995).

Static Functional Connectivity Analysis

For each individual data set, we first calculated the static FC with Pearson correlation analysis. The FC was performed using REST V1.8 package[3]. Pearson's correlation coefficients were computed between the time series of all pairs of brain voxels. Each voxel represents a node in the graph, and each significant functional connection (i.e., Pearson correlation) between any pair of voxels is an edge. As a result, we can obtain an n × n matrix of Pearson's correlation coefficients between any pair of voxels so that the whole brain FC matrix for each participant was constructed. Then, individual correlation matrices were transformed into a Z-score matrix using Fisher's r-to-z transformation to improve normality. After that, the weighted degree centrality strength of a voxel as the sum of the connections (Z-values) between a given brain voxel and all other voxels was computed. As previously described similarly (Gao et al., 2016), we used a Pearson's correlation coefficient threshold at $r > 0.25$ by thresholding each correlation at $p \leq 0.001$.

Dynamic Functional Connectivity Construction

A voxel-to-voxel based dynamic functional connectivity (dynamic FC) construction was performed using the dynamic brain connectivity (dynamic BC) toolbox (Liao et al., 2014a). A time-varying parameter regression equation was employed to describe the dynamic interactions between brain regions. We calculated correlation maps using the Pearson correlation strategy between the time series derived from each voxel to all other brain voxels for a sliding window of 50 volumes (100 s). We obtained a correlation map for each sliding window; then, the correlation map was converted to z-scores using the Fisher r-to-z transformation. The window was then shifted by 0.6 volume (1.2 s) and a new correlation map was calculated. This approach permitted the estimation of FC over time (Liao et al., 2014a,b). Since the time series were composed of 200 volumes, this procedure yielded sliding-time windows and thus resulted in 121 correlation maps.

Statistical Analysis

A paired t-test was performed to investigate the difference between the post-TBS and pre-TBS conditions. A threshold of $p < 0.05$, corrected using Monte Carlo simulations in the AFNI AlphaSim program[4], was used to calculate the probability of false positive detection while accounting for both the individual voxel probability thresholding and cluster size (single voxel $p = 0.05$, FWHM = 6 mm). Using this program, clusters of greater than 85 voxels were applied to the resulting statistical map at a corrected significance level of $p < 0.05$ (Song et al., 2011; Wang et al., 2012).

RESULTS

Group Differences in Static Functional Network Connectivity

As shown in **Figure 2A** and **Table 1**, compared to baseline, post-combined cTBS/iTBS exhibited increased FC in the precuneus (BA 19), left fusiform gyrus (BA 37), and right pre/post-central gyrus (BA 4/3) and showed decreased FC in the posterior cingulate gyrus (PCC) (BA 29) and left inferior parietal lobule (BA 39).

Group Comparison of Dynamic Functional Connectivity

After dynamic FC analysis, we obtained a seven-unit dataset, and from each unit of the dataset, we calculated an FC map. Thus, a total of seven FC T-test maps were obtained. Compared with the pre-TBS condition, in the first window, the post-TBS exhibited decreased FC in the left inferior parietal lobule and left thalamus; in the second window, the PCC showed decreased FC. The left medial superior frontal gyrus displayed increased FC in the third window; the middle occipital gyrus/cuneus demonstrated increased FC in the fourth window; then, in the following windows, multifocal bilateral areas included sensorimotor areas, such as the primary sensorimotor cortex and paracentral lobule, and non-sensorimotor areas, such as the occipital gyrus,

[4]http://afni.nimh.nih.gov/pub/dist/doc/manual/AlphaSim.pdf

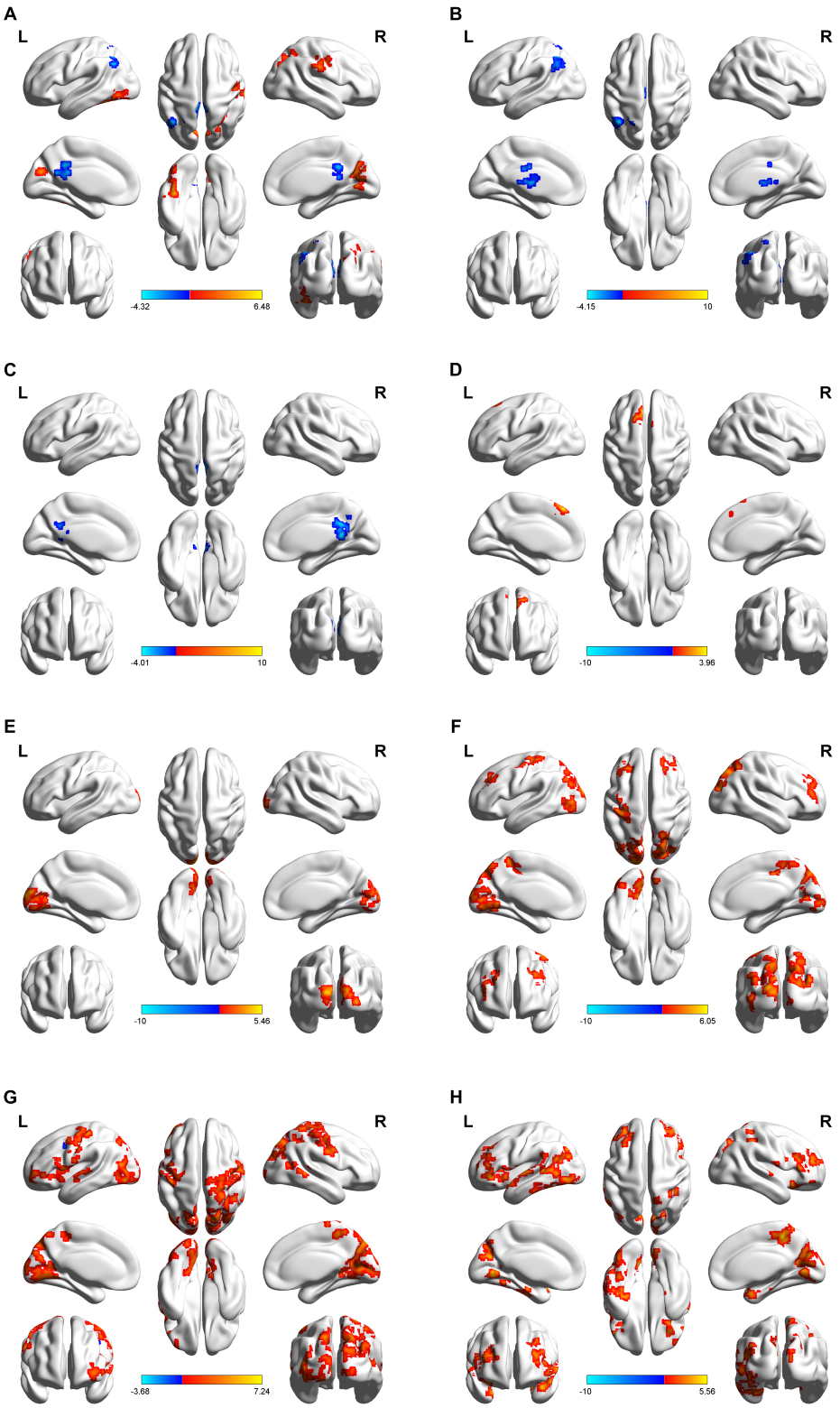

FIGURE 2 | Regional distribution of altered functional connectivity between post-theta-burst stimulation and baseline in healthy subjects. Short-term of aftereffects on brain functional connectivity (FC) induced by intermittent theta burst stimulation (iTBS) followed the contralateral continuous theta burst stimulation (cTBS) (i.e. "virtual lesion") over the suprahyoid muscle cortex. The upper images represent static FC **(A)** and a serial of dynamic FC maps **(B–H)**. Lateral, dorsal, medial, basal and posterior views are shown in every figure. Color bar indicates the *T*-value at the bottom. Areas color-coded in red (blue) indicate the regions in which the values

(Continued)

FIGURE 2 | Continued
of FC corresponding to post-TBS were higher (lower) than those of pre-TBS ($p < 0.05$, AlphaSim correction was performed to correct for multiple comparisons). Surface visualization of regions with abnormal FCs using BrainNet Viewer (http://www.nitrc.org/projects/bnv/). For static FC comparison **(A)**, increased FC was found in the precuneus, left fusiform gyrus, and right pre/post-central gyrus, and decreased FC was observed in posterior cingulate gyrus (PCC) and left inferior parietal lobule. In dynamic FC analysis, post-TBS showed reduced FC in left angular and PCC on the early windows **(B,C)**, in the following windows **(D–H)**, increased FC in multiple cortical areas including bilateral pre- and postcentral gyri and paracentral lobule, and non-sensorimotor areas including a body of prefrontal, temporal and occipital gyrus, and brain stem. The details are presented in **Table 1**.

TABLE 1 | Functional connectivity comparison between post- and pre-TBS on the suprahyoid muscle cortex.

Brain region	BA	Cluster size (voxels)	Peak MNI coordinates (mm)			*T*-value
			X	Y	Z	
Static functional connectivity						
Right pre/postcentral gyrus	4/3	87	56	−19	39	3.1934
Precuneus	19	306	24	−75	36	4.5864
Left fusiform gyrus	37	120	−39	−45	−24	6.4808
Posterior cingulate gyrus	29	144	3	−42	15	−4.1386
Left inferior parietal lobule	39	104	−42	−63	48	−4.3236
Dynamic functional connectivity						
Window 1						
Left thalamus		92	−3	−12	9	−3.9233
Left inferior parietal lobule	40	123	−42	−60	48	−4.1469
Window 2						
Posterior cingulate		153	12	−39	12	−4.0102
window 3						
Left medial superior frontal gyrus	8	87	−9	33	51	3.9604
Window 4						
Middle occipital gyrus/cuneus	18	448	30	−99	0	5.4572
Window 5						
Left precentral gyrus	6	102	−42	0	60	3.7038
Paracentral lobule	5	201	0	−39	51	4.1413
Left cuneus/precuneus	18	795	−21	−93	15	6.0536
Right precuneus	7	377	21	−78	39	4.9914
Right superior frontal gyrus	9	184	24	30	36	3.4375
Left superior frontal gyrus	9	113	−39	36	36	3.7198
Right superior temporal gyrus	39	92	48	−54	15	4.5806
Window 6						
Right postcentral/precentral gyrus	6/4	441	45	−54	60	5.0194
Left postcentral/precentral gyrus	6/4	248	−42	−24	63	4.6705
Precuneus/cuneus	7	1239	−18	−72	45	4.9855
Left inferior frontal operculum	45	245	−42	21	18	4.6498
Left middle occipital gyrus	19	218	−6	−105	6	7.2442
Window 7						
Paracentral lobule/postcentral gyrus	5	252	12	−39	54	5.0432
Precuneus/cuneus	18	375	−12	−66	−3	4.4948
Right middle frontal gyrus	10	348	57	27	30	5.0111
Right inferior frontal gyrus	38	163	27	18	−24	4.9059
Left inferior frontal gyrus	45	258	−54	36	3	5.2874
Left superior temporal gyrus	38	272	−39	15	−21	5.5615
Left middle temporal gyrus	22	401	−57	−42	6	4.6347
Left fusiform gyrus	37	855	−42	−48	−24	502446
Brainstem	NS	85	−6	−24	−33	403195

TBS, continuous theta-burst stimulation; BA, Brodman's area; MNI, Montreal Neurological Institute; cTBS, continuous TBS; iTBS, intermittent TBS.

prefrontal gyrus, temporal gyrus and brain stem (**Figures 2B–H**, details in **Table 1**).

DISCUSSION

In this study, we explored the short-term after-effect of iTBS application to the right motor cortex of the suprahyoid muscles following cTBS, which was used to create a "virtual lesion" in the left suprahyoid muscles cortex in healthy participants. The static and dynamic FC analyses based on the data of Rs-fMRI were implemented to investigate the FC of the brain network at the voxel level for the whole brain. In the static FC measurement, increased FC was found in the precuneus, left fusiform gyrus, and right pre/postcentral gyrus; and decreased FC was observed in the PCC and left inferior parietal lobule. Compared with static FC, the dynamic FC displayed a different distribution of brain FC in the brain networks. From the dynamic FC maps, increased FC in multiple bilateral brain areas including bilateral sensorimotor areas and other non-sensorimotor brain regions were found, while they were not fully displayed in the static FC analysis. The present study, to our knowledge, is the first study to focus on the short-term after-effects of TBS on the swallowing cortex by examining brain network temporal dynamics in a cohort of healthy controls.

Similar to previous studies (Michou et al., 2016), cTBS, an inhibitory TMS, was applied to the left suprahyoid muscles motor area to act as a "virtual lesion," which temporarily and reversibly disrupted a focal region of brain excitability. In contrast, iTBS was used as an excitatory stimulation on the right suprahyoid muscles motor areas in order to verify whether iTBS could alter the brain excitability after forming the contralateral "virtual lesion" and to identify what pattern of alteration of FC could be induced in the whole brain network. As expected, a number of spatially discrete cortical regions exhibited alternation of FC after the TBS application in both static FC and dynamic FC maps.

In the static FC maps, because the right motor cortex of the suprahyoid muscles was the target area for iTBS, the right primary somatosensory cortex displaying an increased FC is not surprising. A body of studies has indicated that the primary somatosensory cortex is implicated in reflexive and volitional swallowing (Hamdy et al., 1999a,b; Ertekin and Aydogdu, 2003; Martin et al., 2007) and plays a role in the initiation of the pharyngeal stage of swallowing (Malandraki et al., 2009). Additionally, the left posterior parietal cortex and PCC exhibited decreased FC in the static FC maps. Similar to the previous study (Ertekin and Aydogdu, 2003), the posterior parietal cortex together with the somatosensory cortex is likely to have a sensory role in the control of swallowing. The precuneus and PCC are components of the default-mode network (DMN) that occurs during the initiation of task-related activities (Raichle et al., 2001). Furthermore, the precuneus is thought to play a role in adjusting volitional swallowing related to swallow-related intent and planning and possibly urges (Hamdy et al., 1999a; Kern M.K. et al., 2001). Moreover, the PCC and precuneus are regarded as association areas, which are thought to play a role in integrating sensory information (Hamdy et al., 1999a). Consistent with a previous report (Jefferson et al., 2009), we did not observe decreased or increased FC in the left sensorimotor cortex, which is the target position of cTBS, and we speculate there is a balance between bilateral hemispheres in brain excitability due to the interaction between iTBS and cTBS over the opposite swallowing motor cortex. Taken together, in the static FC maps, we did not observe the evidence that indicates that iTBS can reverse the aftereffect of the contralateral "virtual lesion" induced by cTBS.

In the dynamic FC maps, we observed alterations in FC induced by TBS in multifocal and bilateral brain regions in different windows. Interestingly, some areas demonstrated in the static FC maps with alteration in FC, such as the left posterior parietal lobule and PCC, also exhibited decreased FC in the first few windows of the dynamic FC maps. Similar to a previous study (Babaei et al., 2013), the lateral parietal, PCC and precuneus regions have close FC among themselves and may be involved in sensory processing in the swallowing brain network. The left thalamus displayed decreased FC in the dynamic FC maps in the present study. It has been proposed that the thalamus is a structure known as a relay station for sensory information traveling into higher cortical areas (Malandraki et al., 2009); and thus, after the ipsilateral swallowing cortex is suppressed, the processing and transferring of sensorimotor information is inhibited accordingly. Apart from the areas with decreased FC on the dynamic FC maps, we found increased dynamic FC in the bilateral primary sensorimotor cortex in the following windows after TBS application. As we mentioned above, the activation of the primary sensorimotor during volitional swallowing has been well documented with imaging studies in the fMRI studies (Hamdy et al., 1999a,b; Mosier et al., 1999; Mihai et al., 2014). In our study, the targeted brain areas were the cortex of the bilateral suprahyoid muscle, and thus, the presence of alterations of brain connectivity in the post- and precentral gyrus is not surprising. These areas are supposed to play an important role in the initiation and regulation of swallowing (Narita et al., 1999; Ertekin and Aydogdu, 2003). In addition, the paracentral lobule and the continuation of the precentral and postcentral gyri displayed increased FC in the dynamic FC maps. The paracentral lobule is associated with sensorimotor functioning and is activated by swallowing tasks (Martin et al., 2007). Except for the sensorimotor brain regions we mentioned above, a number of other non-sensorimotor brain regions displayed alteration in FC in the present study, including the bilateral temporal lobe, frontal cortex and occipital cortex. Swallowing is a complex and dynamic neuromuscular task requiring rapid and precise coordination of numerous cranial nerves and muscle pairs (Ertekin and Aydogdu, 2003). It was supposed that the non-sensorimotor areas may represent swallowing related to intent, planning, decision making, and memory, as well as information processing related to deglutition (Ertekin and Aydogdu, 2003). Specifically, the temporal cortex, together with the prefrontal cortex, is supposed to play a supplementary role in the regulation of swallowing and feeding because of its relationship with taste and imagery of food (Hamdy et al., 1999a). Moreover, the prefrontal cortex has been associated with the perception of body signals, attentional control, and higher order sensorimotor processing (Suntrup et al., 2014). The occipitoparietal regions are

regarded as a hub area for integrating sensory input with motor output (Kern M. et al., 2001). Taken together, we speculate that these non-sensorimotor regions could play a supplementary role in the regulation of swallowing linked to swallow-related intent and planning and possibly urges.

In the present study, the dynamic FC displayed a different pattern of brain areas with altered FC compared with the static FC maps. Other studies using EEG with high temporal resolution signals have shown that the activity of the brain is constantly changing over time at rest (Van de Ville et al., 2010). This indicates that dynamic FC analysis might add additional information to our understanding of the mechanism of iTBS on the swallowing cortex. We observed ipsilateral suppression of FC on the left angular area, left thalamus and PCC in the dynamic FC maps in the early windows. Then, increased FC was observed in multiple regions, including the sensorimotor brain network (bilateral primary sensorimotor cortex and paracentral lobule) and non-sensorimotor brain network (frontal, temporal and occipital gyrus), and was seen in the following windows of the dynamic FC maps. We suppose that the decreased FCs in the early stages may be induced by cTBS that yielded an inhibitory after-effect on spontaneous neuron activity, and the following increased FC in multiple brain areas might be caused by iTBS, which produced an excitatory after-effect. Interestingly, in static FC maps, we did not observe an alteration in FC in the multifocal regions including sensorimotor brain areas and non-sensorimotor brain areas, which instead demonstrated increased FC in the dynamic FC maps. This finding indicates that dynamic FC can provide much more information compared with the static FC method for detecting the aftereffects of TBS over the swallowing cortex. Of note, we observed multiple bilateral brain areas with increased FC in the late stages of dynamic FC maps, and the results indicate contralateral iTBS facilitate brain excitability in bilateral swallowing in the motor cortex instead of interhemispheric inhibition.

It is important to consider the limitations of the present study. First, since previous work has shown that sham TBS over the pharyngeal motor cortex does not alter cortical excitability in an unconditioned system (Mistry et al., 2007, 2012), we did not include a sham stimulation group in the present study. Second, the sample size in this study was relatively small, and a larger dataset would be required to validate the present findings. Finally, considering the issue of cooperation of participants during the imaging study, we did not prolong the scanning time to measure the aftereffects of TBS until it returned to baseline.

Taken together, we explored the short-term aftereffects of iTBS following contralateral cTBS (a virtual lesion) on the suprahyoid muscles motor cortex. We observed increased FC in the bilateral sensorimotor cortex and other non-sensorimotor areas induced by contralateral iTBS, which could not be fully displayed in static FC analysis. The present study indicates that dynamic FC analysis can provide much more information about the brain excitability induced by contralateral iTBS. Our results provide evidence that iTBS could be used as a novel noninvasive tool for rehabilitating swallowing difficulties after brain damage. We suggest that contralateral iTBS might be developed as a therapeutic strategy for swallowing disorders associated with unilateral lesions in the swallowing cortex.

The present study was approved by the clinical research ethics committee of Guangzhou First People's Hospital. The study was conducted in accordance with the Declaration of Helsinki (2008 revision).

AUTHOR CONTRIBUTIONS

XW contributed to the experimental design and writing of the manuscript. GZ, XR, and YuLi were involved in the literature review, data collection, and writing of the manuscript. CG, SY, LL, and XC contributed to the analysis of MRI data. LJ, EL, and YaLi were involved in the data collection. GX, XJ, and YLa contributed to the experimental design and the writing process.

FUNDING

This research was partly supported by the National Natural Science Foundation of China (81371441, 81572230, and 81871846), the Guangdong Provincial Science and Technology Program (2013B051000036 and 2014B020212001), the Guangzhou Municipal Science and Technology Program (2016201604030036), and the Science and Technology Planning Project of Guangzhou (201804010032).

REFERENCES

Andoh, J., Matsushita, R., and Zatorre, R. J. (2015). Asymmetric interhemispheric transfer in the auditory network: evidence from TMS, resting-state fMRI, and diffusion imaging. *J. Neurosci.* 35, 14602–14611. doi: 10.1523/JNEUROSCI.2333-15.2015

Babaei, A., Ward, B. D., Siwiec, R. M., Ahmad, S., Kern, M., Nencka, A., et al. (2013). Functional connectivity of the cortical swallowing network in humans. *Neuroimage* 76, 33–44. doi: 10.1016/j.neuroimage.2013.01.037

Bath, P. M., Bath, F. J., and Smithard, D. G. (2000). Interventions for dysphagia in acute stroke. *Cochrane Database Syst. Rev.* 2:CD000323. doi: 10.1002/14651858.CD000323

Bharath, R. D., Biswal, B. B., Bhaskar, M. V., Gohel, S., Jhunjhunwala, K., Panda, R., et al. (2015). Repetitive transcranial magnetic stimulation induced modulations of resting state motor connectivity in writer's cramp. *Eur. J. Neurol.* 22, 796–805.

Biswal, B., Yetkin, F. Z., Haughton, V. M., and Hyde, J. S. (1995). Functional connectivity in the motor cortex of resting human brain using echo-planar MRI. *Magn. Reson. Med.* 34, 537–541. doi: 10.1002/mrm.1910340409

Clave, P., and Shaker, R. (2015). Dysphagia: current reality and scope of the problem. *Nat. Rev. Gastroenterol. Hepatol.* 12, 259–270. doi: 10.1038/nrgastro.2015.49

Cugy, E., Leroi, A. M., Kerouac-Laplante, J., Dehail, P., Joseph, P. A., Gerardin, E., et al. (2016). Effect of submental sensitive transcutaneous electrical stimulation on virtual lesions of the oropharyngeal cortex. *Ann. Phys. Rehabil. Med.* 59, 94–99. doi: 10.1016/j.rehab.2015.10.010

Dichter, G. S., Gibbs, D., and Smoski, M. J. (2015). A systematic review of relations between resting-state functional-MRI and treatment response in major depressive disorder. *J. Affect. Disord.* 172, 8–17. doi: 10.1016/j.jad.2014.09.028

Doeltgen, S. H., Bradnam, L. V., Young, J. A., and Fong, E. (2015). Transcranial non-invasive brain stimulation in swallowing rehabilitation following stroke–a review of the literature. *Physiol. Behav.* 143, 1–9. doi: 10.1016/j.physbeh.2015.02.025

Ertekin, C., and Aydogdu, I. (2003). Neurophysiology of swallowing. *Clin. Neurophysiol.* 114, 2226–2244. doi: 10.1016/s1388-2457(03)00237-2

Gao, C., Wenhua, L., Liu, Y., Ruan, X., Chen, X., Liu, L., et al. (2016). Decreased subcortical and increased cortical degree centrality in a nonclinical college student sample with subclinical depressive symptoms: a resting-state fMRI Study. *Front. Hum. Neurosci.* 10:617. doi: 10.3389/fnhum.2016.00617

Geeganage, C., Beavan, J., Ellender, S., and Bath, P. M. (2012). Interventions for dysphagia and nutritional support in acute and subacute stroke. *Cochrane Database Syst. Rev.* 10:CD000323. doi: 10.1002/14651858.CD000323.pub2

Geerligs, L., Renken, R. J., Saliasi, E., Maurits, N. M., and Lorist, M. M. (2014). A brain-wide study of age-related changes in functional connectivity. *Cereb. Cortex* 25, 1987–1999. doi: 10.1093/cercor/bhu012

González-Fernández, M., and Daniels, S. K. (2008). Dysphagia in stroke and neurologic disease. *Phys. Med. Rehabil. Clin. N. Am.* 19, 867–888. doi: 10.1016/j.pmr.2008.07.001

Hamdy, S., Aziz, Q., Rothwell, J. C., Power, M., Singh, K. D., Nicholson, D. A., et al. (1998). Recovery of swallowing after dysphagic stroke relates to functional reorganization in the intact motor cortex. *Gastroenterology* 115, 1104–1112. doi: 10.1016/s0016-5085(98)70081-2

Hamdy, S., Mikulis, D. J., Crawley, A., Xue, S., Lau, H., Henry, S., et al. (1999a). Cortical activation during human volitional swallowing: an event-related fMRI study. *Am. J. Physiol.* 277, G219–G225.

Hamdy, S., Rothwell, J. C., Brooks, D. J., Bailey, D., Aziz, Q., and Thompson, D. G. (1999b). Identification of the cerebral loci processing human swallowing with H2(15)O PET activation. *J. Neurophysiol.* 81, 1917–1926. doi: 10.1152/jn.1999.81.4.1917

Huang, Y.-Z., Edwards, M. J., Rounis, E., Bhatia, K. P., and Rothwell, J. C. (2005). Theta burst stimulation of the human motor cortex. *Neuron* 45, 201–206.

Jefferson, S., Mistry, S., Michou, E., Singh, S., Rothwell, J. C., and Hamdy, S. (2009). Reversal of a virtual lesion in human pharyngeal motor cortex by high frequency contralesional brain stimulation. *Gastroenterology* 137, 841–849. doi: 10.1053/j.gastro.2009.04.056

Ji, G. J., Yu, F., Liao, W., and Wang, K. (2017). Dynamic aftereffects in supplementary motor network following inhibitory transcranial magnetic stimulation protocols. *Neuroimage* 149, 285–294. doi: 10.1016/j.neuroimage.2017.01.035

Kern, M., Birn, R., Jaradeh, S., Jesmanowicz, A., Cox, R., Hyde, J., et al. (2001). Swallow-related cerebral cortical activity maps are not specific to deglutition. *Am. J. Physiol. Gastrointest. Liver Physiol.* 280, G531–G538.

Kern, M. K., Jaradeh, S., Arndorfer, R. C., and Shaker, R. (2001). Cerebral cortical representation of reflexive and volitional swallowing in humans. *Am. J. Physiol. Gastrointest. Liver Physiol.* 280, G354–G360.

Khedr, E. M., and Abo-Elfetoh, N. (2010). Therapeutic role of rTMS on recovery of dysphagia in patients with lateral medullary syndrome and brainstem infarction. *J. Neurol. Neurosurg. Psychiatry* 81, 495–499. doi: 10.1136/jnnp.2009.188482

Liao, W., Wu, G. R., Xu, Q., Ji, G. J., Zhang, Z., Zang, Y. F., et al. (2014a). DynamicBC: a MATLAB toolbox for dynamic brain connectome analysis. *Brain Connect* 4, 780–790. doi: 10.1089/brain.2014.0253

Liao, W., Zhang, Z., Mantini, D., Xu, Q., Ji, G. J., Zhang, H., et al. (2014b). Dynamical intrinsic functional architecture of the brain during absence seizures. *Brain Struct. Funct.* 219, 2001–2015. doi: 10.1007/s00429-013-0619-2

Lin, T., Jiang, L., Dou, Z., Wu, C., Liu, F., Xu, G., et al. (2017). Effects of theta burst stimulation on suprahyoid motor cortex excitability in healthy subjects. *Brain Stimul.* 10, 91–98. doi: 10.1016/j.brs.2016.08.011

Liu, F., Wang, Y., Li, M., Wang, W., Li, R., Zhang, Z., et al. (2017). Dynamic functional network connectivity in idiopathic generalized epilepsy with generalized tonic-clonic seizure. *Hum. Brain Mapp.* 38, 957–973. doi: 10.1002/hbm.23430

Malandraki, G. A., Sutton, B. P., Perlman, A. L., Karampinos, D. C., and Conway, C. (2009). Neural activation of swallowing and swallowing-related tasks in healthy young adults: an attempt to separate the components of deglutition. *Hum. Brain Mapp.* 30, 3209–3226. doi: 10.1002/hbm.20743

Martin, R., Barr, A., MacIntosh, B., Smith, R., Stevens, T., Taves, D., et al. (2007). Cerebral cortical processing of swallowing in older adults. *Exp. Brain Res.* 176, 12–22. doi: 10.1007/s00221-006-0592-6

Martino, R., Foley, N., Bhogal, S., Diamant, N., Speechley, M., and Teasell, R. (2005). Dysphagia after stroke: incidence, diagnosis, and pulmonary complications. *Stroke* 36, 2756–2763. doi: 10.1161/01.str.0000190056.76543.eb

Marusak, H. A., Calhoun, V. D., Brown, S., Crespo, L. M., Sala-Hamrick, K., Gotlib, I. H., et al. (2016). Dynamic functional connectivity of neurocognitive networks in children. *Hum. Brain Mapp.* 38, 97–108. doi: 10.1002/hbm.23346

Marusak, H. A., Calhoun, V. D., Brown, S., Crespo, L. M., Sala-Hamrick, K., Gotlib, I. H., et al. (2017). Dynamic functional connectivity of neurocognitive networks in children. *Hum. Brain Mapp.* 38, 97–108. doi: 10.1002/hbm.23346

Michou, E., Mistry, S., Jefferson, S., Singh, S., Rothwell, J., and Hamdy, S. (2012). Targeting unlesioned pharyngeal motor cortex improves swallowing in healthy individuals and after dysphagic stroke. *Gastroenterology* 142, 29–38. doi: 10.1053/j.gastro.2011.09.040

Michou, E., Raginis-Zborowska, A., Watanabe, M., Lodhi, T., and Hamdy, S. (2016). Repetitive transcranial magnetic stimulation: a novel approach for treating oropharyngeal dysphagia. *Curr. Gastroenterol. Rep.* 18:10. doi: 10.1007/s11894-015-0483-8

Mihai, P. G., Otto, M., Platz, T., Eickhoff, S. B., and Lotze, M. (2014). Sequential evolution of cortical activity and effective connectivity of swallowing using fMRI. *Hum. Brain Mapp.* 35, 5962–5973. doi: 10.1002/hbm.22597

Mistry, S., Michou, E., Rothwell, J., and Hamdy, S. (2012). Remote effects of intermittent theta burst stimulation of the human pharyngeal motor system. *Eur. J. Neurosci.* 36, 2493–2499. doi: 10.1111/j.1460-9568.2012.08157.x

Mistry, S., Verin, E., Singh, S., Jefferson, S., Rothwell, J. C., Thompson, D. G., et al. (2007). Unilateral suppression of pharyngeal motor cortex to repetitive transcranial magnetic stimulation reveals functional asymmetry in the hemispheric projections to human swallowing. *J. Physiol.* 585, 525–538. doi: 10.1113/jphysiol.2007.144592

Mosier, K., Patel, R., Liu, W. C., Kalnin, A., Maldjian, J., and Baredes, S. (1999). Cortical representation of swallowing in normal adults: functional implications. *Laryngoscope* 109, 1417–1423. doi: 10.1097/00005537-199909000-00011

Nam, H. S., Beom, J., Oh, B. M., and Han, T. R. (2013). Kinematic effects of hyolaryngeal electrical stimulation therapy on hyoid excursion and laryngeal elevation. *Dysphagia* 28, 548–556. doi: 10.1007/s00455-013-9465-x

Narita, N., Yamamura, K., Yao, D., Martin, R. E., and Sessle, B. J. (1999). Effects of functional disruption of lateral pericentral cerebral cortex on primate swallowing. *Brain Res.* 824, 140–145. doi: 10.1016/s0006-8993(99)01151-8

Pisegna, J. M., Kaneoka, A., Pearson, W. G. Jr., Kumar, S., and Langmore, S. E. (2016). Effects of non-invasive brain stimulation on post-stroke dysphagia: a systematic review and meta-analysis of randomized controlled trials. *Clin. Neurophysiol.* 127, 956–968. doi: 10.1016/j.clinph.2015.04.069

Preti, M. G., Bolton, T. A., and Van De Ville, D. (2016). The dynamic functional connectome: state-of-the-art and perspectives. *Neuroimage* 160, 41–54. doi: 10.1016/j.neuroimage.2016.12.061

Raichle, M. E., MacLeod, A. M., Snyder, A. Z., Powers, W. J., Gusnard, D. A., and Shulman, G. L. (2001). A default mode of brain function. *Proc. Natl. Acad. Sci. U.S.A.* 98, 676–682.

Robinson, L. F., He, X., Barnett, P., Doucet, G. E., Sperling, M. R., Sharan, A., et al. (2017). The temporal instability of resting state network connectivity in intractable epilepsy. *Hum. Brain Mapp.* 38, 528–540. doi: 10.1002/hbm.23400

Ruan, X., Xu, G., Gao, C., Liu, L., Liu, Y., Jiang, L., et al. (2017). Alterations of the amplitude of low-frequency fluctuation in healthy subjects with theta-burst stimulation of the cortex of the suprahyoid muscles. *Neuroscience* 365, 48–56. doi: 10.1016/j.neuroscience.2017.09.027

Song, X. W., Dong, Z. Y., Long, X. Y., Li, S. F., Zuo, X. N., Zhu, C. Z., et al. (2011). REST: a toolkit for resting-state functional magnetic resonance imaging data processing. *PLoS One* 6:e25031. doi: 10.1371/journal.pone.0025031

Steel, A., Song, S., Bageac, D., Knutson, K. M., Keisler, A., Saad, Z. S., et al. (2016). Shifts in connectivity during procedural learning after motor cortex stimulation: a combined transcranial magnetic stimulation/functional magnetic resonance imaging study. *Cortex* 74, 134–148. doi: 10.1016/j.cortex.2015.10.004

Suntrup, S., Teismann, I., Wollbrink, A., Warnecke, T., Winkels, M., Pantev, C., et al. (2014). Altered cortical swallowing processing in patients with functional dysphagia: a preliminary study. *PLoS One* 9:e89665. doi: 10.1371/journal.pone.0089665

Suppa, A., Ortu, E., Zafar, N., Deriu, F., Paulus, W., Berardelli, A., et al. (2008). Theta burst stimulation induces after-effects on contralateral primary motor cortex excitability in humans. *J. Physiol.* 586, 4489–4500. doi: 10.1113/jphysiol.2008.156596

Valchev, N., Curcic-Blake, B., Renken, R. J., Avenanti, A., Keysers, C., Gazzola, V., et al. (2015). cTBS delivered to the left somatosensory cortex changes its functional connectivity during rest. *Neuroimage* 114, 386–397. doi: 10.1016/j.neuroimage.2015.04.017

Van de Ville, D., Britz, J., and Michel, C. M. (2010). EEG microstate sequences in healthy humans at rest reveal scale-free dynamics. *Proc. Natl. Acad. Sci. U.S.A.* 107, 18179–18184. doi: 10.1073/pnas.1007841107

Wang, L., Dai, W., Su, Y., Wang, G., Tan, Y., Jin, Z., et al. (2012). Amplitude of low-frequency oscillations in first-episode, treatment-naive patients with major depressive disorder: a resting-state functional MRI study. *PLoS One* 7:e48658. doi: 10.1371/journal.pone.0048658

Wig, G. S., Schlaggar, B. L., and Petersen, S. E. (2011). Concepts and principles in the analysis of brain networks. *Ann. N. Y. Acad. Sci.* 1224, 126–146. doi: 10.1111/j.1749-6632.2010.05947.x

Wu, S. W., Shahana, N., Huddleston, D. A., and Gilbert, D. L. (2012). Effects of 30Hz theta burst transcranial magnetic stimulation on the primary motor cortex. *J. Neurosci. Methods* 208, 161–164. doi: 10.1016/j.jneumeth.2012.05.01

Yan, C. G., and Zang, Y. F. (2010). DPARSF: A MATLAB Toolbox for "Pipeline" data analysis of resting-state fMRI. *Front. Syst. Neurosci.* 4:13. doi: 10.3389/fnsys.2010.00013

Conflict of Interest Statement: The authors declare that the research was conducted in the absence of any commercial or financial relationships that could be construed as a potential conflict of interest.

frontiers in Neurology

ORIGINAL RESEARCH
published: 24 April 2019
doi: 10.3389/fneur.2019.00394

Reduced Interhemispheric White Matter Asymmetries in Medial Temporal Lobe Epilepsy With Hippocampal Sclerosis

*Xu Zhao[1], Zhi-qiang Zhou[2], Ying Xiong[1], Xu Chen[3], Ke Xu[4], Juan Li[1], Ying Hu[1], Xiao-long Peng[1] and Wen-zhen Zhu[1]**

[1] Department of Radiology, Tongji Hospital, Tongji Medical College, Huazhong University of Science and Technology, Wuhan, China, [2] Department of Anesthesiology and Pain Medicine, Tongji Hospital, Tongji Medical College, Huazhong University of Science and Technology, Wuhan, China, [3] Department of Neurosurgery, Tongji Hospital, Tongji Medical College, Huazhong University of Science and Technology, Wuhan, China, [4] Department of Neurology, Tongji Hospital, Tongji Medical College, Huazhong University of Science and Technology, Wuhan, China

Mesial temporal lobe epilepsy (MTLE), one of the most common types of refractory focal epilepsy, has shown white matter abnormalities both within and beyond the temporal lobe. In particular, the white matter abnormalities in the ipsilateral hemisphere are more obvious than those in the contralateral hemisphere in MTLE, that is, the abnormalities present asymmetrical characteristics. However, very few studies have characterized the white matter microstructure asymmetry in MTLE patients specifically. Thus, we performed diffusion tensor imaging (DTI) to investigate the white matter microstructure asymmetries of patients with MTLE with unilateral hippocampal sclerosis (MTLE-HS). We enrolled 25 MTLE-HS (left MTLE-HS group, $n = 13$; right MTLE-HS group, $n = 12$) and 26 healthy controls (HC). DTI data were analyzed by tract-based spatial statistics (TBSS) to test the hemispheric differences across the entire white matter skeleton. We also conducted a two-sample paired t-test for 21 paired region of interests (ROIs) parceled on the basis of the ICBM-DTI-81 white-matter label atlas of bilateral hemispheres to test the hemispheric differences. An asymmetry index (AI) was calculated to further quantify the differences between the left and right paired-ROIs. It was found that the asymmetries of white matter skeletons were significantly lower in the MTLE-HS groups than in the HC group. In particular, the asymmetry traits were moderately reduced in the RMTLE-HS group and obviously reduced in the LMTLE-HS group. In addition, AI was significantly different in the RMTLE-HS group from the LMTLE-HS or HC group in the limbic system and superior longitudinal fasciculus (SLF). The current study found that the interhemispheric white matter asymmetries were significantly reduced in the MTLE-HS groups than in the HC group. The interhemispheric white matter asymmetries are distinctly affected in left and right MTLE-HS groups. The differences in AI among RMTLE-HS, LMTLE-HS, and HC involved the limbic system and SLF, which may have some pragmatic implications for the diagnosis of MTLE and differentiating LMTLE-HS from RMTLE-HS.

Keywords: medial temporal lobe epilepsy, hippocampal sclerosis, asymmetry, diffusion tensor imaging, tract-based spatial statistics

OPEN ACCESS

Edited by:
Weidong Cai,
University of Sydney, Australia

Reviewed by:
Jingyun Chen,
New York University, United States
Dong-Hoon Lee,
University of Sydney, Australia

****Correspondence:***
Wen-zhen Zhu
zhuwenzhen8612@163.com

Specialty section:
This article was submitted to Applied Neuroimaging, a section of the journal Frontiers in Neurology

Received: *24 December 2018*
Accepted: *01 April 2019*
Published: *24 April 2019*

Citation:
Zhao X, Zhou Z, Xiong Y, Chen X, Xu K, Li J, Hu Y, Peng X and Zhu W (2019) Reduced Interhemispheric White Matter Asymmetries in Medial Temporal Lobe Epilepsy With Hippocampal Sclerosis. Front. Neurol. 10:394. doi: 10.3389/fneur.2019.00394

INTRODUCTION

Both structural and functional asymmetries have long been observed in the human brain and thought to be a central principle of central nervous system architecture and to relate to differences in most cognitive and neurobehavioral functioning. The most consistent structural asymmetries are the rightward asymmetry of the frontal region and the leftward asymmetry of the occipital petalias and the planum temporale. The most striking functional lateralizations are the leftward asymmetry of verbal cognitive function and the rightward asymmetry of spatial cognitive function in most individuals (1–8). The alteration of the hemispheric asymmetries has been reported in some neurodevelopmental and psychiatric disorders, such as schizophrenia (9), prelingual deafness (10), and autism (11).

Mesial temporal lobe epilepsy (MTLE) is one of the most common types of refractory focal epilepsy, among which hippocampal sclerosis (HS) is the most frequent pathological change. About one-third of TLE cases are medically intractable, rendering them good candidates for surgical treatment. A key point for a successful surgery for TLE patients is to correctly recognize an epileptogenic focus, such as HS (12). Numerous studies have shown that the structural and/or functional changes of MTLE not only involve the temporal lobe but also extend beyond the temporal regions (13–16), and these structural and/or functional abnormalities present asymmetric characteristics. A review of the voxel-based morphometry (VBM) of TLE found significant volume reductions in 26 brain regions and a strong preference for asymmetric abnormalities to be observed ipsilateral to the epileptogenic zone (15). The white matter integrity of TLE assessed by diffusion tensor imaging (DTI) also shows more severe impairment in the ipsilateral than the contralateral hemisphere (17). The same asymmetric features of TLE were present in functional connectivity analysis as well (16). In particular, left MTLE (LMTLE) manifests as more widespread abnormalities and involves the contralateral hemisphere more widely than right MTLE (RMTLE) (13, 18–20). In addition, LMTLE often exhibits more intense cognitive impairment than RMTLE (21, 22). These data imply that LMTLE and RMTLE may be two different diseases with different pathogenesis (13, 23, 24).

Previous studies suggested that persistent seizure activities in TLE patients could produce white matter defects, such as reduced axonal density, axonal demyelination, and replacement of axons with glia (25, 26). DTI, as a noninvasive technique that can evaluate the integrity of the white matter microstructure *in vivo* based on measuring the restricted diffusion of water molecules in the brain, has been widely used in the analysis of white matter defects in TLE (27). Fractional anisotropy (FA) is a parameter of DTI that is used widely in describing the degree of anisotropy of a diffusion process and is thought to reflect fiber density, axonal diameter, and myelination in white matter. Mean diffusivity (MD) is another parameter of DTI that measures the extent of the diffusion of water molecules independent of directionality (28). Axial diffusivity (AD, the principal eigenvalue) , also called the longitudinal diffusivity, reflects the diffusivity along the principal axis, and radial diffusivity (RD, the average of the 2 remaining eigenvalues) represents the diffusivity of the two minor axes. White matter anomalies have been found in TLE with using DTI, some of which are asymmetric (23, 29) and can be helpful in discriminating left TLE from right TLE (29). Moreover, recent advances have shown that the white matter asymmetry is probably the missing link between structural and functional lateralization (3, 30). Thus, we believe that asymmetric assessment of white matter in patients with MTLE may contribute to the understanding of its pathogenesis and may be useful in differentiating LMTLE from RMTLE.

However, the white matter asymmetric traits in MTLE are not fully understood. The aforementioned studies compared MTLE patients with controls and found inter-subject differences that could only provide indirect evidence of asymmetry. Although few studies focused on comparing the white matter of the two hemispheres directly, these analyses were restricted to specific fiber tracts and could not provide a comprehensive understanding of the asymmetric characteristics in white matter of MTLE. For example, Ahmadi et al. focused on eight pairs of whiter matter fiber tracts (29), and Kemmotsu et al. only investigated six pairs of fiber tracts that projected from the temporal lobe (23). Moreover, because the ROIs of fiber tracts were manually drawn, there was the possibility of intraoperator error (29). Tract-based spatial statistics (TBSS) is a whole-brain analytical method that requires no a priori assumptions and is widely used for the analysis of white matter microstructure (31). Therefore, in the current study, we examined the white matter asymmetry of DTI indices, including FA, MD, AD, and RD, by TBSS in patients with MTLE by contrasting the left and right hemispheres directly so that each individual served as his own control to diminish the variability between individuals. We also conducted a ROI-based quantitative analysis and compared the four DTI indices (FA, MD, AD, and RD) of 21 paired ROIs of bilateral hemispheres directly to add evidence for white matter asymmetries. The asymmetry index (AI) was compared among the LMTLE, RMTLE, and healthy control (HC) groups to distinguish LMTLE from RMTLE. As a homogeneous group of MTLE, we only included MTLE with unilateral HS (MTLE-HS) in the final statistical analysis to exclude any confounding factors. We hypothesized that the asymmetries of white matter microstructure in MTLE-HS would be different from HC and that AI would provide useful information for differentiating left MTLE-HS (LMTLE-HS) from right MTLE-HS (RMTLE-HS).

MATERIALS AND METHODS

Subjects

We recruited 27 right-handed adult MTLE patients who were referred to Tongji hospital (Wuhan city, Hubei province, China) for the investigation of epilepsy. The diagnosis of MTLE was confirmed in all 27 patients according to the criteria defined by the Commission on Classification and Terminology of the International League Against Epilepsy (32). They were then divided into left MTLE or right MTLE based on clinical manifestations, video electroencephalography (v-EEG), neuroimaging results and/or PET-CT. To exclude the influence of different sides of epileptic foci on outcome, this study only included the homogeneous groups of MTLE patients

with unilateral HS. Among these participants, 12 patients were pathologically confirmed to have HS by the subsequent surgical treatment, and the other 13 cases of HS were diagnosed according to the typical MRI findings (volume reduction of the ipsilateral hippocampus, disturbed internal structure, increased signal intensity on T2FLAIR, widening of ipsilateral temporal angle) (33). The exclusion criteria included a mismatch between seizure semiology, v-EEG and neuroimaging results; bilateral HS; lesions other than HS seen on MRI; and other neurologic disorders. One patient was excluded because of the discrepancy of v-EEG and MRI. Another 1 patient was excluded owing to excessive motion during the MRI, resulting in 25 patients with unilateral HS (LMTLE-HS group, $n = 13$; RMTLE-HS group, $n = 12$) whose imaging data were used in the final analysis. The age of first seizure and the epilepsy duration of these patients were also collected. Twenty-six right-handed healthy adults with matched age and gender were included as controls. There were no lesions on MRI and no history of neurologic or psychiatric illness in any controls. All 26 HCs were included in the final analysis. Consistency in age and gender among the RMTLE-HS, LMTLE-HS and HC groups was determined with 1-way ANOVA with Bonferroni corrected *post hoc* analysis and the $\chi 2$ test respectively. We conducted the Mann–Whitney U test for the age of first seizure and the epilepsy duration of RMTLE-HS and LMTLE-HS groups in SPSS 24, and the significance level was set at $p < 0.05$. All patients and controls included in this study gave written informed consent in accordance with the Declaration of Helsinki. This study was approved by the Ethical Committee of Tongji Hospital of Tongji Medical College of Huazhong University of Science and Technology.

Image Acquisition

MR images were acquired using a 3.0-T MR scanner (Discovery MR750; GE Healthcare, Milwaukee, Wisconsin) with a 32-channel head coil. The subjects were padded with flexible foam to limit head motion. To exclude possible lesions specified in the exclusion criteria, all subjects underwent the standard structural brain scan, including axial T1WI, T2WI, T2FLAIR (TR/TE/TI 8400/160/2100 ms, section thickness 5 mm, section spacing 1.5 mm, matrix size 256 × 256, FOV 24.0 × 24.0 cm^2, and NEX = 1). A sagittal three-dimensional T1-weighted-imaging brain volume (3D-T1BRAVO) (TR/TE/TI 8.2/3.2/450 ms, flip angle 12°, slice thickness 1 mm, sagittal slices 166, matrix size 256 × 256 × 160, FOV 25.6 × 25.6 cm^2, and NEX = 1) and an oblique coronal T2FLAIR perpendicular to the long axis of the hippocampus were also acquired to observe the hippocampus and temporal lobe better. DTI data were obtained in the axial plane by using a single-shot diffusion-weighted echo-planar imaging pulse sequence with the following scanning protocol: TR/TE 8500/66.3 ms, FOV 25.6 × 25.6 cm^2, matrix size 128 × 128, slice thickness 2 mm, number of slices 70, number of diffusion gradient directions 64, b = 0 and 1000 s/mm^2, number of images at a b-value of 0 s/mm^2 = 5, acceleration factor 2, and scan time 9 min 55 s.

DTI Processing

The DTI data were preprocessing by the following steps: (1) Format transformation: MRIcron (http://www.nitrc.org/projects/mricron) was used to convert the image files in DICOM format into NIFTI format for further processing. (2) Eddy current correction: A FSL "eddy" tool (http://www.fmrib.ox.ac.uk/fsl/fslwiki/eddy) was used and all raw DTI images were aligned to the corresponding b0 images to correct eddy current distortions and motion artifacts. (3) Brain extraction: the nonbrain tissues such as scalp and skull were removed by using the Brain Extraction Tool (BET) (34). The robust brain center estimation was chosen and fractional intensity threshold was set as 0.2. (4) DTIFIT was used to calculate maps of FA, MD, AD, and RD for each subject.

We used TBSS (http://fsl.fmrib.ox.ac.uk/fsl/fslwiki/TBSS) to perform voxel-wise statistical analysis of the FA/MD/AD/RD images with the following steps (35): (1) Align all the FA images into the FMRIB58_FA_1 mm standard-space image through a nonlinear registration. (2) Write the nonlinear transform parameters to individual subjects and generate a mean FA skeleton from the actual subjects in our study, which represented the centers of all tracts common to the entire group. (3) Set an FA threshold of 0.2 to exclude nonskeleton voxels and generate individual skeletonized FA data. Each subject's MD, AD, RD images were then projected onto this skeleton. (4) Use the script "tbss_sym" to test the hemispheric differences. Firstly, the original asymmetric skeleton was dilated by one voxel. Next, the symmetric mean FA data was generated by flipping and averaging the original mean FA data, and then they were skeletonized to generate the initial symmetric skeleton. This skeleton was masked by the dilated original skeleton and was flipped and masked by the non-flipped image to ensure the skeleton was exactly symmetrical. Finally, a symmetrized skeleton was created for subsequent analysis. Each subject's aligned DTI data were projected onto this symmetrized skeleton. Asymmetry images were then created by the flipped minus original skeleton projected data, and the left side of the images were then zeroed. The resulting images were fed into voxelwise statistical analysis.

Statistical Analysis

To test the asymmetry of FA/MD/AD/RD, we ran the permutation-based nonparametric 1-sample t-test (FSL Randomize tool with 5,000 permutations; http://fsl.fmrib.ox.ac.uk/fsl/fslwiki/randomise) twice separately (positive stands for left>right, negative stands for left<right). The significance level for t-tests (one-tailed) was set at $P < 0.05$, corrected for multiple comparisons by using Threshold-Free Cluster Enhancement (TFCE) with the familywise error (FWE) rate controlled. The rightward/leftward asymmetry on FA/MD/AD/RD was defined as having a larger/smaller FA/MD/AD/RD value of the right brain voxel/ROI than the left.

ROI-Based Quantitative Analysis

We used the ICBM-DTI-81 white-matter label atlas (36) as a standard to parcel the white matter into 48 ROIs. To test the hemisphere symmetry, 21 paired ROIs of bilateral hemispheres were included in the final analysis, excluding six ROIs in the midline involved both hemispheres. FA/MD/AD/RD was calculated by averaging the pixel values in these 21 paired ROIs for each subject separately. To eliminate potential confounders

related to the innate asymmetry of human brain, we normalized all the DTI indices by using z scores based on the mean of the control group in a given hemisphere. We conducted the two-sample paired *t*-test for each paired ROI of each group by using SPSS, and the significance level was set at $P < 0.05$.

Asymmetry Index Calculation

An asymmetry index (AI) was calculated using the formula AI = $100 * (\text{Right} - \text{Left})/[(\text{Right} + \text{Left})/2]$ (11, 37) to further quantify the differences between the left and right paired ROIs mentioned above. A positive AI value indicated that the ROI value of the right hemisphere was greater than the corresponding left ROI, that is, rightward asymmetry, while a negative value stood for the opposite, that is, leftward asymmetry. For the statistical comparison of AIs among the three groups, a univariate ANOVA was used, and a *post hoc* analysis with Bonferroni correction was included for multiple comparisons and to determine the direction of AI differences among groups.

RESULTS

Clinical Data

The clinical and demographic characteristics of the 3 subject groups are summarized in **Table 1**. No significant differences were found among the LMTLE-HS, RMTLE-HS, and HC in age ($P = 0.531$) or gender ($P = 0.654$). The age of first seizure and epilepsy duration did not show significant differences between the LMTLE-HS and RMTLE-HS groups ($P = 0.611$, $P = 0.186$, respectively) either.

The TBSS Results of the Whole-Brain White Matter Asymmetry

As shown in **Figure 1A**, the TBSS skeleton analysis of asymmetry images showed a large proportion of leftward and rightward asymmetries across the whole brain of the HC group in FA, while both the LMTLE-HS and RMTLE-HS group displayed significantly reduced asymmetries than the HC group. The leftward asymmetry reductions in LMTLE-HS included the cingulum, superior corona radiata, external capsule, posterior limb of the internal capsule, and uncinate fasciculus (UF), and those in RMTLE-HS included the body of the corpus callosum, superior corona radiata, external capsule, and posterior limb of the internal capsule. The rightward asymmetry reductions in LMTLE-HS included the anterior corona radiate (ACR) and corpus callosum, and those in RMTLE-HS included the superior longitudinal fasciculus (SLF). In particular, the leftward asymmetry of the fornix (FORX) in FA seen in the HC group was reversed in the LMTLE-HS group. The MD map presented a relatively small area of asymmetry in the HC group compared to the FA map and a smaller area in the LMTLE-HS and RMTLE-HS group (**Figure 1B**). Asymmetric patterns of AD and RD were largely consistent with MD for the three groups (**Figure S1**).

Results of ROI-Based Quantitative Analysis

The ROI-based quantitative analysis of FA also showed a large number of rightward and leftward asymmetries among the 21 paired ROIs (17 paired ROIs showed asymmetry features, among which nine showed rightward asymmetry and eight showed leftward asymmetry) in the HC group (**Table S1**). For MD, 16 paired ROIs presented asymmetric traits in the HC group, among which nine showed rightward asymmetry and seven showed leftward asymmetry (**Table S2**). AD and RD showed similar asymmetric features in the HC group as MD (**Tables S3, S4**).

Compared to HC, the asymmetry traits were moderately reduced in the RMTLE-HS group and obviously reduced in the LMTLE-HS group. After eliminating the innate asymmetry of the human brain seen in the HC group, only eight paired ROIs [corticospinal tract (CST) ($P = 0.02$), medial lemniscus ($P = 0.009$), cerebral peduncle ($P = 0.03$), external capsule ($P = 0.003$), parahippocampal cingulum (PHC) ($P = 0.01$), FORX ($P = 0.02$), superior fronto-occipital fasciculus (SFOF) ($P = 0.01$), and tapetum ($P = 0.04$)] showed leftward asymmetry in FA, and 5 paired ROIs [cingulum (cingulate gyrus) (CG) ($P = 0.004$), PHC ($P = 0.004$), FORX ($P = 0.01$), SLF ($P = 0.04$) and UF ($P = 0.01$)] showed rightward asymmetry in MD in the RMTLE-HS group. Meanwhile, only two paired ROIs [posterior thalamic radiation ($P = 0.01$) and sagittal stratum ($P = 0.01$)] showed rightward asymmetry in FA and one paired ROI (UF) ($P = 0.02$) showed leftward asymmetry in MD in the LMTLE-HS group (**Figure 2**). Similarly, the results of ROI-based quantitative analysis of AD/RD were largely consistent with MD in both the LMTLE-HS and RMTLE-HS groups (**Figure S2**).

Analysis of the Whole-Brain White Matter Asymmetry Index

The between-group analysis of AIs for the three groups showed no significant differences between HC and LMTLE-HS among all paired-ROIs. However, some differences were observed between HC and RMTLE-HS, such as PHC ($P = 0.01$) in FA (**Figure 3A**), and PHC ($P = 0.002$), FORX ($P = 0.003$), SLF ($P = 0.02$), and SFOF ($P = 0.03$) in MD (**Figure 3B**). The external capsule ($P = 0.003$) and PHC ($P = 0.001$) in FA (**Figure 3A**) and the

TABLE 1 | Demographic characteristics of the subjects.

	LMTLE-HS ($n = 13$)	RMTLE-HS ($n = 12$)	HC ($n = 26$)	Significant differences (*P*-value)
Age (mean ± SD years)	28.54 ± 9.84	31.25 ± 9.75	27.73 ± 8.08	0.531
Gender (male/female)	9/4	7/5	14/12	0.654
Median age at first seizure (years)	16	13	NA	0.611
Median epilepsy duration (years)	10	14	NA	0.186

LMTLE-HS, left mesial temporal lobe epilepsy with hippocampal sclerosis; RMTLE-HS, right mesial temporal lobe epilepsy with hippocampal sclerosis; HC, healthy control; SD, standard deviation; NA, not applicable.

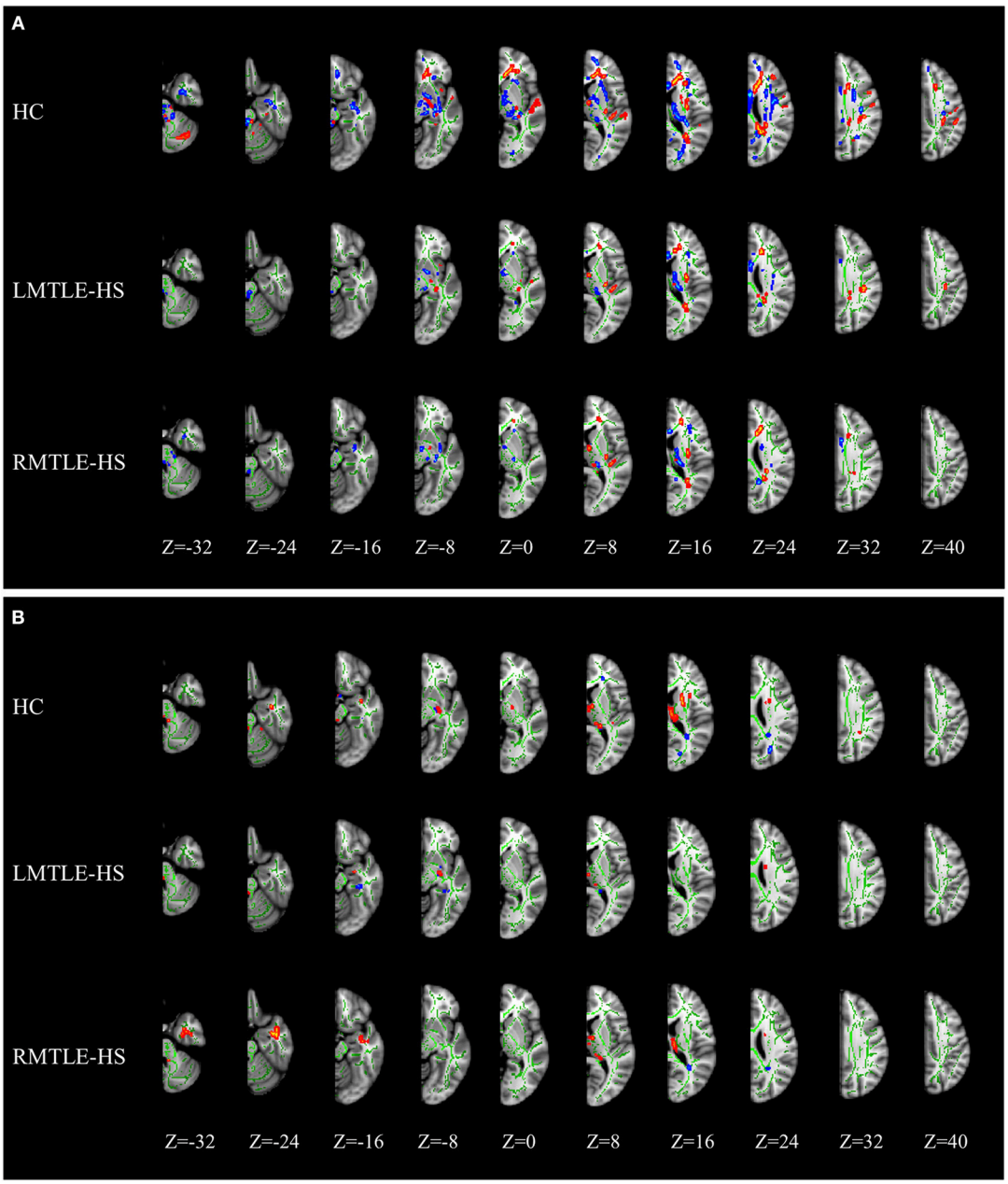

FIGURE 1 | MRI images of significant tract-based spatial statistics (TBSS) clusters of white matter asymmetry in healthy controls, patients with left mesial temporal lobe epilepsy with hippocampal sclerosis (LMTLE-HS) and patients with right MTLE-HS. **(A)** Represents fractional anisotropy (FA) and **(B)** represents mean diffusivity (MD). Results are presented on the left hemisphere of the symmetric TBSS skeleton (depicted in green). Rightward asymmetry that was defined as having a larger FA/MD value of the right brain (R) than the left (L) (R > L) depicted in blue-light-blue and leftward asymmetry (L > R) in red-yellow.

ACR ($P = 0.04$), CG ($P = 0.01$), PHC ($P = 0.002$), FORX ($P = 0.004$), SLF ($P = 0.01$), and SFOF ($P = 0.0001$) in MD (**Figure 3B**) also showed significant differences between LMTLE-HS and RMTLE-HS. The AIs analysis in RD was similar to MD among the three groups (**Figure S3B**). In AD, FORX ($P = 0.009$) showed significant differences between HC and LMTLE-HS, and medial lemniscus ($P = 0.01$) and sagittal stratum ($P = 0.03$) showed significant differences between LMTLE-HS and RMTLE-HS (**Figure S3A**).

DISCUSSION

The structural asymmetry of white matter microstructure in patients with MTLE-HS has not yet been comprehensively investigated. In this study, we used DTI to investigate the hemispheric asymmetry of the white matter microstructure in patients with MTLE-HS. Our findings showed that interhemispheric asymmetries were significantly lower in the MTLE-HS groups than in the HC group. In particular,

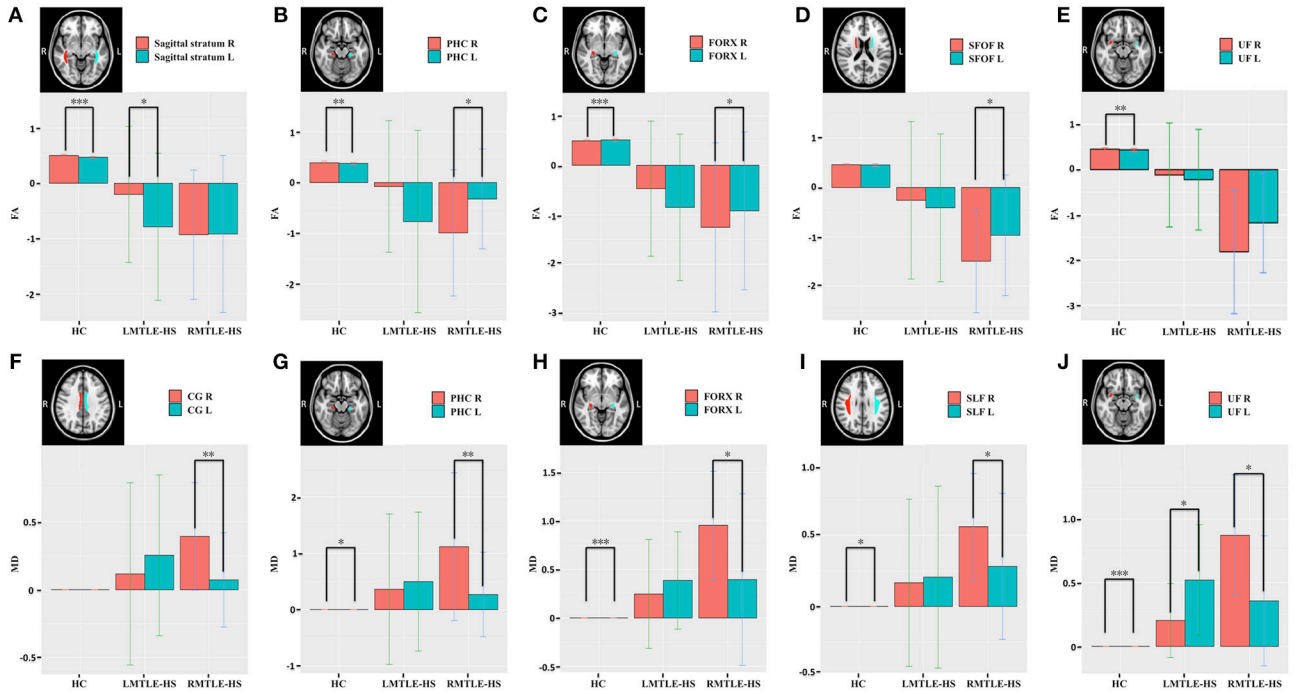

FIGURE 2 | The paired-ROIs asymmetries in HC, LMTLE-HS, and RMTLE-HS were calculated by comparing the FA **(A–E)** or MD **(F–J)** values of the paired-ROIs in bilateral hemispheres. The FA and MD values of LMTLE-HS and RMTLE-HS were calculated by using z scores based on the mean of the HC in a given hemisphere. Red represents the FA or MD values of the right hemisphere and blue represents the FA or MD values of the left hemisphere. Rightward asymmetry was defined as having a larger FA/MD value of the right brain than the left, and leftward asymmetry was left ROI value larger than right (*$P < 0.05$; **$P < 0.01$; ***$P < 0.001$). PHC, parahippocampal cingulum; FORX, fornix; SFOF, superior fronto-occipital fasciculus; UF, uncinate fasciculus; CG, cingulum fibers within the cingulate gyrus; SLF, superior longitudinal fasciculus.

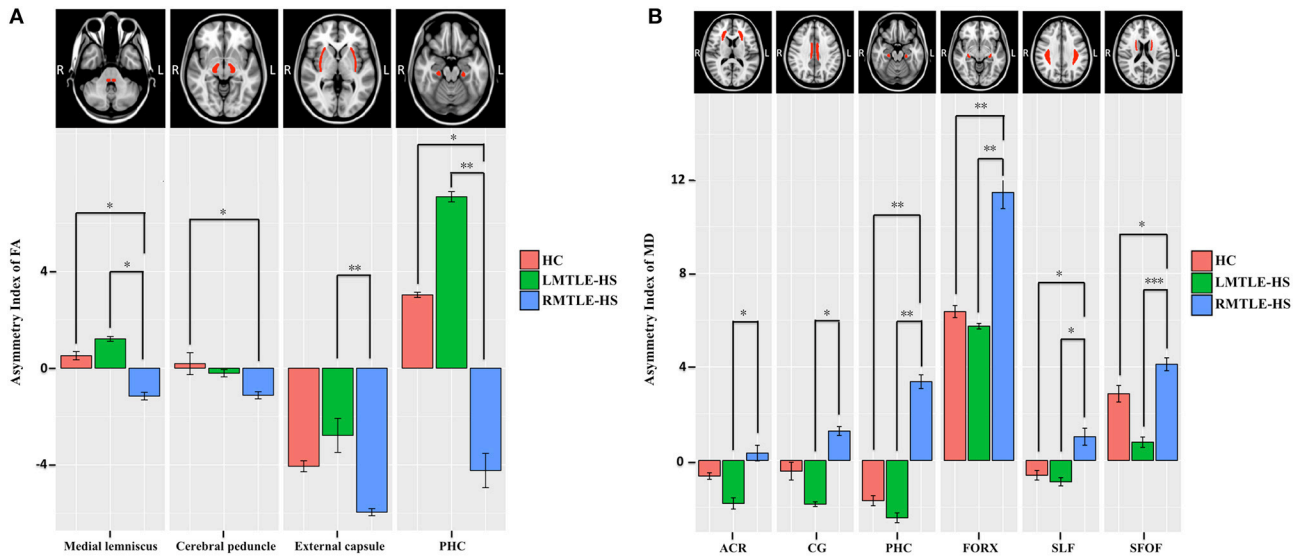

FIGURE 3 | The asymmetry index (AI) differences of the paired-ROIs in bilateral hemispheres among HC, LMTLE-HS, and RMTLE-HS. **(A)** Represents the AI of FA and **(B)** represents the AI of MD. Red represents FA or MD values in HC; green, patients with LMTLE-HS; blue, patients with RMTLE-HS (*$P < 0.05$; **$P < 0.01$; ***$P < 0.001$). PHC, parahippocampal cingulum; ACR, anterior corona radiate; CG, cingulum fibers within the cingulate gyrus; FORX, fornix; SLF, superior longitudinal fasciculus; SFOF, superior fronto-occipital fasciculus.

the asymmetric areas were smaller in the LMTLE-HS than the RMTLE-HS group. In addition, AI was significantly different in the RMTLE-HS group from that in the LMTLE-HS or HC group in the limbic system and SLF. Taken together, our results indicate that reductions of asymmetry of the white matter microstructure in patients with MTLE-HS compared to HC and the asymmetric alterations might be a useful clue in understanding the lateralization of seizure foci.

Brain Asymmetry in Patients With MTLE

MTLE-HS is one of the most common types of refractory focal epilepsy. Although many studies have shown that both structural and functional abnormalities were asymmetric in MTLE patients (13, 16, 19, 22, 23, 29), these findings have not been found consistently. Some studies have reported that the alterations in the ipsilateral hemisphere were more severe than those in the contralateral hemisphere in MTLE (15, 17). In particular, the majority of these studies showed that the LMTLE patients presented more diffused and bilateral abnormalities than the RMTLE patients (13, 16, 18–20, 23, 29). In contrast, some other studies reported the opposite results (24, 38) that alterations in the RMTLE group were more severe than in the LMTLE group. However, very few studies have focused specifically on patients with MTLE to characterize the asymmetry. The different asymmetric patterns between LMTLE and RMTLE remain unclear, and the importance of these asymmetries for understanding MTLE should be noted. First, the abnormal asymmetry of MTLE is associated with lateralization of seizure. For example, M.E. Ahmadi et al. found that using the asymmetric features of some fiber tracts could increase the lateralization of seizure foci to 90% of all cases (29). Concha et al. also found that tract segments correctly lateralized 87% of patients (39). Second, abnormal asymmetry of MTLE might be associated with the cognitive dysfunction in MTLE. For example, previous studies reported that the LMTLE-HS group showed worse performance on many neuropsychological tests (including verbal memory, general memory, and delayed recall) than the RMTLE-HS group (16). Therefore, understanding the underlying mechanisms of the differences in asymmetry between MTLE and HCs may play an important role in the clinic.

Asymmetry Abnormalities of White Matter Microstructure in MTLE-HS

TBSS analysis showed significant reductions of the asymmetries of whole-brain white matter in FA in the MTLE-HS groups compared to the HC group. These findings indicate that the interhemispheric asymmetry of patients with MTLE-HS is impaired (11). Structural asymmetry is a characteristic of human brain organization and is beneficial for the functional specializations of the two hemispheres, in particular cognitive processes (1, 5, 7, 40). Gotts et al. provides direct evidence that the strength of functional lateralization is correlated with the level of cognitive ability in humans (41). Furthermore, aberrant interhemispheric asymmetries are associated with some neuropathologies, such as prelingual deafness, autism, schizophrenia, and epilepsy (9–11, 42). Therefore, we assumed that the reduction of white matter asymmetry of MTLE-HS might be related to the reported cognitive dysfunctions (16).

Some previous studies indicated that the innate side-to-side cerebral asymmetry could contribute to the observed difference between LTLE and RTLE (43). However, whether the asymmetric changes of MTLE patients are associated with the innate human brain asymmetry needs further analysis. Here, to eliminate the probable influences of innate human brain asymmetry, we normalized all the DTI indices by using z scores based on the mean of the control group in a given hemisphere. Specifically, after eliminating the innate asymmetry of the human brain seen in the HC group, we found only rightward asymmetry in FA and only leftward asymmetry in MD in the LMTLE-HS group and only leftward asymmetry in FA and only rightward asymmetry in MD in the RMTLE-HS group. The AD and RD showed similar asymmetric features as MD. Our findings support the previous results that more pronounced changes ipsilateral to the seizure focus were presented in LMTLE/RMTLE by using whole-brain analysis and by comparing the bilateral hemispheres directly (17, 23, 29). The FA reduction and MD increase in the ipsilateral hemisphere to the seizure focus of MTLE have been consistently reported. We speculated that RMTLE-HS/LMTLE-HS influenced the ipsilateral side of these paired ROIs more severely, resulting in reduced/elevated FA/MD values of the ipsilateral side and thus manifesting as asymmetric features.

The Different White Matter Asymmetrical Patterns Between LMTLE-HS and RMTLE-HS

The asymmetry alterations appeared differently between LMTLE-HS and RMTLE-HS. The asymmetric ROIs were smaller in the LMTLE-HS group than in the RMTLE-HS group. A possible explanation for this finding is that LMTLE-HS affected the bilateral hemispheres almost equally and thus the innate asymmetry of the human brain was nearly not affected by LMTLE-HS. The reliability of these findings is further supported by the ROI result that the AI between LMTLE-HS and HC did not present significant differences. Our findings were partially consistent with many previous studies. Abnormalities in LMTLE-HS are more widespread and bilateral than those in RMTLE-HS (13, 20, 23). For example, Kemmotsu et al. reported that patients with LTLE showed smaller FA values in the ipsilateral hemisphere of the UF and ILF, as well as a similar trend in the PHC, ARC and IFOF. RTLE patients showed a trend of smaller ipsilateral FA values only in the PHC (23). Recently, a large-scale brain network study also showed that LMTLE-HS had a more intricate bihemispheric dysfunction than RMTLE-HS (13). For RMTLE-HS, the impairment was relatively more confined to the ipsilateral hemisphere, and therefore, the innate asymmetry of the human brain was changed. The exact underlying mechanisms remain to be elucidated. They might have some relationship with the greater vulnerability of the left hemisphere to early insults and the wider propagation of left hemisphere seizures (23). It is also possible that LMTLE and RMTLE are etiologically distinct and pathologically different syndromes from the outset (29).

The Different Asymmetry Alterations of the Limbic System and SLF Among the Three Groups

Some differences were observed in AI analysis among the three groups, such as in the CG, PHC, and FORX. It should be noted that the CG, PHC, and FORX are parts of the limbic system. Within this system, the FORX serves as the internal ring that projects from the hippocampus to the mammillary bodies, while the cingulum serves as the external ring interconnecting the entorhinal cortex and the cingulate gyrus (44, 45). It has long been proposed that TLE may be a probable manifestation of limbic system dysfunction (46), and the relevance of the limbic system as a MTLE-HS neural circuit has been well established (47, 48). For example, Despina Liacu et al. found that the bilateral cingulum and FORX in MTLE-HS groups showed significant DTI index abnormalities compared with controls (47). H. Urbach also found a bilateral reduction of the streamline counts of cingulum association fibers projecting from the cingulate gyrus to the parahippocampal gyrus in MTLE-HS (48). Thus, the differences in AI of these components of the limbic system among HC, RMTLE-HS, and LMTLE-HS may have some pragmatic implications as to the diagnosis MTLE and the differentiation of LMTLE-HS from RMTLE-HS.

Furthermore, the AI of SLF in MD also showed significant differences among HC, RMTLE-HS and LMTLE-HS. SLF is a bilateral white matter association fiber tract connecting the frontal, occipital, parietal, and temporal lobes (49). SLF plays an important role in many complex cognitive processes, including working memory, and language processing (50, 51). The abnormalities of SLF in TLE have been found in many studies (23, 29), and the association between SLF and memory and language impairments have also been presented in TLE (52). For example, the arcuate fasciculus (AF), a part of the SLF of TLE, has been associated with poorer verbal memory and naming performance. Regression analyses revealed that AF independently predicted cognitive performance after controlling for hippocampal volume (52). Thus, the different AIs of the SLF among the three groups in our study might indicate the different cognitive functions associated with SLF, but this inference needs further verification because of the lack of cognitive function evaluation in the current study.

LIMITATION

Some limitations of the current study should be mentioned. First, we did not evaluate the subjects' cognitive functions and thus could not clarify the relationship between asymmetry and cognitive functions. Such cognitive functions as language have been observed to be associated with brain asymmetry (5). We would include cognitive evaluation in future studies. Second, we only analyzed the white matter asymmetry of MTLE patients. Further research about the functional and other structural asymmetries should be included in future studies, which might provide a comprehensive understanding of the asymmetry characteristics of MTLE.

CONCLUSION

The current study found that the interhemispheric asymmetries in FA were significantly lower in both the LMTLE-HS group and the RMTLE-HS group than in the HC group. The ROI-based quantitative analysis provided further evidence for the previous result that RMTLE-HS/LMTLE-HS influences the ipsilateral hemisphere more severely and that impairment in LMTLE-HS may be more diffuse and bilateral than that in RMTLE-HS. The differences in AI among RMTLE-HS, LMTLE-HS, and HC involved the limbic system and the SLF, which may have some pragmatic implications as to the diagnosis of MTLE and the differentiation of LMTLE-HS from RMTLE-HS.

ETHICS STATEMENT

This study was carried out in accordance with the recommendations of the Ethical Committee of Tongji Hospital of Tongji Medical College of Huazhong University of Science and Technology with written informed consent from all subjects. All subjects gave written informed consent in accordance with the Declaration of Helsinki. The protocol was approved by the Ethical Committee of Tongji Hospital of Tongji Medical College of Huazhong University of Science and Technology.

AUTHOR CONTRIBUTIONS

XZ, ZZ, and WZ were responsible for the study design, data interpretation and writing the manuscript. YX, XZ, XP, and ZZ contributed to MRI data acquisition, TBSS processing, ROI-based quantitative analyzing and AI analyzing. XC, KX, JL, and YH assisted in recruiting subjects, acquiring MRI data and collecting clinical data. WZ revised the first draft of the manuscript. All authors critically reviewed and approved the submitted version.

FUNDING

This work is supported by the National Natural Science Foundation of China (No. 81570462, 81730049, 81601480).

ACKNOWLEDGMENTS

The authors are grateful to Prof. Suiqiang Zhu, Dr. Huicong Kang, and Dr. Xiaoyan Liu, Department of Neurology, Tongji Hospital, Tongji Medical College of Huazhong University of Science and Technology, for helpful in diagnosing of MTLE.

SUPPLEMENTARY MATERIAL

The Supplementary Material for this article can be found online at: https://www.frontiersin.org/articles/10.3389/fneur.2019.00394/full#supplementary-material

REFERENCES

1. Cabeza R. Hemispheric asymmetry reduction in older adults: the HAROLD model. *Psychol Aging.* (2002) 17:85–100. doi: 10.1037/0882-7974.17.1.85
2. Good CD, Johnsrude I, Ashburner J, Henson RN, Friston KJ, Frackowiak RS. Cerebral asymmetry and the effects of sex and handedness on brain structure: a voxel-based morphometric analysis of 465 normal adult human brains. *Neuroimage.* (2001) 14:685–700. doi: 10.1006/nimg.2001.0857
3. Ocklenburg S, Friedrich P, Gunturkun O, Genc E. Intrahemispheric white matter asymmetries: the missing link between brain structure and functional lateralization? *Rev Neurosci.* (2016) 27:465–80. doi: 10.1515/revneuro-2015-0052
4. Ocklenburg S, Gunturkun O, Beste C. Lateralized neural mechanisms underlying the modulation of response inhibition processes. *Neuroimage.* (2011) 55:1771–8. doi: 10.1016/j.neuroimage.2011.01.035
5. Toga AW, Thompson PM. Mapping brain asymmetry. *Nat Rev Neurosci.* (2003) 4:37–48. doi: 10.1038/nrn1009
6. Vogel JJ, Bowers CA, Vogel DS. Cerebral lateralization of spatial abilities: a meta-analysis. *Brain Cogn.* (2003) 52:197–204. doi: 10.1016/S0278-2626(03)00056-3
7. Yin X, Han Y, Ge H, Xu W, Huang R, Zhang D, et al. Inferior frontal white matter asymmetry correlates with executive control of attention. *Hum Brain Mapp.* (2013) 34:796–813. doi: 10.1002/hbm.21477
8. Takao H, Hayashi N, Ohtomo K. White matter asymmetry in healthy individuals: a diffusion tensor imaging study using tract-based spatial statistics. *Neuroscience.* (2011) 193:291–9. doi: 10.1016/j.neuroscience.2011.07.041
9. Kawasaki Y, Suzuki M, Takahashi T, Nohara S, McGuire PK, Seto H, et al. Anomalous cerebral asymmetry in patients with schizophrenia demonstrated by voxel-based morphometry. *Biol Psychiatry.* (2008) 63:793–800. doi: 10.1016/j.biopsych.2007.08.008
10. Li W, Li J, Xian J, Lv B, Li M, Wang C, et al. Alterations of grey matter asymmetries in adolescents with prelingual deafness: a combined VBM and cortical thickness analysis. *Restor Neurol Neurosci.* (2013) 31:1–17. doi: 10.3233/RNN-2012-120269
11. Carper RA, Treiber JM, DeJesus SY, Muller RA. Reduced hemispheric asymmetry of white matter microstructure in autism spectrum disorder. *J Am Acad Child Adolesc Psychiatry.* (2016) 55:1073–80. doi: 10.1016/j.jaac.2016.09.491
12. Pustina D, Avants B, Sperling M, Gorniak R, He X, Doucet G, et al. Predicting the laterality of temporal lobe epilepsy from PET, MRI, and DTI: a multimodal study. *NeuroImage Clinical.* (2015) 9:20–31. doi: 10.1016/j.nicl.2015.07.010
13. de Campos BM, Coan AC, Lin Yasuda C, Casseb RF, Cendes F. Large-scale brain networks are distinctly affected in right and left mesial temporal lobe epilepsy. *Hum Brain Mapp.* (2016) 37:3137–52. doi: 10.1002/hbm.23231
14. Gross DW, Concha L, Beaulieu C. Extratemporal white matter abnormalities in mesial temporal lobe epilepsy demonstrated with diffusion tensor imaging. *Epilepsia.* (2006) 47:1360–3. doi: 10.1111/j.1528-1167.2006.00603.x
15. Keller SS, Roberts N. Voxel-based morphometry of temporal lobe epilepsy: an introduction and review of the literature. *Epilepsia.* (2008) 49:741–57. doi: 10.1111/j.1528-1167.2007.01485.x
16. Pereira FR, Alessio A, Sercheli MS, Pedro T, Bilevicius E, Rondina JM, et al. Asymmetrical hippocampal connectivity in mesial temporal lobe epilepsy: evidence from resting state fMRI. *BMC Neurosci.* (2010) 11:66. doi: 10.1186/1471-2202-11-66
17. Otte WM, van Eijsden P, Sander JW, Duncan JS, Dijkhuizen RM, Braun KPJ. A meta-analysis of white matter changes in temporal lobe epilepsy as studied with diffusion tensor imaging. *Epilepsia.* (2012) 53:659–67. doi: 10.1111/j.1528-1167.2012.03426.x
18. Coan AC, Appenzeller S, Bonilha L, Li LM, Cendes F. Seizure frequency and lateralization affect progression of atrophy in temporal lobe epilepsy. *Neurology.* (2009) 73:834–42. doi: 10.1212/WNL.0b013e3181b783dd
19. Haneef Z, Lenartowicz A, Yeh HJ, Levin HS, Engel J Jr., Stern JM. Functional connectivity of hippocampal networks in temporal lobe epilepsy. *Epilepsia.* (2014) 55:137–45. doi: 10.1111/epi.12476
20. Keller SS, Schoene-Bake JC, Gerdes JS, Weber B, Deppe M. Concomitant fractional anisotropy and volumetric abnormalities in temporal lobe epilepsy: cross-sectional evidence for progressive neurologic injury. *PLoS ONE.* (2012) 7:e46791. doi: 10.1371/journal.pone.0046791
21. Alessio A, Bonilha L, Rorden C, Kobayashi E, Min LL, Damasceno BP, et al. Memory and language impairments and their relationships to hippocampal and perirhinal cortex damage in patients with medial temporal lobe epilepsy. *Epilepsy Behav.* (2006) 8:593–600. doi: 10.1016/j.yebeh.2006.01.007
22. Bonilha L, Rorden C, Halford JJ, Eckert M, Appenzeller S, Cendes F, et al. Asymmetrical extra-hippocampal grey matter loss related to hippocampal atrophy in patients with medial temporal lobe epilepsy. *J Neurol Neurosurg Psychiatr.* (2007) 78:286–94. doi: 10.1136/jnnp.2006.103994
23. Kemmotsu N, Girard HM, Bernhardt BC, Bonilha L, Lin JJ, Tecoma ES, et al. MRI analysis in temporal lobe epilepsy: cortical thinning and white matter disruptions are related to side of seizure onset. *Epilepsia.* (2011) 52:2257–66. doi: 10.1111/j.1528-1167.2011.03278.x
24. Pail M, Brazdil M, Marecek R, Mikl M. An optimized voxel-based morphometric study of gray matter changes in patients with left-sided and right-sided mesial temporal lobe epilepsy and hippocampal sclerosis (MTLE/HS). *Epilepsia.* (2010) 51:511–8. doi: 10.1111/j.1528-1167.2009.02324.x
25. Rodriguez-Cruces R, Concha L. White matter in temporal lobe epilepsy: clinico-pathological correlates of water diffusion abnormalities. *Quant Imaging Med Surg.* (2015) 5:264–78. doi: 10.3978/j.issn.2223-4292.2015.02.06
26. Sutula TP, Hagen J, Pitkanen A. Do epileptic seizures damage the brain? *Curr Opin Neurol.* (2003) 16:189–95. doi: 10.1097/00019052-200304000-00012
27. Pierpaoli C, Jezzard P, Basser PJ, Barnett A, Di Chiro G. Diffusion tensor MR imaging of the human brain. *Radiology.* (1996) 201:637–48. doi: 10.1148/radiology.201.3.8939209
28. Le Bihan D, Mangin JF, Poupon C, Clark CA, Pappata S, Molko N, et al. Diffusion tensor imaging: concepts and applications. *J Magn Reson Imaging.* (2001) 13:534–46. doi: 10.1002/jmri.1076
29. Ahmadi ME, Hagler DJ Jr., McDonald CR, Tecoma ES, Iragui VJ, Dale AM, et al. Side matters: diffusion tensor imaging tractography in left and right temporal lobe epilepsy. *AJNR Am J Neuroradiol.* (2009) 30:1740–7. doi: 10.3174/ajnr.A1650
30. Liu M, Bernhardt BC, Hong SJ, Caldairou B, Bernasconi A, Bernasconi N. The superficial white matter in temporal lobe epilepsy: a key link between structural and functional network disruptions. *Brain.* (2016) 139(Pt 9):2431–40. doi: 10.1093/brain/aww167
31. Beaulieu C. The basis of anisotropic water diffusion in the nervous system - a technical review. *NMR Biomed.* (2002) 15:435–55. doi: 10.1002/nbm.782
32. Berg AT, Berkovic SF, Brodie MJ, Buchhalter J, Cross JH, van Emde Boas W, et al. Revised terminology and concepts for organization of seizures and epilepsies: report of the ILAE Commission on Classification and Terminology, 2005-2009. *Epilepsia.* (2010) 51:676–85. doi: 10.1111/j.1528-1167.2010.02522.x
33. Malmgren K, Thom M. Hippocampal sclerosis–origins and imaging. *Epilepsia.* (2012) 53(Suppl. 4):19–33. doi: 10.1111/j.1528-1167.2012.03610.x
34. Smith SM. Fast robust automated brain extraction. *Hum Brain Mapp.* (2002) 17:143–55. doi: 10.1002/hbm.10062
35. Smith SM, Jenkinson M, Johansen-Berg H, Rueckert D, Nichols TE, Mackay CE, et al. Tract-based spatial statistics: voxelwise analysis of multi-subject diffusion data. *Neuroimage.* (2006) 31:1487–505. doi: 10.1016/j.neuroimage.2006.02.024
36. Mori S, Oishi K, Jiang H, Jiang L, Li X, Akhter K, et al. Stereotaxic white matter atlas based on diffusion tensor imaging in an ICBM template. *Neuroimage.* (2008) 40:570–82. doi: 10.1016/j.neuroimage.2007.12.035
37. Boscolo Galazzo I, Mattoli MV, Pizzini FB, De Vita E, Barnes A, Duncan JS, et al. Cerebral metabolism and perfusion in MR-negative individuals with refractory focal epilepsy assessed by simultaneous acquisition of (18)F-FDG PET and arterial spin labeling. *Neuroimage Clin.* (2016) 11:648–57. doi: 10.1016/j.nicl.2016.04.005
38. Voets NL, Beckmann CF, Cole DM, Hong S, Bernasconi A, Bernasconi N. Structural substrates for resting network disruption in temporal lobe epilepsy. *Brain.* (2012) 135(Pt 8):2350–7. doi: 10.1093/brain/aws137

39. Concha L, Kim H, Bernasconi A, Bernhardt BC, Bernasconi N. Spatial patterns of water diffusion along white matter tracts in temporal lobe epilepsy. *Neurology*. (2012) 79:455–62. doi: 10.1212/WNL.0b013e31826170b6
40. Duboc V, Dufourcq P, Blader P, Roussigne M. Asymmetry of the brain: development and implications. *Annu Rev Genet*. (2015) 49:647–72. doi: 10.1146/annurev-genet-112414-055322
41. Gotts SJ, Jo HJ, Wallace GL, Saad ZS, Cox RW, Martin A. Two distinct forms of functional lateralization in the human brain. *Proc Natl Acad Sci USA*. (2013) 110:E3435–44. doi: 10.1073/pnas.1302581110
42. Cao W, Zhang Y, Hou C, Yang F, Gong J, Jiang S, et al. Abnormal asymmetry in benign epilepsy with unilateral and bilateral centrotemporal spikes: a combined fMRI and DTI study. *Epilepsy Res*. (2017) 135:56–63. doi: 10.1016/j.eplepsyres.2017.06.004
43. Haneef Z, Lenartowicz A, Yeh HJ, Engel J Jr., Stern JM. Effect of lateralized temporal lobe epilepsy on the default mode network. *Epilepsy Behav*. (2012) 25:350–7. doi: 10.1016/j.yebeh.2012.07.019
44. Jang SH, Yeo SS. Thalamocortical tract between anterior thalamic nuclei and cingulate gyrus in the human brain: diffusion tensor tractography study. *Brain Imaging Behav*. (2013) 7:236–41. doi: 10.1007/s11682-013-9222-7
45. Kwon HG, Hong JH, Jang SH. Mammillothalamic tract in human brain: diffusion tensor tractography study. *Neurosci Lett*. (2010) 481:51–3. doi: 10.1016/j.neulet.2010.06.052
46. Reimer DR, Mohan J, Nagaswami S. Temporal lobe epilepsy as a probable manifestation of limbic system dysfunction. *Bull Menninger Clin*. (1975) 39:357–63.
47. Liacu D, Idy-Peretti I, Ducreux D, Bouilleret V, de Marco G. Diffusion tensor imaging tractography parameters of limbic system bundles in temporal lobe epilepsy patients. *J Magn Reson Imaging*. (2012) 36:561–8. doi: 10.1002/jmri.23678
48. Urbach H, Egger K, Rutkowski K, Nakagawa JM, Schmeiser B, Reisert M, et al. Bilateral cingulum fiber reductions in temporal lobe epilepsy with unilateral hippocampal sclerosis. *Eur J Radiol*. (2017) 94:53–7. doi: 10.1016/j.ejrad.2017.07.015
49. Schmahmann JD, Smith EE, Eichler FS, Filley CM. Cerebral white matter: neuroanatomy, clinical neurology, and neurobehavioral correlates. *Ann N Y Acad Sci*. (2008) 1142:266–309. doi: 10.1196/annals.1444.017
50. Burzynska AZ, Nagel IE, Preuschhof C, Li SC, Lindenberger U, Backman L, et al. Microstructure of frontoparietal connections predicts cortical responsivity and working memory performance. *Cereb Cortex*. (2011) 21:2261–71. doi: 10.1093/cercor/bhq293
51. Fitzgerald J, Leemans A, Kehoe E, O'Hanlon E, Gallagher L, McGrath J. Abnormal fronto-parietal white matter organisation in the superior longitudinal fasciculus branches in autism spectrum disorders. *Eur J Neurosci*. (2018) 47:652–61. doi: 10.1111/ejn.13655
52. McDonald CR, Ahmadi ME, Hagler DJ, Tecoma ES, Iragui VJ, Gharapetian L, et al. Diffusion tensor imaging correlates of memory and language impairments in temporal lobe epilepsy. *Neurology*. (2008) 71:1869–76. doi: 10.1212/01.wnl.0000327824.05348.3b

Conflict of Interest Statement: The authors declare that the research was conducted in the absence of any commercial or financial relationships that could be construed as a potential conflict of interest.

frontiers in Neuroscience

ORIGINAL RESEARCH
published: 10 July 2019
doi: 10.3389/fnins.2019.00679

Intra-Scanner and Inter-Scanner Reproducibility of Automatic White Matter Hyperintensities Quantification

Chunjie Guo[1†], Kai Niu[2†], Yishan Luo[3], Lin Shi[3,4], Zhuo Wang[1], Meng Zhao[5], Defeng Wang[1,4], Wan'an Zhu[1], Huimao Zhang[1†] and Li Sun[5*†]*

[1] Department of Radiology, The First Hospital of Jilin University, Changchun, China, [2] Department of Otorhinolaryngology Head and Neck Surgery, The First Hospital of Jilin University, Changchun, China, [3] BrainNow Medical Technology Limited, Sha Tin, Hong Kong, [4] Department of Imaging and Interventional Radiology, The Chinese University of Hong Kong, Sha Tin, Hong Kong, [5] Department of Neurology and Neuroscience Center, The First Hospital of Jilin University, Changchun, China

OPEN ACCESS

Edited by:
Ching-Po Lin,
National Yang-Ming University, Taiwan

Reviewed by:
Yi Su,
Banner Alzheimer's Institute, United States
Xin Di,
New Jersey Institute of Technology, United States

***Correspondence:**
Huimao Zhang
huimaozhanglinda@163.com
Li Sun
sjnksunli@163.com

[†] These authors have contributed equally to this work

Specialty section:
This article was submitted to Brain Imaging Methods, a section of the journal Frontiers in Neuroscience

Received: 11 January 2019
Accepted: 13 June 2019
Published: 10 July 2019

Citation:
Guo C, Niu K, Luo Y, Shi L, Wang Z, Zhao M, Wang D, Zhu W, Zhang H and Sun L (2019) Intra-Scanner and Inter-Scanner Reproducibility of Automatic White Matter Hyperintensities Quantification. Front. Neurosci. 13:679. doi: 10.3389/fnins.2019.00679

Objectives: To evaluate white matter hyperintensities (WMH) quantification reproducibility from multiple aspects of view and examine the effects of scan–rescan procedure, types of scanner, imaging protocols, scanner software upgrade, and automatic segmentation tools on WMH quantification results using magnetic resonance imaging (MRI).

Methods: Six post-stroke subjects (4 males; mean age = 62.8, range = 58–72 years) were scanned and rescanned with both 3D T1-weighted, 2D and 3D T2-weighted fluid-attenuated inversion recovery (T2-FLAIR) MRI across four different MRI scanners within 12 h. Two automated WMH segmentation and quantification tools were used to measure WMH volume based on each MR scan. Robustness was assessed using the coefficient of variation (CV), Dice similarity coefficient (DSC), and intra-class correlation (ICC).

Results: Experimental results show that the best reproducibility was achieved by using 3D T2-FLAIR MRI under intra-scanner setting with CV ranging from 2.69 to 2.97%, while the largest variability resulted from comparing WMH volumes measured based on 2D T2-FLAIR MRI with those of 3D T2-FLAIR MRI, with CV values in the range of 15.62%–29.33%. The WMH quantification variability based on 2D MRIs is larger than 3D MRIs due to their large slice thickness. The DSC of WMH segmentation labels between intra-scanner MRIs ranges from 0.63 to 0.77, while that for inter-scanner MRIs is in the range of 0.63–0.65. In addition to image acquisition, the choice of automatic WMH segmentation tool also has a large impact on WMH quantification.

Conclusion: WMH reproducibility is one of the primary issues to be considered in multicenter and longitudinal studies. The study provides solid guidance in assisting multicenter and longitudinal study design to achieve meaningful results with enough power.

KEY POINTS

- The intra-scanner and inter-scanner WMH reproducibility study in the same cohort.
- The best reproducibility was achieved by using 3D T2-FLAIR MRI under intra-scanner setting.
- There is a large variability in comparing WMH quantification results based on 2D T2-FLAIR MRI with those of 3D T2-FLAIR MRI.

Keywords: reproducibility of results, white matter, magnetic resonance imaging, brain, imaging, three-dimensional

INTRODUCTION

White matter hyperintensities, commonly found on T2-weighted T2-FLAIR brain MR images in the elderly, are associated with a number of neuropsychiatric disorders, including multiple sclerosis (MS) (Filippi et al., 2016),vascular dementia, Alzheimer's disease (AD) (Fazekas et al., 1996; Hirono et al., 2000), mild cognitive impairment (DeCarli et al., 2001), stroke (Fazekas et al., 1993), and Parkinson's disease (Marshall et al., 2006), and even in patients with primary mental disorders including mood disorders and schizophrenia spectrum disorders (Brown et al., 1995). Many studies have provided evidence that WMH have a strong impact on cognitive functioning (Gunning-Dixon and Raz, 2000) and they have been associated with impairment in a number of domains (Cees De Groot et al., 2000; Prins et al., 2004). WMH usually have a higher signal intensity compared to the normal-appearing white matter on FLAIR sequences and may appear iso- or hypointense on T1-weighted MR images. It can be measured quantitatively and non-invasively on large population samples and have been proposed as an intermediate marker, which could be used for the identification of new risk factors and potentially as a surrogate end point in clinical trials (Schmidt et al., 2004).

One challenging issue in studying WMH is the accurate and robust quantification and localization, given their variability and scattered spatial distribution. There are a number of automatic or semiautomatic methods and tools studying WMH segmentation and quantification, including thresholding method (Payne et al., 2002; Gibson et al., 2010; Simões et al., 2013), clustering methods (Admiraal-Behloul et al., 2005; Schmidt et al., 2012; Jain et al., 2015), and machine learning algorithms (Sweeney et al., 2014; López-Zorrilla et al., 2017; Rachmadi et al., 2018). While there are so many methods studying the accuracy of WMH segmentation and quantification, few studies examined the reproducibility of WMH quantification.

Accurate WMH quantification is of vital importance not only because it is associated with an increased risk of stroke, cognitive decline, dementia, and death, but also because their progression has been studied in association with cognitive decline, with increasing progression predicting a more rapid decline in global cognitive performance and executive function (Mungas et al., 2005; van den Heuvel et al., 2006; Kramer et al., 2007). In addition, WMH may also have a role as a surrogate marker to assess treatment efficacy. The impact of progression of WMH on stroke and dementia are also needed to help design therapeutic trials incorporating progression of WMH as an intermediate end point. In order to accurately observe the progression of WMH, the reproducibility of WMH measurement is of critical significance. The reliability of WMH quantification based on images acquiring from different scanners in multiple centers is of crucial importance in multi-center and follow-up studies. It is thought that a direct comparison of images or WMH quantities from different scanners in different centers may induce great variation, but no study examined the extent of this variation compared with within-center variability. The uncertain or lower reproducibility of WMH quantification across centers can contribute to a major concern for carrying out multicenter and longitudinal research, as well as clinical trials.

In this study, we carry out the study on the reproducibility of WMH quantification, which covers both intra-scanner and inter-scanner variability, 2D–3D magnetic resonance imaging (MRI) variability, MR system upgrade variability, and image processing tools variability in WMH quantification. The results of this study can provide great help and guidance in multicenter and longitudinal WMH study design.

Abbreviations: 95% CI, 95% confidence interval; CV, coefficient of variation; DSC, Dice similarity coefficient; FLAIR, fluid-attenuated inversion recovery; ICC, intra-class coefficient; SPM, statistical parametric mapping; WMH, white matter hyperintensities.

MATERIALS AND METHODS

Participants

Six post-stroke patients with last onset more than 6 months (4 male and 2 female; mean age = 62.8 years; range = 58–72 years) were prospectively recruited from the outpatient clinic at the Department of Neurology, the First Hospital of Jilin University, P.R. China. Exclusion criteria were cortical infarction > 1/3 hemisphere, severe neuropsychiatric disorders, and a history of traumatic brain injury or tumors. In addition, to exclude the confounding effect of edema, all the participants had been without treatment with dehydrating agent or steroid within 4 weeks before MRI scans. Based on visual assessment of WM lesions, Fazekas scale was assessed on all 3D T2-FLAIR images by an experienced radiologist (CJG), and the mean Fazekas scale score of each subject was recorded. The median Fazekas scale score of all participants was 2.2 (range 1–3) (Fazekas et al., 1987). The study was approved by the local ethics committee and written informed consent was obtained from all participants.

Image Acquisition

All participants were scanned within 12 h across four clinical MRI systems: MR1: 1.5-T Siemens Avanto (software: syngo MR B15); MR2: 1.5-T Siemens Avanto (software: syngo MR B17) (Siemens Healthcare, Erlangen, Germany); MR3: 3.0-T Philips Ingenia (Philips Healthcare, Best, the Netherlands), and MR4: 3.0-T Siemens Trio (Siemens Healthcare, Erlangen, Germany). 3D T1-weighted MRI sequence was obtained for assisting accurate WMH segmentation. 3D T2-FLAIR and 2D T2-FLAIR were acquired twice with repositioning in-between on each MRI system, resulting in a total of 16 T2-FLAIR volumes per participant. All the 2D T2-FLAIR parameters were from the default clinical sequences. The MRI acquisition parameters are detailed in **Table 1**.

Image Processing

Two fully automated WMH segmentation and quantification software were used for WMH segmentation and volumetric measurement. One is AccuBrain® (BrainNow Medical Technology Ltd.) and the other is lesion growth algorithm [16] as implemented in the Lesion Segmentation Toolbox (LST[1]). AccuBrain® is an automated brain segmentation and quantification software. It can segment a list of brain structures based on T1w MRI. Given additional T2-FLAIR MRI, it can also segment and quantify WMH (Shi et al., 2013). AccuBrain® segments T1w MRI and produces brain structure masks and tissue masks. Then, it coregisters T1w MRI with T2-FLAIR MRI and transforms the structure and tissue masks onto T2-FLAIR space. Using a set of morphological techniques, it extracts WMH on T2-FLAIR MRI and refines it using the transformed brain structure mask from T1w MRI. AccuBrain® is a cloud-based computing tool, which only requires MRI scans as input with no other tunable parameters.

LST is an open source toolbox of SPM used to segment T2 hyperintense lesions in FLAIR images. LST also relies on both T1w and T2-FLAIR MRI to segment WMH. It determines the three tissue classes of gray and white matter as well as cerebrospinal fluid from the T1w MRI and then uses the T2-FLAIR intensity distribution of each tissue class to detect outliers. The neighboring voxels are analyzed and assigned to lesions under certain conditions. This is done iteratively until no further voxels are assigned to lesions. Herein, the likelihood of belonging to WM or GM is weighed against the likelihood of belonging to lesions. We used the default parameters in LST toolbox, initial threshold: 0.3, MRF parameter: 1, and maximum iterations: 50.

[1]https://www.applied-statistics.de/lst.html

Reproducibility Analysis

To measure the reproducibility, several metrics, i.e., volume difference percentage, CV, DSC, and ICC, were computed. Volume difference percentage is defined as the percentage of quantified WMH volume difference between the two sequential scans of the average WMH volume value of the two scans:

$$\text{volume difference percentage} = \frac{|scan - rescan|}{(scan + rescan)/2} \times 100\%$$

TABLE 1 | MRI acquisition parameters.

	MR1	MR2	MR3	MR4
Manufacturer	Siemens	Siemens	Philips	Siemens
Model name	Avanto	Avanto	Ingenia	TrioTim
Station name	MEDPC26921	MRC25494	3FCD991	MRC35363
System version	syngo MR B15	syngo MR B17	R6.0.531.1	syngo MR B15
Field strength (T)	1.5	1.5	3	3
2D FLAIR				
Voxel size, mm^3	0.5 × 0.5 × 6.0	0.5 × 0.5 × 6.0	0.5 × 0.5 × 6.0	0.5 × 0.5 × 6.0
Number of slices	20	20	18	20
Repetition time (ms)	9,000	9,000	7,000	8,000
Echo time (ms)	99	103	93	93
Flip angle (°)	150	150	90	130
Voxel size, mm^3	1.0 × 1.0 × 1.0	1.0 × 1.0 × 1.0	1.0 × 1.0 × 1.0	1.0 × 1.0 × 1.0
Number of slices	176	176	344	176
Repetition time (ms)	7,500	7,500	4,800	7,500
Echo time (ms)	402	396	310	389
Flip angle (°)	120	120	90	120
3D T1WI				
Voxel size, mm^3	1.0 × 1.0 × 1.0	1.0 × 1.0 × 1.0	1.0 × 1.0 × 1.0	1.0 × 1.0 × 1.0
Number of slices	176	176	192	176
Repetition time (ms)	1,900	1,900	7.07	1,900
Echo time (ms)	3.37	3.37	3.19	2.96
Flip angle (°)	15	15	7	9

FLAIR, fluid-attenuated inversion recovery; T1WI, T1-weighted images.

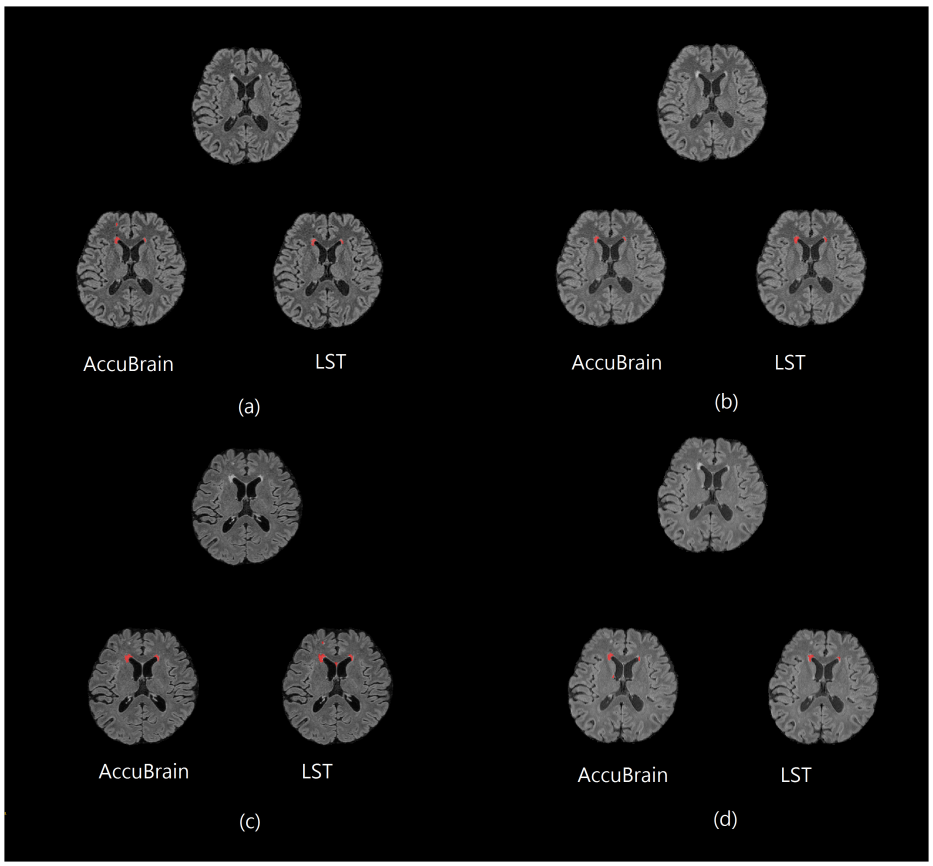

FIGURE 1 | One subject's 3D T2-FLAIR MR images from different scanners together with their WMH segmentation results (red overlay) using AccuBrain® and LST. **(a)** MR1; **(b)** MR2; **(c)** MR3; and **(d)** MR4.

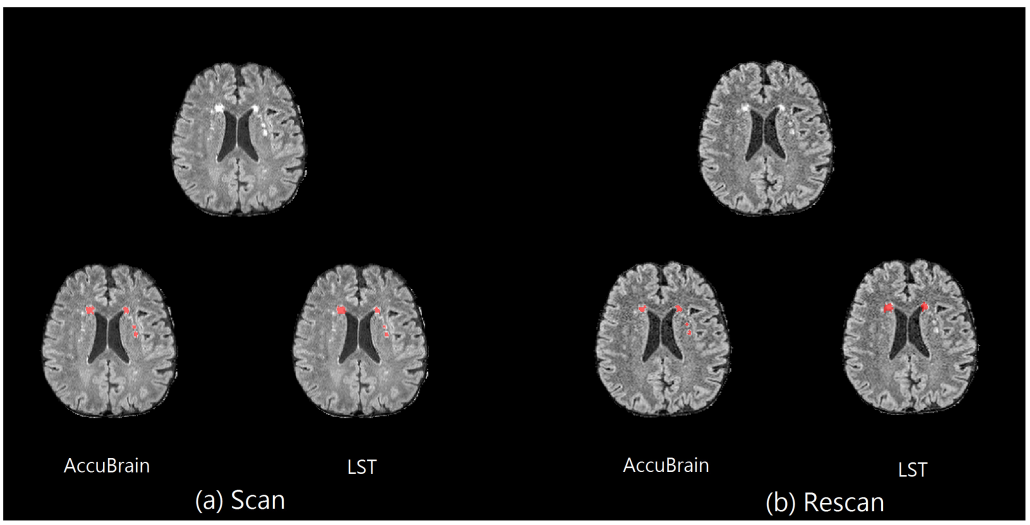

FIGURE 2 | Scan–rescan example on MR1. The corresponding T2-FLAIR MRI slice from a 3D T2-FLAIR MRI scan–rescan experiment on MR1 scanner, together with their WMH segmentation results using AccuBrain® and LST. **(a)** The first 3D T2-FLAIR scan. **(b)** Rescan with the subject's position change.

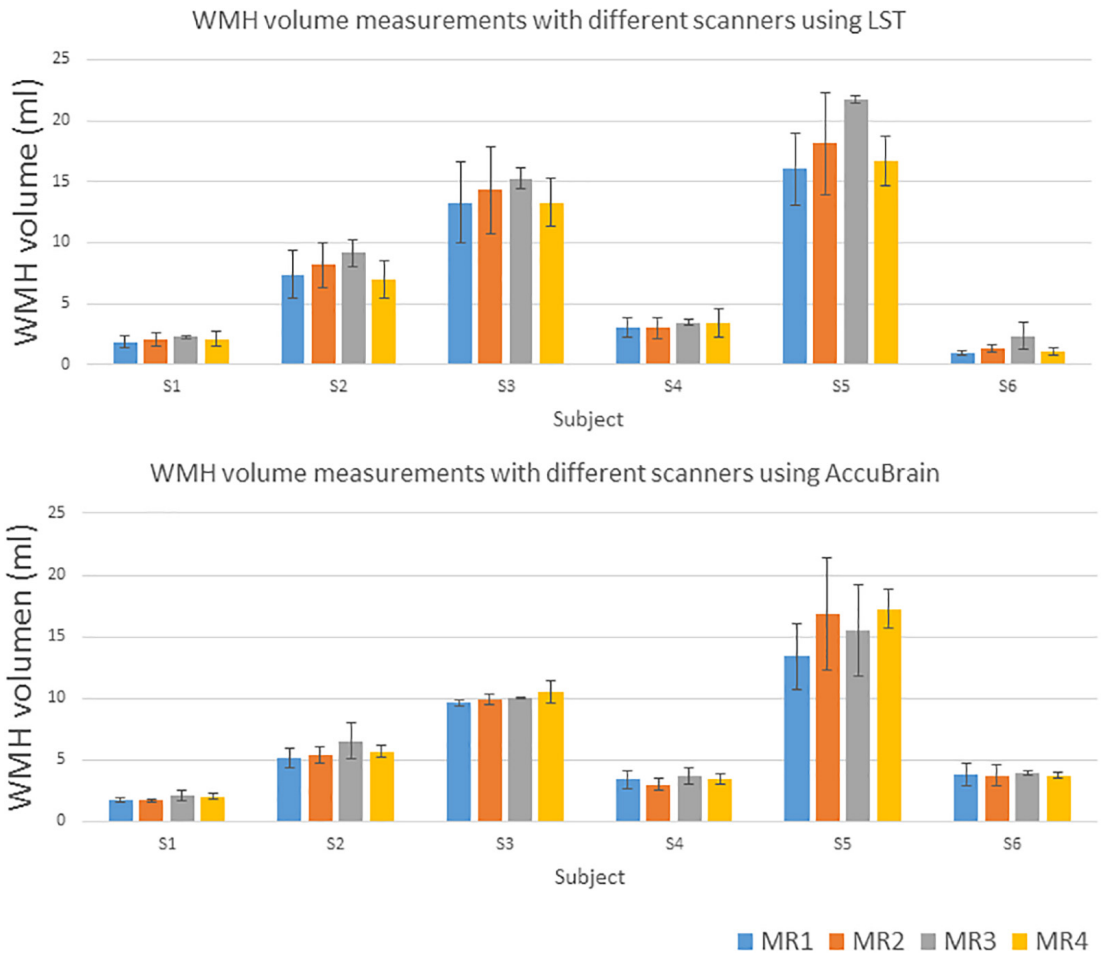

FIGURE 3 | WMH volume measurements using LST and AccuBrain® with MRIs from different scanners.

CV is defined as the ratio of the standard deviation to the mean of the multiple measurements and is expressed in percentages.

$$CV = \frac{\sigma}{\mu} \times 100\%$$

DSC is defined as the volume overlap of two segmentations:

$$DSC\,(A, B) = \frac{2\,(A \cap B)}{|A| + |B|}$$

In this study, we first aligned all the WMH results in the MR1 3D FLAIR MRI space, used the STAPLE algorithm (Warfield et al., 2004) to combine the WMH segmentation labels of all the scans, and created a fused label as reference label; each segmentation label was compared with the reference label in terms of DSC.

ICC was computed using two-way mixed method with 95% CIs in IBM SPSS Statistics 20 software.

The reproducibility of WMH quantification was assessed from four aspects.

Intra-Scanner Reproducibility

Each subject has a set of scanned 3D T1w, 2D T2-FLAIR, and 3D T2-FLAIR MRIs and re-scanned 2D T2-FLAIR and 3D T2-FLAIR MRIs on each MR scanner. The set of scan–rescan T2-FLAIR MRIs were used for examining within-scanner repeatability in a single center. The volume difference percentage, CV, DSC, and ICC between two sequential WMH measures using scan–rescan images were computed.

Inter-Scanner Reproducibility

The studying subjects were scanned with the same set of image sequences (3D T1w, 2D T2-FLAIR, and 3D T2-FLAIR) across four different scanners within 12-h interval. The inter-scanner variability was evaluated using CV, DSC, and ICC values of the same subject's different WMH measurements.

MR System Software Variability

Two of the four studying MRI scanners (MR1 and MR2) are the same MRI system from the same vendor (Siemens Avanto) but different in MRI system software (syngo MR B15 and syngo MR B17) and settled place. The effects of MR system upgrade

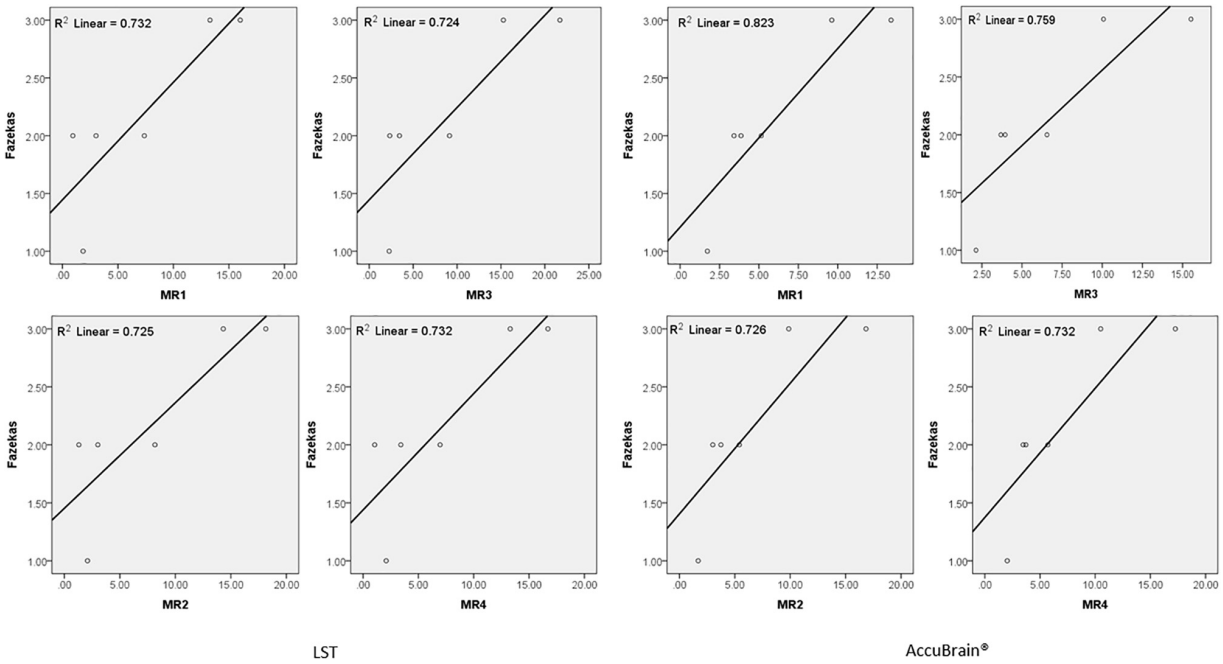

FIGURE 4 | The correlation between Fazekas score and WMH volume measurements using LST and AccuBrain® with MRIs from different scanners.

and examination place on WMH volume measurements were examined using this experiment.

2D and 3D T2-FLAIR Variability

As each subject was scanned using both 2D and 3D T2-FLAIR on the same scanner, the WMH volume measurement difference between 2D and 3D T2-FLAIR images was studied.

RESULTS

Segmentation

Figure 1 shows some representative axial slices of one subject's 3D T2-FLAIR MR images from different acquisitions and their corresponding automatic WMH segmentation results of the two software. It can be observed that the T2-FLAIR MRIs have a large variability in appearance across scanners, which brings great challenge in obtaining consistent WMH volumetric measurement.

In addition, on the same scanner, the subject's imaging position change can also have an impact on T2-FLAIR MRI appearance and WMH segmentation results. One example can be seen in **Figure 2**, where images from a 3D T2-FLAIR scan–rescan test are shown. Even if the same scanner and imaging parameters are used within a short time period, the T2-FLAIR MRIs look different in tissue and WMH contrast.

We quantified all the subjects' segmented WMH using both LST and AccuBrain® with all the MRIs from different scanners,

TABLE 2 | Intra-scanner WMH volume measurement reproducibility using different image processing software.

		Volume difference percentage (%) (mean ± std)		CV (%) (mean ± std)		DSC (mean ± std)		ICC (95% CI)	
3D	**Scanner**	**AccuBrain®**	**LST**	**AccuBrain®**	**LST**	**AccuBrain®**	**LST**	**AccuBrain®**	**LST**
	All	3.81 ± 2.97	4.20 ± 5.15	2.69 ± 2.10	2.97 ± 3.64	0.73 ± 0.06	0.74 ± 0.07	0.996 (0.992–0.998)	1 (0.999–1)
	MR1	4.35 ± 0.15	7.25 ± 0.11	3.07 ± 1.98	5.12 ± 6.34	0.70 ± 0.04	0.73 ± 0.10	0.995 (0.965–0.999)	0.999 (0.994–1)
	MR2	3.36 ± 0.10	2.17 ± 0.11	2.37 ± 2.80	1.53 ± 0.74	0.74 ± 0.09	0.70 ± 0.06	0.999 (0.996–1)	1 (0.998–1)
	MR3	4.13 ± 0.21	2.40 ± 0.14	2.92 ± 2.58	1.70 ± 1.38	0.77 ± 0.04	0.75 ± 0.05	0.992 (0.943–0.999)	1 (0.998–1)
	MR4	3.41 ± 0.11	4.97 ± 0.07	2.41 ± 1.19	3.51 ± 2.82	0.73 ± 0.05	0.77 ± 0.05	0.999 (0.989–1)	0.999 (0.996–1)
2D	All	7.35 ± 5.86	8.07 ± 8.06	5.19 ± 4.14	5.71 ± 5.70	0.68 ± 0.10	0.68 ± 0.12	0.969 (0.930–0.986)	0.997 (0.993–0.999)
	MR1	4.11 ± 2.98	6.48 ± 4.77	2.90 ± 2.11	4.58 ± 3.37	0.67 ± 0.12	0.63 ± 0.14	0.998 (0.989–1)	0.999 (0.990–1)
	MR2	9.68 ± 7.35	10.56 ± 13.32	6.84 ± 5.20	7.46 ± 9.42	0.68 ± 0.12	0.70 ± 0.15	0.980 (0.866–0.997)	0.998 (0.982–1)
	MR3	10.1 ± 6.39	10.76 ± 7.67	7.14 ± 4.52	7.60 ± 5.42	0.65 ± 0.08	0.70 ± 0.09	0.959 (0.741–0.994)	0.995 (0.968–0.999)
	MR4	5.51 ± 4.65	4.48 ± 2.31	3.89 ± 3.29	3.16 ± 1.63	0.69 ± 0.08	0.67 ± 0.09	0.981 (0.871–0.997)	0.998 (0.985–1)

FLAIR, fluid-attenuated inversion recovery; CV, coefficient of variation; DSC, Dice similarity coefficient; ICC, intra-class coefficient; 95% CI, 95% confidence interval.

TABLE 3 | Inter-scanner WMH volume measurement reproducibility using different image processing software.

	CV				DSC	ICC
	All scanners	95% CI of the difference	MR1 vs. MR2	95% CI of the difference	All scanners	All scanners
3D T2-FLAIR						
AccuBrain®	10.54 ± 4.09	(6.239–14.84)	5.01 ± 2.35	(2.538–4.485)	0.64 ± 0.082	0.985 (0.947–0.998)
LST	29.36 ± 24.37	(3.785–54.95)	6.97 ± 4.29	(2.466–11.47)	0.62 ± 0.129	0.950 (0.837–0.992)
2D T2-FLAIR						
AccuBrain®	11.49 ± 4.62	(6.646–16.34)	8.37 ± 5.41	(2.683–14.05)	0.63 ± 0.079	0.967 (0.888–0.995)
LST	10.89 ± 4.81	(5.836–15.95)	11.39 ± 7.61	(3.401–19.38)	0.65 ± 0.118	0.985 (0.949–0.998)

FLAIR, fluid-attenuated inversion recovery; CV, coefficient of variation; DSC, Dice similarity coefficient; ICC, Intra-class coefficient; 95% CI, 95% confidence interval.

TABLE 4 | Comparison of WMH quantification based on 2D and 3D T2-FLAIR.

	Intra-scanner CV		Inter-scanner CV	
	Mean ± std	95% CI of the difference	Mean ± std	95% CI of the difference
AccuBrain®	15.62 ± 8.73	(11.93–19.31)	17.17 ± 5.81	(11.07–23.27)
LST	24.19 ± 11.82	(19.19–29.18)	29.33 ± 15.01	(13.57–45.08)

CV, coefficient of variation; 95% CI, 95% confidence interval.

as shown in **Figure 3**. The WMH volumes range from 1 to 20 ml for different subjects. We quantified all the subjects' segmented WMH using both LST and AccuBrain® with all the MRIs from different scanners, as shown in **Figure 3**. The WMH volumes range from 1 to 20 ml for different subjects. S1–S6's mean Fazekas scale score is 1, 2, 3, 2, 3, and 2, respectively. The Pearson correlation between mean Fazekas scale score and LST quantified WMH volumes is 0.856 (MR1), 0.851 (MR2), 0.851 (MR3), and 0.856 (MR4), while the correlation is 0.907 (MR1), 0.852 (MR2), 0.871 (MR3), and 0.856 (MR4) with AccuBrain® quantified WMH volume, as shown in **Figure 4**.

Reproducibility

Table 2 shows the intra-scanner reproducibility results in the scan–rescan experiments. In general, the intra-scanner reproducibility results of different segmentation methods show relatively small differences with a mean volume difference percentage of 3.81% (3D) and 7.35% (2D) using AccuBrain®, and 4.20% (3D) and 8.07% (2D) using LST, and mean CV is 2.69% (3D) and 5.19% (2D) using AccuBrain®, and 2.97% (3D) and 5.71% (2D) using LST. The mean DSC is 0.73 (3D) and 0.68 (2D) using AccuBrain®, and 0.74 (3D) and 0.68 (2D) using LST. Comparatively, using 3D T2-FLAIR MRI brings more consistent WMH quantification results than using 2D-FLAIR MRI.

Table 3 compares the WMH volume measurement variability across different scanners. It shows that inter-scanner CV values are much larger than those of the intra-scanner experiment. Moreover, variability can also come from image processing software, where AccuBrain® has an average inter-scanner CV value of 10.54% (3D), while LST's inter-scanner CV value is 29.36% (3D) on average. In addition, MR1 and MR2 are two MRI scanners of the same type (Siemens Avanto) but with different versions of software installed and different rooms to be settled. There are still some variations between the quantifications on the two machines, but much smaller than that from different types of scanners.

In **Table 4**, the differences between 2D T2-FLAIR and 3D T2-FLAIR MRI were calculated and compared. It can be observed that in both intra-scanner and inter-scanner settings, the WMH volume measurement variations between 2D and 3D MRI are large and vary across different image processing tools.

DISCUSSION

In this study, we examined the reproducibility of WMH quantification. To achieve this, subjects with different levels of WMH load have undertaken MRI acquisitions (3D T1w, 2D and 3D T2-FLAIR sequences) across four different MRI scanners. On each scanner, a scan–rescan procedure was performed to examine intra-scanner variability, while the inter-scanner variability was tested across the four scanners. Meanwhile, the effect of software upgrade and settled place was examined using the same type of scanner but installed with different versions of software and in different examination rooms. In addition, comparison of WMH volume measurements between 2D and 3D T2-FLAIR was also made in both intra-scanner and inter-scanner setting.

In the intra-scanner experiments, it has shown that 3D T2-FLAIR MRIs generally achieved much better reproducibility than 2D T2-FLAIR MRIs regardless of image processing software, where the between-scan volume difference percentage is 3.81–4.20% for 3D T2-FLAIR and 7.35–8.07% for 2D T2-FLAIR. The larger variability of 2D scans indicates that the large slice thickness of 2D MRI scan can bring large variation in WMH volume measurement due to the irregular pattern of WMH across slices. An average 4% volume difference percentage was achieved in the scan–rescan procedure using 3D T2-FLAIR MRI. This implies that for a subject with low WMH load, e.g., 2 ml, a deviation of 0.08 ml may be induced on average with the same imaging setting; meanwhile, for a subject with

high WMH load, e.g., 10 ml, an average of 0.4 ml deviation may be induced. The scan–rescan reproducibility results can provide important clinical information in aiding doctor's further assessment or diagnosis.

There are several existing works studying the within-center reproducibility WMH volumetric measurement using a scan–rescan procedure in a single center. For example, de Boer et al. (2010) assessed whiter matter lesion segmentation reproducibility by comparing the automatic segmentations (by trained kNN method) of 30 subjects who were scanned twice within a short time interval; the mean CV is 5.87% using 3D T1w and 3D T2-FLAIR MRI. Another study assessed reproducibility of three automated segmentation pipelines for quantitative MRI measurement of brain white matter signal abnormalities (WMSA) on 30 subjects who were positioned and imaged twice within 30 min and achieved a range of 2.57–7.76% CV values using different pipelines (Wei et al., 2002). Ramirez et al. evaluated Lesion Explorer (LE), an MRI-derived tissue segmentation and brain region parcellation processing pipeline for obtaining intracranial tissue and subcortical hyperintensity volumetry in a short-term scan–rescan reliability test on 20 volunteers, with a reported intra-class correlation coefficient (ICC) of 0.9998 for subcortical hyperintensity measurement (Ramirez et al., 2013). In general, our reported intra-scanner CV values [CV: 2.69%, ICC: 0.996 (0.992–0.998) using AccuBrain® and CV: 2.97%, ICC: 1 (0.999–1) using LST] are close to the reported indices in a previous study. However, the previous studies mainly focused on 3D T2-FLAIR MRI. As the commonly used protocol in clinical practice, WMH quantification based on 2D T2-FLAIR MRI is also of great interest to clinicians. It is validated in our experiments that CV values of WMH quantification based on 2D MRI is in the range of 2.90–7.60% using different MRI scanners and processing software. In the inter-scanner experiments, the inter-scanner CV values (10.54% using AccuBrain® and 29.36% using LST) are around four to six times of the intra-scanner CV values (2.69% using AccuBrain® and 2.97% using LST). The large inter-scanner variability is mainly due to various T2-FLAIR MRI appearances resulting from different imaging parameters on different scanners. If the same scanner and imaging parameters are used, the difference can be smaller, where 5.01% and 6.97% CV value was achieved with AccuBrain® and LST, respectively, using the same Siemens Avanto scanner but with different versions of software and installation places. This variability is in the same level of intra-scanner variability, implying that machine software upgrade and installation place can have little impact on the measurement of WMH volume. However, it still suggests that centers should consider having some assessment or calibration for quality assurance and to calculate differences across time when scanner upgrade or replacement are considered.

In comparing quantification using both 2D and 3D T2-FLAIR, it has revealed that the variability is quite high under both intra-scanner and inter-scanner setting. 2D T2-FLAIR MRI is commonly accepted in clinical practice for diagnosis or assessment due to its relatively short acquisition time. However, WMH quantification results based on 2D MRI cannot be directly compared with the 3D MRI quantities, even with some resampling techniques, as it is easy to underestimate or overestimate WMH volume using 2D MRI.

Recommendations for multicenter WMH quantitative study:

(1) Acquire 3D T2-FLAIR MRIs using the same imaging parameters on the same scanner. Intra-scanner 3D T2-FLAIR reproducibility is much higher than others regardless of automatic quantification tools. Followed is the reproducibility of the same scanner but with upgraded software and resettled place. It indicates that in order to achieve the highest reproducibility, acquiring 3D T2-FLAIR MRIs in the same scanner is preferred in a multicenter study or a longitudinal study.
(2) WMH quantification on 2D T2-FLAIR MRIs is not comparable with that on 3D T2-FLAIR MRIs. Due to large slice thickness and irregular WMH pattern across slices, the variability of WMH volumetric measurement based on 2D T2-FLAIR MRI is much larger than 3D T2-FLAIR MRI. Although 2D T2-FLAIR MRI is commonly used in clinical practice, it is not preferable in a multicenter study or follow-up comparison. In particular, a direct comparison of quantitative results between 2D and 3D MRI can result in large deviation.
(3) WMH segmentation methods have a large impact on the quantification results and reproducibility. It can be observed that the scan–rescan reproducibility is relatively stable among different segmentation tools. However, the inter-scanner reproducibility is various among different tools. Choosing and comparing different image processing software is also an important issue in reliable WMH measurement.
(4) Before multicenter clinical trial is carried out, if different scanners are involved, protocol optimization and harmonization should be implemented first in each scanner. A reproducibility experiment with phantom or volunteer assessments for quality assurance is important to calculate differences in brain quantification.
(5) In a multicenter study, when images from different scanners have already been acquired, it is advised to (1) choose proper WMH quantification tools that are designed robust to scanner change and (2) use dedicated statistical models to adjust on scanner or use random-effects models.

Our study has several limitations. First, the subject number is not yet large enough for us to draw a statistically meaningful conclusion. Due to the long acquisition time for each subject to complete the whole procedure within 1 day, it is difficult to recruit many subjects in the current study. Second, MRI data acquisition was held in a single center. Although inter-scanner acquisitions were performed on different scanners and in different rooms to simulate multi-center study design, it is necessary in the future to launch multi-center reproducibility study based on a large population.

CONCLUSION

In conclusion, we compared WMH quantification reproducibility in different experimental settings. In general, the reproducibility

was the best when performing WMH segmentation on 3D MRI acquired by the same type of MRI scanner and same imaging parameters regardless of automatic segmentation tools. This study gives evidence on the extent of variability of WMH measurement across centers and can also aid in designing multicenter and longitudinal study to have enough power.

ETHICS STATEMENT

This study was carried out in accordance with the recommendations of the First Hospital of Jilin University, China local ethics committee with written informed consent from all subjects. All subjects gave written informed consent in accordance with the Declaration of Helsinki. The protocol was approved by the First Hospital of Jilin University, China ethics committee.

AUTHOR CONTRIBUTIONS

CG, KN, YL, LSh, HZ, and LSu contributed to the study concept and design. CG, ZW, and MZ contributed to acquisition of the data. CG, KN, YL, LSh, DW, WZ, HZ, and LSu contributed to analysis and interpretation. CG, KN, YL, LSh, HZ, and LSu drafted the manuscript. All authors contributed to the critical revision of the manuscript for important intellectual content.

FUNDING

This study was supported by the grant provided by the Major Chronic Disease Program of the Ministry of Science and Technology of China (No. 2018YFC1312301), the Young Scholars Program of the National Natural Science Foundation of China (No. 81600923), and the General Program of Jilin Provincial Science and Technology Development of China (No. 2017C020).

REFERENCES

Admiraal-Behloul, F., van den Heuvel, D. M., Olofsen, H., van Osch, M. J., van der Grond, J., van Buchem, M. A., et al. (2005). Fully automatic segmentation of white matter hyperintensities in MR images of the elderly. *Neuroimage* 28, 607–617. doi: 10.1016/j.neuroimage.2005.06.061

Brown, F. W., Lewine, R. R. J., and Hudgins, P. A. (1995). White matter hyperintensity signals associated with vascular risk factors in schizophrenia. *Prog. Neuropsychopharmacol. Biol. Psychiatry* 19, 39–45. doi: 10.1016/0278-5846(94)00102-N

Cees De Groot, J., de Leeuw, F. E., Oudkerk, M., van Gijn, J., Hofman, A., Jolles, J., et al. (2000). Cerebral white matter lesions and cognitive function: the Rotterdam scan study. *Ann. Neurol.* 47, 145–151.

de Boer, R., Vrooman, H. A., Ikram, M. A., Vernooij, M. W., Breteler, M. M., van der Lugt, A., et al. (2010). Accuracy and reproducibility study of automatic MRI brain tissue segmentation methods. *Neuroimage* 51, 1047–1056. doi: 10.1016/j.neuroimage.2010.03.012

DeCarli, C., Miller, B. L., Swan, G. E., Reed, T., Wolf, P. A., Carmelli, D., et al. (2001). Cerebrovascular and brain morphologic correlates of mild cognitive impairment in the national heart, lung, and blood institute twin study. *Arch. Neurol.* 58, 643–647. doi: 10.1001/archneur.58.4.643

Fazekas, F., Chawluk, J. B., Alavi, A., Hurtig, H. I., and Zimmerman, R. A. (1987). MR signal abnormalities at 1.5 T in Alzheimer's dementia and normal aging. *Am. J. Roentgenol.* 149, 351–356. doi: 10.2214/ajr.149.2.351

Fazekas, F., Kapeller, P., Schmidt, R., Offenbacher, H., Payer, F., Fazekas, G., et al. (1996). The relation of cerebral magnetic resonance signal hyperintensities to Alzheimer's disease. *J. Neurol. Sci.* 142, 121–125. doi: 10.1016/0022-510X(96)00169-4

Fazekas, F., Kleinert, R., Offenbacher, H., Schmidt, R., Kleinert, G., Payer, F., et al. (1993). Pathologic correlates of incidental MRI white matter signal hyperintensities. *Neurology* 43, 1683–1683. doi: 10.1212/wnl.43.9.1683

Filippi, M., Rocca, M. A., Ciccarelli, O., De Stefano, N., Evangelou, N., Kappos, L., et al. (2016). MRI criteria for the diagnosis of multiple sclerosis: MAGNIMS consensus guidelines. *Lancet Neurol.* 15, 292–303. doi: 10.1016/S1474-4422(15)00393-2

Gibson, E., Gao, F., Black, S. E., and Lobaugh, N. J. (2010). Automatic segmentation of white matter hyperintensities in the elderly using FLAIR images at 3T. *J. Magn. Reson. Imaging* 31, 1311–1322. doi: 10.1002/jmri.22004

Gunning-Dixon, F. M., and Raz, N. (2000). The cognitive correlates of white matter abnormalities in normal aging. *Quant. Rev.* 14:224. doi: 10.1037/0894-4105.14.2.224

Hirono, N., Kitagaki, H., Kazui, H., Hashimoto, M., and Mori, E. (2000). Impact of white matter changes on clinical manifestation of Alzheimer's disease: a quantitative study. *Stroke* 31, 2182–2188. doi: 10.1161/01.str.31.9.2182

Jain, S., Sima, D. M., Ribbens, A., Cambron, M., Maertens, A., Van Hecke, W., et al. (2015). Automatic segmentation and volumetry of multiple sclerosis brain lesions from MR images. *Neuroimage* 8, 367–375. doi: 10.1016/j.nicl.2015.05.003

Kramer, J. H., Mungas, D., Reed, B. R., Wetzel, M. E., Burnett, M. M., Miller, B. L., et al. (2007). Longitudinal MRI and cognitive change in healthy elderly. *Neuropsychology* 21, 412–418. doi: 10.1037/0894-4105.21.4.412

López-Zorrilla, A., de Velasco-Vázquez, M., Serradilla-Casado, O., Roa-Barco, L., Graña, M., Chyzhyk, D., et al. (2017). "Brain White Matter Lesion Segmentation with 2D/3D CNN," in *Natural and Artificial Computation for Biomedicine and Neuroscience*, eds J. Ferrández Vicente, J. Álvarez-Sánchez , F. de la Paz López, cpsfnmMoreo Jcpefnm Toledo, and H. Adeli (Berlin: Springer International Publishing), 394–403.

Marshall, G. A., Shchelchkov, E., Kaufer, D. I., Ivanco, L. S., and Bohnen, N. I. (2006). White matter hyperintensities and cortical acetylcholinesterase activity in parkinsonian dementia. *Acta Neurol. Scand.* 113, 87–91. doi: 10.1111/j.1600-0404.2005.00553.x

Mungas, D., Harvey, D., Reed, B. R., Jagust, W. J., DeCarli, C., Beckett, L., et al. (2005). Longitudinal volumetric MRI change and rate of cognitive decline. *Neurology* 65, 565–571. doi: 10.1212/01.wnl.0000172913.88973.0d

Payne, M. E., Fetzer, D. L., MacFall, J. R., Provenzale, J. M., Byrum, C. E., Krishnan, K. R., et al. (2002). Development of a semi-automated method for quantification of MRI gray and white matter lesions in geriatric subjects. *Psychiat. Res. Neuroim.* 115, 63–77. doi: 10.1016/S0925-4927(02)00009-4

Prins, N. D., van Straaten, E. C., van Dijk, E. J., Simoni, M., van Schijndel, R. A., Vrooman, H. A., et al. (2004). Measuring progression of cerebral white matter lesions on MRI. *Vis. Rat. volumetr.* 62, 1533–1539. doi: 10.1212/01.wnl.0000123264.40498.b6

Rachmadi, M. F., Valdés-Hernández, M. D. C., Agan, M. L. F., Di Perri, C., and Komura, T. (2018). Segmentation of white matter hyperintensities using convolutional neural networks with global spatial information in routine clinical brain MRI with none or mild vascular pathology. *Comput. Med. Imaging Graph.* 66, 28–43. doi: 10.1016/j.compmedimag.2018.02.002

Ramirez, J., Scott, C. J. M., and Black, S. E. (2013). A short-term scan–rescan reliability test measuring brain tissue and subcortical hyperintensity volumetrics obtained using the lesion explorer structural MRI processing pipeline. *Brain Topogr.* 26, 35–38. doi: 10.1007/s10548-012-0228-z

Schmidt, P., Gaser, C., Arsic, M., Buck, D., Förschler, A., Berthele, A., et al. (2012). An automated tool for detection of FLAIR-hyperintense white-matter lesions in

multiple sclerosis. *Neuroimage* 59, 3774–3783. doi: 10.1016/j.neuroimage.2011.11.032

Schmidt, R., Scheltens, P., Erkinjuntti, T., Pantoni, L., Markus, H. S., and Wallin, A. (2004). White matter lesion progression. *Surrog. Endpoint Trials Cereb. Small Vessel Dis.* 63, 139–144. doi: 10.1212/01.wnl.0000132635.75819.e5

Shi, L., Wang, D., Liu, S., Pu, Y., Wang, Y., Chu, W. C., et al. (2013). Automated quantification of white matter lesion in magnetic resonance imaging of patients with acute infarction. *J. Neurosci. Methods* 213, 138–146. doi: 10.1016/j.jneumeth.2012.12.014

Simões, R., Mönninghoff, C., Dlugaj, M., Weimar, C., Wanke, I., van Cappellen van Walsum, A. M., et al. (2013). Automatic segmentation of cerebral white matter hyperintensities using only 3D FLAIR images. *Magn. Reson. Imaging* 31, 1182–1189. doi: 10.1016/j.mri.2012.12.004

Sweeney, E. M., Vogelstein, J. T., Cuzzocreo, J. L., Calabresi, P. A., Reich, D. S., Crainiceanu, C. M., et al. (2014). A comparison of supervised machine learning algorithms and feature vectors for MS lesion segmentation using multimodal structural MRI. *PLoS One* 9:e95753. doi: 10.1371/journal.pone.0095753

van den Heuvel, D. M. J., ten Dam, V. H., de Craen, A. J., Admiraal-Behloul, F., Olofsen, H., Bollen, E. L., et al. (2006). Increase in periventricular white matter hyperintensities parallels decline in mental processing speed in a non-demented elderly population. *J. Neurol. Neurosurg. Psychiatry* 77, 149–153. doi: 10.1136/jnnp.2005.070193

Warfield, S. K., Zou, K. H., and Wells, W. M. (2004). Simultaneous truth and performance level estimation (STAPLE): An algorithm for the validation of image segmentation. *IEEE Trans. Med. Imaging* 23, 903–921. doi: 10.1109/TMI.2004.828354

Wei, X., Warfield, S. K., Zou, K. H., Wu, Y., Li, X., Guimond, A., et al. (2002). Quantitative analysis of MRI signal abnormalities of brain white matter with high reproducibility and accuracy. *J. Magn. Reson. Imaging* 15, 203–209. doi: 10.1002/jmri.10053

Conflict of Interest Statement: LSh was the director of BrainNow Medical Technology Limited. YL was an employee of BrainNow Medical Technology Limited, which developed AccuBrain® used in this manuscript.

The remaining authors declare that the research was conducted in the absence of any commercial or financial relationships that could be construed as a potential conflict of interest.

frontiers in Neurology

ORIGINAL RESEARCH
published: 16 July 2019
doi: 10.3389/fneur.2019.00752

Aberrant Brain Activity at Early Delay Stage Post-radiotherapy as a Biomarker for Predicting Neurocognitive Dysfunction Late-Delayed in Patients With Nasopharyngeal Carcinoma

Yadi Yang[1†], Xiaoshan Lin[2†], Jing Li[1†], Lujun Han[1], Zhipeng Li[1], Shiliang Liu[3], Gangqiang Hou[4], Chuanmiao Xie[1], Xiaofei Lv[1] and Yingwei Qiu[2*]*

[1] Department of Medical Imaging, Sun Yat-sen University Cancer Center, State Key Laboratory of Oncology in South China, Collaborative Innovation Center for Cancer Medicine, Guangdong Key Laboratory of Nasopharyngeal Carcinoma Diagnosis and Therapy, Guangzhou, China, [2] Department of Radiology, The Third Affiliated Hospital of Guangzhou Medical University, Guangzhou Medical University, Guangzhou, China, [3] Department of Radiation Oncology, Sun Yat-sen University Cancer Center, State Key Laboratory of Oncology in South China, Collaborative Innovation Center for Cancer Medicine, Guangdong Key Laboratory of Nasopharyngeal Carcinoma Diagnosis and Therapy, Guangzhou, China, [4] Shenzhen Kangning Hospital, Shenzhen Mental Health Center, Shenzhen, China

Background: Increasing evidence indicates that early radiation-induced subtle cerebral changes may be the precursors to permanent brain dysfunction at the late-delayed (LDS) post-radiotherapy (RT) stage. In this study, we aim to track the RT-related longitudinal brain activity in nasopharyngeal carcinoma (NPC) patients and to determine whether early abnormal brain activity can predict late neurocognitive dysfunction after RT.

Methods: Thirty-three NPC patients were finally included and longitudinally followed up at the following time points: prior to treatment initiation, early-delayed stage (EDS, 1–3 months), and LDS (six months) after RT. Fifteen comparable healthy controls (HCs) were finally included and followed up in parallel. Montreal Cognitive Assessment (MoCA) was used to assess the general cognitive function. Brain activity was recorded via resting-state fMRI and regional homogeneity (ReHo). A whole-brain voxel-wise-based one-way repeated-measure analysis of variance (ANOVA) was conducted to evaluate the longitudinal ReHo changes among the three time points for NPC patients and HCs, respectively. Results were reported at the significant level of a threshold of two-tailed voxel-wise $P < 0.01$ and cluster level $P < 0.05$ with Gaussian Random Field (GRF) correction. Finally, the efficacies of the aberrant ReHo at EDS for predicting the cognitive impairment at LDS in NPC patients were evaluated.

Results: Significant differences were detected in ReHo among the three time points in NPC patients but not in HCs. Aberrant ReHo was distributed in the bilateral cerebellum, the right temporal lobe, and the left insular areas, which showed different dynamic changes patterns over time. Logistic regression model combining the mean ReHo, age, and irradiation dose on the bilateral temporal lobe had the highest diagnostic efficiency according to the area under the curve (AUC) score (AUC = 0.752, $P = 0.023$).

OPEN ACCESS

Edited by:
Feng Feng,
Peking Union Medical College Hospital (CAMS), China

Reviewed by:
Bo Gao,
Affiliated Hospital of Guizhou Medical University, China
Jordi A. Matias-Guiu,
Servicio de Neurología, Hospital Clínico San Carlos, Spain

***Correspondence:**
Xiaofei Lv
lvxf@sysucc.org.cn
Yingwei Qiu
qiuyw1201@gmail.com

[†]These authors have contributed equally to this work

Specialty section:
This article was submitted to Applied Neuroimaging, a section of the journal Frontiers in Neurology

Received: *30 March 2019*
Accepted: *27 June 2019*
Published: *16 July 2019*

Citation:
Yang Y, Lin X, Li J, Han L, Li Z, Liu S, Hou G, Xie C, Lv X and Qiu Y (2019) Aberrant Brain Activity at Early Delay Stage Post-radiotherapy as a Biomarker for Predicting Neurocognitive Dysfunction Late-Delayed in Patients With Nasopharyngeal Carcinoma. Front. Neurol. 10:752. doi: 10.3389/fneur.2019.00752

Conclusions: The post-RT brain activity revealed by ReHo in NPC patients was dynamic, complex, and multifactorial. Furthermore, the combination of the aberrant ReHo at EDS, age, and irradiation dose may serve as a potential biomarker of the RT-induced cognitive impairments at LDS.

Keywords: radiotherapy, radiation-induced injury, regional homogeneity, resting-state fMRI, nasopharyngeal carcinoma, neurocognitive dysfunction

INTRODUCTION

There were an estimated 129,000 new cases of nasopharyngeal carcinoma (NPC) and 73,000 deaths in 2018 (1). According to world area, incidence rates are highest in South-Eastern Asia, including Malaysia, Indonesia, Singapore, and South-Eastern China (2). The standard treatment for NPC is radiotherapy (RT) due to the radio-sensitivity of the tumor (3). The survival rate of NPC patients is generally favorable, thus long-term side effects of RT are of concern in survivors. Radiation-induced brain injury is a major neurologic complication following RT. Classically, it is classified into an acute stage (days to weeks post-irradiation), early-delayed stage (EDS) (1–4 months post-irradiation), and late-delayed stage (LDS) (more than 4–6 months post-irradiation) (4). Radiation-related neurocognitive decline, which may be attributed to the brain injury, is a significant but largely unrecognized sequela that appears after irradiation in NPC patients (4, 5). Reportedly, it has been described as part of a biphasic pattern of cognitive loss. Following RT there is an initial deterioration in cognitive function, after which there is a transient recovery at post-RT EDS, and then a progressive, irreversible deterioration in the cognitive functioning at post-RT LDS (6). Historically, the primary research focus has been placed on markers of brain damage and cognitive decline appearing over 6 months to 1 year or later after irradiation (7). However, such knowledge cannot ameliorate the progression of the brain injury and cognition dysfunction, which is irreversible at post-RT LDS (6). Recent evidence indicates that early radiation-induced subtle changes in the brain may be the precursors to long-term, permanent brain dysfunction at post-RT LDS (4, 7, 8). Thus, consideration of early forms of RT-induced brain damage and how they can evolve over time may not only shed light on the complicated pathogenesis of RT-induced neurocognitive impairment, but also facilitate the early identification and treatment, which can reverse the degenerative processes before they have caused permanent disability.

Earlier research has suggested that brain activity in the resting-state reflects the baseline status of the whole brain and is a promising indicator in the investigation of the pathophysiological characteristics of nervous system diseases (9). Recently, resting-state brain activity was used to explore the post-RT brain dysfunction in NPC patients, which yielded inspiring findings (10–13). Two cross-sectional studies (11, 14), comparing between NPC patients who had already finished RT with those who had not received RT, revealed RT-related aberrant whole-brain and cerebellar-cerebral functional connectivity (FC), respectively. Another cross-sectional study (13), compared pre- and post-RT NPC individuals with multiple groups of different time points, which discovered that the brain activity underwent dynamic post-RT changes. Furthermore, the increased local brain activity in the inferior temporal lobe at EDS may be used to predict the occurrence of severe brain necrosis many years later (13). However, it is difficult to obtain a clear picture from these cross-sectional results, given that the post-RT cohort effects and diverse time points in different studies (11, 13). Extant longitudinal studies revealed that disruption of the FC of the hippocampal-related cortices occurred in the NPC patients (10) or intra- and inter-network disconnection within a few months after RT (12). Unfortunately, these longitudinal studies did not involve cognitive tests (10) or focused only on one post-RT time point (12), which hampered the determination of the relation of the dynamic alteration to the cognitive dysfunction. Furthermore, whether the early brain activity changes can be used for predicting late-delayed cognitive dysfunction in NPC patients is still debatable.

Regional homogeneity (ReHo) is an important research method for mapping the level of local activity across the whole brain of an individual, which reflects the local temporal homogeneity of the regional blood oxygen level-dependent signal in the resting state (15, 16). This data-driven method provides analysis of the region-to-region interactions and voxel-by-voxel neural activity with remarkably high test-retest reliabilities at the functional level, based on the intrinsic activity of the resting brain (16). Accumulating evidence indicates that the regional properties of the intrinsic brain dynamics can reliably reflect aspects of cognitive function (17–19). Furthermore, increasingly more studies have suggested the potential of ReHo changes as a prognostic imaging tool to identify the disease-related progression treatment response and outcomes for various neuropsychiatric disorders (19–21). Thus, the application of this method might be helpful for the better characterization of the relationship between the functional evolutional processes and the late-delayed cognitive dysfunction in post-RT NPC.

Given that the previous evidence of a dynamic brain activity alteration pattern during the different post-RT phases and early increased local brain functional activity was predictive of severe later temporal lobe necrosis (13), we hypothesized that: (1) Compared with pre-RT, aberrant ReHo can be detected in brains of post-RT NPC patients at EDS and LDS, which would undergo a dynamic alteration from EDS to LDS; (2) The global cognitive function would be impaired in post-RT NPC patients; (3) The abnormal ReHo index at EDS may be used as a biomarker for prediction of impaired cognitive function at LDS.

MATERIALS AND METHODS

Participants

This prospective study was approved by the local institutional review board. Written informed consent was obtained from all subjects. From December 2014 to May 2018, 38 newly diagnosed, treatment-naive patients with NPC and 20 comparable healthy controls were initially included. Ten subjects (5 NPC patients and 5 healthy controls) were discarded due to excessive head motion. Finally, 33 patients with NPC (21 male and 12 female, 18–55 years old, mean age of 38.91 ± 9.38 years) and 15 comparable healthy controls (10 males and 5 females; aged 26–55 years, mean age 40.33 ± 10.33 years) were included. The following inclusion criteria were used for all participants: aged 18–60 years, dextromanuality, no intracranial invasion, no distant metastases, no brain tumors, no alcoholism, no substance dependence, no prior substantial head trauma, no diabetes, no viral hepatitis, no positive human immunodeficiency virus status, no neurological or psychiatric diseases or other major medical issues, routine brain MR examination was negative, and baseline MoCA scores were more than or equal to 26. The exclusion criteria for all participants were as follows: age lower than 18 or above 60 years, left-handedness, alcoholism, diabetes, brain tumors, history of cranial trauma, history of any psychiatric or neurological disease, any current medications that may affect cognitive function, contraindications for MRI scanning, and excessive head movement during the functional MRI (fMRI) acquisition. The additional exclusion employed criteria for NPC patients were intracranial invasion and distant metastases. Each NPC patient underwent a detailed pre-treatment evaluation, and the clinical stages of NPC were classified according to the 7th edition of the American Joint Committee (AJCC) staging system (22).

Treatment

All patients received one fraction of intensity-modulated radiation therapy (IMRT) ($n = 30$) or tomotherapy ($n = 3$) daily for five consecutive days per week. The prescribed radiation doses for patients treated were 62–70 Gy at 2.0–2.33 Gy/fraction over 30–33 fractions to the planning target volume (PTV) of the nasopharynx tumor volume (GTVnx) and gross tumor volume of malignant lymph nodes (GTVnd), with 56–60 Gy to the PTV of clinical target volume 1 (CTV1) (high-risk regions) and 50–56 Gy to the PTV of CTV2 (low-risk regions and neck nodal regions). The details of the RT techniques were identical to those reported in previous studies (23, 24). Dose evaluation was performed based on the data from the dose–volume histogram for the targets (24). The main evaluation parameters were maximum dose (Dmax), mean dose (Dmean), and minimum dose (Dmin) received by bilateral temporal lobe (**Table 1**). In addition, of the 33 patients, 1 (3.0%) underwent only RT, 16 (48.5%) were administered concurrent chemoradiotherapy, and 16 (48.5%) received a combination of neoadjuvant and concurrent chemoradiotherapy. Neoadjuvant therapy consisted of cisplatin with 5-fluorouracil (PF), cisplatin with docetaxel (TP), or cisplatin with 5-fluorouracil and docetaxel (TPF) every 3 weeks for ≥2 cycles. The concurrent chemotherapy consisted of cisplatin/nedaplatin or paclitaxel administered weekly for at least 4–7 cycles or in weeks 1, 4, and 7 of radiation therapy.

Image Acquisition

All MRI scans were performed on a GE Discovery MR750 3.0 scanner (GE Medical Systems, Milwaukee, WI, USA) with a 16-channel head and neck coil (GE Medical Systems) at the Department of Medical Imaging, Sun Yat-sen University Cancer Center. To detect intracranial lesions, routine imaging examinations were performed of axial T1-weighted images [repetition time (TR)/echo time (TE) = 596/8 ms] and T2-weighted images (TR/TE = 3,223/89 ms) and T2-FLAIR images [TR/TE/inversion time (TI) = 9,000/93/2,475 ms], obtained for every subject. Then, a resting-state fMRI scan with an echo-planar imaging sequence and a high-resolution structural MRI scan with T1 weighted three-dimensional brain volume imaging (3D-BRAVO) sequence were sequentially conducted. The imaging parameters were as follows: (1) Resting-state fMRI: TR/TE = 2,000/30ms, flip angle = 90°, thickness/gap = 3/0.8 mm, acquisition matrix = 64 × 64, field of view (FOV) = 240 × 240 mm^2, voxel size = 3.75 × 3.75 × 3.8 mm^3, 39 axial slices and 240 time points (8 min). (2) 3D-BRAVO: TR/TE = 8.16/3.18 ms, inversion time = 800 ms, flip angle = 8°, acquisition matrix = 256 × 256, FOV = 256 × 256 mm^2, voxel size = 1 × 1 × 1 mm^3, 176 sagittal slices with no inter-slice gap. For the resting-state fMRI scan, subjects were instructed to avoid falling asleep, keep their eyes closed, and avoid thinking about anything.

Neurocognitive Tests

General cognitive function was assessed through the Montreal Cognitive Assessment (MoCA, Beijing Version) test, which assesses different cognitive domains: attention and concentration, executive functions, memory, language, visuo-constructional skills, conceptual thinking, calculations, and orientation. The MoCA was reported to be a feasible and relative sensitive instrument for routine cognitive screening for NPC patients with radiation-induced injury (25). Cutoff scores for the MoCA was determined at 26 (scores of 25 or below will indicate cognitive impairment) (26). The time to administer the MoCA was approximately 10 min. The MoCA scores ranged from 0 to 30; higher scores indicated a better cognitive performance. After an appropriate explanation, all subjects completed the MoCA test on the same day of MRI scanning.

TABLE 1 | Dose–volume statistics of the bilateral temporal lobe for 33 patients with nasopharyngeal carcinoma treated with radiation therapy (Gy).

Temporal lobe	Maximum dose (Dmax)	Minimum dose (Dmin)	Mean dose (Dmean)
Left	65.51 ± 12.36	1.82 ± 0.78	17.97 ± 5.35
Right	67.59 ± 6.46	1.77 ± 0.66	18.02 ± 4.71

All data are presented as mean ± standard deviation.

Follow-Up Procedure

To investigate the dynamic alteration of whole-brain ReHo and cognitive function dysfunction at an early stage after RT, all 33 patients with NPC were longitudinally evaluated at three time points: prior to treatment initiation, EDS (1–3 months after RT completion), and LDS (6 months after the completion of RT). MRI data and MoCA tests were acquired at each time point. Meanwhile, all 15 healthy controls were followed up in parallel (baseline, 6 months, 9 months) and completed MRI scans and MoCA measurements were conducted at each time point. The procedures for the follow-up of all participants are presented in **Figure 1**.

Data Preprocessing and Computation of ReHo Maps

All preprocessing steps were carried out using the toolkit of Data Processing & Analysis of Brain Imaging (DPABI_V3.0_171210, http://rfmri.org/DPABI), an extension of Statistical Parametric Mapping (SPM8) (http://www.fil.ion.ucl.ac.uk/spm). The first 10 volumes of each functional time series were discarded from analysis to allow for magnetization equilibrium and for the adaptation of the subjects to the scanning situation. The remaining 230 volumes were corrected for the acquisition time delay between the different slices as well as for geometrical displacements according to the estimated head movement and were then realigned to the first volume. Head motion parameters were computed by estimating the translation in each direction and the angular rotation on each axis for each volume. Any subject who had a maximum displacement in any of the three cardinal directions (x, y, z) $>$ 2.0 mm or a maximum spin (x, y, z) $>$ 2.0° was excluded from the study. The realigned fMRI data were spatially normalized to the Montreal neurological institute (MNI) space using the normalization parameters estimated by T1 structural image unified segmentation and was resampled to $3 \times 3 \times 3$ mm^3 voxels. Several sources of spurious variances, including the estimated motion parameters, the linear drift, and the average time series in the cerebrospinal fluid and white matter regions, were removed from the data through linear regression. After that, a temporal filter (0.01–0.08 Hz) was performed to reduce the effect of low-frequency drift sand high-frequency uninteresting signals.

The calculation procedure of ReHo maps calculation was the same as that reported earlier (17, 18, 21). In brief, this was accomplished on a voxel-by-voxel basis by calculating Kendall coefficient of concordance (KCC) of time series of a given voxel with those of its nearest 26 neighbors. A larger value for a given voxel indicated a higher regional homogeneity within a cluster made up of the voxel and its nearest neighbors. A whole-brain map of ReHo values for each subject was calculated. Then, each ReHo map was scaled by its global mean, and finally smoothed with a 6 mm full-width at half maximum (FWHM) Gaussian kernel.

Statistical Analysis

Statistical Analysis of the NPC Patients and Healthy Controls at the Baseline

Two-sample *t*-test was applied to compare the group difference in age, education level and MOCA between NPC patients and healthy controls at baseline. Pearson's chi-squared test was used to evaluate gender differences between the two groups. Analyses were conducted using SPSS 18.0 (SPSS for Windows, Chicago, IL, USA), and a $P < 0.05$ was deemed significant.

To investigate differences in ReHo between the two groups at baseline, a two-sample *t*-test was executed on the individual ReHo maps in a voxel-by-voxel manner using age, gender, and years of formal education as covariates.

Longitudinal Changes in Cognitive Function

Repeat measurement ANOVA and multiple comparisons (*post-hoc* Dunnett's tests) were employed to investigate the difference

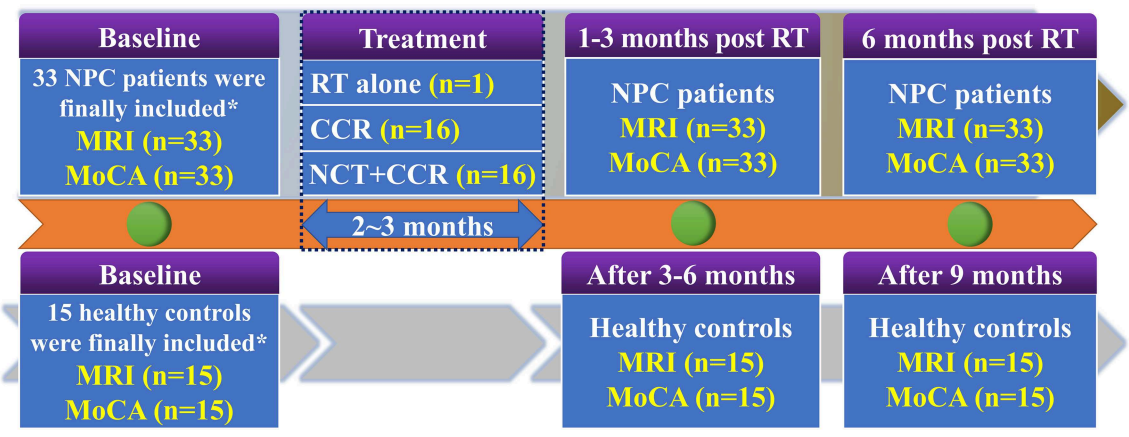

FIGURE 1 | Enrolment and follow-up procedures for patients with NPC and healthy controls. CCR, Concurrent Chemotherapy and Radiotherapy; MoCA, Montreal Cognitive Assessment; NCT, Neoadjuvant Chemotherapy; NPC, nasopharyngeal carcinoma; RT, radiation therapy. *38 newly diagnosed patients with NPC and 20 comparable healthy controls were initially included. Ten subjects (5 NPC patients and 5 healthy controls) were discarded due to excessive head motion. Finally, 33 patients with NPC and 15 comparable healthy controls were included.

between the MOCA score among pre-RT, EDS and LDS in patients with NPC and healthy controls. Cognitive function impairment was defined if the MoCA score is <26 during the follow-up according to previous studies.

Longitudinal Changes of ReHo

To explore the longitudinal ReHo differences among pre-RT, EDS and LDS in patients with NPC. A whole-brain voxel-wise-based one-way repeated-measure analysis of variance (ANOVA), with head motion parameters as covariates, was conducted to evaluate the ReHo changes among the three time points. Results were reported at the significant level of a threshold of two-tailed voxel-wise $P < 0.01$ and cluster level $P < 0.05$ with Gaussian Random Field (GRF) correction. We then extracted the mean ReHo values that showed significant differences among the three time points for all individuals. One-way repeated measure ANOVA *post-hoc* Dunnett's tests with were performed to detect the dynamic alteration. Also, to exclude the aging effects, we also investigated the longitudinal ReHo differences for the normal controls using the same statistical methods.

Prediction of Impaired Cognitive Function in LDS Using the ReHo Index in EDS

To explore whether the ReHo alterations at EDS can be used to predict the cognitive impairment at LDS in patients with NPC, multivariate logistic regression and receiver operating characteristic curve (ROC) analyses were performed to determine the efficacies of the average ReHo value within all the clusters that showed significant changes among three time points at EDS and the clinical characteristics (age and the maximum irradiation dose of bilateral temporal lobe) alone or combined to predict impaired cognitive function at LDS. A *P*-value was considered significant if it was 0.05 or less at a confidence interval of 95%.

RESULTS

Demographic Characteristics and the Comparison Results of ReHo at Baseline

The demographic and clinical characteristics of NPC patients and healthy controls at the baseline are summarized in **Table 2**. No significant differences were found in age, gender, education level, and MoCA scores between the two groups at the baseline. Additionally, no significant difference was detected in the whole-brain ReHo between the two groups at the baseline.

Longitudinal Changes in the Cognitive Function

In total, 99 and 45 MoCA data were collected for NPC patients and healthy controls, respectively. A significant decrease in the MoCA scores was detected in the NPC patients during the longitudinal following ($F = 23.214$, $P < 0.001$; **Figure 2**); furthermore, there were significant differences in the MoCA scores between pre-RT and EDS ($P = 0.003$), between pre-RT and LDS ($P < 0.001$), and between EDS and LDS ($P < 0.001$) (**Figure 2**). In the controls, no significant difference was detected in the MoCA scores among the three time points ($P = 0.257$). Ten NPC patients with post-RT NPC at LDS had cognitive function impairment.

Longitudinal ReHo Changes During Three Periods

The ReHo changes among three periods in patients with NPC are shown in **Figure 3** and **Table 3**. There was a significant difference in the bilateral cerebellum, the right inferior temporal gyrus (ITG), the right temporal pole: the middle temporal gyrus (TPOmid) and the left insula. In healthy controls, there were no significant ReHo changes in any brain region among the three time points.

TABLE 2 | Demographic and clinical characteristics of the patients with nasopharyngeal carcinoma (NPC) and healthy controls at the baseline.

Demographic information	NPC patients	Healthy controls	t/χ^2 values	*P*-values
Numbers	33	15	NA	NA
Age (years)*	39.91 ± 9.38	40.33 ± 10.33	−0.473	0.639
Gender (male/female)	21/12	10/5	0.041	0.839
Education (years)	12.42 ± 2.98	12.80 ± 3.36	−0.389	0.699
MoCA	29.18 ± 1.16	28.73 ± 0.96	1.307	0.198
T-classification (T1/T2/T3/T4)	2/5/15/11	NA	NA	NA
N-classification (N0/N1/N2/N3)	5/11/13/4	NA	NA	NA
M-classification (M0/M1)	33/0	NA	NA	NA
AJCC TMN stage (I/II/III/IV)	0/4/14/15	NA	NA	NA
RT technology (IMRT/TOMO)	30/3	NA	NA	NA
Therapeutic regimens (RT alone/CCR/NCT+CCR)	1/16/16	NA	NA	NA

**Data are mean ± standard deviation. AJCC, American Joint Committee on Cancer; IMRT, intensity-modulated radiation therapy; MoCA, Montreal Cognitive Assessment; NA, not available; RT, radiotherapy; TOMO, tomotherapy; T-classification describes the size of the primary tumor and whether it has invaded nearby tissue. N-classification describes nearby lymph nodes that are involved. M-classification defines distant metastasis. AJCC TMN stage was obtained based on the T-, N-, and M-classification results. Therapeutic regimens include radiotherapy alone (RT alone), concurrent chemoradiotherapy (CCR) and Neoadjuvant/adjuvant chemotherapy combined with concurrent chemoradiotherapy (NCT+CCR).*

The dynamic change curves of mean ReHo extracted from each brain region in patients with NPC across the three stages are depicted in **Figure 3**. In detail, there were three patterns of dynamic change for the ReHo index: "increase-decrease-recover" pattern in the right cerebellum, the right ITGs and the left cerebellum; "increase without recovery" pattern in the right TPOmid; "decrease without recovery" pattern in the left insula.

Prediction of Impaired Cognitive Function in LDS Period Using the ReHo Index in EDS

According to the established logistic regression models, the ROC curves for mean ReHo (showed groups differences) at EDS, age, dose (the irradiation dose to bilateral temporal lobe) alone, and three combined models were qualified to determine the efficacies of predicting the impaired cognitive function in LDS (**Figure 4**; **Supplementary Table 1**). The multivariate regression analysis showed that the logistic regression model combining the three variables had the highest diagnostic efficiency based on the area under the curve (AUC) score of the ROC curves (AUC = 0.752, $P = 0.023$).

DISCUSSION

To the best of our knowledge, this is the first study to dynamically and longitudinally explore the RT-related aberrant spontaneous brain activity from EDS to LDS in NPC patients. We found that the brain regions showing aberrant ReHo were located in the right ITG, the right TPOmid, the bilateral cerebellum, and the left insula in post-RT NPC patients. Furthermore, these regions showed different patterns of dynamic changes of ReHo: "increase-decrease-recover," "increase pattern," and "decrease pattern." Moreover, the logistic regression model combining the mean ReHo at EDS, age and irradiation dose had the highest efficiency to predict cognitive dysfunction at LDS in patients with NPC. Identification of the aberrant and dynamic ReHo changes in multiple brain regions would contribute to obtaining a better understanding of the characteristics of functional evolutional processes during different phase post RT in NPC patients. Importantly, the combination of the ReHo alterations at EDS, age, and irradiation dose may serve as a potential biomarker for the RT-induced brain functional impairments at LDS.

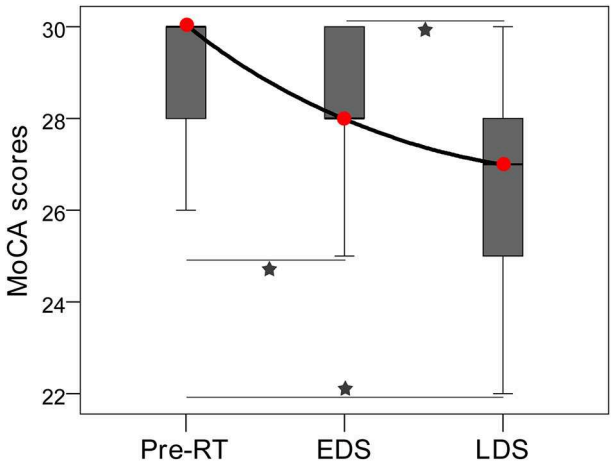

FIGURE 2 | Box plot showing the longitudinal changes in MoCA performance of patients with nasopharyngeal carcinoma. A significant decrease in the MoCA scores was detected among the three stages; there were significant differences in MoCA scores between pre-RT and EDS, between Pre-RT and LDS, and between EDS and LDS. Red circles indicate median MoCA scores of each stages. Pentagrams indicate significant differences with *post-hoc* Dunnett's tests ($P < 0.05$). EDS, early-delayed stage; LDS, late-delayed stage; MoCA, Montreal Cognitive Assessment; RT, radiation therapy.

RT-induced brain injury in the temporal lobe and cerebellum has been well-documented in previous studies (12, 27–30), and these findings are not surprising, given that anatomically they are all close to or overlapped by the CTV, which may cause unnecessary radiation and results in the radioactive damage. In the present study, we observed that the abnormal ReHo in the bilateral cerebellum and the right ITG manifested dynamic changes with an "increase-decrease-recover" pattern. The blood-oxygen level dependent (BOLD) signal is mostly contributed by cerebral blood flow (CBF), and large CBF change has been postulated to produce large BOLD signal variability (31). Thus, abnormal RT-related ReHo observed in present study may also be due to the aberrant RT-induced brain CBF, which in turn relate to the RT-related vascular injury. It is well-known that radiation has profound time-dependent effects on the vasculature (8, 32, 33). Shortly after RT, vascular structure and function can be altered, including blood vessel dilatation, endothelial cell enlargement, increased vascularity, which can lead to acute blood brain barrier (BBB) disruption and increased permeability (34, 35). Then, these acute post-RT alterations were reported to be followed by a recovery process, such as full or partial recovery of the endothelial density, vessel density, and vessel length, though the duration and extent of this recovery seemed to vary among the reports (8, 32). Intriguingly, the present finding that the "increase-decrease-recover" pattern of ReHo in the bilateral cerebellum and right ITG was coincident with the dynamic time course of the vascular post-RT damage, further confirmed the hypothesis that the aberrant ReHo in these regions were associated with vascular injury. Moreover, this hypothesis was also highly supported by the findings of a recent study, through measuring CBF by arterial spin labeling (ASL)-MRI, Hu et al. revealed that elevated CBF in the left cerebellum in post-RT NPC patients at EDS, which recovered to the baseline level at the LDS (28). Additionally, this dynamic pattern was also consistent with other *in vivo* studies by using diverse MRI models, reporting increased fALFF in the ITG (13), as well as decreased diffusion tensor imaging (DTI) and magnetic resonance spectroscopy (MRS) metrics in the temporal lobe at the early stage but partially recovered later (36, 37). Taken together, it is reasonable to conclude that findings of "increase-decrease-recover" change pattern of ReHo in the bilateral cerebellum and the right ITG might be associated with the dynamic interaction between RT-induced vascular disruption and recovery processes.

Notably, we also found abnormal ReHo in the right TPOmid, which showed an "increase without recovery" pattern, whereas a "decrease without recovery" pattern

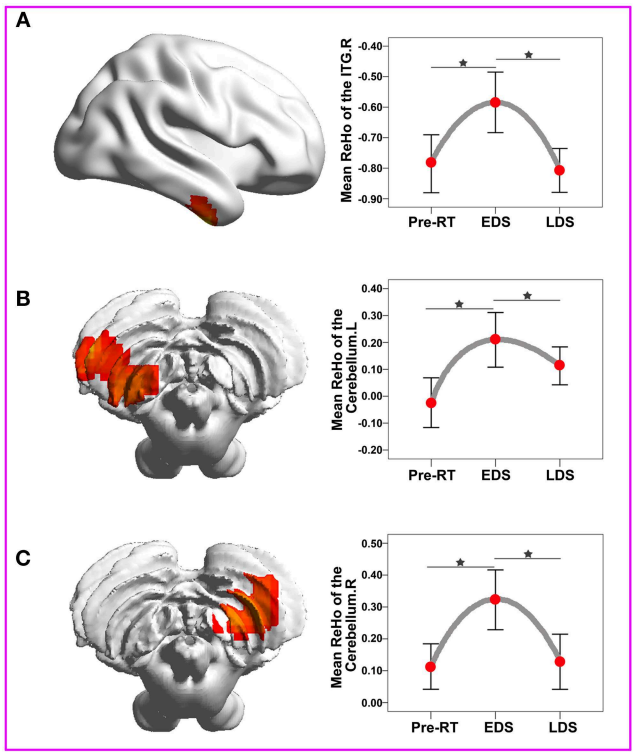

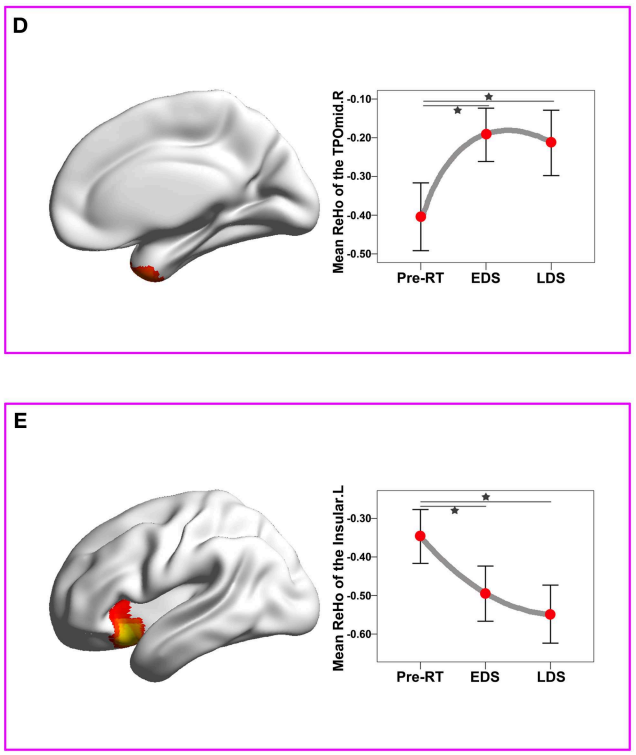

FIGURE 3 | ReHo changes among the three time points compared with a whole-brain voxel-wise based one-way repeated measure ANOVA and *post-hoc* tests. There were three patterns of dynamic change for the ReHo index: "increase-decrease-recover" pattern **(A–C)**, with full-recovery in the right cerebellum **(A)** and right ITGs **(B)**, and with partial-recovery in the left cerebellum **(C)**; "increase" pattern without significant recovery in the right TPOmid **(D)**; "decrease" pattern without significant recovery in the left insula **(E)**. Brain regions were reported at the significant level of a threshold of two-tailed voxel-wise $P < 0.01$ and cluster level $P < 0.05$ with Gaussian Random Field correction. Error bars indicate two standard errors, and pentagrams indicate significant differences revealed by ANOVA *post-hoc* tests with Dunnett's tests ($P < 0.05$). ANOVA, analysis of variance; EDS, early-delayed stage; L, left; LDS, late-delayed stage; ITG, inferior temporal gyrus; MNI, Montreal Neurological Institute; R, right; ReHo, regional homogeneity; TPOmid, temporal pole: middle temporal gyrus; RT, radiotherapy.

TABLE 3 | Regions of the brain in which the ReHo differ significantly among the pre-RT, EDS, and LDS in the patients with nasopharyngeal carcinoma post RT.

Brain areas	No. of voxels	BA	MNI coordinate			Mean ReHo value			Peak *t*-values
			X	*Y*	*Z*	Pre-RT	EDS	LDS	
Right cerebellum	103	-	24	−60	−54	0.113 ± 0.201	0.322 ± 0.265	0.128 ± 0.244	9.390
Left cerebellum	57	-	−48	−66	−54	−0.024 ± 0.261	0.210 ± 0.287	0.113 ± 0.199	13.067
Right ITG	64	20	42	−9	−39	−0.404 ± 0.247	−0.192 ± 0.194	−0.213 ± 0.238	12.236
Right TPOmid	85	38	42	18	−36	−0.785 ± 0.268	−0.584 ± 0.280	−0.807 ± 0.203	8.978
Left insula	71	47	−30	15	−12	−0.347 ± 0.197	−0.495 ± 0.202	−0.548 ± 0.212	12.3708

BA, Broadmann Areas; EDS, early-delayed stage; LDS, late-delayed stage; ITG, inferior temporal gyrus; MNI, Montreal Neurological Institute; ReHo, regional homogeneity; TPOmid, temporal pole: middle temporal gyrus; RT, radiotherapy.

was established in the left insula. Although the underlying biological mechanisms of these diverse patterns are unclear, the dose of the irradiation may explain these phenomena. The dose-volume effects on the brain have been consistently studied previously (23, 29, 38). The temporal pole, which covers the anterior-most end of the temporal lobe, is the brain region that receives the highest dose of radiation. This relatively high dose may lead to a sustained injury without recovery.

Nevertheless, the left insula, which is not exposed to the high dose of RT, showed a "decrease without recovery" pattern; the decreased ReHo in these areas may be interpreted as indirect RT-induced injury. Of note, the insula not only integrates the multimodal sensory information due to the presence of dense connections with other brain regions, such as the frontal and temporal ones, but is also involved in the multiple resting-state networks (12, 39, 40). Recently, we found that the changes of the right insular FC correlated with the maximum dose in the right

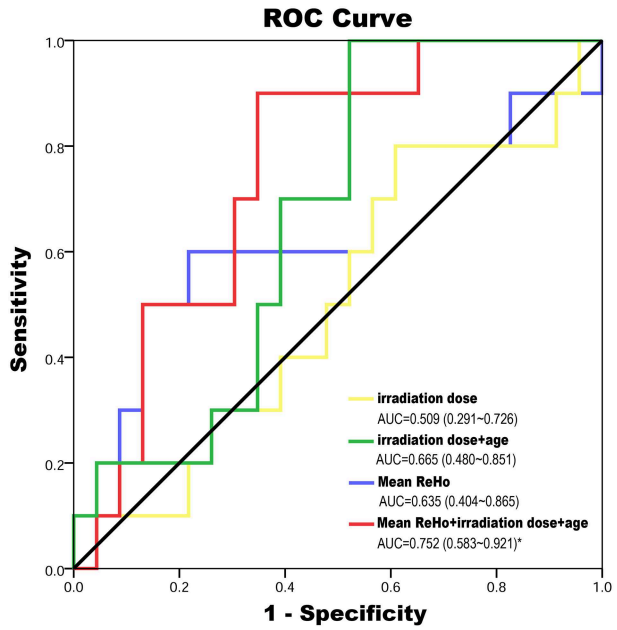

FIGURE 4 | The ROC curves for mean ReHo (showed groups differences) at EDS, age, dose (the maximum irradiation dose to bilateral temporal lobe) alone and three combined model were qualified to determine the efficacies of predicting of impaired cognitive function in LDS. The multivariate regression analysis showed that the logistic regression model combining the three variables has the highest diagnostic efficiency according to the AUC score of the ROC curves (AUC = 0.752, $P = 0.023$). AUC, area under the curve; EDS, early-delayed stage; LDS, late-delayed stage; ReHo, regional homogeneity; ROC, receiver operating characteristic curve; RT, radiotherapy.

temporal lobe (12), which indicated that the FC impairment in the right insular may be related to the RT-induced injury in the right temporal lobe. Therefore, it is possible that the decreased ReHo in the left insula could be a secondary RT-induced change caused through the formation of abnormal connections between the insula and a certain vulnerable region (such as the temporal lobe). The finding that a sustained reduced ReHo in NPC patients at both EDS and LDS post RT was supported by previous resting-state fMRI studies. In post-RT NPC patients, not only significantly reduced FC was detected in the right insular within the salience network in NPC patients at the EDS (3 months post-RT) (12), but also aberrant FC related to insula at the LDS (from 6 to 87 months post-RT) (11), However, further studies are needed to elucidate the underlying biological mechanisms.

Interesting, that the combination of brain activity at EDS, irradiation dose and age can be used to predict cognitive impairment at LDS in NPC patients. Given that cognitive impairment is considered to be progressive and irreversible during the LDS (4, 33, 41), the early indications at the reversible stage would be extremely helpful. Our finding was in line with the increasing evidence from recent studies using other MRI modalities, such as dynamic contrast-enhanced (DCE) MRI and DTI (7, 38), which showed that the early hippocampal vascular dose response and the early diffusivity changes in the parahippocampal cingulum can be useful as a biomarker for predicting late-delayed cognitive decline. Our findings also supported the hypothesis that the process of RT-induced cognitive function impairment at LDS is multifactorial (4, 7, 38, 42, 43). Irradiation dose-dependent brain cognitive function changes have been well-documented in previous studies (4, 43). Recently, increasing evidence reveals that radiation-induced cognitive dysfunction is significantly influenced by age (38, 42). Thus, our findings added to the current literature that the RT-induced cognitive impairment is a multifactorial influenced process, and the combination of the ReHo alterations at EDS, age, and irradiation dose may serve as a potential biomarker of the RT-induced brain cognitive impairments at LDS.

Nevertheless, still some limitations in this study should be mentioned. First, the MoCA used in the present study is a brief cognitive screening tool not highly sensitive to certain domains (26), such as the verbal and visual memory, attention and executive functions, impaired by RT as documented in previous studies (7, 33). Further studies with a complex cognitive evaluation are warranted to focus on the relationship between specific cognitive impairments and abnormal ReHo to fully assess the effect of RT-induced early brain activity changes on late-delayed cognitive decline in NPC patients. Second, in the current study, we longitudinally observed the alterations of the spontaneous brain activity and the general cognition within 6 months post RT in NPC patients. Thus, whether these phenomena were permanent or transient is still an open question, and future studies with longer follow-up periods are needed to obtain a better understanding of the characteristics of the processes of functional changes. Third, in this preliminary study, the diagnostic performances of the model to predict the cognitive late-delayed impairments after RT was moderate (AUC = 0.752), with a relative high specificity (90%) but a low sensitivity (65.2%). A more comprehensive models incorporating clinical and multiple parameters derived from multimodal MRI is warranted to improve the diagnostic efficiency in the future. Finally, another limitation could be a potential learning effect of neurocognitive testing due to repeated use (three times in 6 months) of the MoCA test. This could be reduced or avoided by using parallel versions when possible and by a well-structured time scheduling in the future study (44).

CONCLUSION

Longitudinal analyses of brain activity changes provide new important insights into radiation-induced brain functional impairments in NPC patients after RT. We found that aberrant ReHo was mainly distributed in the temporal lobe and the cerebellum, which received a comparatively higher dose of irradiation. Furthermore, alterations of ReHo in these brain regions manifested as different patterns over time, which revealed that the pathophysiology of post-RT brain injury is dynamic, complex, and multifactorial. More importantly, the combination of the ReHo alterations at EDS, age, and irradiation dose may serve as a potential biomarker for the cognitive late-delayed impairments after RT. Therefore, our preliminary findings will

provide guidance for critically important early interventions before permanent and irreversible disability has occurred at LDS.

ETHICS STATEMENT

This study was carried out in accordance with the recommendations of name of guidelines, name of committee with written informed consent from all subjects. All subjects gave written informed consent in accordance with the Declaration of Helsinki. The protocol was approved by the Sun Yat-sen University Cancer Center.

AUTHOR CONTRIBUTIONS

YY, XLv, and YQ designed of the study and carried out data collection and wrote the manuscript. XLin screened the clinical data of the study. JL and LH completed the acquisition of functional imaging data. ZL and SL sorted the data. YQ carried out data analysis. CX and GH contributed to conceptualization of the study and revision of the manuscript.

FUNDING

This work was funded by grants from the Natural Scientific Foundation of China (grant numbers: 81401399, 81560283, and 81201084), Natural Scientific Foundation of Jiangxi Province, China (grant number: 20151BAB205049), Fundamental Research Funds for the Central Universities (Grant number: 15ykpy35), and Medical Scientific Research Foundation of Guangdong Province (Grant numbers: B2014162, A2017620).

SUPPLEMENTARY MATERIAL

The Supplementary Material for this article can be found online at: https://www.frontiersin.org/articles/10.3389/fneur.2019.00752/full#supplementary-material

REFERENCES

1. Bray F, Ferlay J, Soerjomataram I, Siegel RL, Torre LA, Jemal A. Global cancer statistics 2018: GLOBOCAN estimates of incidence and mortality worldwide for 36 cancers in 185 countries. *CA Cancer J Clin*. (2018) 68:394–424. doi: 10.3322/caac.21492
2. Torre LA, Bray F, Siegel RL, Ferlay J, Lortet-Tieulent J, Jemal A. Global cancer statistics, 2012. *CA Cancer J Clin*. (2015) 65:87–108. doi: 10.3322/caac.21262
3. Lee AW, Ma BB, Ng WT, Chan AT. Management of nasopharyngeal carcinoma: current practice and future perspective. *J Clin Oncol*. (2015) 33:3356–64. doi: 10.1200/JCO.2015.60.9347
4. Makale MT, McDonald CR, Hattangadi-Gluth JA, Kesari S. Mechanisms of radiotherapy-associated cognitive disability in patients with brain tumours. *Nat Rev Neurol*. (2017) 13:52–64. doi: 10.1038/nrneurol.2016.185
5. Hsiao KY, Yeh SA, Chang CC, Tsai PC, Wu JM, Gau JS. Cognitive function before and after intensity-modulated radiation therapy in patients with nasopharyngeal carcinoma: a prospective study. *Int J Radiat Oncol Biol Phys*. (2010) 77:722–6. doi: 10.1016/j.ijrobp.2009.06.080
6. McTyre E, Scott J, Chinnaiyan P. Whole brain radiotherapy for brain metastasis. *Surg Neurol Int*. (2013) 4:S236–44. doi: 10.4103/2152-7806.111301
7. Chapman CH, Nagesh V, Sundgren PC, Buchtel H, Chenevert TL, Junck L, et al. Diffusion tensor imaging of normal-appearing white matter as biomarker for radiation-induced late delayed cognitive decline. *Int J Radiat Oncol Biol Phys*. (2012) 82:2033–40. doi: 10.1016/j.ijrobp.2011.01.068
8. Brown WR, Thore CR, Moody DM, Robbins ME, Wheeler KT. Vascular damage after fractionated whole-brain irradiation in rats. *Radiat Res*. (2005) 164:662–8. doi: 10.1667/RR3453.1
9. Zhang D, Raichle ME. Disease and the brain's dark energy. *Nat Rev Neurol*. (2010) 6:15–28. doi: 10.1038/nrneurol.2009.198
10. Chen SC, Abe Y, Fang PT, Hsieh YJ, Yang YI, Lu TY, et al. Prognosis of hippocampal function after sub-lethal irradiation brain injury in patients with nasopharyngeal carcinoma. *Sci Rep*. (2017) 7:14697. doi: 10.1038/s41598-017-13972-2
11. Ma Q, Wu D, Zeng LL, Shen H, Hu D, Qiu S. Radiation-induced functional connectivity alterations in nasopharyngeal carcinoma patients with radiotherapy. *Medicine*. (2016) 95:e4275. doi: 10.1097/MD.0000000000004275
12. Qiu Y, Guo Z, Han L, Yang Y, Li J, Liu S, et al. Network-level dysconnectivity in patients with nasopharyngeal carcinoma (NPC) early post-radiotherapy: longitudinal resting state fMRI study. *Brain Imaging Behav*. (2018) 12:1279–89. doi: 10.1007/s11682-017-9801-0
13. Ding Z, Zhang H, Lv XF, Xie F, Liu L, Qiu S, et al. Radiation-induced brain structural and functional abnormalities in presymptomatic phase and outcome prediction. *Hum Brain Mapp*. (2018) 39:407–27. doi: 10.1002/hbm.23852
14. Ma Q, Zeng LL, Qin J, Luo Z, Su J, Wu D, et al. Radiation-induced cerebellar-cerebral functional connectivity alterations in nasopharyngeal carcinoma patients. *Neuroreport*. (2017) 28:705–11. doi: 10.1097/WNR.0000000000000813
15. Zang Y, Jiang T, Lu Y, He Y, Tian L. Regional homogeneity approach to fMRI data analysis. *Neuroimage*. (2004) 22:394–400. doi: 10.1016/j.neuroimage.2003.12.030
16. Zuo XN, Xing XX. Test-retest reliabilities of resting-state FMRI measurements in human brain functional connectomics: a systems neuroscience perspective. *Neurosci Biobehav Rev*. (2014) 45:100–18. doi: 10.1016/j.neubiorev.2014.05.009
17. Lv XF, Qiu YW, Tian JZ, Xie CM, Han LJ, Su HH, et al. Abnormal regional homogeneity of resting-state brain activity in patients with HBV-related cirrhosis without overt hepatic encephalopathy. *Liver Int*. (2013) 33:375–83. doi: 10.1111/liv.12096
18. Qiu Y, Lv X, Su H, Jiang G, Tian J, Zhuo F, et al. Reduced regional homogeneity in bilateral frontostriatal system relates to higher impulsivity behavior in codeine-containing cough syrups dependent individuals. *PLoS ONE*. (2013) 8:e78738. doi: 10.1371/journal.pone.0078738
19. Zhao Z, Tang C, Yin D, Wu J, Gong J, Sun L, et al. Frequency-specific alterations of regional homogeneity in subcortical stroke patients with different outcomes in hand function. *Hum Brain Mapp*. (2018) 39:4373–84. doi: 10.1002/hbm.24277
20. Lin WC, Hsu TW, Chen CL, Lu CH, Chen HL, Cheng YF. Resting State-fMRI with ReHo analysis as a non-invasive modality for the prognosis of cirrhotic patients with overt hepatic encephalopathy. *PLoS ONE*. (2015) 10:e0126834. doi: 10.1371/journal.pone.0126834
21. An L, Cao XH, Cao QJ, Sun L, Yang L, Zou QH, et al. Methylphenidate normalizes resting-state brain dysfunction in boys with attention deficit hyperactivity disorder. *Neuropsychopharmacol*. (2013) 38:1287–95. doi: 10.1038/npp.2013.27
22. Edge SB, Compton CC. The American Joint Committee on Cancer: the 7th edition of the AJCC cancer staging manual and the future of TNM. *Ann Surg Oncol*. (2010) 17:1471–4. doi: 10.1245/s10434-010-0985-4
23. Lv X, He H, Yang Y, Han L, Guo Z, Chen H, et al. Radiation-induced hippocampal atrophy in patients with nasopharyngeal carcinoma early after

radiotherapy: a longitudinal MR-based hippocampal subfield analysis. *Brain Imaging Behav.* (2018). doi: 10.1007/s11682-018-9931-z. [Epub ahead of print].
24. Sun Y, Yu XL, Luo W, Lee AW, Wee JT, Lee N, et al. Recommendation for a contouring method and atlas of organs at risk in nasopharyngeal carcinoma patients receiving intensity-modulated radiotherapy. *Radiother Oncol.* (2014) 110:390–7. doi: 10.1016/j.radonc.2013.10.035
25. Wu X, Gu M, Zhou G, Xu X, Wu M, Huang H. Cognitive and neuropsychiatric impairment in cerebral radionecrosis patients after radiotherapy of nasopharyngeal carcinoma. *BMC Neurol.* (2014) 14:10. doi: 10.1186/1471-2377-14-10
26. Nasreddine ZS, Phillips NA, Bedirian V, Charbonneau S, Whitehead V, Collin I, et al. The montreal cognitive assessment, MoCA: a brief screening tool for mild cognitive impairment. *J Am Geriatr Soc.* (2005) 53:695–9. doi: 10.1111/j.1532-5415.2005.53221.x
27. Gazdzinski LM, Cormier K, Lu FG, Lerch JP, Wong CS, Nieman BJ. Radiation-induced alterations in mouse brain development characterized by magnetic resonance imaging. *Int J Radiat Oncol Biol Phys*. (2012) 84:e631–8. doi: 10.1016/j.ijrobp.2012.06.053
28. Hu F, Li T, Wang Z, Zhang S, Wang X, Zhou H, et al. Use of 3D-ASL and VBM to analyze abnormal changes in brain perfusion and gray areas in nasopharyngeal carcinoma patients undergoing. *Biomed Res*. (2017) 28:7879–85.
29. Lv XF, Zheng XL, Zhang WD, Liu LZ, Zhang YM, Chen MY, et al. Radiation-induced changes in normal-appearing gray matter in patients with nasopharyngeal carcinoma: a magnetic resonance imaging voxel-based morphometry study. *Neuroradiology*. (2014) 56:423–30. doi: 10.1007/s00234-014-1338-y
30. Guo Z, Han L, Yang Y, He H, Li J, Chen H, et al. Longitudinal brain structural alterations in patients with nasopharyngeal carcinoma early after radiotherapy. *Neuroimage Clin*. (2018) 19:252–9. doi: 10.1016/j.nicl.2018.04.019
31. Mulderink TA, Gitelman DR, Mesulam MM, Parrish TB. On the use of caffeine as a contrast booster for BOLD fMRI studies. *Neuroimage*. (2002) 15:37–44. doi: 10.1006/nimg.2001.0973
32. Li YQ, Chen P, Jain V, Reilly RM, Wong CS. Early radiation-induced endothelial cell loss and blood-spinal cord barrier breakdown in the rat spinal cord. *Radiat. Res.* (2004) 161:143–52. doi: 10.1667/RR3117
33. Greene-Schloesser D, Robbins ME, Peiffer AM, Shaw EG, Wheeler KT, Chan MD. Radiation-induced brain injury: a review. *Front Oncol*. (2012) 2:73. doi: 10.3389/fonc.2012.00073
34. Diserbo M, Agin A, Lamproglou I, Mauris J, Staali F, Multon E, et al. Blood-brain barrier permeability after gamma whole-body irradiation: an *in vivo* microdialysis study. *Can J Physiol Pharmacol*. (2002) 80:670–8. doi: 10.1139/y02-070
35. Liu Y, Xiao S, Liu J, Zhou H, Liu Z, Xin Y, et al. An experimental study of acute radiation-induced cognitive dysfunction in a young rat model. *AJNR Am J Neuroradiol*. (2010) 31:383–7. doi: 10.3174/ajnr.A1801
36. Wang HZ, Qiu SJ, Lv XF, Wang YY, Liang Y, Xiong WF, et al. Diffusion tensor imaging and 1H-MRS study on radiation-induced brain injury after nasopharyngeal carcinoma radiotherapy. *Clin Radiol.* (2012) 67:340–5. doi: 10.1016/j.crad.2011.09.008
37. Xiong WF, Qiu SJ, Wang HZ, Lv XF. 1H-MR spectroscopy and diffusion tensor imaging of normal-appearing temporal white matter in patients with nasopharyngeal carcinoma after irradiation: initial experience. *J Magn Reson Imaging*. (2013) 37:101–8. doi: 10.1002/jmri.23788
38. Farjam R, Pramanik P, Aryal MP, Srinivasan A, Chapman CH, Tsien CI, et al. A radiation-induced hippocampal vascular injury surrogate marker predicts late neurocognitive dysfunction. *Int J Radiat Oncol Biol Phys*. (2015) 93:908–15. doi: 10.1016/j.ijrobp.2015.08.014
39. Cauda F, D'Agata F, Sacco K, Duca S, Geminiani G, Vercelli A. Functional connectivity of the insula in the resting brain. *Neuroimage*. (2011) 55:8–23. doi: 10.1016/j.neuroimage.2010.11.049
40. Olson IR, Plotzker A, Ezzyat Y. The Enigmatic temporal pole: a review of findings on social and emotional processing. *Brain*. (2007) 130:1718–31. doi: 10.1093/brain/awm052
41. Kiang A, Weinberg VK, Cheung KH, Shugard E, Chen J, Quivey JM, et al. Long-term disease-specific and cognitive quality of life after intensity-modulated radiation therapy: a cross-sectional survey of nasopharyngeal carcinoma survivors. *Radiat. Oncol.* (2016) 11:127. doi: 10.1186/s13014-016-0704-9
42. Schindler MK, Forbes ME, Robbins ME, Riddle DR. Aging-dependent changes in the radiation response of the adult rat brain. *Int J Radiat Oncol Biol Phys*. (2008) 70:826–34. doi: 10.1016/j.ijrobp.2007.10.054
43. Hahn CA, Zhou SM, Raynor R, Tisch A, Light K, Shafman T, et al. Dose-dependent effects of radiation therapy on cerebral blood flow, metabolism, and neurocognitive dysfunction. *Int J Radiat Oncol Biol Phys*. (2009) 73:1082–7. doi: 10.1016/j.ijrobp.2008.05.061
44. Fabbri L, Mosca IE, Gerli F, Martini L, Pancani S, Lucidi G, et al. The Games for Older Adults Active Life (GOAL) project for people with mild cognitive impairment and vascular cognitive impairment: a study protocol for a randomized controlled trial. *Front Neurol.* (2018) 9:1040. doi: 10.3389/fneur.2018.01040

Conflict of Interest Statement: The authors declare that the research was conducted in the absence of any commercial or financial relationships that could be construed as a potential conflict of interest.

frontiers in Neuroscience

ORIGINAL RESEARCH
published: 20 August 2019
doi: 10.3389/fnins.2019.00785

Gamma-Aminobutyric Acid Levels in the Anterior Cingulate Cortex of Perimenopausal Women With Depression: A Magnetic Resonance Spectroscopy Study

Dan Wang[1], Xuan Wang[1], Meng-Ting Luo[2], Hui Wang[3]† and Yue-Hua Li[1]*†*

[1] Institute of Diagnostic and Interventional Radiology, Shanghai Sixth People's Hospital, Shanghai Jiao Tong University, Shanghai, China, [2] Department of Radiology, Henan Provincial People's Hospital, Zhengzhou, China, [3] Department of Otolaryngology Head and Neck Surgery, Shanghai Sixth People's Hospital, Shanghai Jiao Tong University, Shanghai, China

Objective: The anterior cingulate cortex (ACC) is associated with the processing of negative emotions. Gamma-aminobutyric acid (GABA) metabolism plays an important role in the pathogenesis of mental disorders. We aimed to determine the changes in GABA levels in the ACC of perimenopausal women with depression.

Methods: We recruited 120 perimenopausal women, who were followed up for 18–24 months. After reaching menopause, the participants were divided into a control group (n = 71), an anxiety group (n = 30), and a depression group (n = 19). The participants were examined using proton magnetic resonance spectroscopy (MRS). TARQUIN software was used to calculate the GABA concentrations in the ACC before and after menopause. The relationship of the GABA levels with the patients' scores on the 14-item Hamilton Anxiety Scale and 17-item Hamilton Depression Scale was determined.

Results: GABA decreased with time. The postmenopausal GABA levels were significantly lower in the depression group than in the anxiety group and were significantly lower in both these groups than in the normal group. The postmenopausal GABA levels were significantly lower than the premenopausal levels in the normal, anxiety, and depression groups (P = 0.014, <0.001, and <0.001, respectively). The premenopausal GABA levels did not significantly differ between the normal vs. anxiety group (P = 0.907), normal vs. depression group (P = 0.495), and anxiety vs. depression group. The postmenopausal GABA levels were significantly lower in the depression group than in the anxiety group and were significantly lower in both these groups than

OPEN ACCESS

Edited by:
Feng Feng,
Peking Union Medical College Hospital (CAMS), China

Reviewed by:
Laura M. Rowland,
University of Maryland, Baltimore, United States
Meredith A. Reid,
Auburn University, United States

***Correspondence:**
Hui Wang
wangh2014@163.com
Yue-Hua Li
liyuehua312@163.com

† These authors have contributed equally to this work

Specialty section:
This article was submitted to Brain Imaging Methods, a section of the journal Frontiers in Neuroscience

Received: *12 January 2019*
Accepted: *15 July 2019*
Published: *20 August 2019*

Citation:
Wang D, Wang X, Luo M-T, Wang H and Li Y-H (2019) Gamma-Aminobutyric Acid Levels in the Anterior Cingulate Cortex of Perimenopausal Women With Depression: A Magnetic Resonance Spectroscopy Study. Front. Neurosci. 13:785. doi: 10.3389/fnins.2019.00785

in the normal group, normal vs. anxiety group ($P = 0.022$), normal vs. depression group ($P < 0.001$), and anxiety vs. depression group ($P = 0.047$).

Conclusion: Changes in GABA concentrations in the anterior cingulate cortex are related with the pathophysiological mechanism and symptoms of perimenopausal depression.

Keywords: magnetic resonance spectroscopy, gamma-aminobutyric acid, postmenopausal, depression, anxiety, anterior cingulate cortex

INTRODUCTION

The anterior cingulate cortex (ACC) is closely related to the occurrence and development of depression. The ACC occupies the rostral portions of Brodmann areas 24, 25, 32, and 33, and is activated by diverse tasks, ranging from emotion processing and regulation to attention and cognitive control (Ferrone et al., 2007). Many previous studies have confirmed the significant association of the ACC, especially the subgenual ACC, with the processing of negative emotions. The pregenual ACC is considered to be associated with cognitive functions such as social cognition, including theory of mind tasks and conflict monitoring (Ferrone et al., 2007; Formica et al., 2007; Ferolla et al., 2011).

Perimenopausal depression is a mental disorder that first occurs in women during the perimenopausal period and is mainly characterized by symptoms of hypothymia, anxiety, nervousness, and loss of interest, accompanied with autonomic and endocrine dysfunction, especially recession of the gonads. Women with severe symptoms may have a tendency to commit suicide. A meta-analysis has shown that women in the perimenopausal period were particularly vulnerable to anxiety or depression, and had more severe symptoms than women in the premenopausal period (de Kruif et al., 2016). However, the pathophysiological mechanisms of perimenopausal depression are still unknown.

Gamma-aminobutyric acid (GABA) is the main inhibitory neurotransmitter in the central nervous system. It combines with GABA receptors and inhibits excitatory neural activity. Abnormal GABA metabolism plays an important role in the pathogenesis of mental disorders such as depression and schizophrenia (Levy and Degnan, 2013; Rowland et al., 2013). An increasing body of preclinical and clinical evidence has proved that a close relationship exists between GABA and depression. Magnetic resonance spectroscopy (MRS) is a non-invasive technique for quantifying metabolites in the brain. MRS has been successfully applied in studies of depression and has detected changes in many metabolites in different brain regions (Puts and Edden, 2012). MRS plays an important role in exploring the treatments and mechanisms of depression. However, due to the chemical shift and the scalar coupling effect, the GABA spectrum overlaps with signals of other major metabolites. It is therefore difficult to detect GABA by using conventional ^{1}H-MRS. An improved MRS method—MEGA-PRESS, based on partially refocused J-couplings—has been used to detect GABA in studies of healthy brains and psychiatric diseases.

In this study, we used the MEGA-PRESS technique to detect GABA in the anterior cingulate cortex (ACC) of perimenopausal women. The Totally automatic robust quantitation in nuclear MR (TARQUIN) software was used as the post-processing method to calculate GABA concentrations. We aimed to characterize the pathophysiological mechanisms of perimenopausal depression by determining whether changes in GABA concentrations in the ACC were associated with perimenopausal anxiety/depression.

MATERIALS AND METHODS

Participants

We recruited 131 perimenopausal women. After the exclusion of 11 participants, 120 participants remained. The inclusion criteria for the experimental group were as follows: (1) women in the perimenopausal stage, as defined by the Stages of Reproductive Aging Workshop (Soules et al., 2001), i.e., a persistent ≥7-day difference in menstrual cycle length in consecutive cycles (persistence was defined as recurrence within 10 cycles of the first cycle with variable length), and (2) education up to junior high school level or above. The exclusion criteria were as follows: (1) GABA values could not be detected (6 of the 131 participants were excluded due to this reason), (2) diagnosis of a somatic disease (hypertension or diabetes mellitus); (3) presence of a hypothalamic-pituitary-adrenal axis or thyroid disease; (4) history of depression or other related mental illnesses, or presence of dementia or other organic mental disorders; (5) use of oral contraceptives or hormone therapy within 3 months of entering the study; (6) a history of non-depressive disorders in the participant or a family member (including immediate family by blood and collateral blood relatives within three generations); (7) smoking and/or dependence on alcohol; and (8) poor GABA quality (5 of the 131 participants were excluded because of this reason) (**Figure 1**).

Estrogen Measurements

A fasting blood specimen (3 mL) was collected into a 5-mL sterile plain tube without anticoagulant at 9:00–11:00 a.m. on the second or third day of the menstrual cycle. However, if a timely sample could not be obtained (as was the case for the late stage perimenopausal women), a fasting sample was taken when the endometrium was <5 mm thick as determined using transvaginal Doppler ultrasonography. In this study, estrogen levels fluctuated during the perimenopausal period, but the overall trend was downward.

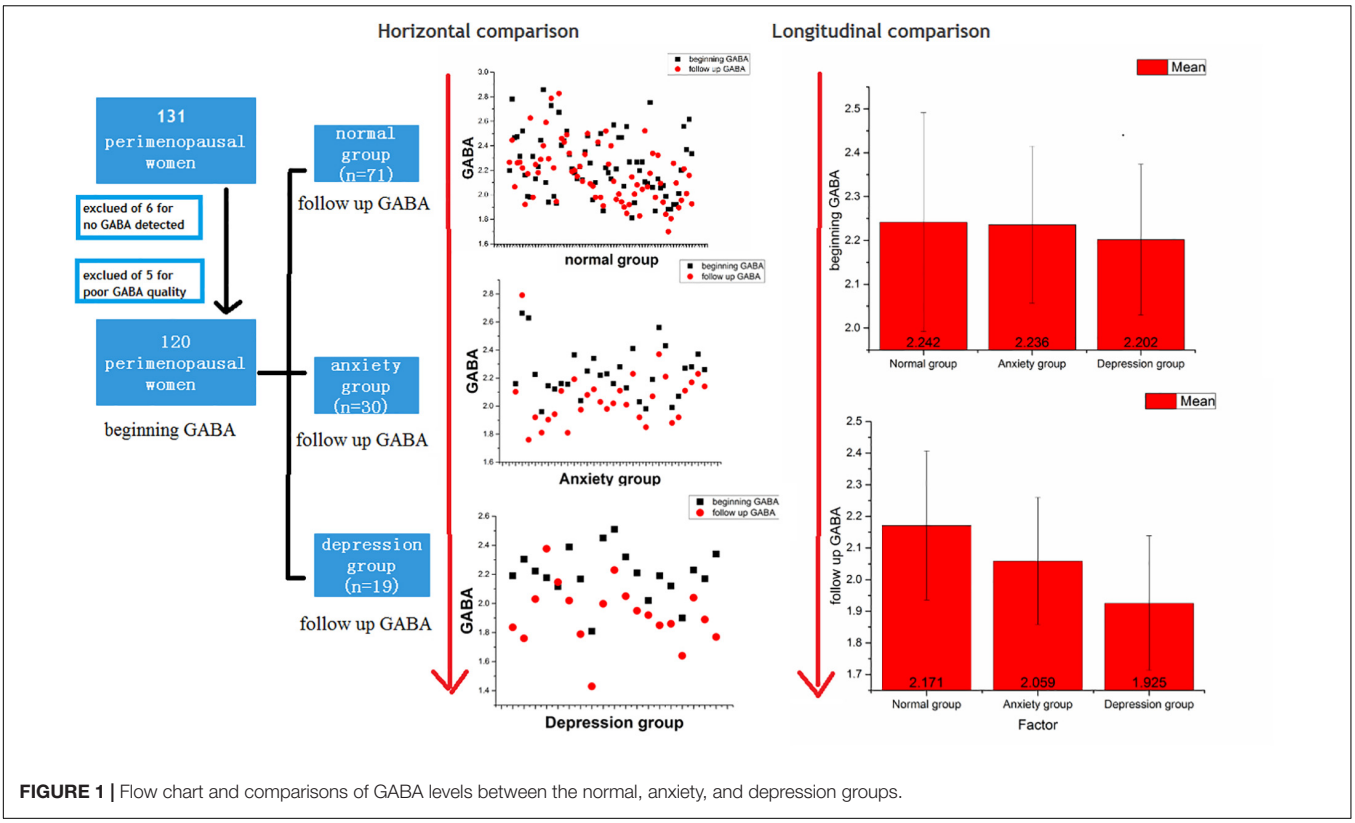

FIGURE 1 | Flow chart and comparisons of GABA levels between the normal, anxiety, and depression groups.

This study was approved by the ethics committee of the Shanghai Sixth People's Hospital, Shanghai Jiao Tong University), and all participants signed informed consent forms before being entered into the study.

MRI and MRS Analyses

In all subjects, MR data were acquired using a 3.0-T MR scanner (MAGETOM, Verio, Siemens Healthcare, Erlangen, Germany) equipped with a 32-channel phased-array head coil as the transmitting and receiving coils. First, a T1-weighted turbo field echo sequence was used to obtain high-resolution three-dimensional (3D) axial images of the brain structure, with the following scanning parameters: field of vision (FOV), 230 mm; repetition time (TR)/echo time (TE), 1500/2.96 ms; flip angle, 9°; voxel size, 0.9 mm × 0.9 mm × 1 mm; slice thickness, 1 mm; and distance factor, 50%. The MEGA-PRESS sequence was used to detect GABA in the regions of interest (ROIs), with the following scanning parameters: TE, 68 ms; TR, 1500 ms; acquisition bandwidth, 1200 Hz; pulse placement, 1.9 ppm, and number of excitations, 64 on and 64 off. Unsuppressed water was used for water scaling and correction of frequency and phase. The spectra were fitted using TARQUIN software (Wilson et al., 2011; Mullins et al., 2014; Harris et al., 2017). GABA peaks were quantified calculated using the water-scaled method, as described previously (Wilson et al., 2011; Mullins et al., 2014; Harris et al., 2017).

A radiologist with 10 years of experience placed two ROIs measuring 2 cm × 2 cm × 2 cm each bilaterally in the subgenual ACC in the sagittal plane and adjusted them accordingly in the coronal and axial planes. The average GABA value of the right and left sides (ROIs) was calculated. The edges of all ROIs were positioned to avoid the lateral ventricles and skull. All images were post-processed by the same radiologist with 10 years of experience, and the TARQUIN software was used to calculate GABA concentrations in the ROIs (**Figure 2**).

Gray matter and white matter tissue proportion of interest has been evaluated for each patient using manual segmentation available in ITK-SNAP[1], where the bounding box was redrawn from the saved planning volume of interest.

Quality Control

In order to gain a high success ratio acquiring GABA spectra, we defined a pre-requirement for performing GABA acquisition: magnetic field inhomogeneity <15 Hz for the defined ROI. After the GABA acquisition, we visually inspected the spectra, and the quality control parameters for spectral fitting were reviewed to verify that the spectra were not qualitatively abnormal. All full widths at half maximum were ≤0.12 ppm. Poorly fitted spectra higher than 20% of the GABA estimate were excluded from further analysis, and this led to the exclusion of 5 of the 131 participants.

Statistical Analysis

For all statistical tests, the level of significance was set at $P < 0.05$. The following analyses were carried out (**Figure 3**).

[1]http://www.itksnap.org

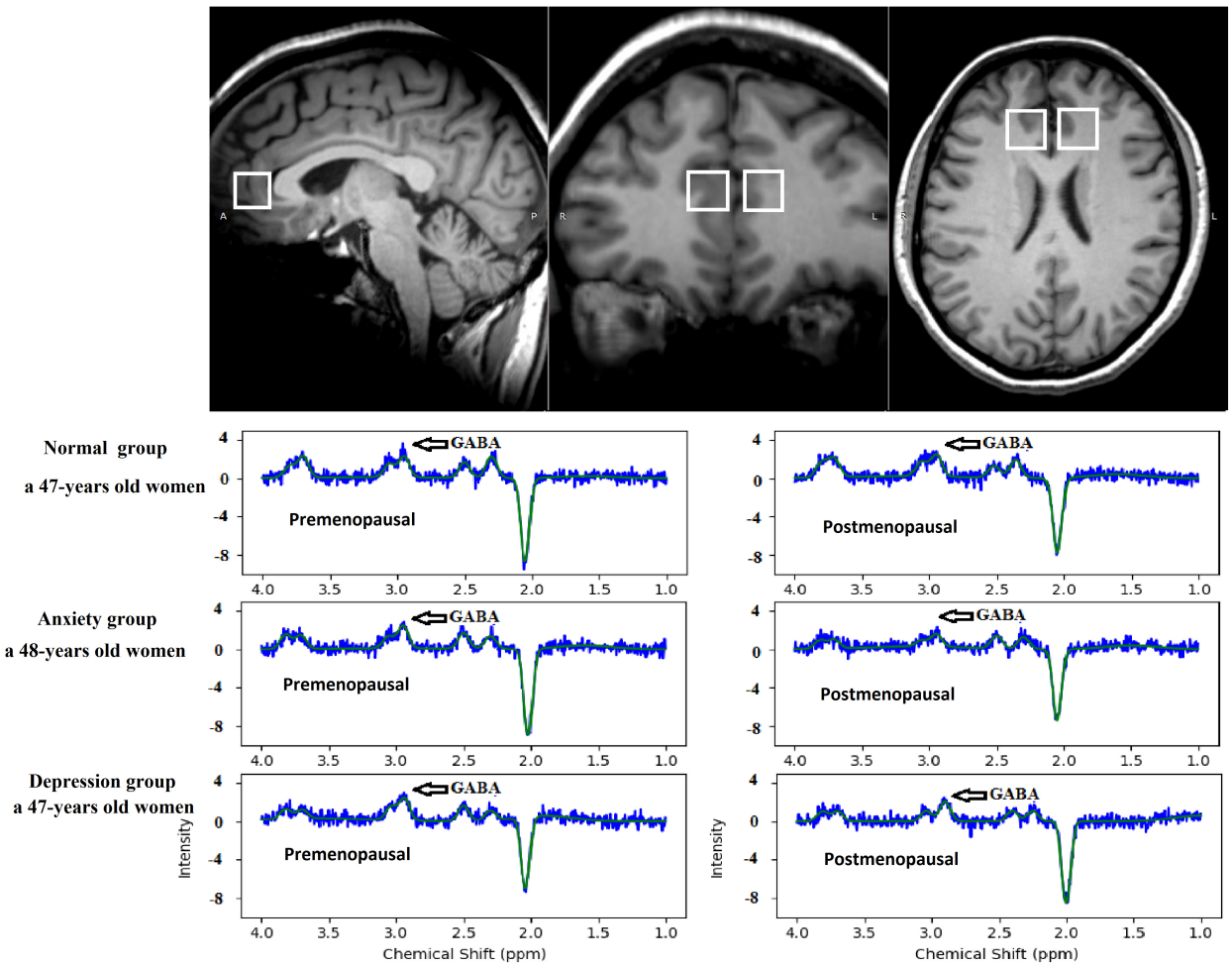

FIGURE 2 | The region of interest in the anterior cingulate cortex on MEGA-PRESS in the axial, sagittal, and coronal planes. TARQUIN edited spectrum GABA in the normal, anxiety, and depression groups. The edited spectrum of the premenopausal and postmenopausal GABA levels located at 3.0 ppm.

(1) Two-way repeated ANOVA with time (pre-menopausal, post-menopausal) and three groups (normal, depression, anxiety group) was used to compared changes GABA with time and groups. Both of the main effect of the group and the time effect were done.
Main effect compared the difference between normal group, depression group and anxiety group at premenopausal stage (i.e., normal group vs. anxiety group, normal group vs. depression group, and anxiety group vs. depression group). It also compared the difference between the three groups at postmenopausal stage.
Time effect was used to compare the difference of pre- and postmenopausal GABA concentrations in the normal group (n = 71), anxiety group (n = 30), and depression group (n = 19).
(2) The Pearson correlation coefficient was used to analyze the correlation of GABA with the Hamilton Anxiety Scale (HAMA)-14 scores in the anxiety group and with the Hamilton Depression Scale (HAMD)-17 scores in the depression group. A two-tailed test of significance was used, with a P value <0.05 considered statistically significant.
(3) Receiver operating characteristic (ROC) curves and the area under the curve (AUC) were calculated to evaluate the diagnostic performance of GABA concentration in the control, anxiety, and depression groups.
(4) Retrospective calculated the gray matter/white matter ratio, as this ratio changes at the two time points (beginning and follow up), one-way ANOVA was used to compare the difference.

RESULTS

General Information

The 120 women remaining in this study were followed up for 18–24 months. All women underwent MRS with a 3.0-T MR

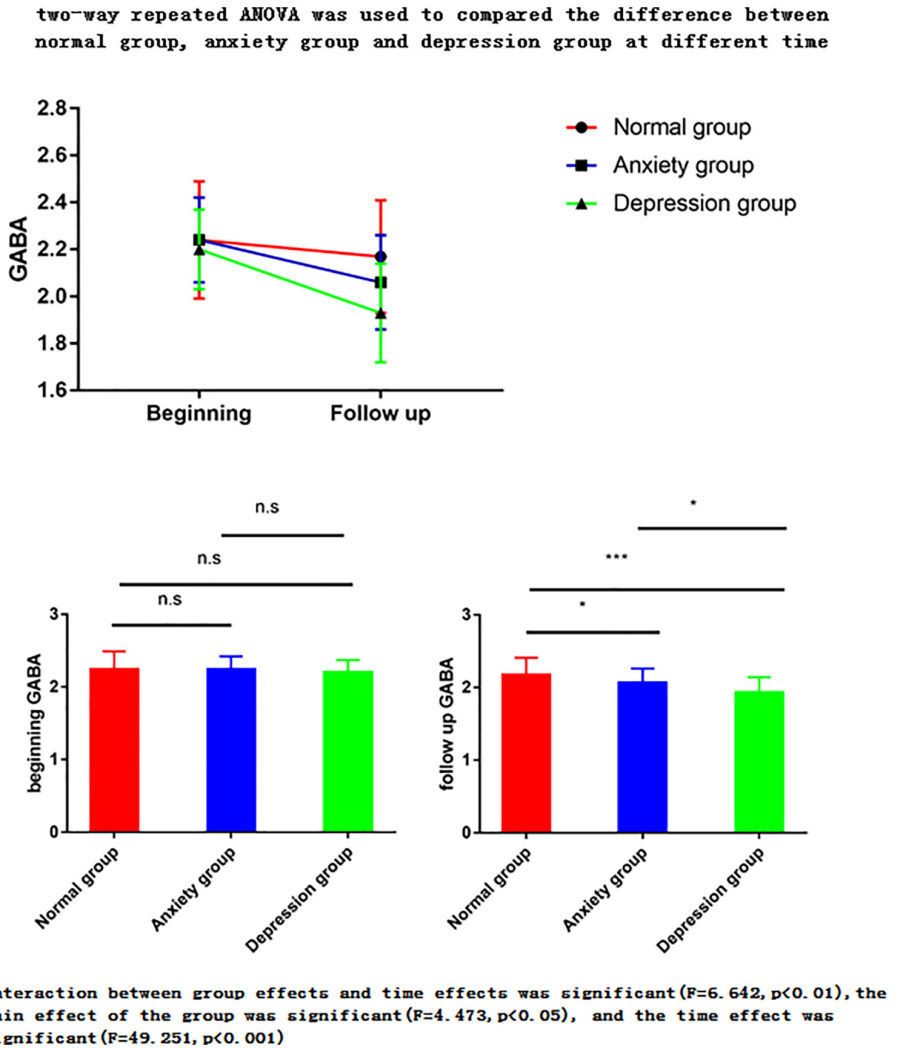

FIGURE 3 | Two-way repeated ANOVA was used to compare the difference between normal group, anxiety group and depression group at different times. The ANOVA for repeated measures is used to perform the data analysis. Interaction between group effects and time effects was significant ($F = 6.642$, $p < 0.01$), the main effect of the group was significant ($F = 4.473$, $p < 0.05$), and the time effect was significant ($F = 49.251$, $p < 0.001$). (1) The main effect showed no statistical difference between any two groups in the three groups at the start time point, but there was a statistical difference between the two groups in the follow-up time point ($p < 0.05$). (2) The time effect shows that there are differences between the two time points in the normal group, there are differences between the two time points of the anxiety group, and there are also differences between the two time points in the depression group. $^{*}P < 0.05$; $^{**}P < 0.01$; $^{***}P < 0.001$.

scanner assessed before and after menopause. The participants were divided into three groups: normal group ($n = 71$), anxiety group ($n = 30$), and depression group ($n = 19$). These diagnoses were based on the Diagnostic and Statistical Manual of Mental Disorders, fifth edition (DSM-V) and were made by two psychiatrists (with 8 and 10 years of experience). These two psychiatrists also assessed the HAMA-14 and HAMD-17 scores before and after menopause. HAMD-17 scores ≥ 17 suggest depression, while HAMA-14 scores > 14 suggest anxiety (**Figure 1**).

The general information of the three groups is displayed in **Table 1**. Blood pressure, blood glucose and triglyceride levels, and body mass index did not significantly differ between the three study groups ($P > 0.05$; **Table 1**).

MRS Data

By means of the MEGA-PRESS sequence, we successfully acquired edited spectra of GABA from the ACC region in 120 subjects.

GABA

The two-way repeated ANOVA results showed that the interaction between group effects and time effects was significant ($F = 6.642$, $p < 0.01$), the main effect of the group was significant ($F = 4.473$, $p < 0.05$), and the time effect was significant ($F = 49.251$, $p < 0.001$) (**Tables 2–4**).

(1) The main effect showed no statistical difference between any two groups in the three groups at the

TABLE 1 | General information.

	Normal group		Anxiety group		Depression group		*P*		
	Mean	***SD***	**Mean**	***SD***	**Mean**	***SD***	**P1**	**P2**	**P3**
Patients (n)	71		30		19		–	–	–
Age (years)	46.80	1.98	47.57	1.99	47.68	1.86	0.076	0.085	0.839
Systolic pressure (mmHg)	80.83	7.46	86.7	3.82	87.79	4.72	<0.05*	<0.05*	0.559
Diastolic pressure (mmHg)	122.96	7.96	125.83	6.16	126.74	6.73	0.075	0.049	0.676
Triglyceride (mmol/L)	1.414	0.306	1.551	0.237	1.452	0.274	0.030*	0.612	0.238
BMI (kg/m^2)	22.910	1.923	23.967	2.950	23.595	3.027	0.046	0.272	0.599
Premenopausal Serum estradiol (mmol/L)	83.170	31.204	81.142	33.245	92.588	30.500	0.769	0.251	0.219
Postmenopausal Serum estradiol (mmol/L)	75.858	17.334	63.478	22.195	54.020	18.483	0.003	<0.01*	0.089
Premenopausal HAMD score					4.789	0.713	0.462	0.382	0.738
Postmenopausal HAMD score					20.737	2.579	<0.05*	<0.05*	<0.05*
Premenopausal HAMA score			3.700	1.088			0.126	0.140	0.868
Postmenopausal HAMA score			18.1	3.356			<0.05*	<0.05*	<0.05*

*P1, normal vs. anxiety group, independent-samples t-test; P2, normal vs. depression group, independent-samples t-test; P3, anxiety vs. depression group, independent-samples t-test. *P < 0.05 was statistically significant. BMI, body mass index; HAMD, hamilton depression scale; HAMA, hamilton anxiety scale.*

TABLE 2 | Two-way repeated ANOVA was used to compare the difference between normal group, anxiety group and depression group at different times.

Group	Beginning GABA	Follow up GABA	F time	F group	F time × group
Normal group	2.242 + 0.250	2.172 + 0.235	49.251***	4.473*	6.642**
Anxiety group	2.236 + 0.180	2.059 + 0.201			
Depression group	2.202 + 0.172	1.923 + 0.213			

*Interaction between group effects and time effects was significant (F = 6.642, p < 0.01), the main effect of the group was significant (F = 4.473, p < 0.05), and the time effect was significant (F = 49.251, p < 0.001).*P < 0.05; **P < 0.01; ***P < 0.001.*

TABLE 3 | Difference between normal group, depression group and anxiety group at premenopausal and postmenopausal time.

Time	(I) Group	(J) Group	Mean Difference (I−J)	Standard Error	Significant	95% Confidence interval for difference	
						Lower Bound	**Upper Bound**
Beginning	Normal group	Anxiety group	0.006	0.049	0.907	−0.091	0.102
		Depression group	0.040	0.058	0.495	−0.075	0.154
	Anxiety group	Normal group	−0.006	0.049	0.907	−0.102	0.091
		Depression group	0.034	0.066	0.606	−0.096	0.164
	Depression group	Normal group	−0.040	0.058	0.495	−0.154	0.075
		Anxiety group	−0.034	0.066	0.606	−0.164	0.096
Follow up	Normal group	Anxiety group	0.113*	0.049	0.022*	0.017	0.210
		Depression group	0.245*	0.058	0.000***	0.131	0.360
	Anxiety group	Normal group	−0.113*	0.049	0.022*	−0.210	−0.017
		Depression group	0.132*	0.066	0.047*	0.002	0.262
	Depression group	Normal group	−0.245*	0.058	0.000***	−0.360	−0.131
		Anxiety group	−0.132*	0.066	0.047*	−0.262	−0.002

*The simple effect showed no statistical difference between any two groups in the three groups at the start time point, but there was a statistical difference between the two groups in the follow-up time point (p < 0.05). *P < 0.05; ***P < 0.001.*

premenopausal time point, but there was a statistical difference between the two groups in the follow-up time point ($p < 0.05$).

The postmenopausal GABA levels significantly differed between the normal vs. anxiety group ($P = 0.022$), normal vs. depression group ($P < 0.001$), and anxiety vs. depression group ($P = 0.047$). The postmenopausal GABA levels were significantly lower in the depression group than in the anxiety group and were significantly lower in both these groups than in the normal group.

The premenopausal GABA levels did not significantly differ between the normal vs. anxiety group ($P = 0.907$),

TABLE 4 | Difference between premenopausal (time 1) and postmenopausal time (time 2) of the normal group, depression group and anxiety group.

Group	(I) time	(J) time	Mean Difference (I-J)	Std. Error	Sig.	95% Confidence interval for difference	
						Lower bound	Upper bound
Normal group	1	2	0.070*	0.028	0.014*	0.015	0.125
	2	1	−0.070*	0.028	0.014*	−0.125	−0.015
Anxiety group	1	2	0.178*	0.043	0.000***	0.092	0.263
	2	1	−0.178*	0.043	0.000***	−0.263	−0.092
Depression group	1	2	0.276*	0.054	0.000***	0.169	0.383
	2	1	−0.276*	0.054	0.000***	−0.383	−0.169

*The simple effect shows that there are differences between the two time points in the normal group, there are differences between the two time points of the anxiety group, and there are also differences between the two time points in the depression group. *P < 0.05; ***P < 0.001.*

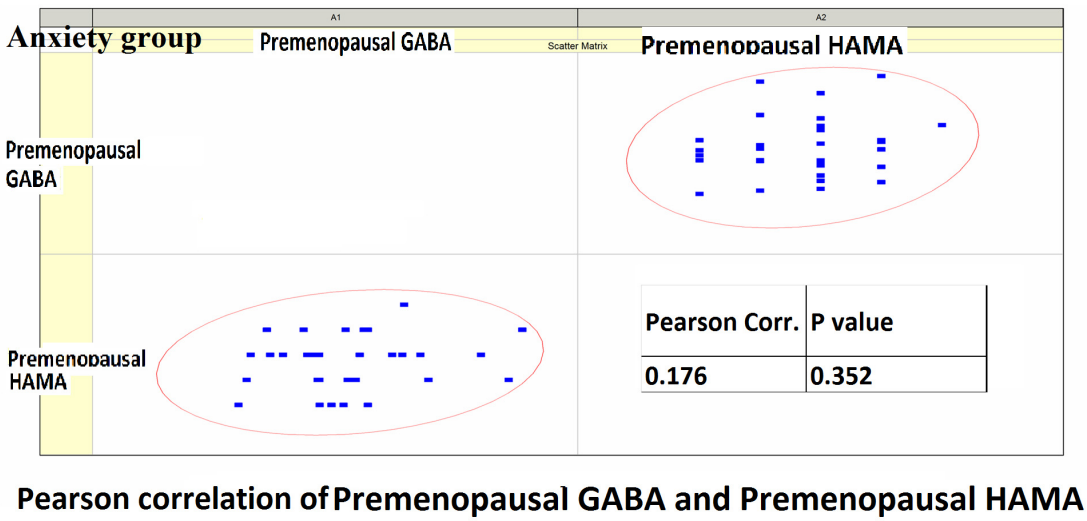

FIGURE 4 | Pearson correlation coefficients for premenopausal GABA levels in the anxiety group and the premenopausal HAMA-14 scores.

normal vs. depression group ($P = 0.495$), and anxiety vs. depression group ($P = 0.606$).

(2) The time effect shows that there are differences between the two time points in the normal group, there are differences between the two time points of the anxiety group, and there are also differences between the two time points in the depression group. This means there is difference between postmenopausal groups, and GABA decreased with time.

The postmenopausal GABA levels were significantly lower than the premenopausal levels in the normal, anxiety, and depression groups ($P = 0.014$, <0.001, and <0.001, respectively).

Pearson Correlation Analysis

Pearson correlation analysis revealed the following: (1) The premenopausal GABA levels were not significantly correlated with the HAMA-14 scores in the anxiety group ($r = 0.176$, $P = 0.352$) or with HAMD-17 scores in the depression group ($r = -0.191$, $P = 0.433$). (2) The postmenopausal GABA levels were significantly correlated with the HAMA-14 score in the anxiety group ($r = -0.365$, $P = 0.048$), but not with the HAMD-17 score in the depression group ($r = -0.428$, $P = 0.068$; **Figures 4–7** and **Table 5**).

Receiver operating characteristic curve and AUC results: The postmenopausal GABA diagnostic performance in normal and mental disorders (both anxiety and depression) was as follows: AUC value 0.703 ($P < 0.001$). Postmenopausal GABA diagnostic performance in anxiety and depression was as follows: AUC value 0.677 ($P = 0.038$). The ratio of GABA decline to premenopausal GABA diagnostic performance in normal and mental disorders (both anxiety and depression) was as follows: AUC value 0.683 ($P < 0.001$). The ratio of GABA decline to premenopausal GABA diagnostic performance in anxiety and depression was as follows: AUC value 0.774 ($P = 0.001$; **Figure 8**).

Gray Matter/White Matter Ratio

There is no significant difference between groups and times; gray matter/white matter ratio did not drive the GABA comparison results (**Table 6**).

GABA SNR%SD were calculated between groups and two time points, there is no significant difference.

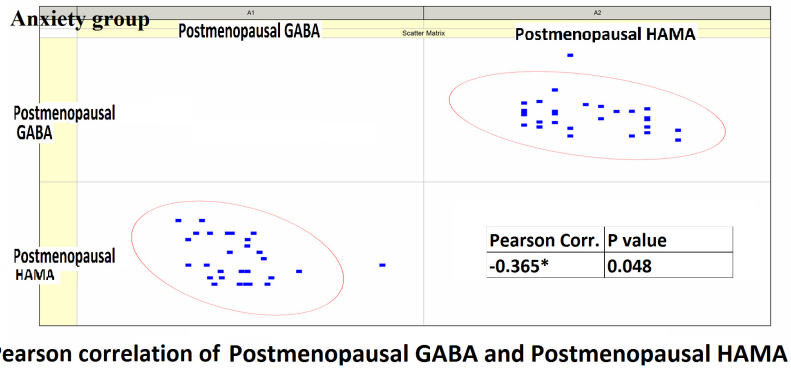

FIGURE 5 | Pearson correlation coefficients for postmenopausal GABA levels in the anxiety group and the postmenopausal HAMA-14 scores.

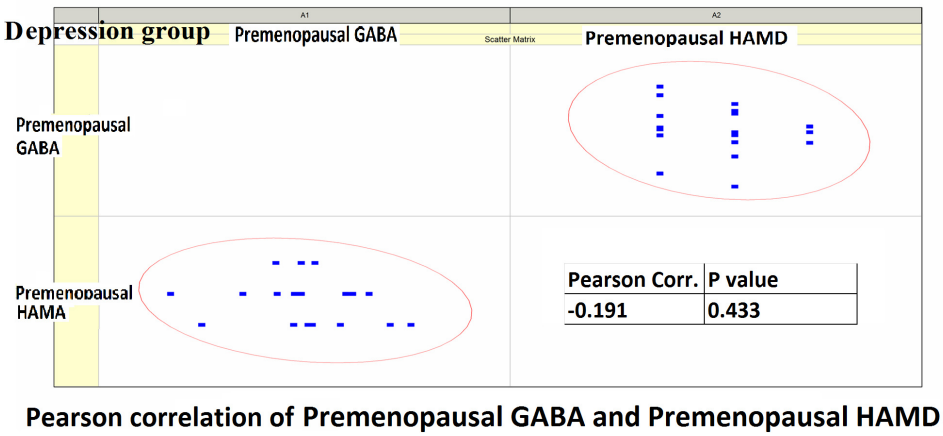

FIGURE 6 | Pearson correlation coefficients for premenopausal GABA levels in the depression group and premenopausal HAMD-17 scores.

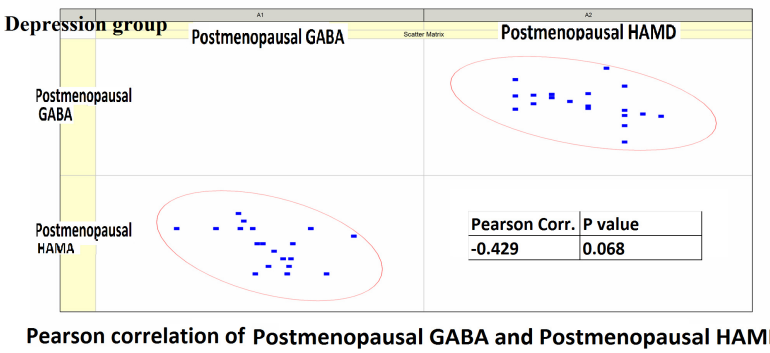

FIGURE 7 | Pearson correlation coefficients for postmenopausal GABA levels in the depression group and postmenopausal HAMD-17 scores.

DISCUSSION

In this study, we have provided preliminary evidence that GABA levels in the ACC region of perimenopausal women with depression were significantly lower after menopause and were significantly lower than the levels in the control group ($P < 0.05$). This finding suggests that a reduction in GABA levels in the ACC is associated with the pathophysiological mechanism of perimenopausal depression, and that there might be a lack of GABA in the perimenopausal period. The study also found that after menopause, the concentration of GABA was significantly lower in the depression group than in the anxiety group, and

TABLE 5 | Pearson correlation coefficients for HAMA scores and GABA of anxiety group, Pearson correlation coefficients for HAMD scores and GABA of depression group.

	Premenopausal				Postmenopausal			
	HAMA score	GABA	Pearson correlation	*P* value	HAMA score	GABA	Pearson correlation	*P* value
Anxiety group	3.700 + 1.088	2.236 + 0.180	0.176	0.352	18.1 + 3.356	2.059 + 0.201	−0.365*	0.048
	Premenopausal				**Postmenopausal**			
	HAMD score	**GABA**			**HAMD score**	**GABA**		
Depression group	4.789 + 0.713	2.202 + 0.172	−0.191	0.433	20.737 + 2.579	1.923 + 0.213	−0.42857	0.068

*Two-tailed Pearson correlation test of significance was used. *Correlations were significant at the 0.05 probability level.*

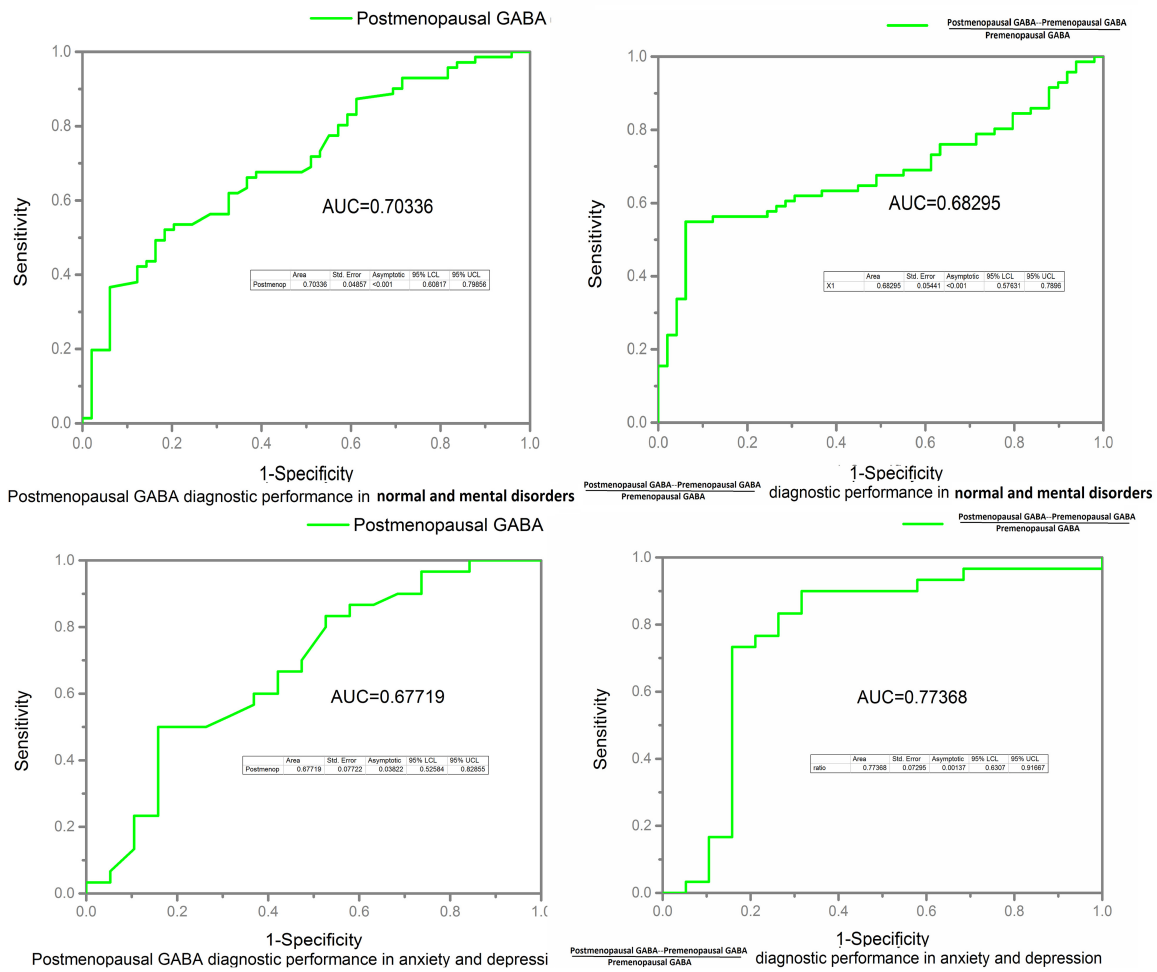

FIGURE 8 | Receiver operating characteristic (ROC) curves and area under the curve (AUC) value were calculated to assess the diagnostic performance of GABA in the normal, anxiety, and depression groups.

significantly lower in the anxiety group than in the normal group. This further suggested an association between a reduction in GABA levels and depression. We also observed dynamic changes in GABA levels during the transition from the premenopausal to the postmenopausal period.

Many investigators have focused on the relationship between GABA levels and depression. GABA concentrations in the plasma and cerebrospinal fluid of depressive patients are lower than those in healthy controls. Smiley et al. (2016) found that GABA-neuron density in the auditory cerebral cortex is reduced in subjects with

TABLE 6 | Gray matter/white matter ratio comparison between three groups (normal group, anxiety group, and depression group) at beginning time and follow up time.

		Number	Lesion		Comparison between groups		
			Mean	*SD*		*T* value	*P* value
Beginning	Normal group	71	0.774	0.013	Anxiety group Normal group	−0.176	0.860
	Anxiety group	30	0.773	0.013	Depression group Normal group	1.686	0.094
	Depression group	19	0.779	0.015	Depression group Anxiety group	1.616	0.109
Follow up	Normal group	71	0.778	0.019	Anxiety group Normal group	−0.929	0.355
	Anxiety group	30	0.774	0.017	Depression group Normal group	0.686	0.494
	Depression group	19	0.774	0.019	Depression group Anxiety group	0.086	0.932

There is no significant difference between groups and times of Gray matter/white matter ratio.

major depressive disorder. Using MRS studies, Hasler et al. (2007) found lower GABA levels in the prefrontal cortex in subjects with major depression than in healthy controls. Many studies have found that patients with depression have lower GABA levels in the occipital lobe and ACC than do healthy controls (Sanacora et al., 2004; Bhagwagar et al., 2008). Sanacora et al. (2004) have suggested that GABA concentrations vary among the different subtypes of depression and that a change in the ratio of excitatory–inhibitory neurotransmitter levels might be associated with abnormal brain function. In investigations of female physiological cycles related with depression, Liu et al. (2015) found that GABA levels in the ACC, prefrontal lobe, and left basal ganglia region were significantly reduced in women with premenstrual dysphoric disorder. Wang et al. (2016) found that GABA levels in the ACC and medial prefrontal lobe were decreased in postmenopausal women. In our study, we also detected reduced GABA levels in the ACC of perimenopausal women with depression, which was consistent with the results of the above studies. However, GABA was too low to be detected in some participants.

An imbalance of the limbic-cortical-striatal-pallidal-thalamic loop is the generally acknowledged neurological model of depression. The activity of the anterior cingulate gyrus and dorsal lateral frontal lobe has been shown to be decreased in depressive patients. Wang et al. (2016) detected significantly low GABA levels in the ACC/medial prefrontal cortex of postmenopausal women with depression. Dubin et al. (2016) found that after repetitive transcranial magnetic stimulation, the GABA levels in the medial prefrontal cortex significantly increased. Therefore, in this study, we selected the ACC region as the ROI, as this region is closely related with emotional function. We did not choose the occipital lobe as in the study by Bhagwagar et al. (2008) because the size of the ROI in our study was relatively large, and ROIs placed in the occipital lobe can be easily disturbed by other structural signals in the base of the skull. Hasler et al. (2007) detected reduced GABA levels in the prefrontal regions in patients with major depressive disorder, including parts of the ACC, but the GABA values in their study were lower than the GABA values in this study, possibly because of differences in ROI sizes, channels of the head coil, and calculation methods. We retrospectively calculated the gray matter/white matter ratio, as this ratio changes at the two time points (beginning and follow up); there was no significant difference between groups and times. Gray matter/white matter ratio did not drive the GABA results.

There are some limitations to this study. First, this is a cohort study, and the sample size needs to be increased in future. The follow-up period was relatively short. To explain the relationship between GABA levels and the pathogenesis of perimenopausal depression, more experiments need to be performed. GABA spectroscopy was poor due to movement, and GABA spectroscopy could not be acquired due to the participant requesting to end the scan prematurely. Furthermore, we only selected the ACC as the ROI; the prefrontal cortex and other brain regions related to emotional circuits were not included in this study. The differences between the left and right ROIs were not assessed. The manually prescribed ROIs were subjective and could have led to deviations in the results of different subjects. Moreover, it has been suggested that the GABA levels in the brain decrease with age (Gao et al., 2013). During the perimenopausal period, hormone levels fluctuate significantly. Studies have suggested that decreased estrogen levels affect perimenopausal depression (Schmidt et al., 1994). And the gray matter/white matter ratio was retrospectively calculated, and a small amount of cerebrospinal fluid was not considered and may lead to some small deviation.

CONCLUSION

In summary, this study examined the changes in the GABA levels in the ACC region in perimenopausal women with depression and anxiety as well as healthy women (controls). The results suggested that the GABA levels in the ACC decreased during the perimenopausal period, and that this decrease was closely associated with depression and anxiety. We calculated GABA concentrations by using the MEGA-PRESS sequence; the results were highly reliable and stable. Advances in MRS technology will be important in the exploration of pathogenesis and the development of targeted drugs for perimenopausal depression.

ETHICS STATEMENT

This study was approved by the local ethics committee (The ethics committee of Shanghai Sixth Affiliated People's Hospital,

Shanghai Jiao Tong University), and all participants signed informed consent forms before entering the study.

AUTHOR CONTRIBUTIONS

DW wrote the manuscript. DW, XW, and M-TL calculated the statistical data. Y-HL and HW designed the research content and research direction.

FUNDING

This study was supported by the National Natural Science Youth Project Foundation of China, No. 81501460, Shanghai Jiao Tong University crossing Biomedical Engineering Research Fund No. YG2015MS16, Shanghai Municipal Health & Family Planning Commission research projects No. 201640160, and Shanghai Science and Technology Commission Medical Guidance Project No. 18411967600. This study was also supported by the National Natural Science Foundation of China Nos. 81471656, 81671673, and 81570908/H1304, the Shanghai Municipal Natural Science Foundation No. 14ZR1432100, the Shanghai Talent Development Fund No. 201555, the Shanghai Municipal Education Commission-Gaofeng Clinical Medicine Grant Support No. 2016427, the Clinical Science and Technology Innovation Project of Shanghai Shen Kang Hospital Development Center No. SHDC22015038, and the Shanghai Municipal Science and Technology Commission Medical Guide Project No. 16411968900.

REFERENCES

Bhagwagar, Z., Wylezinska, M., Jezzard, P., Evans, J., Boorman, E., Matthews, M. P., et al. (2008). Low GABA concentrations in occipital cortex and anterior cingulate cortex in medication-free, recovered depressed patients. *Int. J. Neuropsychopharmacol.* 11, 255–260. doi: 10.1017/s1461145707007924

de Kruif, M., Spijker, A. T., and Molendijk, M. L. (2016). Depression during the perimenopause: a meta-analysis. *J. Affect. Disord.* 206, 174–180. doi: 10.1016/j.jad.2016.07.040

Dubin, M. J., Mao, X., Banerjee, S., Goodman, Z., Lapidus, K. A., Kang, G., et al. (2016). Elevated prefrontal cortex GABA in patients with major depressive disorder after TMS treatment measured with proton magnetic resonance spectroscopy. *J. Psychiatry Neurosci.* 41, E37–E45.

Ferolla, P., Faggiano, A., Grimaldi, F., Ferone, D., Scarpelli, G., Ramundo, V., et al. (2011). Shortened interval of octreotide LAR administration is effective in patients with well differentiated neuroendocrine carcinomas in progression on standard doses. *J. Endocrinol. Invest.* 35, 326–331. doi: 10.3275/7869

Ferrone, C. R., Tang, L. H., Tomlinson, J., Gonen, M., Hochwald, S. N., Brennan, M. F., et al. (2007). Determining prognosis in patients with pancreatic endocrine neoplasms: can the WHO classification system be simplified? *J. Clin. Oncol.* 25, 5609–5615. doi: 10.1200/JCO.2007.12.9809

Formica, V., Wotherspoon, A., Cunningham, D., Norman, A. R., Sirohi, B., Oates, J., et al. (2007). The prognostic role of WHO classification, urinary 5-hydroxyindoleacetic acid and liver function tests in metastatic neuroendocrine carcinomas of the gastroenteropancreatic tract. *Br. J. Cancer* 96, 1178–1182. doi: 10.1038/sj.bjc.6603699

Gao, F., Edden, R. A., Li, M., Puts, N. A., Wang, G., Liu, C., et al. (2013). Edited magnetic resonance spectroscopy detects an age-related decline in brain GABA levels. *Neuroimage* 78, 75–82. doi: 10.1016/j.neuroimage.2013.04.012

Harris, A. D., Puts, N. A. J., Wijtenburg, S. A., Rowland, L. M., Mikkelsen, M., Barker, P. B., et al. (2017). Normalizing data from GABA-edited MEGA-PRESS implementations at 3 Tesla. *Magn. Reson. Imaging* 42, 8–15. doi: 10.1016/j.mri.2017.04.013

Hasler, G., van der Veen, J. W., Tumonis, T., Meyers, N., Shen, J., and Drevets, W. C. (2007). Reduced prefrontal glutamate/glutamine and gamma-aminobutyric acid levels in major depression determined using proton magnetic resonance spectroscopy. *Arch. Gen. Psychiatry* 64, 193–200. doi: 10.1001/archpsyc.64.2.193

Levy, L. M., and Degnan, A. J. (2013). GABA-based evaluation of neurologic conditions: MR spectroscopy. *AJNR Am. J. Neuroradiol.* 34, 259–265. doi: 10.3174/ajnr.A2902

Liu, B., Wang, G., Gao, D., Gao, F., Zhao, B., Qiao, M., et al. (2015). Alterations of GABA and glutamate-glutamine levels in premenstrual dysphoric disorder: a 3T proton magnetic resonance spectroscopy study. *Psychiatry Res.* 231, 64–70. doi: 10.1016/j.pscychresns.2014.10.020

Mullins, P. G., McGonigle, D. J., O'Gorman, R. L., Puts, N. A., Vidyasagar, R., Evans, C. J., et al. (2014). Current practice in the use of MEGA-PRESS spectroscopy for the detection of GABA. *Neuroimage* 86, 43–52. doi: 10.1016/j.neuroimage.2012.12.004

Puts, N. A., and Edden, R. A. (2012). In vivo magnetic resonance spectroscopy of GABA: a methodological review. *Prog. Nucl. Magn. Reson. Spectrosc.* 60, 29–41. doi: 10.1016/j.pnmrs.2011.06.001

Rowland, L. M., Kontson, K., West, J., Edden, R. A., Zhu, H., Wijtenburg, S. A., et al. (2013). In vivo measurements of glutamate, GABA, and NAAG in schizophrenia. *Schizophr. Bull.* 39, 1096–1104. doi: 10.1093/schbul/sbs092

Sanacora, G., Gueorguieva, R., Epperson, C. N., Wu, Y. T., Appel, M., Rothman, D. L., et al. (2004). Subtype-specific alterations of gamma-aminobutyric acid and glutamate in patients with major depression. *Arch. Gen. Psychiatry* 61, 705–713. doi: 10.1001/archpsyc.61.7.705

Schmidt, P. J., Purdy, R. H., Moore, P. H. Jr., Paul, S. M., and Rubinow, D. R. (1994). Circulating levels of anxiolytic steroids in the luteal phase in women with premenstrual syndrome and in control subjects. *J. Clin. Endocrinol. Metab.* 79, 1256–1260. doi: 10.1210/jcem.79.5.7962316

Smiley, J. F., Hackett, T. A., Bleiwas, C., Petkova, E., Stankov, A., Mann, J. J., et al. (2016). Reduced GABA neuron density in auditory cerebral cortex of subjects with major depressive disorder. *J. Chem. Neuroanat.* 76, 108–121. doi: 10.1016/j.jchemneu.2015.10.008

Soules, M. R., Sherman, S., Parrott, E., Rebar, R., Santoro, N., Utian, W., et al. (2001). Executive summary: stages of reproductive aging workshop (STRAW). *Fertil. Steril.* 76, 874–878. doi: 10.1016/s0015-0282(01)02909-0

Wang, Z., Zhang, A., Zhao, B., Gan, J., Wang, G., Gao, F., et al. (2016). GABA+ levels in postmenopausal women with mild-to-moderate depression: a preliminary study. *Medicine* 95:e4918. doi: 10.1097/md.0000000000004918

Wilson, M., Reynolds, G., Kauppinen, R. A., Arvanitis, T. N., and Peet, A. C. (2011). A constrained least-squares approach to the automated quantitation of in vivo (1)H magnetic resonance spectroscopy data. *Magn. Reson. Med.* 65, 1–12. doi: 10.1002/mrm.22579

Conflict of Interest Statement: The authors declare that the research was conducted in the absence of any commercial or financial relationships that could be construed as a potential conflict of interest.

frontiers in Neuroscience

ORIGINAL RESEARCH
published: 29 August 2019
doi: 10.3389/fnins.2019.00903

Intracranial Atherosclerotic Disease-Related Acute Middle Cerebral Artery Occlusion Can Be Predicted by Diffusion-Weighted Imaging

Huijun Zhang[1†], Xuan Sun[2†], Qiong Huang[1], Xiangming Wang[1], Yunhua Yue[3], Mingfeng Ju[1], Xiaoping Wang[1], Ji Ding[1] and Zhongrong Miao[2]*

[1] Department of Neurology, Tong Ren Hospital, Shanghai Jiao Tong University School of Medicine, Shanghai, China, [2] Department of Interventional Neurology, Beijing Tiantan Hospital, Capital Medical University, China National Clinical Research Center for Neurological Diseases, Center of Stroke, Beijing Institute for Brain Disorders, Beijing, China, [3] Department of Neurology, Yangpu Hospital, Tongji University School of Medicine, Shanghai, China

OPEN ACCESS

Edited by:
Lin Shi,
The Chinese University of Hong Kong, China

Reviewed by:
Dong-Hoon Lee,
The University of Sydney, Australia
Sidong Liu,
Macquarie University, Australia

***Correspondence:**
Zhongrong Miao
miaozhongrong123@126.com

[†] These authors have contributed equally to this work

Specialty section:
This article was submitted to Brain Imaging Methods, a section of the journal Frontiers in Neuroscience

Received: 03 December 2018
Accepted: 13 August 2019
Published: 29 August 2019

Citation:
Zhang H, Sun X, Huang Q, Wang X, Yue Y, Ju M, Wang X, Ding J and Miao Z (2019) Intracranial Atherosclerotic Disease-Related Acute Middle Cerebral Artery Occlusion Can Be Predicted by Diffusion-Weighted Imaging. Front. Neurosci. 13:903. doi: 10.3389/fnins.2019.00903

Background: The differentiation of large vessel occlusion caused by intracranial atherosclerotic stenosis (ICAS) or intracranial embolism significantly impacts the course of treatment (i.e., intravenous thrombolysis versus mechanical thrombectomy) for acute cerebral infarction. Currently, there is no objective evidence to indicate ICAS-related middle cerebral artery M1 segment occlusion before treatment. In cases of ICAS, it is often observed that the infarct core caused by ICAS-related M1 segment middle cerebral artery occlusion (MCAO) is located in deeper parts of the brain (basal ganglia or semiovoid region).

Objective: To evaluate whether the location of the infarct core, identified using diffusion-weighted imaging (DWI), can be used to differentiate ICAS from intracranial embolism.

Methods: Thirty-one consecutive patients diagnosed with acute cerebral infarction caused by middle cerebral artery M1 segment occlusion were retrospectively included based on angiographic findings to distinguish ICAS from embolic occlusion. Patients were divided into two groups based on the location of the infarct core on DWI: in the deep part of the brain (basal ganglia or semiovoid region) or more superficially (i.e., cortex).

Results: In 16 patients, the infarct core was mainly in the deep part of the brain on DWI [14 of 16 patients in the ICAS group and only 2 in the non-ICAS group

(93.3 vs. 6.7%, respectively; $P < 0.001$)]. The diagnostic sensitivity of DWI for ICAS was 93.3%, with a specificity of 87.5%, a Positive predictive value (PPV) of 87.5%, and an Negative predictive value (NPV) of 93.3%, the accuracy was 88.5%.

Conclusion: Intracranial atherosclerotic disease-related acute MCAO can be predicted using DWI.

Keywords: intracranial atherosclerotic stenosis, diffusion-weighted imaging, middle cerebral artery occlusion, intracranial embolism, acute ischemic stroke

INTRODUCTION

More than 80% of strokes are ischemic in nature, 25–35% of which result from large vessel occlusion. Patients with large vessel occlusion often experience severe neurological deficits (Kidwell et al., 2013). Without timely and appropriate treatment, these patients have a poor prognosis. Large vessel occlusions are usually caused by intracranial atherosclerotic stenosis (ICAS) or intracranial embolism. ICAS accounts for 22.9% of cases in Asia (Yoon et al., 2015).

For acute ischemic stroke caused by intracranial embolism (Berkhemer et al., 2015; Goyal et al., 2015; Jovin et al., 2015; Lee et al., 2015; Powers et al., 2015; Saver et al., 2015), mechanical thrombectomy is an effective treatment. Patients diagnosed with cerebral embolism can be directly treated with mechanical thrombectomy without intravenous thrombolysis for shortening the recanalization time. For patients with large vessel occlusion caused by ICAS, however, platelet aggregation can cause re-occlusion of the culprit vessels after mechanical thrombectomy, even if remedial measures are administered (Heo et al., 2003; Gao et al., 2015; Yoon et al., 2015). For patients in this category, a loading dose of antiplatelet agents can be used to reduce aggregation before and during surgery. Therefore, it is very important to differentiate ICAS from intracranial embolism before operating.

Intracranial atherosclerotic stenosis can be detected and assessed using high-resolution angiographic-magnetic resonance (MR) imaging (MRI) before treatment (Dieleman et al., 2014; Natori et al., 2014; Kim et al., 2015; van der Kolk et al., 2015); however, this is expensive and without definite diagnostic criteria. It can also be predicted by microcatheter "first-pass effect" during mechanical thrombectomy (Yi et al., 2018); however, there is no objective evidence to indicate intracranial atherosclerotic disease-related occlusion before surgery.

Magnetic resonance (MR) imaging plays an important role in the diagnosis and treatment of acute ischemic cerebrovascular disease. In the present study, patients with acute middle cerebral artery occlusion (MCAO) underwent diffusion-weighted imaging (DWI) to evaluate whether the location of the infarct core could be used to differentiate ICAS from intracranial embolism.

Abbreviations: ADC, apparent diffusion coefficient; DWI, diffusion-weighted image; HAS, hyper-dense artery sign; ICAS, intracranial atherosclerotic stenosis; MCAO, middle cerebral artery occlusion; NIHSS, NIH stroke scale; NPV, negative predictive value; PPV, positive predictive value; TICI, thrombolysis in cerebral infarction.

MATERIALS AND METHODS

Patients

Thirty-one consecutive patients, who experienced acute stroke and underwent endovascular therapy between May 2017 and August 2018, were identified in the Beijing Tiantan Hospital (Beijing, China) database according to the following criteria: exhibited MCAO; time between symptom onset and admission was 6 h or >6 h for a moderate-to-large hypoperfusion area as depicted on multimodal MRI; underwent vascular recanalization, which was subsequently confirmed; age >18 years; and the prestroke modified Rankin Scale score was 0–1. Patients in whom stroke was the result of dissection, moyamoya disease or vasculitis, those with unexplained MCAO, those who did not undergo MRI before surgery or cerebrovascular examination within 1 week after the operation, and those with carotid T and carotid L collaterals were excluded. Informed consent was obtained from all participants or their relatives, and the protocol was approved by the Institutional Review Board of Beijing Tiantan Hospital.

Demographic information and patient characteristics are summarized in **Table 1**. The patients (18 men, 13 women) had a mean (±standard error of the mean) age of 61 ± 2 years. Seventeen (54.8%) patients were smokers. The prevalence of hypertension, diabetes, hyperlipidemia, atrial fibrillation and/or rheumatic heart disease, and transient ischemic attack in the 31 patients were 58.1, 32.3, 16.1, 32.3, and 6.45%, respectively.

Operational Definitions of ICAS and Embolic Occlusion

Angiographic findings distinguishing ICAS from embolic occlusion were based on those described in a previous study (Yi et al., 2018). Evidenced by final angiography or during endovascular treatment, ICAS was defined as a significant fixed

TABLE 1 | Clinical characteristics of all the patients (n = 31).

Sex (male, *n*)	18 (58.1%)
Age	61.13 (years)
Smoker	17 (54.8%)
Hypertension, *n*(%)	18 (58.1%)
Diabetes mellitus, *n*(%)	10 (32.3%)
Hyperlipidemia, *n*(%)	5 (16.1%)
Atrial fibrillation and/or rheumatic heart disease	10 (32.3%)
Transient ischemic attack	2 (6.45%)

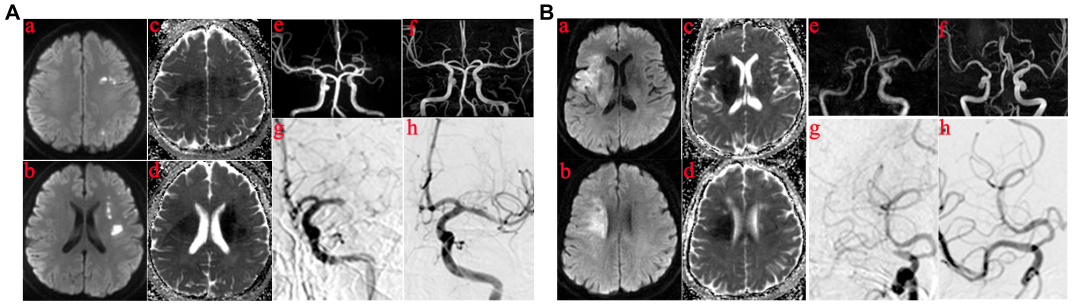

FIGURE 1 | Those in whom the infarct core was mainly in the basal ganglia or semiovoid region and those in whom the infarct core was mainly in cortex. **(A)** The infarct core was mainly in basal ganglia or semiovoid region. **(a–d)** The presentation of infarcts on DWI and Apparent diffusion coefficient (ADC) mapping; **(e)** Right middle cerebral artery occlusion before operation on MRA; **(f)** MRA performed within 1 week showed severe residual stenosis in the responsibility lesions of right middle cerebral artery; **(g,h)** DSA demonstrated the results of MRA. **(B)** The infarct core was mainly in cortex. **(a–d)** The presentation of infarcts on DWI and ADC mapping; **(e)** Left middle cerebral artery occlusion before operation on MRA; **(f)** Postoperative MRA showed no residual stenosis in the responsibility lesions of right middle cerebral artery; **(g,h)** DSA demonstrated the results of MRA.

focal stenosis that could be resolved using angioplasty or stent insertion (Lee et al., 2015; Yi et al., 2018) at the site of occlusion (**Figures 1Ag,h**). Significant stenosis was defined as fixed stenosis ≥70% or fixed stenosis ≥50%, besides either angiographically evident of impaired perfusion or evidence of re-occlusion after appropriate treatment using a stent retriever. The cause of MCAO (**Figures 1Ae,Be**) was classified as embolism based on the following: no focal stenosis after clot retrieval during operation (**Figures 1Bg,h**), and confirmed on MR angiography (**Figures 1Af,Bf**) or computed tomography angiography performed within 1 week after the procedure; and an embolus removed using a stent retriever.

DWI and Clinical Assessment

Before surgery, MRI included DWI and a three-dimensional-time-of-flight-MR angiography. T1-, T2-weighted imaging, and fluid attenuated inversion recovery were performed in all patients using a 3.0 Tesla scanner (Discovery 750, GE Healthcare, Milwaukee, WI, United States) equipped with a 32-channel head coil. A single-shot echo-planar imaging DWI sequence was performed using the following parameters: repetition time/echo time, 2300/63.60 ms; b, 1000 s/mm2; slice thickness, 5 mm; slice number, 24; field of view, 240 mm; and matrix, 128 × 128. The related apparent diffusion coefficient (ADC) and exponential ADC maps were obtained. A focal hyperintensity on DWI and hypointensity on the ADC was defined as an infarct core. The site of the infarct [located deep in the brain (e.g., basal ganglia or semiovoid region, or mainly in cortex)] was investigated. DWI findings were evaluated by two neuroradiologists blinded to the clinical symptoms and surgical findings.

Neurological function in all patients was assessed on admission using the National Institutes of Health Stroke Scale (NIHSS). Patients were radiologically assessed using the Thrombolysis in Cerebral Infarction (TICI) scale, and successful reperfusion was defined as a TICI grade of 2b or 3 after endovascular treatment (Zaidat et al., 2013).

Clinical characteristics of the patients, risk factors for arteriosclerosis, heart disease, previous transient ischemic attack, NIHSS score on admission, the hyper-dense artery sign (HAS) on non-enhanced CT, and angiographic information were collected. All images were retrospectively reviewed by two neurologists blinded to patient information and study protocol; discrepancies between the reviewers were resolved by consensus discussion.

Statistical Analysis

Differences in clinical characteristics, risk factors, and imaging features between patients in whom the infarct core was mainly in the deep part of the brain and those in whom the infarct core was mainly in the cortex were examined using bivariate analysis, as between patients with ICAS and those with intracranial embolism. The Student's *t*-test was used to compare continuous variables, while the $\chi 2$ test was used to compare categorical variables. Diagnostic performance including sensitivity, specificity, positive predictive value (PPV), negative predictive value (NPV), and diagnostic accuracy of the location of infarct core for the prediction of ICAS, were calculated. All statistical analyses were performed using Prism version 5 (Mac OS X, Apple Inc., Cupertino, CA, United States); $P \leq 0.05$ was considered to be statistically significant.

RESULTS

Patients With ICAS vs. Patients With Embolism

Data from 15 patients diagnosed with ICAS and 16 diagnosed with embolism were compared using the $\chi 2$ test; the results are summarized in **Table 2**.

Patients with ICAS were more likely to have hypertension (80 vs. 37.5%; $P = 0.029$), less likely to have atrial fibrillation and/or rheumatoid heart disease (6.67 vs. 56.2%; $P = 0.006$), and less likely to exhibit HAS on non-enhanced CT (20 vs. 75%, $P = 0.003$). Twelve of the 15 (80%) patients with ICAS required emergency angioplasty for successful recanalization (**Table 2**).

TABLE 2 | Clinical characteristics and endovascular therapy of patients in the ICAS group and embolism group.

	ICAS group (*n* = 15)	Embolism group (*n* = 16)	*P*-value
Sex (male, *n*)	9 (60%)	9 (56.2%)	1.000
Age (mean, years)	61±2	63±3	0.575
Smoker	9 (60%)	8 (50%)	0.722
Hypertension, n(%)	12 (80%)	6 (37.5%)	0.029
Diabetes mellitus, *n*(%)	5 (33.3%)	5 (31.3%)	1.000
Hyperlipidemia, *n*(%)	3 (20%)	2 (12.5%)	0.654
Atrial fibrillation and/or rheumatic heart disease	1 (6.67)	9 (56.2%)	0.006
Transient ischemic attack	2 (13.3)	0	0.226
Admission NHISS	12±1	15±2	0.235
HAS on CT, *n* (%)	3 (20%)	12 (75%)	0.003
With balloon or stent	12 (80%)	1 (6.25%)	< 0.001
Hemorrhage	3 (20%)	7 (43.8%)	0.458
Occlusion again, *n*(%)	1 (6.67)	0 (0%)	0.484

TABLE 3 | Clinical characteristics of the two groups patients the infarct core were mainly in deep of the brain and cortex, respectively.

	Deep of the brain (*n* = 16)	Cortex (*n* = 15)	*P*-value
Sex (male, *n*)	10 (62.5%)	8 (53.3%)	0.722
Age (mean, years)	60±3	65±2	0.142
Smoker	10 (60%)	7 (50%)	0.724
Hypertension, *n*(%)	12 (80%)	6 (37.5%)	0.029
Diabetes mellitus, *n*(%)	6 (37.5%)	4 (26.7%	0.704
Hyperlipidemia, *n*(%)	4 (25%)	1 (6.7%)	0.333
Atrial fibrillation and/or rheumatic Heart disease	1 (6.67)	9 (56.2%)	0.006
Transient ischemic attack	2 (13.3)	0	0.226

Patients Whose Infarct Core Was Mainly in the Deep of the Brain and Those Whose Infarct Core Was Mainly in Cortex

According to DWI and ADC, patients were divided into two categories, as shown in **Figures 1A (a–d)**. For some, the infarct core was mainly in the deep part of the brain (e.g., basal ganglia or semiovoid region) and, as shown in **Figures 1B (a–d)**, there were some whose infarct core was mainly in the cortex, respectively. Clinical characteristics of the two patient groups are summarized in **Table 3**. Patients in whom the infarct core was mainly in the basal ganglia or semiovoid region group, compared with those whose infarct core mainly in cortex group, were more likely to have hypertension (80 vs. 37.5%; $P = 0.029$) and less likely to have atrial fibrillation and/or rheumatoid heart disease (6.67 vs. 56.2%; $P = 0.006$), respectively.

Diagnostic Performance of the DWI

There were 16 patients in whom the infarct core was mainly in the basal ganglia or semiovoid region on DWI (14 of the 16 patients in the ICAS group and only 2 in the non-ICAS group [93.3 vs. 6.7%, respectively; $P < 0.001$]). The diagnostic sensitivity of DWI for ICAS was 93.3%, with a specificity of 87.5%, a PPV of 87.5%, and an NPV of 93.3%, the accuracy was 88.5%.

DISCUSSION

The purpose of our study was to explore objective evidence for discerning ICAS from intracranial embolism resulting in M1 occlusion before surgery. CT and MRI are mainly used in the diagnosis and treatment of acute cerebral infarction. However, the following advantages of MRI become necessary for examination (Bang et al., 2018). First, DWI combined with ADC is superior to any CT techniques for imaging the infarct core (Kohrmann and Schellinger, 2009). Second, mismatch between DWI and FLAIR can be used to guide intravenous recombinant tissue plasminogen activator treatment in "Wake-up" patients with acute ischemic stroke with an unknown time of onset (Thomalla et al., 2018). Finally, using MRI to assess collaterals and the infarct core can expand the scope of application of endovascular treatment (Albers et al., 2018; Nogueira et al., 2018). Thus, MRI was chosen as the main research tool for diagnosis and treatment of acute cerebral infarction.

Our data revealed no significant difference in sex or age between those with ICAS and those with embolization. One possible explanation is that our findings were based on a single-center experience and that the sample size was insufficient, or only focused on occlusion of the M1 segment of the middle cerebral artery. Consistent with a previous study (Yi et al., 2018), we also found that the ICAS patients were more likely to have hypertension (80 vs. 37.5%; $P = 0.029$), which is a risk factor for arteriosclerosis (Lee et al., 2015), less likely to have atrial fibrillation and/or rheumatoid heart disease (6.67 vs. 56.2%; $P = 0.006$) and exhibit HAS on non-enhanced CT (20 vs. 75%; $P = 0.003$), which is related to cardiac-embolic stroke (Kirchhof et al., 2003; Cho et al., 2005; Kim et al., 2008; Moftakhar et al., 2013). Twelve of the 15 (80%) patients with ICAS required emergency angioplasty for successful recanalization (**Table 2**).

Although DWI had been used to analyze causes of posterior cerebral artery infarction (Lee et al., 2009), there has been no research using DWI to study the characteristics of infarcts caused by MCAO of the M1 segment in ICAS. In assessing DWI results of patients with acute MCAO, we found that the infarction core of the patients with ICAS were primarily located in the deeper parts of the brain (basal ganglia and semiovoid regions), and the infarction core of occlusions caused by intracranial embolism were located more superficially (i.e., cortex). Our study revealed a significant association between the location of the infarct core detected on DWI and causes of middle cerebral artery M1 occlusion. There were 16 patients whose infarct core was mainly in the deep of the brain on DWI. The diagnostic sensitivity of DWI for ICAS was 93.3%, with a specificity of 87.5%, a PPV of 87.5%, and an NPV of 93.3%, the accuracy was 88.5%. Our study demonstrated that the infarct core in patients with ICAS was located primarily in the deeper parts of the brain, which has two possible explanations.

First, in ICAS, the collateral circulation in the cortex is abundant. Second, chronic ischemia may increase the ischemic tolerance of cortical neurons. As our investigation was a single-center retrospective study, a multicenter study involving a larger sample size or a randomized controlled trial are needed to further verify our results.

CONCLUSION

The features of infarction on DWI can predict MCAO caused by ICAS preoperatively, which may reflect the ischemic tolerance of cortical neurons. Increased ICAS can guide therapeutic strategies in patients with acute cerebral infarction. First, patients diagnosed with cerebral embolism can be directly treated with mechanical thrombectomy without intravenous thrombolysis for shortening the recanalization time. Second, for these patients, intravenous thrombolysis for within "time window" or dual antiplatelet loading dose for out of "time window" is a better option. Third, if diagnosed with ICAS, it should be considered preoperatively, and stent or balloon expansion therapy should be administered in time to reduce vascular injury caused by repeated thrombolysis. Finally, the correct diagnosis provides an appropriate basis for secondary prevention of stroke.

ETHICS STATEMENT

Our access to patients' records for data collection and analysis of the data were approved by Beijing Tiantan Hospital, Capital Medical University medical ethics committee.

AUTHOR CONTRIBUTIONS

HZ and XS designed the research. HZ, XS, and ZM performed the research. QH, XmW, YY, MJ, XpW, and JD analyzed the data. ZM wrote the manuscript.

FUNDING

This study was supported by grants from National Key Research and Development Program of China (Grant Number 2016YFC1301501).

REFERENCES

Albers, G. W., Marks, M. P., Kemp, S., Christensen, S., Tsai, J. P., Ortega-Gutierrez, S., et al. (2018). Thrombectomy for stroke at 6 to 16 hours with selection by perfusion imaging. *N. Engl. J. Med.* 378, 708–718. doi: 10.1056/NEJMoa1713973

Bang, O. Y., Chung, J. W., Son, J. P., Ryu, W. S., Kim, D. E., Seo, W. K., et al. (2018). Multimodal MRI-based triage for acute stroke therapy: challenges and progress. *Front. Neurol.* 9:586. doi: 10.3389/fneur.2018.00586

Berkhemer, O. A., Fransen, P. S., Beumer, D., van den Berg, L. A., Lingsma, H. F., Yoo, A. J., et al. (2015). A randomized trial of intraarterial treatment for acute ischemic stroke. *N. Engl. J. Med.* 372, 11–20. doi: 10.1056/NEJMoa1411587

Cho, K. H., Kim, J. S., Kwon, S. U., Cho, A. H., and Kang, D. W. (2005). Significance of susceptibility vessel sign on T2*-weighted gradient echo imaging for identification of stroke subtypes. *Stroke* 36, 2379–2383. doi: 10.1161/01.str.0000185932.73486.7a

Dieleman, N., van der Kolk, A. G., Zwanenburg, J. J., Harteveld, A. A., Biessels, G. J., Luijten, P. R., et al. (2014). Imaging intracranial vessel wall pathology with magnetic resonance imaging: current prospects and future directions. *Circulation* 130, 192–201. doi: 10.1161/circulationaha.113.006919

Gao, F., Lo, W. T., Sun, X., Mo, D. P., Ma, N., and Miao, Z. R. (2015). Combined use of mechanical thrombectomy with angioplasty and stenting for acute basilar occlusions with underlying severe intracranial vertebrobasilar stenosis: preliminary experience from a single chinese center. *AJNR Am. J. Neuroradiol.* 36, 1947–1952. doi: 10.3174/ajnr.A4364

Goyal, M., Demchuk, A. M., Menon, B. K., Eesa, M., Rempel, J. L., Thornton, J., et al. (2015). Randomized assessment of rapid endovascular treatment of ischemic stroke. *N. Engl. J. Med.* 372, 1019–1030.

Heo, J. H., Lee, K. Y., Kim, S. H., and Kim, D. I. (2003). Immediate reocclusion following a successful thrombolysis in acute stroke: a pilot study. *Neurology* 60, 1684–1687. doi: 10.1212/01.wnl.0000063323.23493.98

Jovin, T. G., Chamorro, A., Cobo, E., de Miquel, M. A., Molina, C. A., Rovira, A., et al. (2015). Thrombectomy within 8 hours after symptom onset in ischemic stroke. *N. Engl. J. Med.* 372, 2296–2306. doi: 10.1056/NEJMoa1503780

Kidwell, C. S., Jahan, R., Gornbein, J., Alger, J. R., Nenov, V., Ajani, Z., et al. (2013). A trial of imaging selection and endovascular treatment for ischemic stroke. *N. Engl. J. Med.* 368, 914–923. doi: 10.1056/NEJMoa1212793

Kim, E. Y., Yoo, E., Choi, H. Y., Lee, J. W., and Heo, J. H. (2008). Thrombus volume comparison between patients with and without hyperattenuated artery sign on CT. *AJNR Am. J. Neuroradiol.* 29, 359–362. doi: 10.3174/ajnr.a0800

Kim, S. K., Yoon, W., Heo, T. W., Park, M. S., and Kang, H. K. (2015). Negative susceptibility vessel sign and underlying intracranial atherosclerotic stenosis in acute middle cerebral artery occlusion. *AJNR Am. J. Neuroradiol.* 36, 1266–1271. doi: 10.3174/ajnr.A4280

Kirchhof, K., Welzel, T., Mecke, C., Zoubaa, S., and Sartor, K. (2003). Differentiation of white, mixed, and red thrombi: value of CT in estimation of the prognosis of thrombolysis phantom study. *Radiology* 228, 126–130. doi: 10.1148/radiol.2273020530

Kohrmann, M., and Schellinger, P. D. (2009). Acute stroke triage to intravenous thrombolysis and other therapies with advanced CT or MR imaging: pro MR imaging. *Radiology* 251, 627–633. doi: 10.1148/radiol.2513081074

Lee, E., Kang, D. W., Kwon, S. U., and Kim, J. S. (2009). Posterior cerebral artery infarction: diffusion-weighted MRI analysis of 205 patients. *Cerebrovasc. Dis.* 28, 298–305. doi: 10.1159/000229016

Lee, J. S., Hong, J. M., Lee, K. S., Suh, H. I., Demchuk, A. M., Hwang, Y. H., et al. (2015). Endovascular therapy of cerebral arterial occlusions: intracranial atherosclerosis versus embolism. *J. Stroke Cerebrovasc. Dis.* 24, 2074–2080. doi: 10.1016/j.jstrokecerebrovasdis.2015.05.003

Moftakhar, P., English, J. D., Cooke, D. L., Kim, W. T., Stout, C., Smith, W. S., et al. (2013). Density of thrombus on admission CT predicts revascularization efficacy in large vessel occlusion acute ischemic stroke. *Stroke* 44, 243–245. doi: 10.1161/STROKEAHA.112.674127

Natori, T., Sasaki, M., Miyoshi, M., Ohba, H., Katsura, N., Yamaguchi, M., et al. (2014). Evaluating middle cerebral artery atherosclerotic lesions in acute ischemic stroke using magnetic resonance T1-weighted 3-dimensional vessel wall imaging. *J. Stroke Cerebrovasc. Dis.* 23, 706–711. doi: 10.1016/j.jstrokecerebrovasdis.2013.06.025

Nogueira, R. G., Jadhav, A. P., Haussen, D. C., Bonafe, A., Budzik, R. F., Bhuva, P., et al. (2018). Thrombectomy 6 to 24 hours after stroke with a mismatch between deficit and infarct. *N. Engl. J. Med.* 378, 11–21. doi: 10.1056/NEJMoa1706442

Powers, W. J., Derdeyn, C. P., Biller, J., Coffey, C. S., Hoh, B. L., Jauch, E. C., et al. (2015). 2015 american heart association/american stroke association focused update of the 2013 guidelines for the early management of patients with acute ischemic stroke regarding endovascular treatment: a guideline for healthcare

professionals from the american heart association/american stroke association. *Stroke* 46, 3020–3035. doi: 10.1161/str.0000000000000074

Saver, J. L., Goyal, M., Bonafe, A., Diener, H. C., Levy, E. I., Pereira, V. M., et al. (2015). Stent-retriever thrombectomy after intravenous t-PA vs. t-PA alone in stroke. *N. Engl. J. Med.* 372, 2285–2295. doi: 10.1056/NEJMoa1415061

Thomalla, G., Simonsen, C. Z., Boutitie, F., Andersen, G., Berthezene, Y., Cheng, B., et al. (2018). MRI-Guided thrombolysis for stroke with unknown time of onset. *N. Engl. J. Med.* 379, 611–622. doi: 10.1056/NEJMoa1804355

van der Kolk, A. G., Zwanenburg, J. J., Denswil, N. P., Vink, A., Spliet, W. G., Daemen, M. J., et al. (2015). Imaging the intracranial atherosclerotic vessel wall using 7T MRI: initial comparison with histopathology. *AJNR Am. J. Neuroradiol.* 36, 694–701. doi: 10.3174/ajnr.A4178

Yi, T. Y., Chen, W. H., Wu, Y. M., Zhang, M. F., Zhan, A. L., Chen, Y. H., et al. (2018). Microcatheter "first-pass effect" predicts acute intracranial artery atherosclerotic disease-related occlusion. *Neurosurgery* 84, 1296–1305. doi: 10.1093/neuros/nyy183

Yoon, W., Kim, S. K., Park, M. S., Kim, B. C., and Kang, H. K. (2015). Endovascular treatment and the outcomes of atherosclerotic intracranial stenosis in patients with hyperacute stroke. *Neurosurgery* 76, 680–686. doi: 10.1227/NEU.0000000000000694

Zaidat, O. O., Yoo, A. J., Khatri, P., Tomsick, T. A., von Kummer, R., Saver, J. L., et al. (2013). Recommendations on angiographic revascularization grading standards for acute ischemic stroke: a consensus statement. *Stroke* 44, 2650–2663. doi: 10.1161/strokeaha.113.001972

Conflict of Interest Statement: The authors declare that the research was conducted in the absence of any commercial or financial relationships that could be construed as a potential conflict of interest.

frontiers in Neurology

ORIGINAL RESEARCH
published: 01 October 2019
doi: 10.3389/fneur.2019.01018

Machine Learning Assisted MRI Characterization for Diagnosis of Neonatal Acute Bilirubin Encephalopathy

*Zhou Liu[1,2], Bing Ji[2], Yuzhong Zhang[3], Ge Cui[4], Lijian Liu[1,5], Shuai Man[6], Ling Ding[3], Xiaofeng Yang[4], Hui Mao[2] and Liya Wang[1,3]**

[1] Graduate School, Nanchang University School of Medicine, Nanchang, China, [2] Department of Radiology and Imaging Sciences, Emory University School of Medicine, Atlanta, GA, United States, [3] Department of Radiology, The People's Hospital of Longhua, Southern Medical University, Shenzhen, China, [4] Department of Radiation Oncology, Emory University School of Medicine, Atlanta, GA, United States, [5] Department of Radiology, National Cancer Center/Cancer Hospital & Shenzhen Hospital, Chinese Academy of Medical Sciences and Peking Union Medical College, Shenzhen, China, [6] Department of Pediatrics, The People's Hospital of Longhua, Southern Medical University, Shenzhen, China

OPEN ACCESS

Edited by:
Lin Shi,
The Chinese University of Hong Kong, China

Reviewed by:
Bo Gao,
Affiliated Hospital of Guizhou Medical University, China
Jung Hun Oh,
Memorial Sloan Kettering Cancer Center, United States
Maarten Lequin,
University Medical Center Utrecht, Netherlands

***Correspondence:**
Liya Wang
2718377613@qq.com

Specialty section:
This article was submitted to Applied Neuroimaging, a section of the journal Frontiers in Neurology

Received: 12 March 2019
Accepted: 09 September 2019
Published: 01 October 2019

Citation:
Liu Z, Ji B, Zhang Y, Cui G, Liu L, Man S, Ding L, Yang X, Mao H and Wang L (2019) Machine Learning Assisted MRI Characterization for Diagnosis of Neonatal Acute Bilirubin Encephalopathy. Front. Neurol. 10:1018. doi: 10.3389/fneur.2019.01018

Background: The use of magnetic resonance imaging (MRI) in diagnosis of neonatal acute bilirubin encephalopathy (ABE) in newborns has been limited by its difficulty in differentiating confounding image contrast changes associated with normal myelination. This study aims to demonstrate the feasibility of building a machine learning prediction model based on radiomics features derived from MRI to better characterize and distinguish ABE from normal myelination.

Methods: In this retrospective study, we included 32 neonates with clinically confirmed ABE and 29 age-matched controls with normal myelination. Radiomics features were extracted from the manually segmented region of interest (ROI) on T1-weighted spin echo images, followed by the feature selection using two-sample independent *t*-test, least absolute shrinkage and selection operator (Lasso) regression, and Pearson's correlation matrix. Additional feature quantifying the relative mean intensity of ROI was defined and calculated. A prediction model based on the selected features was built to classify ABE and normal myelination using multiple machine learning classifiers and a leave-one-out cross-validation scheme. Receiver operating characteristics (ROC) analysis was used to evaluate the prediction performance with the area under the curve (AUC) and feature importance ranked based on the Fisher score.

Results: Among 1319 radiomics features, one radiologist-defined intensity-based feature and 12 texture features were selected as the most discriminative features. Based on these features, decision trees had the best classification performance with the largest AUC of 0.946, followed by support vector machine (SVM), tree-bagger, logistic regression, Naïve Bayes, discriminant analysis, and k-nearest neighborhood (KNN), which have an AUC of 0.931, 0.925, 0.905, 0.891, 0.883, and 0.817, respectively. The relative mean intensity outperformed other 12 texture features in differentiating ABE from controls.

Conclusions: The results from this study demonstrated a new strategy of characterizing ABE-induced intensity and morphological changes in MRI, which are difficult to be recognized, interpreted, or quantified by the routine experience and visual-based reading strategy. With more quantitative and objective measurements, the reported machine learning assisted radiomics features-based approach can improve the diagnosis and support clinical decision-making.

Keywords: magnetic resonance imaging, neonate, bilirubin encephalopathy, myelination, machine learning, radiomics

INTRODUCTION

Neonatal jaundice is one of the most prominent clinical concerns during the neonatal period. It is mainly caused by the accumulation of neurotoxic unconjugated bilirubin from the breakdown of old red blood cells that cannot be cleared effectively by newborns (1). Based on a nationwide survey on hospitalized neonates in China, 49.1% developed various degrees of neonatal jaundice and 8–9% developed severe hyperbilirubinemia with as high as 0.9% (357/4,141,535) ended up developing bilirubin encephalopathy due to lack of appropriate diagnosis and prediction of its development or delayed treatment (2). Kernicterus, the brain damage specifically caused by hyperbilirubinemia, is characterized by the intense yellow staining of bilirubin at some specific regions of the brain, which is consistent across the term, preterm, and rare adult with kernicterus (3). Before kernicterus (chronic bilirubin encephalopathy, CBE), a permanent neurological sequela induced by bilirubin toxicity, hyperbilirubinemia and acute bilirubin encephalopathy (ABE) can be reversed with safe and effective treatments (4). Therefore, identifying neonates with a high risk of ABE early to apply the treatment timely is the key to minimize the incidence of permanent bilirubin-induced neurological dysfunction (BIND) and kernicterus (5). However, early detection of jaundiced neonates with the risk of brain damage in the acute stage is challenging in the current clinical practice.

The evaluation of neonatal jaundice is typically done with the standard clinical laboratory test by measuring the total serum bilirubin (TSB) concentration. Because it is not a direct measurement of the actual bilirubin level in the brain, TSB measurement leads to considerably high false-positive and false-negative rates when used as a predictor of ABE (6). Including other serum parameters, such as unconjugated or "free" bilirubin, albumin level, and bilirubin-albumin binding capacity, does not significantly improve the overall prediction power (7, 8). As for clinical manifestations, the early neurological symptoms induced by ABE could be absent, subtle, or non-specific in most cases (9). When a clinical sign of the classic tetrad syndrome caused by CBE appears, the bilirubin toxicity-induced neural injuries have already become permanent and irreversible. Moreover, several comorbidities, such as hemolytic diseases, prematurity, asphyxia, or infection, can all pose neonates with jaundice to a higher risk of ABE, which further compromise the predictive performance of serum measurements and clinical manifestations (10). Therefore, there is a great need in non-invasive and direct detection of bilirubin-induced subtle change in the infant brain to assess the risk of brain damage in ABE.

Magnetic resonance imaging (MRI), as a non-radiation and non-invasive imaging technique, offers superb resolution and soft tissue contrast for visualizing brain structures and abnormalities. Thus, it is well suited for safe and direct imaging of the neonatal brain affected by bilirubin toxicity. It not only can provide brain region-specific evidence for ABE but also enables to exclude hypoxic–ischemic encephalopathy, the most common neonatal encephalopathy (11). During the days to weeks of ABE, MRI shows "classic" T_1-signal hyperintensity in various degrees on T_1-weighted spin echo images in the globus pallidus and subthalamic nuclei, hippocampus, and cerebellum in the neonatal brain accompanied by an unremarkable or subtle signal increase on T_2-weighted images (12–14). However, normal myelination in newborns within the same age span can also lead to slightly increased signal intensity on T_1-weighted images in the same regions similar to the bilirubin-induced hyperintensity in the neonates with ABE (15). Therefore, it is difficult for the conventional signal intensity change-based reading strategy that is commonly used in radiology reading and evaluations to yield accurate diagnosis.

With emerging radiomics and machine learning assisted image analysis, various graphical features, especially those difficult to be recognized by radiologists, can be identified and extracted to generate a large set of data to further correlate with pathological (16), genomic (17), molecular (18), and clinical outcome (19) information. Thus, radiomics analysis can expand the capability of characterizing disease-induced image abnormalities and the underlying pathophysiology in much greater details with parametric variables and high-throughput quantitative measurements to improve the accuracy of diagnosis and predicting prognosis (20, 21).

Herein, we report an initial work of applying the radiomics-based machine learning approach to identify an ABE-specific

Abbreviations: CBE, chronic bilirubin encephalopathy; ABE, acute bilirubin encephalopathy; BIND, bilirubin-induced neurological dysfunction; FLAIR, fluid-attenuated inversion recovery; DWI, diffusion-weighted imaging; ADC, apparent diffusion coefficients; FOV, field of view; TE, echo time; TR, repetition time; ROI, region of interest; Lasso, least absolute shrinkage and selection operator; KNN, k-nearest neighborhood; SVM, support vector machine; AUC, area under the curve; ROC, receiver operating characteristics; GLCM, gray level co-occurrence matrix; GLRLM, gray level run length matrix, NGTDM, neighborhood gray-tone difference matrix; IMC 1 and 2, information measure of correlation 1 and 2.

radiomics pattern based on MRI contrast changes on T_1-weighted spin echo images associated with the bilirubin deposition in neonatal brains and its induced change in tissue properties. The distinct radiomics features were found and used to differentiate ABE from normal myelination.

MATERIALS AND METHODS

Study Subjects

This retrospective study was approved by the Institutional Review Board and carried out in accordance with the Declaration of Helsinki with the written informed consent waived from legal custodians of all subjects for this study. However, as a part of clinical routine procedure, the written informed consent for MRI examinations was obtained from their legal custodians before MRI examinations. We selected 61 neonates based on reviewing their medical records, including 32 ABE neonates with a mean after-birth age of 6.8 ± 3.5 days and 29 age-matched controls (11.6 ± 6.1 days), who had MRI examinations during their hospitalization. For more accurate indication of maturity of the newborns, we used the average equivalent age, defined as gestational age + age after birth. The average equivalent age is 276.1 ± 10.4 days for 32 neonates with suspected ABE and 262.1 ± 22.3 days for 29 age-matched controls, respectively. To minimize the potential age-related factor, we only included those neonates with the age within 3 weeks after birth, during which ABE usually develops. All 32 ABE cases were clinically confirmed based on their medical records. To standardize inclusion criteria, we set stringent inclusion criteria by collecting supportive information for diagnosing ABE from the medical records of all subjects. All ABE positive cases met at least two of three clinical diagnosis criteria, including (1) severe hyperbilirubinemia (peak total serum bilirubin ≥20 mg/dl or 342 μmol/L); (2) positive radiological findings suggestive of ABE; (3) at least one of the ABE-related clinical symptoms with bilirubin-induced neurologic dysfunction (BIND) score ≥ 1 point in which 1, 2, or 3 points were assigned to mild, moderate, or severe symptoms based on the severity of the crying pattern defined for neonates, behavior and mental status, and muscle tone for a total 9 points (22). Neonates with any history of neurological abnormalities caused by perinatal asphyxia, hypoxia–ischemia, intrauterine infection, chromosomal disease, hereditary mitochondrial metabolic disease, carbon monoxide poisoning, and hypermagnesemia and other related diseases were excluded. T_1-weighted images from each case were evaluated for motion artifacts that may affect the image analysis. All cases included have satisfactory image quality for further analysis.

All clinically confirmed ABE cases had a peak TSB level ≥20 mg/dl during hospitalization. With laboratory test and clinical manifestations available for all 32 positive ABE cases during interpretation, previous radiology reports showed that radiologists diagnosed 5 out of 32 cases matching the typical imaging findings of ABE, 18 cases highly likely to have developed ABE, 7 cases likely but indecisive to have ABE, and 2 cases unlikely to have ABE, but they cannot exclude the possibility in reference to the clinical information. Of 32 ABE neonates, 26 developed explicit ABE-specific clinical symptoms with BIND scores ranging from 1 to 6, while 6 ABE cases developed ABE-non-specific clinical symptoms based on the available medical records. In contrast, 29 age-matched control cases were negative in all three criteria mentioned above.

MRI Acquisition

All images were acquired from a 1.5-T whole-body MRI scanner (Achiva, Philips Healthcare, Best, the Netherlands) using a routine clinical brain MRI protocol. The protocol included the following imaging sequences: T_1-weighted spin-echo imaging in the axial and sagittal directions, and T_2-weighted fast spin echo imaging, T_2-weighted fluid-attenuated inversion recovery (FLAIR) imaging, and diffusion-weighted imaging (DWI) in the axial direction. Because the characteristic image appearance for ABE is elevated signal intensity in globus pallidus and subthalamic nuclei on T_1-weighted spin echo images, we only focused on analyzing T_1-weighted spin echo images in this study. The imaging parameters for T_1-weighted spin echo imaging included the following: echo time (TE) of 17 ms, repetition time (TR) of 600 ms, flip angle of 69°, field of view (FOV) of 150 × 133 × 79 mm, and 18 slices with a slice thickness of 4 mm to cover the whole brain.

Image Preprocess

Images from all cases were visually examined first by the radiologists (ZL and LW) for the image quality and artifacts. We then used the Smallest Univalue Segment Assimilating Nucleus (SUSAN) technique (FSL v5.0, FMRIB, Oxford, UK), a filtering technique that preserves the structures depicted in an image by only averaging a central voxel with neighboring voxels that have similar intensities (23), to reduce noise. FMRIB Linear Image Registration Tool (FLIRT) (FSL v5.0, FMRIB, Oxford, UK) (24) was then used to align the images to correct any motion artifacts before any analysis. Then, a histogram stretching algorithm was used for normalizing the image intensity of all images (25).

Lesion Identification and Segmentation

The pipeline of the feature identification and analysis processes is summarized in **Figure 1**. For the current study, we only focused on the abnormalities in globus pallidus, which is one of the earliest and most sensitive regions affected by the bilirubin toxicity in ABE (26). An abnormal appearance of increased signal intensity on T_1-weighted spin echo images in the region is shown in **Figure 2**, allowing for extracting globus pallidus from T_1-weighted images as the region of interest (ROI). In the ABE case with characteristic imaging findings, the bilateral globus pallidus has a sharp contrast with a well-defined margin for manual segmentation. One radiologist (ZL) with more than 5 years of experience in neuroimaging manually contoured the structure of globus pallidus using open source Imaging Biomarker Explorer Software (IBEX software, MD Anderson Cancer Center, Houston, Texas, US) (27). When the contour of globus pallidus was not well-defined, we referenced the cross-sectional gross anatomy of globus pallidus and also used the silhouette of an ABE case with typical image characteristics as the reference (**Figure 2**). Instead of segmenting globus pallidus independently in different groups, we referenced the clear silhouette of ABE

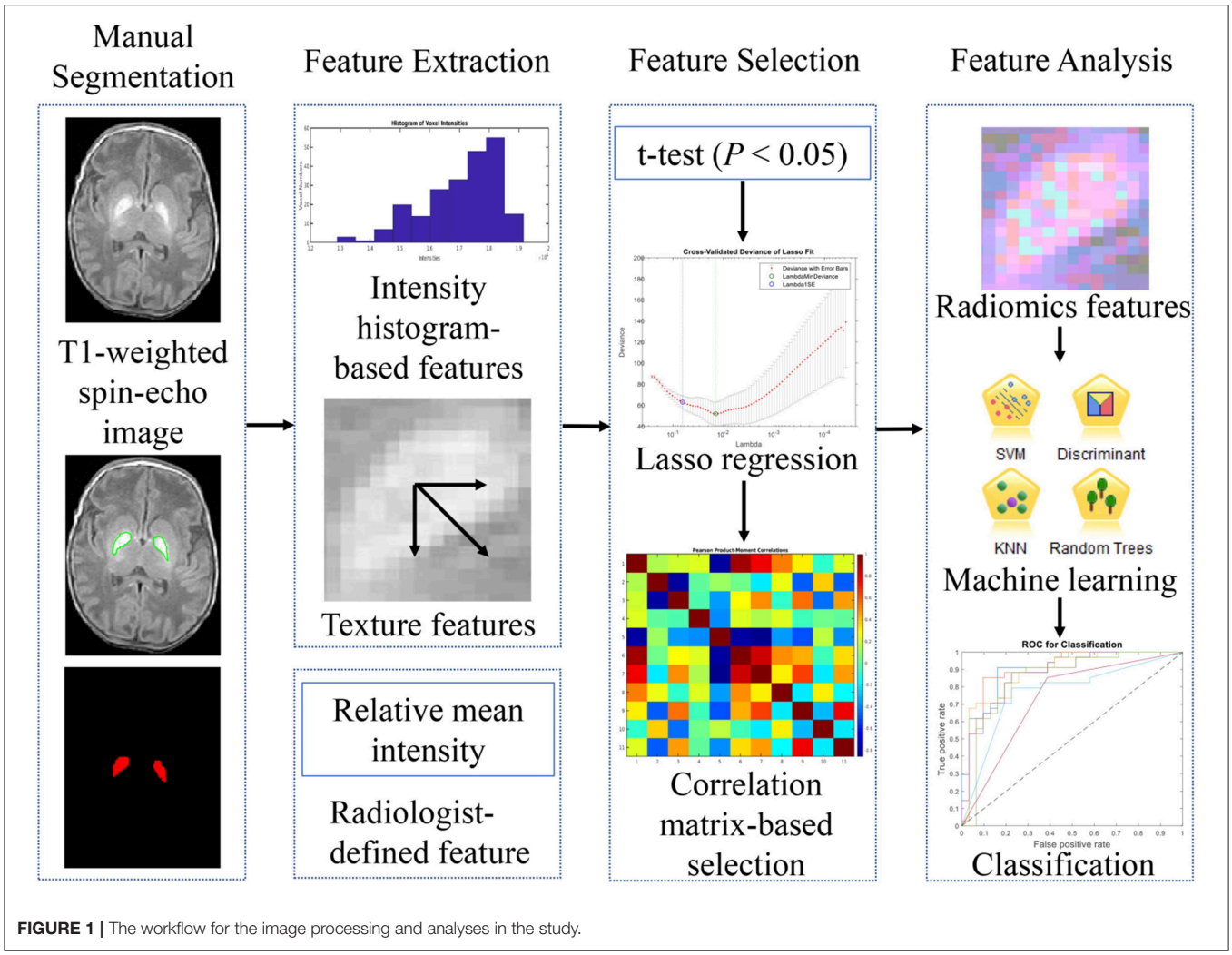

FIGURE 1 | The workflow for the image processing and analyses in the study.

cases with typical imaging findings of ABE in order to ensure that the segmented globus pallidi were comparable in shape between ABE cases and controls. Similarly, we manually delineated the boundary of globus pallidus in control cases based on the cross-sectional neuroanatomy and the corresponding regions of ABE cases with well-defined globus pallidus. In total, three continuous slices containing globus pallidus on T_1-weighted images for each neonate were chosen. After initial segmentation, each ROI was reviewed and adjusted by two radiologists (LW and YZ) with more than 25 years of experience in neuroradiology, with any discrepancy resolved through discussion.

Feature Extraction

Once the segmented globus pallidus was obtained, 1,318 radiomics features from ROIs were extracted using IBEX software. All of the extracted features were then grouped into two main categories and nine subcategories (27), including the first-order statistics (intensity-histogram-based features): (1) intensity histogram gauss fit-based features; (2) histogram gradient orientation-based features; (3) intensity histogram-based features; (4) intensity direct-based features and higher-order statistics (texture features): (5) gray level co-occurrence matrix-based features [GLCM, 2-Dimensions (2-D)]; (6) GLCM (3-D); (7) gray level run length matrix-based features (GLRLM); (8) neighborhood gray-tone difference matrix features (NGTDM, 2-D); and (9) NGTDM (3-D) (28).

To follow the conventional reading strategy and to quantify the average intensity level of globus pallidus, we added a "radiologist-defined feature," i.e., the relative mean intensity of globus pallidus, which corresponds to the average intensity of segmented globus pallidus in the second slice of the three chosen slices normalized by the average intensity of cerebrospinal fluid (CSF) in the segmented region of lateral ventricle of the same slice. Then, two histograms based on the distribution of the relative mean intensity of ABE cases and control cases were generated and curve-fitted by non-linear polynomial regression using MATLAB (2018b, Mathworks, USA).

Feature Selection

To improve the accuracy and efficiency of classifications, irrelevant and redundant features were identified and excluded. We used three feature selection methods sequentially to select

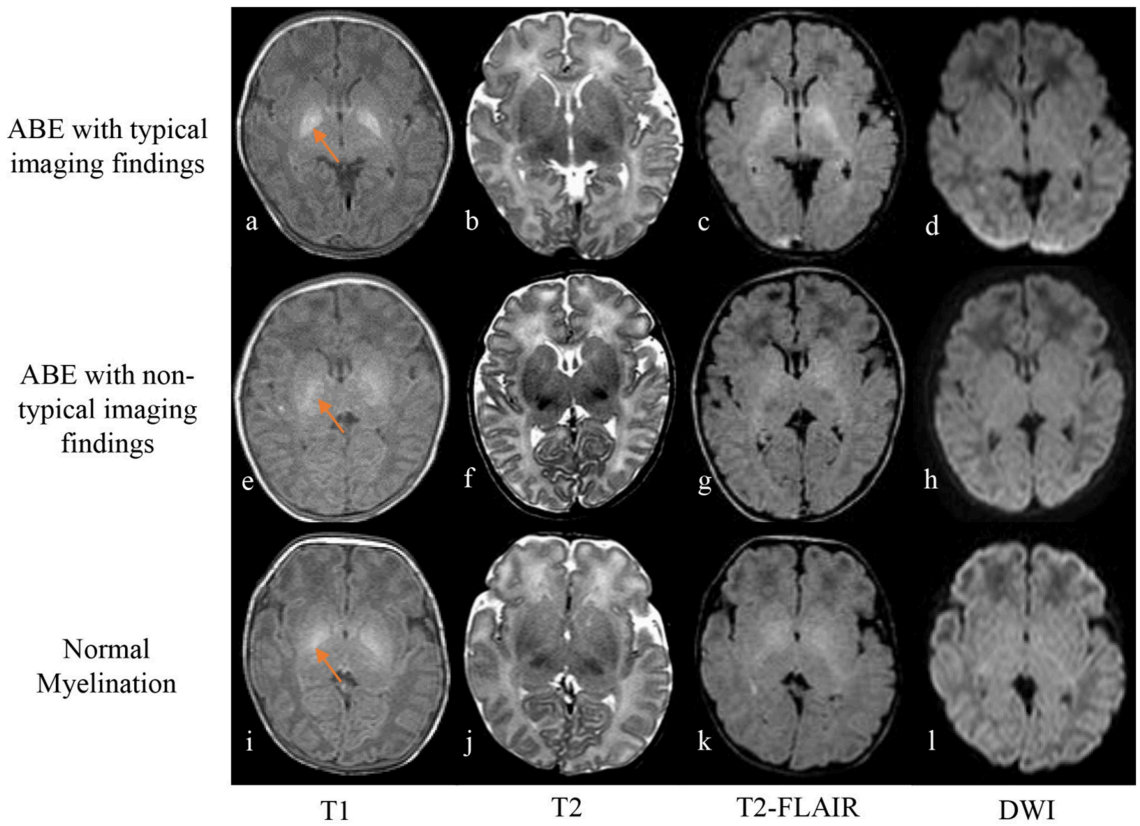

FIGURE 2 | Axial T_1-weighted spin echo image **(a)** shows strikingly hyperintense signal in the globus pallidus with well-defined boundary in a neonate of 10 days old with ABE **(a–d)**, while T_2-weighted fast spin echo image **(b)** and FLAIR image **(c)** show slightly and moderately high signal intensity, compared with the signal intensity of the surrounding basal ganglia region, respectively. No abnormal signal intensity was detected on DWI **(d)**. However, in cases of a 4-day-old neonate with radiologically untypical ABE **(e–h)** and a case of 9-day-old ABE-alike neonate with normal myelination **(i–l)**, imaging findings include hazy slight hyperintensity on T_1-weighted image **(e,i)**, iso-intensity on T_2-weighted image **(f,j)**, slightly high signal intensity on T_2-weighted FLAIR images **(g,k)**, and no obvious abnormal signal intensity on DWI **(h,l)** in the region of globus pallidus with referencing the signal intensity of the surrounding region of basal ganglia.

informative radiomics features from 1,318 graphic features obtained using IBEX software. Firstly, a two-sample *t*-test was used to select those features with statistically significant difference between ABE cases and control cases ($P < 0.05$). To increase the model interpretability and reduce overfitting, the least absolute shrinkage and selection operator (Lasso) regression algorithm (29) was then applied to the remaining features to further reduce irrelevant features. Those features yielding to the lambda (λ) value (a tuning parameter) with minimal deviance were chosen as the most informative features.

Feature Correlation

To follow the principle that good features are highly correlated with the predictive target, but remain to be independent to each other (30), we evaluated the correlation between each pair of the selected features. A correlation-matrix map was generated based on the correlation between each chosen feature to illustrate and determine the redundancy. In correlation-based feature elimination, we did not remove all correlated features like previous studies (31, 32). Instead, we only removed those features with an *r*-value of 1 or −1, termed as linearly correlated features, which usually are calculated using the same formula, but different directions and offsets based on the generated matrix. Then, one representative feature in each group of linearly correlated features was used as the discriminative feature for further analysis, since this feature can represent the other linearly correlated features within the same group. The remaining features ($-1 < r < 1$) were put into the group of relatively independent features.

Classification

The features chosen for classifying ABE and normal myelination conditions included the selected most discriminative features and the radiologist-defined feature. Based on multiple classification algorithms, including logistic regression, discriminant analysis, k-nearest neighborhood (KNN), Naïve Bayes, support vector machine (SVM), decision trees, and ensemble tree-bagger (33), and the chosen features, a prediction model was built to differentiate ABE from normal myelination with a leave-one-out cross-validation scheme used to split the data into training set and testing set randomly. To compare the overall performance of each classifier, the value of the area under the curve (AUC) was calculated based on receiver operating characteristics (ROC)

analysis. Also, the accuracy was obtained from the best cutoff point in the ROC curve for each classifier. Then, features were ranked based on their importance contributing to the classification performance using the Fisher score, an independent filter model aiming to not interact with the bias of a classification learning algorithm (34).

Statistical Analysis

MATLAB (2018b, Mathworks, USA) was used to perform all the statistical analysis, which included calculating the relative mean intensity of the segmented globus pallidus, generating the histogram of relative mean intensity of globus pallidus, feature selection using two-sample *t*-test, Lasso regression algorithm, and correlation-matrix heat map generated using Pearson's correlation, classification using multiple classification algorithms with ROC analysis, and features ranking based on Fisher score. Nonparametric Mood's median test was used to determine whether the medians of the two independent groups (ABE group vs. normal myelination group) from which two samples are drawn are identical, with $P < 0.05$ indicating statistically significant difference. Then, two-sample independent *t*-test was used to compare clinical variables, such as birth weight and different kinds of bilirubin level, with $P < 0.05$ indicating statistically significant difference.

RESULTS

Clinical Findings and Subject Characteristics

In 61 neonates included in this study, we found no statistically significant difference in the average equivalent age ($P = 0.063$) between neonates with ABE ($n = 32$, 276.1 ± 10.4 days) and age-matched controls with normal myelination ($n = 29$, 262.1 ± 22.3 days). It should be noted that controls had more preterm neonates (16/29 vs. 5/32) and slightly lower birth weight (2686.7 ± 918.2 vs. 3027.5 ± 404.6 g) but with no statistical difference ($P = 0.107$). The neonates with ABE had a much higher mean bilirubin level than did controls as shown by the transcutaneous bilirubin level (25.3 ± 5.5 vs. 10.9 ± 2.3 mg/dl), peak TSB (500.1 ± 78.8 vs. 139.3 ± 58.3 μmol/L), and unconjugated serum bilirubin (482.8 ± 73.4 vs. 127.4 ± 58.3 μmol/L) (all $P < 0.00001$). Demographic information is summarized in **Table 1**.

TABLE 1 | Clinical characteristics of neonates with ABE and control neonates.

	Neonates with ABE	Control neonates	*P*-value
Gender (male/female)	15/17	19/10	–
Equivalent age (days)	276.1 ± 10.4	262.1 ± 22.3	0.063
Term/preterm	27/5	13/16	–
Birth weight (g)	3027.9 ± 404.6	2686.7 ± 918.2 (2 NA)	0.106
Transcutaneous bilirubin level (mg/dl)	25.3 ± 5.5 (1 NA)	10.9 ± 2.3 (11 NA)	<0.00001
Peak total serum bilirubin (pTSB) (μmol/L)	500.1 ± 78.8	139.3 ± 58.3 (2 NA)	<0.00001
Unconjugated serum bilirubin (μmol/L)	482.8 ± 73.4	127.4 ± 58.3 (2 NA)	<0.00001

NA, not available; equivalent age = gestational age + age after birth.

Figure 2 shows images of an ABE case with characteristic imaging contrast change in the affected region, an ABE case with ambiguous imaging findings, and a control case with normal myelination. The neonates with radiologically typical ABE (2/32) exhibited bilateral symmetrical pronounced hyperintensity in the globus pallidus on T_1-weighted spin echo images with a well-defined boundary and no obvious signal abnormalities on T_2-weighted spin echo, FLAIR, and DWI (**Figures 2a–d**). However, most ABE cases (30/32) did not present such sharp contrast on T_1-weighted spin echo images in the region of globus pallidus with a well-defined boundary but showed varying degrees of increased signal intensity compared to the signal intensity of the surrounding structures of basal ganglia (**Figures 2e–h**). All the controls also showed slight to moderate elevation of signal intensity in globus pallidus on T_1-weighted spin echo images varied in different degrees (**Figures 2i–l**), consistent with the signal intensity change due to normal myelination in newborns. Such a pattern of signal-intensity increase mimics MRI contrast appearance of a radiologically atypical ABE. For T_2-weighted spin echo images, only 3 ABE cases (3/32) showed slightly high signal intensity in the region of globus pallidus in contrast to the signal intensity of the surrounding basal ganglia region (**Figure 2b**), and no controls showed any obvious signal changes (**Figure 2j**). Interestingly, all the ABE cases and controls with normal myelination showed slightly high signal intensity on T_2-weighted FLAIR images in comparison to the signal intensity of surrounding basal ganglia region (**Figures 2c,g,k**), suggesting that FLAIR sequence may not be a proper imaging method for differentiating ABE from normal myelination. For DWI, no apparent abnormal signal intensity was found in both ABE and control cases, suggesting no substantial effect from ABE and normal myelination on the diffusion properties of the tissue at this point.

Radiomics Features

The feature extraction program automatically identified 1,318 features from ROIs on T_1-weighted spin echo images. Among these, 81 features with statistically significant difference between ABE cases and controls ($P < 0.05$) were selected using two-sample *t*-test. After the Lasso regression algorithm was applied for further feature reduction, 18 features were chosen based on the corresponding lambda (λ) value with minimal deviance (**Figure S1**). **Figure 3** shows the correlation between each pair of these 18 features, presented as a heat map of correlation matrix. We found six non-redundant features ($-1 < r < 1$), with six pairs of linearly correlated features ($r = 1$) in the remaining 12 features. After the correlation-matrix-based feature selection, one representative feature for each linearly correlated feature group ($n = 6$) and six relatively independent features were chosen for further analysis (more details in **Figure 3**). The process of

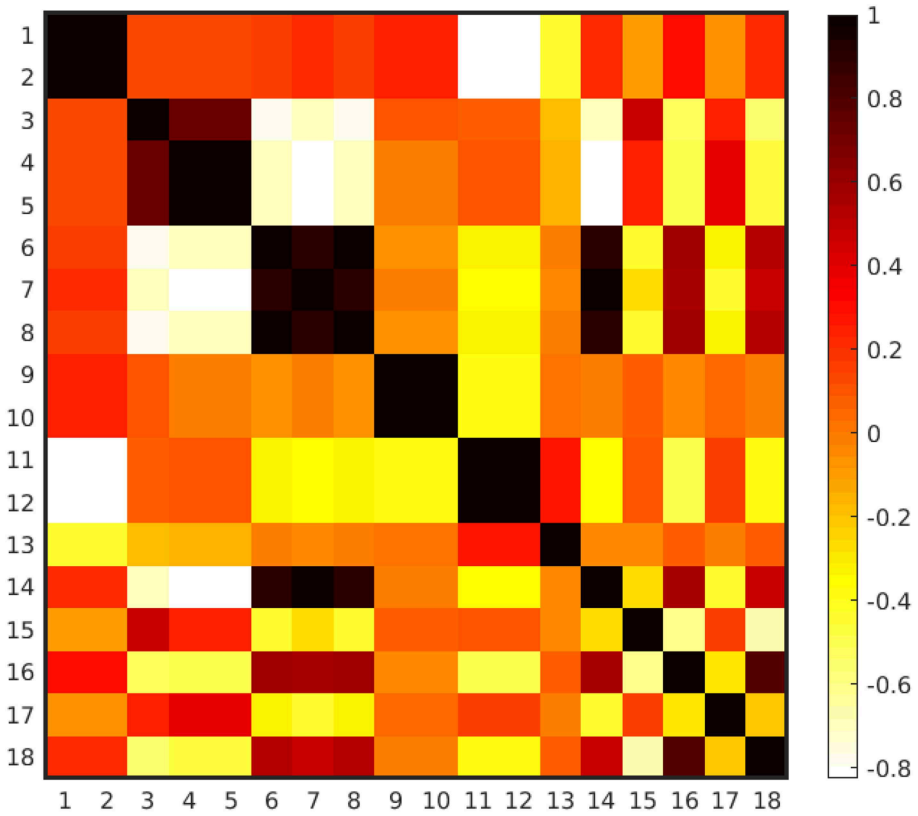

Feature group (r = 1)	Number	Name
group 1	1, 2	Entropy (0-7, 180-7)
group 2	4, 5	IMC1 (45-7, 225-7)
group 3	6, 8	IMC2 (45-4, 225-4)
group 4	7, 14	IMC 2 (45-7, 4-7)
group 5	9, 10	Inverse Variance (135-7, 315-7)
group 6	11, 12	Maximum Probability (135-7, 315-7)
(-1 < r < 1)	3, 13, 15 16, 17 18	IMC1 (-333-7), Cluster shade, Inverse Variance (-333-1), Contrast (2D), Busyness, Contrast (3D)

FIGURE 3 | The correlation-matrix heat map based on the correlation between each feature pair of the selected 18 features. All 18 features were calculated with direction of 0, 45, 90, 135, 180, 225, 270, and 315°, and offset of 1, 4, and 7, respectively. For instance, based on the matrix generated from the segmented globus pallidus, entropy (0°-7) was calculated with direction = 0° and offset = 7, while maximum probability (135°-7) indicates that maximum probability was calculated with direction = 135° and offset = 7.

the feature selection is plotted in **Figure 4** with more detailed information summarized in **Table S1** with descriptions of 12 selected features provided in **Table S2**.

Classifications

Based on the 12 selected features and one radiologist-defined feature, decision trees had the best classification performance with an AUC of 0.946, followed by SVM, tree-bagger, logistic regression, Naïve Bayes, discriminant analysis, and KNN, which have an AUC of 0.931, 0.925, 0.905, 0.891, 0.883, and 0.817, respectively, as shown in **Figure 5A**. On the other hand, when using the misclassification rate to evaluate the accuracy of discriminating ABE neonates and controls, the logistic regression algorithm and tree-bagger performed better than others with 9.38, 0% for misclassifying ABE and 13.79, 24.14% for misclassifying the control condition, respectively. Detailed

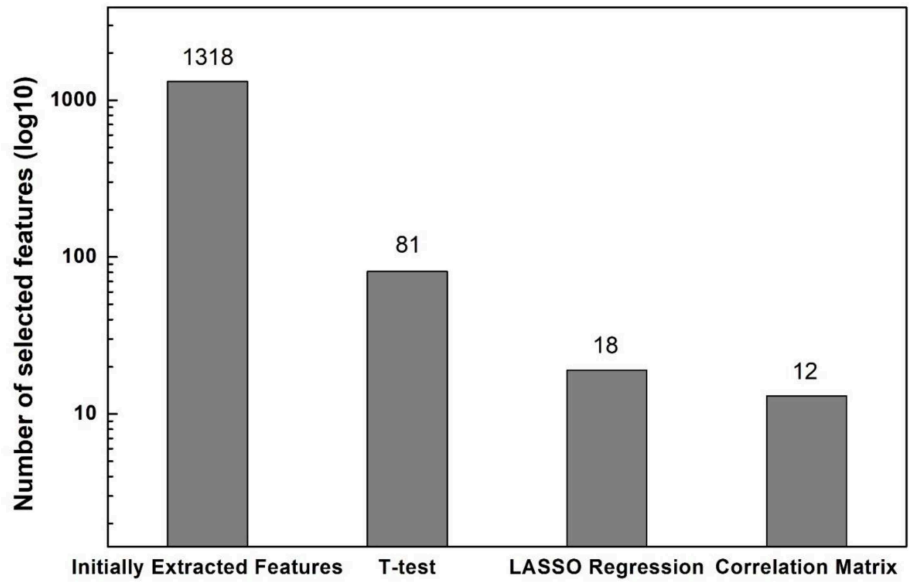

FIGURE 4 | Numbers of features selected after each feature selection method performed sequentially.

comparisons are presented in **Figure 5B**. As a whole, both logistic regression algorithm and tree-bagger had the highest accuracy of 88.5% to differentiate ABE from controls compared to other machine learning classifiers.

Feature Ranking and Contribution

Thirteen features used for classification were ranked using the Fisher score (**Figure 6**) according to their importance in discriminating ABE from the normal myelination. Among them, the relative mean intensity, which reflects the overall brightness of segmented globus pallidus, was the most discriminative feature. It is significantly higher in ABE cases than that in controls ($P < 0.0001$). Importantly, the results from radiomics analysis of image features provided insight into the inherited challenges of using the conventional signal intensity-focused radiology reading strategy to diagnose ABE. Histograms of the relative mean intensity from the segmented globus pallidus in the ABE and control groups shown in **Figure 7** revealed the significant overlap of similar image contrast of ABE and normal myelination conditions that contribute to the difficulty of distinguishing ABE from normal myelination, if it is simply based on the signal intensity change in the images.

In addition, nine different texture features in the GLCM category had significant contributions to the discrimination of ABE from normal myelination. Finally, three other texture features selected in the category of NGTDM, including contrast computed from 2D to 3D images, respectively, and busyness were found to be useful in the classification as they revealed intra-lesion spatial neighbor intensity difference of abnormalities. However, no first-order statistical feature (i.e., intensity histogram-based feature) and feature within the category of GLRLM were found as distinct features based on the current criteria used in this study.

DISCUSSION

Although MRI has been increasingly used to investigate the neuropathology induced by ABE in the neonatal clinical settings, the conventional reading strategy solely based on overall intensity alteration of the globus pallidus on T_1-weighted images is not sufficiently effective and accurate. The current study applied a radiomics-based machine learning approach to extract specific image features to discriminate neonates with ABE from controls with normal myelination. The results suggested that this approach improved the characterization of abnormalities and thus achieved a better classification of these two conditions.

Clinically, most ABE cases do not show characteristic signal abnormalities in MRI and thus are not readily distinguishable from normal myelination. As shown in this study, only two cases with ABE showed typical striking hyperintensity in the region of globus pallidus, while other cases of ABE have various degrees of hyperintense contrast that overlap with the signal changes from normal myelination. In clinical routine, the common reading strategy of radiologists focuses on identifying the relatively higher signal intensity induced by ABE than that of normal myelination on T_1-weighted image, since usually, signal abnormality tends to vary from moderately high to very high for ABE and slightly high to moderately high for normal myelination based on poorly quantitative visual impression. However, depending on the experience and expertise level of radiologists, such a subjective judgment is susceptible to inter- and intra-observer variability in interpreting ABE. Worth noting, the radiologist-defined feature, the relative mean intensity of the segmented globus pallidus outperformed 12 selected texture features as the most discriminative feature to differentiate ABE from normal myelination, suggesting the robustness of the conventional intensity-based reading strategy

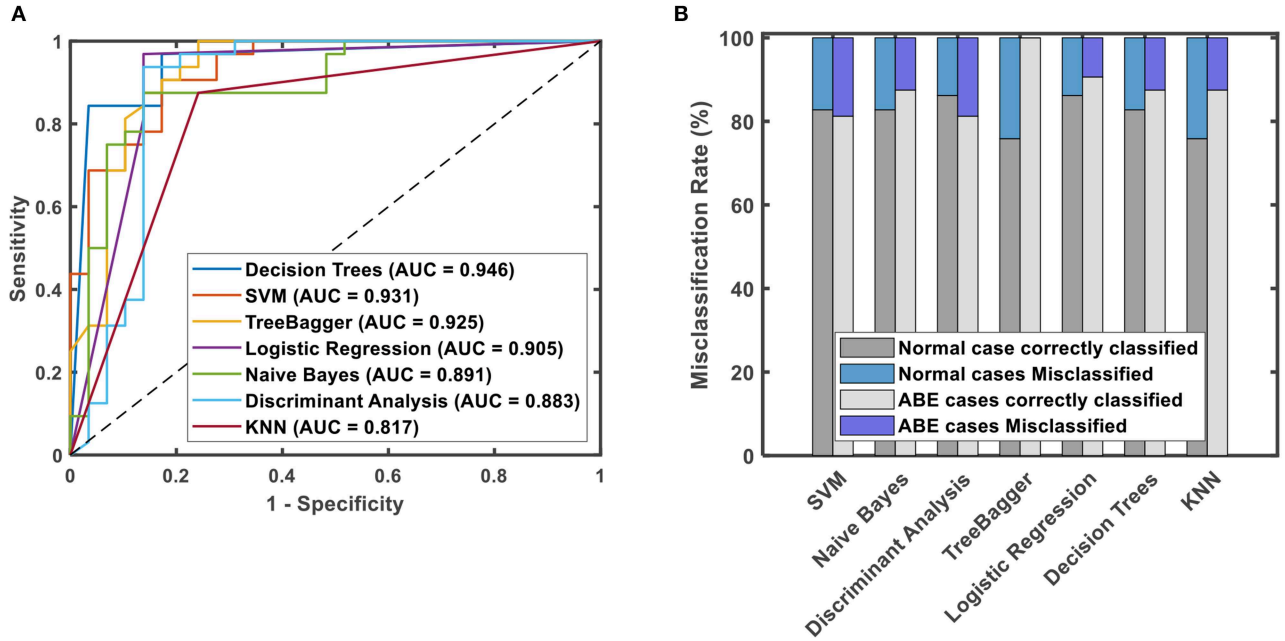

FIGURE 5 | ROC curves with values of AUC for different classification methods using 13 discriminative features **(A)** and misclassification rates for normal cases and ABE cases for different prediction models **(B)**.

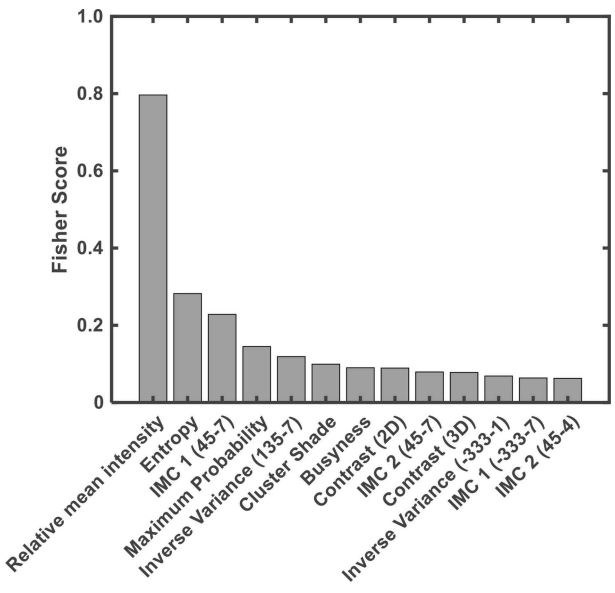

FIGURE 6 | Contributions of features in discriminating ABE and controls were ranked based on their Fisher score. IMC 1 & 2 = information measure of correlation 1 and 2.

used by the radiologists who have developed sufficient experience in recognizing subtle intensity changes and differences caused by the disease. However, compared to the experience-dependent traditional visual-based pattern recognition, using computational algorithms to extract fine graphical features and descriptors on changes in image intensity and contrast in a more quantitative manner can eliminate the inter- and intra-observer subjective variability in interpreting ABE.

The study also showed that additional texture features that are not readily recognized, described, or quantified by radiologists in the clinical routine reading can be identified by computational methods, allowing for using more quantitative parameters to better characterize the lesion and further enhance the discrimination of these two conditions. In our study, we found that three NGTDM features and nine GCLM features contributed to separating ABE from normal myelination. NGTDM features revealed the pattern of intra-lesion spatial intensity difference (28) of ABE associated with tissue relaxation time change induced by bilirubin toxicity. In contrast, GCLM features, which represent the spatial distribution of various gray-level combinations, reveals the regional heterogeneity of the affected tissue (35). The high accuracy in distinguishing ABE from normal myelination based on these morphological heterogeneity-associated texture features demonstrated the feasibility of utilizing additional texture features to detect, describe, and quantify the morphological heterogeneity of the globus pallidus induced by bilirubin accumulation. Importantly, it should be noted that this approach can be potentially expanded to diagnosing other types of neonatal encephalopathy that is diagnosed only based on signal intensity change.

ABE-positive cases included in the study were clinically confirmed with either positive serum indicators, and (or) positive imaging findings, and (or) neurological or behavioral symptoms. However, BIND scores cannot be obtained from some ABE

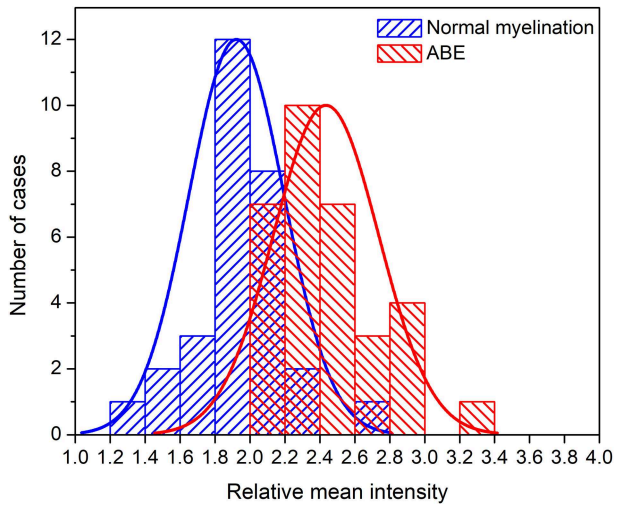

FIGURE 7 | Histograms of the relative mean intensity distribution plots from the groups of ABE and control with normal myelination.

cases due to either overlooked subtle neurological or behavioral symptoms or incomplete medical records in this retrospective study. In the future, a prospective study performing BIND score evaluation for any neonates with suspicious ABE is needed. The current proof-of-concept study only included a limited number of ABE subjects due to that MRI has yet to become a clinical standard practice for evaluating ABE and remaining technical challenges in neonatal MRI. Therefore, we did not attempt to follow these patients and further evaluate the possibility of using radiomics features to sub-classify these ABE cases to determine the severity of the conditions and difference between preterm and term neonates. Besides, we have applied multiple cross-validation methods, such as 10-, 5-fold, and leave-one-out method to reduce overfitting. Finally, we optioned to use leave-one-out method for its resulting relatively lower accuracy and AUC, considering minimizing the possibility of overfitting given a relatively small sample size. It is anticipated that training machine learning algorithms on a large cohort with larger sample size and more heterogeneous data acquired on an MRI scanner with higher magnetic field and testing them on an independent cohort should further validate the robustness of this approach to generalize a clinical feasible predictive model.

Another limitation of the current study is that we used manual contouring for segmentation of ROI, which is prone to inter-observer variability. We ensured to minimize the segmentation inaccuracy by referencing the cross-sectional gross anatomy and the ROIs determined in the ABE cases with typical imaging findings via double-blinded reading by the experienced radiologists. Although manual delineation is time-consuming and subject to introducing the bias from interpreters, it is currently considered as a "gold standard" for segmentation (36). A semiautomatic method, combining expert-based manual delineation and automatic segmentation algorithm, might improve the segmentation accuracy and thus further improve the accuracy of downstream classification in the future. Furthermore, the current study only focused on extracting radiomics features from T_1-weighted images, attempting to follow the conventional reading strategy of interpreting ABE for comparison. It is expected that the classification performance of the reported approach will be further improved by incorporating features extracted from multi-parametric MRI, including those features associated with tissue microenvironment alterations, such as relaxation time change (T_1-mapping), cellularity (DWI), integrity and maturity of white matter tract (diffusion tensor imaging), and metabolism (magnetic resonance spectroscopy).

CONCLUSION

The current study demonstrated the feasibility of using a radiomics-based machine learning approach to analyze overlapped hyperintense signal patterns of globus pallidus on T_1-weighted spin echo images between neonates with ABE and normal myelination to improve the differentiation of these two conditions. Compared to the experience-dependent visual-based conventional reading strategy, incorporating radiomics features improved the lesion characterizations with more descriptors and more quantitative and objective measurements for ABE-induced intensity change and morphological heterogeneity. The results support the potential utility of such an approach to assist the clinical prediction on the risk and development of neurological damages in neonates with hyperbilirubinemia.

DATA AVAILABILITY STATEMENT

The datasets generated for this study are available on request to the corresponding author.

ETHICS STATEMENT

This retrospective study is approved by the Institutional Review Board of the People's Hospital of Longhua, Shenzhen China. The study was carried out in accordance with the Declaration of Helsinki with written informed consent waived from the custodians of all subjects.

AUTHOR CONTRIBUTIONS

LW and HM contributed to project idea and supervision and to manuscript revision, and maintained integrity of this manuscript. ZL implemented the whole study, analyzed the data, and drafted the manuscript. BJ and YZ contributed to statistical analysis and reviewed the manuscript. LD, SM, and LL collected the raw data. GC and XY provided technical support. All authors had reviewed this manuscript critically and approved its final submission.

FUNDING

This work was supported in part by the grant from the China Scholar Council to ZL.

ACKNOWLEDGMENTS

We thank Department of Radiology and Imaging Sciences of Emory University School of Medicine for supporting ZL to study and carry out this project at Emory University.

SUPPLEMENTARY MATERIAL

The Supplementary Material for this article can be found online at: https://www.frontiersin.org/articles/10.3389/fneur.2019.01018/full#supplementary-material

REFERENCES

1. Allen D. Neonatal jaundice. *Nurs Child Young People.* (2016) 28:11. doi: 10.7748/ncyp.28.6.11.s15
2. Wei KL, Yang YJ, Yao YJ, Du LZ, Wang QH, Wang RH, et al. Epidemiologic survey on hospitalized neonates in China. *Transl Pediatr.* (2012) 1:15–22. doi: 10.3978/j.issn.2224-4336.2011.10.01
3. Watchko JF. Kernicterus and the molecular mechanisms of bilirubin-induced CNS injury in newborns. *Neuromolecular Med.* (2006) 8:513–29. doi: 10.1385/NMM:8:4:513
4. Bhutani VK, Wong RJ, Stevenson DK. Hyperbilirubinemia in preterm neonates. *Clin Perinatol.* (2016) 43:215–32. doi: 10.1016/j.clp.2016.01.001
5. Smitherman H, Stark AR, Bhutani VK. Early recognition of neonatal hyperbilirubinemia and its emergent management. *Semin Fetal Neonatal Med.* (2006) 11:214–24. doi: 10.1016/j.siny.2006.02.002
6. Maisels MJ. Managing the jaundiced newborn: a persistent challenge. *CMAJ.* (2015) 187:335–43. doi: 10.1503/cmaj.122117
7. Wennberg R. Unbound bilirubin: a better predictor of kernicterus? *Clin Chem.* (2008) 54:207–8. doi: 10.1373/clinchem.2007.098319
8. Iskander I, Gamaleldin R, El Houchi S, El Shenawy A, Seoud I, El Gharbawi N, et al. Serum bilirubin and bilirubin/albumin ratio as predictors of bilirubin encephalopathy. *Pediatrics.* (2014) 134:e1330–9. doi: 10.1542/peds.2013-1764
9. Bhutani VK, Johnson-Hamerman L. The clinical syndrome of bilirubin-induced neurologic dysfunction. *Semin Fetal Neonatal Med.* (2015) 20:6–13. doi: 10.1016/j.siny.2014.12.008
10. American Academy of Pediatrics Subcommittee on Hyperbilirubinemia. (2004). Management of hyperbilirubinemia in the newborn infant 35 or more weeks of gestation. *Pediatrics.* 114, 297–316. doi: 10.1542/peds.114.1.297
11. Wisnowski JL, Panigrahy A, Painter MJ, Watchko JF. Magnetic resonance imaging of bilirubin encephalopathy: current limitations and future promise. *Semin Perinatol.* (2014) 38:422–8. doi: 10.1053/j.semperi.2014.08.005
12. Coskun A, Yikilmaz A, Kumandas S, Karahan OI, Akcakus M, Manav A. Hyperintense globus pallidus on T1-weighted MR imaging in acute kernicterus: Is it common or rare? *Eur Radiol.* (2005) 15:1263–7. doi: 10.1007/s00330-004-2502-2
13. Gkoltsiou K, Tzoufi M, Counsell S, Rutherford M, Cowan F. Serial brain MRI and ultrasound findings: relation to gestational age, bilirubin level, neonatal neurologic status and neurodevelopmental outcome in infants at risk of kernicterus. *Early Hum Dev.* (2008) 84:829–38. doi: 10.1016/j.earlhumdev.2008.09.008
14. Wang X, Wu W, Hou BL, Zhang P, Chineah A, Liu F, et al. Studying neonatal bilirubin encephalopathy with conventional MRI, MRS, and DWI. *Neuroradiology.* (2008) 50:885–93. doi: 10.1007/s00234-008-0423-5
15. Barkovich AJ. MR of the normal neonatal brain: assessment of deep structures. *AJNR Am J Neuroradiol.* (1998) 19:1397–403.
16. Park YW, Oh J, You SC, Han K, Ahn SS, Choi YS, et al. Radiomics and machine learning may accurately predict the grade and histological subtype in meningiomas using conventional and diffusion tensor imaging. *Eur Radiol.* (2019) 29:4068–76. doi: 10.1007/s00330-018-5830-3
17. Meier A, Veeraraghavan H, Nougaret S, Lakhman Y, Sosa R, Soslow RA, et al. Association between CT-texture-derived tumor heterogeneity, outcomes, and BRCA mutation status in patients with high-grade serous ovarian cancer. *Abdom Radiol.* (2019) 44:2040–7. doi: 10.1007/s00261-018-1840-5
18. Lohmann P, Kocher M, Steger J, Galldiks N. Radiomics derived from amino-acid PET and conventional MRI in patients with high-grade gliomas. *Q J Nucl Med Mol Imaging.* (2018) 62:272–80. doi: 10.23736/S1824-4785.18.03095-9
19. Zheng BH, Liu LZ, Zhang ZZ, Shi JY, Dong LQ, Tian LY, et al. Radiomics score: a potential prognostic imaging feature for postoperative survival of solitary HCC patients. *BMC Cancer.* (2018) 18:1148. doi: 10.1186/s12885-018-5024-z
20. Lambin P, Rios-Velazquez E, Leijenaar R, Carvalho S, van Stiphout RG, Granton P, et al. Radiomics: extracting more information from medical images using advanced feature analysis. *Eur J Cancer.* (2012) 48:441–6. doi: 10.1016/j.ejca.2011.11.036
21. Gillies RJ, Kinahan PE, Hricak H. Radiomics: images are more than pictures, they are data. *Radiology.* (2016) 278:563–77. doi: 10.1148/radiol.2015151169
22. Johnson L, Brown A, Bhutani V. BIND—A clinical score for bilirubin induced neurologic dysfunction in newborns. *Pediatrics.* (1999) 104:746–7.
23. Smith SM, Brady JM. SUSAN—A new approach to low level image processing. *Int J Comput Vis.* (1997) 23:45–78. doi: 10.1023/A:1007963824710
24. Jenkinson M, Bannister P, Brady M, Smith S. Improved optimization for the robust and accurate linear registration and motion correction of brain images. *Neuroimage.* (2002) 17:825–41. doi: 10.1006/nimg.2002.1132
25. Sun XF, Lin S, Luo YS, Yang W, Li HP, Liang PP, et al. Histogram-based normalization technique on human brain magnetic resonance images from different acquisitions. *BioMed Eng Online.* (2015) 14:73. doi: 10.1186/s12938-015-0064-y
26. Sari S, Yavuz A, Batur A, Bora A, Caksen H. Brain magnetic resonance imaging and magnetic resonance spectroscopy findings of children with kernicterus. *Pol J Radiol.* (2015) 80:72–80. doi: 10.12659/PJR.892643
27. Zhang L, Fried DV, Fave XJ, Hunter LA, Yang J, Court LE. IBEX: an open infrastructure software platform to facilitate collaborative work in radiomics. *Med Phys.* (2015) 42:1341–53. doi: 10.1118/1.4908210
28. Amadasun M, King R. Textural features corresponding to textural properties. *IEEE Trans Syst Man Cybern.* (1989) 19:1264–74. doi: 10.1109/21.44046
29. Tibshirani R. Regression shrinkage and selection via the lasso. *J R Stat Soc Ser B.* (1996) 267–88. doi: 10.1111/j.2517-6161.1996.tb02080.x
30. Hall MA. *Correlation-based feature selection for machine learning* (Ph.D. thesis). Department of Computer Science, Waikato University, Hamilton, New Zealand (1999).
31. Liu Y, Kim J, Balagurunathan Y, Li Q, Garcia AL, Stringfield O, et al. Radiomic features are associated with EGFR mutation status in lung adenocarcinomas. *Clin Lung Cancer.* (2016) 17:441–448e446. doi: 10.1016/j.cllc.2016.02.001
32. Wu W, Parmar C, Grossmann P, Quackenbush J, Lambin P, Bussink J, et al. Exploratory study to identify radiomics classifiers for lung cancer histology. *Front Oncol.* (2016) 6:71. doi: 10.3389/fonc.2016.00071
33. Bastanlar Y, Ozuysal M. Introduction to machine learning. *Methods Mol Biol.* (2014) 1107:105–28. doi: 10.1007/978-1-62703-748-8_7
34. Chen Y-W, Lin C-J. Combining SVMs with various feature selection strategies. In: Guyon I, Nikravesh M, Gunn S, Zadeh LA, editors. *Feature Extraction. Studies in Fuzziness and Soft Computing.* Vol. 207. Berlin; Heidelberg: Springer (2006). p. 315–24.
35. Haralick RM, Shanmugam K. Textural features for image classification. *IEEE Trans Syst Man Cybern.* (1973) SMC-3:10–21. doi: 10.1109/TSMC.1973.4309314
36. Kumar V, Gu Y, Basu S, Berglund A, Eschrich SA, Schabath MB, et al. Radiomics: the process and the challenges. *Magn Reson Imaging.* (2012) 30:1234–48. doi: 10.1016/j.mri.2012.06.010

Conflict of Interest: The authors declare that the research was conducted in the absence of any commercial or financial relationships that could be construed as a potential conflict of interest.

frontiers in Neurology

ORIGINAL RESEARCH
published: 25 October 2019
doi: 10.3389/fneur.2019.01097

Machine Learning-Based Framework for Differential Diagnosis Between Vascular Dementia and Alzheimer's Disease Using Structural MRI Features

*Yineng Zheng[1], Haoming Guo[1], Lijuan Zhang[1], Jiahui Wu[1], Qi Li[2] and Fajin Lv[1]**

[1] Department of Radiology, The First Affiliated Hospital of Chongqing Medical University, Chongqing, China, [2] Department of Neurology, The First Affiliated Hospital of Chongqing Medical University, Chongqing, China

OPEN ACCESS

Edited by:
Feng Feng,
Peking Union Medical College Hospital (Chinese Academy of Medical Sciences), China

Reviewed by:
Yi Zhang,
Sichuan University, China
Kun Nie,
Guangdong Provincial People's Hospital, China

***Correspondence:**
Fajin Lv
fajinlv@163.com

Specialty section:
This article was submitted to Applied Neuroimaging, a section of the journal Frontiers in Neurology

Received: *06 March 2019*
Accepted: *30 September 2019*
Published: *25 October 2019*

Citation:
Zheng Y, Guo H, Zhang L, Wu J, Li Q and Lv F (2019) Machine Learning-Based Framework for Differential Diagnosis Between Vascular Dementia and Alzheimer's Disease Using Structural MRI Features. Front. Neurol. 10:1097. doi: 10.3389/fneur.2019.01097

Background and Objective: Vascular dementia (VaD) and Alzheimer's disease (AD) could be characterized by the same syndrome of dementia. This study aims to assess whether multi-parameter features derived from structural MRI can serve as the informative biomarker for differential diagnosis between VaD and AD using machine learning.

Methods: A total of 93 patients imaged with brain MRI including 58 AD and 35 VaD confirmed by two chief physicians were recruited in this study from June 2013 to July 2019. Automated brain tissue segmentation was performed by the AccuBrain tool to extract multi-parameter volumetric measurements from different brain regions. Firstly, a total of 62 structural MRI biomarkers were addressed to select significantly different features between VaD and AD for dimensionality reduction. Then, the least absolute shrinkage and selection operator (LASSO) was further used to construct a feature set that is fed into a support vector machine (SVM) classifier. To ensure the unbiased evaluation of model performance, a comparative study of classification models was implemented by using different machine learning algorithms in order to determine which performs best in the application of differential diagnosis between VaD and AD. The diagnostic performance of the classification models was evaluated by the quantitative metrics derived from the receiver operating characteristic curve (ROC).

Results: The experimental results demonstrate that the SVM with RBF achieved an encouraging performance with sensitivity (SEN), specificity (SPE), and accuracy (ACC) values of 82.65%, 87.17%, and 84.35%, respectively (AUC = 0.861, 95% CI = 0.820–0.902), for the differential diagnosis between VaD and AD.

Conclusions: The proposed computer-aided diagnosis method highlights the potential of combining structural MRI and machine learning to support clinical decision making in distinction of VaD vs. AD.

Keywords: structural MRI, VaD and AD, SVM, machine learning, computer-aided diagnosis

INTRODUCTION

Dementia is a typical clinical syndrome of cognitive decline that interferes with the ability to perform daily activities (1) and occurs due to physical changes of brain structure and function. It is a progressive disease, indicating that it gets worse over time in terms of memory loss, cognitive dysfunction, and behavior. It is reported that the number of patients affected by dementia is believed to be close to 60 million people in 2018, and this number will almost reach 75 million in 2030 and triple with 130 million in 2050. Alzheimer's disease (AD) and vascular dementia (VaD) are the first and second most common forms of dementia, respectively (2). They have several symptoms, pathophysiology, and comorbid clinical manifestation that overlap that make them difficult to distinguish.

At present, the differential diagnosis between AD and VaD is still largely based on clinical guidelines with the exception of the exclusion of other diseases that are able to result in dementia. VaD is usually diagnosed through the combination of neurological examination, cognitive functioning tests, and brain scanning techniques (3). AD is often diagnosed by excluding other causes rather than being able to pinpoint the diagnosis through imageological or biochemical examination (4, 5). Conventional magnetic resonance imaging (MRI) could only discover certain clinical entities such as vascular changes and stroke or ischemic attack occurring in a specific area of brain (6), suggesting their association with VaD. Molecular neuroimaging technique plays an important role in the diagnosis of dementia (7), but it is difficult to determine the types of dementia. However, as is the case with AD, a definite diagnosis of VaD can only be made by brain autopsy. Although some similar cognitive examinations are employed to evaluate brain function (8), there is no test to diagnose AD at this time, so neurological physicians generally rule out other reversible causes of confusion such as normal pressure hydrocephalus, as well as other types of dementia or delirium.

Under attack by AD, the structure changes of temporal lobe, hippocampus, and entorhinal cortex may be changed firstly (4, 9). Hill et al. (10) suggested that structural MRI biomarkers could facilitate the clinical trials of AD. Moreover, several machine learning-based studies have successfully classified and predicted AD and mild cognitive impairment (MCI) using structural MRI features (11–13). It indicates that the changes of structural MRI are sensitive indicators for dementia, but there were no previous studies referring to the distinction between VaD and AD.

A series of studies mentioned above suggest that volumetric measurements of brain MR images are generally a significative type of biomarker. However, to our knowledge, whether multi-parameter structural MRI features can serve as the informative biomarker to detect the differences between VaD and AD is unknown, and little work has been done on machine learning to distinguish VaD from AD. Therefore, despite recent developments in the detection of AD, differential diagnosis between AD and VaD is still challenging and requires further investigation. It is critically important to find a way to be potentially capable of differentiating VaD from AD. In this study, we present a support vector machine (SVM)-based machine learning framework in combination with a range of volumetric measurements of different brain tissues to provide clinical information for differential diagnosis between VaD and AD (**Figure 1**).

MATERIALS AND METHODS

Subjects and Inclusion Criteria

This retrospective study was approved by the Ethics Committee of the First Affiliated Hospital of Chongqing Medical University. The written full informed consents were obtained from all subjects. From June 2013 to July 2019, 122 patients imaged with brain MRI who were hospitalized in the First Affiliated Hospital of Chongqing Medical University were recruited for this study. The diagnosis was confirmed by two chief physicians. VaD patients fulfilled the criteria of NINDS-AIREN (3) and AD patients fulfilled the criteria of NINCDS-ADRDA (14). Exclusion criteria are as follows: (1) patients have both AD and VaD ($n = 8$); (2) patients with suboptimal image quality because of head motion or susceptibility artifacts ($n = 14$); and (3) the areas of hyperintensities are so large that they have little influence on the segmentation accuracy of AD and VaD ($n = 7$). Finally, 58 AD patients and 35 VaD patients were enrolled and the demographic data are summarized in **Table 1**. Sex ratio and age distribution did not differ significantly between both groups (χ^2 test, $P = 0.73$ and Wilcoxon rank-sum test, $P = 0.24$).

MRI Acquisition

All subjects underwent multisequence imaging protocol on a 1.5-T MRI scanner (MAGNETOM ESSENZA, Siemens Healthineers, Germany and Signa HDxt, GE Healthcare, USA). For each patient, two sequences were collected in our study: (1) T1-weighted spin-echo (T1W) image: repetition time/echo time (TR/TE) = 1800/22 ms; matrix size = 512 × 512; field of view (FOV) = 240 × 240 mm^2; slice thickness = 3 mm; gap = 1.5 mm; (2) T2 fluid attenuated inversion recovery (T2 FLAIR) image: TR/TE = 8000/120 ms; matrix size = 512 × 512; field of view (FOV) = 240 × 240 mm^2; slice thickness = 3 mm; gap = 1.5 mm.

Image Pre-processing

Firstly, T1W and T2 FLAIR images are skull-stripped, performed using the FMRIB software library (http://fsl.fmrib.ox.ac.uk/fsl/fslwiki/FSL). Then, the skull-stripped T2 FLAIR images were aligned and registered to T1WI images using SPM12 based on rigid transformation and normalized mutual information (15). After the above operations, N4 bias correction was performed on T1W and T2 FLAIR images to remove low-frequency intensity non-uniformity (http://stnava.github.io/ANTs/).

MRI Structure-Based Feature Extraction and Selection

In our study, multi-parameter structural MRI indexes were used as the feature set to train and test machine learning model. A reliable and robust automated software AccuBrain

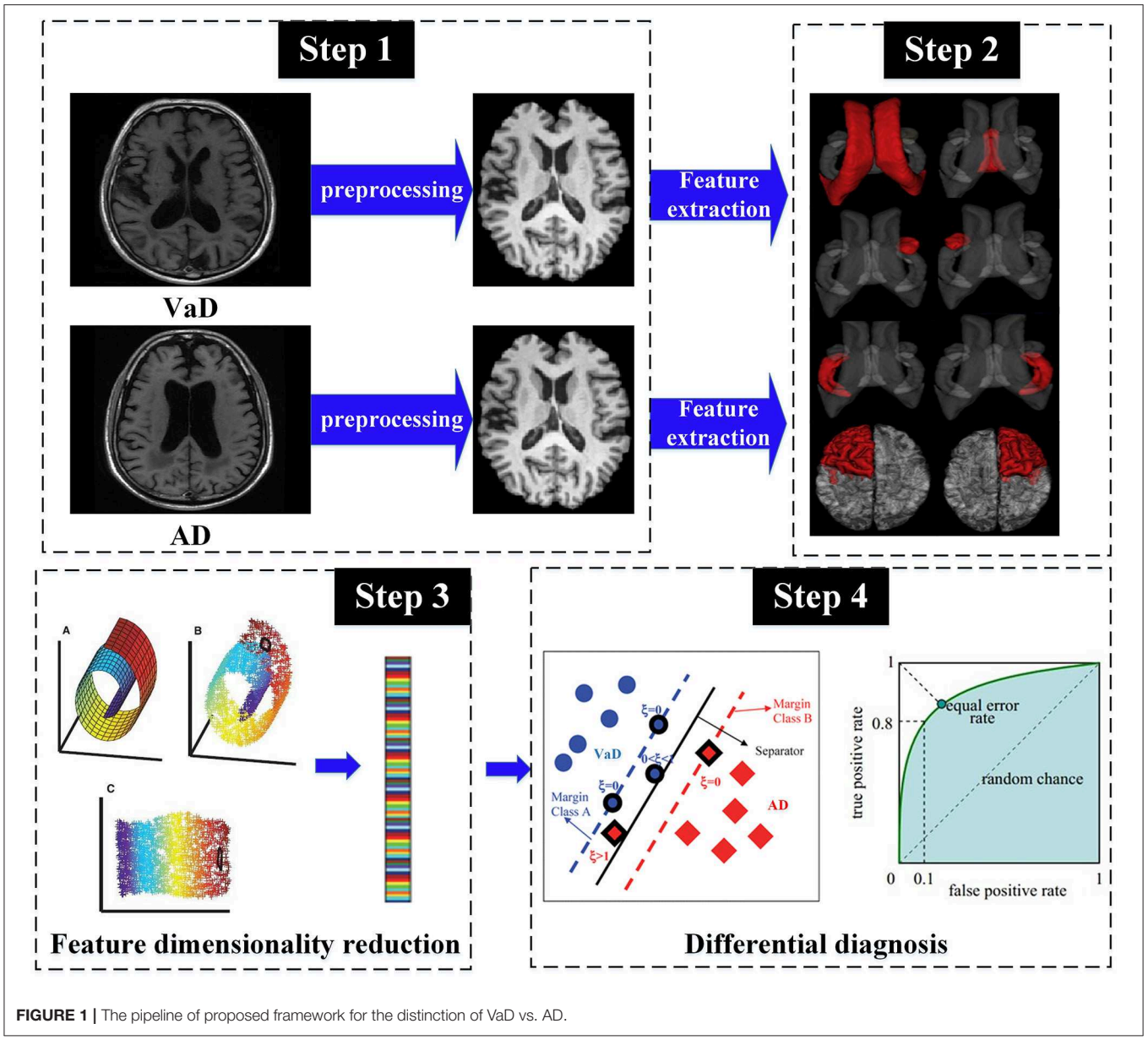

FIGURE 1 | The pipeline of proposed framework for the distinction of VaD vs. AD.

(BrainNow Medical Technology Limited, Hong Kong, China) performs brain structure and tissue segmentation to obtain multiple volumetric measurements of different brain substructures and subcortical tissues (16). It could provide the quantitative volumetry of memory-related cerebral areas in a fully automatic mode. After feature extraction, the next step is construction of the optimal feature subset. As feature selection is an important problem for pattern classification that has become an apparent need in machine learning, the effectiveness of features is directly associated with the performance of classifier. Firstly, normality and homogeneity of variance have been examined by Kolmogorov–Smirnov test and Levene test, respectively, and features with skewed distribution or normal distribution have been compared using the Mann–Whitney *U* test or independent Student *t* test to select certain volumetric indexes with significant difference ($P < 0.05$) as the representative features (17). Then, the least absolute shrinkage and selection operator (LASSO) method was used for the selected features to form the fusion feature signature (feature subset). The feature selection methods were performed with the R software (version 3.5.1; http://www.R-project.org).

Machine Learning Modeling and Performance Evaluation

The typical kernel algorithms in machine learning such as SVM were employed to identify VaD from AD. Based on structural risk minimization, SVM classifier finds an optimal separating hyperplane with maximum margin to distinguish VaD from

AD in the corresponding high-dimension feature space mapped by the input feature subset (18). In this study, we used the LibSVM toolbox (version 3.22) for the implementation of SVM classifier with linear and radial basis kernel functions (19). In addition, genetic algorithm (GA) was conducted to select the optimal parameters of the LibSVM classifier. For performance comparison of classification, we have adopted different machine learning algorithms such as K-nearest neighbor (KNN), logistic regression (LR), and random forest (RF) to test which model performs best in differentiating between VaD and AD, compared with SVM. A brief overview about the corresponding parameters of the classifiers is given in **Table 2**.

In this study, the dataset was divided into two portions called training set and testing set, 70% of which were used as training set, and the remaining 30% were used as test set. In the training set, we used the 10-fold cross-validation (CV) to train and tune the model. The training set was divided into 10 subsets, each as a verification set for monitoring and tuning the parameters of training process, and the other 9 subsets was used for training the model. The test set was used only to assess the performance of the model. In addition, a bootstrap resample method (1,000 times) was used to decrease the bias of overfitting and evaluate the robustness of each diagnostic model. Hence, the accuracy (ACC), sensitivity (SEN), specificity (SPE), and area under the curve (AUC) of model are calculated by taking the average of the results of 1,000 times tests. The detailed procedure of parameter tuning and performance testing is shown in **Figure 2**.

TABLE 1 | Demographic information.

	Patients with VaD	Patients with AD	*P*-value
Number	35	58	
Female/male	16/19	30/28	0.73
Age	72.74 ± 10.19	70.33 ± 9.18	0.24
MMSE	21.79 ± 5.31	22.61 ± 4.87	0.29

TABLE 2 | The implementation details of the different classifiers.

Classifiers	Parameter setting
KNN	20 different values of number of neighbors range from 2 to 21
LR	Penalty: L1, Tol = 0.0001, C = 1.0, Max_ iteration = 500
RF	Ntree = {100, 200, 300, 400, 500}, Mtr = [2:2:50]
SVM	Population_size = 50, Iteration = 1,000, Pc = [0.4, 0.99], Pm = [0.0001, 0.1], Kernel parameter = $\{10^{-2}, 10^{-1}, 10, 10^{2}\}$

KNN, K-nearest neighbor; LR, logistic regression; RF, random forest; SVM, support vector machine.

RESULTS

This section presents the experimental results obtained through the quantitative volumetry of structural MRI using AccuBrain software on T1W and T2 FLAIR imaging, as efficient biomarkers

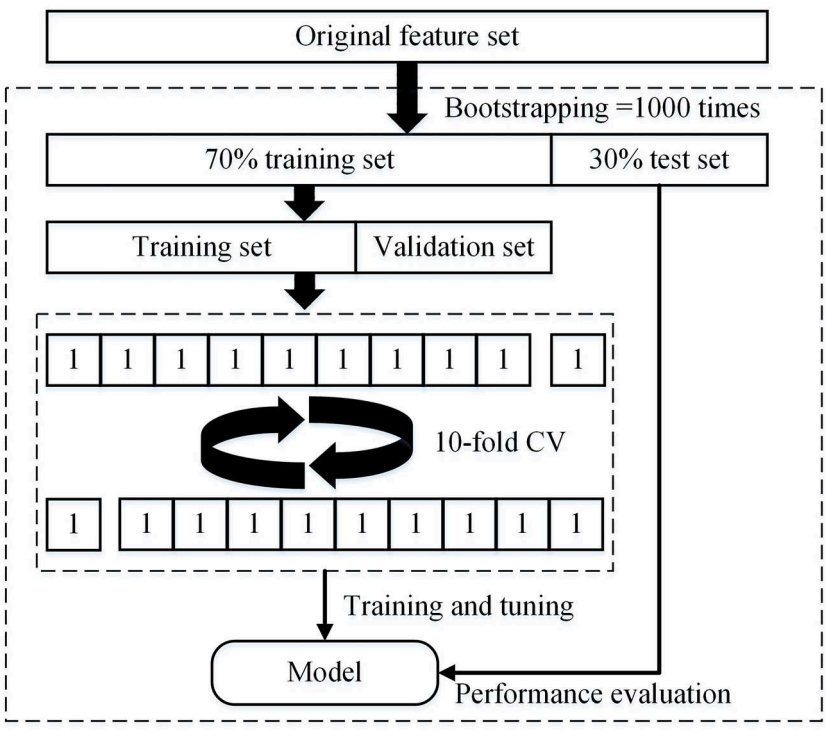

FIGURE 2 | Structure of the nested 10-fold cross-validation for evaluating the performance of machine learning models.

TABLE 3 | The structural MRI features with statistical differences between patients with VaD and AD.

	Brain substructures/regions	Volume (ml)		
		VaD	AD	*P*-value
Brain substructures	Hippocampus	5.62 ± 0.79	5.13 ± 0.74	**0.001**
	Amygdala	3.37 ± 0.49	2.63 ± 0.27	**0.001**
	Pallidum	2.23 ± 0.31	2.49 ± 0.51	**0.031**
	Accumbens nucleus	0.77 ± 0.14	0.68 ± 0.11	**0.003**
Symmetry of brain substructures	Hippocampus (L)	2.90 ± 0.53	2.47 ± 0.42	**0.004**
	Hippocampus (R)	2.87 ± 0.42	2.66 ± 0.31	**0.001**
	Amygdala (L)	1.46 ± 0.27	1.19 ± 0.21	**0.001**
	Amygdala (R)	1.69 ± 0.34	1.39 ± 0.25	**0.001**
	Caudate (L)	3.07 ± 0.51	2.88 ± 0.49	**0.028**
	Pallidum (L)	1.21 ± 0.58	1.29 ± 0.31	**0.031**
	Accumbens nucleus (L)	0.36 ± 0.06	0.32 ± 0.06	**0.012**
	Accumbens nucleus (R)	0.39 ± 0.06	0.35 ± 0.06	**0.013**
Symmetry of brain regions	Frontal lobe (R)	65.14 ± 9.94	62.17 ± 7.86	**0.011**
	Occipital lobe (L)	34.51 ± 6.46	31.28 ± 6.39	**0.001**
	Occipital lobe (R)	31.08 ± 4.97	28.86 ± 5.42	**0.003**
	Temporal lobe (L)	45.46 ± 5.34	43.29 ± 6.47	**0.001**
	Temporal lobe (R)	46.26 ± 6.51	42.93 ± 5.86	**0.002**
	Parietal lobe (L)	36.88 ± 5.75	30.73 ± 4.76	**0.001**
	Parietal lobe (R)	38.12 ± 6.96	31.45 ± 6.85	**0.002**
	Insular (R)	5.67 ± 1.13	5.06 ± 1.07	**0.045**

Bold values indicate the statistically different.

disclosing the significant change of volumes in the memory-related cerebral areas between VaD and AD. On the other hand, the classification performance obtained with or without the feature selection method was compared and analyzed.

Differences in the Volumetric Features of Different Brain Tissues Between VaD and AD

The result presentation of quantitative volumetry in structural MRI was reported for the following cases: (1) volume differences of memory-related cerebral areas between patients who suffer from VaD and AD, (2) symmetry of brain substructures between the patients with VaD and AD, and (3) volume atrophy differences between VaD and AD (**Table 3**). The structural changes of memory-related cerebral areas were obvious and significant between the patients with VaD and AD, while volume differences could have potential to differentiate VaD from AD. When compared to the AD patients, the VaD patients show significantly higher volume values ($P < 0.05$) in brain parenchyma, hippocampus, amygdala, and accumbens nucleus, and significantly lower volume values ($P < 0.05$) in pallidum. The significant difference for the symmetry of certain brain substructures has also been observed between VaD and AD such as hippocampus, amygdala, caudate, pallidum, and accumbens nucleus ($P < 0.05$). The group comparison reveals a significant decline in the volume values of bilateral frontal lobe, occipital lobe, temporal lobe, and parietal lobe as well as significant volume atrophy differences in occipital lobe and parietal lobe in the patients with AD ($P < 0.05$).

Performance Comparison of Machine Learning Models for Differential Diagnosis

This section presents the results of comparing differential diagnosis between VaD and AD obtained by the different machine learning models. The 20 significantly different features (**Table 3**) selected from 62 quantified structural MRI measures obtained by AccuBrain software were ranked by LASSO feature selection. Then, five top-ranked features were selected as the input of machine learning model (**Figure 3**). GA was employed to find the global optimum solution of SVM, the parameters of which were set as follows: population size = 50, iteration times = 1,000, probability of crossover = 0.6 and probability of mutation = 0.1. **Table 4** presents the accuracy rates and the corresponding AUC values of different machine learning models in training, verification, and test set. The overall result of performance comparison is shown in **Figure 4A**. It demonstrated that SVM could achieve more encouraging performance than other frequently used classifiers that are suitable for small datasets in the application of differentiating VaD from AD. The result obtained by SVM classifiers with different kernel functions (linear and RBF kernels) on the raw feature set and the optimal feature subset addressed through the feature selection method is shown in **Figure 4B**. This indicates that the SVM with RBF kernel generally yields higher performance metrics and is more flexible than that with linear kernel, and the combining of machine learning and feature selection can increase the classification performance of the model. The confusion matrix of the proposed SVM model in a single experiment is shown in **Table 5**. When compared to classification using raw

TABLE 4 | The result of different machine learning models in training, verification, and test set.

	Training set		Verification set		Test set	
	Accuracy (%)	AUC	Accuracy (%)	AUC	Accuracy (%)	AUC
KNN	72.63	0.737	70.59	0.722	68.14	0.691
LR	77.14	0.789	74.96	0.754	73.62	0.747
RF	82.89	0.833	83.65	0.845	81.17	0.829
SVM	86.47	0.887	84.71	0.868	84.35	0.861

TABLE 5 | The confusion matrix of SVM model in a single experiment.

		Truth		Recall
		AD	VaD	
Prediction	AD	48	4	0.828
	VaD	10	31	0.886
	Precision	0.923	0.756	0.849

features and the other machine learning models, classification by the selective features and the proposed SVM model improves the accuracy rate to a significant level, which indicates a powerful performance in differential diagnosis between VaD and AD.

DISCUSSION

Many recent neuroimaging studies have focused on the use of advanced machine learning algorithms to solve problems in differential diagnosis, especially cases in the combination of medical science and engineering, such as the identification of the early stage of AD (20) and distinguishing between MCI and AD (21).

VaD characterized by the syndrome of intellectual disability such as hypomnesia and impairment of daily activities or living is very similar to AD. Therefore, accurate differential diagnosis is essential to receive timely clinical treatment that delays the progression of disease (22), which is helpful and required. Research on the biomarkers for differential diagnosis between VaD and AD mainly includes biochemical, genomics, proteomics, and neurophysiology markers such as neurofilament light unit and neurofilament protein levels (23), the ratio of plasma Aβ-38/-40 peptides (24), and phosphorylated tau proteins (25). Moreover, another critical requirement for clinical application is in the pursuit of neuroimaging biomarkers. In our study, a machine learning model derived from an RBF SVM classifier combined with LASSO and GA has been proposed for the differential diagnosis between VaD and AD. To our knowledge, this study is a unique combination of structural MRI biomarkers and machine learning for the differentiation of VaD vs. AD not used before.

Abrigo et al. (16) have affirmed that AccuBrain software could accurately and reliably segment hippocampus in accordance with the EADC-ADNI protocol so as to ensure the robustness, reproducibility, and reliability of structural MRI measurements such as volume, structural symmetry, and atrophy. The present result indicates that the symmetry differences and volume differences of hippocampus, amygdala, accumbens nucleus, and pallidum could have potential to differentiate VaD from AD (10, 26). We found that the involvement of brain regions is a relevant association between the volumetric change or atrophy identified in AD vs. VaD and that identified in AD vs. MCI (27). Because VaD is one of the main categories of senile dementia, the brain structure changes in the patients with VaD are similar to those with AD, which is in accordance with our current findings. Cuingnet et al. (28) found that the main brain area for the differentiation between AD and healthy individuals was the medial temporal lobe, similar to our study.

Our study indicates that the structural MRI measurements could be considered as core biomarkers for the differentiation of not only MCI vs. AD but also VaD vs. AD, combined with other researches (29, 30). It is manifested that the volumetric MRI studies of cerebral areas related with learning and memory such as hippocampus, amygdala, and accumbens nucleus are associated with neurodegeneration and shown to be sensitive to dementia severity (31). The hippocampus is the top-ranked effective indicator for differential diagnosis, which is in agreement with a previous study on the correlation between hippocampal volume and severity degree of dementia (32). Tondelli et al. (33) have suggested that the structural MRI changes occur before cognitive decline in the patients with AD and could potentially detect the regions affected by AD neuropathology. However, it seems possible to detect a similar distribution of brain atrophy accompanied by cognitive disorder caused by alternative VaD or AD. This could potentially explain why many VaD patients were misdiagnosed as AD subjectively by young physicians in the clinic. VaD could be easily confused with AD, especially in the early stages (34, 35). It is believed that the combination of such diverse structural MRI biomarkers containing more of the information in MR scanning contributes to an accurate differentiation between VaD and AD, in comparison with a single biomarker. Machine learning algorithms have been validated to overcome this obstacle. SVM outperforms all other classification methods such as KNN, LR, decision-making trees, and RF in small-sample research. Our results point in the same direction, since the input measures used are very small datasets.

In our experiment, the diagnostic performance of SVM classifier is superior to that of the other machine learning models. This is probably because SVM is trained based on a convex optimization problem so as to obtain a global optimum solution (18). Compared with RF, it is more likely to model more functions with the kernel-based method and reach an optimal separating structure in a small sample training set as well as avoiding suffering from local minimum mistakes and overfitting. In addition, KNN tends to perform very well with a lot of data points and RF is inherently suited for multiclass problems, while SVM is intrinsically constructed for binary classification, and the latter is more suitable to the task of this study. Compared with LR, SVM minimizes hinge loss while LR minimizes logistic

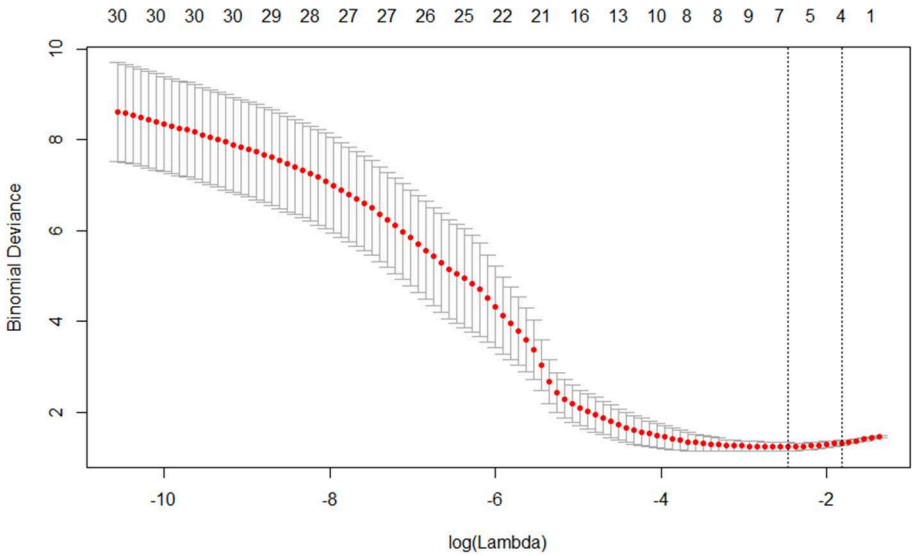

FIGURE 3 | Plot of coefficients-lambda obtained by LASSO.

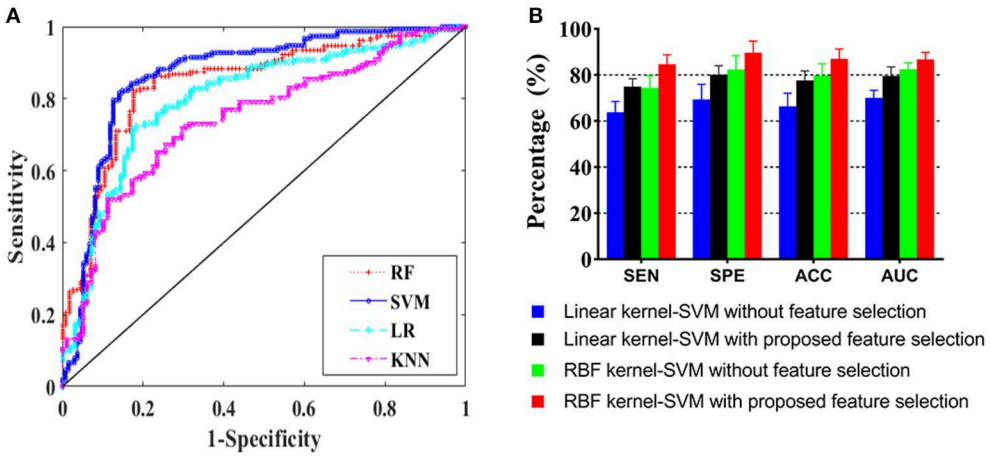

FIGURE 4 | Model performance presentation. **(A)** ROC curves for different machine learning models and **(B)** performance comparison for SVM with linear and radial base function (RBF) kernels on the raw and optimized datasets.

loss. This makes LR more sensitive to outliers because logistic loss diverges quicker than hinge loss. Besides, even though the data are distinguished sufficiently confidently, logistic loss does not reach zero. This might give rise to minor degradation in accuracy. The factors mentioned above support the fact that SVM outperforms the other classifiers in our study.

Some limitations in this study should be considered. First, our study only involved single-center data, and the small sample set was used, especially for VaD data. Transfer learning is an alternative method for the problem of lack of data (36). It is regarded as the use of a pre-trained model as a feature extractor, and then training and testing the classifier using the features that can be derived from fine-tuning the pre-trained model using source data. This will take the place of AccuBrain software as feature extractor. However, one of the purposes of the present study is to confirm that the AccuBrain software could effectively and reliably provide volumetric measurements of structural MRI as independent indicators, which helps to quantify the architectural differences and facilitates computer-aided diagnosis between AD and VaD. So, for this purpose, we did not consider using transfer learning in this study. Nevertheless, further expanding samples and launching multi-center studies in future work, transfer learning could be the best choice. Second, only the indicators from structural MRI are used. Next, a larger number of datasets including multi-center data could be applied to extend our study by combining other MRI-based biomarkers, such as functional parameters (DTI metrics), radiomics features, and brain connectome, which target subtler information. We have reasons to believe that the combination of structural MRI-based volumetric measurements and other markers would

improve the degree to which structural features are sensitive to differentiation between VaD and AD.

DATA AVAILABILITY STATEMENT

All datasets generated for this study are included in the manuscript.

ETHICS STATEMENT

This retrospective study was approved by the Ethics Committee of our hospital. The written full informed consents were obtained from all subjects.

AUTHOR CONTRIBUTIONS

YZ, LZ, QL, and FL designed the study. HG, JW, and QL collected patient data and provided clinical expertise. YZ processed and analyzed the MRI data, and drafted the manuscript. FL and QL interpreted the data for the work. All the authors approved the final version of the manuscript.

FUNDING

The project was funded by the National Natural Science Foundation of China (Grant Nos. 31800823 and 31570003) and the Incubation Foundation of the First Affiliated Hospital of Chongqing Medical University (PYJJ2019-04).

REFERENCES

1. Wu YT, Fratiglioni L, Matthews FE, Lobo A, Breteler MMB, Skoog I, et al. Dementia in western Europe: epidemiological evidence and implications for policy making. *Lancet Neurol.* (2016) 15:116–24. doi: 10.1016/S1474-4422(15)00092-7
2. Leontino B, Annachiara CJNR. Vascular cognitive disorder. A biological and clinical overview. *Neurochem Res.* (2010) 35:1933–8. doi: 10.1007/s11064-010-0346-5
3. Lopez OL, Larumbe MR, Becker JT, Rezek D, Rosen J, Klunk W, et al. Reliability of NINDS-AIREN clinical criteria for the diagnosis of vascular dementia. *Neurology.* (1994) 44:1240–5. doi: 10.1212/WNL.44.7.1240
4. Braak H, Braak EJAN. Neuropathological stageing of Alzheimer-related changes. *Acta Neuropathol.* (1991) 82:239–59. doi: 10.1007/BF00308809
5. Cheng Y, Bai FN. The association of tau with mitochondrial dysfunction in Alzheimer's disease. *Front Neurosci.* (2018) 12:163. doi: 10.3389/fnins.2018.00163
6. Jellinger KA. The enigma of vascular cognitive disorder and vascular dementia. *Acta Neuropathol.* (2007) 113:349–88. doi: 10.1007/s00401-006-0185-2
7. Hall B, Mak E, Cervenka S, Aigbirhio FI, Rowe JB, O'Brien JTJARR. *In vivo* tau PET imaging in dementia: Pathophysiology, radiotracer quantification, and a systematic review of clinical findings. *Ageing Res Rev.* (2017) 36:50–63. doi: 10.1016/j.arr.2017.03.002
8. Mark Y, Xie SX, Kling MA, Toledo JB, Wolk DA, Lee EB, et al. Cerebrovascular atherosclerosis correlates with Alzheimer pathology in neurodegenerative dementias, *Brain*. (2012) 135:3749–56. doi: 10.1093/brain/aws271
9. Velayudhan L, Proitsi P, Westman E, Muehlboeck JS, Mecocci P, Vellas B, et al. Entorhinal cortex thickness predicts cognitive decline in Alzheimer's disease. *J Alzheimers Dis.* (2013) 33:755–66. doi: 10.3233/JAD-2012-121408
10. Pich EM, Jeromin A, Frisoni GB, Hill D, Lockhart A, Schmidt ME, et al. Therapy, Imaging as a biomarker in drug discovery for Alzheimer's disease: is MRI a suitable technology? (2014) 6:51. doi: 10.1186/alzrt276
11. Gómezsancho M, Tohka J, Gómezverdejo VJMRI. Comparison of feature representations in MRI-based MCI-to-AD conversion prediction. *Magn Reson Imaging.* (2018) 50:84–95. doi: 10.1016/j.mri.2018.03.003
12. Leandrou S, Petroudi S, Kyriacou PA, Reyes-Aldasoro CC, Pattichis CSJIRiBE. Quantitative MRI brain studies in mild cognitive impairment and Alzheimer's disease: a methodological review. *IEEE Rev Biomed Eng.* (2018) 11:97–111. doi: 10.1109/RBME.2018.2796598
13. Hu K, Wang Y, Chen K, Hou L, Zhang XJN. Multi-scale features extraction from baseline structure MRI for MCI patient classification and AD early diagnosis. *Neurocomputing.* (2016) 175:132–45. doi: 10.1016/j.neucom.2015.10.043
14. Tierney MC, Fisher RH, Lewis AJ, Zorzitto ML, Snow WG, Reid DW, et al. The NINCDS-ADRDA Work Group criteria for the clinical diagnosis of probable Alzheimer's disease: a clinicopathologic study of 57 cases. *Neurology.* (1988) 38:359–64. doi: 10.1212/WNL.38.3.359
15. Ashburner J, Friston KJ. Diffeomorphic registration using geodesic shooting and Gauss–Newton optimisation. *Neuroimage.* (2011) 55:954–67. doi: 10.1016/j.neuroimage.2010.12.049
16. Abrigo J, Shi L, Luo Y, Chen Q, Chu WCW, Mok VCT, et al. Standardization of hippocampus volumetry using automated brain structure volumetry tool for an initial Alzheimer's disease imaging biomarker. *Acta Radiol.* (2018) 60:769–76. doi: 10.1177/0284185118795327
17. Ruxton GDJBE. The unequal variance t-test is an underused alternative to Student's t-test and the Mann–Whitney U test. *Behav Ecol.* (2010) 17:688–90. doi: 10.1093/beheco/ark016
18. Cortes C, Vapnik V. Support vector networks. *Mach Learn.* (1995) 20:273–97. doi: 10.1007/BF00994018
19. Chang CC, Lin CJ. LIBSVM: a library for support vector machines. *ACM Transact Intellig Syst Technol.* (2011) 2:27. doi: 10.1145/1961189.1961199
20. Khazaee A, Ebrahimzadeh A, Babajani-Feremi AJBBR. Classification of patients with MCI and AD from healthy controls using directed graph measures of resting-state fMRI. *Behav Brain Res.* (2017) 322:339–50. doi: 10.1016/j.bbr.2016.06.043
21. Sørensen L, Igel C, Pai A, Balas I, Anker C, Lillholm M, et al. Differential diagnosis of mild cognitive impairment and Alzheimer's disease usingstructural MRI cortical thickness, hippocampal shape, hippocampal texture, and volumetry^{-}. *Neuroimage Clin.* (2017) 13:470–82. doi: 10.1016/j.nicl.2016.11.025
22. Benedict C, Grillo CAJFiN. Insulin resistance as a therapeutic target in the treatment of Alzheimer's disease: a state-of-the-art review. *Front Neurosci.* (2018) 12:215. doi: 10.3389/fnins.2018.00215
23. Petzold A, Keir G, Warren J, Fox N, Rossor MNJND. A systematic review and meta-analysis of CSF neurofilament protein levels as biomarkers in dementia. *Neurodegener Dis.* (2007) 4:185–94. doi: 10.1159/000101843
24. Mirko B, Hermann E, Brit M, Godehard W, Volker W, Michael L, et al. Blood-based neurochemical diagnosis of vascular dementia: a pilot study. *J Neurochem.* (2010) 103:467–74. doi: 10.1111/j.1471-4159.2007.04763.x
25. Kidemetpiskač S, Leko MB, BlaŽeković A, Langer LH, Klepac N, Sonicki Z, et al. Therapeutics, Evaluation of cerebrospinal fluid phosphorylated tau231 as a biomarker in the differential diagnosis of Alzheimer's disease and vascular dementia. *CNS Neurosci Ther.* (2018) 24:734–40. doi: 10.1111/cns.12814
26. Cedazo-Minguez A, Winblad BJEG. Biomarkers for Alzheimer's disease and other forms of dementia: Clinical needs, limitations and future aspects. *Exp Gerontol.* (2010) 45:5–14. doi: 10.1016/j.exger.2009.09.008
27. Aguilar C, Westman E, Muehlboeck JS, Mecocci P, Vellas B, Tsolaki M, et al. Different multivariate techniques for automated classification of MRI data in Alzheimer's disease and mild cognitive impairment. *Psychiatry Res.* (2013) 212:89–98. doi: 10.1016/j.pscychresns.2012.11.005
28. Cuingnet R, Gerardin E, Tessieras J, Auzias G, Lehéricy S, Habert MO, et al. Automatic classification of patients with Alzheimer's disease from structural MRI: a comparison of ten methods using the ADNI database. *Neuroimage.* (2011) 56:766–81. doi: 10.1016/j.neuroimage.2010.06.013

29. Rathore S, Habes M, Iftikhar MA, Shacklett A, Davatzikos CJN. A review on neuroimaging-based classification studies and associated feature extraction methods for Alzheimer's disease and its prodromal stages. *Neuroimage.* (2017) 155:530–48. doi: 10.1016/j.neuroimage.2017.03.057
30. Beheshti I, Demirel H, Matsuda HJCiB. Classification of Alzheimer's disease and prediction of mild cognitive impairment-to-Alzheimer's conversion from structural magnetic resource imaging using feature ranking and a genetic algorithm. *Comput Biol Med.* (2017) 83:109–19. doi: 10.1016/j.compbiomed.2017.02.011
31. Jack CR, Knopman DS, Jagust WJ, Petersen RC, Weiner MW, Aisen PS, et al. Tracking pathophysiological processes in Alzheimer's disease: an updated hypothetical model of dynamic biomarkers. *Lancet Neurol.* (2013) 12:207–16. doi: 10.1016/S1474-4422(12)70291-0
32. Csernansky JG, Wang L, Price JL, Morris JCJAD, Disorders A. Correlations between antemortem hippocampal volume and postmortem neuropathology in AD subjects. *Alzheimer Dis Assoc Disord.* (2004) 18:190–5.
33. Tondelli M, Wilcock GK, Nichelli PJNoA. Structural MRI changes detectable up to ten years before clinical Alzheimer's disease. *Neurobiol Aging.* (2012) 33:825.e825–36. doi: 10.1016/j.neurobiolaging.2011.05.018
34. Ozkan S, Adapinar DO, Elmaci NT, Arslantas DJND. Apraxia for differentiating Alzheimer's disease from subcortical vascular dementia and mild cognitive impairment. *Neuropsychiatr Dis Treat.* (2013) 2013:947–51. doi: 10.2147/NDT.S47879
35. Kim TY, Kim SY, Kim EG, Kim JW, Park KW, Sung SM, et al. The differences of behavioral and psychological symptoms in the patients of Alzheimer's disease and vascular dementia. *Alzheimers Dementia.* (2006) 2:S260–1. doi: 10.1016/j.jalz.2006.05.932
36. Pan SJ, Yang Q. A survey on transfer learning. *IEEE Trans Knowl Data Eng.* (2010) 22:1345–59. doi: 10.1109/TKDE.2009.191

Conflict of Interest: The authors declare that the research was conducted in the absence of any commercial or financial relationships that could be construed as a potential conflict of interest.

frontiers in Neuroscience

ORIGINAL RESEARCH
published: 01 November 2019
doi: 10.3389/fnins.2019.01183

Diminished Frontal Theta Activity During Gaming in Young Adults With Internet Gaming Disorder

Juri Kim[1†], Jinsick Park[1†], Young Min Park[1], DongPyo Jang[1], Kee Namkoong[2,3], Young-Chul Jung[2,3] and In Young Kim[1]**

[1] Department of Biomedical Engineering, Hanyang University, Seoul, South Korea, [2] Institute of Behavioral Science in Medicine, Yonsei University College of Medicine, Seoul, South Korea, [3] Department of Psychiatry, Yonsei University College of Medicine, Seoul, South Korea

Cognitive control is essential for flexible, top-down, goal-directed behavior. Individuals with Internet gaming disorder (IGD) are characterized by impaired prefrontal cortex function and cognitive control. This results in an increase in stimulus-driven habitual behavior, particularly related to pathological gaming. In the present study, we investigated the electroencephalographic (EEG) activity in individuals with IGD. Twenty-four individuals with IGD and 35 healthy control (HC) subjects were recruited. We analyzed their EEG activity while the subjects played their favorite game (30–40 min duration). We compared the band power between the two groups. During gaming, the left frontal theta, alpha, and beta band activities were lower in subjects with IGD than in HCs. Moreover, the left frontal theta power negatively correlated with IGD severity. These results indicate that left frontal theta power could be used as a neurophysiological biomarker for the detection of diminished cognitive control patterns in individuals with IGD.

Keywords: EEG, left frontal cortex, cognitive control, theta power, internet gaming disorder

OPEN ACCESS

Edited by:
Feng Feng,
Peking Union Medical College Hospital (CAMS), China

Reviewed by:
Koichi Sameshima,
University of São Paulo, Brazil
Saskia Sophie Steinmann,
University Medical Center Hamburg-Eppendorf, Germany

***Correspondence:**
Young-Chul Jung
eugenejung@yuhs.ac
In Young Kim
iykim@hanyang.ac.kr

[†]These authors have contributed equally to this work

Specialty section:
This article was submitted to Brain Imaging Methods, a section of the journal Frontiers in Neuroscience

Received: *04 January 2019*
Accepted: *18 October 2019*
Published: *01 November 2019*

Citation:
Kim J, Park J, Park YM, Jang D, Namkoong K, Jung Y-C and Kim IY (2019) Diminished Frontal Theta Activity During Gaming in Young Adults With Internet Gaming Disorder. Front. Neurosci. 13:1183. doi: 10.3389/fnins.2019.01183

INTRODUCTION

Internet gaming disorder (IGD) is a specific form of Internet addiction characterized by an individual's impaired control over Internet gaming (Kuss, 2013). As with other addictions, individuals with IGD exhibit salience, mood modification, tolerance, withdrawal symptoms, conflicts, and relapses (Chou and Ting, 2003). In the recent 11th Revision of the International Classification of Diseases (ICD-11) from the World Health Organization (WHO), a gaming disorder is defined as a pattern of gaming behavior ("digital-gaming" or "video-gaming") characterized by an impaired control over gaming. Increasing priority is given to gaming over other activities to the extent that gaming takes precedence over other interests and daily activities. The continuation or escalation of gaming persists despite the occurrence of negative consequences (Young, 2018).

Many studies have demonstrated the neurophysiological features of IGD using electroencephalography (EEG). Most previous studies have focused on identifying biomarkers for subjects with IGD in the resting state. A study by Choi et al. (2013) revealed that subjects with IGD had a lower beta band power in all regions and a higher gamma band power in the frontal regions than those of healthy control (HC) subjects. These results were related to impulsivity. In addition,

Lee et al. (2014) demonstrated that the absolute beta band power in all brain regions was lower in subjects with IGD who did not have depression, than in those with depression and in HC subjects. The lower beta activity is correlated with the impulsivity and dysfunctional inhibitory control in subjects with IGD without depression. Park et al. reported that the intra-hemispheric coherence values for the theta band between the T4-T6 and P4-O2 electrodes were higher in subjects with attention-deficit/hyperactivity disorder (ADHD) with comorbid IGD than those in subjects with ADHD without comorbidity (Park et al., 2017). They indicated that the repetitive activation of the brain reward system during continuous gaming may have increased the neuronal connectivity within the parieto-occipital and temporal regions in the subjects with ADHD alone, compared to those with comorbid IGD. These studies provided evidence that the excessive use of Internet games results in cognitive impairment and functional changes in the brain of subjects with IGD.

To prevent the cognitive impairment caused by IGD, it is necessary to monitor the cue-induced neurophysiological responses during gaming. It is assumed that gaming may be associated with excessive rewarding behavior that meets the criteria of addiction. Gaming can elicit a strong motivational state that contributes to cravings and repeated excessive or addictive behaviors (Thalemann et al., 2007). For example, in a study investigating pathological gambling, a significant increase in the mean craving for gambling was found in subjects with pathological gambling who were exposed to visual gambling cues during the assessment period (Crockford et al., 2005). In an IGD study on the cue-reactivity paradigm, the differences in the cue-induced event-related potentials between excessive computer-game players and casual players were significant for game related-cues. However, they were not significant for non-game related cues (Thalemann et al., 2007). Yao et al. (2015) reported inhibition deficits during the performance of a gaming-related Go/No-Go task in subjects with IGD compared with HCs. However, the IGD group did not differ from the HC group in non-gaming-related inhibitory control, as assessed by the Stroop task.

Previous studies have demonstrated that the an addiction cue can lead to strong motivation. This has led to studies that have examined the differences before and after an addiction cue. However, the aforementioned studies did not describe the gaming cue-induced neurophysiological response during gaming in individuals with IGD. A recent study investigated the changes in the heart rate variability (HRV) patterns during gaming as a potential biomarker for IGD (Hong et al., 2018; Lee et al., 2018). Compared with HCs, subjects with IGD exhibited an altered HRV response while playing an online game. This indicates that the dynamics between executive control and reward-seeking may be out of balance during gaming in these subjects. This prompted us to initiate a study of the cue-induced neurophysiological responses during gaming. EEG can be used to measure the neurophysiological responses in real time with a higher temporal resolution than that of fMRI. In addition, EEG can be correlated with cognitive functions and can measure the neural activity directly, with a multidimensional signal encompassing time, space, frequency, and power (Cohen, 2011). In this study, we used EEG to analyze the cue-induced neurophysiological responses during gaming.

We hypothesized that the differences in the brain functions between individuals with and those without IGD would become apparent during gaming. Furthermore, if the activity in specific regions in the brain would be significantly different between the groups, this would be a beneficial biomarker that could be used to classify IGD. Thus, in this study, we examined the changes in the power of the theta, alpha, and beta bands between the resting state and the gaming state using EEG. We compared them between individuals with and those without IGD to determine their significance. The purpose of this study was to clarify whether the brain activity changed during gaming in individuals with IGD without other psychological problems (e.g., depression and anxiety). Since previous studies have reported a difference in motivation between the resting state and after a game-related cue in a cue-related task in IGD, we further investigated the difference in the brain activity while gaming compared with that at the resting state between the IGD and HC groups.

MATERIALS AND METHODS

Participants

We recruited 59 right-handed young males. The subjects were examined for their Internet usage patterns and were administered the Young's Internet Addiction Test (YIAT) (Beard and Wolf, 2001; Young, 2011). Subjects who used the Internet primarily for gaming and whose YIAT scores were more than 50, were classified as the IGD group (n = 24, mean age = 23.3 $\pm$ 2.3 years). They were confirmed to have IGD by a psychiatrist according to the IGD diagnostic criteria of the DSM Fifth Edition (Petry and O'Brien, 2013). Subjects who scored below 50 on the YIAT were classified as HCs (n = 35, mean age = 23.2 $\pm$ 2.5 years). All subjects in this study frequently played "League of Legends (LOL)," (Riot Games, Los Angeles, CA, United States, 2009). This is the most popular multiplayer online battle arena game in Korea (Nuyens et al., 2016, Statista, 2018). To control for differences in skill between the IGD group and the HC group, we included only those who were ranked above the silver tier. There were six tiers in this game, bronze, silver, gold, platinum, diamond and challenger.

All subjects completed several self-reporting questionnaires assessing comorbid psychiatric symptoms of IGD (Kim et al., 2016). The following self-reporting questionnaires were used:

1. The Beck Depression Inventory to test for depression (Beck et al., 1961).
2. The Beck Anxiety Inventory to test for anxiety (Beck et al., 1988).
3. The Barratt Impulsiveness Scale, version 11 to evaluate impulsivity (Patton et al., 1995).
4. The Alcohol Use Disorders Identification Test to identify alcohol-related problems (Reinert and Allen, 2002).

5. The Wender Utah Rating Scale to evaluate for symptoms of ADHD (Ward et al., 1993).

Task and Procedure

Resting-state EEG (PRE) was recorded with the participants in a comfortable sitting position with their eyes open for 5 min (**Figure 1**). Each subject then played the online game LOL three times, (periods GAME1, GAME2, and GAME3) with 5 min of rest between gaming periods. Following the gaming, resting-state EEG was again recorded for 5 min (POST). The Institutional Review Board approved the protocol for this study (HYI-16-044), and all subjects provided signed informed consent before participating.

EEG Data Acquisition and Pre-processing

EEG data were acquired using a Waveguard 64 EEG sensor-cap (CA-105, ANT-Neuro, Enscheda, Netherlands). The signals were sampled at a frequency of 1024 Hz and we used the active G1/G2 ground reference (BRAINBOX EEG-1166 system, Braintronics, Almere, Netherlands) for the ground and reference (G1: FPz, G2: AFz). As a reference, a single channel with bipolar electrodes was attached to the mastoids. Possible line noise artifacts were removed from the data with a notch filter at 60 Hz in the central frequency, IIR notch filter in filter type, and 9.9 Hz in bandwidth. The impedance of each electrode was maintained below 10 kiloohms.

Artifact removal was performed using the EEGLAB toolbox (Version 14.1.1b, Swartz Center for Computational Neuroscience) in Matlab (Version R2016b, The MathWorks, Inc., Natick, MA, United States) (Delorme and Makeig, 2004). Data were filtered using the EEGLAB filter function *pop_eegfiltnew*; high pass, 1 Hz; low pass, 30 Hz. The filtering option in EEGLAB uses linear finite impulse response (FIR) filtering with a second-order Hamming window. It was applied to the EEG signals to eliminate the noise from the subjects' movement, breathing, and muscle electrical activity. After artifact removal, the signals were re-referenced with a common average of potentials at 61 electrodes, except for the ground and reference electrodes, by applying the *pop reref* algorithm. After the application of the common average re-reference (CAR) method, independent component analysis (ICA) was performed by applying the *pop runica* algorithm. After the ICA analysis, to remove the eye-blink noise, we removed components with a large weight (typically 1 and 2 components) in Fp1 and Fp2 while having an eye-blink pattern. A time-frequency representation was generated by a Morlet wavelet transform with a wavelet length of three cycles, a window size of 3000 ms, and a shift time of 100 ms (Akin, 2002). Four frequency bands were integrated: delta (1–4 Hz), theta (4–8 Hz), alpha (8–13 Hz), and beta (13–30 Hz). We focused on the theta, alpha, and beta bands in this study.

EEG Analysis

A percentage value was used to normalize the individuals' baseline, because the absolute amplitude of EEG oscillations is as dependent on skull conductivity and geometry as it is on neuronal dynamics. The change in the EEG power during the task was calculated as a relative change in the average EEG power between the gaming task and baseline, as follows:

$$Percentage\ value = (Power(Task) - Power(Baseline_{PRE})) * \frac{100}{Power(Baseline_{PRE})}$$

As shown in **Figure 2**, we divided the activity at 61 sites into 13 regions by averaging within each region (according to the international 10-10 system): prefrontal (FP1, FP2), left frontal (F7, F3, AF7, AF3, F5), frontal (Fz, F1, F2), right frontal (F4, F8, AF4, AF8, F6), left central (FC5, C3, CP5, FC3, C5, CP3), central (FC1, FC2, Cz, CP1, CP2, FCz, C1, C2, CPz), right central (FC6, C4, CP6, FC4, C6, CP4), left temporal (T7, FT7, TP7), right temporal (T8, FT8, TP8), left parietal (P7, P3, P5, PO5, PO3, PO7), parietal (Pz, P1, P2), right parietal (P4, P8, P6, PO4, PO6, PO8), and occipital (POz, O1, Oz, O2).

Statistical Analysis

Independent-sample *t*-tests were performed to compare the demographic, clinical, and behavioral variables between the two groups. The differences in the EEG data were analyzed by means of a mixed-model analysis of variance (mixed ANOVA). To evaluate the between-group differences in the EEG percentage values in the theta, alpha, and beta bands in 13 ROIs, we used the gaming period (during gaming sessions 1-3 and post) as the within-subjects factor, and the group (IGD or HC group) as the between-subjects factor. *Post hoc* comparisons were applied to determine whether the differences between the groups (independent *t*-tests) and between certain periods (paired *t*-tests) were statistically significant. To avoid multiple comparison problems including three bands and 13 ROIs, a false discovery rate (FDR) correction algorithm was applied to the *p*-values (Groppe et al., 2011). We used an alpha value of 0.05 (2-tailed significance) and an FDR value of 0.2 for the statistics that corresponded to a control of the maximum proportion of false positives among the rejected null hypotheses of <20% (Genovese et al., 2002). The *p*-values as well as corrected

FIGURE 1 | Experimental protocol for recording scalp EEG signals.

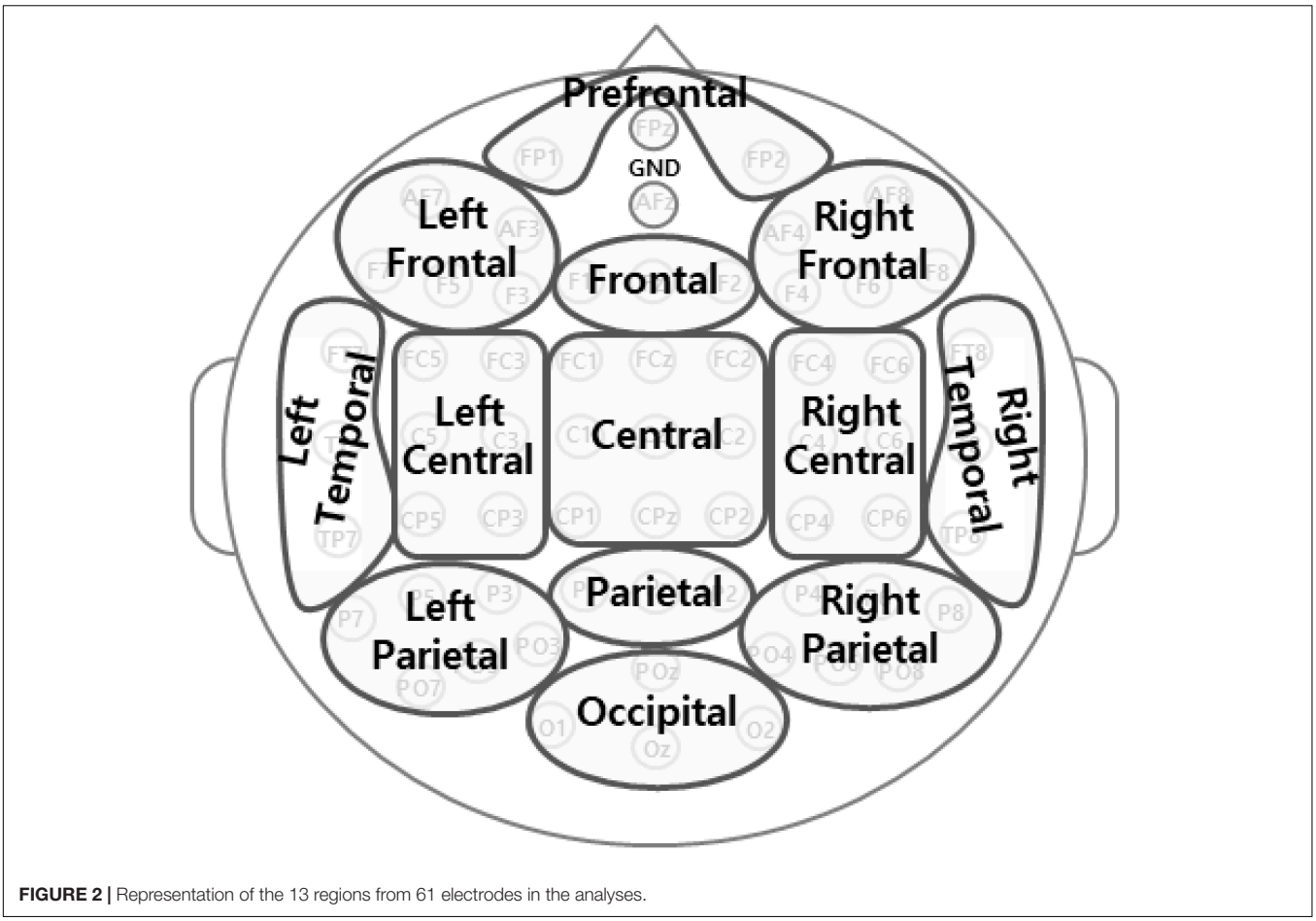

FIGURE 2 | Representation of the 13 regions from 61 electrodes in the analyses.

p-values were included as part of the results. In addition, to determining the relationship between the EEG percentage value in each band and the severity of IGD, we conducted Pearson's correlation analysis between the left frontal percentage value and the YIAT score for each band. All statistical analyses were performed using SPSS software (version 21; IBM, Inc., NY, United States).

RESULTS

Demographics, Clinical Characteristics, and Behavioral Results of the Subjects

The demographics, clinical characteristics, and behavioral results of the subjects are presented in **Table 1**. The groups did not differ in age or IQ. The subjects in the IGD group scored significantly higher in the tests for severity of the online game-related problems (YIAT: $t = 12.088$, $p < 0.001$; K-scale: $t = 5.500$, $p < 0.001$).

The two groups did not differ significantly in self-reported depression, anxiety, alcohol-related problems, and ADHD symptoms. However, the subjects in the IGD group scored significantly higher than those in the HC group in the tests for impulsivity (BIS: $t = 3.352$, $p < 0.005$). The gaming time during the experiment was approximately 30 min, and there was no difference between the two groups.

EEG Activity

Figure 3 displays the scalp topographies of the theta, alpha, and beta bands for the IGD and HC groups. For all bands analyzed by the mixed-model ANOVA, the main effect of the group was found to differ significantly between the groups (**Figure 4**). The data satisfied both normality and homogeneity of variance. In the theta band, left frontal: $F(1,57) = 12.713$, $p = 0.001$, corrected $p = 0.039$, effect size = 0.182; frontal: $F(1,57) = 4.701$, $p = 0.034$, corrected $p = 0.165$, effect size = 0.076; left central: $F(1,57) = 8.707$, $p = 0.005$, corrected $p = 0.065$, effect size = 0.133; central: $F(1,57) = 6.610$, $p = 0.013$, corrected $p = 0.126$, effect size = 0.104; right central: $F(1,57) = 6.619$, $p = 0.013$, corrected $p = 0.101$, effect size = 0.104; left temporal: $F(1,57) = 5.318$, $p = 0.025$, corrected $p = 0.162$, effect size = 0.085 (effect size as partial eta-squared). In the alpha band, left frontal: $F(1,57) = 4.614$, $p = 0.036$, corrected $p = 0.156$, effect size = 0.075. In the beta band, left frontal: $F(1,57) = 10.702$, $p = 0.002$, corrected $p = 0.039$, effect size = 0.158; left temporal: $F(1,57) = 4.598$, $p = 0.036$, corrected $p = 0.1404$, effect size = 0.078; left central: $F(1,57) = 4.834$, $p = 0.032$, corrected $p = 0.178$, effect size = 0.075 (mixed ANOVA; p value <0.05, FDR correction;

TABLE 1 | Demographics, clinical characteristics, and behavioral results of the subjects.

Variables	Internet gaming disorder group (*N* = 24)	Healthy control group (*N* = 35)	*t*	*p*-value
Demographic data				
Age (years)	23.08 (2.71)	23.20 (2.47)	−0.172	0.864
FSIQ	110.79 (15.36)	113.45 (11.22)	−0.770	0.444
Clinical data				
YIAT	63.28 (9.87)	34.28 (8.63)	12.088	< 0.001
K-scale	86.04 (17.48)	62.14 (15.07)	5.500	< 0.001
BDI	8.95 (7.93)	7.45 (5.08)	0.886	0.379
BAI	5.04 (4.72)	5.17 (5.50)	0.118	0.907
BIS	54.76 (8.55)	48.80 (6.13)	3.352	< 0.005
AUDIT	11.52 (7.51)	9.51 (5.40)	1.112	0.271
WURS	24.70 (16.13)	23.85 (13.71)	0.218	0.828
Gaming time				
GAME1	31.50 (7.18)	29.65 (8.39)	0.877	0.384
GAME2	32.91 (10.74)	29.94 (7.22)	1.273	0.208
GAME3	29.29 (7.36)	30.42 (8.88)	−0.517	0.607
Time spent gaming per week, hours	26.63 (24.39)	18.84 (15.64)	1.382	0.134

Data are presented as the mean (SD). FSIQ, full scale intelligence quotient; BDI, beck depression inventory; BAI, beck anxiety inventory; BIS, Barratt Impulsiveness Scale; AUDIT, alcohol use disorder identification test; WURS, Wender Utah Rating Scale for ADHD. Independent-sample t-tests were used.

corrected p value <0.2). The percentage values for all measured bands were lower in the IGD group than those in the HC group. For all bands, the left frontal region differed significantly between the groups.

We also found significant main effects for the period for all bands. The theta band differed significantly in 12 regions (every region except the prefrontal region). The alpha band differed significantly in all 13 regions and the beta band differed significantly in 10 regions (all but the left parietal, right parietal, and occipital regions). The interactions between the groups and the period were not statistically significant in any region.

Correlation Analyses

To investigate whether the activity in the left frontal region could be a biomarker for IGD, we analyzed the relationship between the YIAT score and the power of each band in the left frontal region. We found significant negative correlations between the YIAT score and percentage value in the left frontal region in the theta, alpha, and beta bands in several periods. In the theta band, GAME1: $r = -0.353$, $p = 0.006$; GAME2: $r = -0.328$, $p = 0.011$; GAME3: $r = -0.305$, $p = 0.018$; POST: $r = -0.279$, $p = 0.032$ (**Figure 5**). In the alpha band, GAME1: $r = -0.264$, $p = 0.043$; GAME2: $r = -0.259$, $p = 0.047$. In the beta band, GAME1: $r = -0.257$, $p = 0.049$; GAME2: $r = -0.263$, $p = 0.044$.

DISCUSSION AND CONCLUSION

We investigated the differences in the EEG response patterns in the theta, alpha, and beta bands between the HC and IGD groups during the gaming periods. We recruited individuals with IGD who exhibited only impulsivity, without other accompanying mental illnesses (depression, anxiety, alcohol use disorder [AUD], or ADHD). This is the first study to acquire real-time scalp EEG signals and analyzed longitudinal data during playing the online game LOL, the subjects' primary game. The subjects with IGD had significantly lower theta, alpha, and beta band powers in the left frontal region than those of the HCs during gaming. The association between impaired cognitive control and IGD during gaming is represented by the lower frontal theta activity. This is associated with less cognitive control, whereas the lower frontal alpha activity suggests a lower load on the working memory. It is likely that validation and application of meaningful clinical indicators for IGD diagnosis and treatment will be possible through the addiction-related features of individuals with IGD that appear during gaming. In addition, the left frontal theta activity, which correlates with the severity of addiction, is likely to be used to discriminate individuals with IGD during gaming in real-time.

The frontal theta activity has been shown to be related to cognitive control (Brand et al., 2014; Cavanagh and Frank, 2014). Cognitive control is an executive function in the control system that allows us to regulate our behavior so that it is planned, goal-oriented, flexible, and effective (Shallice and Burgess, 1996; Jurado and Rosselli, 2007; Anderson et al., 2008). IGD is associated with impaired cognitive control, characterized as a behavioral addiction or impulse-control disorder (Dong et al., 2011, 2012, 2013). Additionally, increased alpha activity is related to the load on the working memory (Gundel and Wilson, 1992; Gevins et al., 1997; Klimesch, 2012). Katahira et al. (2018) suggested that the amplitudes of frontal theta and alpha activity were significantly smaller under conditions of boredom (accuracy 99.7%) than under flow conditions (accuracy 54.4%). Our results indicate that lower frontal theta activity can be interpreted as decreased cognitive control, while lower frontal alpha activity can be interpreted as a lower working memory load condition. Furthermore, it is assumed that the individuals with IGD are gaming under boredom conditions, characterized by lower frontal activity of both theta and alpha waves. The reduced frontal beta power in individuals with IGD is associated with impaired inhibitory control and reward feedback (Choi et al., 2013; Lee et al., 2014; HajiHosseini and Holroyd, 2015).

The left region of the brain is related to analytical and strategic thinking, and the LOL game requires strategic thinking. In this study, the HC group showed higher left frontal theta power than those in the IGD group during LOL gaming. In other words, based on the left frontal theta activity, it seems that the HC subjects performed the LOL game with more strategic thinking than individuals with IGD.

Imaging studies on addictive behavior have identified the key role of the prefrontal cortex (PFC), both through its regulation of the limbic reward regions and its involvement in higher-order executive functions (Goldstein and Volkow, 2011). PFC dysfunction is associated with activation of the limbic system, which results in addictive behavior (Crews and Boettiger, 2009). In other words, impaired executive functions contribute to

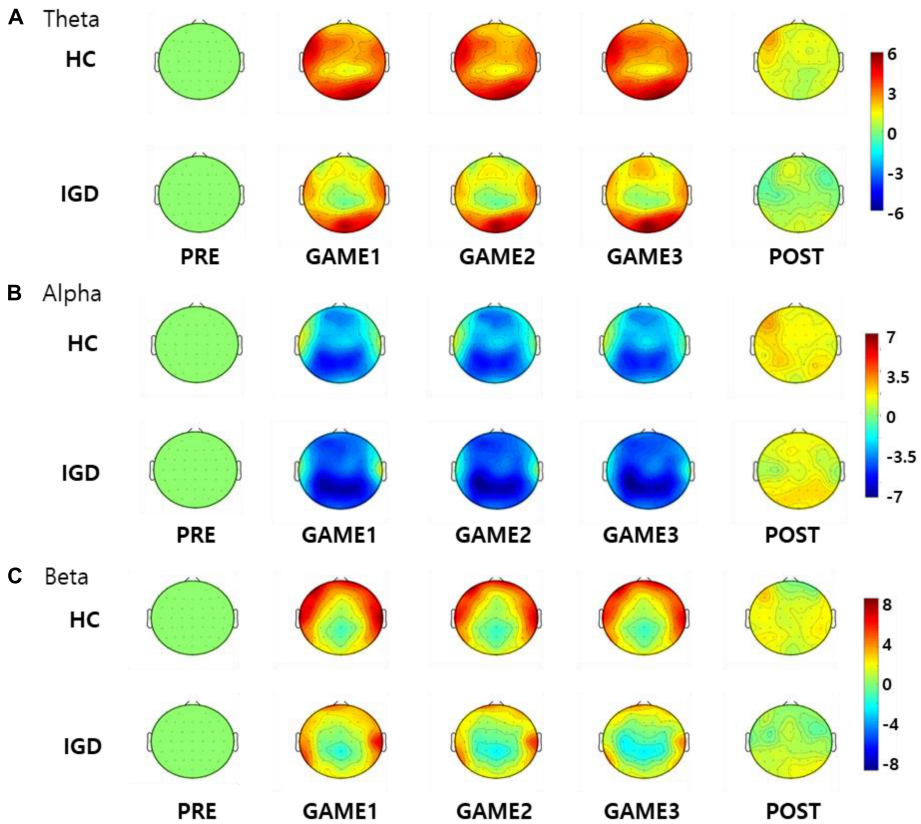

FIGURE 3 | Topographical maps of the percentage values in the **(A)** theta, **(B)** alpha, and **(C)** beta bands in the healthy control (HC) subjects and those with Internet gaming disorder (IGD) during different periods (PRE, GAME1, GAME2, GAME3, and POST). Red represents a higher value, while blue represents a lower value. The IGD group demonstrated reduced percentage values in the theta, alpha, and beta bands compared to those in the HC group. Scales display% for percentage power.

an imbalance between the frontal cortical functions and a hyperactive limbic system that drives impulsive behavior (Bechara, 2005). Lee et al. reported that weaker dorsolateral prefrontal activation is correlated with higher cognitive impulsivity in IGD. The accuracy of the Stroop task was lower in the addiction group than in the normal group (Lee et al., 2015). Koepp et al. (1998) reported that the frontal striatal and limbic brain regions involved in the dopamine mesolimbic pathway are associated with the urge to play games and the reward mechanism.

In terms of reinforcement learning in a gaming environment, the player recognizes the current state and selects actions that maximize reward among the selectable actions (Montague, 1999). A feature of reinforcement learning is that when a player selects an action, the environment changes by his/her reactions to it. In the LOL game, it is difficult for a player to know what another player is thinking. There are those who strive to think strategically and obtain information based on the characteristics of the LOL game; however, there are also those who seek only immediate rewards. Players who only pursue immediate rewards are reward-seeking, and this can easily lead to addiction. In the brain, goal-directed control predicts a future situation based on the given information, establishes a strategy to achieve the goal, and acts as planned. In contrast, stimulus-driven control is not based on the given information and the participant responds to the situation without strategy or planning (Corbetta and Shulman, 2002). Repetitive stimulus-driven control results in individuals losing control over their gaming behavior with a loss of control over gaming.

This study has several limitations. First, as the scalp EEG was recorded during real-time online gaming, it is possible that there was noise in the EEG signals due to physical movements (i.e., wrist movement, neck motion). To reduce this effect, we instructed subjects not to engage in activities unrelated to gaming. Additionally, various filters were used to remove the noise from the data in the analytic processes. Future studies should consider additional biological signals that can reflect the subject's physical condition (i.e., EMG, PPG), which can be effective tools for establishing objective indicators during gaming. In addition, only male subjects were included in this study, which is the reason that generalization of the results of the current study may be limited. Finally, the changes in the scalp EEG signals in response to specific game events were not evaluated in this study. Future studies, including an analysis of the behavioral characteristics of individuals with IGD during specific game events and their accompanying scalp EEG signal responses, may expand on our present study.

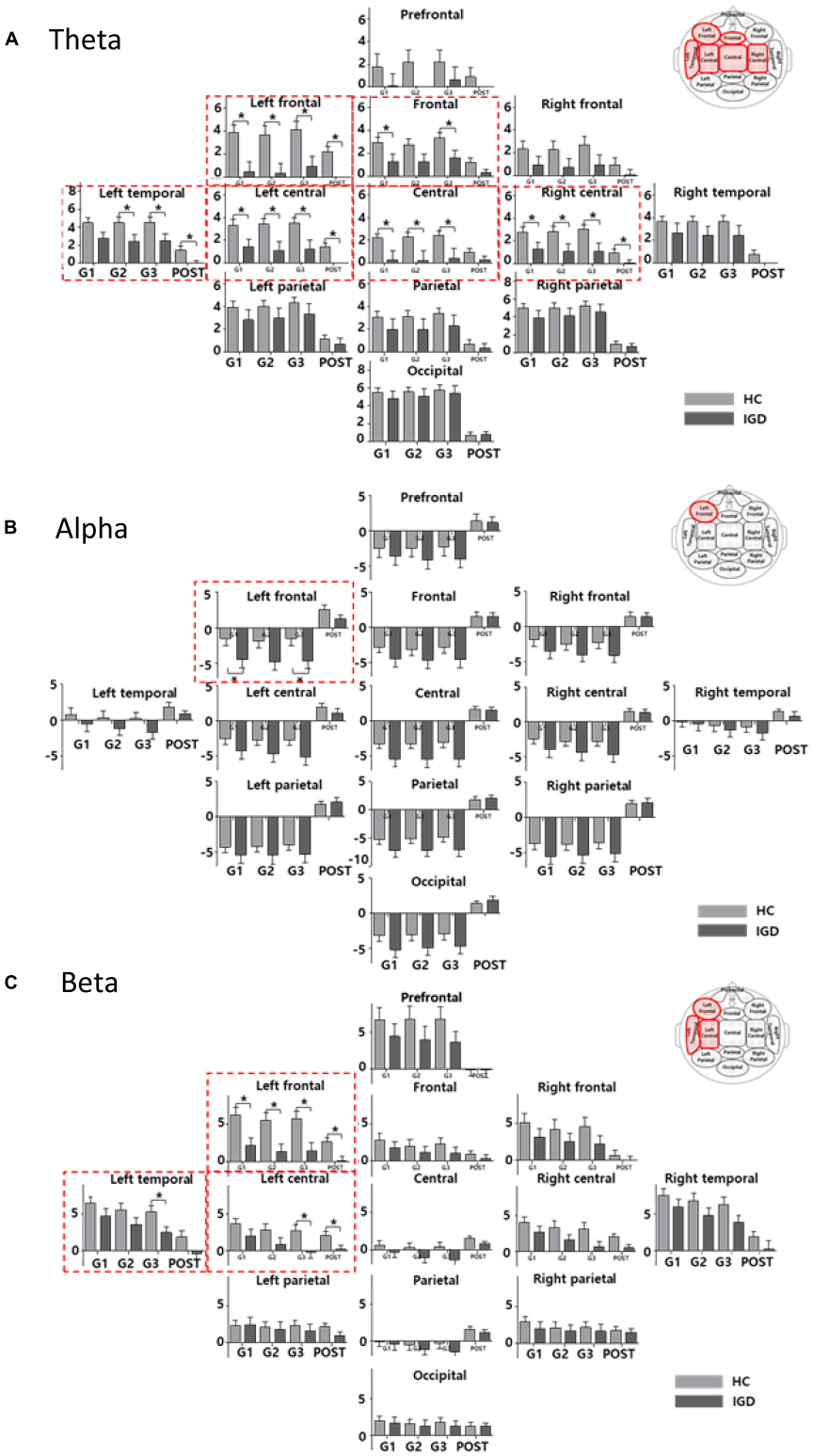

FIGURE 4 | The bar graph represents the results of mixed ANOVA for the 13 regions in the **(A)** theta, **(B)** alpha, and **(C)** beta bands. The X-axis represents the period (GAME1, GAME2, GAME3, and POST) and Y-axis represents percentage values for the 13 regions (light gray: HC, dark gray: IGD). The bar graph is located upward at percentage values greater than 0 and downward at percentage values less than zero. The red box indicates a region with a significant difference for the group effect (mixed ANOVA; $p < 0.05$, FDR correction; corrected $p < 0.2$). The *post hoc* results from the independent *t*-tests between the groups are shown as asterisks (*). Error bars indicate standard error. *$p < 0.05$.

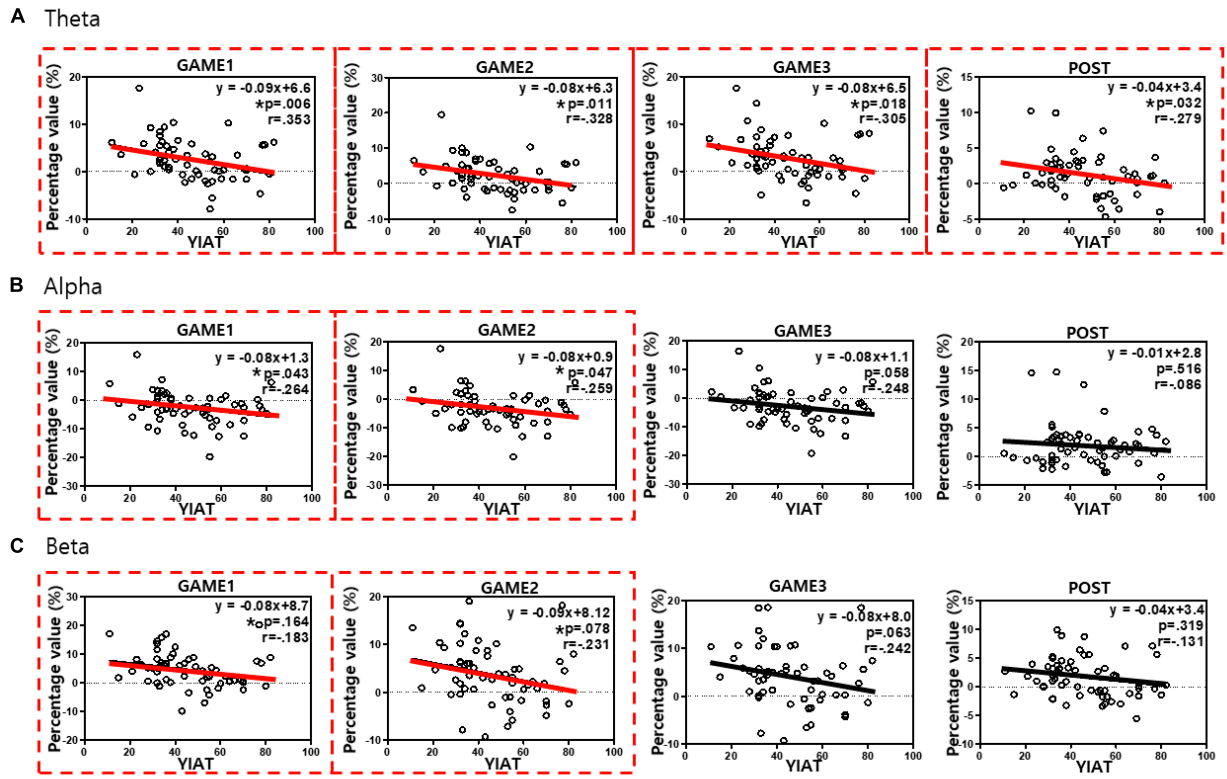

FIGURE 5 | Correlation analyses between the YIAT score and the percentage value in the left frontal region in all subjects in the **(A)** theta, **(B)** alpha, and **(C)** beta bands. The red boxes indicate statistical significance ($p < 0.05$), indicating periods with a weak correlation between the YIAT score and percentage value in the left frontal region. Significant negative correlations were observed in all periods for the theta band, during GAME1 and GAME2 periods for the alpha band, and during GAME1 and GAME2 periods for the beta band. *$p < 0.05$.

There are several strengths associated with this study. First, to the best of our knowledge, this is the first study to compare EEG activity recorded in individuals with IGD and HC subjects during gaming. Most previous studies reported EEG activity measured in the resting state, but we concluded that it is important to observe the reaction of participants to gaming cues in order to understand the addiction (Choi et al., 2013; Lee et al., 2014; Park et al., 2017). In addition, we made considerable efforts to recruit subjects who only exhibited impulsivity, in order to control for other factors. Almost all previous studies conducted in patients with IGD included subjects who had comorbid disorders (depression, anxiety, AUD, and ADHD).

In summary, based on the findings reported here we conclude that an association exists between impaired cognitive control and IGD during gaming. Our data demonstrated that individuals with IGD had significantly lower theta, alpha, and beta power in the left frontal region than that of the HCs while gaming. The collective data on theta, alpha, and beta activity suggest that the low theta and alpha activity indicated a boredom state, while the low beta activity reflected impulsivity and impaired inhibitory control during gaming. In addition, the degree of left frontal theta power suppression was found to be correlated with the severity of IGD during gaming. These findings suggest that reduced percentage values for the responses in the theta, alpha, and beta bands in the left frontal region during gaming have the potential to be neurobiological markers for IGD.

ETHICS STATEMENT

All subjects provided written informed consent before beginning with the experiment. Moreover, the experimental protocols were approved by the Institutional Review Board of Hanyang University (IRB number: HYI-16-044).

AUTHOR CONTRIBUTIONS

JK, JP, YP, DJ, KN, Y-CJ, and IK conceived and designed the experiments. JK and YP conducted the experiments. JP and DJ analyzed the data. KN, YJ, and IK wrote the manuscript. All authors revised and approved the manuscript.

FUNDING

This research was supported by the Original Technology Research Program for Brain Science through the National Research Foundation of Korea funded by the Ministry of Science, ICT and Future Planning (NRF-2015 M3C7A1064789).

REFERENCES

Akin, M. (2002). Comparison of wavelet transform and FFT methods in the analysis of EEG signals. *J. Med. Syst.* 26, 241–247. doi: 10.1023/A:1015075101937

Anderson, V., Anderson, P., and Jacobs, R. (2008). *Executive Functions and the Frontal Lobes: A Lifespan Perspective*. NewYork, NY: Taylor & Francis.

Beard, K. W., and Wolf, E. M. (2001). Modification in the proposed diagnostic criteria for internet addiction. *Cyberpsychol. Behav.* 4, 377–383. doi: 10.1089/109493101300210286

Bechara, A. (2005). Decision making, impulse control and loss of willpower to resist drugs: a neurocognitive perspective. *Nat. Neurosci.* 8, 1458–1463. doi: 10.1038/nn1584

Beck, A. T., Brown, G., Epstein, N., and Steer, R. A. (1988). An inventory for measuring clinical anxiety: psychometric properties. *J. Consult. Clin. Psychol.* 56, 893–897. doi: 10.1037/0022-006X.56.6.893

Beck, A. T., Ward, C. H., Mendelson, M., Mock, J., and Erbaugh, J. (1961). An inventory for measuring depression. *Arch. Gen. Psychiatry* 4, 561–571. doi: 10.1001/archpsyc.1961.01710120031004

Brand, M., Young, K. S., and Laier, C. (2014). Prefrontal control and Internet addiction: a theoretical model and review of neuropsychological and neuroimaging findings. *Front. Hum. Neurosci.* 8:375. doi: 10.3389/fnhum.2014.00375

Cavanagh, J. F., and Frank, M. J. (2014). Frontal theta as a mechanism for cognitive control. *Trends Cogn. Sci.* 18, 414–421. doi: 10.1016/j.tics.2014.04.012

Choi, J. S., Park, S. M., Lee, J., Hwang, J. Y., Jung, H. Y., Choi, S. W., et al. (2013). Resting-state beta and gamma activity in internet addiction. *Int. J. Psychophysiol.* 89, 328–333. doi: 10.1016/j.ijpsycho.2013.06.007

Chou, T. J., and Ting, C. C. (2003). The role of flow experience in cyber-game addiction. *Cyberpsychol. Behav.* 6, 663–675. doi: 10.1089/109493103322725469

Cohen, M. X. (2011). It's about time. *Front. Hum. Neurosci.* 5:2. doi: 10.3389/fnhum.2011.00002

Corbetta, M., and Shulman, G. L. (2002). Control of goal-directed and stimulus-driven attention in the brain. *Nat. Rev. Neurosci.* 3, 201–215. doi: 10.1038/nrn755

Crews, F. T., and Boettiger, C. A. (2009). Impulsivity, frontal lobes and risk for addiction. *Pharmacol. Biochem. Behav.* 93, 237–247. doi: 10.1016/j.pbb.2009.04.018

Crockford, D. N., Goodyear, B., Edwards, J., Quickfall, J., and el-Guebaly, N. (2005). Cue-induced brain activity in pathological gamblers. *Biol. Psychiatry* 58, 787–795. doi: 10.1016/j.biopsych.2005.04.037

Delorme, A., and Makeig, S. (2004). EEGLAB: an open source toolbox for analysis of single-trial EEG dynamics including independent component analysis. *J. Neurosci. Methods* 134, 9–21. doi: 10.1016/j.jneumeth.2003.10.009

Dong, G. H., DeVito, E. E., Du, X. X., and Cui, Z. Y. (2012). Impaired inhibitory control in 'internet addiction disorder': a functional magnetic resonance imaging study. *Psychiatry Res. Neuroimaging* 203, 153–158. doi: 10.1016/j.pscychresns.2012.02.001

Dong, G. H., Shen, Y., Huang, J., and Du, X. X. (2013). Impaired error-monitoring function in people with internet addiction disorder: an event-related fMRI study. *Eur. Addict. Res.* 19, 269–275. doi: 10.1159/000346783

Dong, G. H., Zhou, H., and Zhao, X. (2011). Male internet addicts show impaired executive control ability: evidence from a color-word stroop task. *Neurosci. Lett.* 499, 114–118. doi: 10.1016/j.neulet.2011.05.047

Genovese, C. R., Lazar, N. A., and Nichols, T. (2002). Thresholding of statistical maps in functional neuroimaging using the false discovery rate. *Neuroimage* 15, 870–878. doi: 10.1006/nimg.2001.1037

Gevins, A., Smith, M. E., McEvoy, L., and Yu, D. (1997). High-resolution EEG mapping of cortical activation related to working memory: effects of task difficulty, type of processing, and practice. *Cereb. Cortex* 7, 374–385. doi: 10.1093/cercor/7.4.374

Goldstein, R. Z., and Volkow, N. D. (2011). Dysfunction of the prefrontal cortex in addiction: neuroimaging findings and clinical implications. *Nat. Rev. Neurosci.* 12, 652–669. doi: 10.1038/nrn3119

Groppe, D. M., Urbach, T. P., and Kutas, M. (2011). Mass univariate analysis of event-related brain potentials/fields I: a critical tutorial review. *Psychophysiology* 48, 1711–1725. doi: 10.1111/j.1469-8986.2011.01273.x

Gundel, A., and Wilson, G. F. (1992). Topographical changes in the ongoing EEG related to the difficulty of mental tasks. *Brain Topogr.* 5, 17–25. doi: 10.1007/BF01129966

HajiHosseini, A., and Holroyd, C. B. (2015). Sensitivity of frontal beta oscillations to reward valence but not probability. *Neurosci. Lett.* 602, 99–103. doi: 10.1016/j.neulet.2015.06.054

Hong, S. J., Lee, D., Park, J., Namkoong, K., Lee, J., Jang, D. P., et al. (2018). Altered heart rate variability during gameplay in internet gaming disorder: the impact of situations during the game. *Front. Psychiatry* 9:429. doi: 10.3389/fpsyt.2018.00429

Jurado, M. B., and Rosselli, M. (2007). The elusive nature of executive functions: a review of our current understanding. *Neuropsychol. Rev.* 17, 213–233. doi: 10.1007/s11065-007-9040-z

Katahira, K., Yamazaki, Y., Yamaoka, C., Ozaki, H., Nakagawa, S., and Nagata, N. (2018). EEG correlates of the flow state: a combination of increased frontal theta and moderate frontocentral alpha rhythm in the mental arithmetic task. *Front. Psychol.* 9:300. doi: 10.3389/fpsyg.2018.00300

Kim, N. R., Hwang, S. S., Choi, J. S., Kim, D. J., Demetrovics, Z., Kiraly, O., et al. (2016). Characteristics and psychiatric symptoms of internet gaming disorder among adults using self-reported DSM-5 criteria. *Psychiatry Invest.* 13, 58–66. doi: 10.4306/pi.2016.13.1.58

Klimesch, W. (2012). Alpha-band oscillations, attention, and controlled access to stored information. *Trends Cogn. Sci.* 16, 606–617. doi: 10.1016/j.tics.2012.10.007

Koepp, M. J., Gunn, R. N., Lawrence, A. D., Cunningham, V. J., Dagher, A., Jones, T., et al. (1998). Evidence for striatal dopamine release during a video game. *Nature* 393, 266–268. doi: 10.1038/30498

Kuss, D. J. (2013). Internet gaming addiction: current perspectives. *Psychol. Res. Behav. Manag.* 6, 125–137. doi: 10.2147/PRBM.S39476

Lee, D., Hong, S. J., Jung, Y. C., Park, J., Kim, I. Y., and Namkoong, K. (2018). Altered heart rate variability during gaming in internet gaming disorder. *Cyberpsychol. Behav. Soc. Netw.* 21, 259–267. doi: 10.1089/cyber.2017.0486

Lee, J., Hwang, J. Y., Park, S. M., Jung, H. Y., Choi, S. W., Kim, D. J., et al. (2014). Differential resting-state EEG patterns associated with comorbid depression in internet addiction. *Prog. Neuropsychopharmacol. Biol. Psychiatry* 50, 21–26. doi: 10.1016/j.pnpbp.2013.11.016

Lee, J., Lee, S., Chun, J. W., Cho, H., Kim, D. J., and Jung, Y. C. (2015). Compromised prefrontal cognitive control over emotional interference in adolescents with internet gaming disorder. *Cyberpsychol. Behav. Soc. Netw.* 18, 661–668. doi: 10.1089/cyber.2015.0231

Montague, P. R. (1999). Reinforcement learning: an introduction. *Trends Cogn. Sci.* 3, 360–360. doi: 10.1016/S1364-6613(99)01331-5

Nuyens, F., Deleuze, J., Maurage, P., Griffiths, M. D., Kuss, D. J., and Billieux, J. (2016). Impulsivity in multiplayer online battle arena gamers: preliminary results on experimental and self-report measures. *J. Behav. Addict.* 5, 351–356. doi: 10.1556/2006.5.2016.028

Park, J. H., Hong, J. S., Han, D. H., Min, K. J., Lee, Y. S., Kee, B. S., et al. (2017). Comparison of QEEG findings between adolescents with attention deficit hyperactivity disorder (ADHD) without comorbidity and ADHD comorbid with internet gaming disorder. *J. Korean Med. Sci.* 32, 514–521. doi: 10.3346/jkms.2017.32.3.514

Patton, J. H., Stanford, M. S., and Barratt, E. S. (1995). Factor structure of the barratt impulsiveness scale. *J. Clin. Psychol.* 51, 768–774. doi: 10.1002/1097-4679(199511)51:6<768::aid-jclp2270510607>3.0.co;2-1

Petry, N. M., and O'Brien, C. P. (2013). Internet gaming disorder and the DSM-5. *Addiction* 108, 1186–1187. doi: 10.1111/add.12162

Reinert, D. F., and Allen, J. P. (2002). The alcohol use disorders identification test (AUDIT): a review of recent research. *Alcohol. Clin. Exp. Res.* 26, 272–279. doi: 10.1111/j.1530-0277.2002.tb02534.x

Shallice, T., and Burgess, P. (1996). The domain of supervisory processes and temporal organization of behaviour. *Philos. Trans. R. Soc. Lond. B Biol. Sci.* 351, 1405–1411. doi: 10.1098/rstb.1996.0124

Statista (2018). *League of Legends: Number of League of Legends Monthly Active Users (MAU) from 2011 to 2016 (in millions)*. Available at: https://www.statista.com/statistics/317099/number-lol-registered-users-worldwide/ (accessed Oct 25, 2018).

Thalemann, R., Wolfling, K., and Grusser, S. M. (2007). Specific cue reactivity on computer game-related cues in excessive gamers. *Behav. Neurosci.* 121, 614–618. doi: 10.1037/0735-7044.121.3.614

Ward, M. F., Wender, P. H., and Reimherr, F. W. (1993). The wender utah rating scale: an aid in the retrospective diagnosis of childhood attention deficit hyperactivity disorder. *Am. J. Psychiatry* 150, 885–890. doi: 10.1176/ajp.150.6.885

Yao, Y. W., Wang, L. J., Yip, S. W., Chen, P. R., Li, S., Xu, J. S., et al. (2015). Impaired decision-making under risk is associated with gaming-specific inhibition deficits among college students with internet gaming disorder. *Psychiatry Res.* 229, 302–309. doi: 10.1016/j.psychres.2015.07.004

Young, K. (2018). *WHO Adds Gaming Disorder to ICD-11*. Available at: https://www.jwatch.org/fw114289/2018/06/19/who-adds-gaming-disorder-icd-11 (accessed June 19, 2018).

Young, K. S. (2011). *Clinical Assessment of Internet-Addicted Clients: A Handbook and Guide to Evaluation and Treatment*. Hoboken, NJ: John Wiley & Sons, Inc., 19–34.

Conflict of Interest: The authors declare that the research was conducted in the absence of any commercial or financial relationships that could be construed as a potential conflict of interest.

frontiers in Neuroscience

METHODS
published: 15 November 2019
doi: 10.3389/fnins.2019.01198

Deep Feature Selection and Causal Analysis of Alzheimer's Disease

*Yuanyuan Liu, Zhouxuan Li, Qiyang Ge, Nan Lin and Momiao Xiong**

Department of Biostatistics and Data Science, School of Public Health, The University of Texas Health Science Center, Houston, TX, United States

Deep convolutional neural networks (DCNNs) have achieved great success for image classification in medical research. Deep learning with brain imaging is the imaging method of choice for the diagnosis and prediction of Alzheimer's disease (AD). However, it is also well known that DCNNs are "black boxes" owing to their low interpretability to humans. The lack of transparency of deep learning compromises its application to the prediction and mechanism investigation in AD. To overcome this limitation, we develop a novel general framework that integrates deep leaning, feature selection, causal inference, and genetic-imaging data analysis for predicting and understanding AD. The proposed algorithm not only improves the prediction accuracy but also identifies the brain regions underlying the development of AD and causal paths from genetic variants to AD via image mediation. The proposed algorithm is applied to the Alzheimer's Disease Neuroimaging Initiative (ADNI) dataset with diffusion tensor imaging (DTI) in 151 subjects (51 AD and 100 non-AD) who were measured at four time points of baseline, 6 months, 12 months, and 24 months. The algorithm identified brain regions underlying AD consisting of the temporal lobes (including the hippocampus) and the ventricular system.

Keywords: Alzheimer's disease, diffusion tensor imaging images, deep learning, causal inference, feature selection, genetic-imaging data analysis

OPEN ACCESS

Edited by:
Lin Shi,
The Chinese University of Hong Kong, China

Reviewed by:
Jingyun Chen,
New York University, United States
Liang Zhan,
University of Pittsburgh, United States

***Correspondence:**
Momiao Xiong
Momiao.Xiong@uth.tmc.edu

Specialty section:
This article was submitted to Brain Imaging Methods, a section of the journal Frontiers in Neuroscience

Received: *18 March 2019*
Accepted: *22 October 2019*
Published: *15 November 2019*

Citation:
Liu Y, Li Z, Ge Q, Lin N and Xiong M (2019) Deep Feature Selection and Causal Analysis of Alzheimer's Disease. Front. Neurosci. 13:1198. doi: 10.3389/fnins.2019.01198

INTRODUCTION

Alzheimer's disease (AD) causes progressive brain atrophy and memory loss, is a progressive, irreversible degenerative disease of the brain, and is the most common neurodegenerative disease in the world (Struyfs et al., 2015; Zhuang et al., 2017; Liu et al., 2018a,b). AD is an increasingly prevalent disease affecting an estimated 5.4 million Americans and more than 30 million people in the world. It is estimated that these numbers will be tripled by 2050. AD is the sixth leading cause of death in the United States (Alzheimer's Association, 2016; Leandrou et al., 2018).

Diagnosis and prediction of AD via clinical and psychometric assessments are challenging (Leandrou et al., 2018). The AD patients cannot obtain early and accurate diagnosis through clinical dementia rating and cognitive tests. A final diagnosis of AD is confirmed by histological examination at postmortem biopsy. However, the histological examination of the brain for the living patients is infeasible. Individually varying brain structure, function, and pathological effects can be measured by images. Therefore, imaging plays an important role in improving diagnosis and prediction of AD. According to the recommendation by the National Institute of Neurological

and Communicative Disorders and Stroke–AD and Related Disorders Association (NINCDS-ADRDA) Work Group, the clinical classification of AD should explore the image markers: magnetic resonance imaging (MRI), diffusion tensor imaging (DTI), positron emission tomography (PET), amyloid-PET, tau-PET, and abnormal neuronal cerebrospinal fluid (CSF) markers (tau and/or Aβ) (Dubois et al., 2007; Leandrou et al., 2018; Liu et al., 2018a,b).

As the size of the imaging datasets increases, manual analysis of imaging data is tedious and time-consuming. Computer-aided diagnosis (CAD) of AD that combines computational models and analytical tools for high-dimensional imaging data analysis is emerging as one of the major tools for diagnosis and prediction of AD (Dimitriadis et al., 2018; Leandrou et al., 2018). The widely used machine learning (ML) methods in CAD include discriminant analysis (DA), logistic regression (LR), random forest, neural networks, and support vector machine (SVM) (Lorenzi et al., 2017; Sarica et al., 2017; Dimitriadis et al., 2018; Leandrou et al., 2018). Deep learning, a rapidly resurging subfield of ML, outperforms many classical ML approaches and is emerging as a major analytic platform in ML (Esteva et al., 2019). Deep learning with massive amounts of computational power has produced a revolution in driverless cars, speech recognition, and imaging analysis (Waldrop, 2019) and demonstrated great potential for the diagnosis and predictive power in tuberculosis (Heo et al., 2019), cancer (Esteva et al., 2017; Haenssle et al., 2018; Ghatwary et al., 2019; Ladefoged et al., 2019), diabetic retinopathy (Gulshan et al., 2016), chronic kidney disease (Ravizza et al., 2019), AD (Payan and Montana, 2015; Hosseini-Asl et al., 2016; Sarraf and Tofighi, 2016; Ju et al., 2017; Ding et al., 2018; Wada et al., 2018; Spasov et al., 2019), and conversion from mild cognitive impairment (MCI) to AD (Choi et al., 2018; Spasov et al., 2019). There is a growing interest in the application of deep learning to health care and medicine.

Despite its great progresses in computer vision, natural language processing, control, decision making, diagnosis, and early detection of complex diseases, deep leaning is also well known as a "black box" owing to its low interpretability to humans and still has a serious opacity problem (Waldrop, 2019). Overcoming the limitation of the lack of transparency and interpretation remains a great challenge for deep learning (Dubois et al., 2007). In this paper, we develop a novel general framework that integrates deep leaning and causal inference for image classification. The new framework for image analysis consists of two stages: (1) develop convolutional neural networks (CNN) to classify AD status on the basis of DTI and use of occlusion map to find image regions that are most distinctive for disease status and (2) the use of state-of-the-art causal inference tools to determine if the selected image regions are causal for AD.

Brain anatomy, structural connectivity, and physical connection between brain regions that are characterized through water molecular diffusing within white matter tracts can be measured by DTI. The imaging signals provide intermediate endophenotypes. Genetic variants will influence brain microstructure, function, and disease development. Understanding the role that genetics has in imaging and disease variation is key to understanding the causal chain of complex diseases (Jahanshad et al., 2013; Bycroft et al., 2018; Elliott et al., 2018). Therefore, to further cover the genetic bases of brain structures and function, and mechanism of AD, a joint analysis of the genetic brain images and AD will be carried out. We will assess both association and causal relationships among genetic variants, brain regions, and AD.

MATERIALS AND METHODS

Materials

The DTI images used in this study are downloaded from the Alzheimer's Disease Neuroimaging Initiative (ADNI); the size of each image was $91 \times 109 \times 91$. ADNI is a longitudinal multicenter study designed to develop clinical, imaging, genetic, and biomedical biomarkers for the early detection and tracking of AD[1] (Alzheimer's Disease Neuroimaging Initiative, 2019). DTI images were recorded for every participant from different time points in which they joined the research study. The diagnostic results were normal control (NC), MCI, and AD. In this study, DTI images of 151 individuals from NCs (100 images) and AD (51 images) groups were chosen from four different diagnostic time points: baseline, 6 months, 12 months, and 24 months.

Image Preprocessing

To make sure that all the images for this analysis are comparable, we register all the DTI image data for every subject at every time point to the common template, which can be downloaded from the McConnell Brain Imaging Centre[2]. We utilized a strategy of combination of linear and non-linear registration algorithm to map each individual DTI data to the common template. During the linear image registration procedure, we first map the image data to the common template to make sure all the images are within the standard brain region by using FLIRT (FMRIB's Linear Image Registration Tool) from FSL (FMRIB software library) image analysis suite[3]. Then we further applied non-linear registration algorithm, which is implemented in RNiftyReg to map the image details within the standard brain. The linear image registration process helps us restrain each individual DTI image to a standard template, and the non-linear image registration helps us to make sure that the registered image maintains the structures details as the original data.

Genetic Data Preprocessing

We performed quality control (QC) in both individual level and single-nucleotide polymorphism (SNP) level QC in the plink binary format. For the individual level QC, the following steps were applied to the data:

1. Individuals with discordant gender information were removed from the data.
2. Individuals with missing rate $>10\%$ were removed from the data.

[1]http://adni.loni.usc.edu/about/#core-container

[2]http://www.bic.mni.mcgill.ca/ServicesAtlases/ICBM152NLin2009

[3]http://www.fmrib.ox.ac.uk/fsl/

3. Individuals with heterozygosity rate of more than three standard deviations from the mean were excluded from the data.
4. Individuals with identity by descent (IBD) > 0.185 were excluded from the data.

After the individual level QC was conducted, the following steps for SNP level QC were further applied to the data:

1. SNPs with missing genotype rate >10% were excluded from the data being analyzed.
2. SNPs with *P*-value for Hardy–Weinberg equilibrium (HWE) test <1*E*-6 were excluded from the data.
3. SNPs without polymorphism were removed from the data.

Then pre-imputation QC tool from McCarthy Groups was further applied to check the data against 1000G reference data. The imputation of the genetic data was conducted under the SHAPEIT + IMPUTE2 framework in the internal computational clusters. The 1000G reference data were used as the reference panel for imputation. After the imputation, the SNP level QC steps were applied again to the data to produce the final genetic data for analysis. Finally, a total of 1,589,061 common SNPs in 36,480 genes genotyped in 151 individuals were included in analysis.

Architecture of Convolutional Neural Network

The CNN model Visual Geometry Group (VGG) that won the first and second places in the localization and classification tracks, respectively, in the ImageNet Challenge 2014 was chosen for image classification and prediction (Simonyan and Zisserman, 2014). To improve the classification accuracy, the VGG utilized smaller receptive window size and increased the depth of the network. Furthermore, to prevent overfitting and improve the image region recognition ability of the networks, global average pooling (GAP) layer was used as a structure regularizer and localizer in the model to identify the complete extent of the object and exactly which regions of an image are being used for classification (Zhou et al., 2016).

As is shown in **Figure 1**, the network contained five max pooling layers, followed with a GAP layer before a fully connected softmax layer with two nodes.

Three-dimensional (3D) whole brain images with 109 × 91 × 91 size were input into CNN. DTI measures microscopic random motion of water molecules, which uncovers the orientation of surrounding tissues, and provides tract information on brain structure. Convolution of an image with different filters can perform operations that capture various types of features and directional information of DTI images and can preserve tract of DTI and the relationship between pixels. 3D CNNs (3D-CNN) with five convolutional layers and three fully connected layers were used for AD prediction. A 3D filter was applied to the dataset, and the filter moves in three directions (*X*, *Y*, *Z*) to calculate the low-level feature representations. Specifically, 3D filters were arranged as in **Table 1**.

To overcome the small sample size limitation of medical images, image augmentation techniques were used (Aderghal et al., 2017). The first technique we applied was Gaussian filters to blur the image to mimic the possible variations in the original images. A filter size of 3 × 3, 5× 5, and 7× 7 were used with spread parameters of 0.7, 0.7, and 0.6, respectively. The second augmentation technique we used was translation, where

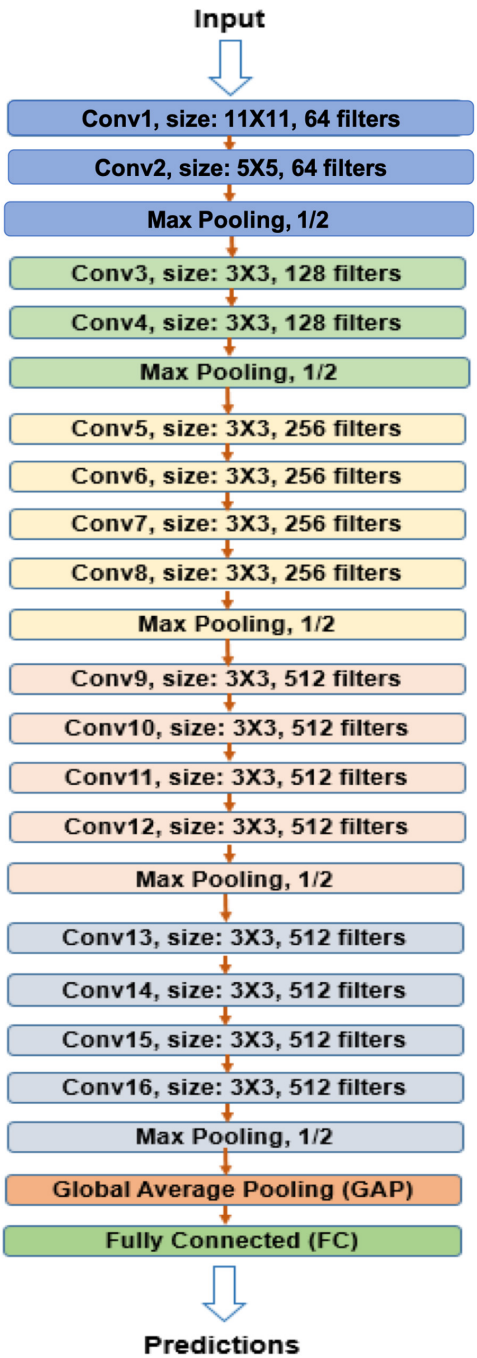

FIGURE 1 | VGG-GAP model architecture. The CNNs in the model included five max pooling layers and one GAP layer before fully connected layer. VGG, Visual Geometry Group; GAP, global average pooling; CNN, convolutional neural network.

TABLE 1 | 3D filters in five convolutional layers.

Conv layer	Filter size	Stride in (*X*, *Y*) direction	Stride in *Z* direction
Conv 1	11 × 11 × 11	4	4
Conv 2	5 × 5 × 5	1	1
Conv 3	3 × 3 × 3	1	1
Conv 4	3 × 3 × 3	1	1
Conv 5	3 × 3 × 3	1	1

3D, three-dimensional.

we shifted the images by ±1 pixel in each dimension. This imitates the possible variations in registration process where the images were aligned with the template. Finally yet importantly, the images were flipped horizontally because some regions of the brain (e.g., the hippocampus) are symmetrical to enlarge our sample size. To balance the data, we randomly duplicated some images from the under-sampled category. Data augmentation and class balancing produced over 20 times more data than the original dataset.

The model was trained in the Texas Advanced Computing Center (TACC) Maverick2 with NVIDIA GTX 1080 Ti GPUs.

Deep Feature Selection for Diffusion Tensor Imaging Images

Prediction difference analysis for visualizing the response of CNN to a specific input was used to select features for DTI image classification (Zintgraf et al., 2017). Specifically, prediction difference analysis estimates the importance of input pixels by calculating the effect of removing information from the imaging on the class prediction precision (Zeiler and Fergus, 2014).

A sliding window (patch) of 3 × 3 × 3 was applied to each image. The imaging signals contained in the sliding window were taken as a feature. Each one 3 × 3 × 3 patch was replaced by randomly sampled values from multivariate normal distributions. The resulting new image where the imaging feature (information) was removed was input into a previously trained CNN model to obtain probability p_1 for predicting AD. Let p_0 be the probability of predicting AD using the original images [without removing the feature (information)]. The relative importance of the feature was evaluated by Zintgraf et al. (2017).

$$d = \log\left(\frac{\frac{p_0}{1-p_0}}{\frac{p_1}{1-p_1}}\right) \quad (1)$$

The sliding window moved across the entire image and a relevance matrix, W of the same size as the whole image was generated, which reflected the relevance importance of all image pixels. A positive value indicated that the pixel contributed evidence for the classification of AD, whereas a negative value showed that the pixel contributed against the classification of AD. For details, please see Zintgraf et al. (2017).

Conditional Generative Adversarial Network and Classifier Two-Sample Tests for Causal Discovery

Three-dimensional functional principal component (FPC) scores were used to summarize the imaging signal information of the brain region (Xiong, 2018). Similarly, 1D FPCs can be used to summarize genetic information in the gene. Conditional generative adversarial networks (CGANs) will be used to discover causal relationships between the brain neuroimaging region and AD and causal relationships between the brain neuroimaging region and gene as well (Goodfellow et al., 2014; Lopez-Paz and Oquab, 2017) (**Figure 2**). Specifically, consider two variables X and Y, which can be binary disease status or continuous FPCs summarizing imaging signals in the brain region or genetic variation in the gene. If X causes Y, denoted by $X \rightarrow Y$, then we have

$$Y = f_Y(X, N_Y),$$

where f_Y is a non-linear function and realized by CGAN where a neural network is used to approximate the non-linear function $f_Y(X, N_Y)$, and N_Y is a noise random variable and is independent of cause X. Similarly, if Y causes $X(Y \rightarrow X)$, then we have

$$X = f_X(X, N_X),$$

where f_X is a non-linear function and N_X is a noise random variable and is independent of cause Y. Assume that n subjects are sampled.

We define dataset $D_w = \{u_i, v_i, i = 1, \ldots, n\}$. We assign label 0 to dataset $D_u = \{u_i, i = 1, \ldots, n\}$ and 1 to dataset $D_v = \{v_i, i = 1, \ldots, n\}$. Let P be the distribution of u_i, $i = 1, \ldots, n$ and Q be the distribution of v_i, $i = 1, \ldots, n$. We use the K *nearest neighbor* (*KNN*) as a binary classifier to classify two datasets and define the test statistic t as the classification accuracy to test the null hypothesis of equal distributions of two datasets $P = Q$. Let z be a random variable.

The procedures for bivariate causal discovery using CGAN are summarized as follows (Lopez-Paz and Oquab, 2017):

1. Use a CGAN from $X \rightarrow Y$ to generate the dataset $D_{X \rightarrow Y} = \{(x_i, \hat{y}_i = f_y(x_i, z_i)),\ i = 1, \ldots, n\}$.
2. Use a CGAN from $Y \rightarrow X$ to generate the dataset $D_{Y \rightarrow X} = \{(\hat{x}_i = f_X(y_i, z_i), y_i),\ i = 1, \ldots, n\}$.
3. Divide the total samples into training samples and test samples.
4. Classify two datasets : $D_u = D_y = \{y_i, i = 1, \ldots, n\}$ versus $D_v = D_{X \rightarrow Y} = \{\hat{y}_i,\ i = 1, \ldots, n\}$ and calculate the two-sample statistic $\hat{t}_{X \rightarrow Y}$.
5. Classify two datasets: $D_u = D_x = \{x_i, i = 1, \ldots, n\}$ versus $D_v = D_{Y \rightarrow X} = \{\hat{x}_i,\ i = 1, \ldots, n\}$ and calculate the two-sample statistic $\hat{t}_{Y \rightarrow X}$.
6. Calculate the test statistic $T = \hat{t}_{X \rightarrow Y} - \hat{t}_{Y \rightarrow X}$. Under the null hypothesis of no causal relationship or test inconclusive, the statistic T is asymptotically distributed as

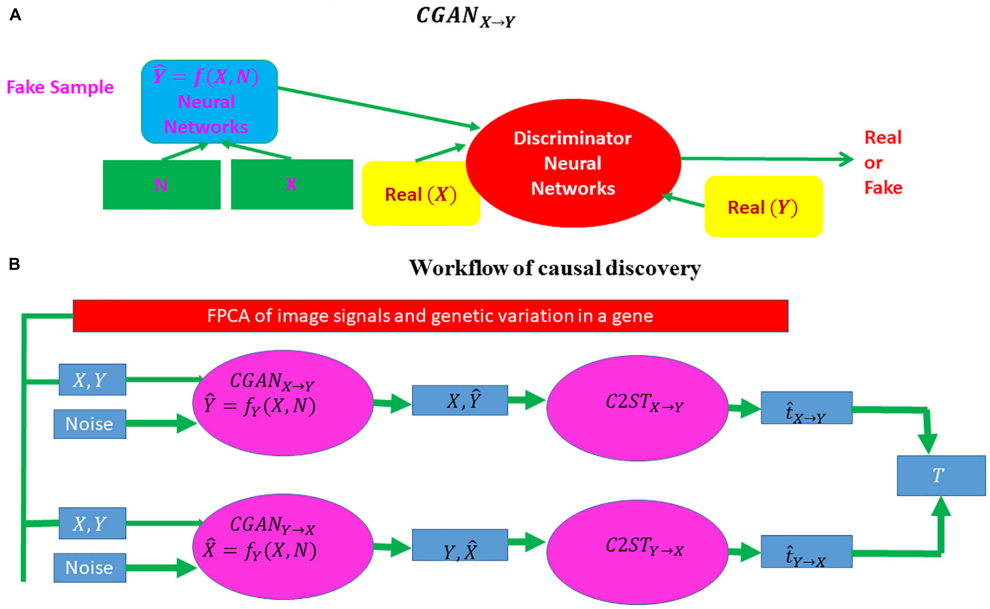

FIGURE 2 | Workflow of causal inference using CGAN and a classifier two-sample test. CGAN, conditional generative adversarial network. **(A)** A visual explanation of CGAN and **(B)** the complete workflow of causal discovery.

TABLE 2 | AD prediction accuracy on fivefold cross validation.

Model development time point	Prediction time point			
	Baseline	6 months	12 months	24 months
Baseline	0.8675	0.9123	0.8864	0.7967
6 months		0.8452	0.8963	0.7791
12 months			0.8335	0.7813
24 months				0.7643

AD, Alzheimer's disease.

$N(0,\sigma^2)$, where $\sigma^2 = \frac{0.5}{n_{\text{test}}} - 2cov(\hat{t}_{X\to Y}, \hat{t}_{Y\to X})$ and n_{test} is the number of subjects in the test set.

Association is defined as measuring the dependence or correlation between two variables and to use these dependencies for prediction that is not dealing with causal problems. Almost all currently used statistical methods in imaging genetics [such as sparse canonical correlation analysis (SCCA), sparse reduced rank regression (SRRR), and parallel independent component analysis (ICA)] are association analysis methods. These methods can detect association between genetic variation and imaging signals. It is well known that correlation or association analysis does not imply causation. The signals identified by association analysis may not have specific pathological relevance to diseases. Association signals provide limited information on the causal mechanism of diseases. Most genetic and imaging analysis questions to uncover the mechanism of the disease are causal in nature. Causation analysis is essential to the genetic analysis of complex phenotypes yet ignored for a long time.

Distinguishing causation from association is an age-old problem. Intuitively, causation implies that changes in one variable will directly make changes in the other. The essential distinction between association and causation relies on what the response will be if we intervene in the system (Lattimore and Ongv, 2018).

There are two types of causal inference: interventional causal inference and observational causal inference. Interventional causal inference learns the effect of taking an action directly via experiments, for example, randomized controlled trials. Interventional experiments are a gold standard for causal inference. However, because in human genetics we cannot change the genetic materials of human subjects, experimental interventions are unethical and infeasible. Therefore, it is essential to develop statistical methods and algorithms to predict the outcomes of an intervention from passive observation.

The additive noise models (ANMs) assume one causal direction $X \to Y$ but no reversible causal direction $Y \to X$. Causation is asymmetric. However, the association of X and Y can be (1) $X \to Y$, (2) $Y \to X$, and (3) $X \to Y$, $Y \to X$. Association is symmetric.

Additive noise models are based on the independence of cause and mechanism (ICM) principle. ICM assumes that causes and mechanisms are chosen independently by nature, which is a recently proposed principle for causal reasoning and causal learning (Peters et al., 2017). ICM assumes that the mechanism that generates effect from its cause contains no information about the cause, which implies that X and N_Y in the ANMs are independent. However, X and N_Y in the non-linear regression model $Y = f_Y(X, N_Y)$ may be dependent.

In summary, association is studied by observed conditional distribution, and causation is investigated by interventional distribution where causal effect is determined by the effect of hypothetic manipulation of an input on an output. In other

TABLE 3 | Average sensitivity and specificity over fivefold cross validation.

Model development time point	Prediction time point			
	Baseline	**6 months**	**12 months**	**24 months**
Baseline	(0.6873, 0.9600)	(0.8073, 0.9700)	(0.7524, 0.9717)	(0.6465, 0.9313)
6 months		(0.6364, 0.9600)	(0.7778, 0.9717)	(0.5977, 0.9417)
12 months			(0.7295, 0.8995)	(0.6674, 0.8833)
24 months				(0.6294, 0.8853)

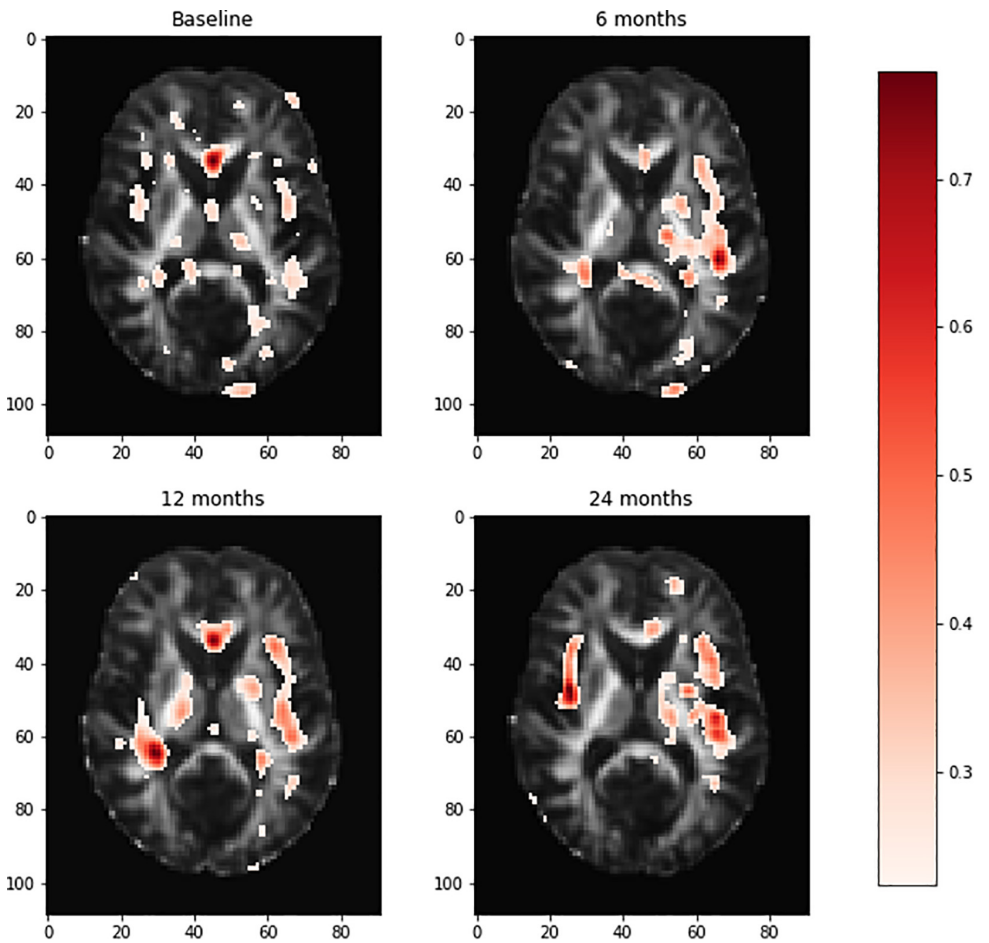

FIGURE 3 | Visualization of the brain regions with relative importance values at the baseline, 6 months, 12 months, and 24 months. The deeper the red color of the brain region, the more important for AD prediction. AD, Alzheimer's disease.

words, association is investigated by seeing, and causation is investigated by doing.

RESULTS

Alzheimer's Disease Classification and Prediction

The VGG network with 3D filters was used for classification and prediction of AD using 3D whole brain DTI images at four different time points: baseline, 6 months, 12 months, and 24 months. We consider two classes: AD and NC. AD prediction accuracy using VGG is listed in **Table 2**, and its sensitivity and specificity are shown in **Table 3**, where the first and second values in the brackets represent sensitivity and specificity, respectively. **Tables 2**, **3** demonstrate that the prediction accuracy, sensitivity, and specificity of VGG using the training dataset at baseline to predict AD in the test datasets at baseline, 6 months, 12 months, and 24 months were 0.8675 (0.6873, 0.9600), 0.8452 (0.6364, 0.9600), 0.8335 (0.7295, 0.8995), and 0.7463 (0.6294, 0.8853), respectively. In other cases, we can observe similar results. The area under the curve (AUC) using the training data at baseline, 6 months, 12 months, and 24 months for prediction of AD in the test datasets at the same time points was 0.8571,

0.8291, 0.8583, and 0.7756, respectively. The low sensitivity of prediction of AD may be due to small and imbalanced sample size (51 AD and 100 controls). A much higher proportion of non-AD controls have decreased sensitivity but increased specificity. Deep VGG that has a large number of parameters to be estimated requires large sample sizes. Although we used data augmentation methods to increase sample sizes, augmentation methods still did not provide large and reliable sample sizes. Large sample sizes are an important issue for increasing the prediction of accuracy.

Region Selection and Interpretation

Relative importance of value d was sorted. Image areas whose relative importance value was in the top 10th percentile were considered as features that contributed substantially to the prediction of AD. We identified 23 important brain regions that contributed substantially to AD prediction. The results are shown in **Figure 3** where each subfigure has 91 × 109 pixel sizes, where the darker the red color is, the more important the brain region is to the prediction accuracy. The brain regions with red color included the temporal lobe (the left temporal, medial, and right temporal lobes), ventricles and enlarged ventricle, occipital lobe, and prefrontal area. To further interpret the image analysis results and increase their transparency, we tested the causal relationships between DTI image ROIs and AD disease at baseline, 6 months, 12 months, and 24 months using CGAN-based statistics. After Bonferroni correction, P-value < 0.0022 was the threshold to declare significance. The number of identified brain regions that showed significant causation to AD at baseline, 6 months, 12 months, and 24 months was 1, 1, 2, and 4, respectively. **Table 4** lists ROIs where P-values for testing causation between the ROI and AD were <0.05. Three remarkable features emerged from these results. First, as time passed, AD progressed from mild (early stage), via moderate (middle stage), to severe (late stage), which resulted in atrophy of more and more brain regions. Therefore, we observed the increased number of significant causal brain regions with AD as the study time of AD increased from the baseline to 24 months. Second, in general, as AD progressed, the significance of causation between the brain region and AD increased (P-values for testing causation decreased). Third, the brain region in ROI 18 (the ventricles and enlarged ventricle) (**Figure 4**) showed significant causation to AD at all four time points (baseline, 6 months, 12 months, and 24 months). The brain regions in ROI 14 (the left temporal lobe) (**Figure 4**) showed significant causation at 12 and 24 months after Bonferroni correction. The literature reports that these regions are related to AD. The left temporal lobe is involved in language and AD (Cretin et al., 2015; Flick et al., 2018; Trimmel et al., 2018), and the right temporal lobe atrophy is involved in severe impairment in emotion recognition (Everhart et al., 2015) and causes frontotemporal dementia (Gliebus, 2014), with the brain ventricles often affected AD (Ferrarini et al., 2006). Ventricle enlargement is a useful structural biomarker for the diagnosis of AD (Anandh et al., 2014).

TABLE 4 | Causations between DTI image ROIs and AD disease status.

Time point	ROI index	*P*-value
Baseline	2	0.0463
	18	0.0005
6 months	8	0.0182
	14	0.0108
	17	0.0155
	18	0.0010
12 months	6	0.0117
	14	0.0018
	17	0.0107
	18	<0.00005
24 months	0	0.0245
	3	0.0133
	5	0.0092
	7	0.0063
	8	0.0030
	9	0.0007
	11	0.0084
	12	0.0002
	13	0.0082
	14	<0.00005
	15	0.0098
	17	0.0239
	18	<0.00005
	19	0.0210
	21	0.0363
	22	0.0166

ROI 14 corresponds to the left temporal lobe and 17 corresponds to the right temporal lobe. ROI 18 corresponds to ventricles and enlarged ventricle and indicates atrophy of cerebral nerve tissue, which is typical in AD patients. DTI, diffusion tensor imaging; ROI, region of interest; AD, Alzheimer's disease.

Genetic Studies of Two Brain Regions

To uncover genetic architecture of brain regions, in addition to genetic-imaging association analysis, we conducted genetic-imaging causal analysis using the CGAN where imaging signals within the brain region and SNPs within the gene were summarized by 2D functional principle scores and classical functional principle scores, respectively (Lopez-Paz and Oquab, 2016). The total number of candidate genes being tested was 61. After Bonferroni correction, the P-value for declaring significance of both causation and association was 0.00082. We presented the results of P-values < 0.05 in causal analysis and association analysis of genetic variation in 61 candidate genes with two brain regions, the left temporal lobe and frontal and temporal left lobe, and the right temporal lobe as seen in **Supplementary Tables S1**, **S2**, respectively, where 61 genes were obtained from genome-wide causation studies of AD in the manuscript (Lin et al., unpublished). In **Supplementary Tables S1**, **S2**, the P-values in bold green denote significant causation or association after Bonferroni corrections. The majority of genes that had causal or association relationships with brain

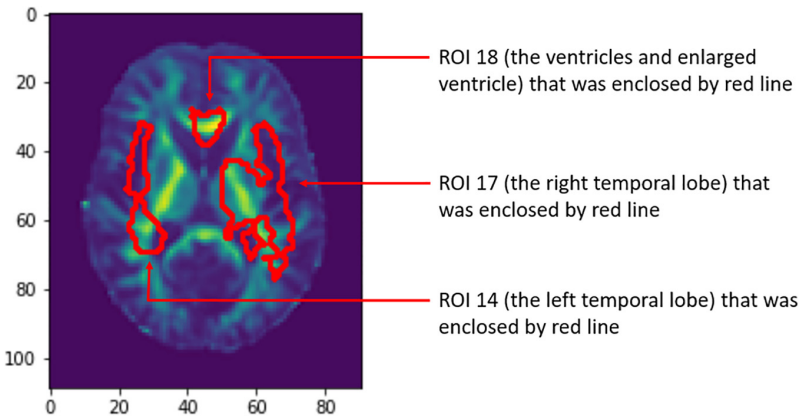

FIGURE 4 | Three brain regions showed causation to AD. AD, Alzheimer's disease.

neuroimaging phenotypes were identified at all time points (baseline, 6 months, 12 months, and 24 months). We also observed that these identified genes had causal or association relationships with both the left temporal lobe and right temporal lobe regions. The identified genes *CD33*, *COBL*, and *APP* that had causal relationships with brain neuroimaging regions were confirmed multiple times in the literature (Bradshaw et al., 2013; Mez et al., 2017; Kovacs et al., 2018; Van Giau et al., 2018; Huang C.C. et al., 2019; Huang C.Y. et al., 2019). It was also reported that gene *FGF4* was involved in neurodevelopmental disorders (Grillo et al., 2014), *FRMD6* was implicated in AD (Hong et al., 2012), *Dock9* played an important role in regulation of morphological changes in hippocampal neurons (Kuramoto et al., 2009), *H3F3B* was associated with a broad schizophrenia phenotype (Manley et al., 2018), *SCYL1* was involved in cerebellar atrophy (Lenz et al., 2018), *AKAP5* played a significant role in the regulation of sympathetic nerve activities (Han et al., 2016), and *PIGC* was involved in epilepsy and intellectual disability (Edvardson et al., 2017).

DISCUSSION

In this paper, we presented a general artificial intelligence (AI) platform for prediction of AD using DTI images. Non-transparency could be a major challenge of deep learning for medical image analysis. To meet this challenge, we introduced three approaches to medical image interpretation: feature selection and visualization, causal analysis of neuroimaging region, and genetic-imaging analysis. Feature selection and visualization methods selected and visualized brain regions as a potential pathology of AD. Further CGAN evaluation and two-sample tests discovered potential causal relationships between the brain neuroimaging regions and AD. We observed the increased number of significant causal brain regions with AD when AD progressed. In general, as AD progressed, the significance of causation between the brain region and AD increased (*P*-values decreased). We observed that the ventricles and enlarged ventricle and the left and right temporal lobes had strong causal relationships with AD. Temporal lobes including the hippocampus are crucial in AD development at the early stages, whereas the ventricles and enlarged ventricle are a useful structural biomarker for the diagnosis of AD. Joint causal analysis of genetic and images of the left and right temporal regions using CGAN evaluation and two-sample tests mapped *CD33*, *COBL*, *FRMD6*, *APP*, and other genes to the left and right temporal brain regions.

Many findings in the paper can be confirmed in the literature. For example, both prediction analysis using deep learning and causal analysis using CGAN and a two-sample test identified the brain temporal lobe region that was involved in AD. The temporal lobe includes the hippocampus and its surrounding regions. It is well known that the temporal lobe consists of structures that are vital for long-term memory. There are numerous reports that the temporal lobe including the left, medial, and right temporal lobes are involved in AD pathology (Kakeda and Korogi, 2010; Li and Chen, 2015; Menéndez-González et al., 2015; Aggleton et al., 2016; Delgado-González et al., 2017; Pettigrew et al., 2017; Wolk et al., 2017; Jung et al., 2018; Kitchigina, 2018; Persson et al., 2018; Grajski and Bressler, 2019; Kenkhuis et al., 2019; Lam et al., 2019; Pasquini et al., 2019; Xie et al., 2019). DTI discovered the functional and structural connectivity between the medial temporal lobe (MTL) and posteromedial cortex (PMC) (Buckner et al., 2008; Pasquini et al., 2019). The MTL includes the hippocampal formation and other cortices. These regions underlie memory processing through interplay with neocortical areas from the PMC. AD-related pathological changes such as tau accumulation and amyloidβ deposition often affect the PMC and MTL regions. The functional and structural disconnections between the MTL and PMC cause the development and progression of AD.

The literature confirmed the identified pathological paths from genetic variants to AD via brain regions: *CD33* → medial temporal and hippocampus (Wang et al., 2019) → AD (Pasquini et al., 2019) and *CD33* → AD (Miles et al., 2019); *APP* → medial and lateral temporal lobe (Huang C.C. et al., 2019) → AD (Buckner et al., 2008) and *APP* → AD (Zhou et al., 2011); *SCYL1* →

cerebellar atrophy (Schmidt et al., 2015) → AD (Gallo et al., 2017); and *SCYL1* → neurodegenerative disease (Schmidt et al., 2007). These provided indirect evidences of identified biomarkers for unraveling mechanism of AD.

The results in this paper are preliminary. Sample sizes need to be increased and additional datasets analyzed to replicate the results. The purpose of this paper is to stimulate further discussions regarding the great challenges we are facing in developing robust deep learning platforms that combine multiple modes of imaging tools and have high accuracy across multiple datasets and uncovering causal pathways from genetic variants to disease via brain imaging regions.

DATA AVAILABILITY STATEMENT

Publicly available datasets were analyzed in this study. This data can be found here: http://adni.loni.usc.edu/.

AUTHOR CONTRIBUTIONS

YL developed the software and conducted the data analysis. ZL contributed to the data preprocessing and partial writing. NL contributed to data preprocessing. QG conducted the partial data analysis. MX designed the study and wrote the manuscript.

FUNDING

YL was supported by the UTHealth Innovation for Cancer Prevention Research Training Program Pre-doctoral Fellowship (Cancer Prevention and Research Institute of Texas Grant No. RP160015).

ACKNOWLEDGMENTS

In this study, data used in the preparation of this article were obtained from the ADNI database (adni.loni.usc.edu). The ADNI was launched in 2003 as a public–private partnership, led by principal investigator Michael W. Weiner, MD. The primary goal of ADNI has been to test whether serial MRI, PET, other biological markers, and clinical and neuropsychological assessment can be combined to measure the progression of MCI and early AD. For up-to-date information, see www.adni-info.org. The authors thank TACC for providing computational resources.

SUPPLEMENTARY MATERIAL

The Supplementary Material for this article can be found online at: https://www.frontiersin.org/articles/10.3389/fnins.2019.01198/full#supplementary-material

REFERENCES

Aderghal, K., Boissenin, M., Benois-Pineau, J., Catheline, G., and Afdel, K. (2017). "Classification of sMRI for AD diagnosis with convolutional neuronal networks: a pilot 2-D+ epsilon Study on ADNI," in *International Conference on Multimedia Modeling*, (New York, NY: Springer) 690–701.

Aggleton, J. P., Pralus, A., Nelson, A. J., and Hornberger, M. (2016). Thalamic pathology and memory loss in early Alzheimer's disease: moving the focus from the medial temporal lobe to Papez circuit. *Brain* 139, 1877–1890. doi: 10.1093/brain/aww083

Alzheimer's Association. (2016). 2016 Alzheimer's disease facts and figures. *Alzheimers Dement.* 12, 459–509. doi: 10.1016/j.jalz.2016.03.001

Alzheimer's Disease Neuroimaging Initiative. (2019). *About ADNI*. Available at: http://adni.loni.usc.edu/about/#core-container (accessed January 12, 2019).

Anandh, K. R., Sujatha, C. M., and Ramakrishnan, S. (2014). Segmentation of ventricles in Alzheimer mr images using anisotropic diffusion filtering and level set method. *Biomed. Sci. Instrum.* 50, 307–313.

Bradshaw, E. M., Chibnik, L. B., Keenan, B. T., Ottoboni, L., Raj, T., Tang, A., et al. (2013). CD33 Alzheimer's disease locus: altered monocyte function and amyloid biology. *Nat. Neurosci.* 16, 848–850. doi: 10.1038/nn.3435

Buckner, R. L., Andrews-Hanna, J. R., and Schacter, D. L. (2008). The brain's default network: anatomy, function, and relevance to disease. *Ann. N. Y. Acad. Sci.* 1124, 1–38. doi: 10.1196/annals.1440.011

Bycroft, C., Freeman, C., Petkova, D., Band, G., Elliott, L. T., Sharp, K., et al. (2018). The UK Biobank resource with deep phenotyping and genomic data. *Nature* 562, 203–209. doi: 10.1038/s41586-018-0579-z

Choi, H., Jin, K. H., and Alzheimer's Disease Neuroimaging Initiative. (2018). Predicting cognitive decline with deep learning of brain metabolism and amyloid imaging. *Behav. Brain Res.* 344, 103–109. doi: 10.1016/j.bbr.2018.02.017

Cretin, B., Laure, D. L., Blanc, F., and Magnin, E. (2015). Left temporal lobe epilepsy revealing left posterior cortical atrophy due to Alzheimer's disease. *J. Alzheimers Dis.* 45, 521–526. doi: 10.3233/JAD-141953

Delgado-González, J. C., Florensa-Vila, J., Mansilla-Legorburo, F., Insausti, R., and Artacho-Pérula, E. (2017). Magnetic resonance imaging and anatomical correlation of human temporal lobe landmarks, in 3d euclidean space: a study of control and Alzheimer's disease subjects. *J. Alzheimers Dis.* 57, 461–473. doi: 10.3233/JAD-160944

Dimitriadis, S. I., Liparas, D., and Alzheimer's Disease Neuroimaging Initiative. (2018). How random is the random forest? Random forest algorithm on the service of structural imaging biomarkers for Alzheimer's disease: from Alzheimer's disease neuroimaging initiative (ADNI) database. *Neural Regen. Res.* 13, 962–970. doi: 10.4103/1673-5374.233433

Ding, Y., Sohn, J. H., Kawczynski, M. G., Trivedi, H., Harnish, R., Jenkins, N. W., et al. (2018). A deep learning model to predict a diagnosis of Alzheimer Disease by using 18F-FDG PET of the brain. *Radiology* 290, 456–464. doi: 10.1148/radiol.2018180958

Dubois, B., Feldman, H. H., Jacova, C., DeKosky, S. T., Barberger-Gateau, P., Cummings, J., et al. (2007). Research criteria for the diagnosis of Alzheimer's disease: revising the NINCDS-ADRDA criteria. *Lancet Neurol.* 6, 734–746. doi: 10.1016/S1474-4422(07)70178-3

Edvardson, S., Murakami, Y., Nguyen, T. T. M., Shahrour, M., St-Denis, A., Shaag, A., et al. (2017). Mutations in the phosphatidylinositol glycan C (PIGC) gene are associated with epilepsy and intellectual disability. *J. Med. Genet.* 54, 196–201. doi: 10.1136/jmedgenet-2016-104202

Elliott, L. T., Sharp, K., Alfaro-Almagro, F., Shi, S., Miller, K. L., Douaud, G., et al. (2018). Genome-wide association studies of brain imaging phenotypes in UK Biobank. *Nature* 562, 210–216. doi: 10.1038/s41586-018-0571-7

Esteva, A., Kuprel, B., Novoa, R. A., Ko, J., Swetter, S. M., Blau, H. M., et al. (2017). Dermatologist-level classification of skin cancer with deep neural networks. *Nature* 542, 115–118. doi: 10.1038/nature21056

Esteva, A., Robicquet, A., Ramsundar, B., Kuleshov, V., DePristo, M., Chou, K., et al. (2019). A guide to deep learning in healthcare. *Nat. Med.* 25, 24–29. doi: 10.1038/s41591-018-0316-z

Everhart, D. E., Watson, E. M., Bickel, K. L., and Stephenson, A. J. (2015). Right temporal lobe atrophy: a case that initially presented as excessive piety. *Clin. Neuropsychol.* 29, 1053–1067. doi: 10.1080/13854046.2015.1104387

Ferrarini, L., Palm, W. M., Olofsen, H., van Buchem, M. A., Reiber, J. H., and Admiraal-Behloul, F. (2006). Shape differences of the brain ventricles in Alzheimer's disease. *Neuroimage* 32, 1060–1069. doi: 10.1016/j.neuroimage.2006.05.048

Flick, G., Oseki, Y., Kaczmarek, A. R., Al Kaabi, M., Marantz, A., and Pylkkänen, L. (2018). Building words and phrases in the left temporal lobe. *Cortex* 106, 213–236. doi: 10.1016/j.cortex.2018.06.004

Gallo, M., Frangipane, F., Cupidi, C., De Bartolo, M., Turone, S., Ferrari, C., et al. (2017). The novel PSEN1 M84V mutation associated to frontal dysexecutive syndrome, spastic paraparesis, and cerebellar atrophy in a dominant Alzheimer's disease family. *Neurobiol. Aging* 56:213.e7-213.e12. doi: 10.1016/j.neurobiolaging.2017.04.017

Ghatwary, N., Zolgharni, M., and Ye, X. (2019). Early esophageal adenocarcinoma detection using deep learning methods. *Int. J. Comput. Assist. Radiol. Surg.* doi: 10.1007/s11548-019-01914-4 [Epub ahead of print].

Gliebus, G. (2014). A case report of anxiety disorder preceding frontotemporal dementia with asymmetric right temporal lobe atrophy. *SAGE Open Med. Case Rep.* 2:2050313X13519977. doi: 10.1177/2050313X13519977

Goodfellow, I., Pouget-Abadie, J., Mirza, M., Xu, B., Warde-Farley, D., Ozair, S., et al. (2014). Generative adversarial nets. *Adv. Neural Inform. Process. Syst.* 2, 2672–2680.

Grajski, K. A., and Bressler, S. L. (2019). Alzheimer's disease neuroimaging initiative. Differential medial temporal lobe and default-mode network functional connectivity and morphometric changes in Alzheimer's disease. *Neuroimage Clin.* 23:101860. doi: 10.1016/j.nicl.2019.101860

Grillo, L., Greco, D., Pettinato, R., Avola, E., Potenza, N., Castiglia, L., et al. (2014). Increased FGF3 and FGF4 gene dosage is a risk factor for craniosynostosis. *Gene* 534, 435–439. doi: 10.1016/j.gene.2013.09.120

Gulshan, V., Peng, L., Coram, M., Stumpe, M. C., Wu, D., Narayanaswamy, A., et al. (2016). Development and validation of a deep learning algorithm for detection of diabetic retinopathy in retinal fundus photographs. *JAMA* 316, 2402–2410. doi: 10.1001/jama.2016.17216

Haenssle, H. A., Fink, C., Schneiderbauer, R., Toberer, F., Buhl, T., Blum, A., et al. (2018). Man against machine: diagnostic performance of a deep learning convolutional neural network for dermoscopic melanoma recognition in comparison to 58 dermatologists. *Ann. Oncol.* 29, 1836–1842. doi: 10.1093/annonc/mdy166

Han, C., Tomita, H., Ohba, T., Nishizaki, K., Ogata, Y., Matsuzaki, Y., et al. (2016). Modified sympathetic nerve regulation in AKAP5-null mice. *Biochem. Biophys. Res. Commun.* 469, 897–902. doi: 10.1016/j.bbrc.2015.12.057

Heo, S. J., Kim, Y., Yun, S., Lim, S. S., Kim, J., Nam, C. M., et al. (2019). Deep learning algorithms with demographic information help to detect tuberculosis in chest radiographs in annual workers' health examination data. *Int. J. Environ. Res. Public Health* 16:E250. doi: 10.3390/ijerph16020250

Hong, M. G., Reynolds, C. A., Feldman, A. L., Kallin, M., Lambert, J. C., Amouyel, P., et al. (2012). Genome-wide and gene-based association implicates FRMD6 in Alzheimer disease. *Hum. Mutat.* 33, 521–529. doi: 10.1002/humu.22009

Hosseini-Asl, E., Keynto, R., and El-Baz, A. (2016). "Alzheimer's disease diagnostics by adaptation of 3D convolutional network," in *Proceedings of the 2016 IEEE International Conference on Image Processing (ICIP)*, (Piscataway, NJ: IEEE), 126–130.

Huang, C. C., Hsiao, I. T., Huang, C. Y., Weng, Y. C., Huang, K. L., Liu, C. H., et al. (2019). Tau PET With 18F-THK-5351 Taiwan Patients With Familial Alzheimer's Disease With the APP p.D678H Mutation. *Front. Neurol.* 10:503. doi: 10.3389/fneur.2019.00503

Huang, C. Y., Hsiao, I. T., Lin, K. J., Huang, K. L., Fung, H. C., Liu, C. H., et al. (2019). Amyloid PET pattern with dementia and amyloid angiopathy in Taiwan familial AD with D678H APP mutation. *J. Neurol. Sci.* 398, 107–116. doi: 10.1016/j.jns.2018.12.039

Jahanshad, N., Kochunov, P. V., Sprooten, E., Mandl, R. C., Nichols, T. E., Almasy, L., et al. (2013). Multi-site genetic analysis of diffusion images and voxelwise heritability analysis: a pilot project of the ENIGMA-DTI working group. *Neuroimage* 90, 470–471. doi: 10.1016/j.neuroimage.2013.04.061

Ju, R., Hu, C., Zhou, P., and Li, Q. (2017). Early diagnosis of Alzheimer's disease based on resting-state brain networks and deep learning. *IEEE/ACM Trans. Comput. Biol. Bioinform.* 16:99. doi: 10.1109/TCBB.2017.2776910

Jung, N. Y., Lee, J. H., Lee, Y. M., Shin, J. H., Shin, M. J., Lee, M. J., et al. (2018). Early stage memory impairment, visual hallucinations, and myoclonus combined with temporal lobe atrophy predict Alzheimer's disease pathology in corticobasal syndrome. *Neurocase* 24, 145–150. doi: 10.1080/13554794.2018.1494290

Kakeda, S., and Korogi, Y. (2010). The efficacy of a voxel-based morphometry on the analysis of imaging in schizophrenia, temporal lobe epilepsy, and Alzheimer's disease/mild cognitive impairment: a review. *Neuroradiology* 52, 711–721. doi: 10.1007/s00234-010-0717-2

Kenkhuis, B., Jonkman, L. E., Bulk, M., Buijs, M., Boon, B. D. C., Bouwman, F. H., et al. (2019). 7T MRI allows detection of disturbed cortical lamination of the medial temporal lobe in patients with Alzheimer's disease. *Neuroimage Clin.* 21:101665. doi: 10.1016/j.nicl.2019.101665

Kitchigina, V. F. (2018). Alterations of Coherent Theta and Gamma Network Oscillations as an Early Biomarker of Temporal Lobe Epilepsy and Alzheimer's Disease. *Front. Integr. Neurosci.* 12:36. doi: 10.3389/fnint.2018.00036

Kovacs, M. D., Burchett, P. F., and Sheafor, D. H. (2018). App review: management guide for incidental findings on CT and MRI. *J. Digit. Imaging.* 31, 154–158. doi: 10.1007/s10278-017-0035-x

Kuramoto, K., Negishi, M., and Katoh, H. (2009). Regulation of dendrite growth by the Cdc42 activator Zizimin1/Dock9 in hippocampal neurons. *J. Neurosci. Res.* 87, 1794–1805. doi: 10.1002/jnr.21997

Ladefoged, C. N., Marner, L., Hindsholm, A., Law, I., Højgaard, L., and Andersen, F. L. (2019). Deep learning based attenuation correction of PET/MRI in pediatric brain tumor patients: evaluation in a clinical setting. *Front. Neurosci.* 12:1005. doi: 10.3389/fnins.2018.01005

Lam, A. D., Cole, A. J., and Cash, S. S. (2019). New approaches to studying silent mesial temporal lobe seizures in alzheimer's disease. *Front. Neurol.* 10:959. doi: 10.3389/fneur.2019.00959

Lattimore, F., and Ongv, C. S. (2018). A Primer on Causal Analysis. *arXiv* [Preprint].,

Leandrou, S., Petroudi, S., Kyriacou, P. A., Reyes-Aldasoro, C. C., and Pattichis, C. S. (2018). Quantitative MRI brain studies in mild cognitive impairment and Alzheimer's disease: a methodological review. *IEEE Rev. Biomed. Eng.* 11, 97–111. doi: 10.1109/RBME.2018.2796598

Lenz, D., McClean, P., Kansu, A., Bonnen, P. E., Ranucci, G., Thiel, C., et al. (2018). SCYL1 variants cause a syndrome with low γ-glutamyl-transferase cholestasis, acute liver failure, and neurodegeneration (CALFAN). *Genet. Med.* 20, 1255–1265. doi: 10.1038/gim.2017.260

Li, B. Y., and Chen, S. D. (2015). Potential similarities in temporal lobe epilepsy and Alzheimer's Disease: from clinic to pathology. *Am. J. Alzheimers Dis. Other Demen.* 30, 723–728. doi: 10.1177/1533317514537547

Liu, X., Chen, K., Wu, T., Weidman, D., Lure, F., and Li, J. (2018a). Use of multimodality imaging and artificial intelligence for diagnosis and prognosis of early stages of Alzheimer's disease. *Transl. Res.* 194, 56–67. doi: 10.1016/j.trsl.2018.01.001

Liu, X., Hou, D., Lin, F., Luo, J., Xie, J., Wang, Y., et al. (2018b). The role of neurovascular unit damage in the occurrence and development of Alzheimer's disease. *Rev. Neurosci.* 30, 477–484. doi: 10.1515/revneuro-2018-0056

Lopez-Paz, D., and Oquab, M. (2016). Revisiting classifier two-sample tests. *arXiv* [Preprint].

Lopez-Paz, D., and Oquab, M. (2017). "Revisiting Classifier Two-Sample Tests for GAN Evaluation and Causal Discovery," in *Proceedings of the International Conference on Learning Representations (ICLR)*, Toulon.

Lorenzi, M., Filippone, M., Frisoni, G. B., Alexander, D. C., Ourselin, S., and Alzheimer's Disease Neuroimaging Initiative. (2017). Probabilistic disease progression modeling to characterize diagnostic uncertainty: application to staging and prediction in Alzheimer's disease. *NeuroImage* 190, 56–68. doi: 10.1016/j.neuroimage.2017.08.059

Manley, W., Moreau, M. P., Azaro, M., Siecinski, S. K., Davis, G., Buyske, S., et al. (2018). Validation of a microRNA target site polymorphism in H3F3B that is potentially associated with a broad schizophrenia phenotype. *PLoS One* 13:e0194233. doi: 10.1371/journal.pone.0194233

Menéndez-González, M., de Celis Alonso, B., Salas-Pacheco, J., and Arias-Carrión, O. (2015). Structural neuroimaging of the medial temporal lobe in Alzheimer's

Disease clinical trials. *J Alzheimers Dis.* 48, 581–589. doi: 10.3233/JAD-150226

Mez, J., Chung, J., Jun, G., Kriegel, J., Bourlas, A. P., Sherva, R., et al. (2017). Two novel loci, COBL and SLC10A2, for Alzheimer's disease in African Americans. *Alzheimers Dement.* 13, 119–129. doi: 10.1016/j.jalz.2016.09.002

Miles, L. A., Hermans, S. J., Crespi, G. A. N., Gooi, J. H., Doughty, L., Nero, T. L., et al. (2019). Small molecule binding to Alzheimer risk factor CD33 promotes Aβ phagocytosis. *Science* 19, 110–118. doi: 10.1016/j.isci.2019.07.023

Pasquini, L., Rahmani, F., Maleki-Balajoo, S., La Joie, R., Zarei, M., Sorg, C., et al. (2019). Medial Temporal Lobe Disconnection and Hyperexcitability Across Alzheimer's Disease Stages. *J. Alzheimers Dis. Rep.* 3, 103–112. doi: 10.3233/ADR-190121

Payan, A., and Montana, G. (2015). Predicting Alzheimer's disease: a neuroimaging study with 3D convolutional neural networks. *arXiv:1502.02506* [Preprint].

Persson, K., Barca, M. L., Cavallin, L., Braekhus, A., Knapskog, A. B., Selbaek, G., et al. (2018). Comparison of automated volumetry of the hippocampus using NeuroQuant and visual assessment of the medial temporal lobe in Alzheimer's disease. *Acta Radiol.* 8, 997–1001. doi: 10.1177/0284185117743778

Peters, J., Janzing, D., and Schölkopf, B. (2017). *Elements of Causal Inference: Foundations and Learning Algorithms*. Boston: The MIT Press.

Pettigrew, C., Soldan, A., Sloane, K., Cai, Q., Wang, J., Wang, M. C., et al. (2017). Progressive medial temporal lobe atrophy during preclinical Alzheimer's disease. *Neuroimage Clin.* 16, 439–446. doi: 10.1016/j.nicl.2017.08.022

Ravizza, S., Huschto, T., Adamov, A., Böhm, L., Büsser, A., Flöther, F. F., et al. (2019). Predicting the early risk of chronic kidney disease in patients with diabetes using real-world data. *Nat. Med.* 25, 57–59. doi: 10.1038/s41591-018-0239-8

Sarica, A., Cerasa, A., and Quattrone, A. (2017). Random forest algorithm for the classification of neuroimaging data in Alzheimer's disease: a systematic review. *Front. Aging Neurosci.* 9:329. doi: 10.3389/fnagi.2017.00329

Sarraf, S., and Tofighi, G. (2016). DeepAD: Alzheimer's disease classification via deep convolutional neural networks using MRI and fMRI. *BioRxiv* [Preprint]. doi: 10.1101/070441,

Schmidt, W. M., Kraus, C., Höger, H., Hochmeister, S., Oberndorfer, F., Branka, M., et al. (2007). Mutation in the Scyl1 gene encoding amino-terminal kinase-like protein causes a recessive form of spinocerebellar neurodegeneration. *EMBO Rep.* 8, 691–697. doi: 10.1038/sj.embor.7401001

Schmidt, W. M., Rutledge, S. L., Schüle, R., Mayerhofer, B., Züchner, S., Boltshauser, E., et al. (2015). Disruptive SCYL1 mutations underlie a syndrome characterized by recurrent episodes of liver failure, peripheral neuropathy, cerebellar atrophy, and ataxia. *Am. J. Hum. Genet.* 97, 855–861. doi: 10.1016/j.ajhg.2015.10.011

Simonyan, K., and Zisserman, A. (2014). Very deep convolutional networks for large-scale image recognition. *arXiv* [Preprint].

Spasov, S., Passamonti, L., Duggento, A., Liò, P., and Toschi, N. (2019). A parameter-efficient deep learning approach to predict conversion from mild cognitive impairment to Alzheimer's disease. *Neuroimage* 189, 276–287. doi: 10.1016/j.neuroimage.2019.01.031

Struyfs, H., Van Hecke, W., Veraart, J., Sijbers, J., Slaets, S., De Belder, M., et al. (2015). Diffusion kurtosis imaging: a possible MRI biomarker for ad diagnosis? *J. Alzheimers Dis.* 48, 937–948. doi: 10.3233/JAD-150253

Trimmel, K., van Graan, A. L., Caciagli, L., Haag, A., Koepp, M. J., Thompson, P. J., et al. (2018). Left temporal lobe language network connectivity in temporal lobe epilepsy. *Brain* 141, 2406–2418. doi: 10.1093/brain/awy164

Van Giau, V., Senanarong, V., Bagyinszky, E., Limwongse, C., An, S. S. A., and Kim, S. (2018). Identification of a novel mutation in APP gene in a Thai subject with early-onset Alzheimer's disease. *Neuropsychiatr. Dis. Treat.* 14, 3015–3023. doi: 10.2147/NDT.S180174

Wada, A., Tsuruta, K., Irie, R., Kamagata, K., Maekawa, T., Fujita, S., et al. (2018). Differentiating Alzheimer's disease from dementia with Lewy bodies using a deep learning technique based on structural brain connectivity. *Magn. Reson. Med. Sci.* doi: 10.2463/mrms.mp.2018-0091 [Epub ahead of print].

Waldrop, M. M. (2019). News feature: what are the limits of deep learning? *Proc. Natl. Acad. Sci. U.S.A.* 116, 1074–1077. doi: 10.1073/pnas.1821594116

Wang, Y. J., Wan, Y., Wang, H. F., Tan, C. C., Li, J. Q., Yu, J. T., et al. (2019). Effects of CD33 variants on neuroimaging biomarkers in non-demented elders. *J. Alzheimers Dis.* 68, 757–766. doi: 10.3233/JAD-181062

Wolk, D. A., Das, S. R., Mueller, S. G., Weiner, M. W., and Yushkevich, P. A., Alzheimer's Disease Neuroimaging Initiative (2017). Medial temporal lobe subregional morphometry using high resolution MRI in Alzheimer's disease. *Neurobiol. Aging* 49, 204–213. doi: 10.1016/j.neurobiolaging.2016.09.011

Xie, L., Wisse, L. E., Pluta, J., de Flores, R., Piskin, V., Manjón, J. V., et al. (2019). Alzheimer's Disease neuroimaging initiative. Automated segmentation of medial temporal lobe subregions on in vivo T1-weighted MRI in early stages of Alzheimer's disease. Human brain mapping. *Hum. Brain Mapp.* 40, 3431–3451. doi: 10.1002/hbm.24607

Xiong, M. M. (2018). *Big Data in Omics and Imaging: (2) Integrated Analysis and Causal Inference*. New York: CRC Press.

Zeiler, M. D., and Fergus, R. (2014). "Visualizing and understanding convolutional networks," in *Proceedings of the European Conference on Computer Vision–ECCV*, (Berlin: Springer), 818–833. doi: 10.1007/978-3-319-10590-1_53

Zhou, B., Khosla, A., Lapedriza, A., Oliva, A., and Torralba, A. (2016). "Learning deep features for discriminative localization," in *Proceedings of the IEEE Conference on Computer Vision and Pattern Recognition*, (Berlin: Springer), 2921–2929.

Zhou, Z. D., Chan, C. H., Ma, Q. H., Xu, X. H., Xiao, Z. C., and Tan, E. K. (2011). The roles of amyloid precursor protein (APP) in neurogenesis: implications to pathogenesis and therapy of Alzheimer disease. *Cell Adh. Migr.* 5, 280–292. doi: 10.4161/cam.5.4.16986

Zhuang, Q. S., Zheng, H., Gu, X. D., Shen, L., and Ji, H. F. (2017). Detecting the genetic link between Alzheimer's disease and obesity using bioinformatics analysis of GWAS data. *Oncotarget* 8, 55915–55919. doi: 10.18632/oncotarget.19115

Zintgraf, L. M., Cohen, T. S., Adel, T., and Welling, M. (2017). Visualizing deep neural network decisions: prediction difference analysis. *arXiv* [Preprint].

Disclaimer: The content is solely the responsibility of the authors and does not necessarily represent the official views of the Cancer Prevention and Research Institute of Texas.

Conflict of Interest: The authors declare that the research was conducted in the absence of any commercial or financial relationships that could be construed as a potential conflict of interest.

frontiers in Neurology

ORIGINAL RESEARCH
published: 29 November 2019
doi: 10.3389/fneur.2019.01199

Differences in Corticoreticulospinal Tract Injuries According to Whiplash in Mild Traumatic Brain Injury Patients

Sung Ho Jang[1], *Sang Seok Yeo*[2], *Jung Won Kwon*[2] *and Young Hyeon Kwon*[1]*

[1] *Department of Physical Medicine and Rehabilitation, College of Medicine, Yeungnam University, Gyeongsan, South Korea,*
[2] *Department of Physical Therapy, College of Health Sciences, Dankook University, Seoul, South Korea*

Background: This study investigated differences in postural control ability (PCA) and corticoreticulospinal tract (CRT) injury severity according to whiplash in patients with mild traumatic brain injury (mTBI).

Methods: Thirty-one patients with mTBI and 21 healthy control subjects were recruited for this study. The balance error scoring system (BESS) was used for PCA assessment. Based on their whiplash history, the patients were classified into two groups: group A—mTBI with whiplash injury; group B—mTBI without whiplash injury. Fractional anisotropy (FA), apparent diffusion coefficient (ADC), and tract volume (TV) values were estimated for the reconstructed CRTs in all subjects.

Results: Significant differences were observed among the total BESS scores of patient groups A and B and the control group ($p < 0.05$). The patient group A BESS score was significantly higher than that of patient group B, and that of the patient group B was significantly higher than that of the control group. No significant differences were detected among the FA and ADC values of the CRTs of the two patient groups and the control group ($p > 0.05$). However, the TV values of the CRT did reveal significant differences; the TV of patient group A was significantly lower than those of patient group B and the control group, and that of patient group B was significantly lower than that of the control group ($p < 0.05$).

Conclusions: We observed greater CRT injury severity and PCA impairment in mTBI patients with whiplash than in mTBI patients without whiplash. The results indicate that whiplash might lead to a greater level of severity in axonal injuries in mTBI patients.

Keywords: corticoreticulospinal tract, diffusion tensor tractography, balance error scoring system, postural control ability, whiplash injury, mild traumatic brain injury

OPEN ACCESS

Edited by:
Feng Feng,
Peking Union Medical College Hospital (CAMS), China

Reviewed by:
Gunnel Peterson,
Uppsala University, Sweden
Ahmed Abdel Razek,
Mansoura University, Egypt
He Jian,
Nanjing Drum Tower Hospital, China

***Correspondence:**
Young Hyeon Kwon
kyh7648764@daum.net

Specialty section:
This article was submitted to Applied Neuroimaging, a section of the journal Frontiers in Neurology

Received: *12 March 2019*
Accepted: *28 October 2019*
Published: *29 November 2019*

Citation:
Jang SH, Yeo SS, Kwon JW and Kwon YH (2019) Differences in Corticoreticulospinal Tract Injuries According to Whiplash in Mild Traumatic Brain Injury Patients. Front. Neurol. 10:1199. doi: 10.3389/fneur.2019.01199

INTRODUCTION

Traumatic brain injury (TBI) can be caused by a sudden impact or an acceleration–deceleration trauma to the head (1). TBI can be classified as mild, moderate, or severe based on the level of injury severity with mild TBI (mTBI) comprising ∼75–90% of all TBI (2, 3). Whiplash is a bony and/or soft tissue injury resulting from acceleration–deceleration energy transfers in the neck (4). Patients

with whiplash often complain of cerebral symptoms suggestive of brain injury, and previous studies have reported evidence that indicates the presence of brain injury in patients with whiplash (5–12). Therefore, whiplash has been considered as a pathogenic mechanism of mTBI (13).

Presence of postural control means the subject has the ability to maintain postural orientation in response to perturbations generated from internal or external sources (14). Impairment of postural control ability (PCA) is a common clinical manifestation following mTBI and/or whiplash (14–20). Previous studies have suggested that mTBI due to whiplash might be associated with greater impairment of PCA than that in patients with mTBI due to other causes (16, 17). The corticoreticulospinal tract (CRT), one of the extrapyramiidal motor pathways in the human brain, mainly mediates movements of proximal and axial muscles (21, 22). As a result, the CRT is involved in postural control responses to perturbations generated from internal or external sources (14, 21, 22).

The introduction of diffusion tensor tractography (DTT), a three-dimensional (3D) modeling process that uses diffusion tensor imaging (DTI) data, has enabled 3D reconstruction and estimation of neural tracts, including the CRT (23). The main advantage of DTT over DTI is that the entire neural tract can be evaluated in terms of DTT parameters. Among the various DTT parameters that can be examined, fractional anisotropy (FA), apparent diffusion coefficient (ADC), and tract volume (TV) parameters are the most commonly used (24–26). The FA value, which indicates the degree of directionality of water diffusion, is used to assess the degree of tract directionality whereas the ADC value indicates the magnitude of the water diffusion (24, 25). Therefore, the values of FA and ADC may be used to suggest the microstructural integrity of white matter microstructures, such as axons, myelin, and microtubules (24, 25, 27, 28). In contrast, the TV value indicates the number of voxels (values on a regular grid within a 3D space) that are included in a neural tract (26). A decrement in TV value without a change in the values of FA and ADC of a neural tract indicates a decrement in the number of neural fibers of that tract without a change in the microstructural integrity of the tract (24–26). Therefore, decreases in the values of the FA and TV, as well as increases in the values of the ADC, indicate the presence of neural injury (24–28). A few studies have used DTT to demonstrate CRT injuries in patients with mTBI (29–31). Among these studies, one demonstrated an association between CRT injury and PCA (31). However, no study has reported on the relationship between CRT injury and PCA impairment according to whiplash status in mTBI patients.

For the present study, we hypothesized that PCA impairment and CRT injury would differ according to whiplash presence in mTBI patients. Therefore, we investigated differences in PCA and CRT injuries in mTBI patients with and without a history of whiplash.

METHODS

Subjects

A total of 39 consecutive patients with mTBI (18 males, 21 females; mean age 46.20 ± 10.92 years; age range 21–64 years; from January 2016 to December 2018) who visited the rehabilitation department of a university hospital and 20 age- and sex-matched normal control subjects (12 male, 9 female; mean age 45.1 ± 8.93 years; age range 30–64 years) with no history of neurologic/psychiatric disease were recruited for this study (**Table 1**).

Inclusion criteria for the 39 patients were: (1) more than 2 weeks had elapsed after mTBI onset, (2) at least one of the following: (i) any period of loss of consciousness; (ii) any loss of memory for events immediately before or after the accident; (iii) any alteration in mental state at the time of the accident (e.g., feeling dazed, disoriented, or confused); or (iv) any focal neurological deficit(s) that may or may not be transient but in which the severity of the injury does not exceed the following: loss of consciousness of approximately 30 min or less; after 30 min post-onset, an initial Glasgow Coma Scale of 13–15; and post-traumatic amnesia (PTA) of <24 h (13, 32, 33), (3) no specific lesion observed on brain magnetic resonance imaging (MRI; T1-weighted, T2-weighted, and fluid-attenuated inversion recovery images), (4) age at the time of head trauma >18 years, (5) an abnormal score on the balance error scoring system (BESS) (cut-off score ≥ 14, range: 0–60; a higher value means more severe postural impairment) (34), and (6) no previous history of neurologic/psychiatric disease. Patients were excluded if impairments could have been due to drugs, alcohol, medications, other injuries, treatment for other injuries, other problems, or the result of a penetrating craniocerebral injury.

We divided the patient group into two groups based on the patient's history of whiplash (indicated by the presence of flexion-hyperextension, lateral flexion, or rotation injury of the head and neck following a motor vehicle collision). Nineteen patients were placed in patient group A (mTBI with whiplash injury; injury causes: motor vehicle accidents, 100%) and 20 patients were assigned to patient group B [mTBI without whiplash injury; injury causes: motor vehicle accidents, 17 (85%); falling, 2 (10%); direct head trauma, 1 (5%)] (**Table 1**). No significant differences in age or sex compositions were detected between patient groups A and B or between the patient and control groups ($p > 05$).

This was a retrospective study, and the study was carried out in accordance with the recommendations of "The CARE of guidelines" with written informed consent obtained from all subjects. The patient provided written informed consent in

TABLE 1 | Demographic and clinical data for the patient and control groups.

	Patient group A ($n = 19$)	Patient group B ($n = 20$)	Control group ($n = 21$)
Gender (male:female)	8:11	10:10	12:9
Mean age, years[a]	49.47 (±10.55)	43.10 (±10.58)	45.10 (±8.93)
Mild traumatic brain injury causal mechanism	Motor vehicle accident (100%)	Motor vehicle accident (85%) Falling (10%) Direct head trauma (5%)	–

[a] *Values represent mean (± standard deviation).*
**Significantly different among patient A, B, and control at $p < 0.05$.*

accordance with the Declaration of Helsinki, and the study protocol was approved by the Institutional Review Board of the Yeungnam University hospital.

Clinical Evaluation

BESS was used for the evaluation of PCA at the time of DTI scanning. Evaluation using BESS has been shown to provide high validity and reliability in normal subjects (35). In addition, BESS can be used to assess the effects of a mild head injury on PCA in the absence of expensive, sophisticated PCA assessment tools (35, 36). Determination of a BESS score requires the subject to stand unsupported with their eyes closed under six conditions involving a combination of two surface types (firm and balance foam) and three stances (double-limb, single-limb, and tandem). In this study, the balance foam (Airex, Sins, Switzerland) was a 6 cm thick piece of medium-density foam (dimensions 50 × 41 cm, density 55 kg/cm^3, tensile strength 260 kPa, elongation to breaking 180%). The non-dominant leg was used as the stance limb during the single-leg trials and it was placed in the rear position during tandem stance trials. The preferred leg to use while kicking a ball was defined as the dominant leg. The order of BESS testing conditions of each individual was randomized by subject and session, with each test lasting 20 s (37). For each test, subjects were asked to assume the required stance by positioning their hands on their iliac crests. A test commenced upon eye closure by the subject. Subjects were instructed to try not to lose their balance but, if needed, make any necessary adjustments and return to the testing position as quickly as possible. Test performance was scored by the addition of one error point for each error committed. An error was assigned when any of the following occurred: (1) lifting hands off the iliac crests; (2) opening the eyes; (3) stepping, stumbling, or falling; (4) moving the hip by more than 30 degrees of flexion or abduction; (5) lifting the forefoot or heel; or (6) remaining out of the testing position for more than 5 s (37). The maximum number of errors for a single stance condition was 10. If the subject could not maintain a stance position for longer than 5 s, subjects were assigned the maximum score for that position. The numbers of errors for each trial were added to obtain a total score (0–60; lower scores indicated better balance) (35).

Diffusion Tensor Imaging and Fiber Tracking

The DTI data obtained for this study were acquired at an average of 14.0 ± 26.2 months after the onset of TBI by using a 1.5 T Philips Gyroscan Intera scanner (Philips, Best, Netherlands) equipped with a Synergy-L sensitivity encoding (SENSE) head coil in order to obtain single-shot, spin-echo, planar-imaging pulse sequences. For each of the 32 non-colinear diffusion sensitizing gradients, 60 contiguous slices were acquired parallel to the anterior commissure–posterior commissure line. Imaging parameters were as follows: acquisition matrix = 96 × 96, reconstructed to matrix = 192 × 192, field of view = 240 × 240 mm, repetition time = 10,398 ms, time to echo = 72 ms, parallel imaging reduction factor (SENSE factor) = 2, EPI factor = 59, and b = 1,000 s/mm^2, number of excitations = 1, and thickness = 2.5 mm. Eddy current-induced image distortions were removed by using affine multiscale two-dimensional registration as provided within the Oxford Centre for Functional Magnetic Resonance Imaging of Brain Software Library (www.fmrib.ox.ac.uk/fsl). DTI-Studio software (CMRM; Johns Hopkins Medical Institute, Baltimore, MD, USA) was used for evaluation of the CRT. The CRT was reconstructed based on fibers passing through two regions of interest (ROIs) on the DTI color map. The first ROI was placed at the reticular formation of the medulla. The second ROI was placed at the tegmentum of the midbrain. Termination criteria used for fiber tracking were a fractional anisotropy (FA) value of <0.2 and an angle of <60 degrees (23). The FA, ADC, and TV values for the DTT-reconstructed CRT were obtained for both hemispheres.

Statistical Analysis

Statistical analysis was performed by using SPSS 21.0 for Windows (SPSS, Chicago, IL, USA). One-way analysis of variance with Fisher's least significant difference *post hoc* test was performed to determine the significance of differences in BESS scores, DTT parameters (FA, ADC, and TV) of the CRT, and age distribution among patient groups A and B and the control group. The chi-squared test was used to examine gender-based differences between patient groups A and B and the control group.

RESULTS

Comparisons of BESS scores and DTT parameter results for the CRTs of the patient and control groups are summarized in **Table 2**. The mean total BESS score for patient group A was significantly higher than those of patient group B and the control group; furthermore, the mean total BESS score for patient group B was significantly higher than that of the control group ($p < 0.05$).

No significant differences were observed in the mean FA and ADC values of the CRTs of patient groups A and B and those of the control group ($p > 0.05$). However, the mean TV value of the CRT of patient group A was significantly lower than those of patient group B and the control group; moreover, the mean TV

TABLE 2 | Clinical data and diffusion tensor imaging parameters for the corticoreticulospinal tracts of patient groups A and B and the control group.

	Patient group A ($n = 19$)	Patient group B ($n = 20$)	Control group ($n = 21$)	F	P
BESS	38.73 (±13.56)[a]	20.42 (±6.23)[b]	10.81 (±3.98)[c]	46.13	<0.00
FA	0.48 (±0.03)	0.48 (±0.03)	0.48 (±0.01)	0.08	0.92
ADC	0.80 (±0.09)	0.79 (±0.05)	0.78 (±0.03)	0.51	0.61
TV	551.63 (±281.74)[a]	870.05 (±327.16)[b]	1,368.52 (±264.86)[c]	39.94	<0.00

Values represent mean (± standard deviation); BESS, balance error scoring system; CRT, corticoreticulospinal tract; FA, fractional anisotropy; ADC, apparent diffusion coefficient; TV, tract volume; One-way ANOVA and the Scheffe post hoc test were used for comparison of diffusion tensor parameters among patient groups A and B and the control group.

Scheffe test result: a < b < c.

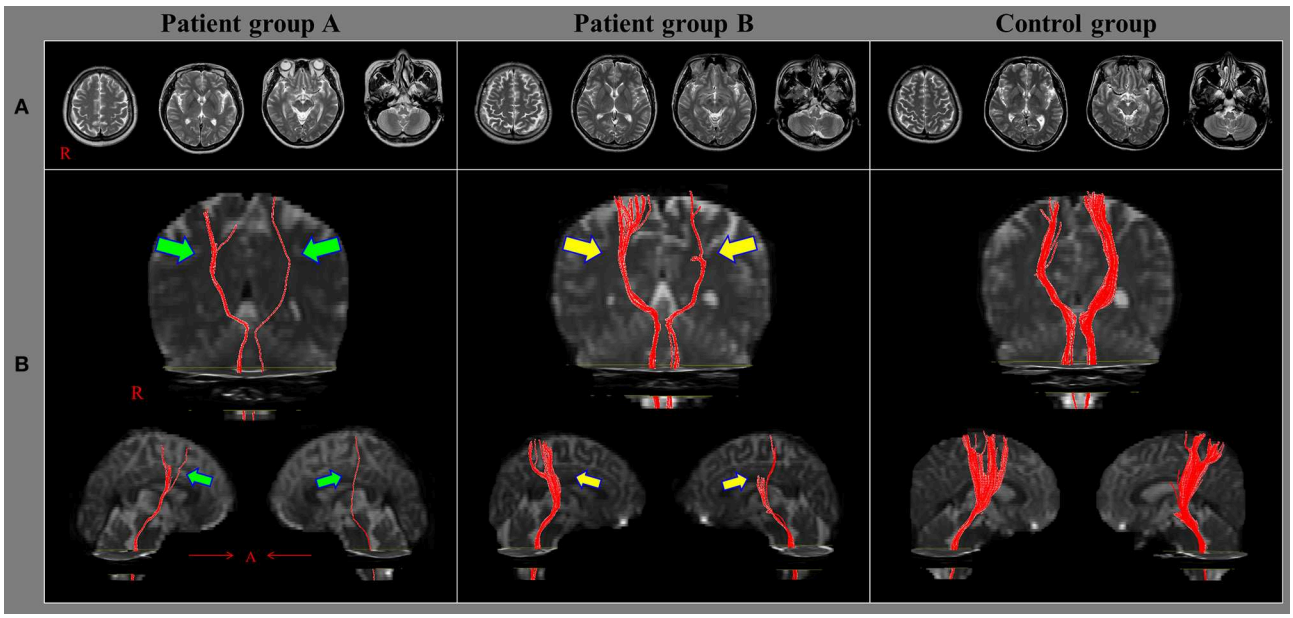

FIGURE 1 | Results of diffusion tensor tractography (DTT) of the corticoreticulospinal tract (CRT). **(A)** T2-weighted brain magnetic resonance images obtained at the time of diffusion tensor imaging in representative subjects of patient group A (51-year-old female), patient group B (49-year-old male), and the control group (56-year-old male); none of the images show an abnormality. **(B)** Results of DTT of the CRT: the CRTs in the group A patient (green arrows) are narrower on both sides than those of the group B patient (yellow arrows). Moreover, the CRTs of the group B patient (yellow arrows) are narrower on both sides than those of the control group patient.

value of the CRT of patient group B was significantly lower than that of the control group ($p < 0.05$) (**Figure 1**).

DISCUSSION

In this study, we investigated differences in PCA and CRT injury among mTBI patients with and without a history of whiplash injury. The results may be summarized as follows: (1) PCA, as determined by BESS testing, became increasingly worse in the following order: control group, patient group B (mTBI without whiplash), and patient group A (mTBI with whiplash); (2) TV values for the CRTs of the three study groups decreased in the same order, but there were no significant differences in FA and ADC values among the groups.

In the clinical evaluation of a patient's PCA, a high BESS score indicates a high level of impairment of PCA. In this study, the most severe PCA impairment was observed in mTBI patients that experienced whiplash with a lower level of impairment observed in mTBI patients that did not have a history of whiplash. These results indicate that whiplash can produce a more severe effect on the PCA of mTBI patients than that from mTBI alone. This result supports those in previous studies which showed that PCA impairment was greater in mTBI patients with a whiplash injury (16, 17).

In 2011, Nacci et al. assessed shifting of the centers of gravity in whiplash patients with and without mTBI and reported that whiplash patients with mTBI showed greater center of gravity shifting than that of whiplash patients without mTBI (16). In 2016, Gandelman-Marton et al. investigated differences in body weight distribution between mTBI patients with and without whiplash and reported that there was a greater change in body weight distribution in mTBI patients with whiplash than in mTBI patients without whiplash (17).

Among the various DTT parameters that can be examined, FA, ADC, and TV are the most commonly used when evaluating the state of neural tracts in patients with brain injury (24–26). Our results showed a decrement in TV value without a change in the FA and ADC values of the CRT, indicating a decrease in the number of neural fibers in the CRT without a change in its microstructural integrity (24–26). As a result, our TV results indicate the presence of CRT injuries in both patient groups, but the CRT injuries exhibited greater severity in mTBI patients with whiplash than that in those without whiplash. The association of CRT injury with PCA appears to be related to the role of the CRT, which, by mediating movements of proximal and axial muscles, is involved in postural control responses to perturbations generated from internal or external sources (14, 21, 22). Because no brain lesions were detected on conventional brain MRI, traumatic axonal injury was considered the most likely pathogenetic mechanism for the CRT injuries identified in our patient groups (38–40). Based on our results, we conclude that the indirect acceleration–deceleration forces transmitted to the whole brain during whiplash might contribute to increasing the severity of axonal injury to the CRT to a level greater than that in mTBI patients with CRT injuries due to other causes (4, 12).

Since the introduction of DTI, a few studies have demonstrated CRT injuries in patients with mTBI (29–31). Two studies reported on patients with mTBI who had more severe weakness in their proximal joints than in their distal joints, which was indicated to be a consequence of CRT injury (29, 30). Jang et al. (31) evaluated PCA and CRT status in 25 mTBI patients and demonstrated that PCA impairment is associated with the presence of CRT injury. Nonetheless, to our best knowledge, this is the first original study to demonstrate that whiplash can lead to increased axonal injury severity in the CRT of mTBI patients.

However, there are some limitations to this study that should be considered. First, DTT analysis is operator-dependent, and regions of fiber complexity and crossing can prevent full reflection of the underlying fiber architecture (41). Second, because our patients were recruited from those who visited the rehabilitation department of a university hospital, there was a possibility that patients with a distinct level of severity of clinical manifestations might be included in this study; thus, our results may not be comparable to those from a broader population of mTBI patients with whiplash injury. Third, we did not perform a clinical examination of the impairments to cervical muscle function due to whiplash; variation in which can affect the CRT (42). Hence, we could not rule out the effect of cervical muscles on our results. Fourth, we recruited patients with chronic stage mTBI (i.e., more than 2 weeks after onset) and the average duration to DTI after onset was heterogeneous (14.0 ± 26.2 months) after TBI onset. As a result, recovery or degeneration of the CRT injuries during that interval may have influenced the results (43–45).

In conclusion, we investigated the association of whiplash with PCA and CRT injury in mTBI patients and observed that CRT injuries and PCA impairments were more severe in mTBI patients with whiplash than in those without whiplash. Our results suggest that whiplash might lead to more severe axonal injury in mTBI. Further studies on the effect of whiplash on other neural tracts are warranted.

DISCLOSURE

Financial disclosure statements have been obtained, and no conflicts of interest have been reported by the authors or by any individuals in control of the content of this article.

DATA AVAILABILITY STATEMENT

The datasets generated for this study are available on request to the corresponding author.

ETHICS STATEMENT

This study was carried out in accordance with the recommendations of The CARE of guidelines with written informed consent from all subjects. The patient signed a written informed consent in accordance with the Declaration of Helsinki, and the study protocol was approved by the Institutional Review Board of the Yeungnam University hospital.

AUTHOR CONTRIBUTIONS

SJ and YK were involved in manuscript development, funding, data acquisition, and manuscript writing. SY and JK helped in conceiving, designing the study, manuscript development, and manuscript writing.

ACKNOWLEDGMENTS

This work was supported by the Medical Research Center Program (2015R1A5A2009124) through the National Research Foundation of Korea (NRF) funded by the Ministry of Science, ICT, and Future Planning.

REFERENCES

1. Vos PE, Battistin L, Birbamer G, Gerstenbrand F, Potapov A, Prevec T, et al. EFNS guideline on mild traumatic brain injury: report of an EFNS task force. *Eur J Neurol.* (2002) 9:207–19. doi: 10.1046/j.1468-1331.2002.00407.x
2. De Kruijk JR, Twijnstra A, Leffers P. Diagnostic criteria and differential diagnosis of mild traumatic brain injury. *Brain Inj.* (2001) 15:99–106. doi: 10.1080/026990501458335
3. Vos PE, Alekseenko Y, Battistin L, Ehler E, Gerstenbrand F, Muresanu DF, et al. Mild traumatic brain injury. *Eur J Neurol.* (2012) 19:191–8. doi: 10.1111/j.1468-1331.2011.03581.x
4. Spitzer WO, Skovron ML, Salmi LR, Cassidy JD, Duranceau J, Suissa S, et al. Scientific monograph of the Quebec task force on whiplash-associated disorders: redefining "whiplash" and its management. *Spine.* (1995) 20:1S−73.
5. Ettlin TM, Kischka U, Reichmann S, Radii EW, Heim S, Wengen D, et al. Cerebral symptoms after whiplash injury of the neck: a prospective clinical and neuropsychological study of whiplash injury. *J Neurol Neurosurg Psychiatry.* (1992) 55:943–8. doi: 10.1136/jnnp.55.10.943
6. Otte A, Ettlin T, Fierz L, Mueller-Brand J. Parieto-occipital hypoperfusion in late whiplash syndrome: first quantitative SPET study using technetium-99m bicisate (ECD). *Eur J Nucl Med.* (1996) 23:72–4. doi: 10.1007/BF01736993
7. Otte A, Ettlin TM, Nitzsche EU, Wachter K, Hoegerle S, Simon GH, et al. PET and SPECT in whiplash syndrome: A new approach to a forgotten brain? *J Neurol Neurosurg Psychiatry.* (1997) 63:368–72. doi: 10.1136/jnnp.63.3.368
8. Otte A, Mueller-Brand J, Nitzsche EU, Wachter K, Ettlin TM. Functional brain imaging in 200 patients after whiplash injury. *J Nucl Med.* (1997);38:1002.
9. Obermann M, Nebel K, Schumann C, Holle D, Gizewski ER, Maschke M, et al. Gray matter changes related to chronic posttraumatic headache. *Neurology.* (2009) 73:978–83. doi: 10.1212/WNL.0b013e3181b8791a
10. Vallez Garcia D, Doorduin J, Willemsen AT, Dierckx RA, Otte A. Altered regional cerebral blood flow in chronic whiplash associated disorders. *EBioMedicine.* (2016) 10:249–57. doi: 10.1016/j.ebiom.2016.07.008
11. Jang SH, Kim SH, Kwon YH. Excessive daytime sleepiness and injury of the ascending reticular activating system following whiplash injury. *Front Neurosci.* (2018) 12:348. doi: 10.3389/fnins.2018.00348
12. Jang SH, Kwon YH. A review of traumatic axonal injury following whiplash injury as demonstrated by diffusion tensor tractography. *Front Neurol.* (2018) 9:57. doi: 10.3389/fneur.2018.00057
13. American Congress of Rehabilitation Medicine. Definition of mild traumatic brain injury. *J Head Trauma Rehabil.* (1993) 8:86–7. doi: 10.1097/00001199-199309000-00010
14. Cavanaugh JT, Guskiewicz KM, Giuliani C, Marshall S, Mercer V, Stergiou N. Detecting altered postural control after cerebral concussion in athletes

with normal postural stability. *Br J Sports Med.* (2005) 39:805–11. doi: 10.1136/bjsm.2004.015909
15. Rubin AM, Woolley SM, Dailey VM, Goebel JA. Postural stability following mild head or whiplash injuries. *Am J Otol.* (1995) 16:216–21.
16. Nacci A, Ferrazzi M, Berrettini S, Panicucci E, Matteucci J, Bruschini L, et al. Vestibular and stabilometric findings in whiplash injury and minor head trauma. *Acta Otorhinolaryngol Ital.* (2011) 31:378–89.
17. Gandelman-Marton R, Arlazoroff A, Dvir Z. Postural stability in patients with different types of head and neck trauma in comparison to healthy subjects. *Brain Inj.* (2016) 30:1612–6. doi: 10.1080/02699052.2016.1199904
18. Lin LF, Liou TH, Hu CJ, Ma HP, Ou JC, Chiang YH, et al. Balance function and sensory integration after mild traumatic brain injury. *Brain Inj.* (2015) 29:41–6. doi: 10.3109/02699052.2014.955881
19. Guskiewicz KM, Ross SE, Marshall SW. Postural stability and neuropsychological deficits after concussion in collegiate athletes. *J Athl Train.* (2001) 36:263–73.
20. Guskiewicz KM, Riemann BL, Perrin DH, Nashner LM. Alternative approaches to the assessment of mild head injury in athletes. *Med Sci Sports Exerc.* (1997) 29:S213–21. doi: 10.1097/00005768-199707001-00003
21. Matsuyama K, Mori F, Nakajima K, Drew T, Aoki M, Mori S. Locomotor role of the corticoreticular-reticulospinal-spinal interneuronal system. *Prog Brain Res.* (2004) 143:239–49. doi: 10.1016/S0079-6123(03)43024-0
22. Mendoza JE, Foundas AL. *Clinical Neuroanatomy: A Neurobehavioral Approach*. New York, NY: Springer (2007). 704 p.
23. Yeo SS, Chang MC, Kwon YH, Jung YJ, Jang SH. Corticoreticular pathway in the human brain: diffusion tensor tractography study. *Neurosci Lett.* (2012) 508:9–12. doi: 10.1016/j.neulet.2011.11.030
24. Mori S, Crain BJ, Chacko VP, van Zijl PC. Three-dimensional tracking of axonal projections in the brain by magnetic resonance imaging. *Ann Neurol.* (1999) 45:265–9. doi: 10.1002/1531-8249(199902)45:2<265::AID-ANA21>3.0.CO;2-3
25. Assaf Y, Pasternak O. Diffusion tensor imaging (DTI)-based white matter mapping in brain research: a review. *J Mol Neurosci.* (2008) 34:51–61. doi: 10.1007/s12031-007-0029-0
26. Pagani E, Agosta F, Rocca MA, Caputo D, Filippi M. Voxel-based analysis derived from fractional anisotropy images of white matter volume changes with aging. *Neuroimage.* (2008) 41:657–67. doi: 10.1016/j.neuroimage.2008.03.021
27. El-Serougy L, Abdel Razek AA, Ezzat A, Eldawoody H, El-Morsy A. Assessment of diffusion tensor imaging metrics in differentiating low-grade from high-grade gliomas. *Neuroradiol J.* (2016) 29:400–7. doi: 10.1177/1971400916665382
28. Razek A, Batouty N, Fathy W, Bassiouny R. Diffusion tensor imaging of the optic disc in idiopathic intracranial hypertension. *Neuroradiology.* (2018) 60:1159–66. doi: 10.1007/s00234-018-2078-1
29. Kwon HG, Jang SH. Delayed gait disturbance due to injury of the corticoreticular pathway in a patient with mild traumatic brain injury. *Brain Inj.* (2014) 28:511–4. doi: 10.3109/02699052.2014.887228
30. Lee HD, Jang SH. Injury of the corticoreticular pathway in patients with mild traumatic brain injury: a diffusion tensor tractography study. *Brain Inj.* (2015) 29:1219–22. doi: 10.3109/02699052.2015.1045028
31. Jang SH, Kim TH, Kwon YH, Lee MY, Lee HD. Postural instability in patients with injury of corticoreticular pathway following mild traumatic brain injury. *Am J Phys Med Rehabil.* (2016) 95:580–7. doi: 10.1097/PHM.0000000000000446
32. Alexander MP. Mild traumatic brain injury: pathophysiology, natural history, and clinical management. *Neurology*. (1995) 45:1253–60. doi: 10.1212/wnl.45.7.1253
33. Ruff RM, Iverson GL, Barth JT, Bush SS, Broshek DK, Policy NAN, et al. Recommendations for diagnosing a mild traumatic brain injury: a national academy of neuropsychology education paper. *Arch Clin Neuropsychol.* (2009) 24:3–10. doi: 10.1093/arclin/acp006
34. Linens SW, Ross SE, Arnold BL, Gayle R, Pidcoe P. Postural-stability tests that identify individuals with chronic ankle instability. *J Athl Train.* (2014) 49:15–23. doi: 10.4085/1062-6050-48.6.09
35. Riemann BL, Guskiewicz KM, Shields EW. Relationship between clinical and forceplate measures of postural stability. *J Sport Rehabil.* (1999) 8:71–82. doi: 10.1123/jsr.8.2.71
36. Lin CC, Roche JL, Steed DP, Musolino MC, Marchetti GF, Furman GR, et al. Test-retest reliability of postural stability on two different foam pads. *J Nat Sci.* (2015) 1:e43.
37. Riemann BL, Guskiewicz KM. Effects of mild head injury on postural stability as measured through clinical balance testing. *J Athl Train.* (2000) 35:19–25.
38. Povlishock JT, Christman CW. The pathobiology of traumatically induced axonal injury in animals and humans: a review of current thoughts. *J Neurotrauma.* (1995) 12:555–64. doi: 10.1089/neu.1995.12.555
39. Shenton ME, Hamoda HM, Schneiderman JS, Bouix S, Pasternak O, Rathi Y, et al. A review of magnetic resonance imaging and diffusion tensor imaging findings in mild traumatic brain injury. *Brain Imaging Behav.* (2012) 6:137–92. doi: 10.1007/s11682-012-9156-5
40. Jang SH. Traumatic axonal injury in mild traumatic brain injury. In: Gorbunoy N, editor. *Traumatic Brain Injury. 1st ed.* London: InTech (2018). p. 137–54.
41. Fillard P, Descoteaux M, Goh A, Gouttard S, Jeurissen B, Malcolm J, et al. Quantitative evaluation of 10 tractography algorithms on a realistic diffusion MR phantom. *Neuroimage.* (2011) 56:220–34. doi: 10.1016/j.neuroimage.2011.01.032
42. Krogh S, Kasch H. Whiplash injury results in sustained impairments of cervical muscle function: a one-year prospective, controlled study. *J Rehabil Med.* (2018) 50:548–55. doi: 10.2340/16501977-2348
43. Murugavel M, Cubon V, Putukian M, Echemendia R, Cabrera J, Osherson D, et al. A longitudinal diffusion tensor imaging study assessing white matter fiber tracts after sports-related concussion. *J Neurotrauma.* (2014) 31:1860–71. doi: 10.1089/neu.2014.3368
44. Jang SH, Seo JP. Delayed degeneration of the left fornical crus with verbal memory impairment in a patient with mild traumatic brain injury: a case report. *Medicine.* (2017) 96:e9219. doi: 10.1097/MD.0000000000009219
45. Yin B, Li DD, Huang H, Gu CH, Bai GH, Hu LX, et al. Longitudinal changes in diffusion tensor imaging following mild traumatic brain injury and correlation with outcome. *Front Neural Circuits.* (2019) 13:28. doi: 10.3389/fncir.2019.00028

Conflict of Interest: The authors declare that the research was conducted in the absence of any commercial or financial relationships that could be construed as a potential conflict of interest.

Advantages of publishing in Frontiers

OPEN ACCESS
Articles are free to read for greatest visibility and readership

FAST PUBLICATION
Around 90 days from submission to decision

HIGH QUALITY PEER-REVIEW
Rigorous, collaborative, and constructive peer-review

TRANSPARENT PEER-REVIEW
Editors and reviewers acknowledged by name on published articles

Frontiers
Avenue du Tribunal-Fédéral 34
1005 Lausanne | Switzerland

Visit us: www.frontiersin.org
Contact us: frontiersin.org/about/contact

REPRODUCIBILITY OF RESEARCH
Support open data and methods to enhance research reproducibility

DIGITAL PUBLISHING
Articles designed for optimal readership across devices

FOLLOW US
@frontiersin

IMPACT METRICS
Advanced article metrics track visibility across digital media

EXTENSIVE PROMOTION
Marketing and promotion of impactful research

LOOP RESEARCH NETWORK
Our network increases your article's readership